Universitat Politècnica de València

Instituto de Tecnología Química

Novel heterogeneous catalysts for the selective hydrogenation of CO_2 to CH_4

Doctoral Thesis presented as part of the requirements to obtain the academic degree of

PhD with International Mention

Written by:

Raul Bruno Machado da Silva

Directed by:

Antonio Chica Lara

Valencia, Spain, December 2024

Universitat Politècnica de València

Instituto de Tecnología Química

INSTITUTO DE TECNOLOGÍA QUÍMICA

EXCELENCIA SEVERO OCHOA
07/2013-06/2017
07/2017-06/2021
2023-2026

CSIC
CONSEJO SUPERIOR DE INVESTIGACIONES CIENTÍFICAS

UNIVERSITAT POLITÈCNICA DE VALÈNCIA

Novel heterogeneous catalysts for the selective hydrogenation of CO_2 to CH_4

External Evaluators:

Italo Odone Mazali, State University of Campinas, Brazil

Laetitia Oliviero, University of Caen, France

Evaluating committee:

President

Sibele B. Castellã Pergher, Federal University of Rio Grande do Norte, Brazil,

Secretary

Cristina Martínez Sánchez, Instituto de Tecnología Química, Spain

Spokesperson

Rubén López Fonseca, University of the Basque Country, Spain

Dr. **ANTONIO CHICA LARA**, Scientific Researcher at the Institute of Chemical Technology (UPV-CSIC).

CERTIFIES that the present doctoral thesis, titled “Novel heterogeneous catalysts for the selective hydrogenation of CO_2 to CH_4,” has been developed by **RAUL BRUNO MACHADO DA SILVA** under his supervision at the Institute of Chemical Technology.

Dr. Antonio Chica Lara

Dedicated to my parents, Isaac and Ana, who showed me through example that critical education is the most powerful tool for social transformation.

Dedicated to all those who made me see that questioning is the best way to transcend borders.

Knowing where you came from is no less
important than knowing where you are going.
Neil deGrasse Tyson

Acknowledgments

Life is truly like a box of chocolates, and each of my choices has brought me precisely to this moment as I begin writing the acknowledgments for my PhD thesis. In a way, it feels fittingly unconventional that the opening section of this work is also the last one written, prompting me to reflect on all those who helped bring me to this point in my academic journey.

My deepest thanks first go to Antonio Chica Lara, my thesis advisor. It feels like only yesterday I arrived in Valencia, unfamiliar with the language and culture of this new land. I am sincerely grateful for the scientific freedom he allowed me and for entrusting me with a doctoral project of such scope, funded by the InPhiNIT fellowship from the *LaCaixa Foundation**, the most prestigious of the Spanish PhD fellowships. I am proud of what we have achieved in realizing this ambitious project.

I also extend special thanks to the maintenance and characterization team at ITQ. There are too many to list exhaustively, and each of you was crucial to this thesis, and you know who you are. Thank you for your time, detailed scientific explanations, and incredible work required to keep a complex institute like ITQ in constant motion like a Swiss watch. This institution embodies true synergy, where the whole is indeed far greater than the sum of its parts. My PhD would not have been possible without the dedication each of you brings to your roles.

To my research group, thank you for sharing these past four years at ITQ. To Javi da Costa, thank you for your support from day one in helping me navigate administrative processes and provide technical help. To Begoña García, Lorena Olmos, Eva López, Pedro Jurado, Isabel Vidal, Daniel Herranz, and Juan Vidal, thank you for all the hours spent together in the lab, for the scientific discussions and for your kindness and patience in introducing me to Spanish culture. I am eager to continue collaborating with you on new and challenging projects.

Among my fellow doctoral candidates, I'd like to express my gratitude to Alessandra de Marcos, Beatriz Moreno, Adrián Plá, José Soriano, and Juan Ignacio Tirado. Despite your distinct personalities, your shared warmth brightened each day and made this journey more enjoyable. The camaraderie we found in discussing the challenges of our respective projects added much-needed lightness to our paths.

I am also grateful to my Italian friends, whom I had the privilege of meeting during this PhD. To Giulia Balestra, Anna Gagliardi, Micaela Pozzati, Rachele Braido, and Ludovica Conte, thank you for infusing our workspace with Italian energy and a Mediterranean spirit that complements that of Spain. Each of you is unique, yet you share an undeniable zest and wit that enriches life. I will always cherish my memories of my trip to Italy. *Grazie mille, ragazze.*

In such an international research environment, I was also fortunate to connect with people worldwide. The experience of working alongside or meeting individuals from diverse backgrounds has profoundly broadened my perspective. To Josephine Goethals, Lyzed Tolosa, Wilson Henao, Niloufar Atashi, Mark Wolf, Nelson Sinisterra, Juan David, Eric Norman, and Jason Giraldo, thank you for helping me see the world in full diversity.

I also thank the team at Professor Hensen's research group at Eindhoven University of Technology in the Netherlands for welcoming me into your laboratory. Your support enabled me to conduct my operando experiments. Professor Nikolay Kosinov, I am deeply grateful for your critical insights and detailed guidance in refining my work on operando studies. To Ariq Attalah, Victor Drozhzhin, Brahim Mezari, Tiny Verhoeven, and Tim Wissink, thank you for the warm welcome during my months in the Netherlands. I fondly remember my biking adventures through your tiny country.

To my friends from undergraduate and master's studies in Campinas, I am grateful that we have remained in contact after all these years. My time at UNICAMP shaped who I am today, and staying in touch with you preserves the precious memories of that chapter. Naíma Orra, Henrique Trevisan, João Marcos Suckow, Gustavo Graf, Lívia Soster, Arthur Gabriel, and so many others, I appreciate how you have scattered across the world, excelling in your fields. Though I am no longer in Campinas, I hold our shared moments dear, as you were instrumental in my academic and personal growth.

To my friends in Fortaleza, thank you so much for keeping in touch with me after all these years. Whether through our trips together or our inspiring conversations, every time I return to Fortaleza, the energy I needed to finish this doctoral thesis also came from you, even though we are far apart. You were there for me during the hard moments of this journey, so my sincerest thanks for maintaining the connection throughout the more than 15 years of friendship we have.

The journey of becoming a new self while preserving one's essence is a delicate art, like walking a tightrope. To my Brazilian friends I met here in Valencia, thank you for providing a sense of home and belonging while navigating this new country. To Rayanne Ferreira, Evandro Silva, Laís Borges, Alechania Misturini, Daniel Freire, Gustavo Andrade, and Carlos Weldo, I am grateful for our conversations on the experience of being racialized and Latin American in a historically white-dominated eurocentric academic environment. We still have much work to do to create a more diverse and inclusive scientific community. Thank you for helping me stay connected to my Brazilian roots when I needed it most. You brought a unique energy to these latitudes.

Spain is one of the five countries where I have had the privilege to live, thanks to the mobility of the academic life. I am immensely grateful for all it has offered me over the years. Besides adding Spanish citizenship to my Brazilian one, I feel honored to be part of a country that, at this pivotal moment, is embracing a more pluralistic identity and confronting its colonial past as it prepares for the challenges of the 21st century.

Valencia itself is almost a character in this story, welcoming me warmly as I pursued this ambitious enterprise. It confirmed to me that life, at its heart, is the art of meeting others despite inevitable partings. In a city where I was far from my blood family, friends have become my constellation of support, surrounding me with warmth and energy and helping me feel part of something greater.

To Beatriz Silva, I am deeply grateful for building a home with you, where we created a safe nest for friends from across the globe. You were the leading biographer of this story. To Bruno Laukmanis, my steadfast friend, who brought reason and calm when things felt stormy, you were the eye of the hurricane. To Alejandro Corona, you were the gravitational center of a diverse circle of friends, creating a safe haven for those far from home. I am lucky to be a part of this. To Álvaro Miralles, for being this curious conversationalist on all topics. I hope to climb many more mountains with you. Your personality of valuing the art of making questions over arriving at answers is inspiring. To Sofía Peña, you showed me how to be a better person through your hard work, patience, and placidness in our workplace.

To Ángel Cabrera, our meeting came about by serendipity, but it ended up having a deeply lasting effect on me. The linear combination of your kindness, critical spirit, and curiosity makes you a singular person, fascinating not only to me but to all those next to you. This thesis is partly yours because you were the impulse to push me forward during the most critical moment of this PhD journey. *Fue divertido contemplar el crecimiento imparable de lo que era solo un juego.* We will always have Benimaclet. Because you became one of my core memories.

Finally, I wish to dedicate this work to my family. Reaching the end of my academic journey with a doctoral degree honors all the years of effort you have devoted to me. To my parents, Isaac and Ana, and my brother, Lucas, for being the firm foundation of my life. Although I left home in Fortaleza at 17 to pursue my academic ambitions, I carry you like a talisman. This thesis is as much yours as it is mine.

In closing, I dedicate this thesis to my grandparents, whose memory is woven into every step of this journey. Recalling you now is an act of historical memory, a tribute to the resilience that shaped my path.

Amid hardship, scarcity, and the military dictatorship Brazil faced during the second half of the 20th century, you were political agents of defiance, choosing education as a beacon of hope for your children. For this very reason, I am here today. It is heartbreaking to know that none of you are here to see me become the first doctor in our family, even though I carry your spirit with me.

As love echoes across time and space, I let this message reach you: I made it.

Thank you for everything.

Your legacy will forever endure.

***The funding provided by the LaCaixa InPhiNIT Predoctoral Fellowship (ID 100010434), code LCF/BQ/DI19/11730019 for accomplishing this PhD project is acknowledged.**

Contents

Abstract

Climate change, along with its wide range of social impacts, represents one of the most significant challenges faced by humankind in the 21st century. To restrain its effects on the planet, it is imperative the development of novel technologies capable of using renewable energy sources while exploiting replacements for the traditional carbon sources aimed at the production and storage of fuels.

An option that merges both goals is the Power-to-Gas (P2G) technology, in which H_2, produced from renewable energy-driven electrolysis, is used to reduce CO_2 and convert it to CH_4. Depending on the purity level in which it is obtained, this fuel can be referred to as biomethane or synthetic natural gas (SNG) and can be distributed by the existing pipeline infrastructure to end-use sectors.

The selective hydrogenation reaction of CO_2 to CH_4 involved in this process, also known as the Sabatier reaction or CO_2 methanation, is regarded as the most competitive one for upscale SNG production using P2G technologies. However, one of the major hurdles in this area is the development of a cost-efficient technology and consequently, employing a catalyst that remains active and can remain operative under mild conditions for an extended duration is crucial to attaining a satisfactory reaction rate.

To develop catalysts for the selective hydrogenation of CO_2 to CH_4, Ni-based catalysts supported on three different families of materials were investigated for the first time. They were characterized using a range of ex-situ and in-situ techniques and tested under different conditions to evaluate their catalytic performance.

Chapter 4 is focused on catalysts supported on zeolitic materials, comparing ferrierite and its delaminated counterpart, ITQ-6, to evaluate the effect of the delamination and Si/Al ratio. ITQ-6-based catalysts exhibited a more dispersed Ni^0 phase, presenting Ni NPs with the optimum size (6-20 nm) for catalytic performance. This had a consequence on the ITQ-6-based catalysts exhibiting higher CO_2 conversion and TOF values attributed to the better dispersion of the Ni^0 phase, and to a higher concentration of surface -OH groups. Regarding the effect of the Si/Al ratio, Si/Al = 30 catalysts exhibited higher CO_2 conversion and TOF values than the pure Si/Al = ∞, which was attributed to the presence of Si-(OH)-Al groups, which increased their CO_2 uptake.

Chapter 5 is centered on oxide-based catalysts to evaluate the effect of the mixed oxide synergy on the CO_2 methanation reaction. $LaAlO_3$-based catalysts exhibited superior performance compared to the individual oxides, which was attributed to a higher concentration of moderate basic sites. Time-resolved operando IR results revealed that these sites are involved in the formation of monodentate carbonates, which are participating intermediates in the reduction of CO_2 to CH_4.

Chapter 6 is focused on catalysts prepared over the porous phyllosilicate sepiolite and the effect of Ce addition as a promoter. A catalyst with 10% wt. Ce exhibited the optimum CH_4 yield values at lower temperatures. This was attributed to the Ce effect to increase the dispersion of the Ni^0 phase to obtain NPs with the optimum size (~ 6 nm) for catalytic performance and improve the concentration of moderate basic sites.

Time-resolved operando IR measurements revealed that Ce-containing catalysts exhibited a mixed dissociative-associative mechanism, differently from the Ce-free one, which only exhibited the dissociative one. The Ce addition led to the formation of monodentate carbonate and formate, which were identified as participating intermediate species.

Chapter 7 is focused on applying catalytic technologies to the biogas upgrade using the selective hydrogenation of CO_2 to CH_4. The catalysts with optimum Ni loading from each chapter were submitted to studies with different WHSV and stability tests with a sweetened synthetic sample biogas sample.

Among all the catalysts tested, the one supported on sepiolite, with 15% wt Ni and 10 % wt. Ce, 15Ni-10Ce-Sep, exhibited the best performance, demonstrating good stability in conversion values throughout the experiment while minimizing coke formation. This was attributed to the effect of Ce to optimize the Ni0 dispersion, increase the concentration of moderate basic sites, and favor the elimination of coke via oxidation. Considering the CH_4 and CO_2 mixture, tests with 15Ni-10Ce-Sep catalysts upgraded a biogas mixture (60% CH_4:40% CO_2) to biomethane (94.1% CH_4/5.9% CO_2) with a CH_4 rate formation of 1211.0 mL CH_4 h^{-1}.

Resumen

El cambio climático, junto con su amplia gama de impactos sociales, representa uno de los desafíos más significativos que enfrenta la humanidad en el siglo XXI. Para mitigar sus efectos en el planeta, es imperativo explorar nuevas tecnologías capaces de utilizar fuentes de energía renovable, al tiempo que se aprovechan fuentes alternativas de carbono para la generación y almacenamiento de combustibles.

Una opción que combina ambas es la tecnología Power-to-Gas (P2G), en la que H_2, producido por electrólisis a partir de energía renovables, es utilizado para reducir el CO_2 y convertirlo en CH_4. Dependiendo del nivel de pureza con el que se obtenga, este combustible puede denominarse biometano o gas natural sintético (GNS), y puede ser distribuido por el sistema de gasoductos existentes a diferentes sectores.

La reacción de hidrogenación selectiva de CO_2 a CH_4 involucrada en este proceso, también conocida como reacción de Sabatier o metanación de CO_2, se considera la más eficiente y competitiva para la producción a gran escala de GNS en aplicaciones P2G. Sin embargo, desarrollar una tecnología de metanación de CO_2 rentable es uno de los mayores desafíos, y por eso, el uso de un catalizador que sea activo y capaz de operar bajo condiciones de operación moderadas durante un largo período de tiempo es clave para lograr una velocidad de reacción adecuada.

Para desarrollar catalizadores de hidrogenación selectiva de CO_2 a CH_4, se ha investigado por primera catalizadores de Ni soportados en tres familias diferentes de materiales. Dichos catalizadores han sido caracterizados utilizando técnicas ex situ e in situ y probados bajo diferentes condiciones para evaluar su comportamiento catalítico.

El **Capítulo 4** se centra en catalizadores soportados en materiales zeolíticos, comparando la zeolita ferrierita y su forma deslaminada correspondiente, ITQ-6, para evaluar el efecto de la deslaminación y la relación Si/Al. Los catalizadores basados en ITQ-6 presentaron una fase Ni^0 más dispersa, con un tamaño óptimo de las nanopartículas de Ni entre 6 y 20 nm. Como consecuencia, los catalizadores de la ITQ-6 exhibieron mayores valores de conversión de CO_2 y TOFs, atribuibles no solo a la mejor dispersión de la fase Ni^o, sino también a una mayor concentración de grupos -OH superficiales. Con respecto al efecto de la relación Si/Al, los catalizadores con Si/Al = 30 exhibieron los mayores valores de conversión de CO_2 y TOF, lo cual se atribuyó a la presencia de grupos Si-(OH)-Al, que incrementaron su capacidad de captura de CO_2.

El **Capítulo 5** se centra en catalizadores basados en óxidos de La y Al. Se evalúa el efecto sinérgico de dichos óxidos. Los catalizadores basados en $LaAlO_3$ exhibieron un rendimiento superior en comparación con los óxidos individuales, lo cual se atribuyó a una mayor concentración de centros básicos de fortaleza moderada. Los resultados de IR operando resueltos

en el tiempo revelaron que estos centros están involucrados en la formación de carbonatos monodentados, que son intermediarios activos en la reducción de CO_2 a CH_4.

El **Capítulo 6** presenta el estudio de catalizadores preparados sobre el filosilicato poroso sepiolita y el efecto promotor del Ce en la reacción de metanación. Un catalizador con 10% de Ce en peso exhibió los valores óptimos de rendimiento de CH_4 a bajas temperaturas. Este resultado se atribuyó al efecto del Ce sobre el aumento de la dispersión de la fase Ni^0 para obtener nanopartículas con un tamaño medio de 6 nm, tamaño óptimo para alcanzar un buen comportamiento catalítico, así como de favorecer un incremento en la concentración de centros básicos de fortaleza moderada.

Los estudios de IR operando resueltos en el tiempo revelaron que los catalizadores que contienen Ce presentaban un mecanismo mixto disociativo-asociativo, diferente del catalizador sin Ce, que solo mostró el mecanismo disociativo. La adición de Ce condujo a la formación de especies intermedias participantes, como carbonatos monodentados y formiatos que explican estás diferencias mecanísticas.

En el **Capítulo 7,** las mejores formulaciones catalíticas desarrolladas en cada familia de catalizadores, se estudiaron en la metanación de biogás simulado, es decir, se llevó a cabo la hidrogenación selectiva de CO_2 en presencia del CH_4 presente en el propio biogás. Los catalizadores con el contenido óptimo de Ni de cada familia se estudiaron a diferentes WHSV y se realizaron pruebas de estabilidad.

Entre todos los catalizadores probados, el soportado en sepiolita, con 15% en peso de Ni y 10% en peso de Ce (15Ni-10Ce-Sep), presentó los mejores resultados, demostrando buena estabilidad y minimizando la formación de coque. Este resultado se atribuyó al efecto del Ce no solo para optimizar la dispersión de Ni^0, sino también para aumentar la concentración de centros básicos de fortaleza moderada y favorecer la eliminación del coque por oxidación. Considerando el biogás simulado (mezcla de CH_4 y CO_2), las pruebas con el catalizador 15Ni-10Ce-Sep permitieron obtener una corriente de biometano (94.1% CH_4/5.9% CO_2), con una tasa de formación de CH_4 de 1211,0 mL CH_4 h^{-1}.

Resum

El canvi climàtic, juntament amb la seua àmplia gamma d'impactes socials, representa un dels desafiaments més significatius que enfronta la humanitat en el segle XXI. Per a mitigar els seus efectes en el planeta, és imperatiu explorar noves tecnologies capaces d'utilitzar fonts d'energia renovable, al mateix temps que s'aprofiten fonts alternatives de carboni per a la generació i emmagatzematge de combustibles.

Una opció que combina ambdues és la tecnologia Power-to-Gas (P2G), en la qual H_2, produït per electròlisi a partir d'energia renovables, és utilitzat per a reduir el CO_2 i convertir-lo en CH_4. Depenent del nivell de puresa amb el qual s'obtinga, este combustible pot denominar-se biometà o gas natural sintètic (SNG), i pot ser distribuït pel sistema de gasoductes existents a diferents sectors.

La reacció d'hidrogenació selectiva de CO_2 a CH_4 involucrada en este procés, també coneguda com a reacció de Sabatier o metanación de CO_2, es considera la més eficient i competitiva per a la producció a gran escala de SNG en aplicacions P2G. No obstant això, desenrotllar una tecnologia de metanación de CO_2 rendible és un dels majors desafiaments, i per això, l'ús d'un catalitzador que siga actiu i capaç d'operar sota condicions moderades durant un llarg període de temps és clau per a aconseguir una velocitat de reacció adequada.

Per a desenrotllar catalitzadors per a la hidrogenació selectiva de CO_2 a CH_4, es van investigar per primera vegada en la literatura catalitzadors de Ni suportats en tres famílies diferents de materials. Van ser caracteritzats utilitzant tècniques ex-situ i in-situ provats sota diferents condicions per a avaluar el seu rendiment catalític.

El **Capítol 4** aborda en els catalitzadors suportats en materials zeolíticos, comparant ferrierita i la seua contrapart deslaminada, ITQ-6, per a avaluar l'efecte de la deslaminación i la relació Si/Al. Els catalitzadors de la ITQ-6 van exhibir una fase Ni^0 més dispersa, presentant nanopartícules de Ni amb la grandària òptima (6-20 nm) per al rendiment catalític. Com a conseqüència, els catalitzadors de la ITQ-6 exhibiren majors valors de conversió de CO_2 i TOF, atribuïbles no sols a la millor dispersió de la fase Ni^0, sinó també a una major concentració de grups -OH superficials. Respecte a l'efecte de la relació Si/Al, els catalitzadors amb $Si/Al = 30$ van exhibir majors valors de conversió de CO_2 i TOF que els de $Si/Al = \infty$, la qual cosa es va atribuir a la presència de grups Si-(OH)-Al, que van incrementar la seua capacitat de captura de CO_2.

El **Capítol 5** aborda en els catalitzadors basats en òxids per a avaluar l'efecte de la sinergia d'òxids mixtos en la reacció de metanación de CO_2. Els catalitzadors basats en $LaAlO_3$ van exhibir un rendiment superior en comparació amb els òxids individuals, la qual cosa es va atribuir a una major concentració de llocs bàsics de fortalesa moderada. Els resultats d'espectroscòpia IR

operando resolts en el temps van revelar que estos llocs estan involucrats en la formació de carbonats *monodentados, que són intermediaris actius en la reducció de CO_2 a CH_4.

El **Capítol 6** aborda en catalitzadors preparats sobre el filosilicato porós sepiolita i l'efecte de l'addició de Ce com a promotor. Un catalitzador amb 10% de Ce en pes va exhibir els valors òptims de rendiment de CH_4 a temperatures més baixes. Això es va atribuir a este efecte del Ce d'augmentar la dispersió de la fase Ni^0 per a obtindre nanopartícules amb la grandària òptima (~6 nm) per al rendiment catalític, així com d'augmentar la concentració de llocs bàsics de fortalesa moderada.

Els estudis d'espectroscòpia IR operando resolts en el temps van revelar que els catalitzadors que contenen Ce van exhibir un mecanisme mixt dissociatiu-associatiu, diferent del catalitzador sense Ce, que només va mostrar el mecanisme dissociatiu. L'addició de Ce va conduir a la formació d'espècies intermèdies participants, com a carbonats monodentados i formiatos.

El **Capítol 7** aborda en l'aplicació de tecnologies catalítiques per a la valorització del biogàs mitjançant la hidrogenació selectiva de CO_2 a CH_4. Els catalitzadors amb el contingut òptim de Ni de cada capítol van ser estudiats amb diferents WHSV i proves d'estabilitat amb una mostra de biogàs sintètic purificat.

Entre tots els catalitzadors provats, el suportat en sepiolita, amb 15% en pes de Ni i 10% en pes de Ce (15Ni-10Ce-Sep), va exhibir el millor rendiment, demostrant bona estabilitat en els valors de conversió i minimitzant la formació de coc. Això es va atribuir a este efecte del Ce no sols per a optimitzar la dispersió de Ni^0, sinó també per a augmentar la concentració de llocs bàsics de fortalesa moderada i afavorir l'eliminació del coc per oxidació. Considerant la mescla de CH_4 i CO_2, les proves amb el catalitzador 15Ni-10Ce-Sep van millorar una mescla de biogàs (60% CH_4: 40% CO_2) a biometà (94.1% CH_4/5.9% CO_2), amb una taxa de formació de CH_4 de 1211,0 ml CH_4 h^{-1}.

Resumo

As alterações climáticas, juntamente com sua ampla gama de impactos sociais, representam um dos desafios mais significativos enfrentados pela humanidade no século XXI. Para conter seus efeitos no planeta, é imperativo explorar novas tecnologias capazes de utilizar fontes de energia renováveis, ao mesmo tempo em que se exploram fontes alternativas de carbono para a geração e armazenamento de combustíveis.

Uma opção que combina ambos é a tecnologia Power-to-Gas (P2G), na qual H_2, produzido a partir da eletrólise impulsionada por energia renovável, é utilizado para reduzir o CO_2 e convertê-lo em CH_4. Dependendo do nível de pureza em que é obtido, esse combustível pode ser denominado biometano ou gás natural sintético (GNS) e pode ser distribuído pela infraestrutura de gasodutos existente para diferentes setores.

A reação de hidrogenação seletiva de CO_2 a CH_4 envolvida neste processo, também conhecida como reação de Sabatier ou metanação de CO_2, é considerada a mais eficiente e competitiva para a produção em larga escala de GNS em aplicações P2G. No entanto, desenvolver uma tecnologia de metanação de CO_2 economicamente viável é um dos maiores desafios, e, por essa razão, o uso de um catalisador que seja ativo e capaz de operar sob condições moderadas por um longo período de tempo é fundamental para alcançar uma taxa de reação adequada.

Para desenvolver catalisadores para a hidrogenação seletiva de CO_2 para CH_4, catalisadores de Ni suportados em três diferentes famílias de materiais foram estudados. Eles foram caracterizados usando técnicas ex-situ e in-situ e testados sob diferentes condições para avaliar seu desempenho catalítico.

O **Capítulo 4** foca em catalisadores suportados em materiais zeolíticos, comparando ferrierita e sua versão delaminada, ITQ-6, para avaliar o efeito da delaminação e da razão Si/Al. Os catalisadores baseados em ITQ-6 exibiram uma fase de Ni^0 mais dispersa, apresentando nanopartículas de Ni com o tamanho ideal (6-20 nm) para o desempenho catalítico. Isso resultou nos catalisadores baseados em ITQ-6 exibindo maiores valores de conversão de CO_2 e TOF, o que se atribuiu não só à melhor dispersão da fase de Ni^0, mas também a uma maior concentração de grupos -OH superficiais. Quanto ao efeito da razão Si/Al, catalisadores com Si/Al = 30 exibiram maiores valores de conversão de CO_2 e TOF do que aqueles com Si/Al = ∞, o que foi atribuído à presença de grupos Si-(OH)-Al, que aumentaram a captura de CO_2.

O **Capítulo 5** centra em catalisadores à base de óxidos para avaliar o efeito da sinergia de óxidos mistos na reação de metanação de CO_2. Os catalisadores à base de $LaAlO_3$ exibiram desempenho superior em comparação com os óxidos individuais, devido a uma maior concentração de centros básicos moderados. Resultados de espectroscopia operando IR com resolução temporal revelaram que esses centros estão envolvidos na formação de carbonatos monodentados, que são centros ativos na redução do CO_2 a CH_4.

O **Capítulo 6** foca em catalisadores preparados sobre o filossilicato poroso sepiolita e o efeito da adição de Ce como promotor. Um catalisador com 10% em peso de Ce exibiu valores ótimos de rendimento a CH_4 a temperaturas mais baixas. Isso se atribuiu ao efeito do Ce em aumentar a dispersão da fase de Ni^0 para obter nanopartículas com o tamanho ideal (~ 6 nm) para o desempenho catalítico e aumentar a concentração de centros básicos moderados.

Resultados de espectroscopia operando IR com resolução temporal revelaram que catalisadores com Ce exibiram um mecanismo misto dissociativo-associativo, diferentemente daqueles sem Ce, que exibiram apenas o mecanismo dissociativo. A adição de Ce levou à formação de carbonato monodentado e formiato, que foram identificados como espécies intermediárias participantes.

O **Capítulo 7** foca na aplicação de tecnologias catalíticas para o aprimoramento do biogás usando a hidrogenação seletiva de CO_2 para CH_4. Os catalisadores com teores ótimos de Ni de cada capítulo foram submetidos a estudos com diferentes WHSV e testes de estabilidade com uma amostra de biogás sintético purificado.

Entre todos os catalisadores testados, aquele suportado em sepiolita, com 15% em peso de Ni e 10% em peso de Ce, 15Ni-10Ce-Sep, exibiu o melhor desempenho, demonstrando boa estabilidade nos valores de conversão ao longo do experimento enquanto minimizava a formação de coque. Isso foi atribuído ao efeito do Ce não apenas para otimizar a dispersão da fase de Ni^0, mas também para aumentar a concentração de centros básicos moderados e favorecer a eliminação do coque por oxidação. Considerando a mistura de CH_4 e CO_2, testes com o catalisador 15Ni-10Ce-Sep aprimoraram uma mistura de biogás (60% CH_4: 40% CO_2) para biometano (94,1% CH_4/5,9% CO_2), com uma taxa de formação de CH_4 de 1211,0 mL CH_4 h^{-1}.

List of Abbreviations

BET	Brunauer-Emmett-Teller
CCS	Carbon Capture and Storage
CCU	Carbon Capture and Utilization
CCUS	Carbon Capture, Utilization, and Storage
CNG	Compressed Natural Gas
DFT	Density Functional Theory
DRIFTS	Diffuse Reflectance Infrared Fourier Transform Spectroscopy
DTA	Differential Thermal Analysis
E_a	Activation Energy
EDS	Energy Dispersive Spectroscopy
EU	European Union
FCC	Face-Centered Cubic
FESEM	Field Emission Scanning Electron Microscopy
FER	Ferrierite
FID	Flame Ionization Detector
FT-IR	Fourier Transform Infrared Spectroscopy
FWHM	Full Width at Half Maximum
GHG	Greenhouse Gases
GHSV	Gas Hourly Space Velocity
$GtCO_2eq$	Gigatonnes of Carbon Dioxide Equivalent
HAADF	High-angle annular Dark Field
ICP-OES	Inductively Coupled Plasma Optical Emission Spectroscopy
IEA	International Energy Agency
IPCC	Intergovernmental Panel on Climate Change
IUPAC	International Union of Pure and Applied Chemistry
IWI	Incipient Wetness Impregnation
JCPDS	Joint Committee on Powder Diffraction Standards
MOF	Metal-Organic Framework
MS	Mass Spectrometry
MW	Molecular Weight
NP	Nanoparticle
PREFER	Precursor of Ferrierite
PROX	Preferential Oxidation
RNG	Renewable Natural Gas

RWGS	Reverse Water-Gas Shift
SEM	Scanning Electron Microscopy
Sep	Sepiolite
S_{ext}	External Surface Area
SMSI	Strong Metal-Support Interaction
S_{BET}	BET Surface Area
STEM	Scanning Transmission Electron Microscopy
TCD	Thermal Conductivity Detector
TEM	Transmission Electron Microscopy
TG	Thermogravimetric Analysis
TOF	Turnover Frequency
TPD	Temperature-Programmed Desorption
TPR	Temperature-Programmed Reduction
WBA	World Biogas Association
WHSV	Weight Hourly Space Velocity
XRD	X-ray Diffraction
X_{CO_2}	CO_2 Conversion
S_{CH_4}	CH_4 Selectivity
Y_{CH_4}	CH_4 Yield

Chapter 1

Introduction

“Every new beginning comes from some other beginning’s end.”
Seneca

Painting: Wanderer above the Sea of Fog, 1818, Caspar David Friedrich.
Public Domain Image.

1.1 – Climate change and the IPCC reports

Climate change and the vast array of social consequences derived from it are some of the main problems faced by humankind in the XXI century [1].

In 2022, the Intergovernmental Panel on Climate Change (IPCC), an institution of the United Nations responsible for assessing scientific data regarding climate change, published the third part of its sixth assessment report, the AR6 [2]. The report sheds some light that climate change is already causing widespread disruption in every region in the world, as confirmed by the increasing number of withering droughts, extreme heat episodes, and record floods, which threaten world food security for millions of people, most of them inhabitants of the Global South.

Furthermore, the report corroborates once again that human activities related to the emissions of greenhouse gases (GHGs) emissions are climate change's primary cause and that urgent and substantial action is needed to limit further warming and mitigate the impacts of climate change, such as decarbonizing industrial processes and reducing the CO_2 levels in the atmosphere.

The greenhouse effect is a natural phenomenon on Earth that takes place when certain gases in the Earth's atmosphere, the previously mentioned GHGs, trap heat from the sun and prevent it from escaping into space by transforming radiation into vibrational energy [3]. This phenomenon is entirely natural and has been taking place for billions of years, providing regulation on Earth's temperature and keeping it within a range that is habitable for humans and other forms of life. The average temperature of the Earth's surface would be much lower without it, at roughly -18 °C as opposed to the current average of approximately 15 °C [3].

As confirmed by the IPCC report, since the beginning of the Industrial Revolution, which began in the mid-18th century, the GHGs atmospheric concentration significantly increased, enhancing the greenhouse effect with a consequent increase in the average temperature on Earth.

Compared to the beginning of the Industrial Revolution, the concentration of GHGs significantly escalated, with CO_2 concentration increasing from about 280 ppm to over 410 ppm in 2019, the highest level in at least 2 million years (**Figure 1.1**) [2]. The concentration of CH_4 has also increased from pre-industrial levels of about 700 ppb to almost 1,900 ppb in 2019, and the concentration of N_2O, from about 270 ppb to over 330 ppb.

Measurements of land and ocean temperatures in a similar period after the Industrial Revolution reveal that ocean surfaces and land temperatures increased by 0.7 °C and 1.6 °C, respectively, following the trend in GHGs concentration augmentation over the same period (**Figure 1.2**).

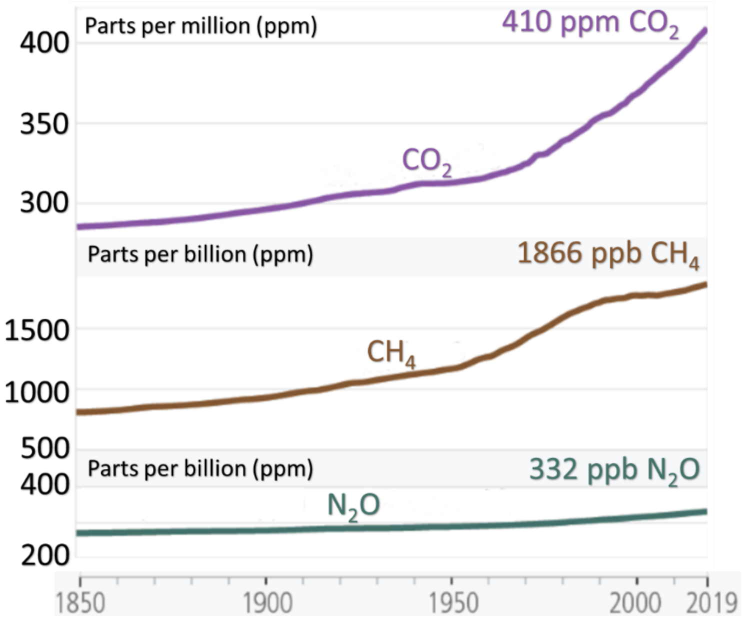

Figure 1.1. Evolution of some of three of the GHGs (CO_2, CH_4, and N_2O) in the period between 1850 and 2019. Data obtained from the IPCC AR6 data report [2].

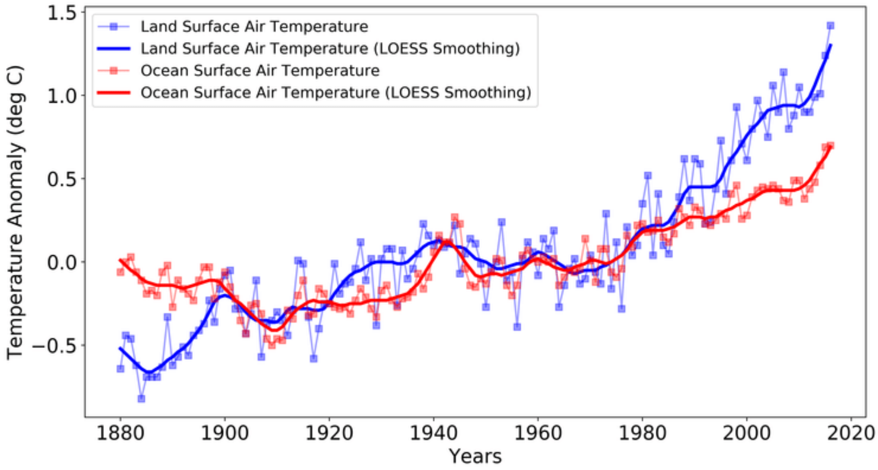

Figure 1.2. Surface temperature anomaly when compared to pre-industrial levels for ocean and land surface for the period comprised between 1880 and 2019. Data compiled by NASA and published by Lenssen et al. [4].

The most recent IPCC report states that there is no question that human-caused greenhouse gas emissions are the primary driver of climate change and are at an all-time high. An estimated 2040 ± 310 gigatons of CO_2 equivalent (GtCO2eq) have been released into the atmosphere due to human activities like burning fossil fuels, deforestation, and intensive agriculture since the mid-18th century when the Industrial Revolution began.

In the early part of the 20th century, the use of fossil fuels was still relatively low, and CO_2 emissions were kept at low levels. However, with the growth of industrialization, population, and economic activity, the consumption of fossil fuels grew rapidly, leading to a sharp increase in CO_2 emissions.

In fact, around 66% of the cumulative emitted CO_2 previously mentioned has occurred since the end of World War II (1939 – 1945), primarily attributed to the global economy's rapid post-war expansion [5]. This is attributed to significant technological advancements, increased manufacturing, and a population boom, which led to a surge in energy consumption.

Between 1970 and 2010, global GHG emissions have risen more than 80%, and about 70% of the CO_2 emissions in 2010 were derived from burning fossil fuels. Besides CO_2, other GHGs, such as CH_4, N_2O, SF_6, and halogenated compounds also experienced a significant increase in their emissions (**Figure 1.3**).

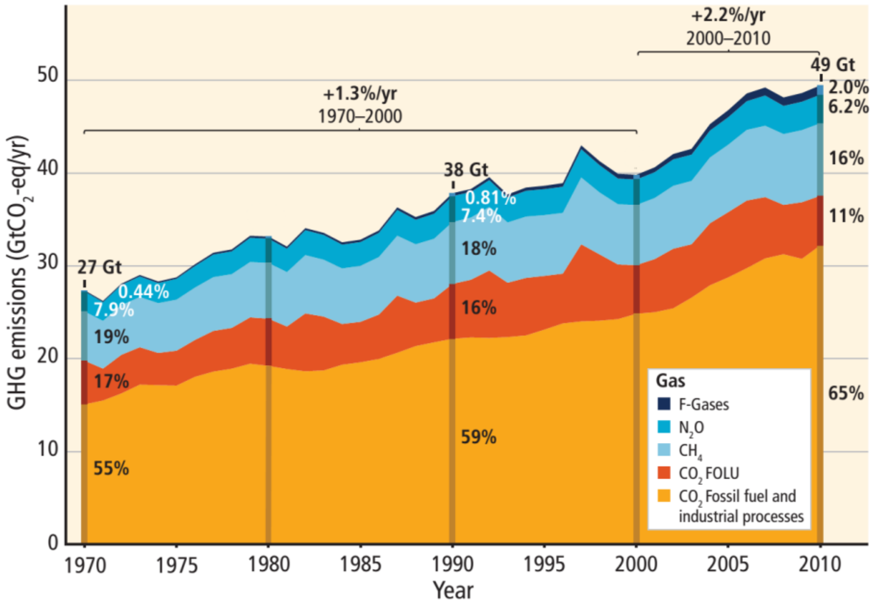

Figure 1.3. Annual emissions of GHGs evolution between 1970 and 2010: F-gases (fluorinated gases), N_2O, CH_4, FOLU-CO_2 (CO_2 emitted from forestry and other land uses), and CO_2 emitted from fossil fuels combustion and industrial processes.

The primary sources of these GHG emissions are subdivided into four categories (**Figure 1.4**).

Energy: The primary cause of greenhouse gas emissions comes from the combustion of fossil fuels, such as coal, oil, and natural gas, which is done to produce electricity and fuel for transportation.

Forestry and other land use (FOLU): Deforestation and other changes in land use, including agriculture, also greatly increase greenhouse gas emissions. Major contributors include N_2O emissions from fertilizers and soil management techniques, livestock, and rice fields, as well as CH_4 emissions from these sources.

Industrial Processes: Industrial processes such as chemical manufacturing, cement production, and iron and steel production also produce GHG emissions.

Waste sources: Organic waste in landfills and wastewater decomposes anaerobically, producing CH_4. Manure from livestock and other agricultural waste can produce CH_4 and N_2O during decomposition, also being a significant source of GHGs emissions.

Since 1970, there has been a drastic increase in all four categories. A general trend indicates that CO_2 emissions from forestry and other land uses, as well as those from industrial processes and the burning of fossil fuels, account for the most significant portion of GHG emissions overall.

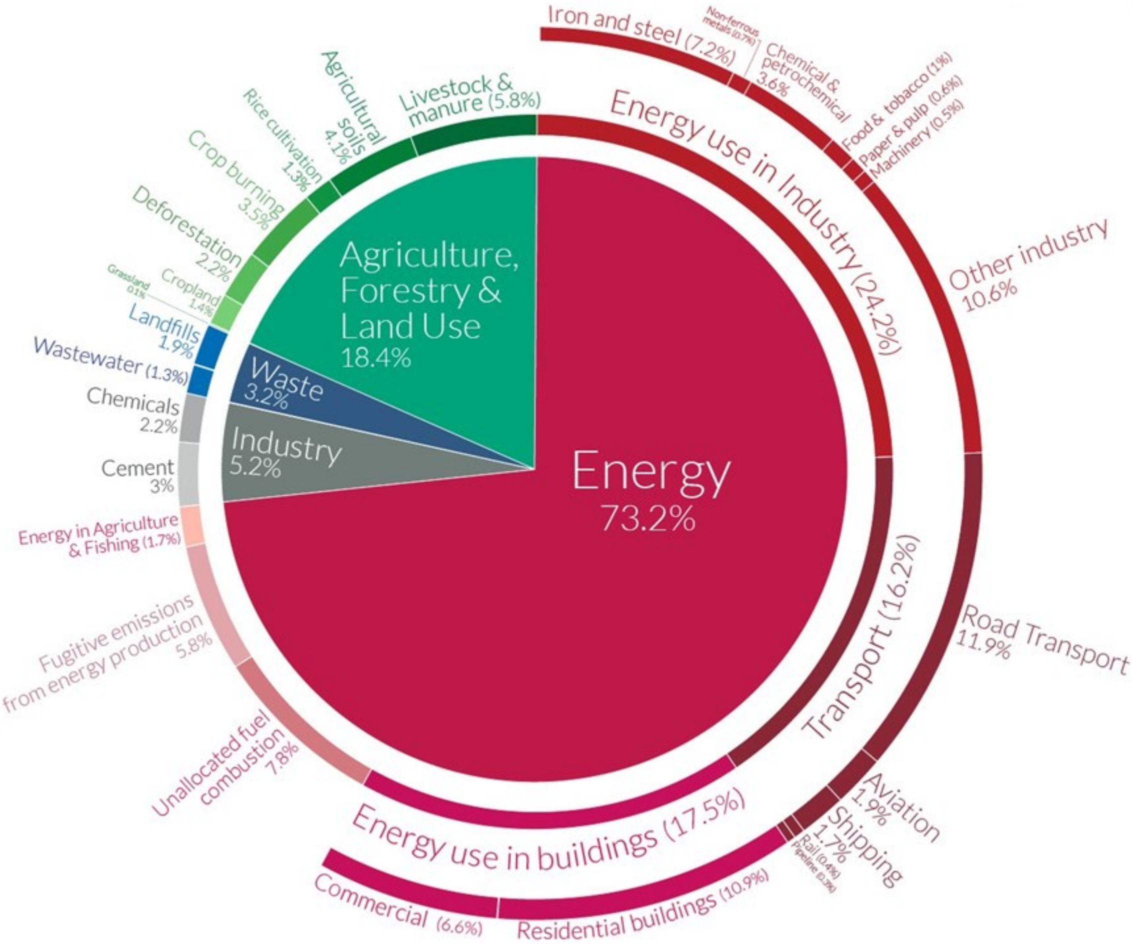

Figure 1.4. Global greenhouse gas emissions by sector in 2016 subdivided in four primary categories (Energy, Agriculture, Forest and Land Use, Industry, and Waste) and subcategories. Image published using the data published by Thomas et al. [6].

1.2 – CO_2 historical emissions and climate justice

As previously discussed in the last section, although there are various types of GHGs, CO_2 is considered the primary greenhouse gas, constituting almost 80% of the total GHGs emissions, as depicted in **Figure 1.3**.

Beyond this, CO_2 has a relatively long atmospheric lifetime, remaining in the atmosphere for a significantly longer period than the other GHGs. It also actively participates in the carbon cycle, making it possible to assess its atmospheric evolution with methods that are less sophisticated than those used for the other GHGs. Thus, discussions about GHGs emissions often focus on CO_2 emissions, even though all of them contribute partially to the harmful effects of global warming.

As discussed in the preceding section, in spite of the fact that climate change will inflict damage at a global level, there are variations not only in the share of responsibility among regions for the occurrence thereof but also in the countries where the effects of climate change will manifest.

Climate change affects different countries, regions, and communities in diverse ways, depending on their geographical location, vulnerability, and adaptive capacity. Data results published by Friedlingstein et al. reveal that the Global North is accountable for 57% of the total CO_2 emissions (870 billion tonnes of CO_2 out of the overall 1529 billion tonnes) [7], even though its current population constitutes only 16% of the total global population current as of 2024 (**Figure 1.5**). This underscores the historical inequality in which countries have disparately contributed to climate change.

Beyond the overall emission analysis, another dimension to consider is the current per capita emissions, which highlight the individual contribution to emissions in different regions, as developed countries have higher per capita emissions than developing nations, as seen in **Figure 1.6**.

Inequality is laid bare in light of the findings presented in the AR6 report published by the Intergovernmental Panel on Climate Change, wherein it becomes evident that climate change will impact countries in a markedly heterogeneous manner, with nations in the Global South bearing a disproportionately greater burden from rising temperatures.

In 2022, for the first time in the historical series of publications regarding climate change, the AR6 report is the first one to finally conclude that geographical differences in vulnerability to climate change result from historical patterns of inequality, such as colonialism and imperialism.

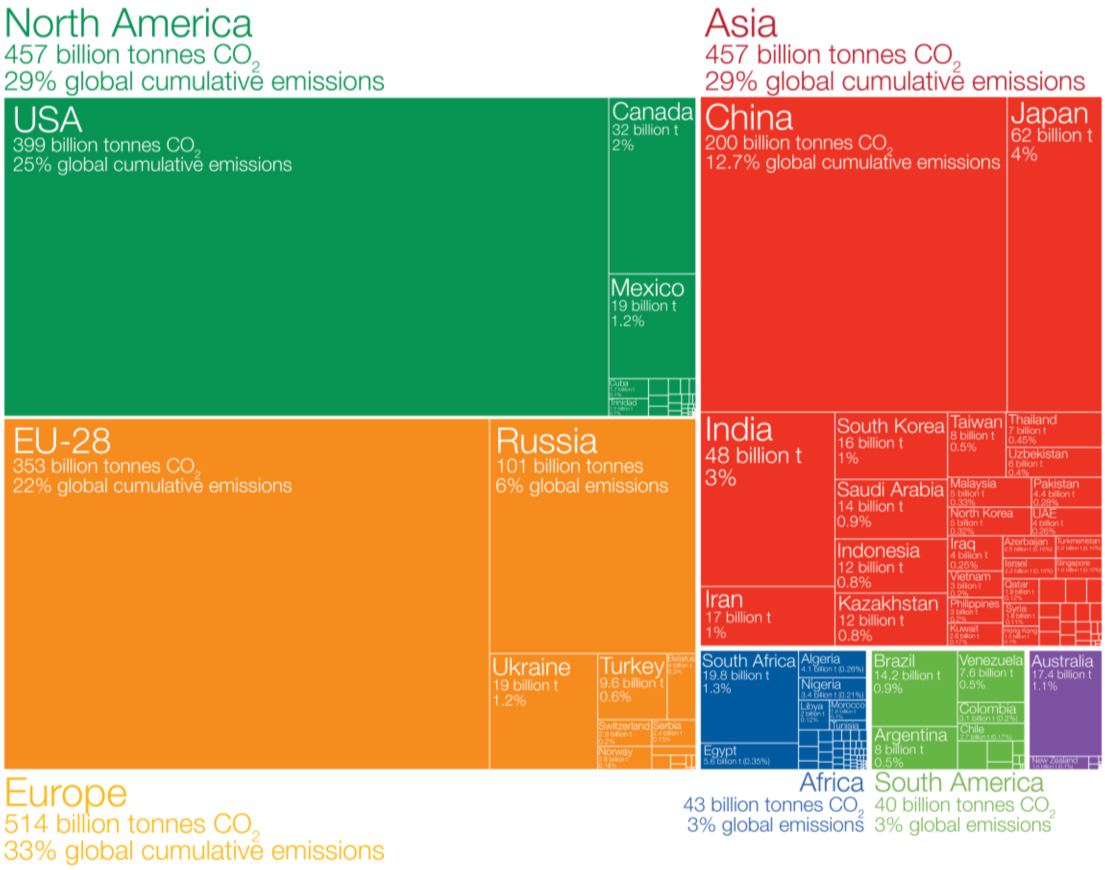

Figure 1.5. Total carbon dioxide emissions from 1751 to 2017, as of 2017. Figures are based on production-based emissions, which include the burning of fossil fuels and industrial processes. The UK was still regarded as a member of the European Union, and emissions from foreign travel are not included. Data extracted and adapted from Friedlingstein et al. [7].

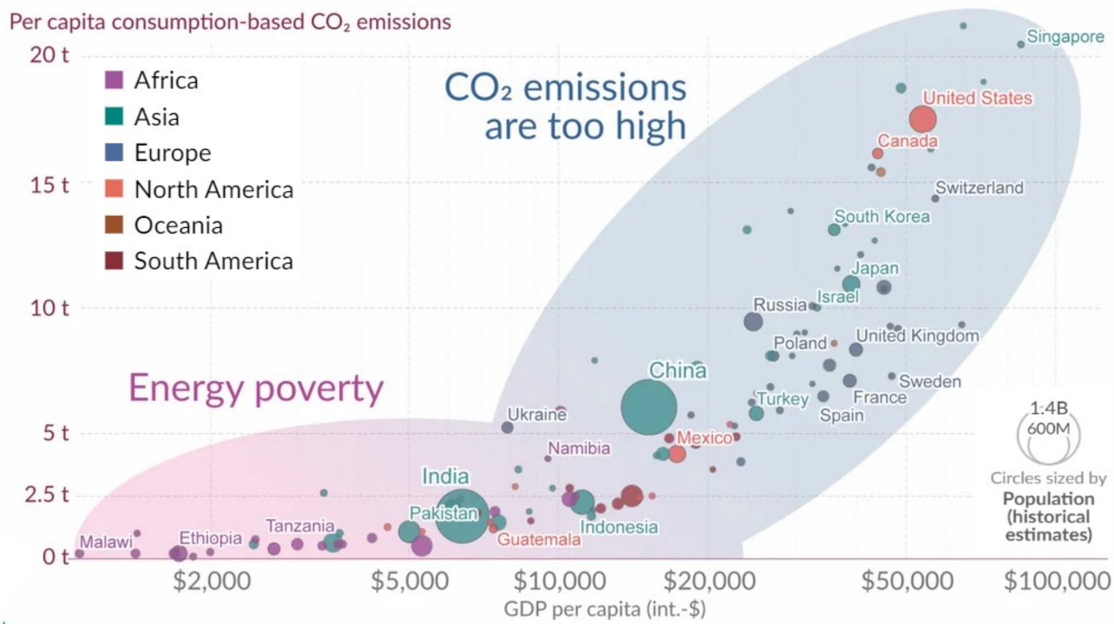

Figure 1.6. Dependance of per capita consumption-based CO_2 emissions on the Gross Domestic Product (GDP) per capita, for different countries in 2017. Data adapted from Ritchie et al. [9].

Building upon the findings of this report, Deivanayagam et al. discuss that climate change is a consequence of the very evolution of the capitalist system, which relied on colonialism, resource appropriation, and primitive accumulation of capital based on exploited labor [8]. Initially, this exploitation occurred within a slave-based system, later transitioning into a structurally precarious wage labor system.

Continuing their historical analysis, they also assert that this inequality has racist origins, as European countries developed pseudoscientific theories to justify the violent invasion and plunder of Global South countries, whose social consequences are still felt today.[10] This led to a continued resource transfer from the Global South to the Global North, enabling early industrialization, initially in Europe and subsequently in North America, which would directly impact the higher GHGs emissions from these countries.

This exploitative dynamic has shaped the current global landscape, where regions aligned with the former exploitation centers exhibit wealth and capital accumulation, characterized by high energy consumption and cumulative GHGs emissions. In parallel, regions that were exploited show significantly lower income and capital accumulation, lower GHGs emissions, and yet, higher vulnerability to the climate change consequences.

Within this dynamic, where there is prior inequality among countries responsible for greenhouse gas emissions, a report published by Burke et al. has revealed that the effects of global warming will further accentuate regional disparities [11].

In a macroeconomic assessment aimed at evaluating the impact of the rise in global temperatures on the gross domestic product (GDP) per capita of different countries by 2100, they concluded that countries in the Global North will be much less adversely affected by the effects than those in the Global South. While developed countries may experience GDP reductions ranging from -49% to 0%, or even increases in their GDP, the majority of developing countries are projected to suffer much more significant GDP losses, falling between -100% and -50% [11] (**Figure 1.7**).

Beyond the economic effect of climate change, a thorough report carried out by World Health Organization and published by Deivanayagam et al. reveals that, between 2030 and 2050, climatic anomalies will result in around 250,000 extra fatalities annually [8] (**Figure 1.8**). This ominous prediction is attributable solely to factors such as malnutrition, malaria, diarrhea, and heat-related stress, and 90 % of these deaths will take place in developing countries, where a robust public health system is absent.

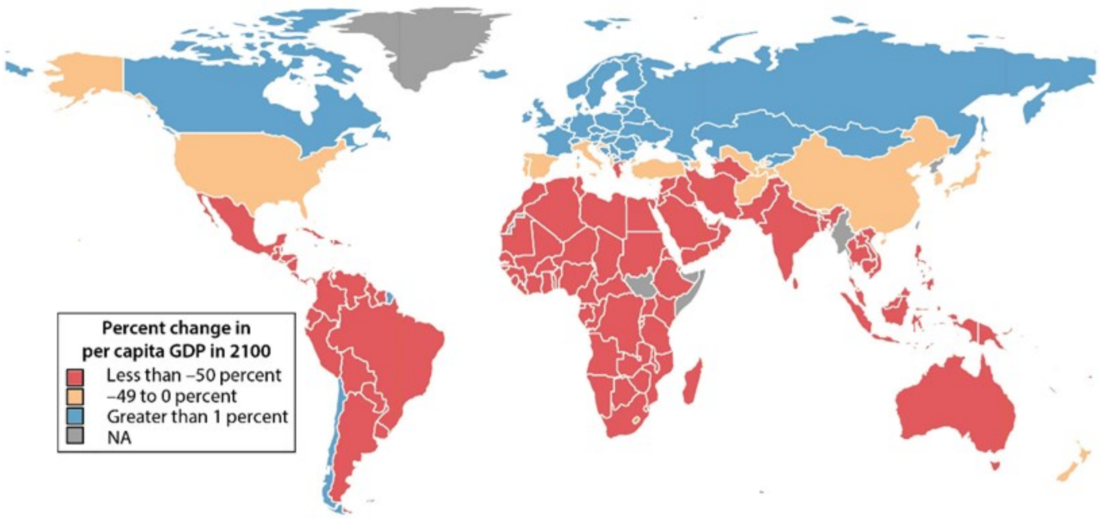

Figure 1.7. Projected impact of global temperature changes on per capita GDP values in different countries for the year 2100. Data adapted from Burke et al. [11].

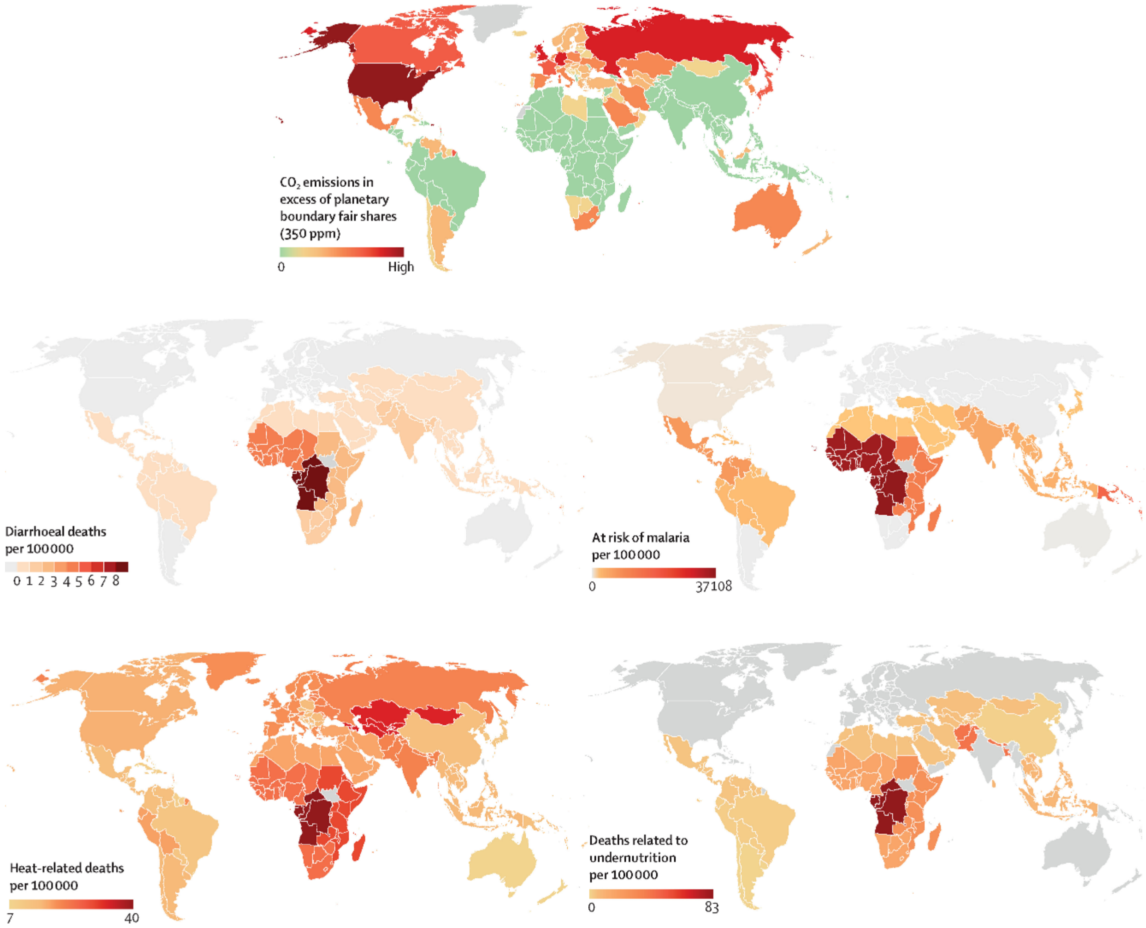

Figure 1.8. Depiction of geographic unequal share of responsibility for climatic alteration and projected inequality of health concerns among countries of Global North and South. CO_2 emissions are cumulatively considered for the 1850-2015 period. Countries depicted with the light grey color present a mortality rate of less than 0.01. Image adapted from Deivanayagam et al. [8].

Extending past the previously mentioned inequality in the emission of CO_2 already present in the atmosphere, leading to inflicted climate changes, there is also a disparity in the extent to which countries can implement measures to reduce CO_2 emissions to meet the limits set by international organizations to mitigate the effects of climate change.

Countries in the Global North exhibit more complex and robust economic frameworks, affording them greater ease in implementing measures to reduce per capita CO_2 emissions. In contrast, Global South countries have less diversified economic matrices lagged down in various stages of industrialization, making them reliant on less clean energy sources with higher contamination potential.

This becomes evident by the results published by Hubacek et al. that show several Global North countries managed to increase their GDP per capita while simultaneously reducing CO_2 emissions in the 2010-2020 timespan [12]. This achievement is attributed to the diversification of their energy matrices, electrification of certain industrial sectors, and the migration of high CO_2-emitting industrial sectors to Asian countries such as China and India.

Furthermore, as previously observed in the data published by Burke et al. [11], some countries in the Global North will experience an increase in their GDP per capita values due to the effects of rising global temperatures. This derives from the fact that some countries in the Global North, such as Sweden, Canada, or Finland, will benefit from the increase in global temperatures and the consequent melting of permafrost in their soils. This combined effect will have a positive impact on the agricultural sector in these regions, as it will increase the yield of crop production and even enable the cultivation of plant species that currently do not adapt well to such high latitudes [13].

Meanwhile, Global South countries struggle to decouple the growth of their GDP from the increase in CO_2 emissions, notably observed in emerging countries, like China, India, and Brazil. As these are nations undergoing late-stage industrialization, they experience a phenomenon similar to the increase in CO_2 emissions associated with an improvement in living standards observed in European countries or the United States during the post-war economic boom.

Many of the Global South's countries are primarily dependent on agriculture because they lack robust industrial and service sectors. As a result, they are more susceptible to variations in rainfall patterns, average temperature, and severe weather events, which will have an impact on crop yields, food security, and livelihoods.

Faced with a panorama of this degree of complexity, where it is evident that climate change has the potential to exacerbate historical inequalities stemming from the capitalist economic system, a series of measures is being undertaken to guarantee what is called climate justice. There is broad academic consensus that the world is undergoing a shift towards a multipolar geopolitical landscape, particularly since the dissolution of the USSR and the rise of regional powers, such as the initial members of the intergovernmental BRICS bloc (Brazil, Russia, China, India, and South Africa), which exhibit growing economic and geopolitical significance [14, 15].

As the world navigates through this multipolarization process, it is an academic consensus the recognition of the interconnectedness of geopolitical shifts and climate change, as the evolving geopolitical landscape introduces new challenges and opportunities for addressing climate-related issues collaboratively.

The multipolar shift may foster both cooperation and competition in addressing climate change, as countries may compete for technological leadership in renewable energy while also cooperating on global initiatives and agreements to mitigate climate change. This is currently in course with the growing prominence of international efforts such as the Paris Agreement (2015), where nations commit to collective targets to limit global temperature rise.

The multipolar framework, however, introduces complexities in negotiations, as diverse national interests and priorities come into play. While some countries may prioritize economic growth over stringent environmental regulations, others may push for more aggressive climate action, reflecting the intricate dynamics of this evolving geopolitical landscape.

One of the critical necessities in addressing climate change within this multipolar context lies in ensuring a decolonial approach on the formulation of new environmental policies to rectify historical injustices that have exacerbated the climate crisis [16]. Rooted in the understanding of how colonialism and imperialism have shaped socio-economic structures, this approach emphasizes the importance of environmental justice, particularly for marginalized communities disproportionately affected by climate change despite minimal contributions to its causes [17]. Historically, vulnerable and marginalized communities have borne the brunt of environmental degradation, and there is a growing awareness that climate action must be inclusive and considerate of social justice principles.

Developing countries face challenges in adapting to climate change and implementing mitigation measures due to economic constraints and the need for development. They recognize past emissions and their effects, and contend that developed nations should bear more of the financial burden for adaptation and mitigation initiatives in the Global South.

Initiatives aimed at transitioning to sustainable practices need to be mindful of avoiding further marginalization and should prioritize the empowerment of communities disproportionately affected by climate change [18].

In this evolving landscape, technology plays a pivotal role and the competition for technological leadership in renewable energy sources is not only a race for economic advantages but also a means to influence global environmental standards. Countries investing in and sharing innovative green technologies contribute not only to their own development but also to the broader global effort to combat climate change and reduce GHGs emissions. Collaborative research initiatives and knowledge-sharing platforms become essential in navigating the complexities of a multipolar world striving for sustainable solutions.

International agreements such as the Paris Agreement, even though with its flaws, recognize the principle of common but differentiated responsibilities, acknowledging the historical responsibility of developed nations, however, there are ongoing debates on how to effectively address and rectify the inequalities in emissions and climate impacts.

In summary, addressing the inequality of CO_2 emissions between the Global North and Global South is crucial for achieving global climate goals. It requires a cooperative and equitable approach that considers historical responsibility, current emission patterns, and the disproportionate impacts on vulnerable regions, while fostering international collaboration to mitigate and adapt to the effects of climate change.

1.3 – Measures to fight against climate change

Thus, as mentioned in the preceding sections and considering the academic consensus that global warming may lead to consequences jeopardizing the well-being of the human species on Earth, a series of scientific and political efforts are underway to devise strategic plans capable of mitigating its effects.

In this context, the Fifth Assessment Report (AR5) published by the Intergovernmental Panel on Climate Change (IPCC) presented various models depicting potential temperature increases on the Earth's surface under different scenarios, considering the current trajectory of global GHGs emissions (**Figure 1.9**).

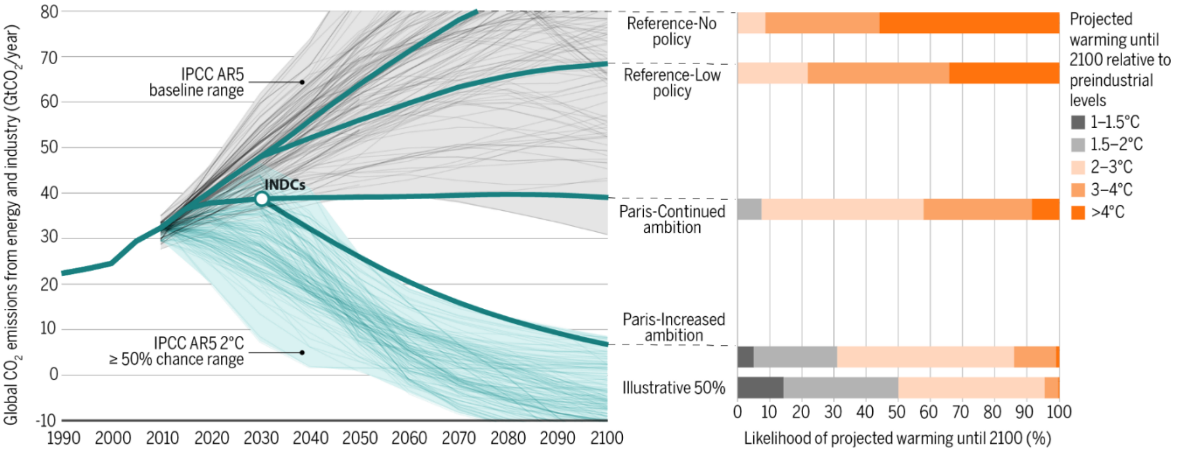

Figure 1.9. Different global CO_2 emissions scenarios and correspondent probabilistic likelihood of temperature increase relative to preindustrial levels by 2100. Image adapted from Fawcett [19].

The results published by the AR5 report in November 2014 laid the scientific foundation for discussions that took place at the UN Climate Change Conference (COP21). These discussions ultimately led to the signing of the Paris Agreement, often cited in the literature as the primary intergovernmental mechanism guiding the formulation of measures to mitigate the effects of global warming.

To prevent more frequent and intense extreme heat events, rising water levels, and disruptions to ecosystems, the Agreement's main goal is to limit global warming to well below 2 °C above pre-industrial levels, with increased efforts to limit the increase to 1.5 °C.

Considering the models proposed by the AR5, the 1.5 °C target was also reached based on scientific evidence and the recognition that even small increases in global temperatures can have significant and potentially irreversible consequences for the planet and its ecosystems. The report finds that emissions of CO_2 need to decline by about 45% from 2010 levels by 2030 and reach net-zero around mid-century to limit global warming to 1.5°C to limit the most severe impacts of climate change. Limiting global warming to the 1.5 °C target is expected to help preserve biodiversity and ecosystems, protect low-lying coastal areas from more severe consequences, such as increased flooding and loss of land, and minimize the adverse impacts on livability and well-being of human societies due to episodes of extreme heat.

In the Paris Agreement, a key concept is the "Nationally Determined Contributions (NDC)", which are basically the pledges made by every nation to describe their climate action plans and contributions to the international effort to mitigate climate change. Thus, different scenarios may unfold depending on the extent to which countries can implement their NDC's and these are summarized below.

- **No policy scenario**

In this hypothetical situation, countries and the global community do not implement any new policies or measures to address greenhouse gas emissions and climate change mitigation. This scenario serves as a baseline or reference point for assessing the potential future trajectory of emissions and their impact on the climate if no additional actions are taken beyond existing policies and commitments. As seen in **Figure 1.9**, the probability of reaching global average temperatures higher than 4 °C by 2100 under this scenario would be above 50%.

- **Low-policy scenario**

In the intermediate zone between the no-policy scenario and the scenario in which measures outlined in the Paris Agreement are implemented, a significant number of scenarios fall under the category of low-policy scenarios. This model encompasses a range of scenarios where only limited or modest policies and measures are adopted to address greenhouse gas emissions and mitigate climate change. In this sequence of scenarios, the probability of temperature increases exceeding 4 °C is lower than in the first scenario. However, it presents a very low probability of achieving the objective set by the Paris Agreement to limit the temperature increase to 2 °C.

- **Paris continued ambition**

Under the initial targets set by the Paris Agreement, if the global CO_2 emission remained the same as the ones observed during the beginning of the 2020 decade, the probability of keeping the increase in global temperature below 2 °C would be below 10%. For this reason, and as extensively critiqued in recent academic discussions, there is a need for the development of a set of targets, which would be encompassed in the " Paris increased ambition” scenario. In this framework, signatory countries should not only reduce the amount of CO_2 emitted into the atmosphere but also accelerate the pace of this reduction from 2030 onwards, with the goal of minimizing the global temperature increase as much as possible.

- **Paris increased ambition and “net zero” scenarios**

As observed in **Figure 1.9**, the scenarios that enhance the probability of keeping the planet's surface temperature below 2 °C, thus aligning with the goals of the Paris Agreement, are the ones that are even more ambitious and bold than the ones initially formulated in the agreement. Among these are the so-called "net zero scenarios."

The "net zero scenario", also known as carbon neutrality, refers to the situation in which the GHG emissions are balanced by removing an equivalent amount of those gases from the atmosphere by removal or sequestration processes, resulting in a net zero emission of GHG into the atmosphere.

As part of the global efforts to combat climate change and transition towards a sustainable, low-carbon future, an increasing number of countries and institutions are actively formulating and implementing policies with the shared objective of achieving net-zero emissions over the coming years, as seen in **Figure 1.10**.

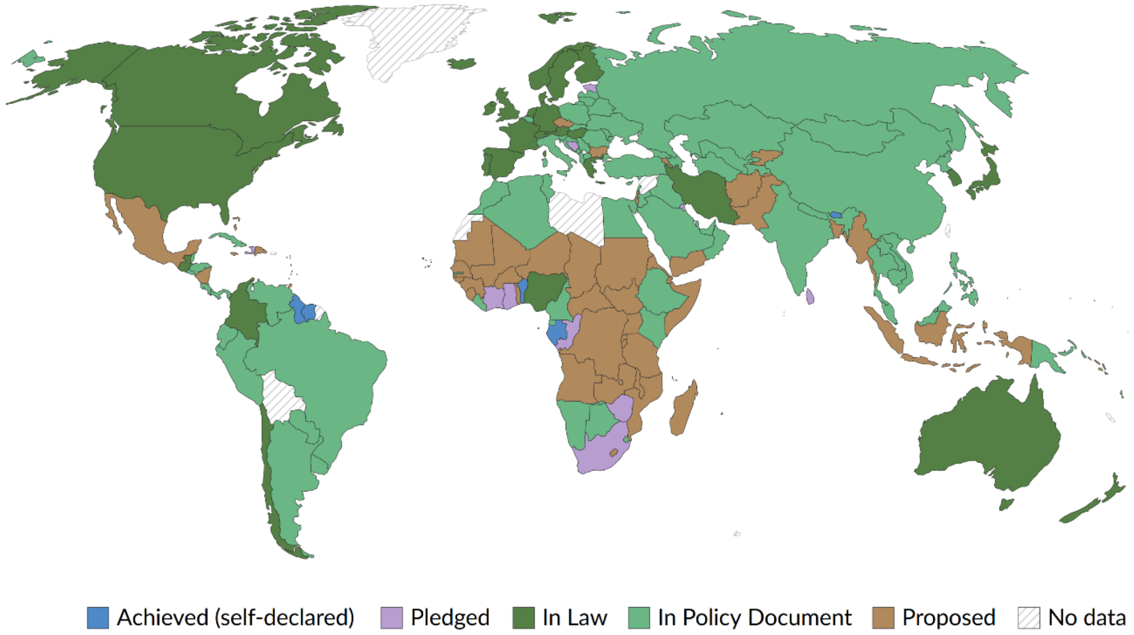

Figure 1.10. Countries with established particular legal frameworks, policy documents, or explicit time-bound pledges to reach carbon neutrality by the target year. Image prepared by the Energy and Climate Intelligence Unit with data extracted from the one published by the United Nations Framework Convention on Climate Change [20].

As discussed in the last section, the race for carbon neutrality is marked by significant geographical inequality in the current capacities to implement sustainable practices, resulting in some parts of the world reaching carbon neutrality before others.

The European Union's pledge to achieve net-zero emissions is one well-known example of a government-level commitment. The European Green Deal comprises programs to boost energy efficiency, expand renewable energy sources, and encourage a circular economy. It functions as a comprehensive policy framework to make the EU's economy sustainable and achieve climate neutrality by 2050.

Similarly, during President Joe Biden's administration, the United States has set an ambitious goal of achieving a carbon-neutral economy by 2050, as the country rejoined the Paris Agreement, signaling a renewed commitment to international cooperation in addressing climate change.

In September 2020, the Chinese administration led by Xi Jinping confirmed a pledge to reduce, even though it was not legally binding. As of 2024, China has been the largest and fastest-growing producer of renewable energy during the last decade, and it will play a significant role in the global effort to reduce GHG emissions.

China also leads the way in cooperation between countries of the Global South, under the framework of the New Silk Road Initiative, which is involved in investments in Latin America and Africa for various infrastructure projects, such as the construction of hydroelectric dams in Africa, and solar and wind power plants in Latin America.

Brazil has also presented a plan to achieve carbon neutrality by 2060. In 2023, it generated almost 93% of its domestically consumed electricity from renewable sources, the highest share in the world, and taking into account the overall energy consumption, the country presents one of the highest shares from renewable sources, too, which is due to its elevated hydropower and biomass potential.

Brazil is home to the largest portion of the Amazon rainforest, the largest tropical rainforest in the world, with approximately 60% of it located within Brazil's border. The forest is known for its incredible biodiversity and plays a crucial role in the country's pledge to reduce GHG emissions, as it acts as a natural carbon sink. Aware of the strategic importance of forest preservation to reach net-zero goals, the Amazon Fund, a financial mechanism created by the Brazilian government in collaboration with international partners to support initiatives to reduce deforestation, was reactivated under the Lula administration.

In addition to the government-level commitment to net-zero emissions, in the 2023 UN Climate Change Conference, 50 of the largest oil and gas companies signed an agreement to reach net-zero GHGs emissions by 2050, signaling a significant shift towards more sustainable practices within the industry. Notable announcements include Saudi Aramco, Exxonmobil, BP, TotalEnergies, Shell, Repsol, and Petrobras.

Furthermore, several banks and financial institutions have made commitments to align their activities with net-zero emissions goals or have taken steps toward sustainable finance, representing a landmark for reaching the Paris Agreement targets.

Achieving net-zero emissions poses a formidable array of technological challenges that require innovative solutions and unprecedented advancements across various sectors, and some of these strategies will be discussed in the next section.

1.4 – Strategies aimed at the reduction of CO_2 emission

As previously stated, the forecast of the negative impact that climate change might have on the planet requires the immediate application of technologies to reduce the emission of GHGs and fulfill the thresholds established by international organizations. Even though different approaches will have to be taken for each one of the GHGs, the development of particular strategies to decrease CO_2 emissions plays a pivotal role, as this gas presents the highest level of emissions among all of them, as seen in section 1.2.

For this necessary transition towards a new sustainable energy model, the development of appropriate technology and infrastructure is essential, and such development requires time and a considerable amount of investment.

Some of the strategies for mitigating CO_2 emissions are:

1. Increasing energy efficiency, by improving the thermal insulation of buildings, appliances, and vehicles. This includes upgrading building codes, promoting energy-efficient appliances, and optimizing industrial processes. Governments can incentivize businesses and individuals to adopt energy-efficient practices through tax breaks, subsidies, and awareness campaigns. Smart grid technologies and demand-response programs can further enhance energy efficiency by intelligently managing and distributing power.

2. Transitioning to renewable energy, by shifting to low-carbon energy sources, such as solar, wind, hydropower, and geothermal. Research into advanced materials and energy storage technologies ensures a reliable and consistent power supply. Decentralized energy systems, such as community-based microgrids, can enhance resilience and reduce dependence on centralized fossil fuel-based power plants, and policies promoting renewable energy adoption, along with financial incentives, can accelerate this critical transition.

3. Electrifying transportation and lowering emissions from the transportation sector, by switching from conventional internal combustion engine vehicles to electric vehicles (EVs). Governments can incentivize EV adoption through subsidies, infrastructure development, and regulatory measures, while expanding renewable energy capacity for EV charging infrastructure in order to maximize the environmental benefits of electrification.

4. Improving land use practices, reducing deforestation, promoting afforestation and reforestation, and improving agricultural practices, as these measures play crucial roles in carbon sequestration, biodiversity conservation. This encompasses developing strategic plans for afforestation, identifying suitable areas for tree planting based on ecological conditions, climate, and land use.

5. Deploying Carbon Capture, Utilization, and Storage (CCUS) processes.

This technology can be thought of as a combination of two processes. The foundation of carbon capture and storage (CCS) is the permanent storage of CO_2 emissions from high-output industrial sources, like power plants and factories, preventing their release into the atmosphere.

The carbon capture and utilization (CCU), different from the other type, represents a cutting-edge approach and uses sequestered CO_2 instead of simply storing it underground.

Presently, CCS is being investigated for emission abatement from industrial processes, such as the production of chemicals, steel, and cement, and is being used in certain power plants, especially those that rely significantly on coal.

Once captured, the transportation of CO_2 to storage sites is a critical step. Common methods include pipelines, similar to those used for natural gas, as well as ships and trucks, especially for remote or offshore storage locations, and afterwards, the storage phase typically involves injecting CO_2 into geological formations, like coal seams that cannot be mined, deep salt formations, and depleted gas an oil fields.

The CCU processes go beyond the traditional approach covered by the CCS technologies, presenting one key advantage: the introduction of economic incentives. By transforming CO_2 into marketable products, industries have the potential to offset the costs associated with capturing and utilizing CO_2, making it an economically viable and sustainable solution.

Combining CCS and CCU is often discussed as an integrated strategy, sometimes referred to as CCUS (Carbon Capture, Utilization, and Storage), as this integrated approach seeks to maximize the benefits of both storage and utilization, allowing for a more comprehensive and economically viable solution to the challenge of reducing CO_2 emissions.

The CCUS technologies present the advantage in comparison with the other strategies in the list by being the only one which can effectively tackle CO_2 emissions in flue gas produced by high emitting industry sectors, such as cement, steel and chemicals production, which account for more than 15% of global GHGs emissions, as seen in **Figure 1.4**.

Presently, operational facilities equipped with CCUS technologies can sequester approximately 90% of the CO_2 content in flue gas, even though it has already been proposed that it is technologically feasible to attain higher capture efficiencies. Additionally, the direct capture of CO_2 from the atmosphere is achievable by employing air-drawing mechanisms facilitated by fans and subsequently passing the air through a medium comprising solid sorbents or liquid solvents. However, it is important to note that this approach is characterized by greater energy intensity and, consequently, elevated costs, primarily due to the comparatively lower concentration of CO2 in the atmosphere compared to flue gas.

This way, after CO_2 is captured, the utilization pathway can be:

1. Enhanced Oil Recovery (EOR): Captured CO_2 can occasionally be used for enhanced oil recovery, a technique that involves pumping CO_2 into reservoirs to boost oil production, while storing the gas underground.

2. Carbon Utilization in Products: CO_2 can be used as a feedstock in the production of various materials, such as urea, polycarbonate, cyclic carbonates, or salicylic acid.

3. Carbon Utilization for Fuels Production: CO_2 can also be converted into fuels, such as in hydrocarbons or alcohols. These processes can take place via Fischer-Tropsch, hydrogenation reactions, or electrolysis, as synthesized in Figure 1.11.

The beginning of using as feedstock for chemical reactions is not a novelty in the XXI century, since the first use dates back to the end of the XIX century, when processes such as the urea synthesis, the Solvay process and the production of salicylic acid, which use CO_2 as reactant, were first conceived.

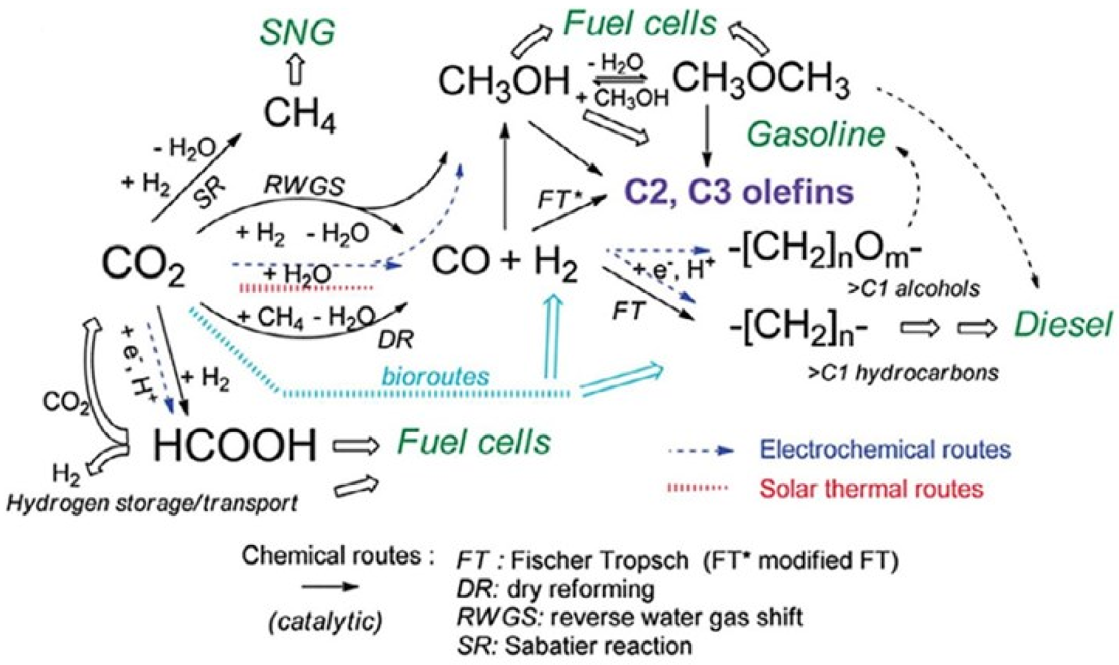

Figure 1.11. Schematic representation of possible reactions that might be used to convert CO_2 using CCU technologies. Image adapted from Centi et al. [21].

In the 1900s, CO_2 was overshadowed by the "golden era" of carbon monoxide chemistry for producing chemicals and fuels. However, starting in the 1970s, there was a renewed interest in the exploitation of CO_2. This resurgence coincided with its application as an additive in the selective hydrogenation of CO to CH_3OH and its utilization in organic applied chemistry, such as the formation of organic carbonates from epoxides.

Despite these developments, CO_2 has not been extensively employed as a raw material in industrial processes due to its high stability. This inertness of CO_2 is attributed to the high oxidation state of the carbon atom in the CO_2 molecule (i.e., 4+), necessitating a substantial energy input for transforming the molecule into higher-valued chemicals.

Thermodynamically, this is translated by the values of Gibbs energy of formation for the series of a C1 species (**Figure 1.12**) that reveals that the conversion reactions of CO_2 into most of the other C1 species are endergonic processes, which means that, under standard conditions, these reactions are not spontaneous. For these reactions to be carried out, an external energy source needs to be provided, which might be heat, an electric current, or light irradiation, which gives rise to thermal, electrochemical, and photochemical processes, respectively.

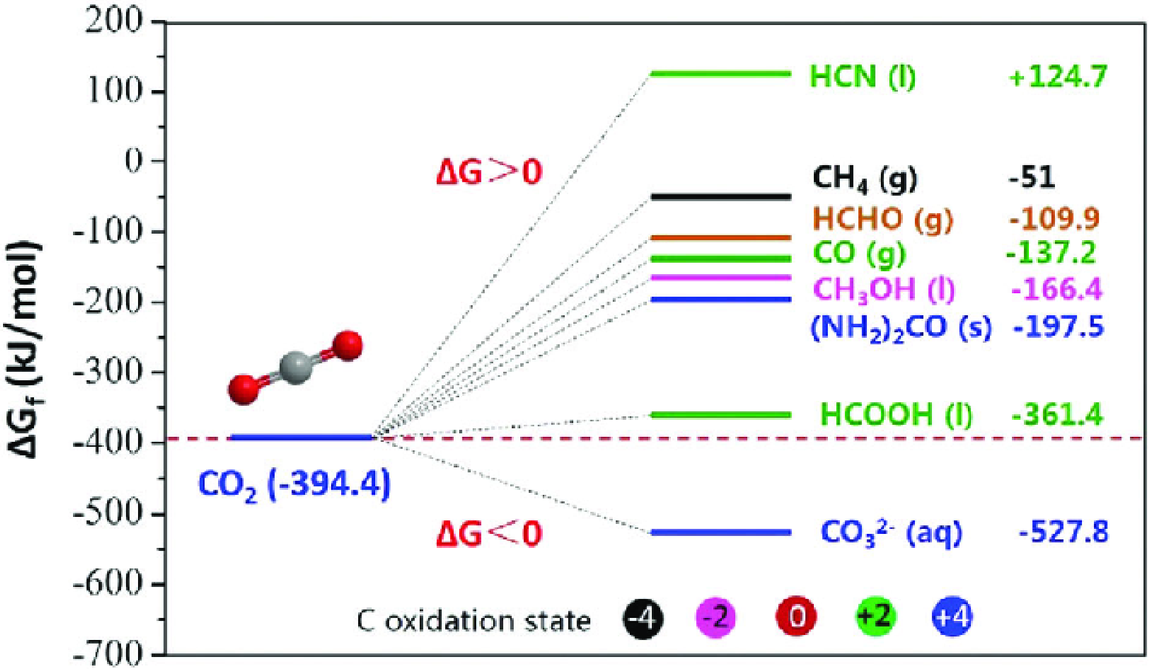

Figure 1.12. Gibbs free energy of formation for a series of C1 species compared to the CO_2 one for comparison standards. Image adapted from Zheng [22].

Nevertheless, even though there are a series of challenges posed in executing these chemical reactions, there is a continuous scientific and industrial interest in optimizing the reaction conditions for these processes and, in parallel, developing more efficient, robust, and stable catalysts. These catalysts should be capable of enhancing the rates of these processes at lower temperatures.

Within the context of all the reactions that can be employed, with CO_2 serving as a feedstock, the CO_2 methanation reaction stands out due to a series of advantages compared to others, which will be addressed in the following section. This will lead to the discussion of the scientific motivation behind this doctoral thesis, which focuses on developing more effective catalysts for the CO_2 methanation reaction.

1.5 – CO_2 methanation reaction

The CO_2 methanation reaction emerges as one of the most promising ones that might receive more attention as a strategy to use CO_2 inside the context of CCU technologies and it is described in **Equation 1.1** below:

$$CO_{2(g)} + 4H_{2(g)} \rightleftharpoons CH_{4(g)} + 2H_2O_{(g)} \qquad \text{Equation 1.1}$$

This reaction is also known as the Sabatier Reaction, named after Paul Sabatier, a French chemist who laid the foundation of the studies of this process at the end of the XIX century and was the recipient of the Nobel Prize in Chemistry in 1912 for his discoveries regarding hydrogenation reactions. Since then, this reaction received increasing interest due to the key role it might play in developing CCU technologies and the more favorable economic viability, which is attributed to the advances in catalyst designs and process energetic optimization.

Nowadays, this reaction is an alternative that allows for obtaining CH_4 through selective hydrogenation of CO_2. Inside the current context, this process offers a triple benefit: (i) it avoids the direct emission of CO_2 into the atmosphere, (ii) it allows for obtaining an energy source such as CH_4, which can be transported using the pipeline infrastructure that already exists and, (iii) it offers an alternative for storing energy from renewable sources, as the reduction process can use green H_2, obtained from more sustainable origin, such as wind or solar power.

Technologies based on the CO_2 methanation reaction belong to the set of processes known as Power to Gas (P2G). P2G processes convert excess electricity from renewable sources, such as wind or solar power, into gaseous fuels, typically hydrogen or methane. These versatile processes contribute to integrating renewable energy into existing infrastructure, providing a means to store and utilize clean energy efficiently across multiple sectors.

Over the following sections, a review of the thermodynamics and the conditions of the reaction, the catalysts used for this chemical process, the reaction mechanism, and a prospect of the technological processes that might use this reaction to mitigate the emission of CO_2 will be presented.

1.5.1 – Thermodynamics

The process behind the CO_2 methanation reaction is intricate and involves several side reactions, each one with its own thermodynamic particularities. Hussain et al. conducted an extensive review and theoretical study and determined the thermodynamic parameters, such as the Gibbs energy change (ΔG), entropy change (ΔS), enthalpy change (ΔH), and equilibrium constant ($\ln K$) for many chemical reactions that might take place simultaneously with the CO_2 methanation reaction. This data is summarized in **Table 1.1** and **Figure 1.13**.

Table 1.1. Values of equilibrium constant (lnK), standard Gibbs Free energy change (Δ_rG^o), standard entropy change (Δ_rS^o), and standard enthalpy change (Δ_rH^o) at T = 25 °C and P = 1 bar for possible reactions related to the CO_2 methanation. Data extracted from Hussain et al. [23].

Number	Chemical Reaction	lnK	$\Delta_rG^{o\ a}$	$\Delta_rS^{o\ a}$	$\Delta_rH^{o\ a}$
1	$CO_{2(g)} + 4H_{2(g)} \rightleftharpoons CH_{4(g)} + 2H_2O_{(g)}$	+24.9	-141.9	-214.5	-164.7
2	$CO_{2(g)} + 2H_{2(g)} \rightleftharpoons C_{(s)} + 2H_2O_{(g)}$	+11.0	-62.8	-91.7	-90.1
3	$CO_{2(g)} + 3H_{2(g)} \rightleftharpoons CH_3OH_{(g)} + 4H_2O_{(g)}$	-0.6	+3.5	-177.1	-49.3
4	$CO_{2(g)} + 2H_{2(g)} \rightleftharpoons CO_{(g)} + H_2O_{(g)}$	-5.0	+28.6	+42.0	+41.1
5	$2CO_{2(g)} + 7H_{2(g)} \rightleftharpoons C_2H_{6(g)} + 4H_2O_{(g)}$	+27.8	-158.4	-357.4	-265.0
6	$CO_{2(g)} + CH_{4(g)} \rightleftharpoons 2CO_{(g)} + 2H_{2(g)}$	-29.8	+170.5	+256.5	+247.0
7	$2CO_{(g)} \rightleftharpoons C_{(s)} + CO_{2(g)}$	+21.0	-120.0	-175.8	-172.4
8	$CH_{4(g)} \rightleftharpoons C_{(s)} + 2H_{2(g)}$	-8.8	+50.5	+80.7	+74.6
9	$CO_{(g)} + 3H_{2(g)} \rightleftharpoons CH_{4(g)} + H_2O_{(g)}$	+19.9	-113.3	-172.4	+206.0
10	$CO_{(g)} + 2H_{2(g)} \rightleftharpoons CH_3OH_{(g)}$	+4.4	-25.1	-219.2	-90.5
11	$CO_{(g)} + H_{2(g)} \rightleftharpoons C_{(s)} + H_2O_{(g)}$	+16.0	-91.4	-133.8	-131.3
12	$2CO_{2(g)} + 5H_{2(g)} \rightleftharpoons C_2H_{6(g)} + 2H_2O_{(g)}$	+37.8	-215.6	-441.4	-347.2

$^a\Delta_rG^o$ and Δ_rH^o units are kJ mol^{-1}. Δ_rS^o unit is kJ K^{-1} mol^{-1}

The chemical reactions CO_2 methanation (1), CO_2 reduction to carbon (2), CO_2 reduction to C_2H_6 (5), Boudouard reaction (7), CO methanation (9), CO reduction to carbon (11), and CO reduction to C_2H_6 (12) exhibit positive lnK values and negative ΔG and ΔH values. This indicates that these reactions are highly spontaneous and exothermic at T = 25 °C and P = 1 bar.

On the other hand, the RWGS reaction (4), dry reforming of methane (6), and CH_4 cracking reaction have negative lnK and positive ΔG and ΔH values. This suggests that these reactions may be impractical or require an input of energy during the methanation process, particularly at lower temperatures. However, with an increase in temperature, these reactions become increasingly significant and achievable.

In the literature, there are thermodynamic studies that allow for the determination of the mole fraction of reactants, products, and side products involved in the CO_2 methanation reaction in equilibrium, such as the one published by Gao et al. [24].

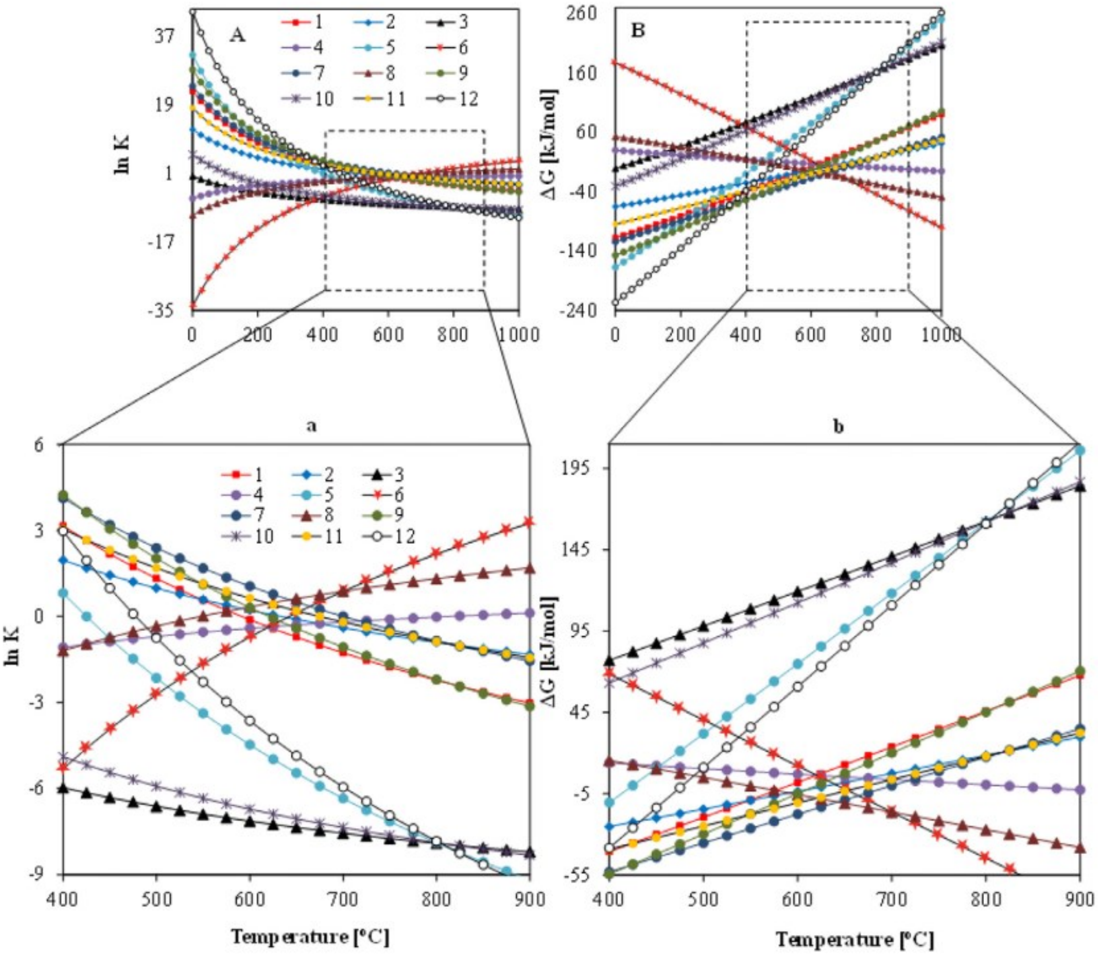

Figure 1.13. (a) lnK and (b) Δ_rG^o values of the side reactions that might occur with CO_2 methanation activity. Adapted from Hussain et al. [23].

The results of such a study, considering P = 1 atm and employing the method to minimize Gibbs free energies considering all the reactions previously mentioned are illustrated in **Figure 1.14.** As observed, the predominant products at low temperatures (200-250 °C) are CH_4 and H_2O, whereas at temperatures exceeding 450 °C, CO becomes more significant due to an increase in the significance of the reverse water-gas shift (RWGS) reaction.

Once the CO_2 methanation reaction is an exothermic process, increasing temperature is not favorable for this reaction, which explains why the CO_2 mole fraction in equilibrium increases when the temperature is increased too. At around 550 °C, however, the equilibrium molar fraction of CO_2 starts decreasing again due to the predominance of the RWGS reaction. Gao's calculations also predict that coke formation does not take place under the tested conditions in a significant extension [24].

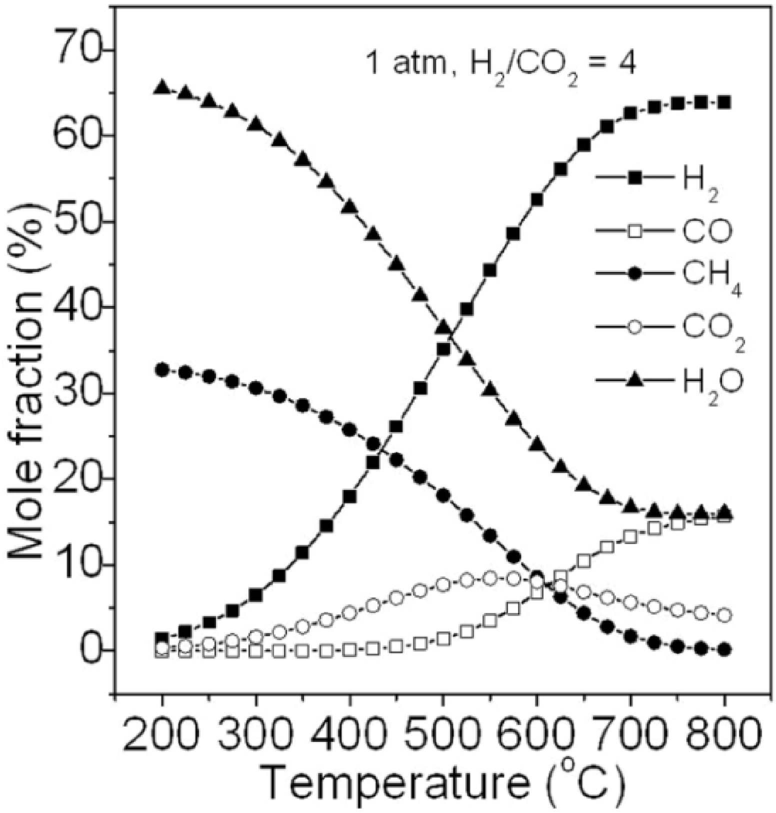

Figure 1.14. Molar fraction of components in equilibrium in a chemical system designed for the CO_2 methanation reaction. Reactions conditions: $H_2/CO_2 = 4$; P = 1 atm. Image adapted from Gao et al. [24].

It should be noted that the reactions of CO_2 hydrogenation and CO hydrogenation are more prominent and viable in the temperature range of 250-400 °C, and they become impractical beyond 500 °C.

Therefore, with all this considered, it is evident that the CO_2 methanation reaction is an elaborate chemical process involving several side reactions and thermodynamic considerations. For this reason, optimizing the reaction conditions is of utmost importance to maximize the CO_2 conversion and selectivity to CH_4, which will be covered in the next section.

1.5.2 – Reaction conditions

The Le Chatelier's principle states that altering various factors, including pressure, temperature, and CO_2/H_2 ratios, can modify the equilibrium composition in a system for the CO_2 methanation reaction. For instance, the findings of Miguel et al. have demonstrated that applying high pressure can enhance the CO_2 conversion and selectivity to CH_4, as seen in **Figure 1.15**, which is expected because the reaction reduces volume [25].

Nevertheless, from an industrial and economical approach, an ongoing endeavor is to develop CO_2 methanation reactor designs that operate at low pressure, using intermediate temperatures [26]. This is due to a series of reasons, such as the interest to couple this system with atmospheric pressure systems in CCUS methodologies, lower energy consumption, which reduces overall operational costs, and safety considerations, which are considered for the high inflammability and low compressibility observed for H_2.

Another important reason is the potential application of the CO_2 methanation reaction for biogas samples upgrade with enrichment of CH_4 content, as it will be more thoroughly evaluated in section 1.5.5. Sweetened biogas samples are usually directly available at atmospheric pressure, and due to this, the development of reactor designs that operate at atmospheric pressure would enable the direct application for biogas upgrade.

As seen in **Figure 1.15** and **Figure 1.16**, the stoichiometric ratio H_2/CO_2 also affects the reaction performance.

When the $H_2/CO_2 = 2$, for example, CO_2 conversion values are in the 50–70% range, and the CH_4 selectivity reaches a maximum of 73.0% and 88.0%, at the pressures of 1 atm and 30 atm, respectively. The higher the H_2/CO_2 ratio, the higher the CO_2 conversion and selectivity towards CH4 values that can be attained.

The H_2/CO_2 ratio also influences the outcome of the reaction if there is a formation of elemental carbon, i.e., coke, which might pose a significant drawback for the design of reactional systems, as coke can plug the reactor setup or irreversibly poison the system’s catalysts. When $H_2/CO_2 = 2$, a significant amount of CO_2 of up to 50% can be reduced to elemental carbon at temperatures lower than 500 °C, but when $H_2/CO_2 = 4$, on the other hand, no coke formation is observed.

In summary, the utilization of the appropriate stoichiometric H_2/CO_2 ratio, coupled with moderate temperatures (250 °C – 450 °C) and suitable pressures, favors the carbon dioxide methanation reaction. Nevertheless, due to the fact the reduction of CO_2 to CH_4 involves the transfer of 8 electrons, the reaction presents a substantial kinetic barrier, which requires the use of optimized catalytic systems to obtain appropriate kinetic rates under the experimental conditions.

The forthcoming section will delve into a comprehensive literature review on catalysts used for this reaction, focusing on their structural attributes and mechanistic insight. By exploring a spectrum of catalytic strategies, the section seeks to provide a nuanced understanding of the evolving landscape, laying the groundwork for subsequent discussions on innovative methodologies and emerging trends.

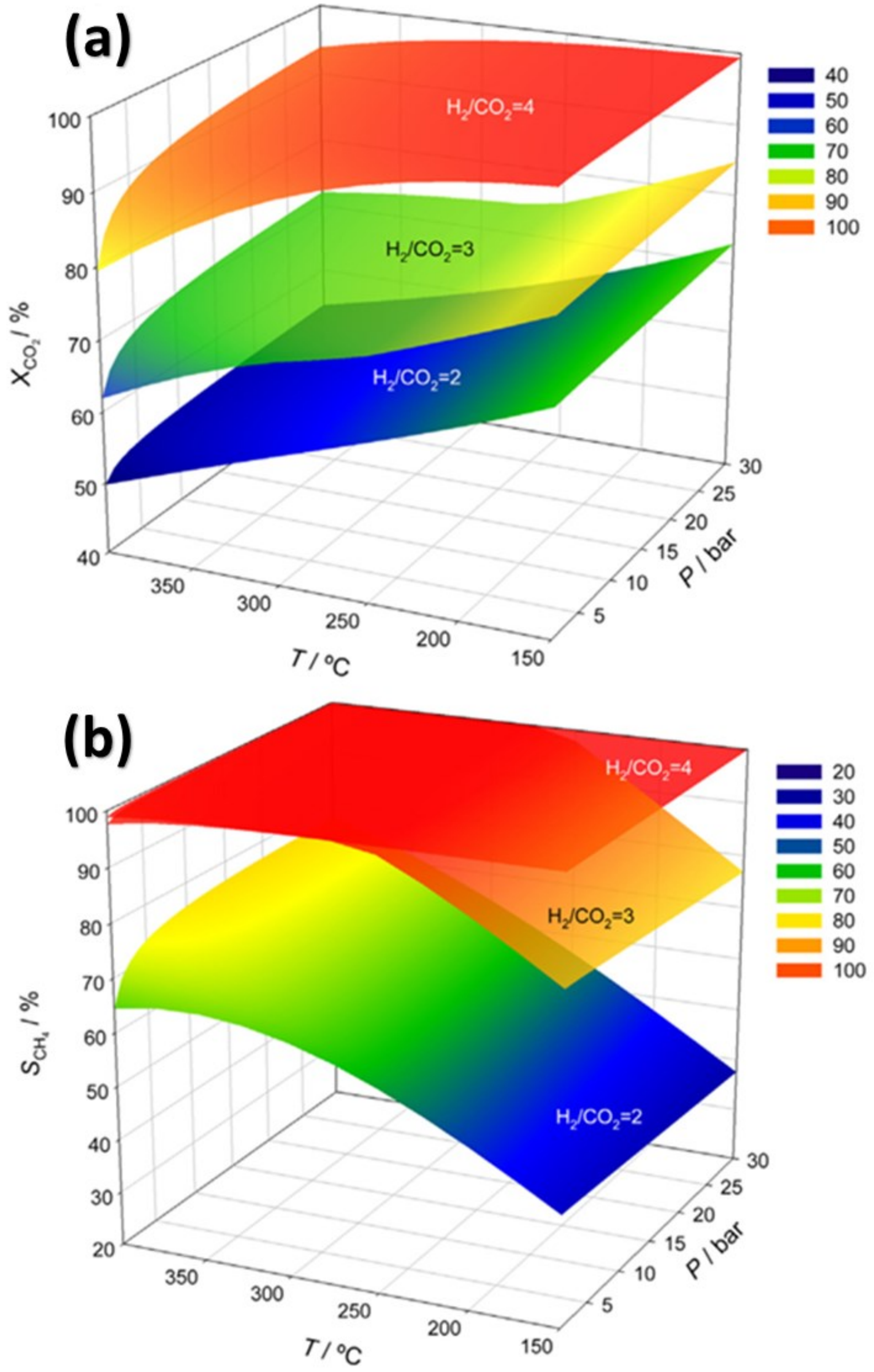

Figure 1.15. Effect of the H_2/CO_2 ratio on (a) CO_2 conversion, X_{CO_2}, and (b) selectivity towards CH_4, S_{CH_4}, at different temperatures and pressures. Image adapted from Miguel et al. [25].

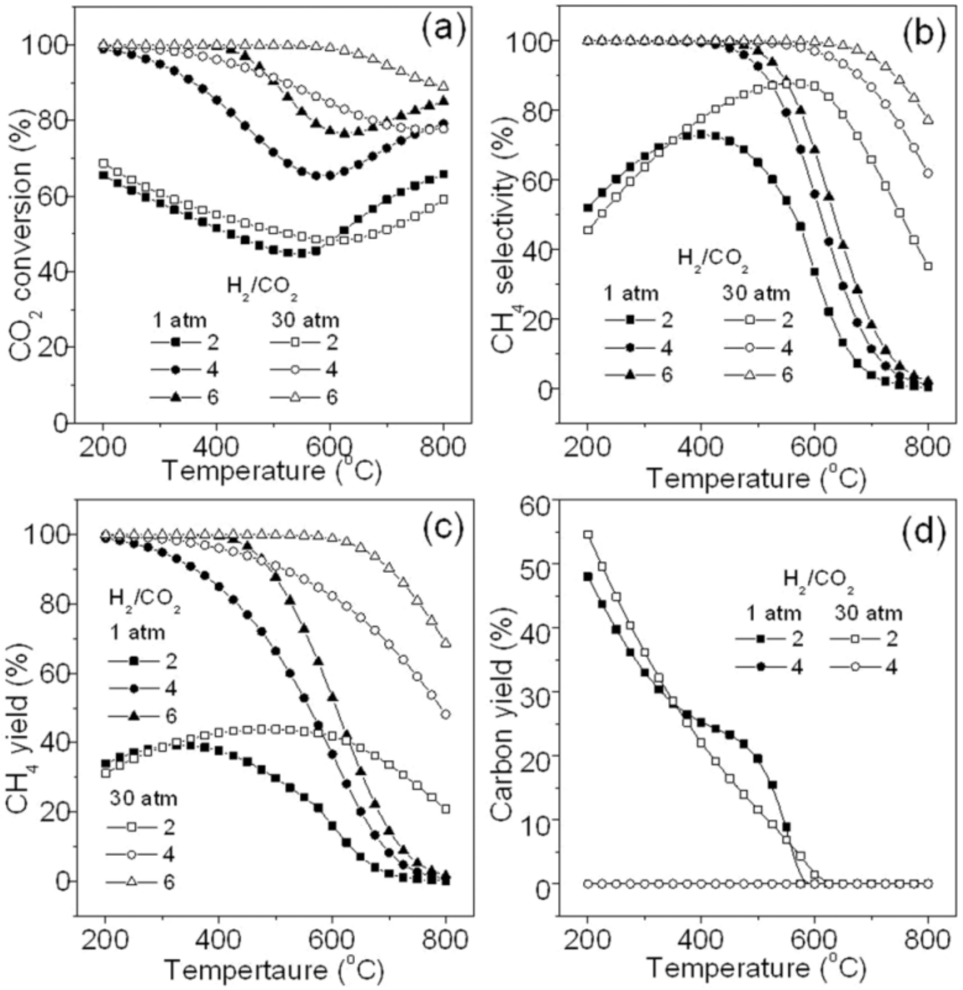

Figure 1.16. Effect of different stoichiometric ratios H2/CO_2 on the CO_2 methanation reaction: (a) CO_2 conversion, (b) CH_4 selectivity, (c) CH_4 yield, and (d) carbon yield.

1.5.3 – Catalysts for CO_2 methanation reaction

Metals from groups 8-10 of the Periodic Table have shown a solid capability to activate and hydrogenate CO and CO_2 in methanation processes. Poutsma et al. [27], Vannice [28], and Mills et al. [29] conducted different studies on these metals and utilized them as unsupported metal catalysts for methanation reactions, with the reactivity results shown in **Figure 1.17**.

It should be acknowledged, however, that these reactivity trends for metals are only a general indication and may vary in specific cases due to factors such as interactions with the catalyst support, temperatures of reduction, or activation. The selectivity of CO_2 methanation is also influenced by other experimental factors, such as the choice of metal and pressure applied. Catalysts based on Pd [30, 31], Fe [32-34], Pt [35-37], and Cu [38] predominantly produce CO through RWGS reaction, while Rh [39, 40], Ru [41, 42], Co [43, 44], and Ni-based [45, 46] are more selective to CH_4, as synthesized in **Figure 1.18**.

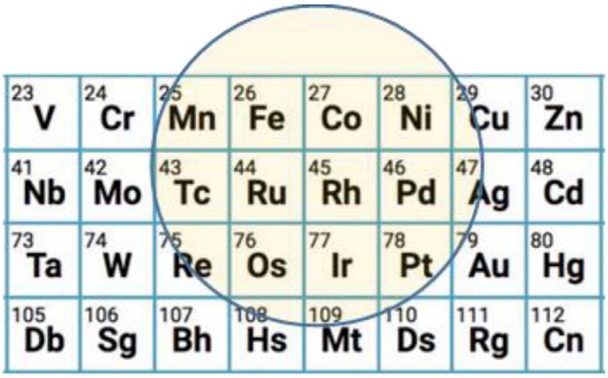

1 **Reactivity:** Ru > Ir > Rh > Ni > CO > Os > Pt > Fe > Mo >Pd > Ag

2 **Reactivity:** Ru > Fe > Ni > Co > Rh > Pd > Pt > Ir
Selectivity: Pd > Pt > Ir > Ni > Rh > Co > Fe > Ru

3 **Reactivity:** Ru > Fe > Ni > Co > Mo
Selectivity: Ni > Co > Fe > Ru

Figure 1.17. Common metals used in catalysts for CO and CO_2 methanation and reactivity and selectivity order as described by three different studies provided by Poutsma et al., Vannice, and Mills et al. [27-29].

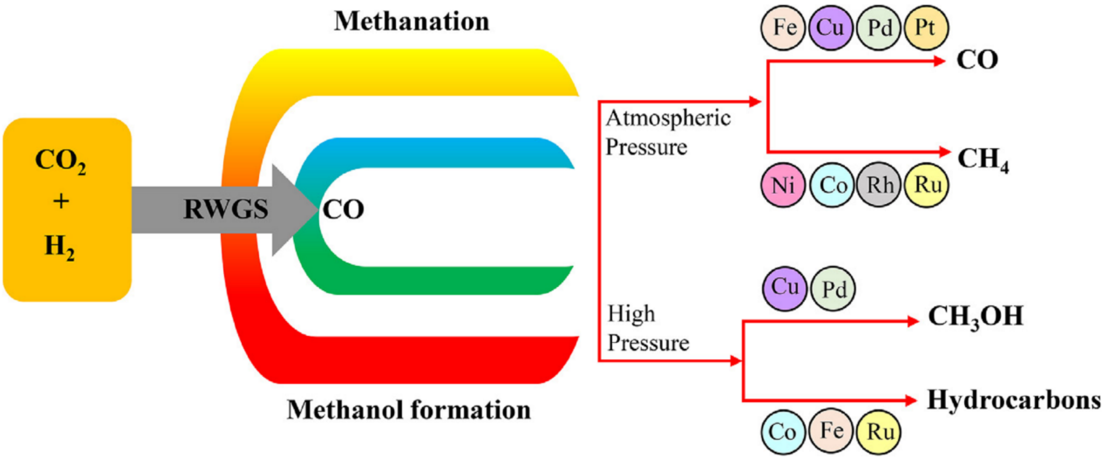

Figure 1.18. Schematic diagram showing possible products formed in CO_2 hydrogenation regarding the reaction pressure and metal used in the catalyst composition. Image adapted from Hussain et al. [23].

As it will be discussed in the following sections, the adsorption of CO and CO_2 species onto the surface of the catalyst's metallic particle might be a crucial step in forming reaction products during CO_2 methanation reactions. Bligaard et al. conducted a research study to examine the correlation between the dissociative CO chemisorption energy on different metal surfaces and their respective catalytic activity in CO methanation [47]. The findings demonstrated a curve that resembled a volcano shape, as illustrated in **Figure 1.19**, when establishing a relationship between the catalytic performance and the dissociative CO adsorption energy for a series of metals.

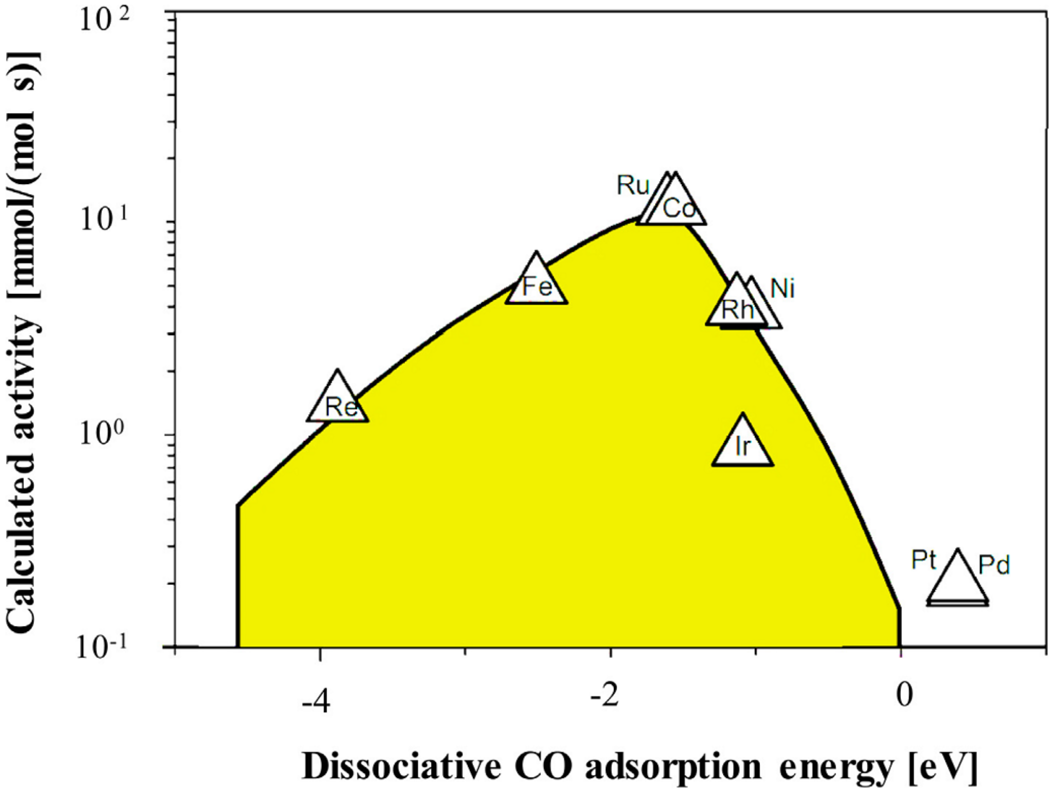

Figure 1.19. Dependence of the CO methanation reaction catalytic activity on the dissociative CO adsorption enthalpy for different transition metals. Data adapted from Bligaard et al. [47].

The observed volcano-like behavior in **Figure 1.19** of the catalyst provides insight into how each metal behaves differently depending on its electronic structure. For instance, Ir, Pt, and Pd, elements on the far-right side of the periodic table, have high dissociative energies that limit the reaction rate, as the C-O bond dissociation lags down the mechanistic pathway, which explains why these metals are not among the most active ones.

Therefore, according to the available evidence, metals positioned in the middle of the periodic table, like Ru, appear to possess an optimal chemisorption energy of around 150 kJ mol^{-1}, which accounts for the fact that Ru exhibits better catalytic performance than other elements that are also from groups 8-10 regarding methanation reactions [48].

Among all the metals with high activity, selectivity, and stability in catalysts, nickel is the one that presents the best catalytic activity-cost relation, as, due to its larger availability in nature compared to the other ones, its price is significantly more competitive than the other ones. Just as a matter of comparison, the Ni price is approximately 18 USD kg^{-1}, lower than the one presented by Co (61 USD kg^{-1}), and significantly lower than the ones presented by the other high-activity metals, such as Rh (USD 638,000 kg^{-1}) or Ru (USD 319,000 kg^{-1}) [49].

So, considering the catalytic activity and the feasibility of scaling up the catalysts developed, nickel was the chosen metal used to develop catalysts in this project.

1.5.4 – Support influence

The type of support chosen for the catalysts for the reaction plays a very significant role, as they provide a matrix to finely disperse metallic nanoparticles. This property is intrinsically related to achieving reasonable dispersion of the supported metal and avoiding or, at least, hindering sintering. Altogether, this is a crucial consideration considering the exothermic nature of the reaction, which poses a significant danger of hotspot concentration in the commonly employed reactors [50].

Consequently, as illustrated in **Figure 1.20**, selecting appropriate support involves striking a balance between two opposing factors: on one side, ensuring sufficient contact with the support to achieve optimal metallic dispersion during operation, and on the other, selecting materials that allow the metallic species to be easily reduced at low temperatures without causing undesirable sintering.

Previous reports in the literature also pointed out that the support may play a role in the mechanism, having an effect on CO_2 adsorption and subsequent activation. The support also influences the amount and the strength of basic sites, which are frequently mentioned as the chemical spot where a significant parcel of CO_2 molecules is anchored before undergoing transformation, which significantly impacts the catalytic performance.

Moreover, the interfacial zone between the metallic phase and the support is crucial for the development of the reaction, as it contains potentially active sites capable of activating CO_2. The H atoms at this peripheral zone aid in the hydrogenation of CO_2 and, additionally, strong metal-support and electronic interactions were recognized as key factors influencing the activity of the reaction.

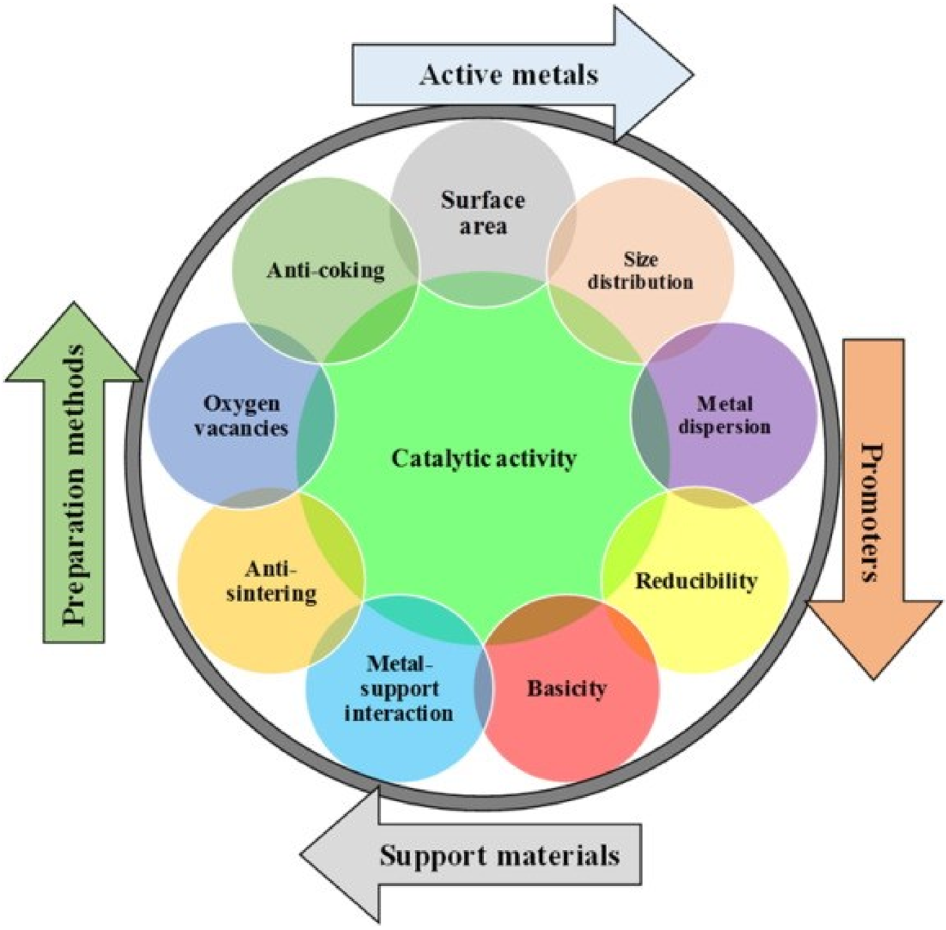

Figure 1.20. Schematic representation of the factors that interfere with the performance of the CO_2 selective hydrogenation to methane. Image adapted from Hussain et al. [23].

Conventional supports

For many industrial processes, conventional catalytic supports based on inorganic oxides are commonly used. One commonly used for the development of catalysts for the CO_2 methanation reaction is aluminum oxide, Al_2O_3. Al_2O_3 is more complex than other metal oxides due to its several crystallographic alterations, which include the α, γ, κ, δ, and θ phases [51].

While α-Al_2O_3 is not usually regarded as a support for CO_2 methanation catalysts, γ-Al_2O_3, on the other hand, finds application, which is attributed to its acid-base properties and porous oriented structure [52]. Zheng et al. reported the use of stable Ru/Al_2O_3 catalysts that kept good activity towards CO_2 conversion under cyclic operational conditions, attributing this to the efficient dispersion of Ru^0 particles over the support high surface area and large average pore [53]. Even with this series of advantages, γ-Al_2O_3-based catalysts are prone to coke formation and metallic particle agglomeration, which might pose a problem for their industrial application [51].

Reducible metal oxides are commonly used as supports for the development of heterogeneous catalysts in CO_2 methanation. These materials possess favorable chemical properties, as they are prone to form oxygen vacancies and assume various oxidation states.

Among these supports, TiO_2 is a highly effective semiconductor material with abundant defects for catalytic applications. Research indicates that Ni catalysts supported on TiO_2 exhibit exceptional performance in CO_2 methanation reactions. This can be attributed to the incorporation of Ni particles into the TiO_2 lattice, which generates oxygen vacancies. The non-stoichiometric nature of the support facilitates electron transfer from Ti atoms to Ni nanoparticles on the catalyst surface, enhancing hydrogen adsorption and promoting subsequent spillover onto the support material. As a result, CO_2 molecules experience improved activation and dissociation at lower temperatures than other catalyst systems.

TiO_2 is considered an effective defect-rich semiconductor material for support with applications in heterogeneous catalysis. Studies have shown that Ni catalysts supported on TiO_2 exhibited better catalytic performance, attributed to a partial exchange of Ni species in the TiO_2 lattice, enhancing the formation of oxygen vacancies [54]. This way, the non-stoichiometric lattice increases the electronic density on the Ni_0 phase and facilitates the dissociation of H species and spillover. As a consequence, this increases the CH_4 formation rate at lower temperatures.

Non-stoichiometric TiO_x provides electrons to Ni atoms on the catalyst surface, facilitating hydrogen adsorption on Ni nanoparticles and subsequently spilling over the support. This, in turn, improves the activation and dissociation of CO_2 molecules, resulting in comparatively higher CO_2 methanation activity at low temperatures.

Because of their redox characteristics, which enhance CO_2 activation by transferring electrons from the support to the metallic phase, CeO_2 and ZrO_2 oxides have also been studied. Tada and collaborators studied the CO_2 methanation potential over different oxides [55]. Their results show that the CeO_2 catalyst had the maximum activity, which can be attributable to its stronger basicity and higher concentration of oxygen vacancies.

The researchers Jia et al. synthesized a catalyst using ZrO_2 as the supporting material for CO_2 methanation, which displays CH_4 yield above 70% at 300 °C [56]. This activity was attributed to factors such as high basicity, well-dispersed Ni nanoparticles, and the formation of oxygen vacancies in the lattice structure. These characteristics promoted efficient activation of CO_2. Additionally, dissociative adsorption of H_2 took place rapidly at the Ni nanoparticles, resulting in hydrogen atoms interacting with carbon intermediates on the ZrO_2 support to produce methane.

Regarding ZrO_2 as support, Da Silva and collaborators [57] compared 10 wt.% Ni catalysts supported over ZrO_2 and SiO_2. The ZrO_2 catalysts exhibited better results, which was attributed to the higher Ni dispersion in the ZrO_2 catalyst and the significantly weaker interaction between CO_2 and the SiO_2 support. Furthermore, Lu et al., using $ZrO(NO_3)_2$ as Zr precursor, modified a mesoporous clay using a hydrothermal procedure [58]. The catalysts supported on zirconia-modified clays were found to exhibit higher activity towards the CO_2 methanation reaction, which was attributed to the higher metallic dispersion achieved by the bimodal pore structure found in the zirconia-modified material and lower coke deposition.

Zeolites

Over the last few years, zeolites received more attention as catalysts' support for the CO_2 methanation reaction due to their high surface area, thermal activity and capability of anchoring metallic nanoparticles while hindering sintering effects.

Recently, Bacariza et al. published a review, in which, zeolites were compared regarding their catalytic activity with other similar materials, such as Al_2O_3 and MgO [59]. Bando et al. [60], and Aziz et al. [61] found out that a catalyst supported on a Y-type zeolite exhibited better activity than reference catalysts supported on SiO_2 and Al_2O_3, using Rh and Ni as active centers, respectively.

Meanwhile, Guo et al., comparing a series of zeolite and oxide materials, observed that the ZSM-5 presented the highest catalytic activity, which was attributed to the basic and porous properties of the support, which created a positive effect with the Ni^0 phase and enhanced the catalytic performance [62].

Metal-organic frameworks (MOF)

Metal-organic frameworks (MOF's) represent another class of materials being explored as supports for catalysts in CO_2 methanation reactions. These materials comprise multidentate organic linkers and transition-metal cations connected by coordination bonds. Also referred to as porous coordination networks, MOF's are notable for their exceptionally high surface areas and the ability to engineer their composition by adjusting the metal and organic ligand components. This versatility allows for the creation of a wide variety of support types.

Recent studies have employed MOF-based catalysts in CO_2 methanation. For instance, Zhen and colleagues investigated the reaction using a Ni-doped MOF-5 catalyst. They found that the strong metal-support interaction between the uniformly dispersed Ni nanoparticles and the MOF-5 support led to high catalytic activity, selectivity, and thermal stability [63].

Similarly, Lippi et al. tested a Ru catalyst prepared over UiO-66 catalyst for CO_2 methanation. The catalyst demonstrated remarkable activity, which was attributed to the unique MOF morphology, which enabled the distribution of Ru^0 nanoparticles across the material framework after reduction [64].

Xu et al. conducted a related study in which they reported that a Ru-doped UiO-66 catalyst achieved efficient catalytic performance because the Ru nanoparticles were encapsulated within the zeolite framework, which allowed good dispersion [65].

Similarly, Li et al. explored a Co catalyst supported on a ZIF-67-like support focusing on how variations in particle size and morphology impacted CO_2 methanation. The optimum performance of the catalysts was attributed to the highly dispersed Co NP's (in the size range between 8 and 20 nm) embedded within a carbon matrix [66].

1.5.5 – Metallic loading influence

The metallic loading in catalysts affects the catalytic performance, as its variation causes changes in the extent of metal dispersion. In this way, low metal loadings will result in high dispersion, even reaching atomic dispersion, while the use of high metal contents will result in catalysts with larger metal nanoparticles or clusters. The presence of the metal in this form of dispersed atoms or nanoparticles has been shown to have a significant effect on the final catalyst activity.

Quindimil et al. evaluated the effect of metallic loading and compared a series of catalysts based on Ni and Ru supported in alumina, with the Ni metal loading ranging from 4 to 20%, and the Ru ones, from 1 to 5% [67]. They found out that the higher the metallic loading, the lower the dispersion as expected, and the lower the reduction event peak temperature, attributed to stronger SMSI in the catalysts with increased dispersion, based on the XPS results. Due to CO_2 saturation effects, the best formulations were the 12%Ni/Al_2O_3 and the 4%Ru/Al_2O_3, providing similar results to higher loading catalysts.

For catalysts supported on mesoporous materials, Graça et al. evaluated the Ni loading ranging from 2 to 14 wt% and verified that the CO_2 conversion increased with higher Ni loadings, which was attributed to an increase in percentual metallic reducibility [68].

Aziz et al. studied catalysts supported on mesoporous silica nanoparticles (MSN) with Ni loadings ranging from 1 to 10 wt. % and noticed that catalytic activity increased with higher Ni contents, with a saturation effect between the 5% wt. and the 10% wt. samples [61]. This was because even though the higher loading sample had more active sites, the metallic incorporation reduced the catalyst's crystallinity, surface area, and the number of basic sites.

The variation of the metal loading usually causes changes in the degree of metal dispersion. Thus, low metal loadings will lead to high dispersion, even reaching atomic dispersion, while the use of high metal contents will lead to catalysts with larger metal nanoparticles or clusters. The presence of the metal in the form of dispersed atoms or as nanoparticles was demonstrated to play a role in the final activity in catalysts based on Rh [69, 70], Ru [71], Ni [72], and Pd [73]. The results point out that much smaller metallic crystallites present higher selectivity towards CO, while larger crystallites, achieved with higher metallic loading, increase the selectivity towards CH_4 (**Figure 1.21**) [73].

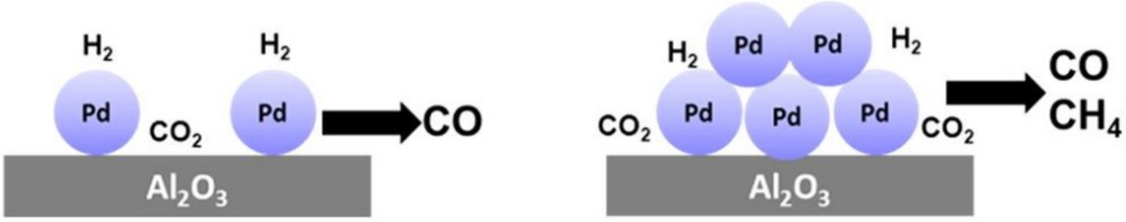

Figure 1.21. Metallic particle size influence on the CO_2 methanation selectivity towards the products. Smaller particles generally present more selectivity towards CO formation, while larger ones to CH_4 formation. Image adapted from Kwak et al. [73].

1.5.6– Promoter's addition influence

An auspicious approach to enhance the catalytic efficiency and endurance of catalysts involves incorporating promoters or additives, which bolster the resistance of catalysts to sintering and coking. Promoters are commonly classified into two groups, namely chemical and textural.

Chemical promoters are employed to increase the number of active sites that improve the electronic properties, including basicity and redox properties. On the other hand, textural promoters are typically utilized to impede and prevent sintering by boosting the textural properties. Usually, alkali and alkaline earth metals, transition metals, and metal oxides are used as promoters in this class.

Petala et al. reported a Ru/TiO_2 catalyst promoted with many alkali metals, and among these, the Na-promoted catalyst exhibited a catalytic performance approximately three times higher than that of the unpromoted Ru/TiO_2 [74]. This enhanced activity was attributed to the improved interaction between the small Na^+ cations and the TiO_2 surface, creating additional active sites for the reactants to bind.

Adding CeO_2 as a promoter is another common strategy to enhance catalytic activity, and several studies have explored CeO_2-promoted catalysts [75-77]. For instance, Liu et al. used an Al_2O_3 catalyst with CeO_2 as a promoter and found that the catalytic activity was sensitive to the amount of CeO_2 [78]. The catalyst with 2% wt. CeO_2 showed the highest catalytic activity and thermal stability, which was linked to the high reducibility of the Ni nanoparticles. CeO_2 addition lowered the reduction temperature and enhanced the catalyst's overall reducibility by altering the interaction between Al_2O_3 and the Ni phase.

1.5.7 – Reaction mechanism

To advance the development of state-of-the-art catalysts for CO_2 methanation, it is essential to thoroughly investigate the underlying reaction mechanism. Although the reaction appears stoichiometrically simple, uncertainties remain about the nature and role of intermediate surface species involved in methane formation. Understanding these intermediates is crucial for optimizing catalyst performance and improving the efficiency of the methanation process [79]. The mechanism pathways can be classified as follows and are summarized in **Figure 1.22**.

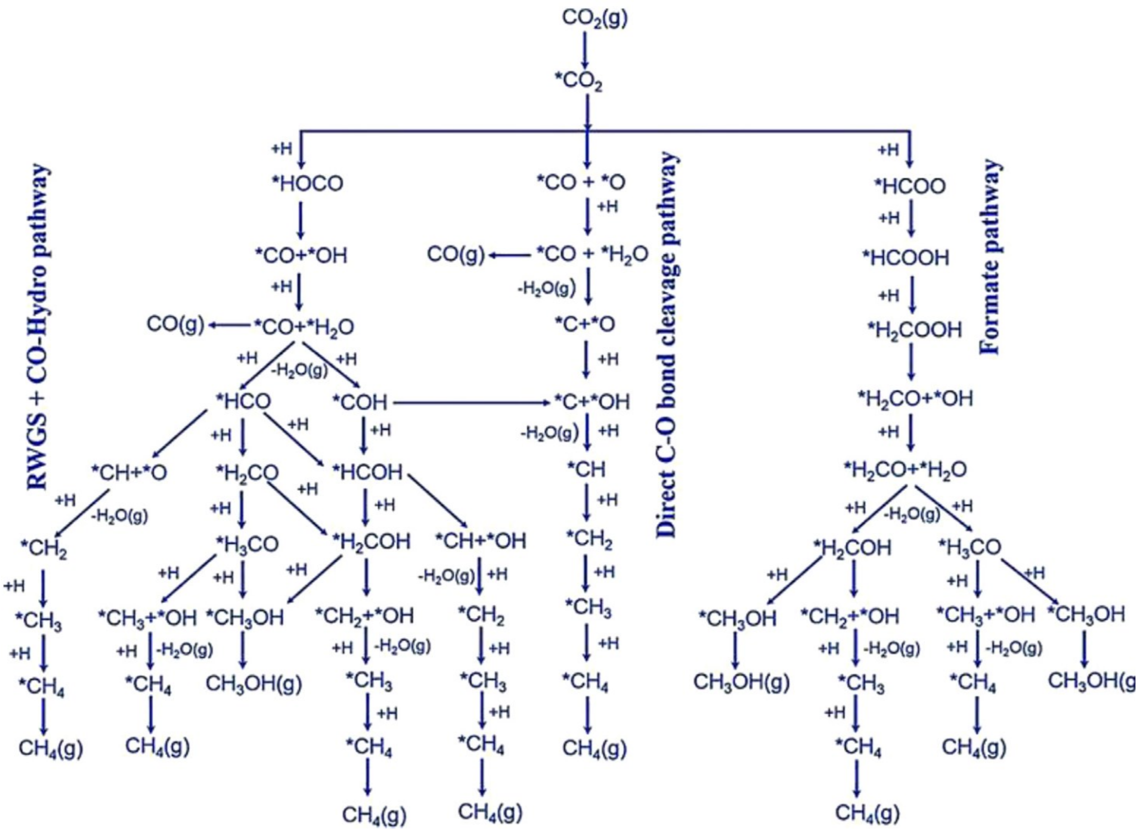

Figure 1.22. Diagram depicting the reaction mechanistic pathways of CO_2 hydrogenation forming different products depending on the degree of hydrogenation. (*) refers to adsorbed surface species. Image adapted from Kattel et al. [36].

(i) the <u>dissociative mechanism</u>, which involved the break-up of the C=O bond during the initial steps of the mechanism.

(ii) the <u>associative mechanism</u>, also known as the formate pathway, involves forming carboxylate species, such as formate, through the CO_2 C-extremity hydrogenation.

(iii) Reverse water gas shift pathway coupled with CO hydro pathway, which involves the hydrogenation of the CO_2 O-extremity to COOH species.

The presence of various active sites plays a key role in facilitating the activation of the reactants, leading to the formation of expected products through various intermediate species. Recent in situ and operando studies, making a cross-section panorama between experimental and theoretical results, have provided valuable insights into the reaction intermediates and the elementary steps. These studies help clarify the complex mechanisms at play, contributing to the design of more efficient catalysts [80].

(i) the dissociative mechanism

Via this pathway, the activated CO_2 molecule, CO_2*, dissociates into CO* and O*, which can further evolve to elemental carbon species (*C), that can be hydrogenated to CH_4 by H species present on the surface of the metallic phase. The *O species, on the other hand, can react with hydrogen to produce H_2O.

By using in-situ operando DRIFTS, Cerdá-Moreno et al. observed that this pathway is observed in Ni catalysts prepared over the sepiolite clay. They reported that in this system, not only monobonded but also bridge-bonded Ni^0-CO species were participating species in the CH_4 formation [81].

Bukhari et al. reported that in a Ni/SBA-15 catalyst, the mechanism also followed the dissociative pathway, with the observation that the CO^* species were reduced to CH_4 by the adsorbed H species [82].

Similarly, Eckle et al. performed a study based on an isotopic exchange using $^{12}CO_2$ and $^{13}CO_2$ to study the reaction intermediates on Ru catalysts on Al_2O_3, under H_2-rich atmospheric pressure conditions by DRIFTS [83]. When the reactants feed was switched from $^{12}CO_2$ to $^{13}CO_2$, the intensity of the $^{12}CO_{(ads)}$ peak reduced, accompanied by an equivalent increase in the $^{13}CO_{(ads)}$ band, indicating that carbonyl is formed by a dissociative pathway in this catalytic system.

On the other hand, during the isotope exchange experiments, the band intensity of the formate bands did not change significantly, suggesting that these species were spectators during the methanation steps.

(ii) the associative mechanism

Through the associative mechanism, the CO_2 species are converted into formates (HCOO) and, eventually, to formic acid (HCOOH), which is ultimately transformed into CH_4.

In the literature, several authors published that the reaction follows the formate pathway in Ni-catalysts supported over different supports, such as MgO [84], Al_2O_3 [85], Y_2O_3[86], ZrO_2 [87], and USY zeolite [88]. Aldana et al. reported that the associative pathway was the main one followed by a CeO_2-ZrO_2 catalyst [89].

Operando FTIR spectra revealed the formation of adsorbed carbonates and carbonyls over the Ni^0 phase, as seen in **Figure 1.23**. When the temperature was increased, the carbonate species were hydrogenated to bicarbonate, which quickly dehydrated to formate, while the CO_{ad} bands did not change significantly.

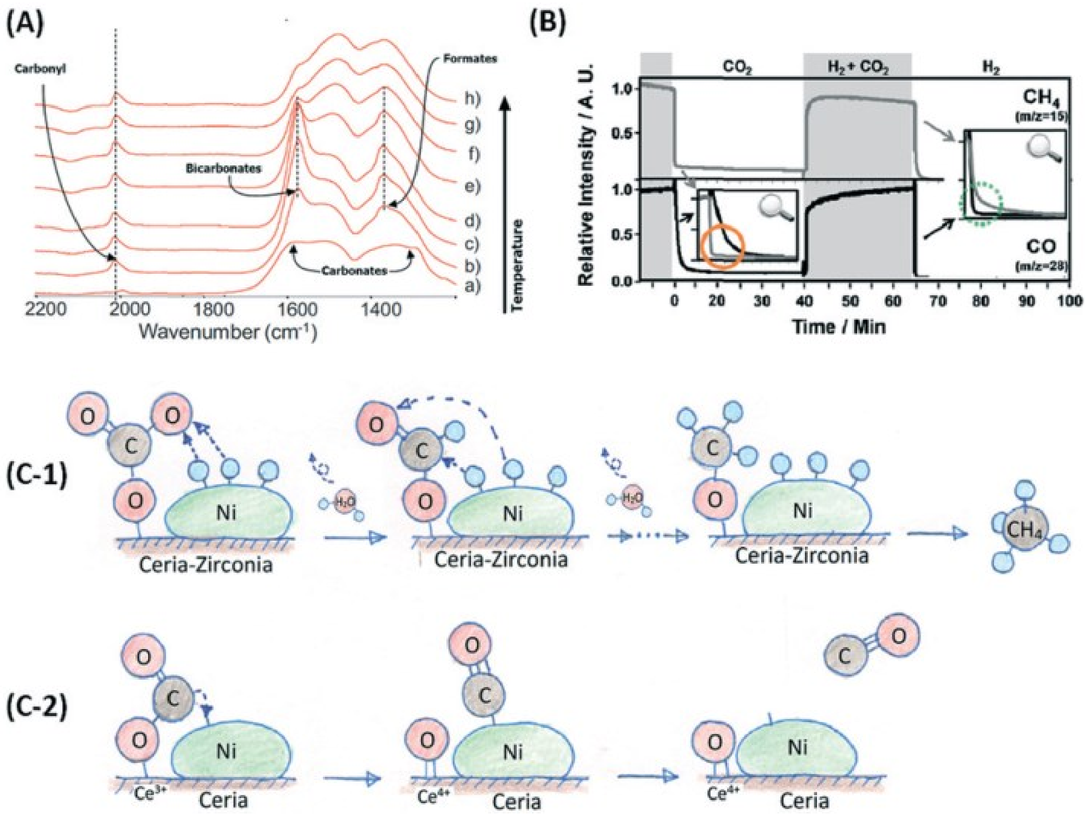

Figure 1.23. (a) Operando DRIFTS-IR spectra obtained for CO_2 hydrogenation catalytic system based on Ni-CeO_2-ZrO_2. CH_4 is formed by the associative mechanism with bicarbonates and carbonates as intermediates. (b) Transient experiments at 400 °C on the same systems analyzing CH_4 and CO formation when inlet composition was altered; and proposed mechanistic pathways for the formation of (c1) CH_4 and (c2) CO. Image adapted from Aldana et al. [89].

Transient experiment with alternate inlet gas compositions, as seen in **Figure 1.23**(b) revealed an immediate stop in CH_4 formation when H_2 was removed from the inlet flow. There was also an immediate stop in CO formation, when CO_2 was removed from the inlet flow. This confirmed that CH_4 was mainly formed by an associative mechanism at the oxide-metal interface, while CO was formed by CO_2 disassociation over the support, as seen in **Figure 1.23** (c1) and (c2).

In a mechanistic study based on in-situ IR studies, Pan et al. compared the reaction pathway on Ni catalysts supported in γ-Al_2O_3 and $Ce_{0.5}Zr_{0.5}O_2$. They observed that the second one exhibited higher TOF and conversion values [90]. Taking into account the spectroscopic results, this was attributed to the fact that on the Ni/$Ce_{0.5}Zr_{0.5}O_2$ system, CO_2 adsorption takes place on intermediate basicity sites, forming monodentate carbonates that undergo hydrogenation at a lower activation energy cost than the species formed Ni/γ-Al_2O_3, which presented more basic sites. Their results seem to confirm that the moderate basicity sites enhance reaction performance the most.

Generally, the intermediate species and steps involved can vary across different systems, largely influenced by the active metal properties, supports, and synergic interactions. Although the exact mechanism of CO_2 methanation remains a subject of ongoing debate, considerable progress has been made in understanding the reaction pathways. In situ or operando DRIFTS and DFT (Density Functional Theory) calculations have provided new insights, offering novel perspectives on catalyst design for CO_2 methanation. These advanced techniques have deepened the comprehension of the reaction mechanisms, paving the way for developing more effective catalysts.

1.5.8 – Pilot plants and upgrade projects

A major obstacle to the large-scale industrial adoption of CO_2 methanation is securing a reliable supply of renewable hydrogen, an essential input for the process. However, as renewable energy becomes increasingly competitive compared to fossil fuels, renewable hydrogen production costs are expected to decrease, making CO_2 methanation more economically viable (**Figure 1.24**).

Considering the international agreements and regulations aimed at protecting the environment, including those set by the United Nations in the Paris Agreement [91-93], there is a significant opportunity for catalytic CO_2 methanation to help mitigate the emission of this gas and meet energy demands. The European Union (EU) aims to achieve carbon neutrality by 2050, a central objective of the European Green Deal [91], an initiative that spurred the development of a whole economic ecosystem for companies seeking to achieve decarbonization goals, as the prices of renewable energies become increasingly competitive.

Companies such as Audi, Siemens, and Shell are investing in this technology, with Audi developing a pilot plant in Germany that uses CO_2 methanation to produce renewable SNG from surplus renewable electricity. The plant is located in Werlte in Lower Saxony, and has a capacity of 6.3 MW, making it one of the largest of its kind in the world. The process involves producing green hydrogen by electrolysis, combined with carbon dioxide captured from a nearby biogas plant, forming methane and increasing the concentration of this gas in the biogas flow.

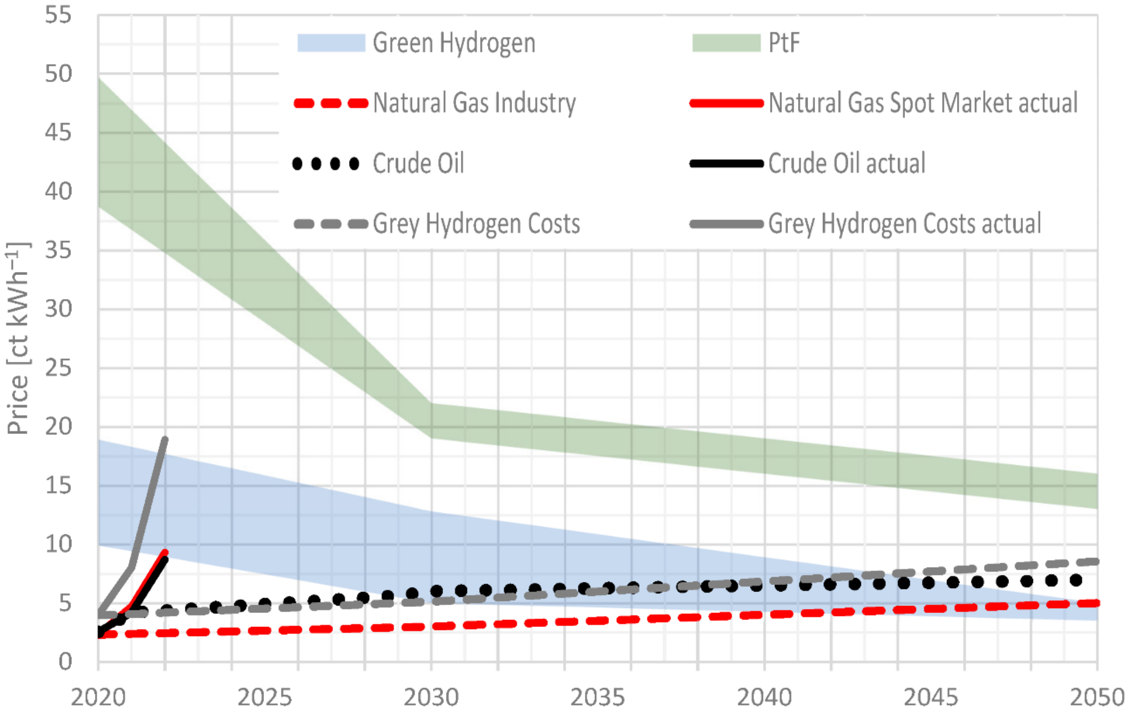

Figure 1.24. Projected costs of green H_2 and synthetic fuels (obtained from Power to Fuel – PtF) until 2050 compared to anticipated trends in grey H_2, industrial natural gas prices, and crude oil rates (dashed lines). The solid lines illustrate the current price trajectories for grey H_2, natural gas, and crude oil. Image adapted from Schnuelle et al. [92].

In another initiative, the Karlsruhe Institute of Technology (KIT), in Germany, in collaboration with the EU's Seventh Framework Program, has developed an industrial-scale plant for CO_2 methanation [93]. This project involves integrating an exothermic methanation plant with an endothermic electrolysis system, resulting in a more efficient hydrogen generation process than traditional water electrolysis, with an efficiency 85% higher than uncoupled processes (**Figure 1.25**).

Another area of interest in the utilization of the CO_2 methanation reaction is in cement or steel production. Companies such as Thyssenkrupp and Salzgitter are exploring the use of it to reduce emissions from their steel production processes [94]. Thyssenkrupp is developing a pilot project called Carbon2Chem, aiming to achieve the economic feasibility of using the reaction to reduce emissions from steel production. The project involves capturing CO_2 emissions and converting them into CH_4 or other chemicals, using green H_2, and using the produced CH_4 directly as a fuel for the own production process, reducing the need for coal to keep the blast furnaces on.

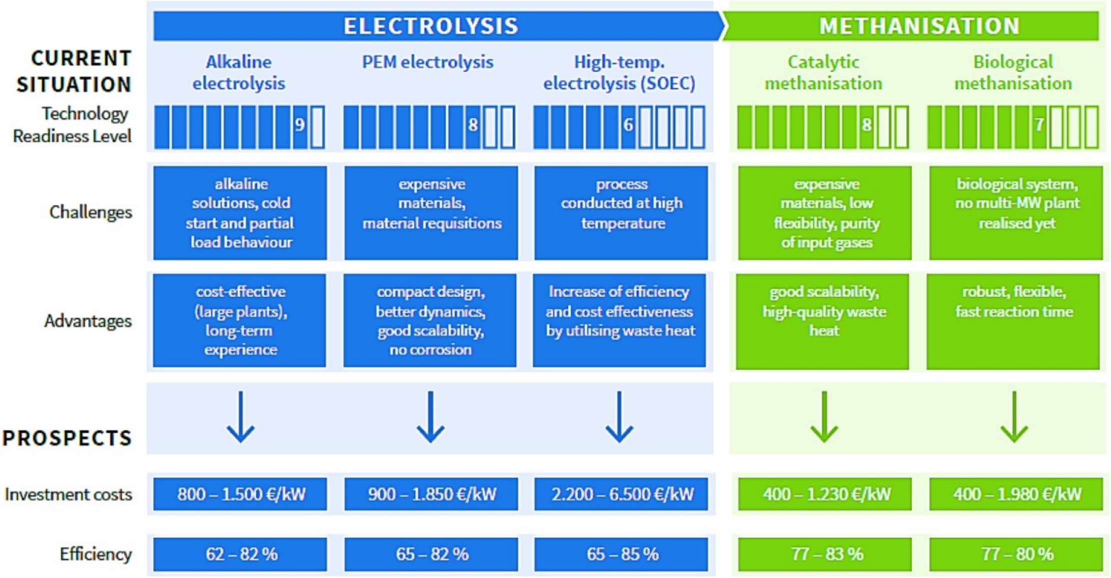

	ELECTROLYSIS			METHANISATION	
CURRENT SITUATION	Alkaline electrolysis	PEM electrolysis	High-temp. electrolysis (SOEC)	Catalytic methanisation	Biological methanisation
Technology Readiness Level	9	8	6	8	7
Challenges	alkaline solutions, cold start and partial load behaviour	expensive materials, material requisitions	process conducted at high temperature	expensive materials, low flexibility, purity of input gases	biological system, no multi-MW plant realised yet
Advantages	cost-effective (large plants), long-term experience	compact design, better dynamics, good scalability, no corrosion	Increase of efficiency and cost effectiveness by utilising waste heat	good scalability, high-quality waste heat	robust, flexible, fast reaction time
PROSPECTS					
Investment costs	800 – 1.500 €/kW	900 – 1.850 €/kW	2.200 – 6.500 €/kW	400 – 1.230 €/kW	400 – 1.980 €/kW
Efficiency	62 – 82 %	65 – 82 %	65 – 85 %	77 – 83 %	77 – 80 %

Figure 1.25. Current situation features and prospects for implementation of methanization-based technologies. Images adapted from Hussain [95].

In the energy sector, CO_2 methanation is being considered to store renewable energy in the form of methane. This is particularly relevant for regions with high renewable energy penetration, where excess renewable energy may not be directly used or stored in batteries [96-98]. Companies, such as E.ON and RWE are exploring using CO_2 methanation for energy storage and grid balancing.

Furthermore, there are several startups and smaller companies that are focusing on CO_2 methanation technology, such as Electrochaea, Sunfire, and Carbon Clean Solutions [99]. These companies are developing innovative approaches to CO_2 methanation, such as using biogenic CO_2 as a feedstock or integrating CO_2 methanation with other processes, such as biogas upgrading.

Overall, there is a growing interest and investment in CO_2 methanation technology, with companies and industrial sectors exploring its potential. As the technology develops and costs decrease, further investment will likely occur.

1.5.9 – Biogas upgrade

Biogas is a renewable fuel generated from the anaerobic decomposition of organic feedstocks such as food waste, farm waste, municipal waste, and energy crops. Generally, biogas contains CH_4 (50-75%), CO_2 (25-50%), and trace amounts of N_2 (2-8%). Additionally, the composition of biogas varies depending on the feedstock, and it contains small quantities of H_2S, NH_3, H_2, and various other volatile organic compounds, such as siloxanes [100].

During the natural decomposition of organic waste, harmful methane emissions are produced. However, if the waste is collected and processed through anaerobic digestion, these emissions can be prevented, and the waste can be converted into valuable green resources. These resources include natural fertilizers, bio-products, and biogas. The biogas obtained during this step, after purification procedures as it will be discussed, can be used as a source of energy, providing an alternative to the extraction and use of fossil fuels in a win-win strategy [101]. The direct emission of CH_4 (whose global warming potential is 20 times higher than CO_2) is prevented, while carbon is taken back to the natural carbon cycle, contributing to defossilization efforts, as seen in **Figure 1.26**.

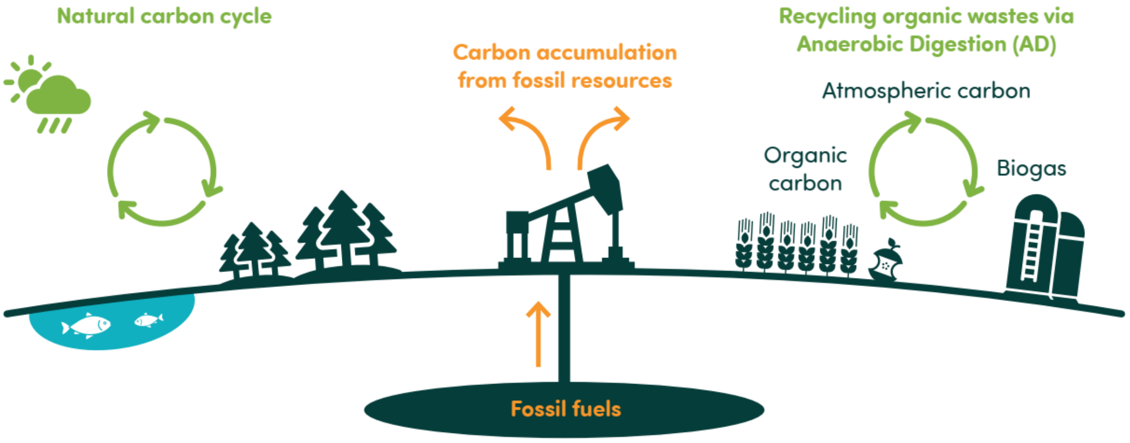

Figure 1.26. Schematic representation on how biogas anaerobic digestion provides a strategy to reduce the emission of atmospheric carbon, as part of the defossilization efforts by providing an energy alternative to fossil fuels obtained from the decomposition of organic matter. Image adapted from Biogas Report provided by the World Biogas Association [102].

Biogas contains energy in the form of methane, but some of the other components previously mentioned limit its application as a fuel, as they cause corrosion on metallic parts and, reduce its calorific value, and are also hazardous to human health upon exposure.

These adverse effects of biogas contaminants can be avoided by upgrading biogas to remove the pollutants through a series of processes known as biogas upgrading [100]. The concentrated biogas obtained after the purification steps, whose CH_4 concentration is close to 100%, is called ‘biomethane’ or ‘renewable natural gas’ (RNG) [102] and can be used as a renewable fuel in different applications (**Figure 1.27**).

One application is electricity and heat generation in combined heat and power systems, enhancing the total efficiency of the process. In this setup, RNG is combusted in an engine or turbine to generate electricity, while the residual heat from the process is utilized for space or water heating.

RNG can also be used as transportation fuel, as it is similar to traditional natural gas and can be directly employed in vehicles as compressed natural gas (CNG) or converted to liquefied natural gas (LNG) for use in heavy-duty vehicles. Furthermore, RNG might also find an application as cooking fuel in households or small businesses, which can be reached by using the preexisting distribution gas grid, providing a clean and efficient alternative to traditional cooking fuels such as wood, charcoal, or kerosene.

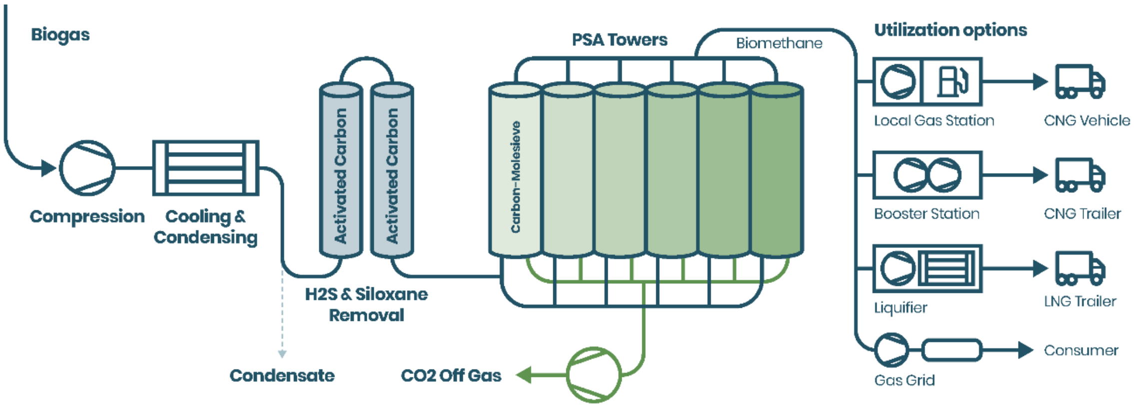

Figure 1.27. Schematic representation of the steps taken during upgrading biogas to remove impurities and possible utilization options for the purified biogas version. Image adapted from Ryckebosch et al. [100].

As of 2020, the global production of biogas was approximately 80 billion cubic meters (bcm) per year, and according to some IEA projections, these numbers are expected to increase by almost 50% by 2030, reaching a total of 120 bcm per year, even though the same reports point that the global technical potential for biogas production is approximately 260 bcm per year [102].

According to the same IEA projections [103], with the biogas production growth perspective around the world, biogas could provide an important alternative to the commonly used natural gas and, together with other related low-carbon footprint energy sources, could take more than 25% of global gas energy demands, as seen in **Figure 1.28**.

Overall, the potential economic benefits of biogas production and use are significant, with estimates ranging from billions to trillions of dollars. A report by the World Biogas Association (WBA) in 2021 estimated that the global biogas market could cut GHGs emissions by 10% by 2023 and be worth $50 billion by 2025, driven by increased demand for renewable energy and government incentives to reduce greenhouse gas emissions [104]. An even more ambitious report from the IEA published in 2022 estimated that biogas could contribute up to 12% of the world's total energy supply from biofuels by 2040, a potential market value of over USD 500 billion.

As governments and businesses continue to prioritize renewable energy and decarbonization efforts, the demand for biogas as an energy source is expected to increase, further driving the growth and economic potential of the industry [103].

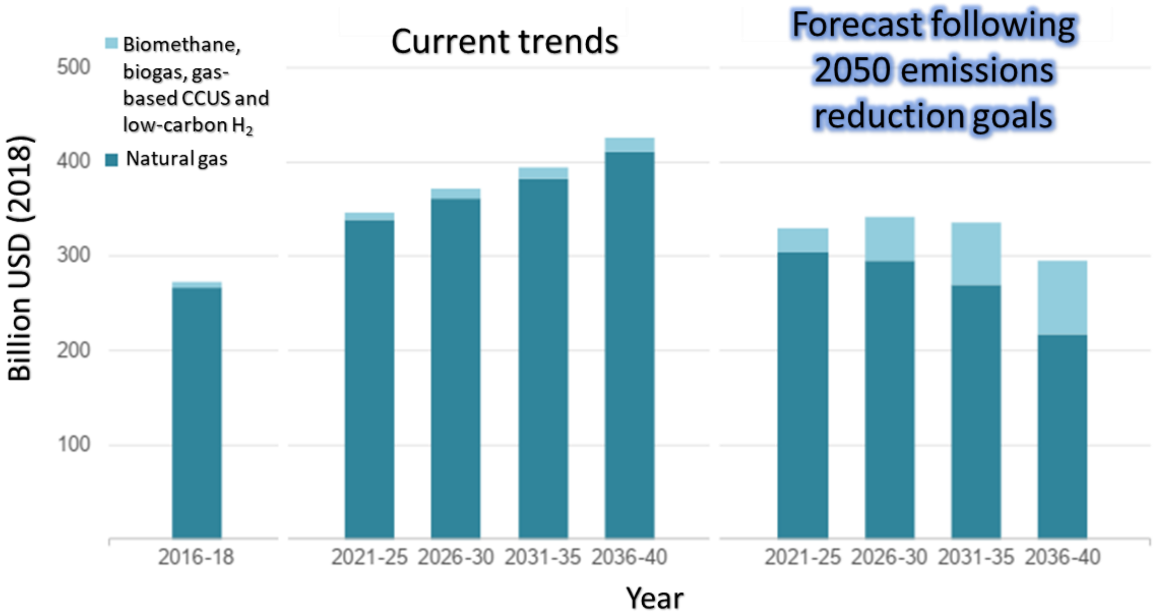

Figure 1.28. Average annual investment in gas as an energy source in different scenarios until 2040. Image adapted from IEA report "Outlook for biogas and biomethane" [102].

The WBA reports also reveal that the most considerable growth in biogas production is projected in Asia, with China leading the way. However, Europe, North America, India, and Brazil are also expected to see significant growth in biogas production.

According to the same report, China is expected to be a significant player in this market too, as they set a target to increase objective regarding their overall energy mix to reach a percentage of 20% of non-fossil fuel energy by 2030, which will have an impact on the growth of the biogas market.

Brazil is a major biogas producer as a renewable energy source and one of the largest in the world in 2020. According to the IEA, Brazil had an estimated biogas production of 6.4 billion cubic meters (bcm), resulting from a well-developed agricultural sector that allows biogas production from livestock waste and sugarcane bagasse. In addition, Brazil has implemented policies and programs to promote biogas production and use, including tax incentives, financing programs, and renewable energy auctions [105].

The European Union (EU) has outlined bold objectives to boost the adoption of renewable energy sources, including biogas, as a critical component of its strategy to address climate change and curb greenhouse gas emissions. In 2023, the Biomethane Industrial Partnership (BIP) was launched by the European Commission and industry leaders committed to the transition towards green energy. This public-private partnership is part of the REPowerEU Plan, and its aim is to support the goal of increasing the annual production and usage of biomethane to 35 billion cubic meters by 2030 [106]. The initiative is anticipated to decrease Europe's reliance on natural gas imports from Russia, particularly in light of the international economic sanctions declared during the escalation of the Russo-Ukrainian War (2014-present) that restricted the amount of imported natural gas.

Therefore, inside this context, instead of the biogas upgrading approaches, a new one is considered in this study. Even though the purification steps to remove hazardous contaminants, such as H_2S and NH_3, are still necessary, the main difference relies on the fact that, instead of throwing away CO_2, this gas is converted into CH_4 in catalytic reactors by the methanation reaction, increasing the concentration of CH_4 in the gas flow. Using green hydrogen from renewable sources, CO_2 would be hydrogenated to CH_4 in an industrial unit set to perform the exothermic reaction, whose excess energy would be coupled to an electrolysis unit operating the endothermic process of water electrolysis.

Then, taking into account this whole panorama presented in this chapter and the importance of finding new sustainable energy sources alternative to the current model, this thesis will discuss the development of new catalytic materials based on nickel deposited in different supports for improving and optimizing the CO_2 methanation reaction and its application for biogas upgrading.

Chapter 2 will present the work objectives. Chapter 3 will present the methodology and experimental procedures used to prepare, study, and characterize the catalysts. Chapters 4 to 7 will provide a more thorough discussion of each one of the different classes of catalysts studied. Chapter 8 will present the catalytic test with simulated biogas samples, discussing the possibility of application of these catalytic systems for actual application for biogas upgrading. Finally, Chapter 9 will present the general conclusion of this work.

1.6 – References

[1] Lee HR, J. Climate Change 2023: Synthesis Report. Geneva, Switzerland2023. p. IPCC.

[2] Masson-Delmotte VZ, P.; Pirani, A.; Connors, S. L; Péan, C.; Berger, S.; Caud, N.; Chen, Y.; Goldfarb, L. Gomis, M. I. IPCC Climate Change 2021 AR6: The Physical Science Basis. 2021.

[3] Costanza R. Climate adaptation: Hold atmosphere in trust for all. Nature. 2016;529:466.

[4] Lenssen NJL, Schmidt GA, Hansen JE, Menne MJ, Persin A, Ruedy R, et al. Improvements in the GISTEMP Uncertainty Model. Journal of Geophysical Research: Atmospheres. 2019;124:6307-26.

[5] Dietz S, Venmans F. Cumulative carbon emissions and economic policy: In search of general principles. Journal of Environmental Economics and Management. 2019;96:108-29.

[6] Thomas CES. Greenhouse gases by sector. Lecture Notes in Energy2017. p. 9-11.

[7] Friedlingstein P, et al. Global Carbon Budget 2022. Earth System Science Data. 2022;14:4811-900.

[8] Deivanayagam TA, English S, Hickel J, Bonifacio J, Guinto RR, Hill KX, et al. Envisioning environmental equity: climate change, health, and racial justice. The Lancet. 2023;402:64-78.

[9] Ritchie HR, P.; Roser M. CO_2 and Greenhouse Gas Emissions. Our World in Data. 2023.

[10] Nobles M, Womack C, Wonkam A, Wathuti E. Ending racism is key to better science: a message from Nature's guest editors. Nature. 2022;610:419-20.

[11] Burke M, Hsiang SM, Miguel E. Global non-linear effect of temperature on economic production. Nature. 2015;527:235-9.

[12] Hubacek K, Chen X, Feng K, Wiedmann T, Shan Y. Evidence of decoupling consumption-based CO2 emissions from economic growth. Advances in Applied Energy. 2021;4:100074.

[13] Ward Jones MK, Schwoerer T, Gannon GM, Jones BM, Kanevskiy MZ, Sutton I, et al. Climate-driven expansion of northern agriculture must consider permafrost. Nature Climate Change. 2022;12:699-703.

[14] Onar NF, Nicolaïdis K. The Decentring Agenda: Europe as a post-colonial power. Cooperation and Conflict. 2013;48:283-303.

[15] Wade RH. Emerging world order? from multipolarity to multilateralism in the g20, the world bank, and the imf. Politics and Society. 2011;39:347-78.

[16] Wilkens J, Datchoua-Tirvaudey ARC. Researching climate justice: a decolonial approach to global climate governance. International Affairs. 2022;98:125-43.

[17] Menton M, Larrea C, Latorre S, Martinez-Alier J, Peck M, Temper L, et al. Environmental justice and the SDGs: from synergies to gaps and contradictions. Sustainability Science. 2020;15:1621-36.

[18] Stein S. The Ethical and Ecological Limits of Sustainability: A Decolonial Approach to Climate Change in Higher Education. Australian Journal of Environmental Education. 2019;35:198-212.

[19] Fawcett AA, Iyer GC, Clarke LE, Edmonds JA, Hultman NE, McJeon HC, et al. Can Paris pledges avert severe climate change? Science. 2015;350:1168-9.

[20] UNFCCC. Synthesis report - Nationally determined contributions under the Paris Agreement. UN Climate Change Conference. 2023.

[21] Centi G, Quadrelli EA, Perathoner S. Catalysis for CO2 conversion: a key technology for rapid introduction of renewable energy in the value chain of chemical industries. Energy & Environmental Science. 2013;6:1711-31.

[22] Zheng Y, Wang J, Yu B, Zhang W, Chen J, Qiao J, et al. A review of high temperature co-electrolysis of H2O and CO2 to produce sustainable fuels using solid oxide electrolysis cells (SOECs): advanced materials and technology. Chemical Society Reviews. 2017;46:1427-63.

[23] Hussain I, Jalil AA, Hassan NS, Hamid MYS. Recent advances in catalytic systems for CO2 conversion to substitute natural gas (SNG): Perspective and challenges. Journal of Energy Chemistry. 2021;62:377-407.

[24] Gao J, Wang Y, Ping Y, Hu D, Xu G, Gu F, et al. A thermodynamic analysis of methanation reactions of carbon oxides for the production of synthetic natural gas. RSC Advances. 2012;2:2358-68.

[25] Miguel CV, Soria MA, Mendes A, Madeira LM. Direct CO2 hydrogenation to methane or methanol from post-combustion exhaust streams - A thermodynamic study. Journal of Natural Gas Science and Engineering. 2015;22:1-8.

[26] Tripodi A, Conte F, Rossetti I. Carbon Dioxide Methanation: Design of a Fully Integrated Plant. Energy and Fuels. 2020;34:7242-56.

[27] Poutsma ML, Elek LF, Ibarbia PA, Risch AP, Rabo JA. Selective formation of methanol from synthesis gas over palladium catalysts. Journal of Catalysis. 1978;52:157-68.

[28] Vannice MA. The Catalytic Synthesis of Hydrocarbons from Carbon Monoxide and Hydrogen. Catalysis Reviews. 2006;14:153-91.

[29] Mills GA, Steffgen FW. Catalytic Methanation. Catalysis Reviews - Science and Engineering. 2006;8:159-210.

[30] Martin NM, Velin P, Skoglundh M, Bauer M, Carlsson PA. Catalytic hydrogenation of CO2 to methane over supported Pd, Rh and Ni catalysts. Catalysis Science & Technology. 2017;7:1086-94.

[31] Park JY, Krauthammer T. Development of an LEFM dynamic crack criterion for correlated size and rate effects in concrete beams. International Journal of Impact Engineering. 2009;36:92-7.

[32] Weatherbee GD, Bartholomew CH. Hydrogenation of CO2 on group VIII metals: IV. Specific activities and selectivities of silica-supported Co, Fe, and Ru. Journal of Catalysis. 1984;87:352-62.

[33] Winter LR, Gomez E, Yan B, Yao S, Chen JG. Tuning Ni-catalyzed CO2 hydrogenation selectivity via Ni-ceria support interactions and Ni-Fe bimetallic formation. Applied Catalysis B: Environmental. 2018;224:442-50.

[34] Zhu J, Zhang G, Li W, Zhang X, Ding F, Song C, et al. Deconvolution of the Particle Size Effect on CO2Hydrogenation over Iron-Based Catalysts. ACS Catalysis. 2020;10:7424-33.

[35] Chen X, Su X, Liang B, Yang X, Ren X, Duan H, et al. Identification of relevant active sites and a mechanism study for reverse water gas shift reaction over Pt/CeO2 catalysts. Journal of Energy Chemistry. 2016;25:1051-7.

[36] Kattel S, Yan B, Chen JG, Liu P. CO2 hydrogenation on Pt, Pt/SiO2 and Pt/TiO2: Importance of synergy between Pt and oxide support. Journal of Catalysis. 2016;343:115-26.

[37] Kim SS, Lee HH, Hong SC. A study on the effect of support's reducibility on the reverse water-gas shift reaction over Pt catalysts. Applied Catalysis A: General. 2012;423-424:100-7.

[38] Qiu M, Tao H, Li Y, Zhang Y. Insight into the mechanism of CO2 and CO methanation over Cu(100) and Co-modified Cu(100) surfaces: A DFT study. Applied Surface Science. 2019;495:143457.

[39] Beuls A, Swalus C, Jacquemin M, Heyen G, Karelovic A, Ruiz P. Methanation of CO2: Further insight into the mechanism over Rh/γ-Al2O3 catalyst. Applied Catalysis B: Environmental. 2012;113-114:2-10.

[40] Martin NM, Hemmingsson F, Wang X, Merte LR, Hejral U, Gustafson J, et al. Structure–function relationship during CO2 methanation over Rh/Al2O3 and Rh/SiO2 catalysts under atmospheric pressure conditions. Catalysis Science & Technology. 2018;8:2686-96.

[41] Mutschler R, Moioli E, Luo W, Gallandat N, Züttel A. CO2 hydrogenation reaction over pristine Fe, Co, Ni, Cu and Al2O3 supported Ru: Comparison and determination of the activation energies. Journal of Catalysis. 2018;366:139-49.

[42] Petala A, Panagiotopoulou P. Methanation of CO2 over alkali-promoted Ru/TiO2 catalysts: I. Effect of alkali additives on catalytic activity and selectivity. Applied Catalysis B: Environmental. 2018;224:919-27.

[43] Parastaev A, Muravev V, Osta EH, Kimpel TF, Simons JFM, van Hoof AJF, et al. Breaking structure sensitivity in CO2 hydrogenation by tuning metal–oxide interfaces in supported cobalt nanoparticles. Nature Catalysis. 2022;5:1051-60.

[44] Gholampour N, Zhao Y, Devred F, Sassoye C, Casale S, Debecker DP. CO2 Methanation over Cobalt Nanoparticles Embedded in ZIF-L–Derived Porous Carbon. ChemCatChem. 2023;15:e202201338.

[45] Wang W, Duong-Viet C, Truong-Phuoc L, Nhut J-M, Vidal L, Pham-Huu C. Activated carbon supported nickel catalyst for selective CO2 hydrogenation to synthetic methane under contactless induction heating. Catalysis Today. 2023;418:114073-.

[46] Schumacher J, Meyer D, Friedland J, Güttel R. Methanation of CO/CO2mixtures: Evaluation of pellet size effect on methane formation rate and reactant selectivity. Chemical Engineering Journal. 2023:142451-.

[47] Bligaard T, Nørskov JK, Dahl S, Matthiesen J, Christensen CH, Sehested J. The Brønsted–Evans–Polanyi relation and the volcano curve in heterogeneous catalysis. Journal of Catalysis. 2004;224:206-17.

[48] Lausche AC, Medford AJ, Khan TS, Xu Y, Bligaard T, Abild-Pedersen F, et al. On the effect of coverage-dependent adsorbate-adsorbate interactions for CO methanation on transition metal surfaces. Journal of Catalysis. 2013;307:275-82.

[49] Liu F, Zhang C, Tang M. The impacts of oil price shocks and jumps on China's nonferrous metal markets. Resources Policy. 2021;73:102228-.

[50] Lee WJ, Li C, Prajitno H, Yoo J, Patel J, Yang Y, et al. Recent trend in thermal catalytic low temperature CO2 methanation: A critical review. Catalysis Today. 2021;368:2-19.

[51] Gao J, Liu Q, Gu F, Liu B, Zhong Z, Su F. Recent advances in methanation catalysts for the production of synthetic natural gas. RSC Advances. 2015;5:22759-76.

[52] Cai M, Wen J, Chu W, Cheng X, Li Z. Methanation of carbon dioxide on Ni/ZrO2-Al2O 3 catalysts: Effects of ZrO2 promoter and preparation method of novel ZrO2-Al2O3 carrier. Journal of Natural Gas Chemistry. 2011;20:318-24.

[53] Zheng Q, Farrauto R, Chau Nguyen A. Adsorption and Methanation of Flue Gas CO2 with Dual Functional Catalytic Materials: A Parametric Study. Industrial and Engineering Chemistry Research. 2016;55:6768-76.

[54] Liu J, Li C, Wang F, He S, Chen H, Zhao Y, et al. Enhanced low-temperature activity of CO2 methanation over highly-dispersed Ni/TiO2 catalyst. Catalysis Science & Technology. 2013;3:2627-33.

[55] Tada S, Shimizu T, Kameyama H, Haneda T, Kikuchi R. Ni/CeO2 catalysts with high CO2 methanation activity and high CH4 selectivity at low temperatures. International Journal of Hydrogen Energy. 2012;37:5527-31.

[56] Jia X, Zhang X, Rui N, Hu X, Liu Cj. Structural effect of Ni/ZrO2 catalyst on CO2 methanation with enhanced activity. Applied Catalysis B: Environmental. 2019;244:159-69.

[57] Da Silva DCD, Letichevsky S, Borges LEP, Appel LG. The Ni/ZrO2 catalyst and the methanation of CO and CO2. International Journal of Hydrogen Energy. 2012;37:8923-8.

[58] Lu B, Ju Y, Abe T, Kawamoto K. Grafting Ni particles onto SBA-15, and their enhanced performance for CO 2 methanation †. RSC Advances. 2015:56444-54.

[59] Bacariza MC, Spataru D, Karam L, Lopes JM, Henriques C. Promising catalytic systems for CO2 hydrogenation into CH4: A review of recent studies. Processes. 2020;8:1-45.

[60] Bando KK, Soga K, Kunimori K, Ichikuni N, Okabe K, Kusama H, et al. CO2 hydrogenation activity and surface structure of zeolite-supported Rh catalysts. Applied Catalysis A: General. 1998;173:47-60.

[61] Aziz MAA, Jalil AA, Triwahyono S, Ahmad A. CO2 methanation over heterogeneous catalysts: Recent progress and future prospects. Green Chemistry. 2015;17:2647-63.

[62] Guo X, Traitangwong A, Hu M, Zuo C, Meeyoo V, Peng Z, et al. Carbon Dioxide Methanation over Nickel-Based Catalysts Supported on Various Mesoporous Material. Energy and Fuels. 2018;32:3681-9.

[63] Zhen W, Li B, Lu G, Ma J. Enhancing catalytic activity and stability for CO2 methanation on Ni@MOF-5 via control of active species dispersion. Chemical Communications. 2015;51:1728-31.

[64] Lippi R, Howard SC, Barron H, Easton CD, Madsen IC, Waddington LJ, et al. Highly active catalyst for CO2 methanation derived from a metal organic framework template. Journal of Materials Chemistry A. 2017;5:12990-7.

[65] Xu W, Dong M, Di L, Zhang X. A Facile Method for Preparing UiO-66 Encapsulated Ru Catalyst and its Application in Plasma-Assisted CO2 Methanation. Nanomaterials 2019, Vol 9, Page 1432. 2019;9:1432-.

[66] Li W, Zhang A, Jiang X, Chen C, Liu Z, Song C, et al. Low Temperature CO2 Methanation: ZIF-67-Derived Co-Based Porous Carbon Catalysts with Controlled Crystal Morphology and Size. ACS Sustainable Chemistry and Engineering. 2017;5:7824-31.

[67] Quindimil A, De-La-Torre U, Pereda-Ayo B, Davó-Quiñonero A, Bailón-García E, Lozano-Castelló D, et al. Effect of metal loading on the CO2 methanation: A comparison between alumina supported Ni and Ru catalysts. Catalysis Today. 2020;356:419-32.

[68] Graça I, González LV, Bacariza MC, Fernandes A, Henriques C, Lopes JM, et al. CO2 hydrogenation into CH4 on NiHNaUSY zeolites. Applied Catalysis B: Environmental. 2014;147:101-10.

[69] Matsubu JC, Yang VN, Christopher P. Isolated metal active site concentration and stability control catalytic CO2 reduction selectivity. Journal of the American Chemical Society. 2015;137:3076-84.

[70] Karelovic A, Ruiz P. CO2 hydrogenation at low temperature over Rh/γ-Al2O3 catalysts: Effect of the metal particle size on catalytic performances and reaction mechanism. Applied Catalysis B: Environmental. 2012;113-114:237-49.

[71] Kwak JH, Kovarik L, Szanyi J. CO2 reduction on supported Ru/Al2O3 catalysts: Cluster size dependence of product selectivity. ACS Catalysis. 2013;3:2449-55.

[72] Wu HC, Chang YC, Wu JH, Lin JH, Lin IK, Chen CS. Methanation of CO2 and reverse water gas shift reactions on Ni/SiO2 catalysts: the influence of particle size on selectivity and reaction pathway. Catalysis Science and Technology. 2015;5:4154-63.

[73] Kwak JH, Kovarik L, Szanyi J. Heterogeneous catalysis on atomically dispersed supported metals: CO 2 reduction on multifunctional Pd catalysts. ACS Catalysis. 2013;3:2094-100.

[74] Petala A, Panagiotopoulou P. Methanation of CO2 over alkali-promoted Ru/TiO2 catalysts: I. Effect of alkali additives on catalytic activity and selectivity. Applied Catalysis B: Environmental. 2018;224:919-27.

[75] Xu Y, Wan H, Du X, Yao B, Wei S, Chen Y, et al. Highly active Ni/CeO2/SiO2 catalyst for low-temperature CO2 methanation: Synergistic effect of small Ni particles and optimal amount of CeO2. Fuel Processing Technology. 2022;236:107418.

[76] Van NTT, Loc LC, Anh NP, Cuong HT, Tri N. Positive effects of CeO2 promoter and Co-reactant/CO on methanation of CO2-rich gas over Ni/SBA-15 catalyst. Materials Transactions. 2020;61:1332-8.

[77] Ahmad KN, Wan Isahak WNR, Rosli MI, Yusop MR, Kassim MB, Yarmo MA. Rare earth metal doped nickel catalysts supported on exfoliated graphitic carbon nitride for highly selective CO and CO2 methanation. Applied Surface Science. 2022;571:151321-.

[78] Liu H, Zou X, Wang X, Lu X, Ding W. Effect of CeO2 addition on Ni/Al2O3 catalysts for methanation of carbon dioxide with hydrogen. Journal of Natural Gas Chemistry. 2012;21:703-7.

[79] Tan CH, Nomanbhay S, Shamsuddin AH, Park YK, Hernández-Cocoletzi H, Show PL. Current Developments in Catalytic Methanation of Carbon Dioxide—A Review. Frontiers in Energy Research. 2022;9:1-8.

[80] Li L, Zeng W, Song M, Wu X, Li G, Hu C. Research Progress and Reaction Mechanism of CO2 Methanation over Ni-Based Catalysts at Low Temperature: A Review. Catalysts. 2022;12:1-24.

[81] Cerdá-Moreno C, Chica A, Keller S, Rautenberg C, Bentrup U. Ni-sepiolite and Ni-todorokite as efficient CO2 methanation catalysts: Mechanistic insight by operando DRIFTS. Applied Catalysis B: Environmental. 2020;264:118546-.

[82] Bukhari SN, Chong CC, Setiabudi HD, Cheng YW, Teh LP, Jalil AA. Ni/Fibrous type SBA-15: Highly active and coke resistant catalyst for CO2 methanation. Chemical Engineering Science. 2021;229:116141-.

[83] Eckle S, Anfang HG, Behm RJ. Reaction intermediates and side products in the methanation of CO and CO2 over supported Ru catalysts in H2-rich reformate gases. Journal of Physical Chemistry C. 2011;115:1361-7.

[84] Huang J, Li X, Wang X, Fang X, Wang H, Xu X. New insights into CO2 methanation mechanisms on Ni/MgO catalysts by DFT calculations: Elucidating Ni and MgO roles and support effects. Journal of CO2 Utilization. 2019;33:55-63.

[85] Le TA, Kim J, Kang JK, Park ED. CO and CO2 methanation over M (MMn, Ce, Zr, Mg, K, Zn, or V)-promoted Ni/Al@Al2O3 catalysts. Catalysis Today. 2020;348:80-8.

[86] Hasan M, Asakoshi T, Muroyama H, Matsui T, Eguchi K. CO2 methanation mechanism over Ni/Y2O3: an in situ diffuse reflectance infrared Fourier transform spectroscopic study. Physical Chemistry Chemical Physics. 2021;23:5551-8.

[87] Solis-Garcia A, Louvier-Hernandez JF, Almendarez-Camarillo A, Fierro-Gonzalez JC. Participation of surface bicarbonate, formate and methoxy species in the carbon dioxide methanation catalyzed by ZrO2-supported Ni. Applied Catalysis B: Environmental. 2017;218:611-20.

[88] Westermann A, Azambre B, Bacariza MC, Graça I, Ribeiro MF, Lopes JM, et al. Insight into CO2 methanation mechanism over NiUSY zeolites: An operando IR study. Applied Catalysis B: Environmental. 2015;174-175:120-5.

[89] Aldana PAU, Ocampo F, Kobl K, Louis B, Thibault-Starzyk F, Daturi M, et al. Catalytic CO2 valorization into CH4 on Ni-based ceria-zirconia. Reaction mechanism by operando IR spectroscopy. Catalysis Today. 2013;215:201-7.

[90] Pan Q, Peng J, Sun T, Wang S, Wang S. Insight into the reaction route of CO2 methanation: Promotion effect of medium basic sites. Catalysis Communications. 2014;45:74-8.

[91] Pe'er G, Bonn A, Bruelheide H, Dieker P, Eisenhauer N, Feindt PH, et al. Action needed for the EU Common Agricultural Policy to address sustainability challenges. People and Nature. 2020;2:305-16.

[92] Schnuelle C, Wassermann T, Stuehrmann T. Mind the Gap—A Socio-Economic Analysis on Price Developments of Green Hydrogen, Synthetic Fuels, and Conventional Energy Carriers in Germany. Energies2022.

[93] Held M, Schollenberger D, Sauerschell S, Bajohr S, Kolb T. Power-to-Gas: CO2 Methanation Concepts for SNG Production at the Engler-Bunte-Institut. Chemie-Ingenieur-Technik. 2020;92:595-602.

[94] Peters M, Geitner C, Verhoeven BF. Experimental Investigation of Electrothermal Desorption of Steel Mill Gases from Activated Carbon. Chemie-Ingenieur-Technik. 2022;94:1458-65.

[95] Hussain I, Jalil AA, Hassan NS, Farooq M, Mujtaba MA, Hamid MYS, et al. Contemporary thrust and emerging prospects of catalytic systems for substitute natural gas production by CO methanation. Fuel. 2022;311:122604.

[96] Park S, Choi K, Lee C, Kim S, Yoo Y, Chang D. Techno-economic analysis of adiabatic four-stage CO2 methanation process for optimization and evaluation of power-to-gas technology. International Journal of Hydrogen Energy. 2021;46:21303-17.

[97] Schaaf T, Grünig J, Schuster MR, Rothenfluh T, Orth A. Methanation of CO2 - storage of renewable energy in a gas distribution system. Energy, Sustainability and Society. 2014;4:1-14.

[98] Uebbing J, Rihko-Struckmann LK, Sundmacher K. Exergetic assessment of CO2 methanation processes for the chemical storage of renewable energies. Applied Energy. 2019;233-234:271-82.

[99] Bhérer-Breton A, Feldman J, Bray B, Hafenbrad D. Small microorganisms to decarbonize big industries: Archaea as an innovative solution for the cement industry. Cement International. 2022;20:24-9.

[100] Ryckebosch E, Drouillon M, Vervaeren H. Techniques for transformation of biogas to biomethane. Pergamon; 2011. p. 1633-45.

[101] Angelidaki I, Alves M, Bolzonella D, Borzacconi L, Campos JL, Guwy AJ, et al. Defining the biomethane potential (BMP) of solid organic wastes and energy crops: A proposed protocol for batch assays. Water Science and Technology. 2009;59:927-34.

[102] International Energy A. Outlook for biogas and biomethane. Prospects for organic growth. IEA Publications. 2020:1-93.

[103] International Energy A. World Energy Outlook 2022. International Energy Agency (IEA) 2022:524-.

[104] Primmer N. Biogas: Pathways to 2030 - Report. World Biogas Association. 2021:128-.

[105] Kopetz H. Renewable resources: Build a biomass energy market. Nature. 2013;494:29-31.

[106] Calero M, Godoy V, Heras CG, Lozano E, Arjandas S, Martín-Lara MA. Current state of biogas and biomethane production and its implications for Spain. Sustainable Energy & Fuels. 2023;7:3584-602.

Chapter 2

Objectives and structure of the thesis

"A prudent question is one-half of wisdom."
Francis Bacon

Painting: The Tower of Babel, 1563, Pieter Bruegel the Elder.
Public Domain Image.

2.1 – General Objective

The general objective of this PhD Thesis is the development of innovative catalytic materials for the CO_2 methanation reaction and their ulterior application for the biogas upgrade.

2.2 – Secondary Objectives

According to the fundamental principles of Green Chemistry, new catalysts must be developed based on three directing goals: **catalytic stability**, **atom economy**, and **energy efficiency**, which include the novel catalysts for the CO_2 methanation reaction.

Related to each one of these principles, the secondary objectives of the PhD thesis are:

1) Develop materials that can keep high yields to CH_4 under long-term experiments (**catalytic stability**).

2) Develop materials that present high selectivity to CH_4, while minimizing the formation of by-products (**atom economy**).

3) Develop materials that can be operated at moderate temperatures while efficiently upgrading the energetic content of biogas samples (**energy efficiency**).

Each of these secondary objectives will be more thoroughly discussed in the sequence.

2.2.1 – Catalytic stability

Catalytic stability refers to the ability of a catalyst to maintain its activity and effectiveness over an extended period of time under specific reaction conditions. In other words, a catalyst is considered stable if it can continue to facilitate a chemical reaction without a significant decrease in its performance or activity over time.

In the case of Ni-based catalysts used for the CO_2 methanation reaction, such as the ones used in this study, sintering of the metallic particles might pose a problem for the catalytic stability for long-term use.

Due to the complex interactions that the metallic phase can have with the reactants, leading to the formation of intermediates, such as Ni-H and Ni-CO, or many others, these species can interact with each other, resulting in the agglomeration of the metallic phase into larger particles.

The metallic phase can also react with the support via intermediation of the reactant molecules, leading to the formation of phases that were not initially present before the start of the catalytic test. In the case that phenomena like these take place, the metallic surface and amount of available active centers change throughout the catalytic test, with the possibility of decreasing CO_2 conversion and CH_4 selectivity values.

Therefore, there is an ongoing interest in developing more robust catalysts able to resist the sintering effect with good catalytic activity. With this, it is possible to design materials that are economically more viable and sustainable without the need to replace the catalytic bed so frequently while also maintaining high values of CO_2 conversion and CH_4 selectivity.

2.2.2 – Atom economy

Atom economy inside the scope of Green Chemistry, is a concept that measures the proportion of atoms in a chemical reaction that ends up in the desired final product. This concept is related to the catalyst selectivity and is a measure of how effectively a chemical reaction converts reactants into useful products while minimizing waste.

This concept is an important consideration in Green Chemistry and sustainable chemical processes, which is directly involved in the preparation of more environmentally friendly processes, minimizing the use of raw materials, and reducing waste generation.

Inside the context of the CO_2 methanation, increasing the atom efficiency is designing catalysts that exhibit high selectivity values towards CH_4 while reducing the proportion of non-desired products, such as coke, $C_{(s)}$, carbon monoxide, CO or methanol, CH_3OH.

2.2.3 – Energy efficiency

In the context of catalysis, energy efficiency refers to the effectiveness of a catalytic process in converting reactants into the desired products while minimizing the amount of energy input required to drive the process.

As previously stated in Chapter 1, even though the CO_2 methanation reaction is theoretically exergonic and spontaneous at standard conditions of temperature and pressure, it does not take place due to kinetic limitations. For this reason, it is necessary to carry out catalytic processes based on this reaction at higher temperatures when high values of CO_2 conversion and CH_4 selectivity can be achieved. Due to the energetic cost of keeping the reactor at high temperatures and with the interest in designing sustainable and moneywise larger-scale processes, there is an ongoing interest in designing catalysts that exhibit higher CO_2 conversion and selectivity towards CH_4 at lower temperatures.

In addition to this, regarding the application of these catalysts for biogas upgrade, developing catalytic technologies to increase the CH_4 content in biogas samples, without separating CO_2 from the raw mixture also increases the overall energy efficiency, avoiding the extra CO_2 purification step. The biogas upgrade also increases the energetic density of the resulting fuel by incrementing the concentration of the combustible chemical, CH_4, increasing the energy efficiency for the end-use sector.

These goals and each chapter in each one of them is addressed are summarized in **Table 2.1.**

Table 2.1. Summary of directing goals set as secondary objectives for the design and development of the catalysts for the CO_2 methanation reaction studied in the PhD Thesis.

Directing goals	Application for the CO_2 methanation reaction	Chapters in which the topic is addressed
Catalytic stability	Reducing the sintering effect and keeping high yield values to CH_4 long-term experiments	4 and 7
Atom efficiency	Increasing the selectivity towards CH_4, while preventing the formation of subproducts such as CO and C	4 and 6
Energy efficiency	Reduce the reactor operating temperature, while providing application for biogas upgrade	4, 5, 6 and 7

2.3 – Structure of the thesis

Chapter 3 will describe the methodology used in this work and the experimental techniques employed to characterize the catalysts. Moreover, the different types of catalytic tests conducted in this study will also be described.

In **Chapter 4**, we will focus on catalysts supported over zeolitic materials. In this chapter, the motivation arises from using a class of zeolites developed at our research institute, known as delaminated zeolites, with particular attention to the ITQ-6 zeolite, the delaminated counterpart of the ferrierite zeolite. Therefore, in this study, ferrierite and ITQ-6 zeolites with different Si/Al ratios were prepared by hydrothermal synthesis and, subsequently, served as support to prepare Ni-based catalysts for the CO_2 methanation reaction, and the best support was found to be ITQ-6 (Si/Al = 30).

All the catalysts were analyzed by a multi-technique approach with different techniques, such as XRD, H_2-TPR, FT-IR, H_2-chemisorption, N_2 adsorption, and SEM-TEM, to rationalize their performance towards the CO_2 methanation reaction.

In **Chapter 5**, we will discuss a family of Ni-based catalysts prepared over a perovskite-structure support, lanthanum aluminate $LaAlO_3$. Unlike Al_2O_3 and La_2O_3, which are common supports already widely discussed for the CO_2 methanation reaction, $LaAlO_3$, on the other hand has been barely described in the literature. The motivation for this study was to explore the metal mixed oxide synergy phenomenon, which has not yet been thoroughly described for the CO_2 methanation reaction.

For this study, all the materials were analyzed by different techniques, such as XRD, H_2-TPR, operando FT-IR, H_2-chemisorption, N_2 adsorption, SEM-TEM, CO_2-TPD, to shed some light on their behavior towards the CO_2 methanation reaction.

In **Chapter 6**, we will address supported catalysts prepared over a porous phyllosilicate known as sepiolite. The motivation for conducting this study stems from prior work conducted by our research group that demonstrated the significant potential of this sepiolite as a support for catalysts aimed at the CO_2 methanation reaction. This was attributed to its high surface area, the possibility of providing a good metallic dispersion, its porous structure, and its high CO_2 uptake, attributed to the presence of surface-OH groups.

Apart from that, at the current stage of the development of catalysts with commercial potential for the CO_2 methanation reaction, it is of utmost importance to design moneywise catalysts. In this aspect, sepiolite-based catalysts emerge as a class of very competitive materials, as this material's production cost and final price are considerably lower than other conventional inorganic supports probed for this reaction. Spain is the largest producer of sepiolite in the world, and, in this sense, the development of a series of sepiolite-based could significantly bring aggregated value to this material and fulfill an important geostrategic role for Spain's energy transition policies.

In this study, a series of Ni-based catalysts were prepared over sepiolite with the addition of cerium as a promoter, and the catalysts were analyzed by a multi-technique approach, with techniques such as XRD, H_2-TPR, FT-IR, CO_2-TPD-MS, H_2-chemisorption, N_2 adsorption, and SEM-TEM microscopy.

Furthermore, in collaboration with Dr. Emiel Hensen's research group at the Eindhoven University of Technology, in the Netherlands, these catalysts were analyzed by advanced time-resolved operando IR spectroscopy to determine which species are involved in the reaction mechanism.

In **Chapter 7**, wrapping up the work from the three last chapters, there will be a discussion about the best catalysts from each one of the previous chapters and their assessment for the biogas upgrade tests. For this, instead of the CO_2 methanation conditions employed in the previous experiments, a flow of simulated sweetened biogas was employed, i.e., samples that had been purified by the elimination of contaminants, such as H_2S and NH_3. Therefore, long-term stability tests were conducted to verify the feasibility of using these systems on an industrial scale. In addition to that, the catalysts were also assessed by TEM microscopy (to assess the modification of textural properties), and elemental composition analysis (to verify the eventual formation of coke).

And finally, **Chapter 8** will present the general conclusions from the four previous chapters.

Figure 2.1 summarizes the structure of the thesis, the distinct features that will be addressed in each one of the chapters, and, finally, the application of these classes of catalytic materials for the biogas upgrade tests.

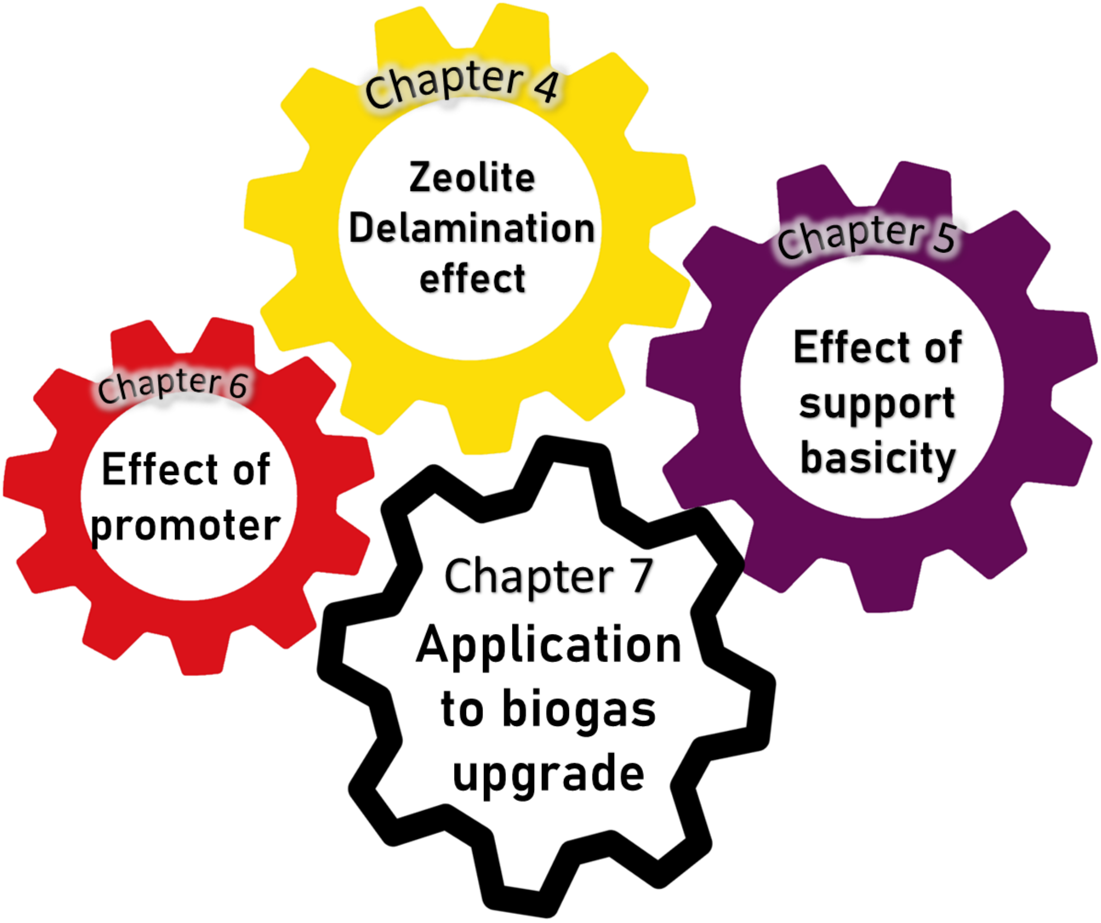

Figure 2.1. Schematic depiction of the main aspects covered in each one of the chapters of the different classes of catalysts studied in this thesis.

Chapter 3

Methodology and Experimental Procedures

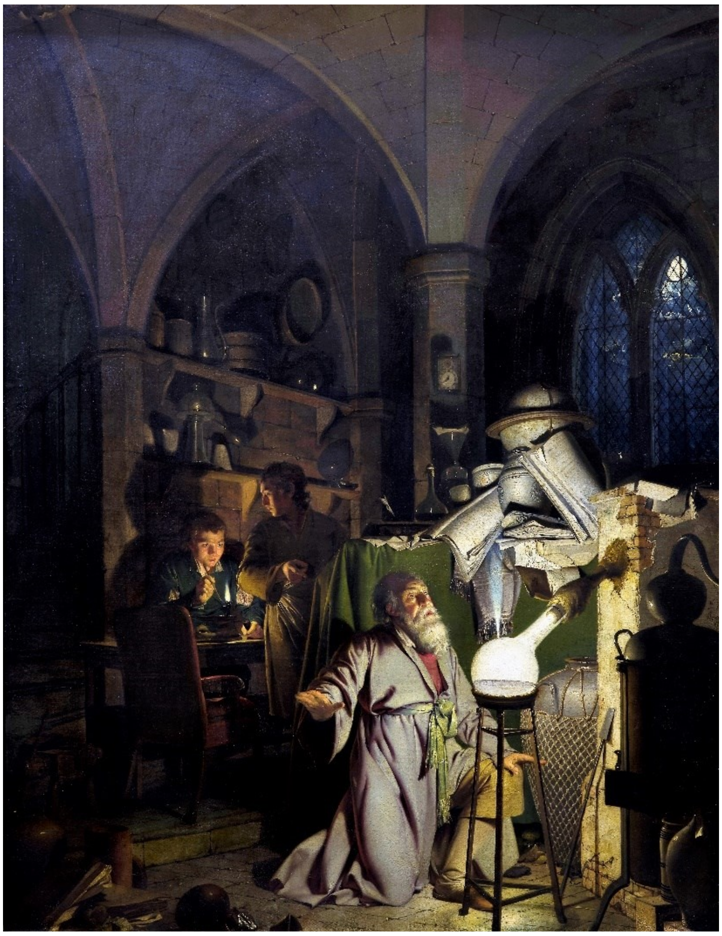

"In all affairs, it's a healthy thing now and then to hang a question mark on the things you have long taken for granted."

Bertrand Russel

Painting: The Alchemist Discovering Phosphorus, 1771, Joseph Wright of Derby.
Public Domain Image.

3.1 – Chemicals

The chemicals used for this study's development and each product's commercial supplier are listed below. They are classified and grouped according to the physical states in which they are found when purchased. For clarity, throughout this work, whenever water is mentioned for the experimental procedures without further mention, it refers to Milli-Q water, i.e., ultra-deionized water.

Solid chemicals:

- Hexahydrate nickel nitrate, $Ni(NO_3)_2 \cdot 6H_2O$ (Sigma-Aldrich)

- Zeolites-based catalysts:

FER and ITQ-6:
Silica, SiO_2 (Aerosil 200, Degussa)
Alumina, Al_2O_3 (boehmite, Catapal B)
Ammonium fluoride, NH_4F ((Aldrich, 98% purity)
Hydrofluoric acid, HF (Aldrich, 49.8% concentration)
Cetyl-trimethylammonium bromide (CTAB (Sigma-Aldrich, 98% purity)
4-amino-2,2,6,6-tetramethylpiperidine (Fluka, 98% purity)

- $LaAlO_3$-based catalysts:

α-Aluminum oxide, Al_2O_3 (Sigma-Aldrich).
Lanthanum oxide, $LaAlO_3$ (Sigma-Aldrich).
Hexahydrate lanthanum nitrate, $La(NO_3)_2 \cdot 6H_2O$ (Sigma-Aldrich).
Nonahydrate aluminium nitrate, $Al(NO_3)_3 \cdot 9H_2O$ (Sigma-Aldrich).

- Sepiolite-based catalysts:

Sepiolite Pangel S9 (Tolsa).
Hexahydrate lanthanum nitrate, $La(NO_3)_2 \cdot 6H_2O$ (Sigma-Aldrich).
Nonahydrate cerium nitrate, $Ce(NO_3)_3 \cdot 9H_2O$ (Sigma-Aldrich).
Sodium hydroxide, NaOH (Scharlau).

- Silicon carbide, SiC (Fisher Scientific).

Liquid chemicals:

Milli-Q water, H_2O.
37% hydrochloric acid, HCl (Fisher Scientific).
48% hydrofluoric acid, HF, (Fisher Scientific).

70% nitric acid, HNO_3, (Fisher Scientific).
Polyethylene glycol, $H-(O-CH_2-CH_2)_n-OH$ (Sigma-Aldrich).
Pyridine (Merck).
50% H_3PO_2 (Sigma-Aldrich).

Gaseous chemicals:
Carbon dioxide, CO_2 (Abelló Linde).
Carbon monoxide, CO (Abelló Linde).
Hydrogen, H_2 (Abelló Linde).
Nitrogen, N_2 (Abelló Linde).
Methane, CH_4 (Abelló Linde).
Gas mixture: CO_2 (15%), H_2 (48%), N_2 (20%), CH_4 (15%), CO (2%) (Abelló Linde).

3.2 – Catalysts Preparation

As discussed in the introduction, the catalysts used for the CO_2 methanation reaction commonly consist of a metallic phase dispersed over the surface of an inorganic support, so for this reason, the preparation of the catalysts used in this work consisted of preparation of the support, incorporation of the Ni phase, calcination and in-situ reduction. However, in the case of some of the $LaAlO_3$-based catalysts, the nickel was added directly during the support synthesis, as it will be discussed in the sequence. The methods used to prepare the support and incorporation of the nickel phase will also be discussed in the next section.

Regarding the calcination and in-situ reduction steps, calcination is conducted in a muffle furnace following the temperature program described in **Figure 3.1**. In contrast, in-situ reduction takes place in the reactor where the reaction occurs. This is accomplished by using a H_2 flow at 150 mL min^{-1}, at a temperature of 450 °C for 2 hours, with a ramp rate of 10 °C min^{-1} until reaching the specified temperature.

In all cases, the number preceding Ni (or Ce) indicates the nominal weight percentage of the catalyst. Furthermore, the symbol "/" signifies that Ni was incorporated via the incipient wetness impregnation (IWI) method. In contrast, the notation "-" is employed when Ni incorporation is via precipitation, as seen for the sepiolite-based catalysts.

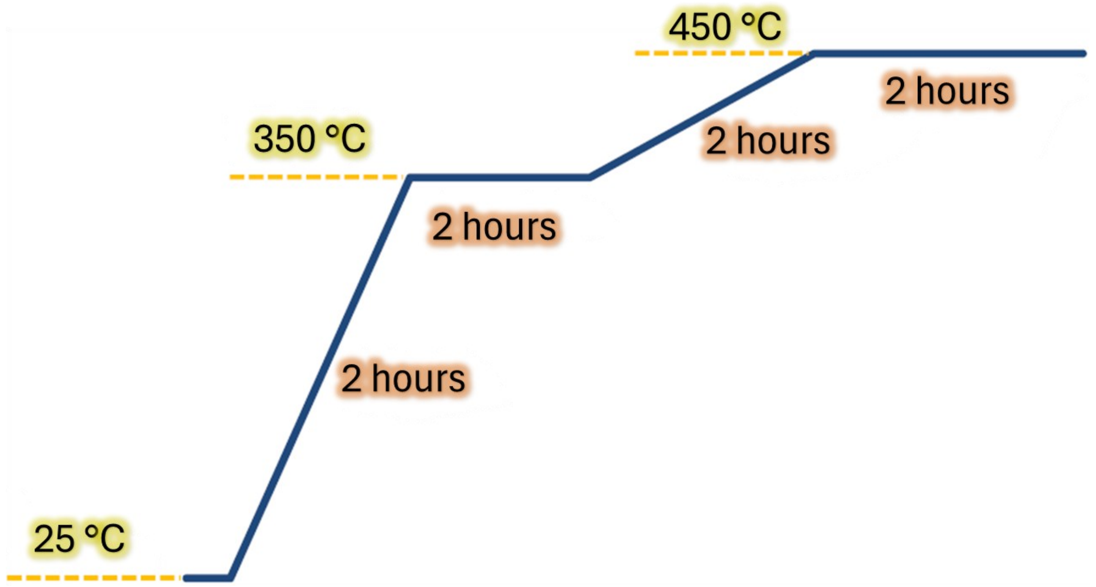

Figure 3.1. Standard calcination step sequence for preparing the Ni-based catalysts used in this study.

3.2.1 – Catalysts supported on zeolites

For the zeolite materials, there will be a number between parenthesis after the notation (e.g., ITQ-6 (30)), which refers to the zeolite Si/Al molar ratio. A Si/Al = ∞ molar ratio refers to a pure silica zeolite.

Synthesis of pure silica zeolites (Si/Al = ∞)

For a standard synthesis, the same procedure described by Chica was followed [1].

10 g of silica, 9.2g of NH_4F, 3.1 g of HF, 26 g of the structure directing agent (SDA), 4-amino-2,2,6,6-tetramethylpiperidine, were mixed with 27.9 mL of water in a Teflon-sealed cup and kept inside an autoclave at 448 K for 5 days. Afterward, the resulting slurry, which consists of the PREFER material, was filtered, washed thrice, and kept overnight inside a drying oven at 333 K. Then, the PREFER was dispersed in a solution of cetyltrimethylammonium bromide (CTAB) and tetrapropylammonium hydroxide (TPAOH) and kept on reflux for 16 h at 368 K. After this step, the obtained material is the expanded ferrierite (FER) (**Figure 3.2**). At this point, two materials can be obtained: if the expanded ferrierite is directly calcined at 853 K for 7 h, the FER (∞) zeolite is obtained. Otherwise, another synthetic route can be followed. The expanded ferrierite slurry can be dispersed on a NaOH solution (pH = 12.5) and kept in a heater ultrasound bath at 323 K, then washed thoroughly until pH = 7 is obtained, dried at 373 K, and then calcined at 853 K for 7 h. In this case, the ITQ-6 (∞) is obtained, as seen in Figure 3.2.

Synthesis of zeolites (Si/Al molar ratio = 30)

For obtaining the Si/Al = 30 zeolites, the exact procedure as described before is followed, with the only difference being that 2.3 g of alumina is added during the hydrothermal synthesis step. The rest is carried out the exact same way.

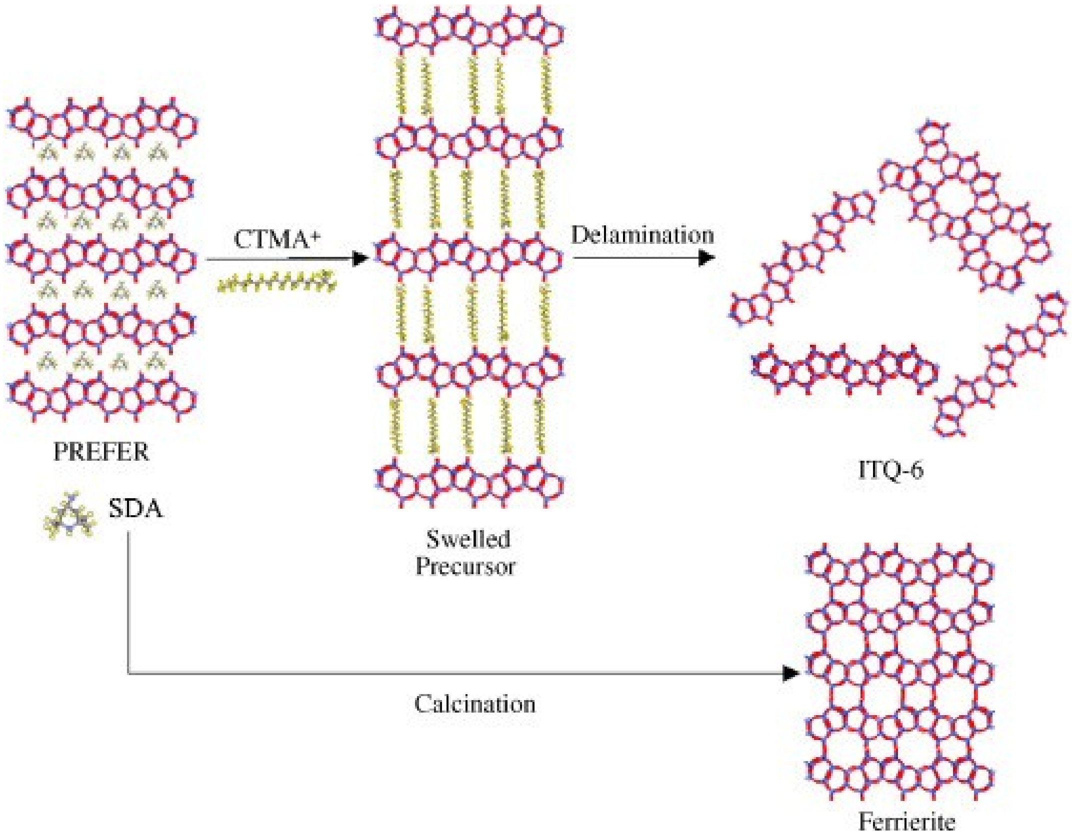

Figure 3.2. Simplified representation on the synthetical route to obtain the FER or the ITQ-6, depending on whether the swelling step with cetyltrimethylammonium bromide (CTAB) is followed before the calcination step. Image adapted from Chica et al. [1].

Incorporation of Ni into zeolite supports

The incorporation of Ni into the different zeolitic supports was performed using the incipient wetness impregnation (IWI) technique. The first step involves determining the volume necessary to fill the material's pores. Water is initially added to a known mass of the support and mixed to achieve a homogeneous mixture until a sludge-like state is attained. This point marks the saturation of the material's pores, and the material will not absorb any additional water added.

To ensure that the total volume of the solution matches the volume of water, as determined in the previous step to reach the pore volume, the next step entails dissolving the appropriate amount of the metallic precursor, in this case, nickel (II) nitrate hexahydrate ($Ni(NO_3)_2 \cdot 6H_2O$ in a suitable volume of water.

Next, this solution containing the Ni precursor is added dropwise onto the support, continuously mixing to ensure the mixture remains as homogeneous as possible. Once the entire volume has been added, the obtained solid is dried at 100 °C for 8 hours and then calcined as previously described.

The amount of $Ni(NO_3)_2 \cdot 6H_2O$ used in the preparation depends on the theoretical Ni loading in the catalyst.

3.2.2 – Catalysts supported on sepiolite

Preparation of support

The support employed for this group of catalysts is commercially available and did not undergo any additional treatment. Specifically, it is the commercial product Pangel S9 by Tolsa.

Incorporation of Ni and the promoter, Ce, into the sepiolite support

For the sepiolite-based catalysts, the co-precipitation method was employed to synthesize the Ni and Ce-based catalysts, adapted from a procedure published by Chen [2].

These catalysts are denominated **x**Ni-**y**Ce-Sep, with the **x** and **y** being the nominal weight proportion of nickel and cerium, respectively. For the preparation step, sepiolite (Pangel S9, Tolsa) was first dispersed in a solution of $Ni(NO_3)_2$ and $Ce(NO_3)_3$ with the theoretical amounts to achieve the x and y nominal proportions. Afterward, pH was slowly increased by dropwise addition of a 5 mol L^{-1} NaOH solution until reaching pH = 10 and kept under stirring for 2 h. After that, the synthesis cake underwent a thorough washing, 12 hours of drying at 100 °C, and calcination at 450 °C during 2 h.

3.2.3 – Catalysts supported on oxides

Preparation of supports

Commercial oxides (Sigma-Aldrich) were used to prepare the La_2O_3 and Al_2O_3-based catalysts. The Al_2O_3 support used in this study was the α-phase one with a similar surface area to the other supports. $LaAlO_3$ was synthesized following the procedure described in the literature via the Pechini method [3, 4].

$La(NO_3)_3 \cdot 6H_2O$ and $Al(NO_3)_3 \cdot 9H_2O$, in the correct molar proportion, were dissolved in 300 mL of isopropanol under stirring for 30 min at 60 °C. The La concentration in this solution was 0.39 mol L^{-1}. The mixture was stirred for 30 minutes while 200 ml of polyethylene glycol was added (2.25 ml min-1). The mixture was heated to 80 °C, kept under stirring for 1 h to evaporate isopropanol, and afterward calcined for 4 hours at 1050 °C.

Incorporation of Ni into the oxide supports

The incorporation of Ni into the different aluminate supports was carried out by incipient wetness impregnation, as previously described for the zeolite supports.

Two types of catalysts were synthesized in this section. The first one was the catalysts prepared by IWI using $Ni(NO_3)_2$ as Ni precursor. These catalysts were impregnated and calcined at 450 °C for 2 h. These catalysts receive the "**x**Ni/support" denomination, where x is the nominal Ni weight content.

The other method employed was ex-solution, in which a 5% wt. Ni-doped $LaAlO_3$ ($5NiLaAlO_3$-ex) was synthesized by following the same procedure previously mentioned for the $LaAlO_3$, with a mixture of the salts $Ni(NO_3)_2 \cdot 6H_2O$, $Al(NO_3)_3 \cdot 9H_2O$, and $La(NO_3)_3 \cdot 6H_2O$ in the correct molar proportion instead. To reduce the calcined catalysts, they were exposed to a H_2 flow (150 mL min^{-1}) at 450 °C (10 °C min^{-1}) and denominated **(catalyst's name)_R**.

This way, the summarized list of the catalysts analyzed in this study is summarized below.

Catalysts supported on zeolites:

5Ni/FER (Si/Al = ∞)
5Ni/ITQ-6 (Si/Al = ∞)
5Ni/FER (Si/Al = 30)
5Ni/ITQ-6 (Si/Al = 30)
10Ni/ITQ-6 (Si/Al = 30)
15Ni/ITQ-6 (Si/Al = 30)
20Ni/ITQ-6 (Si/Al = 30)

Catalysts supported on oxides:

$5Ni/Al_2O_3$
$5Ni/La_2O_3$
$5Ni/LaAlO_3$
$5NiLaAlO_3$-ex
$10Ni/LaAlO_3$
$15Ni/LaAlO_3$

Catalysts supported on sepiolite:

0Ni-10Ce-Sep
5Ni-0Ce-Sep
5Ni-1Ce-Sep
5Ni-10Ce-Sep
5Ni-30Ce-Sep
10Ni-10Ce-Sep
15Ni-10Ce-Sep
20Ni-10Ce-Sep

3.3 – Characterization techniques

In order to obtain the most pertinent physical-chemical properties from the catalysts and establish possible correlations between these properties and the materials' catalytic performance, the following characterization techniques were used to characterize the materials studied in this work. An insight into how these techniques work will be provided in each of the following subsections.

3.3.1 – X-ray diffraction (XRD)

To examine the structure of crystalline materials, the technique of X-ray diffraction (XRD) is utilized. Its mechanism is based on the constructive and destructive interference of X-rays with the regular arrangement of atoms or ions in a crystal lattice [5]. The key structural parameters can be extracted from the diffraction pattern that results, which offers insights into the arrangement of these species.

This technique is grounded in the phenomena of scattering that occur when a monochromatic X-ray beam of photons impacts the crystalline layers of a solid-state sample. As the monochromatic X-ray beam reaches the initial layer of atoms on the sample surface, a portion of the radiation is scattered, while the remainder proceeds to the second layer of atoms. Within this second layer, the same phenomenon takes place; namely, a portion of the beam is scattered, while the non-scattered portion advances to the subsequent layer of atoms within the material, in which this same phenomenon iteratively takes place.

This way, the resulting scattered radiation can interact in two ways, either in destructive interference, when the scattered photons are out of phase, which does not result in the accumulation of these scatterings; or in constructive interference when the leaving photons are in phase, leading to an accumulation of the sequential scattering and allows the observance of a signal in the detector (**Figure 3.3**).

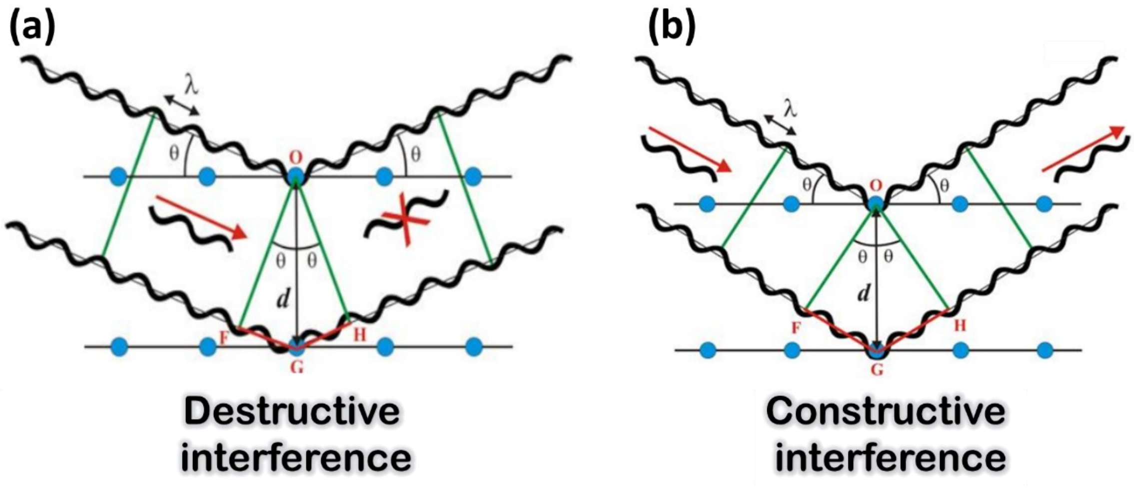

Figure 3.3. Representation of the different interference patterns that take place in X-ray diffraction: (a) destructive interference, when the leaving photons are out of phase, or (b) constructive interference when the leaving photons are in phase. Image adapted from Ameh et al. [5].

The interference will be constructive when the diffraction phenomenon fulfills Bragg's Law requirements, as seen in the following **Equation 3.1**:

$$n\lambda = 2d_{hkl} \cdot \sin\theta$$ **Equation 3.1**

In which,

- n is an integer number.
- λ is the wavelength of the incident X-ray beam.
- d_{hkl} is the interplanar distance between crystallographic planes with the hkl Miller indices.
- θ is the X-ray incidence angle.

Moreover, this technique allows for the estimation of the average crystallite size, as the width of the X-ray diffraction signal is associated with imperfections in the crystal structure of the phase. This degree of imperfection in the structure is, in turn, primarily linked to the crystal size. Hence, smaller crystals yield diffraction signals of greater width [6].

This concept forms the basis of the Scherrer equation (**Equation 3.2**), which correlates the signal intensity at full width at half maximum (FWHM) with the average crystal size, as defined in Equation 3.2:

$$D = \frac{K \cdot \lambda}{\text{FWHM} \cdot \cos\theta}$$ **Equation 3.2**

In which,

D is the average crystal size.

K is a dimensionless shape factor which stands for the crystal's shape and internal structure and considers the influence of crystal morphology and defects on the observed diffraction peak broadening.

λ is the X-ray wavelength.

FWHM stands for Full Width at Half Maximum, in radians (corrected by subtraction with instrumental peak width).

θ is the Bragg angle.

In this work, the XRD technique was employed to identify the different supports used for the development of catalysts and the characteristics of the Ni phase after the calcination, when nickel was present as NiO. The technique was also used to analyze the Ni phase after reduction or reaction when part of the NiO had been reduced to metallic Ni^0. Furthermore, the analyses were used to quantitatively estimate the average crystallite size of reduced metallic nickel, Ni^0, and nickel oxide (NiO) crystalline phases, employing the Scherrer equation (Equation 3.2), as previously described.

Measurements were conducted in a PANalytical CUBIX diffractometer equipped with an X'Celerator detector, utilizing Cu Kα X-ray radiation (λ_1 = 1.5406 Å, λ_2 = 1.5444 Å, I_2/I_1 = 0.5). The samples that consisted of a fine powder were placed on the specific sample holder, ensuring compactness and a flat measuring surface. The operational conditions of the equipment were set at 45 kV and 40 mA, respectively, and two measurement modes were employed:

General mode: 2θ = 3.5 - 90.0° range, 0.040° per scanning step with 35 s of accumulation for each step.

Low θ mode: 2θ = 2.0° - 40.0° range, 0.040° per scanning step with 35 s of accumulation for each step, when it was necessary to analyze peaks at low angles.

3.3.2 – N_2 adsorption-desorption technique

The N_2 adsorption technique characterizes materials' surface area and porosity, particularly porous solids like catalysts, adsorbents, and nanomaterials. It is based on the adsorption phenomenon, by which gas molecules adhere to the surface of a solid or liquid material [7].

When the surface of a solid comes into contact with gas molecules, it can be retained due to attractive forces. As the gas pressure increases, the likelihood of contact also increases, increasing the amount of retained gas. As the amount of adsorbed gas increases, multilayer adsorption occurs on the free surface and within the pore walls. Eventually, the surface becomes entirely covered, and the pores are filled [8].

The adsorption isotherm is the amount of gas adsorbed as a function of the gaseous phase's external pressure or as a function of relative pressure, which is the ratio of the pressure to the pure gas's saturation pressure at the measurement temperature. The majority of materials' adsorption isotherms can be divided into six categories in accordance with rules established by the International Union of Pure and Applied Chemistry (IUPAC) (**Figure 3.4**).

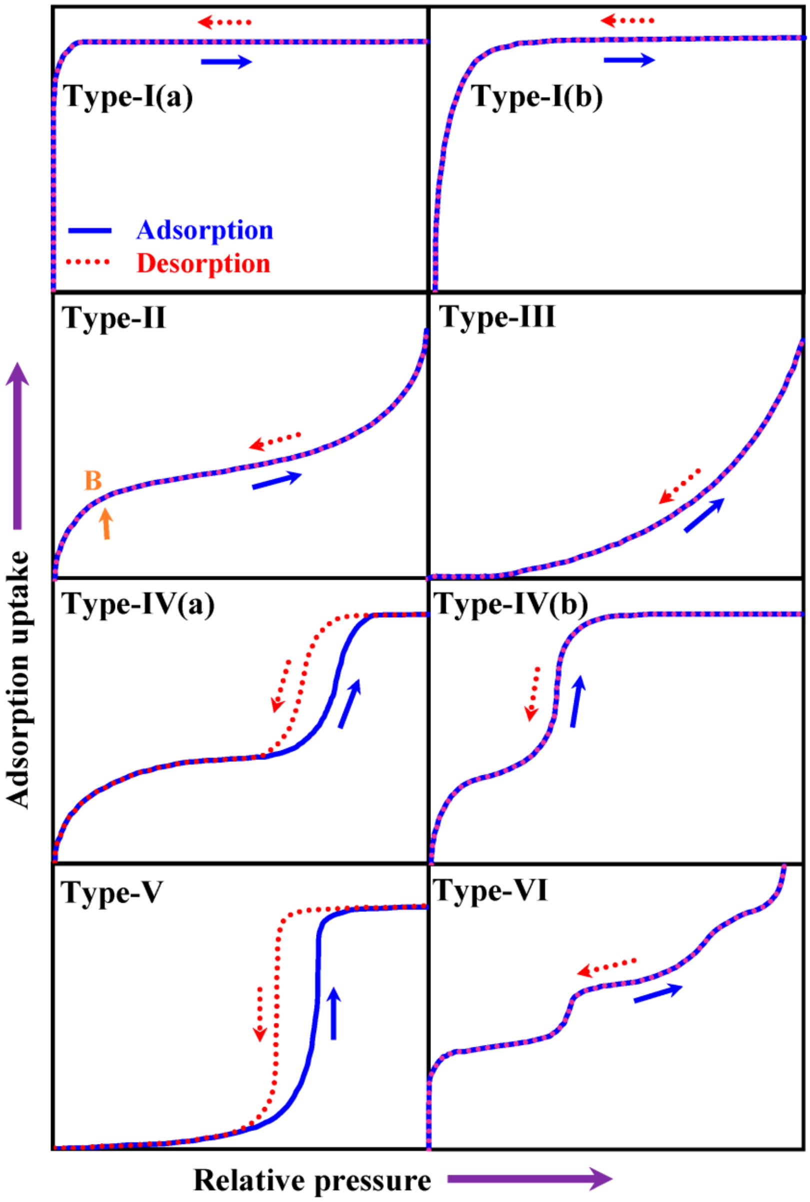

Figure 3.4. Classification of the six types of adsorption that might take place over a material according to the IUPAC guidelines. Image adapted from Rahman et al. [7].

With the data obtained from the adsorption data and the methodology and approximations made by Brunauer, Emmet, and Teller (or BET, the acronym which is commonly used), it is possible to calculate the BET specific surface of a solid sample, S_{BET}. At first, the volume of gas necessary to form monolayer is calculated with Equation 3.3.

$$\frac{1}{V \cdot \left(\frac{P_0}{P} - 1\right)} = \frac{1}{V_m \cdot C} + \frac{C - 1}{V_m \cdot C} \cdot \frac{P}{P_0}$$ **Equation 3.3**

In which,

P is the equilibrium pressure.
V is the volume of adsorbed gas at pressure P.
V_m is the volume of gas required to cover the monolayer.
P_0 is the N_2 saturation at the measurement temperature.
C is a constant associated with the subtraction between the enthalpy of adsorption of the first layer and the enthalpy of liquefaction (involved in the formation of the subsequent layers).

This way, by performing a linear plot of $1/(V \cdot ((P_o/P) - 1)))$ against P/P_0, V_m and C can be estimated with the y-intercept and the slope values obtained with the function linear regression. Once these values are obtained, S_{BET} can be estimated with Equation 3.4.

$$S_{BET} = \frac{V_m}{\bar{V}} \cdot N_a \cdot \sigma$$ **Equation 3.4**

In which,

S_{BET} is the BET specific surface area.
V_m is the volume of gas to cover a monolayer.
$\bar{V}$ is the molar volume of an ideal gas at 25 °C and 1 atm, which is a constant equal to 22.414 L mol^{-1}.
N_a is the Avogadro constant, $6.022 \cdot 10^{23}$ mol^{-1}.
σ is the surface area occupied by one gas molecule (for N_2, $\sigma = 16.2$ Å^2) [9].

The micropore volume can be obtained with the procedure known as the t-plot [10]. To begin with, the parameter "t" is defined as the statistical thickness of an adsorbed layer in meso and macropores. The Harkins and Jura equation (**Equation 3.5**) is typically used to calculate this "t" parameter.

$$t(\text{Å}) = \left(\frac{13.99}{0.034 - \log\left(\frac{P}{P_0}\right)}\right)^{1/2}$$ **Equation 3.5**

In which,

P is the equilibrium pressure.

P_0 is the saturation pressure of the pure gas at the measurement temperature.

Next, by plotting the adsorbed volume against this parameter "t," a set of points whose linear regression gives a line that intersects the ordinate axis, giving the value n. Finally, the micropore volume is calculated by multiplying this n value by the N_2 density factor according to Equation 3.6 :

$$V_{micro}\left(\frac{cm^3}{g}\right) = 0.0015468 \cdot n \qquad \textbf{Equation 3.6}$$

In which,

V_{micro} is the micropore volume of the material.

n is the ordinate intercept of the line obtained when plotting the adsorbed volume against the parameter t.

Furthermore, the t-plot can also be used for estimation of the external surface area. When plotting the adsorbed volume against the parameter t, the slope of the obtained line is the value m. With this value m, the external surface area can be obtained with **Equation 3.7**.

$$S_{ext} = 15.47 \cdot m \qquad \textbf{Equation 3.7}$$

In which,

S_{ext} is the external surface area.

m is the slope of the linear regression graph obtained when the adsorbed volume is plotted against the parameter t.

In this work, N_2 adsorption has been employed to determine the specific surface area (S_{BET}) of various catalysts and the supports used in their preparation. Additionally, for catalysts supported on sepiolite and zeolites, external surface values, micropore surface values, and micropore volume have been considered.

The N_2 adsorption isotherms were recorded using Micromeritics ASAP 2420 and Micromeritics TriStar 3000 equipment at -196 °C. Initially, the sample (approximately 200 mg with particle sizes ranging from 0.250 to 0.425 mm) undergoes a vacuum pre-treatment overnight at a specific temperature to clean the solid's surface. Generally, the temperature used for this pre-treatment has been 350 °C, although in some cases, it has been lowered to 80 °C to preserve the material's structure. Subsequently, the solid is weighed, cooled to 196 °C, and exposed to N_2 pulses while recording the volume of adsorbed gas against pressure variation until the equilibrium condition was attained.

3.3.3 – Inductively Coupled Plasma Optical Emission Spectroscopy (ICP-OES)

The analytical method known as Inductively Coupled Plasma Optical Emission Spectroscopy (ICP-OES) is used to determine elemental composition in a sample both quantitatively and qualitatively. It uses an inductively coupled plasma (ICP) as the excitation source and applies the concepts of atomic emission spectroscopy, as detailed in **Figure 3.5**.

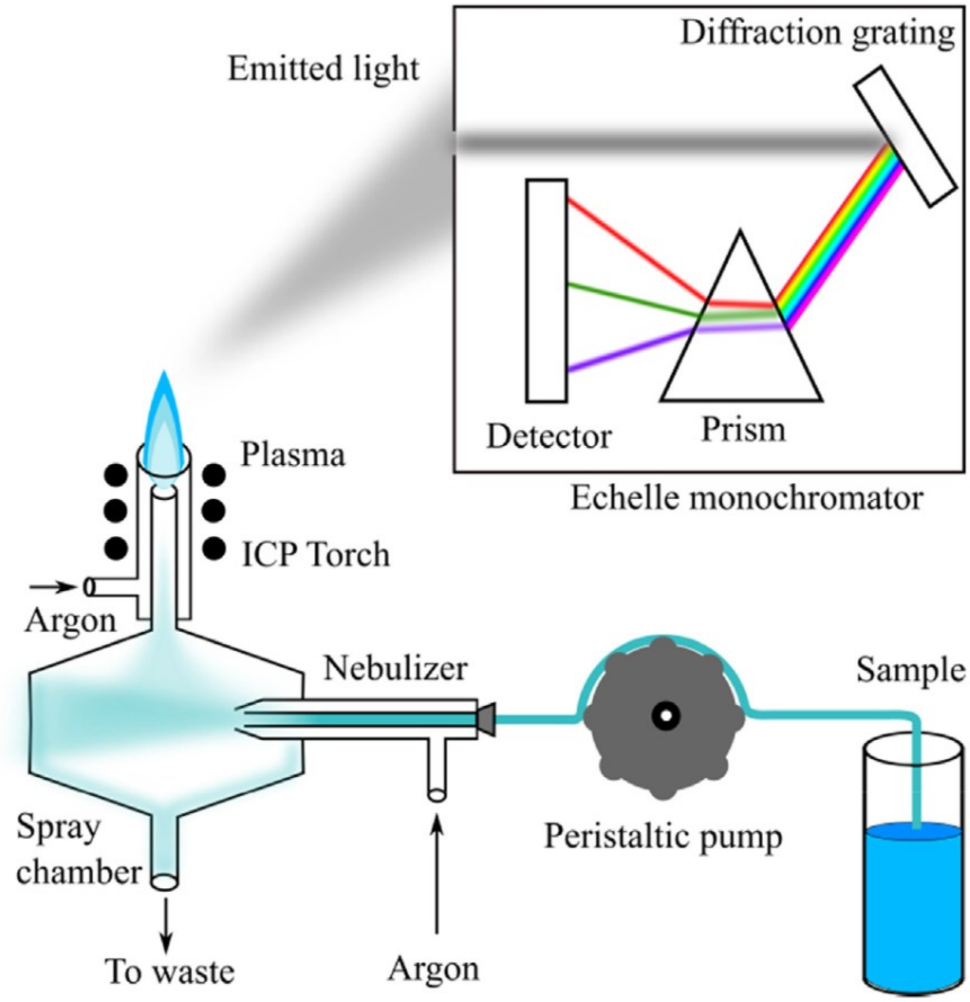

Figure 3.5. Simplified scheme depicting the experimental setup for the analysis with the ICP-OES technique. Image adapted from Cherevko et al. [11].

For this technique, the sample to be analyzed, either a liquid solution or a solid that had been previously digested, is introduced into the equipment where a high-temperature plasma had been created in an RF coil, which leads to the atomization and excitation of the ions present in solution [12].

These excited ions release energy in the form of light, which is collected and passed through a monochromator, which breaks down the light into its different wavelengths, creating an emission spectrum (**Figure 3.5**).

As each element produces a unique emission spectrum due to its specific electronic structure, the elemental loading can be estimated by measuring the intensity of emitted light at characteristic wavelengths.

In the specific case of this work, this technique was used to quantify the metals present in the catalysts with a particular interest in Ni to verify if the actual weight content in the catalyst was close to the nominal one set during the preparation step.

The measurements have been conducted using a Varian 715-ES instrument. For the analysis of solid samples, typically between 20 and 30 mg of the sample are first dissolved in an acidic medium (HNO_3/HF/HCl in a volumetric ratio of 1/1/3) for 24 hours and then diluted with water. For the specific case of the aluminate samples, which were insoluble in this acidic solution, the digestion was performed with H_3PO_2, by dissolving 50 mg of the solid sample in 10 mL of an H_3PO_2 50% solution at 140 °C under stirring at 140 rpm for 10 minutes.

In the case of liquid samples, they can be directly introduced into the instrument.

Once the sample is in liquid form, they are pumped continuously into the nebulization chamber, where it is converted into an aerosol and then transported to the plasma torch. In the plasma, the analytes are excited due to the high temperatures generated, leading to the production of their characteristic emission spectra. In all cases, the calibration curve was adjusted to the approximate expected concentration of the analyte and determined using standard solutions.

3.3.4 – Elemental Analysis

The elemental analysis technique allows for determining the total content of C, H, N, and S in a sample. This technique is based on quantifying combustion products (CO_2, H_2O, N_2, and SO_x) that are generated from the combustion of the sample [13].

In this study, the elemental analysis technique has been used to investigate the potential generation of coke during the reaction, and samples were analyzed after conducting the catalytic or stability tests.

Measurements were conducted in a EuroVector EuroEA instrument, and for each analysis, between 0.5 and 1.5 mg of the sample is required. Firstly, the samples are weighed in a tin capsule. Subsequently, the sample is introduced into the instrument and burnt to combustion under a pure O_2 flow within a furnace at 1020 °C. The gases produced during this combustion (CO_2, H_2O, N_2, and SO_x) are carried by a He stream and separated within a chromatographic column, thus enabling the quantification of each gas with a thermal conductivity detector (TCD).

3.3.5 – Hydrogen Temperature Programmed Reduction (H_2-TPR)

Hydrogen Temperature Programmed Reduction (H_2-TPR) is a technique utilized in the field of catalysis and surface science to elucidate the reducibility and redox properties of materials, mainly metal oxides. This method involves the controlled introduction of H_2 as a reducing agent in a quartz reactor while increasing its temperature under a controlled temperature gradient [14]. At the same time, systematic monitoring of H_2 leaving the analysis cell takes place, typically employing techniques like mass spectrometry (MS) or thermal conductivity detection (TCD). The signal variation from this monitoring offers information at what temperature ranges the material's reduction events take place.

In the case of the samples used in this study, TPR was employed to investigate the reducibility of the Ni species present in the prepared catalysts. Additionally, it provides insights into the various types of interactions that can occur between Ni and different supports, which are directly dependent on the temperature. Furthermore, a series of experiments were conducted to estimate the extent of reduction exhibited by the catalysts under reaction conditions. To achieve this, **Equation 3.8** was used.

$$Reducibility(\%) = \frac{A_{reduction}}{A_{total}} \qquad \textbf{Equation 3.8}$$

In which,

$A_{reduction}$ is the area under the TPR curve up to the reduction temperature. Commonly in this work, 450 °C was the standard reduction temperature for the catalysts studied, so this refers to the area under the curve up to this temperature.

A_{total} is the total area under the TPR curve.

The TPR measurements were conducted using a Micromeritics Autochem 2910 instrument. Firstly, approximately 50 mg of sample previously sieved (0.2 – 0.4 mm) were weighed and loaded into a U-shaped quartz reactor. Subsequently, a pre-treatment step was carried out in an Ar flow at room temperature for 15 minutes, followed by a switch to a mixture of H_2 and Ar (50 mL min^{-1}, 10% by volume of H_2), and then, the temperature was increased up to 900 °C at a ramp rate of 10 °C/min. A trap was positioned at the outlet to collect the formed water, and a thermal conductivity detector, which had been previously calibrated using CuO reduction as a standard, was used to record the H_2 consumption.

3.3.6 – H_2-Chemisorption

Chemisorption analysis studies the interaction between a solid surface (usually a catalyst or adsorbent material) and gas molecules based on their chemical sorption over the material's surface. Unlike the physisorption phenomenon, where weak van der Waals forces are involved, chemisorption involves the bonding between the adsorbate molecules and the surface, which are much stronger than the ones observed in physisorption. These interactions involve the sharing or transfer of electrons between the gas molecule and the catalyst's active centers [15].

Additionally, a specific stoichiometry is involved since it involves a chemical reaction. In the case of H_2, which was the gas used for the analysis in this study, the dihydrogen molecule chemisorbs dissociatively on metals with a clear stoichiometry of Metal/H_2 = 2 for a large number of group VIII metals when the particle sizes are larger than 1 nm [16]. This makes this technique a quantifiable one, making it possible to determine physical-chemical properties, such as H_2 uptake, available metallic surface area, and metallic dispersion, with the data obtained with the amount of chemisorbed H_2 as described in the classical article published by Bartholomew [17].

As with the calculations to determine textural properties with N_2 adsorption, the first step is calculating the amount of gas needed to form the monolayer. The moles of H_2 adsorbed per gram of sample are given by **Equation 3.9**:

$$N_m = \frac{P \cdot V_{mono}}{m \cdot R \cdot T}$$ **Equation 3.9**

In which,

N_m is the amount of chemisorbed H_2 per unit of mass of catalyst.
V_{mono} is the H_2 volume measured for the formation of a monolayer. This value can be determined by extrapolation at P = 0 atm for the chemisorption isotherm.
m is the catalyst's mass.
R is the ideal gas constant, 8.314 J K^{-1} mol^{-1}.
P and T are the pressure and temperature employed during the chemisorption analysis condition.

With N_m determination, the metallic surface, S_{Metal}, can be calculated with Equation 3.10:

$$S_{Metal} = N_m \cdot F_s \cdot N_a \cdot A_{Metal}$$ **Equation 3.10**

In which,

N_m is the amount of chemisorbed H_2 per unit of mass of catalyst.
F_s is the stoichiometric factor (which is 2 for Ni in these conditions).
N_a is the Avogadro constant, $6.022 \cdot 10^{23}$ mol^{-1}
A_{Metal} is the cross-sectional area of each surface-active atom (which is 6.494 Å²/Ni atom) [17].

Also, in a more simplified way, the molar quantity of Ni^0 sites per unit of mass in a catalyst, which is a physical quantity that will be further discussed in the catalytic tests section for the determination of turnover frequencies (TOF) can be determined by **Equation 3.11**:

$$\overline{N}_{available,\ Ni} = N_m \cdot F_s \qquad \textbf{Equation 3.11}$$

In the particular case of this thesis, the technique of H_2 chemisorption was employed to determine the metallic surface of Ni in a series of different catalysts. H_2 was used as the gas since its adsorption presents fewer problems than CO, mainly because for the case of H_2, the stoichiometry is one H atom per Ni atom, whereas with CO chemisorption, up to four different ways of binding to the surface Ni atoms have been identified, making it difficult to establish the stoichiometry of the process [16].

The chemisorption measurements were taken using a Quantachrome Autosorb-1C apparatus. For this type of measurement, about 300 mg of a sieved sample (0.2 – 0.4 mm) were loaded into the reactor and then reduced under the same conditions as the in situ process before the reaction, i.e., under a H_2 flow (150 mL min^{-1}) at 450 °C (heating ramp: 10 °C min^{-1}) for 2 hours. After the reduction step, the sample is exposed to a vacuum without changing temperature and, afterward, the sample is cooled down to 30 °C under a N_2 flow. Then, H_2 is added on pulses sequentially to the sample while the adsorbed volume is registered to obtain the isotherm which accounts for the chemisorption and physisorption phenomena combined. After the first data collection, the sample was degasified again under vacuum, which removed the physiosorbed H_2 molecules, while the chemisorbed H_2 ones remained strongly bound to the Ni^0 metallic surface.

After this evacuation step, H_2 is reintroduced in pulses into the system, but this time, only physical adsorption takes place, resulting in the physisorption isotherm. At last, the chemisorption isotherm can be obtained by taking the difference between the combined adsorption isotherm and the physisorption isotherm.

3.3.7 – Carbon Dioxide Temperature Programmed Desorption coupled with Mass Spectrometry (CO_2-TPD-MS)

Temperature-programmed desorption (TPD) is a technique that received significant attention, particularly in catalysis studies, once it provides reliable information on how gas molecules interact with material surfaces. With this technique, it is possible to obtain insights into the nature of surface interactions, the strength of adsorption, and the presence of active sites on the catalyst' surface [18].

Among the many gases that can be used for the TPD technique, the CO_2-TPD is the one that evaluates the desorption of carbon dioxide from the material's surface and is of particular interest for the analysis of catalysts aimed at the CO_2 methanation reaction. This is because it directly studies how these molecules interact with species on the catalyst surface, such as hydroxyl or oxide groups, which account for a material basicity [19].

The technique is based on inserting the material inside a temperature-controlled tube and then thermally treating it at high temperatures to release volatile contaminants (**Figure 3.6**). Afterwards, the temperature is lowered, and the material is exposed to CO_2 until adsorption saturation is achieved and then, the sample is gradually heated while monitoring the amount of desorbed CO_2 gas as a function of temperature, which is typically performed using mass spectrometry or other analytical techniques. The rate at which CO_2 desorbs from the surface depends on the strength of the CO_2-material interaction, which is related to the material's surface properties, and it is observed as a sequence of peaks that can be quantified [20]. This data can provide information about CO_2 uptake and also CO_2 desorption activation energy, which can help to gather information on how the catalysts' surface interacts with CO_2 molecules.

In the particular case of this thesis, the CO_2-TPD was used to determine the materials' CO_2 uptake and, after the peak deconvolution, the temperatures at which the desorption events occur. Once it is known that in the CO_2 methanation reaction, the CO_2 sorption step is an important one in the reaction mechanism, this data provided reliable information to understand the reaction mechanism taking place in each class of the studied materials.

The CO_2-TPD analyses were carried out by placing 100 mg of the catalyst in a steel tube system, as seen in **Figure 3.6**. Afterwards, a He flow (50 mL min^{-1}) was introduced into the tube and then, it was gradually heated to 200 °C (10°C min^{-1}) and maintained at this temperature for 1 hour. Subsequently, the reactor's temperature was lowered to the adsorption temperature (40 °C), and the tube was loaded with a CO_2 flow mixed with He (total flow: 80 mL min^{-1}, 40% v/v CO_2). Following saturation, the reactor's temperature was raised to 650 °C (10 °C min^{-1}), while the released molecules were then examined using a Balzers Prisma Quadrupole QME 200 MS-spectrometer (**Figure 3.6**). Detection of CO_2 desorption was achieved by monitoring the signal at m/z 44.01.

Quantification of CO_2 uptake was carried out by comparison with the standard desorption spectra of sepiolite, which has CO_2 uptake value and a well known desorption profile in the literature [21]. For this, the total area under the curve for the m/z 44.01 signal for the sepiolite was obtained and used as a reference for all other measurements.

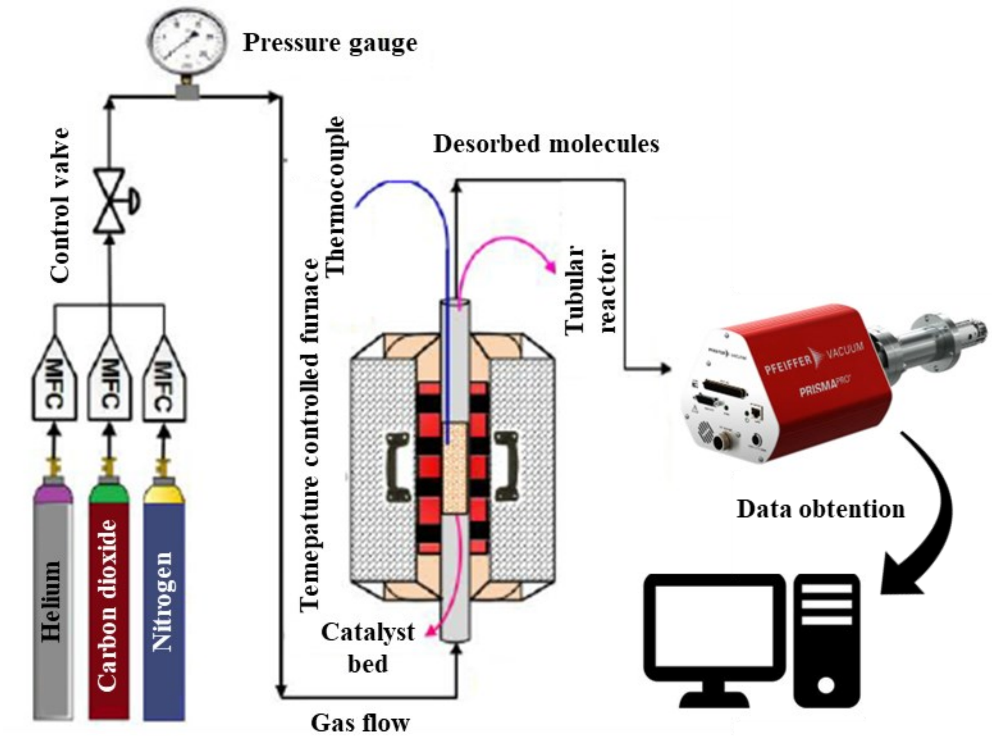

Figure 3.6. Schematic diagram of the experimental setup used for the CO_2-TPD-MS analyses carried out in this study. Image adapted from Naeem [22].

3.3.8 – Fourier Transform Infrared (FT-IR) Spectroscopy

The Fourier Transform Infrared (FT-IR) Spectroscopy is a technique that has significant application in catalysis and materials science because it allows for the determination of molecular structures and enables quantitative and qualitative identification of chemical species [23].

This technique is based on the phenomenon that molecular bonds vibrate at particular frequencies. If this vibration results in a dipole moment change, this bond can be absorbed and excited by infrared radiation photons at a characteristic frequency. This way, if a sample is exposed to a broad range of IR frequencies, and the intensity of the transmitted or reflected radiation is evaluated, information about the type of molecular bonds found in a material can be obtained [24].

Since chemical elements have different electronegativity values and can make single, double, or triple bonds, every chemical bond has a characteristic vibration frequency. **Figure 3.7** shows the different wavenumber zones in which the chemical bond vibration frequencies can be found. In general, the stronger the bond, the more energy will be necessary to excite the vibration mode, which is why double and triple bonds require photons of higher energy than the single bond equivalent.

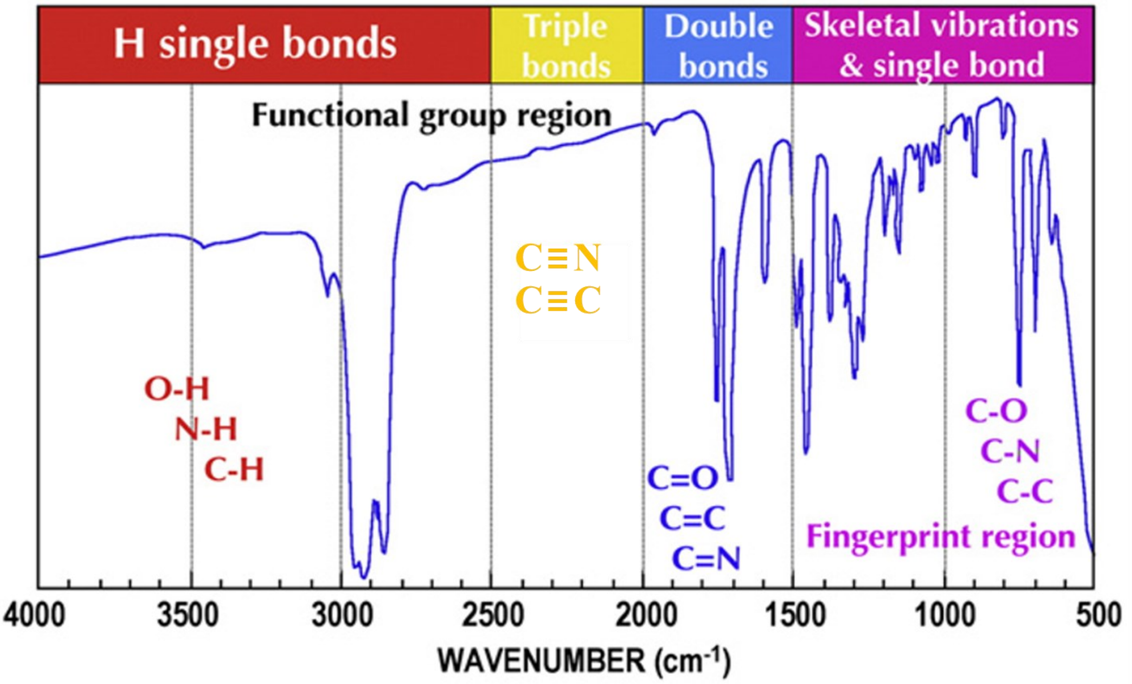

Figure 3.7. Schematic representation of a generic mid-IR transmission spectrum showing typical absorption lines associated with vibrational modes of different chemical bonds. Image adapted from Marcelli [25].

In this study, FT-IR spectroscopy was used for two different applications. The first one was for the characterization of some of the surface of the materials under dry conditions and the determination of surface hydroxyl groups and acidity and basicity by carrying out some pyridine-assisted analyses. This one will be described hereinafter.

For some of the catalysts, there was an interest in determining the presence and concentration of surface hydroxyl groups. For this, a typical transmission IR study enables determining their presence. For a typical analysis, 100 mg of a previously dried sample is squeezed to take the shape of a self-sustaining wafer and inserted into a transmission chamber. The wafer was dried under a vacuum at 400 °C overnight to eliminate traces of water and possible contaminants. Then, a transmission spectrum of the material is obtained in a Nicolet iS 10 FT-IR spectrometer in the 1200-4000 cm^{-1} range.

The second application was for reaction mechanism studies under operando conditions, which allowed the determination of reaction intermediates, such as carbonates, bicarbonates, formates, etc., and it will be more thoroughly described in section **3.3.11**, after the catalytic tests section, for clarity reasons.

3.3.9 – Microscopy measurements

Electron microscopy is a powerful technique that enables the acquisition of high-resolution images of materials. It provides valuable insights into their structure, morphology, topology, chemical composition, and defect characterization, generated through the interaction between a beam of electrons and the sample (**Figure 3.8**).

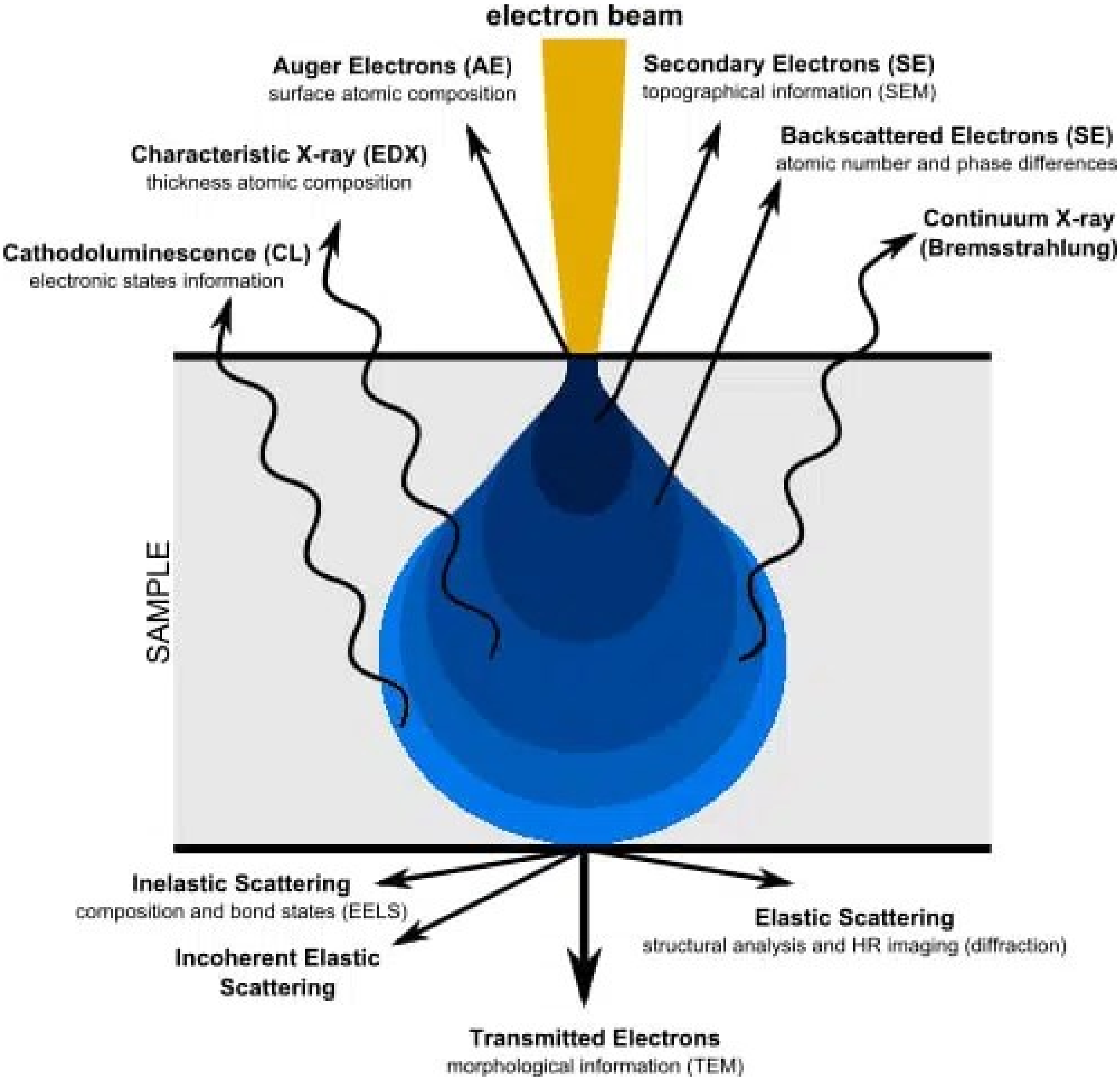

Figure 3.8. Simplified depiction of the effects that take place by the interaction of an electron beam with matter. Image adapted from Ezahmouly et al. [26].

The utilization of electrons distinguishes electron microscopy from optical microscopy by offering superior resolution capabilities due to the shorter wavelength and higher energy exhibited by electrons compared to photons in visible light [27]. As a result, electron microscopy allows for greater magnification levels and even atomic resolutions that surpass the limitations imposed by optical microscopes operating within visible light wavelengths. Two types of microscopy techniques were employed in this work, and they are described after this.

Transmission electron microscopy (TEM)

The first of the microscopy techniques used in this study is the Transmission Electron Microscopy (TEM), which uses accelerated electrons focused by lenses to examine samples. By capturing and concentrating the transmitted and dispersed beams, TEM produces images with varying levels of gray intensity, which correspond to the extent of dispersion of the incident electrons [28, 29].

Two different imaging modes can be employed: bright field mode (whereby dark objects appear against a light background when using transmitted beams) or dark field mode (which uses scattered electrons leading to bright object appearances against a dark background), which is more commonly utilized in practice.

Moreover, by utilizing this method, diffraction patterns can be acquired when examining crystalline samples. These diffractograms furnish insights into the orientation and structure of the constituent crystalline phases. Additionally, valuable information regarding material composition can also be obtained. Combining this technique with an energy-dispersive X-ray Spectroscopy (EDS) analyzer, chemical composition details can be derived from characteristic X-rays emitted by the sample upon electron bombardment (**Figure 3.8**).

A variant of TEM involves detecting transmitted electrons while scanning through a specimen, known as Scanning Transmission Electron Microscopy. STEM offers an advantage over conventional TEM in terms of reduced radiation damage since the beam is mobile rather than fixed and sweeps across the sample during imaging [30].

The microscope used in this study was the JEM 2100F model from JEOL, a high-resolution 200 kV transmission electron microscope. For the preparation of the samples, it is necessary to consider that the sample must be permeable to the electrons. To achieve this, a small amount of the catalyst is dispersed in isopropanol, and then two droplets are placed over a carbon-coated Cu grid.

After obtaining the microscopy images, particle size distribution was analyzed using Image J software, which involved counting a determined number of particles for each sample. The data was fitted to a normal distribution and used to estimate the average Ni^0 particle size.

Scanning Electron Microscopy (SEM)

Scanning Electron Microscopy (SEM), a potent technique used to visualize the surface morphology and topography of a wide range of materials at very high magnifications, was the second microscopy technique used in this study.

This method involves exposing the sample to a high-energy electron beam. The electrons interact with the sample to produce various forms of radiation, which are then captured by detectors and converted into images. Two kinds of electrons stand out among these radiation types produced when the beam interacts with the sample in SEM microscopy: secondary and backscattered electrons (**Figure 3.8**).

Secondary electrons are low-speed ones resulting from the emission corresponding to the atoms closest to the surface, while backscattered electrons are the ones that interact with the nuclei of the atoms in the sample and are reflected in the opposite direction. The emission intensity of backscattered electrons depends on the atomic number of the sample's atoms, with heavier atoms producing more backscattered electrons. This way, an image generated from this type of electrons can contrast the differences to reveal details about chemical composition.

In this work, a variant type of this microscopy mode, called Field Emission Scanning Electron Microscopy (FESEM), was also used. Like SEM, FESEM allows for detailed information about the surface of the sample, but with the difference that the electron beam is generated with a field emission gun, which can emit electrons with higher energy than the ones generated by the sources commonly used in the traditional SEM. With this, the FESEM technique can produce images with even higher resolution and contrast than the ones generated by SEM.

FESEM has been used to understand the surface morphology of catalysts prepared over FER and ITQ-6 zeolites to identify the topological alteration during the delamination procedure and obtain information about the changes after calcination, reduction, and reaction. Additionally, SEM microscopy assessed catalysts supported on sepiolite and lanthanum aluminates to obtain information about textural properties and Ni^0 size distribution.

For this purpose, a Zeiss Ultra 55 microscope, a field emission scanning electron microscope equipped with various detectors (for secondary and backscattered electrons), was used. Sample preparation involves depositing a small amount of solid onto a double-sided adhesive tape previously attached to a sample holder. Then, any remaining loosely adhered solid is removed by blowing, and finally, the sample is introduced inside the equipment holder.

3.3.10 – Catalytic tests

Catalytic tests were used to evaluate each catalyst for the CO_2 methanation reaction. These tests were carried out following the description provided in the following sections, which include additional information about the standard test, the experimental setup used, and the computations needed to determine each catalyst's catalytic activity and selectivity. Furthermore, other catalytic tests, in addition to the standard ones described, will be described thoroughly.

Equipment Setup Description

The equipment employed for the catalytic tests is schematically depicted in **Figure 3.9** and can be divided into three parts: feeding system, reaction system, and product analysis.

The feeding system comprises three mass flow meters provided by Bronkhorst High-Tech B.V., enabling the delivery of desired quantities of CO_2, H_2, and N_2, which were calibrated beforehand using a conventional burette flow meter. At the exit of these mass flow controllers, a check valve is positioned in each gas line to prevent any potential backflow of compounds from the equipment into the feed lines. Furthermore, a pressure relief valve is installed to prevent possible overpressure issues within the system, and a preheater ensures that the inlet gases enter the system at the desired temperature.

The reaction system features a network of heated lines and valves to direct the fed gases through the rest of the setup. Adequate heating of the system is essential to prevent possible condensation of reaction products and to achieve this, various thermocouples and controllers maintain the system at the desired temperature.

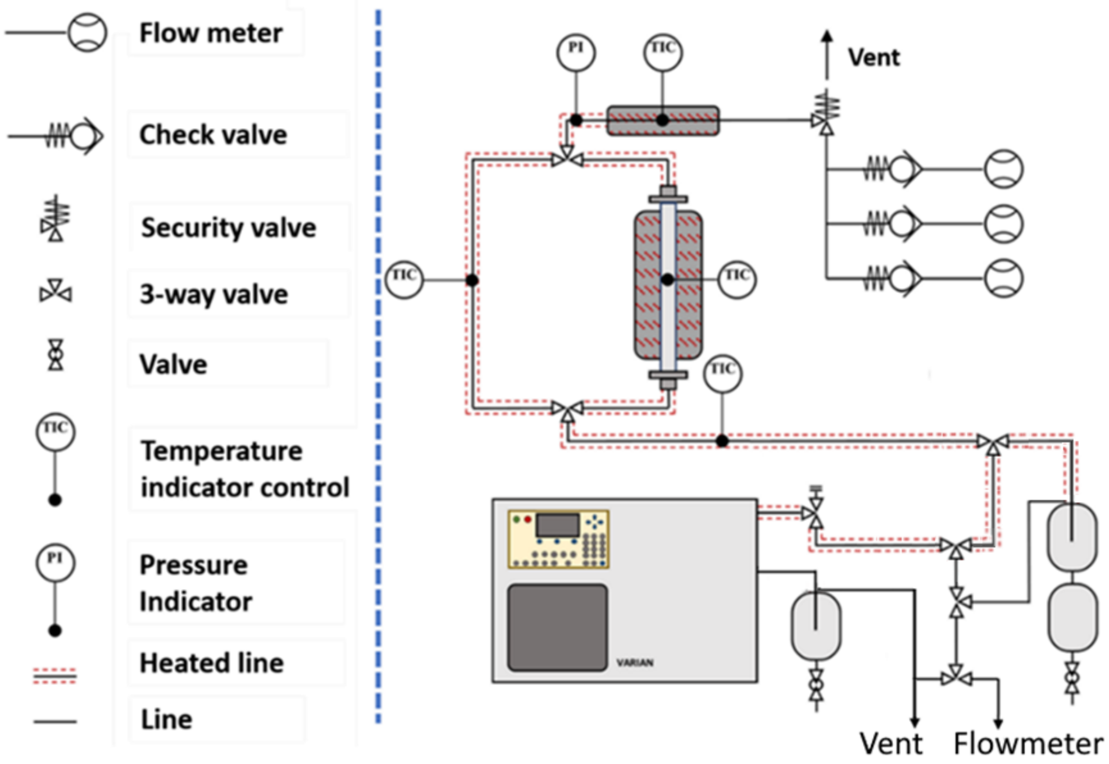

Figure 3.9. Scheme of the catalytical unit used to perform the tests.

The initial valves downstream of the feeding system direct the gas flow to either the reaction zone or the bypass. The reaction zone comprises a heating furnace enveloping a fixed-bed tubular reactor (**Figure 3.10**) that houses the catalyst bed. The bypass zone allows the analysis of gas composition fed into the reactor without passing through the reactor itself.

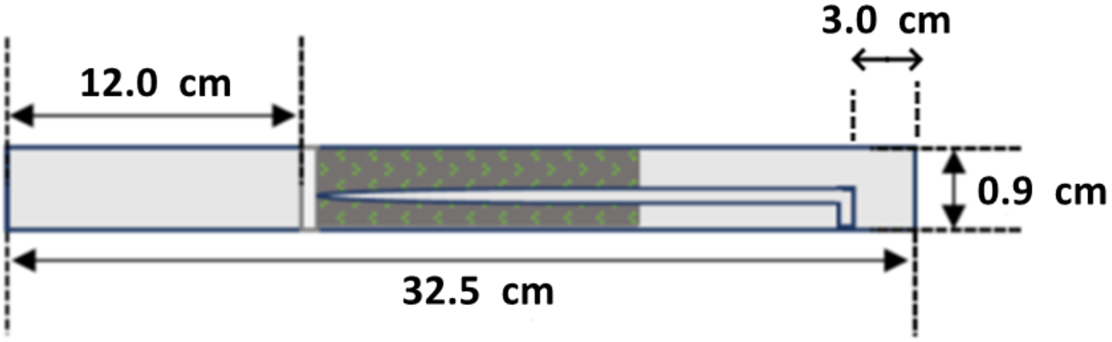

Figure 3.10. Schematic representation of the fixed-bed tubular reactor dimensions used for the catalytic tests.

The catalyst bed within the reactor consists of catalyst particles (previously sieved to size in the range of 0.2-0.4 mm) mixed with silicon carbide particles (size larger than 0.600 mm), an inert material that keeps the catalyst bed volume constant at 5.0 mL. The reactor containing the catalyst bed is a quartz reactor with an inner sheath that accommodates a thermocouple placed halfway through the catalyst bed to control its temperature. Given the specified reactor measurements depicted in **Figure 3.10**, the catalyst bed has a height of 7.9 cm, satisfying the conditions between catalytic bed length ($L_{reactor}$), reactor diameter ($d_{reactor}$), and average particle diameter (d_{cat}) of: $L_{reactor}/d_{cat} > 50$ and $d_{reactor}/d_{cat} > 10$, confirming the plug flow behavior, which regards the fixed bed with homogeneous porosity [31].

The final part of the reaction system involves a refrigerated reservoir where condensable reaction products are liquefied and separated from gaseous products.

This segment of the reaction system is directly connected to the product analysis system, which consists of a gas chromatograph (Varian 3800 GC) that employs Ar as the carrier gas. Specifically, this gas chromatograph is equipped with:

-two types of detectors: a Thermal Conductivity Detector (TCD) and a Flame Ionization Detector (FID).

-two chromatographic columns: HayeSep Q (1/8", 2 m) and MolSieve 13X (1/8", 1.5 m), for separating the analyzed gases.

-a methanizer unit, which is a component that contains a catalyst and promotes the conversion of CO and CO_2 into CH_4, so they can also be analyzed in the FID.

- Description of a standard experiment

The catalytic tests were conducted at 1 atm and between 250 and 450 °C. In standard tests, the weight hourly space velocity (WHSV) was 38,000 mL/(g_{cat}·h), defined based on the flow rates of the reactants, CO_2, and H_2. In contrast, the total gas flow was set at 250 mL min^{-1}

with a molar composition of CO_2:H_2:N_2 = 18:72:10. Consequently, the molar ratio of H_2:CO_2 in the inlet stream was 4:1, which is the stoichiometric ratio for the CO_2 methanation reaction. Alternatively, there might be a reference of the gas hourly space velocity (GHSV), which for these conditions is equal to 80,000 h^{-1}, by considering the catalyst volume.

Therefore, the procedure for a standard catalytic test involves the following steps:

Loading of the reactor: The necessary amount of catalyst is weighed according to the experiment's space velocity conditions (0.350 g for a standard assay), and its volume is measured. Then, the required volume of silicon carbide is added to achieve a total bed volume of 5 mL. For the loading, the catalysts are used as a fine powder previously sieved (size range: 0.2-0.4 mm) and mixed with SiC particles whose size are larger than 0.6 mm ensuring maximum homogeneity before introducing into the reactor.

Leakage check: The loaded reactor is placed within the reaction system, and a check is performed to ensure that the system is airtight – meaning all introduced gases circulate through the system, and no leakages are present.

Catalyst activation: The H_2 flow is set to 150 mL/min, and the temperature controllers within the system are activated, set at 150 °C for all lines except the reactor-containing furnace, where it is set to 450 °C. The temperature ramp used for all controllers is 10 °C min^{-1}. Once the indicated reactor temperature (450 °C) is reached, these conditions are maintained for an additional 2 hours. After this time, N_2 (50 mL min^{-1}) is introduced into the system, while the system cools down to 150 °C.

Catalytic tests: The reactor temperature is raised to the initial reaction temperature, typically 250 °C, and the cooling system for the reservoir where liquid reaction products condense is activated. Upon reaching the set temperature, the flow is directed toward the bypass line, and the flow rates of CO_2, H_2, and N_2 are set (45, 180, and 25 mL min^{-1}, respectively, in a standard assay). Under these conditions, the weight hour space velocity is 38,000 mL $(g_{cat} \cdot h)^{-1}$.

After performing three analyses of this feed mixture, the flow is directed to the reactor with the catalytic bed, and the temperature is incrementally raised, usually in 50 °C intervals. At each temperature, three analyses of the reaction products at the reactor outlet are conducted. **Figure 3.11** and **Figure 3.12** display two examples of typical chromatograms for bypass and reaction analyses, respectively. In the bypass chromatograms (**Figure 3.11**), peaks corresponding to H_2, N_2, and CO_2 are observed in the TCD, while only CO_2 is detected in the FID, due to the fact that is previously transformed into CH_4 in the methanizer unit. On the other hand, in the reaction chromatograms (**Figure 3.12**), peaks corresponding to H_2, N_2, CO, CH_4, and CO_2 are discernible in the TCD, and in the FID, CH_4 originated from the transformation of CO and CO_2 via the methanizer and the reaction-derived CH_4 are observed.

Extra experiments which were also conducted

In addition to the standard experiment described previously, other types of catalytic tests were conducted during this study. These are described below, and their conditions are summarized in **Table 3.1**.

Table 3.1. Outline the experimental conditions used for the catalytic experiments and tests carried out in this study.

Experiment	**T (°C)**	**Inlet components and molar fraction** [a]	**Total flow ($mL\ min^{-1}$)**	**WHSV [$mL\ (g_{cat}\cdot h)^{-1}$]**
Standard	250-450	CO_2 (18):H_2 (72):N_2 (10)	250	38,000
Lower WHSV	250-450	CO_2 (18):H_2 (72):N_2 (10)	31.25-250	4,750 - 38,000
CO methanation	250-450	CO_2 (18):H_2 (72):N_2 (10)	250	38,000
Biogas	320	CO_2 (12.6):H_2 (50.4):N_2 (7.9):CH_4 (18.9)	317.5	38,000
Biogas stability	320	CO_2 (12.6):H_2 (50.4):N_2 (7.9):CH_4 (18.9)	317.5	38,000

[a] The number between parenthesis refers to the corresponding molar percentage in the gas inlet mixture. In standard experiments in this study, CO_2 and H_2 were mixed in stoichiometric proportion, i.e., 4:1, and in the sweetened biogas tests, the CH_4:CO_2 proportion was 6:4.

CO methanation tests

To study the mechanism of the CO_2 methanation reaction, and as it is widely known from the literature that CO can be one of the reaction intermediates, catalytic tests for the CO methanation reaction were also carried out for some of the zeolite-based materials.

The catalytic conditions were basically the same as the ones used for the CO_2 methanation reaction, with the difference that the inlet flow was composed of flow rates of CO, H_2, and N_2 set at 45, 180, and 25 mL min^{-1}, respectively, in a standard test. The rest of the conditions were kept exactly the same.

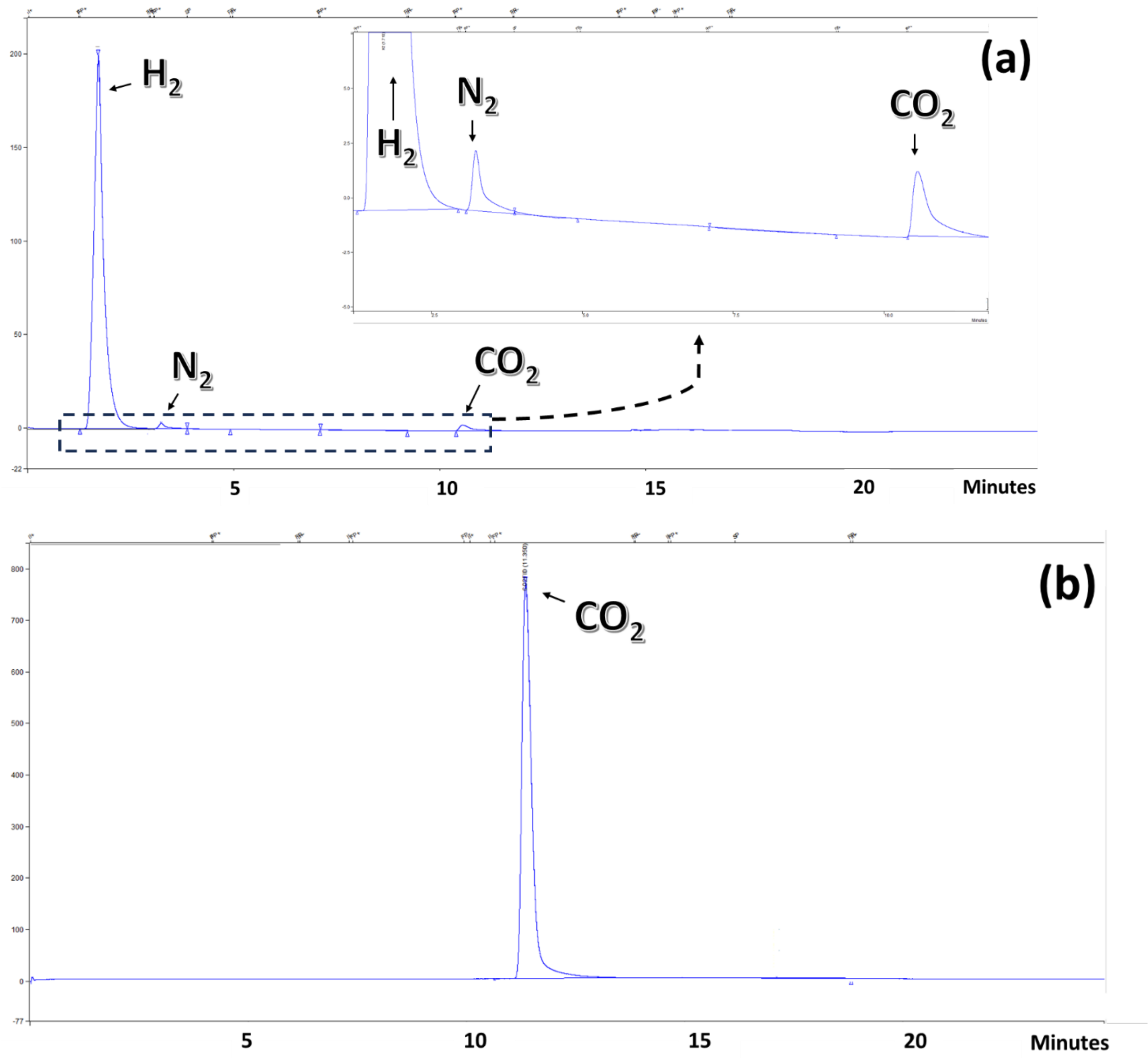

Figure 3.11. Chromatograms obtained for the bypass analyses as detected by the (a) TCD and (b) FID. In the upper figure, a zoom-in of the highlighted region is depicted to show with more clarity the peak separation.

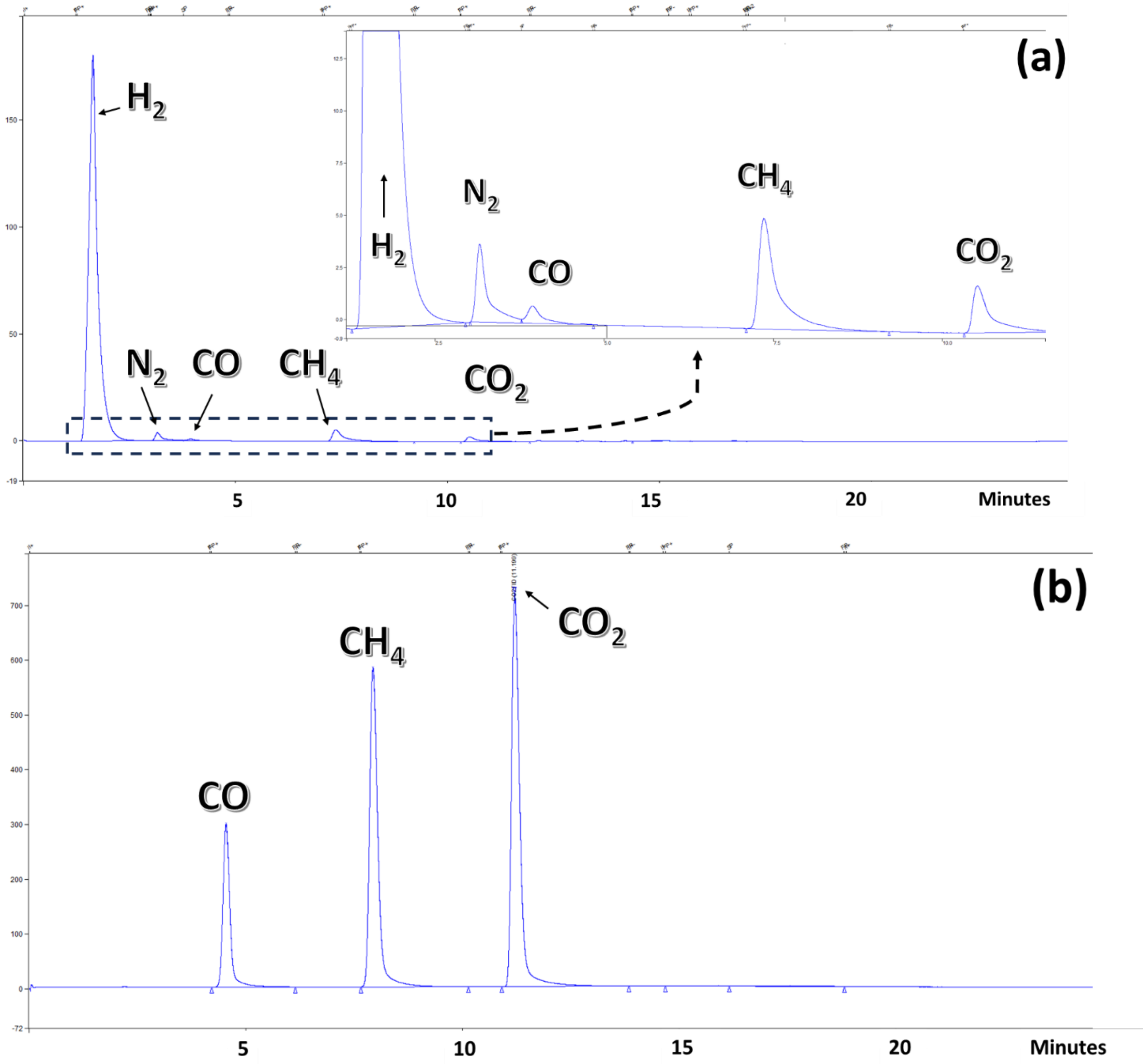

Figure 3.12. Chromatograms obtained for a typical analysis when a CO_2 hydrogenation catalytic test is carried out as detected by the (a) TCD and (b) FID. In the upper figure, a zoom-in of the highlighted region is depicted to show with more clarity the peak separation.

<u>Experiments at lower gas hourly space velocities (WHSV)</u>

To increase the contact time of the reactants for some catalysts, experiments at lower WHSV values were also carried out. Differently from the standard experiment, in which the WHSV was 38,000 mL $(g_{cat}\cdot h)^{-1}$, lower WHSV values were tested, such as 20,000 mL $(g_{cat}\cdot h)^{-1}$, and 10,000 mL $(g_{cat}\cdot h)^{-1}$. To carry out this, the amount of catalyst was kept the same, while the inlet flow rates were proportionally reduced.

Experiments with a simulated sweetened sample of biogas

The simulated sweetened biogas mixture contains a CO_2:CH_4 ratio of 40:60, a typical proportion of these two gases found in real samples [32]. These experiments were conducted maintaining the same speed velocity regarding the reactant gases (CO_2 and H_2). Therefore, in the biogas simulation tests, the inlet composition consisted of CO_2, H_2, N_2, and CH_4 flows set at 45, 180, 25, and 67.5 mL min^{-1}, with the total flow at 317.5 mL min^{-1}. The reaction temperature for these tests was 320 °C, and the WHSV was kept at 38,000 mL/(g_{cat}·h).

Stability experiments

And finally, after the catalysts were tested using sweetened biogas samples emulating real samples, stability tests were carried out at WHSV = 38,000 mL $(g_{cat}\cdot h)^{-1}$ at 320 °C, with the inlet composition consisting of CO_2, H_2, N_2, and CH_4 flows set at 45, 180, 25 and 67.5 mL min^{-1}. Under these conditions, all the catalysts tested in this study presented CH_4 yield values lower than the one set by the thermodynamical equilibrium, which makes this analysis sensitive if the catalysts are deactivated to some extent.

Data treatment

As stated before, the analyses conducted through gas chromatography enable the calculation of the quantities of each gas within the mixture reaching the chromatograph. Based on these values, parameters such as CO_2 conversion or selectivity to reaction products are determined. This quantification is feasible due to the relationship between the area of each peak, associated with a specific compound, and the amount of that compound in the mixture.

The quantification of each gas via chromatography is achieved by using N_2 as a standard gas for quantification and applying response factors. Initially, the response factors (RF) of the TCD and FID are calculated from the analysis of a gas mixture with a known composition: CO_2 (15%), H_2 (48%), N_2 (20%), CH_4 (15%), CO (2%), using **Equation 3.12** and **Equation 3.13**.

$$RF_{TCD} = \frac{\left(\frac{A}{n}\right)_{analyte}}{\left(\frac{A}{n}\right)_{N_2}}$$ **Equation 3.12**

$$RF_{FID} = \frac{\left(\frac{A}{n \cdot MW}\right)_{analyte}}{\left(\frac{A}{n \cdot MW}\right)_{CH_4}}$$ **Equation 3.13**

In which,

RF_X is the response factor of each compound or analyte in the TCD or in the FID.

A is the area under the peak corresponding to the analyte or the reference gas (N_2 for the TCD, and CH_4 for the FID).

n is the molar amount of the corresponding gas.

MW is the gas molecular weight.

Once the response factors are determined, the quantities of each detected compound by the TCD are derived from the area under the peak assigned to that compound. This calculation is carried out assuming that the introduced N_2 does not undergo any reaction as it is an inert gas, which is a quite realistic assumption for the experimental conditions. Consequently, the N_2 molar flow rate entering the reactor is equal to the molar flow rate exiting the reactor.

For the quantification of the FID results, the response factor is calculated by using the TCD-determined CH_4 amount as a reference, but instead of calculating in terms of molar amount, it is calculated in terms of mass, as the FID is weight-sensitive.

Once the response factor for each one of the compounds have been determined, the molar flows of each one of the gas components can be calculated with the following equation:

$$\dot{n}_X = RF_{TCD} \cdot \dot{n}_{N_2}$$ **Equation 3.14**

In which,

$\dot{n}_X$ is molar flow, in mol h^{-1}, either for the analyte X, which was used as standard gas.

$RF_{TCD,\ X}$ is the TCD response factor for the analyte X, as determined in **Equation 3.12**.

After the molar flows have been determined, for CO_2 methanation reaction, CO_2 conversion (X_{CO_2}), selectivity towards CH_4 (S_{CH_4}), yield to CH_4 (Y_{CH_4}), and turnover frequency number towards CH_4 (TOF_{CH_4}) were calculated using the following expressions. The ***in*** **subscript** refers to inlet flow, while the ***out*** **subscript** to the outlet one.

$$X_{CO_2} = \frac{\dot{n}_{CO_2,in} - \dot{n}_{CO_2,out}}{\dot{n}_{CO_2,in}} \times 100\%$$ **Equation 3.15**

$$S_{CH_4} = \frac{\dot{n}_{CH_4,out}}{\dot{n}_{CH_4,out} + \dot{n}_{CO,out}} \times 100\%$$ **Equation 3.16**

$$Y_{CH_4} = X_{CO_2} \times S_{CH_4}$$ **Equation 3.17**

$$TOF_{CH_4} = \frac{\dot{n}_{CH_4,out}}{0.350\ g \times \overline{N}_{available,\ Ni}}$$ **Equation 3.18**

For CO methanation reaction, CO conversion (X_{CO}) and turnover frequency number towards CH_4 (TOF_{CO}) were calculated using the following expressions:

$$X_{CO} = \frac{\dot{n}_{CO,in} - \dot{n}_{CO,out}}{\dot{n}_{CO,in}} \times 100\%$$ **Equation 3.19**

$$TOF_{CO} = \frac{\dot{n}_{CH_4,out}}{0.350\ g \times \overline{N}_{available,\ Ni}}$$ **Equation 3.20**

Finally, to confirm the validity of the results obtained, the carbon balance (C balance) for each analysis was calculated, which basically consisted of calculating the number of moles in the inlet and outlet flows of the reactor, using **Equation 3.21**. The C balance is correct when the number of moles of C introduced to the reactor is equal to the number of moles of C at the exit of the reactor.

$$C\ balance(\%) = \frac{\sum\left(n_i \cdot \left(\frac{mol}{h}\right)_i\right)_{out}}{\sum\left(n_i \cdot \left(\frac{mol}{h}\right)_i\right)_{in}} \cdot 100$$ **Equation 3.21**

In all the catalytic tests, the C balance was 100 ±5 %.

3.3.11 – FT-IR Mechanistic studies

In this work, the reaction mechanism studies have been conducted using operando conditions with infrared spectroscopy. When an analysis is performed on operando conditions, the measurements are conducted under real operating conditions. For this reason, it is possible to identify the different types of bonds formed by the interaction between reactants and products on the catalyst's surface. Therefore, with this technique, it is possible to identify the reaction intermediates formed and their interaction with the catalyst, ultimately making it feasible to propose a mechanism pathway by which the reaction takes place [33].

In this work, the technique was used to study the sepiolite-based catalysts to rationalize the catalytic results and propose a possible mechanistic pathway by which the CO_2 methanation reaction might be taking over this class of materials.

The operando measurements were carried out in a system as the one depicted in **Figure 3.13**, in which it is possible to see the Nicolet 6700 FTIR spectrometer used for carrying out the analyses by following these steps. **Figure 3.14** depicts the custom-made cell located inside the spectrometer.

Figure 3.13. Nicolet 6700 FT-IR spectrometer used for the operando FT-IR measurements carried out in this work. The custom-made cell is located inside the spectrometer where the IR beam could orthogonally hit the catalyst's surface.

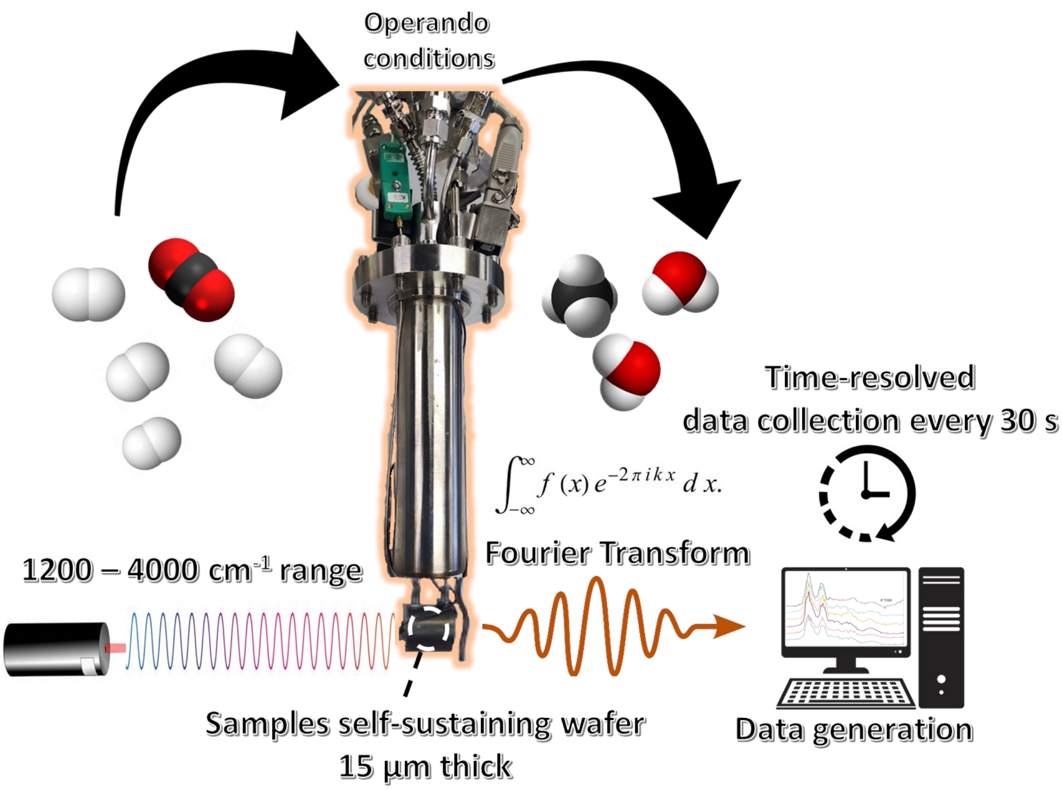

Figure 3.14. Photograph of the custom-made IR cell used in this study and schematic representation of the process used to obtain the operando FT-IR spectra. 15- µm-thick wafers were prepared from the solid samples and positioned orthogonally to the beam pathway.

This way, these are the steps while conducting an operando FT-IR experiment:

1. Sample Preparation

For a standard procedure, first, the catalyst powder, which had been thoroughly dried, is pressed into 15 µm thick circular self-sustaining wafers (radius = 2 cm). Then, the wafer was inserted inside the custom-made transmission cell, where the IR beam could hit the surface orthogonally and pass through, as seen in **Figure 3.14**.

2. Catalyst reduction and background reference spectrum obtention

The catalyst was then reduced under the same conditions used in a catalytic test, i.e., at 450 °C under a 150 mL min^{-1} H_2 flow for 2 hours, before being cooled to 50 °C under a 25 mL min^{-1} He flow. At this point, a background spectrum is obtained, and it will be subtracted from all the others obtained after this one. This is performed to reduce surface interference in the measurements and make it possible to focus on the formation of the reaction intermediates.

3. Operando experiments

After the background spectrum is obtained, two types of experiments can be carried out.

The first type is the operando per se experiment, in which the sample is exposed to the reaction reactant flow diluted in He (CO_2, H_2, and He; 45, 180, and 25 mL min^{-1}, respectively). Then, the temperature is raised to 250 °C and kept under 20 minutes while an IR spectrum is continuously obtained every 30 seconds. After the 20-minute period, the cell is heated successively to 450 °C with 50 °C intervals, repeating the 20-minute retaining time at each temperature.

The second type is the transient operando experiments. In this type of experiment, the sample is first heated to 250 °C, and then, the continuous IR measurements are performed every 30 seconds. Then, a CO_2 flow diluted in He (CO_2 and He; 45 and 25 mL min^{-1}, respectively) is inserted into the chamber, while the sample is left at this temperature for 20 minutes. After this time, the CO_2 flow is exchanged by a H_2 flow diluted in He (H_2 and He; 180 and 25 mL min^{-1}, respectively), and the sample is left under this condition for another 20 minutes under continuous IR analysis. Upon finishing this time, the sample is heated successively to 450 °C with 50 °C intervals, with transient injections of CO_2 and H_2 repeated the same way as done at 250 °C.

4. Finishing the experiment

After the measurements are concluded, the cell chamber temperature is reduced again to room temperature, and another spectrum is obtained for a safety check comparison with the reference spectrum.

3.4 – References

[1] Chica A, Diaz U, Fornés V, Corma A. Changing the hydroisomerization to hydrocracking ratio of long chain alkanes by varying the level of delamination in zeolitic (ITQ-6) materials. Catalysis Today. 2009;147:179-85.

[2] Chen M, Wang C, Wang Y, Tang Z, Yang Z, Zhang H, et al. Hydrogen production from ethanol steam reforming: Effect of Ce content on catalytic performance of Co/Sepiolite catalyst. Fuel. 2019;247:344-55.

[3] Torrez-Herrera JJ, Korili SA, Gil A. Effect of the synthesis method on the morphology, textural properties and catalytic performance of La-hexaaluminates in the dry reforming of methane. Journal of Environmental Chemical Engineering. 2021;9:105298-.

[4] Jana P, Jayan PS, Mandal S, Biswas K. Effect of seeding on the formation of lanthanum hexaaluminates synthesized through advanced sol gel process. Journal of Crystal Growth. 2014;408:7-13.

[5] Ameh ES. A review of basic crystallography and x-ray diffraction applications. The International Journal of Advanced Manufacturing Technology. 2019;105:3289-302.

[6] Muniz FTL, Miranda MAR, Morilla dos Santos C, Sasaki JM. The Scherrer equation and the dynamical theory of X-ray diffraction. Acta Crystallographica Section A. 2016;72:385-90.

[7] Rahman MM, Muttakin M, Pal A, Shafiullah AZ, Saha BB. A Statistical Approach to Determine Optimal Models for IUPAC-Classified Adsorption Isotherms. 2019;12:4565.

[8] Kuila U, Prasad M. Specific surface area and pore-size distribution in clays and shales. 2013;61:341-62.

[9] Zou J, Fan C, Liu X. Effects of Molecular Cross-Sectional Areas of Adsorbed Nitrogen on the Brunauer-Emmett-Teller Analysis for Carbon-Based Slit Pores. Langmuir : the ACS journal of surfaces and colloids. 2020;36:14656-65.

[10] Lippens BC, de Boer JH. Studies on pore systems in catalysts: V. The t method. Journal of Catalysis. 1965;4:319-23.

[11] Cherevko S, Mayrhofer KJJ. On-Line Inductively Coupled Plasma Spectrometry in Electrochemistry: Basic Principles and Applications. In: Wandelt K, editor. Encyclopedia of Interfacial Chemistry. Oxford: Elsevier; 2018. p. 326-35.

[12] Donati GL, Amais RS, Williams CB. Recent advances in inductively coupled plasma optical emission spectrometry. Journal of Analytical Atomic Spectrometry. 2017;32:1283-96.

[13] Kandioller W, Theiner J, Keppler BK, Kowol CR. Elemental analysis: an important purity control but prone to manipulations. Inorganic Chemistry Frontiers. 2022;9:412-6.

[14] Jehng J-M, Wachs IE, Patience GS, Dai Y-M. Experimental methods in chemical engineering: Temperature programmed surface reaction spectroscopy—TPSR. 2021;99:423-34.

[15] Vesselli E, Peressi M. Chapter 8 - Nanoscale Control of Metal Clusters on Templating Supports. In: Fornasiero P, Cargnello M, editors. Studies in Surface Science and Catalysis: Elsevier; 2017. p. 285-315.

[16] Almithn AS, Hibbitts DD. Supra-monolayer coverages on small metal clusters and their effects on H2 chemisorption particle size estimates. 2018;64:3109-20.

[17] Bartholomew CH, Pannell RB. The stoichiometry of hydrogen and carbon monoxide chemisorption on alumina- and silica-supported nickel. Journal of Catalysis. 1980;65:390-401.

[18] Nishi Y, Inagaki M. Chapter 11 - Gas Adsorption/Desorption Isotherm for Pore Structure Characterization. In: Inagaki M, Kang F, editors. Materials Science and Engineering of Carbon: Butterworth-Heinemann; 2016. p. 227-47.

[19] Ishii T, Kyotani T. Chapter 14 - Temperature Programmed Desorption. In: Inagaki M, Kang F, editors. Materials Science and Engineering of Carbon: Butterworth-Heinemann; 2016. p. 287-305.

[20] Cvetanović RJ, Amenomiya Y. Application of a Temperature-Programmed Desorption Technique to Catalyst Studies. In: Eley DD, Pines H, Weisz PB, editors. Advances in Catalysis: Academic Press; 1967. p. 103-49.

[21] Güngör N, Işçi S, Günister E, Miśta W, Teterycz H, Klimkiewicz R. Characterization of sepiolite as a support of silver catalyst in soot combustion. Applied Clay Science. 2006;32:291-6.

[22] Naeem MA, Al-Fatesh AS, Fakeeha AH, Abasaeed AE. Hydrogen production from methane dry reforming over nickel-based nanocatalysts using surfactant-assisted or polyol method. International Journal of Hydrogen Energy. 2014;39:17009-23.

[23] Hunger M, Weitkamp J. In situ IR, NMR, EPR, and UV/Vis Spectroscopy: Tools for New Insight into the Mechanisms of Heterogeneous Catalysis. 2001;40:2954-71.

[24] Eischens RP. Infrared Spectroscopy and Catalysis Research. 1964;146:486-93.

[25] Marcelli A, Cricenti A, Kwiatek WM, Petibois C. Biological applications of synchrotron radiation infrared spectromicroscopy. Biotechnology Advances. 2012;30:1390-404.

[26] Ezzahmouly M, Elmoutaouakkil A, Ed-Dhahraouy M, Khallok H, Elouahli A, Mazurier A, et al. Micro-computed tomographic and SEM study of porous bioceramics using an adaptive method based on the mathematical morphological operations. Heliyon. 2019;5:e02557.

[27] Amelinckx S, Van Dyck D, Van Landuyt J, Van Tendeloo G. Electron Microscopy: Principles and Fundamentals2007.

[28] Kim H, Murata MM, Chang H, Lee SH, Kim J, Lee JH, et al. Optical and Electron Microscopy for Analysis of Nanomaterials. Advances in Experimental Medicine and Biology2021. p. 277-87.

[29] Wan W, Su J, Zou XD, Willhammar T. Transmission electron microscopy as an important tool for characterization of zeolite structures. Inorganic Chemistry Frontiers. 2018;5:2836-55.

[30] Su D. Advanced electron microscopy characterization of nanomaterials for catalysis. Green Energy & Environment. 2017;2:70-83.

[31] Khodakov AY, Chu W, Fongarland P. Advances in the Development of Novel Cobalt Fischer−Tropsch Catalysts for Synthesis of Long-Chain Hydrocarbons and Clean Fuels. Chemical Reviews. 2007;107:1692-744.

[32] Li Y, Alaimo CP, Kim M, Kado NY, Peppers J, Xue J, et al. Composition and Toxicity of Biogas Produced from Different Feedstocks in California. Environmental science & technology. 2019;53:11569-79.

[33] Savara A, Weitz E. Elucidation of Intermediates and Mechanisms in Heterogeneous Catalysis Using Infrared Spectroscopy. 2014;65:249-73.

Chapter 4

Zeolite-based catalysts

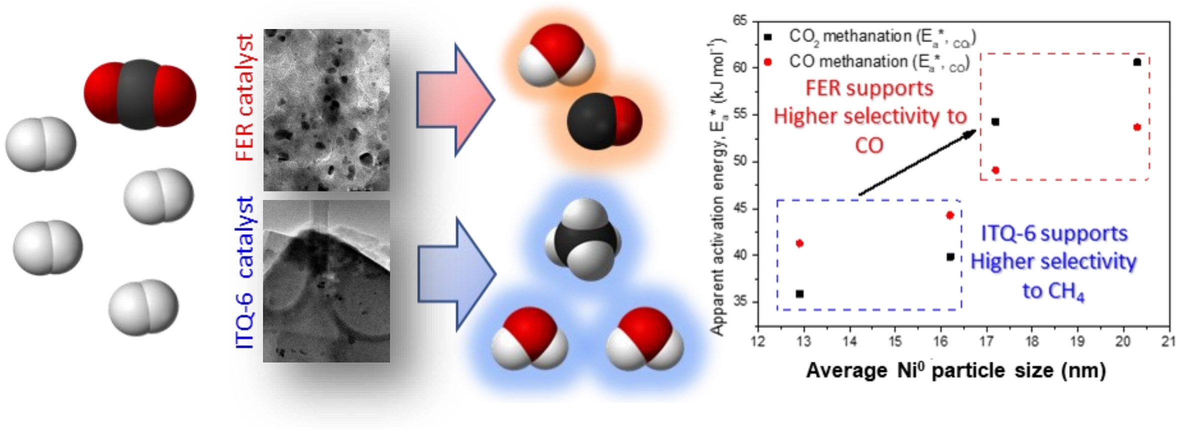

This chapter was adapted with permission from an article previously distributed by Elsevier Corporation.

This article was published in *Journal of Catalysis*, 436, Machado-Silva, R. B.; Costa-Serra, J. F.; Chica, A.; Enhancement of catalytic activity in CO_2 methanation in Ni-based catalysts supported on delaminated ITQ-6 zeolite, 115609, Copyright Elsevier (**2024**).

DOI: 10.1016/j.jcat.2024.115609

4.1 – Introduction

Zeolites are crystalline microporous materials characterized by a well-defined system of channels and cavities with molecular dimensions (3-12 Å). The term "zeolite" originates from the Greek words "zeo (ζέω)" (to boil) and "lithos (λίθος)" (stone), first used by Axel Cronstedt in 1756 when he observed that heating the mineral stilbite caused it to lose water and release it as steam [1].

These materials can be found in natural deposits, predominantly in regions with significant volcanic activity, in which they are formed by chemical alteration of magmatic materials. The specific conditions, including temperature, pressure, and the presence of various ions, contribute to the formation of different zeolite structures and compositions. As a result, naturally occurring zeolites often exhibit a wide variety of physical and chemical properties, depending on the geological setting in which they were formed [2].

In addition to their natural occurrence, zeolites can be precisely synthesized in the laboratory. This synthetic approach allows for the meticulous control of their chemical composition and structural properties, facilitating the production of zeolites with specific characteristics tailored to particular applications, such as adsorption, ion exchange, and molecular sieving [3].

Structurally, these materials consist of a three-dimensional framework of interconnected tetrahedra, each composed of a central silicon or aluminum atom surrounded by four oxygen atoms [4, 5]. In terms of composition, they are aluminosilicates, in which the introduction of aluminum into the network induces a negative charge balanced by the presence of cations (Na^+, K^+, Mg^{2+}, Ca^{2+}, NH_4^+, or H^+) [4].

In addition to silicon and aluminum, the zeolite framework can accommodate a variety of other heteroatoms, such as B, P, Sn, Ti, Fe, Ge, Ta, and V, which can be incorporated into the structure by isomorphous substitution and alter the zeolite's chemical, electronic, and catalytic properties.

Thus, zeolites form a versatile group of materials, both in their chemical composition and structure, making them suitable for a wide range of applications. They have been used for soil and water decontamination, particularly in the removal of inorganic contaminants, such as heavy metals, organic, and even radioactive contaminants [6]. Their adsorption capacity depends on specific properties, such as the Si/Al molar ratio or the type and concentration of the compensation cation. These properties can be modified to enhance the material's efficiency through various treatments (acidic/basic, ion exchange, surfactant treatments, etc.) [7, 8].

Additionally, zeolites have been utilized in other fields, such as for microorganism immobilization [9], soil improvement [10], and in more innovative applications, such as antimicrobial materials, photovoltaic cells, and medical devices [11].

On a large scale, zeolites are employed in the production of detergents and the petrochemical industry as catalysts, in which they hold great commercial values[1, 12]. In the petrochemical industry, the introduction of synthetic faujasite-type zeolites (zeolites X and Y) into an industrial-scale Fluid Catalytic Cracking (FCC) unit in 1962 marked a milestone in the development and application of these materials [13]. The zeolites used were not only more active compared to the previously used silica-alumina catalysts, but they also improved the yield of gasoline fraction, the most valuable product of these FCC units [13].

Since then, zeolites have been employed in the petrochemical industry as highly efficient and selective catalysts in processes such as cracking, isomerization, alkylation, reforming, dewaxing, and desulfurization [1, 12, 14, 15]. The success of these materials is associated with their acidic properties, which can vary in terms of the type (Bronsted or Lewis), the density of active sites, strength, and location. Additionally, due to their microporous structure and the effect on molecular diffusion, zeolites possess shape-selective properties concerning the formation of transition states in the mechanistic pathway, enabling the selective formation of specific products [13].

In addition to their use in the petrochemical industry, zeolites are applied as catalysts in other reactions, such as those involved in biomass conversion for the production of chemicals and fuels [16], NO_x reduction [17], and Fischer-Tropsch synthesis [18].

In recent years, numerous studies have focused on the application of zeolite-based materials as catalysts for the CO_2 methanation reaction. Regarding the porous structure of the zeolites, for example, Bando et al. [19] and Aziz et al. [20] reported that catalysts based on a Y-type zeolite showed superior catalytic performance when they were compared to Al_2O_3 and MgO-based catalysts.

Additionally, Scirè et al. [21] investigated the impact of the support material by comparing Ru-based catalysts supported on H-ZSM-5 and SiO_2 supports via operando FT-IR studies. Their findings indicated that the zeolite-based catalyst exhibited superior performance, attributed to more favorable Ru-zeolite interactions, which accounted for the higher values of CH_4 selectivity.

Similarly, Guo et al. [22] compared the effect of the zeolite framework and reported that a Ni-based catalyst supported on ZSM-5 showed the highest catalytic activity among the tested supports (SiO_2, Al_2O_3, MCM-41, SBA-15, and ZSM-5). This was rationalized by the higher basicity of the first material and its optimum dispersion of the Ni^0 phase, which increased the synergistic interaction between the metallic phase and the support.

Another feature that is also considered when considering zeolites as supports for catalysts for the CO_2 methanation reaction is their basicity. For example, there are reports that Ni-loaded USY and beta zeolites exhibited higher activity when these zeolites do not present low Si/Al molar ratios [23, 24], as higher Si/Al ratio might be associated with higher basicity, which has a positive effect on the CO_2 conversion and selectivity to CH4. The zeolite's compensation cation also affects the basicity and, consequently, the catalytic performance. Bacariza et al. [25] studied a series of catalysts based on the USY zeolite exchanged with a series of monovalent and divalent cations. The results indicated that, depending on the cation, differences in catalytic activity are observed in the order: $Cs^+ > Na^+ > Li^+ > K^+ > H^+$, for monovalent cations and $Mg^{2+} > Ca^{2+} > Ba^{2+}$, for divalent cations. These differences are related to the enhanced CO_2 adsorption capacity and increased basicity of the materials.

The Si/Al molar ratio also affects the hydrophobicity of zeolites, which also has a consequence on the CO_2 methanation reaction performance, as water molecules are one of the reaction products. Bacariza et al., in a report with Ni-based catalysts, prepared over Y zeolite [24], emphasized that Si/Al molar ratios at intermediate values contribute to a better performance in the CO_2 methanation reaction. They found that Si/Al = 3 zeolites exhibited poorer performance than Si/Al = 38 ones, which was attributed to the higher hydrophobicity of the latter, which facilitated the removal of water from the reaction site and promoted methane formation.

Moreover, zeolites have been utilized in other CO_2-related applications beyond catalysis for the CO_2 methanation reaction, such as studies on CO_2 adsorption [26-29]. Various authors reported that zeolites with a low Si/Al ratio exhibit higher CO_2 adsorption capacity compared to those with a higher ratio [26, 27], which was explained by the fact that CO_2 is a molecule with a quadrupole moment and that the substitution of Si by Al leads to a charge deficiency. Consequently, a material with a low Si/Al ratio will exhibit a greater charge deficiency and, thus, a stronger interaction with the CO_2 molecule.

Palomino et al. [27] determine an optimal Si/Al ratio at which CO_2 adsorption is maximized for LTA-type zeolites. As the Al content increases and the Si/Al ratio decreases, the adsorption capacity increases, reaching a maximum at a Si/Al ratio of 2. For higher Al contents, i.e., Si/Al ratios lower than 2, the adsorption capacity decreases.

Considering altogether these characteristics, such as the CO_2 adsorption capacity and the high surface area of zeolites, along with the considerable versatility of their structure and chemical composition, it can be concluded that these materials exhibit significant potential for CO_2 methanation reactions.

In this study, for the first time in the literature, the ferrierite (FER) zeolite and its delaminated counterpart, the ITQ-6 zeolite, were explored as supports for Ni-based catalysts in CO_2 methanation reactions.

Ferrierite (FER) crystallizes under the orthorhombic system and presents a bidimensional porous system composed of 10-MR channels (0.43 nm x 0.55 nm) orthogonally intersected by 8-MR (0.38 nm x 0.55 nm), creating a pile of zeolitic layers (**Figure 4.1**) [30].

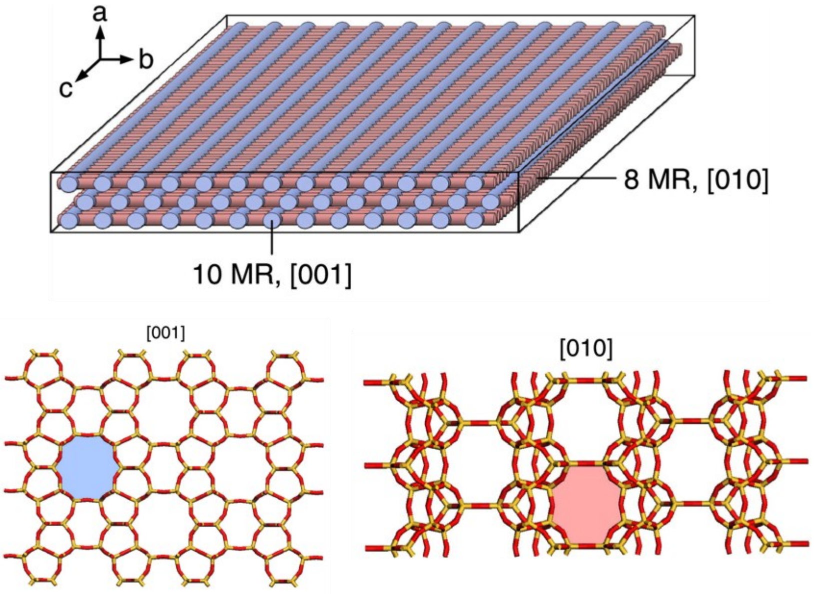

Figure 4.1. Representation of the structure of the ferrierite zeolite along the [001] and [010] directions. The opening of the 8-MR and the 10-MR channels are highlighted. Image adapted from Bonilla et al. [31].

Previous results published by Corma et al. allowed the development of a synthetic procedure, which consisted of a swelling step followed by a delamination of one of the FER zeolitic layers, which led to the production, for the first time, of the delaminated version of the FER, the ITQ-6, as seen in **Figure 4.2** [32, 33].

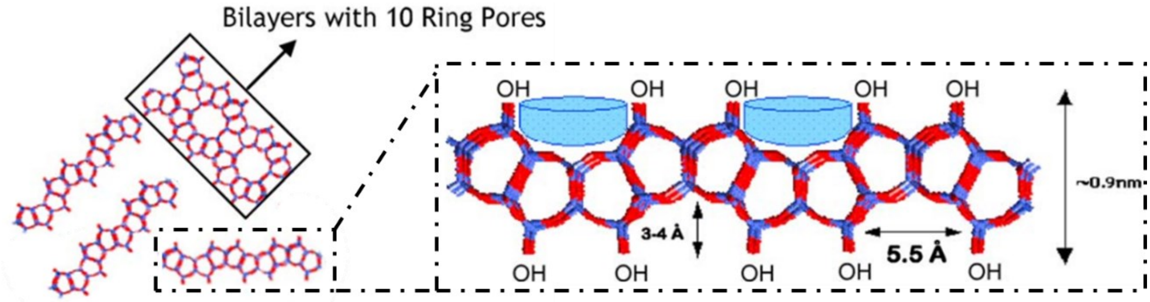

Figure 4.2. Artistic representation of delaminated ITQ-6, revealing the "molecular cups" formed after delamination of the ferrierite structure. Image adapted from Chica et al. [34].

ITQ-6 is primarily composed of delaminated zeolitic layers, which make up a "house-of-cards-like" structure that exhibits "molecular cups" formed in the sites where the 10-MR channels used to be [34]. This delaminated structure significantly increases the material's mesoporous volume and surface area, which might reach values higher than 590 m^2 g^{-1}.

Due to its unique porous and catalytical properties, ITQ-6 has been described as catalyst support for several chemical reactions, such as alkanes hydroisomerization and hydrocracking [34], organic sulfides oxidation [35], Fischer-Tropsch synthesis [36], dehydrogenation [37], and ethanol steam reforming [38]. The article in which these results were published by Machado-Silva et al. is the first report in the literature using this zeolite as support for catalysts aimed at the CO_2 and CO methanation reactions [39].

In this work, Ni-based catalysts over delaminated zeolites (Ni/ITQ-6) were tested to check their performance towards the CO_2 and CO methanation reaction and studied regarding the impact of aluminum content with different techniques, such as XRD, SEM-TEM analyses, H_2-TPR, FT-IR, H_2-chemisorption and N_2 physisorption isotherms determination. With this, the objective of this work was to assess if the ITQ-6 support allows for higher Ni^0 dispersion, and if this had an improving effect on the CO_2 methanation reaction, increasing conversion and selectivity towards CH_4. The incorporation of aluminum into the zeolitic network was also assessed by FT-IR measurements, regarding its effect on the support's concentration of surface hydroxyl groups, and the impact on basicity, hydrophilicity and Ni^0 phase dispersion.

Finally, after identifying that the aluminum-containing ITQ-6 was the best support among the ones tested, Ni loading on this support was optimized and the catalyst was probed to evaluate the potential prospects of using these delaminated zeolites to prepare efficient catalysts for CH_4 production by the Sabatier reaction.

More information was provided in Chapter 3 about the preparation of the catalysts used in this chapter, but their description is summarized in **Table 4.1**. The notation "_R" after the catalyst name indicates it was previously reduced.

Table 4.1. Denomination employed in this chapter for the zeolite-based catalysts prepared over ferrierite (FER) and ITQ-6 zeolites. All Ni loading refers to nominal values established during their preparation.

5Ni/FER (∞)	5% wt. Ni catalyst prepared over FER (Si/Al = ∞)
5Ni/ITQ-6 (∞)	5% wt. Ni catalyst prepared over ITQ-6 (Si/Al = ∞)
5Ni/FER (30)	5% wt. Ni catalyst prepared over FER (Si/Al = 30)
5Ni/ITQ-6 (30)	5% wt. Ni catalyst prepared over ITQ-6 (Si/Al = 30)
10Ni/ITQ-6 (30)	10% wt. Ni catalyst prepared over ITQ-6 Si/Al = 30)
15Ni/ITQ-6 (30)	15% wt. Ni catalyst prepared over ITQ-6 (Si/Al = 30)
20Ni/ITQ-6 (30)	20% wt. Ni catalyst prepared over ITQ-6 (Si/Al = 30)

4.2 – Experimental Results and Discussion

4.2.1 – Support and catalysts characterization

The zeolites ITQ-6 and FER were obtained with different Si/Al ratios (30 and ∞) by preparing the same layered precursor (PREFER) but with different Si/Al ratios. The direct calcination of this precursor led to a multilayer condensation and the formation of the microporous-structured FER zeolites, FER (30), and FER (∞) [40].

For ITQ-6 zeolites, the PREFER precursor is exposed to swelling with $CTMA^+$ for its intercalation in the middle of the interlayer space of the PREFER. Upon sonication in an ultrasound bath, the structure is delaminated, and after ulterior calcination, ITQ-6 zeolites with different Si/Al ratios [FER (30) and FER (∞)] are obtained, as seen by the XRD diffractograms (**Figure 4.3**).

ITQ-6 zeolites exhibited lower intensity in the XRD peaks associated with the planes ($h00$) compared to their FER counterpart, which points out that there was a loss of crystallinity order along the a-axis [41], suggesting the delamination process took place in this direction (**Figure 4.3**). ITQ-6 (30) and ITQ-6 (∞) preserve the (200) and (400) planes diffraction peaks, even though with smaller intensity, suggesting part of the sample was not delaminated, as it will be confirmed by t-plot micropore volume calculations.

Regarding now the catalysts after Ni incorporation into the supports (FER and ITQ-6), the TG/DTA patterns for all catalysts (See **Chapter 9 - Supplementary Information**) show that after the incorporation of the Ni precursor, at the calcination temperature (450ºC), $Ni(NO_3)_2$ is decomposed to form a NiO phase. This is evidenced by the XRD patterns, where all calcined samples exhibit the typical peaks associated with the presence of crystalline NiO [42]: 37.40° (111), 43.46° (200), and 63.24° (220) (**Figure 4.4**). The results also confirm that the calcination step did not alter the crystalline structure of zeolite supports, as most of the peaks were preserved in shape and intensity.

All calcined catalysts present Ni weight content close to the nominal one, as revealed by ICP results (**Table 4.2**).

By measuring the average NiO crystallite size with the Scherrer Equation for the most intense peak attributed to NiO, i.e., the one centered at 43.46°, one notices that for the same Ni content (5 %), it is smaller over the ITQ-6-type catalysts (**Table 4.2**).

For the ITQ samples with higher Ni content (10%, 15%, and 20%), the higher the Ni loading, the more intense and narrower the NiO peaks become due to the presence of larger NiO crystallites (**Figure 4.5**), which is reflected in the average NiO crystallite size trend.

Table 4.2. NiO crystallite size for the zeolite-based catalysts (D_{NiO}), corresponding Ni^0 crystallite size after the reduction step (D_{Ni^0}) and Ni loading.

Catalyst	D_{NiO} (nm)[a]	D_{Ni^0}(nm)[b]	D_{Ni^0}(nm)[c]	Ni loading (%) [d]
5Ni/FER (∞)	19	16	27	5.4
5Ni/ITQ-6 (∞)	11	11	20	5.0
5Ni/FER (30)	15	14	23	4.9
5Ni/ITQ-6 (30)	8	6	16	5.4
10Ni/ITQ-6 (30)	14	17	-	10.4
15Ni/ITQ-6 (30)	17	18	-	15.4
20Ni/ITQ-6 (30)	21	19	-	20.8

[a] Determined by Scherrer Equation using NiO (200) plane peak intensity.

[b] Determined in the samples after reduction using Ni (111) plane peak intensity.

[c] Determined by HAADF-STEM images with particle size counting.

[d] Determined by ICP-OES.

After the samples were reduced, the peaks arising from the NiO phase disappeared and gave rise instead to the peaks corresponding to the presence of Ni^0 particles found at $2\theta° = 44.50°$ (111) and 51.85° (200) (**Figure 4.5**). Furthermore, in the higher Ni loading samples, it is even possible to see the peak located at $2\theta° = 76.38°$ (220). With this data, it was possible to calculate the average Ni^0 crystallite size (**Table 4.2**) which followed the same trend observed for the NiO crystallite size.

Reduced catalysts based on Si/Al = 30 supports do not exhibit peaks associated with the presence of $NiAl_2O_4$ phase (JCPDS 10-0339), as the formation of these aluminate phases occurs at higher temperatures (> 900 °C) for stabilization of the spinel structure, confirming that NiO is exclusively reduced to Ni^0 [43].

From HAADF-STEM dark field and TEM images (**Figure 4.6** through **Figure 4.12**) of the reduced catalysts, 500 Ni^0 particles were measured, and the size distributions (**Figure 4.13**) confirm the trend observed for the crystallite size obtained from the Scherrer Equation (**Table 4.2**).

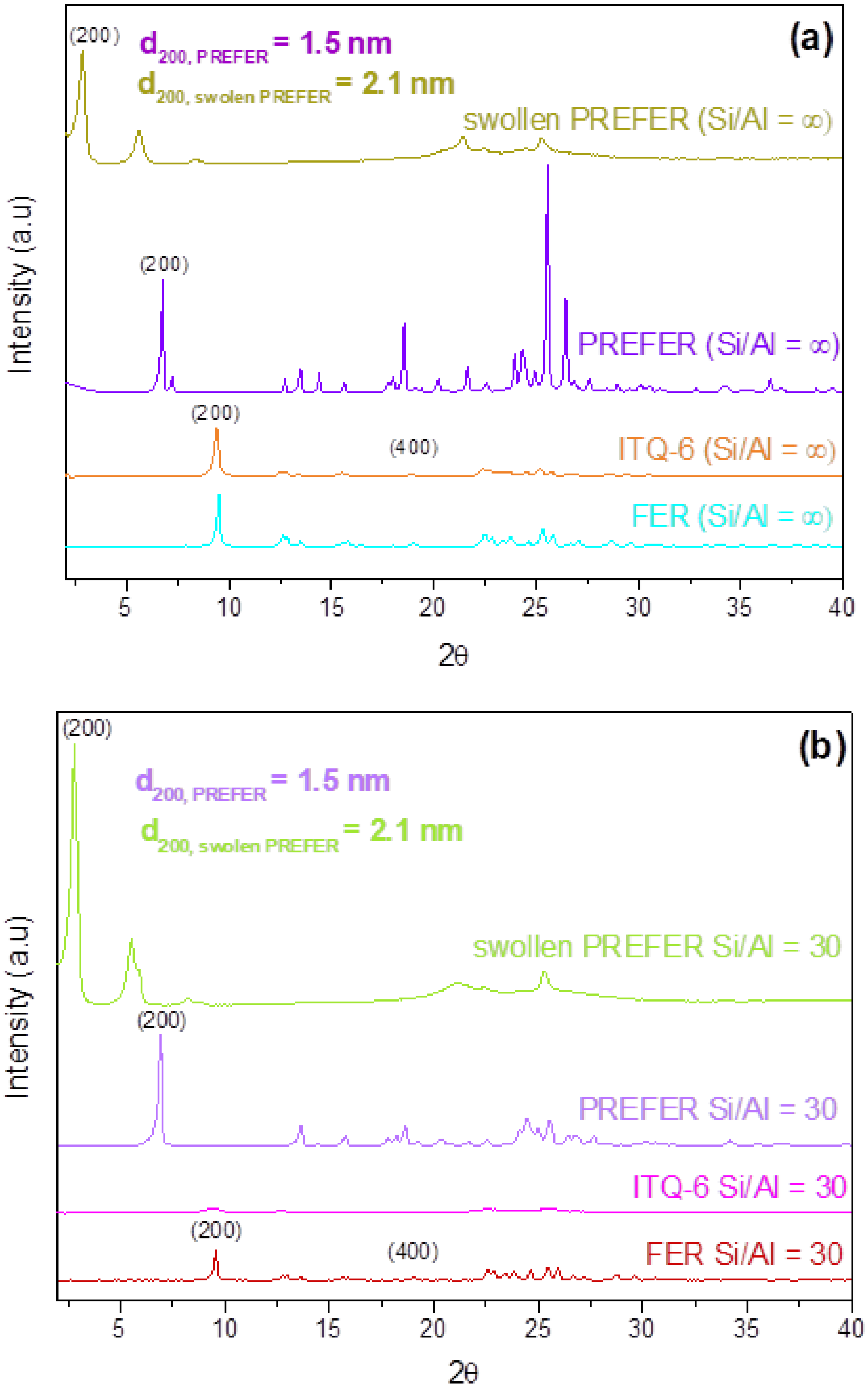

Figure 4.3. X-ray diffraction patterns for FER, ITQ-6, PREFER, and swollen PREFER with Si/Al molar ratios of (a) ∞ and (b) 30.

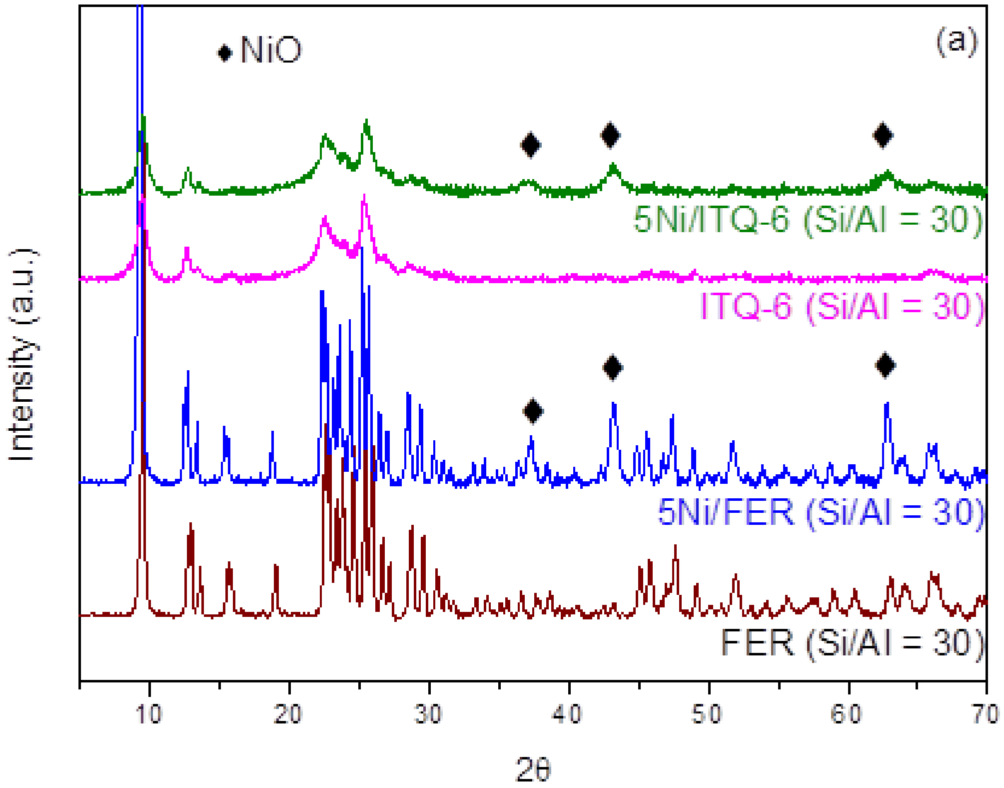

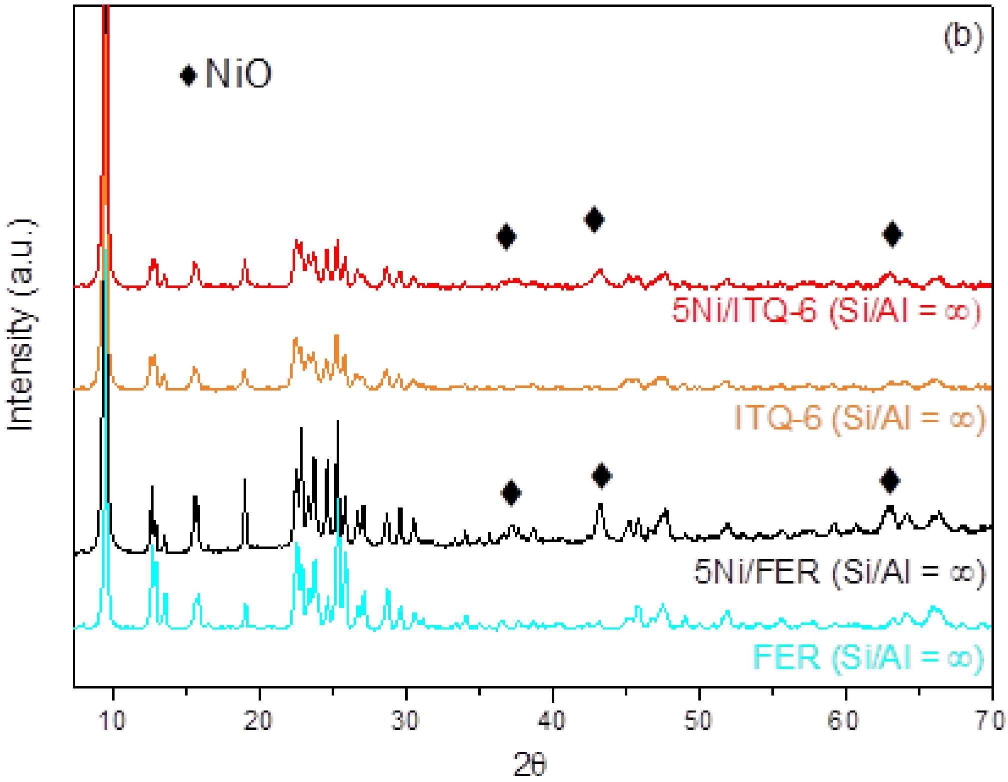

Figure 4.4. X-ray diffractograms of 5 wt. % Ni-based catalysts supported on FER and ITQ-6 zeolites between the range 2θ =5°-70° with Si/Al ratios of (a) infinite and (b) 30. The diffractograms of the bare supports are also depicted for comparison.

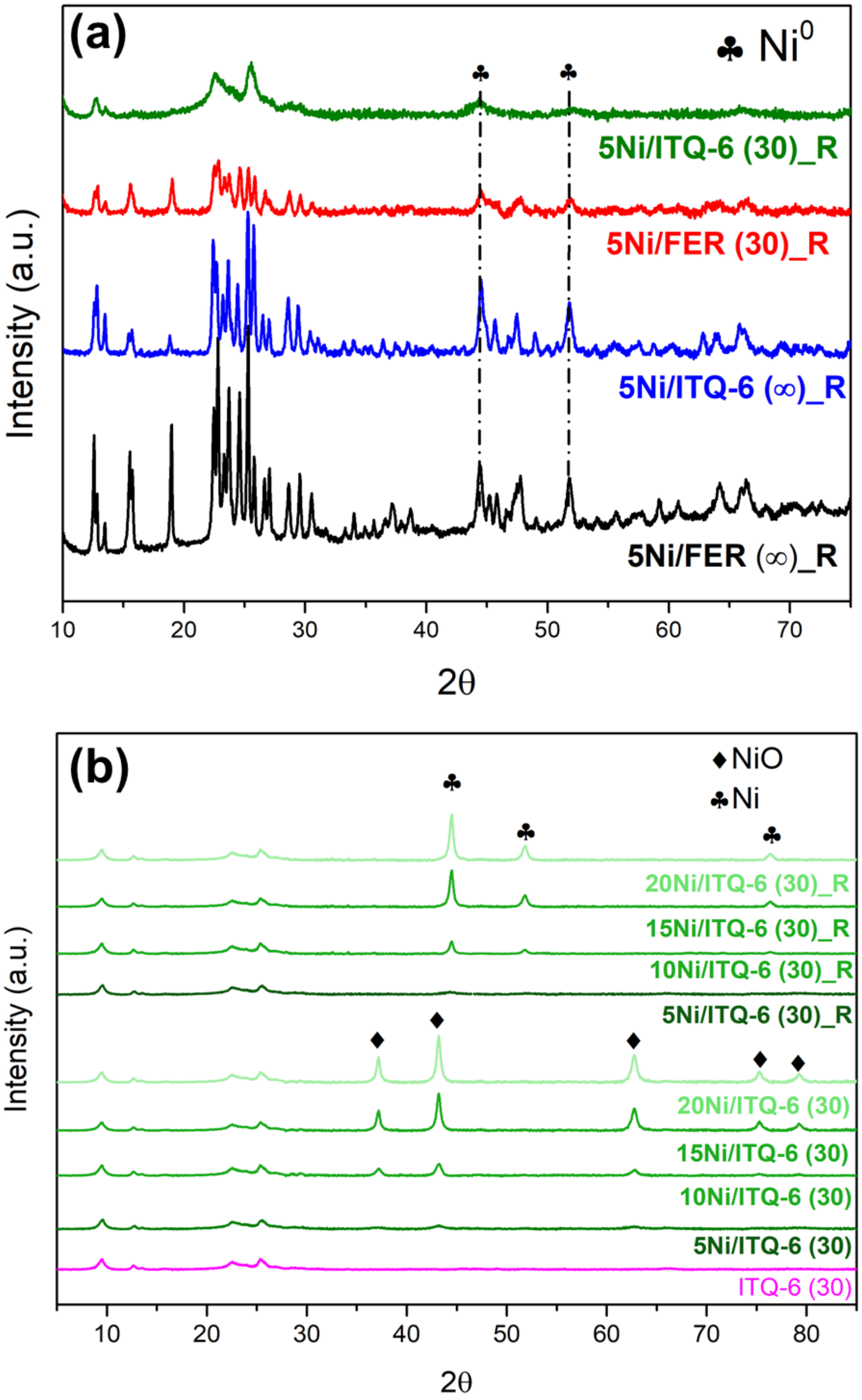

Figure 4.5. X-ray diffractograms of (a) reduced 5% wt. Ni-based catalysts supported on FER and ITQ-6 zeolites, and (b) higher Ni loading catalysts supported on ITQ-6 (30).

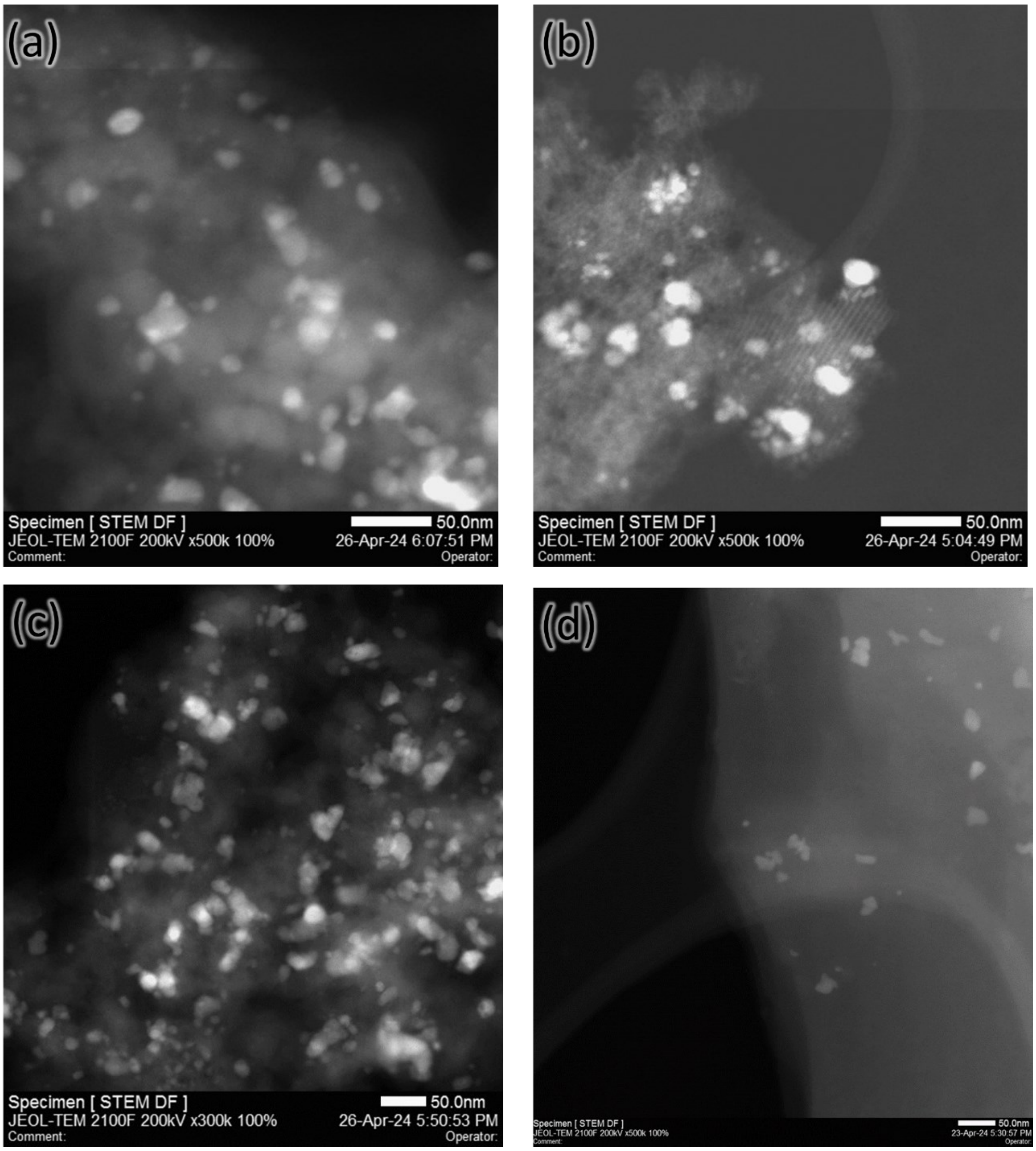

Figure 4.6. HAADF-STEM dark field images of the reduced catalysts: (a) 5Ni/FER (∞), (b) 5Ni/ITQ-6 (∞), (c) 5Ni/FER (30), and (d) 5Ni/ITQ-6 (30).

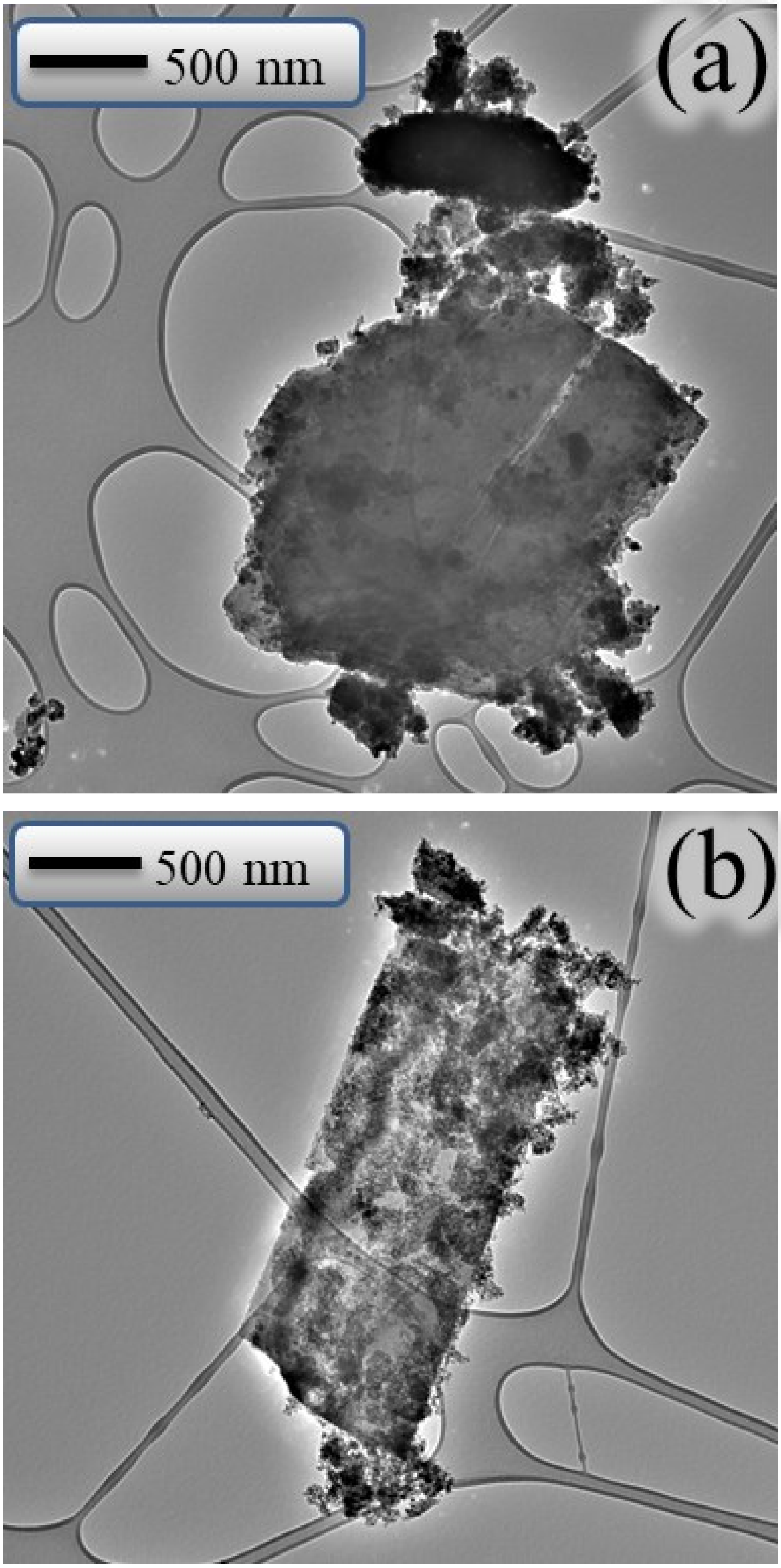

Figure 4.7. TEM images of the reduced 5% wt. Ni-based catalysts supported on aluminum-free supports: (a) 5Ni/FER (Si/Al = ∞) and (b) 5Ni/ITQ-6 (Si/Al = ∞).

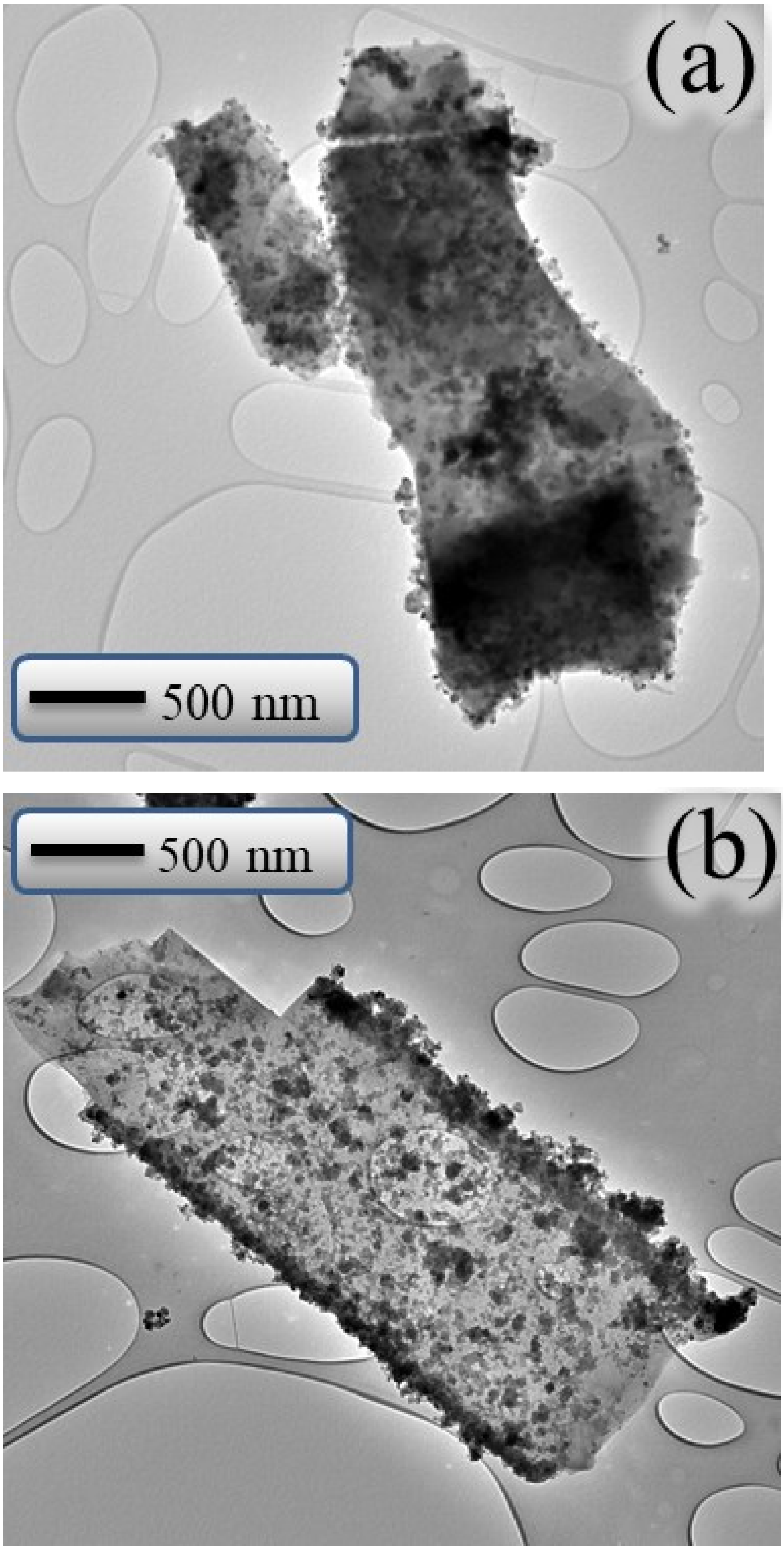

Figure 4.8. TEM images of the reduced 5% wt. Ni-based catalysts supported of the aluminum-containing catalysts: (a) 5Ni/FER (Si/Al = 30), and (b) 5Ni/ITQ-6 (Si/Al = 30).

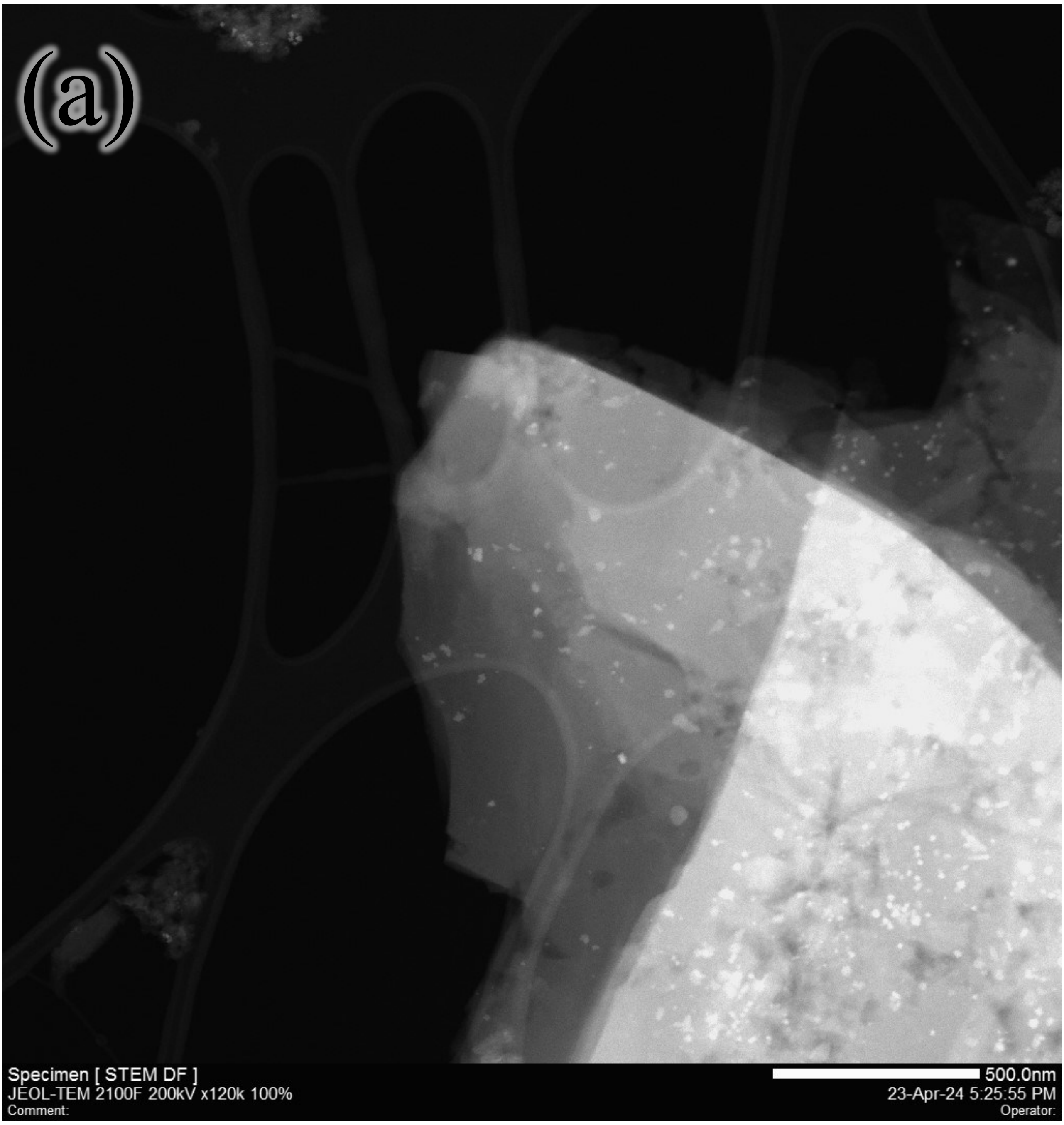
(a)
Specimen [STEM DF]
JEOL-TEM 2100F 200kV x120k 100%
Comment:
500.0nm
23-Apr-24 5:25:55 PM
Operator:


(b)
Specimen [STEM DF]
JEOL-TEM 2100F 200kV x500k 100%
Comment:
100.0nm
23-Apr-24 5:30:57 PM
Operator:

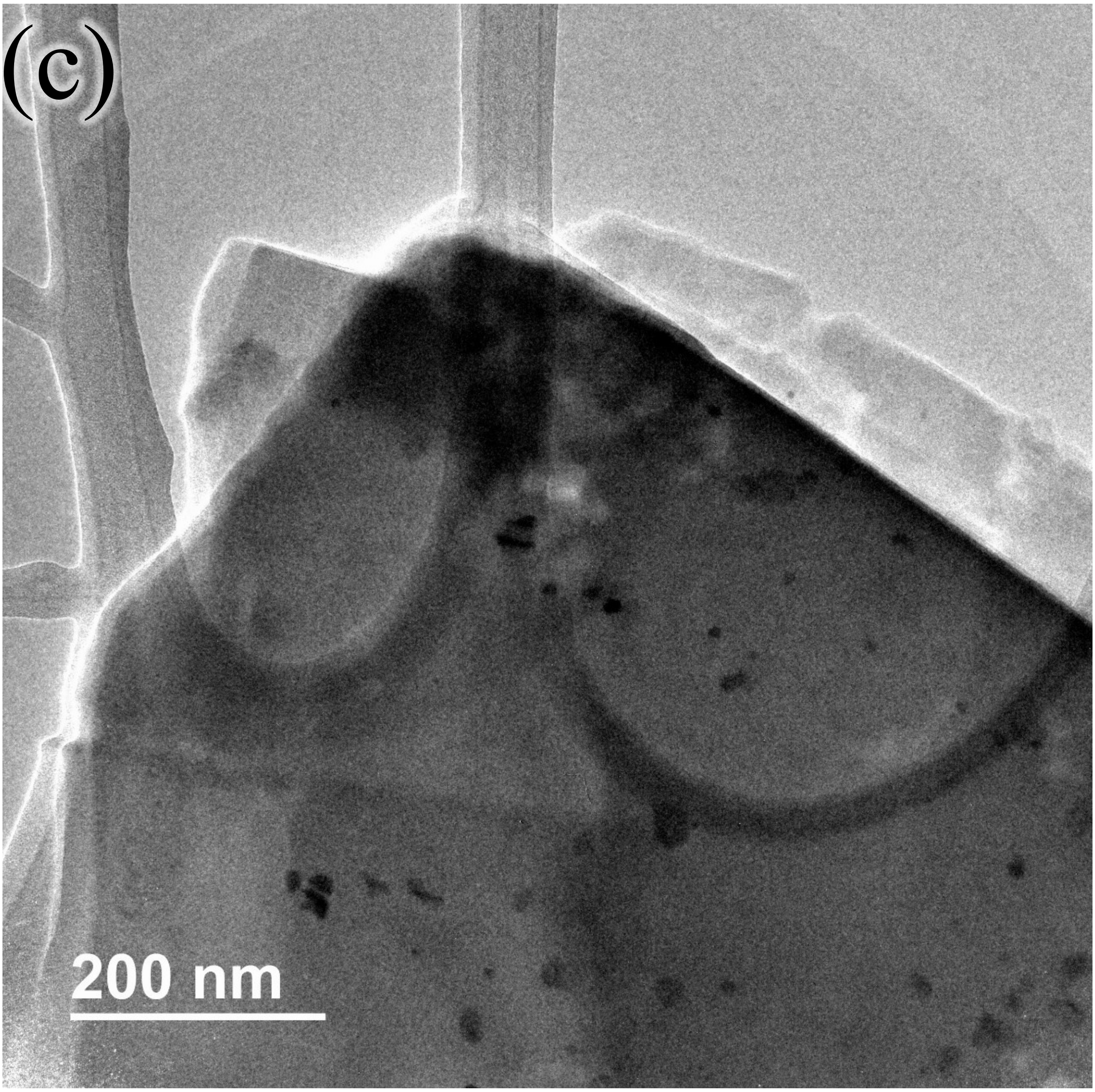

Figure 4.9. (a), (b) HAADF-STEM dark field and (c) TEM bright-field images for the 5Ni/ITQ-6 (30).

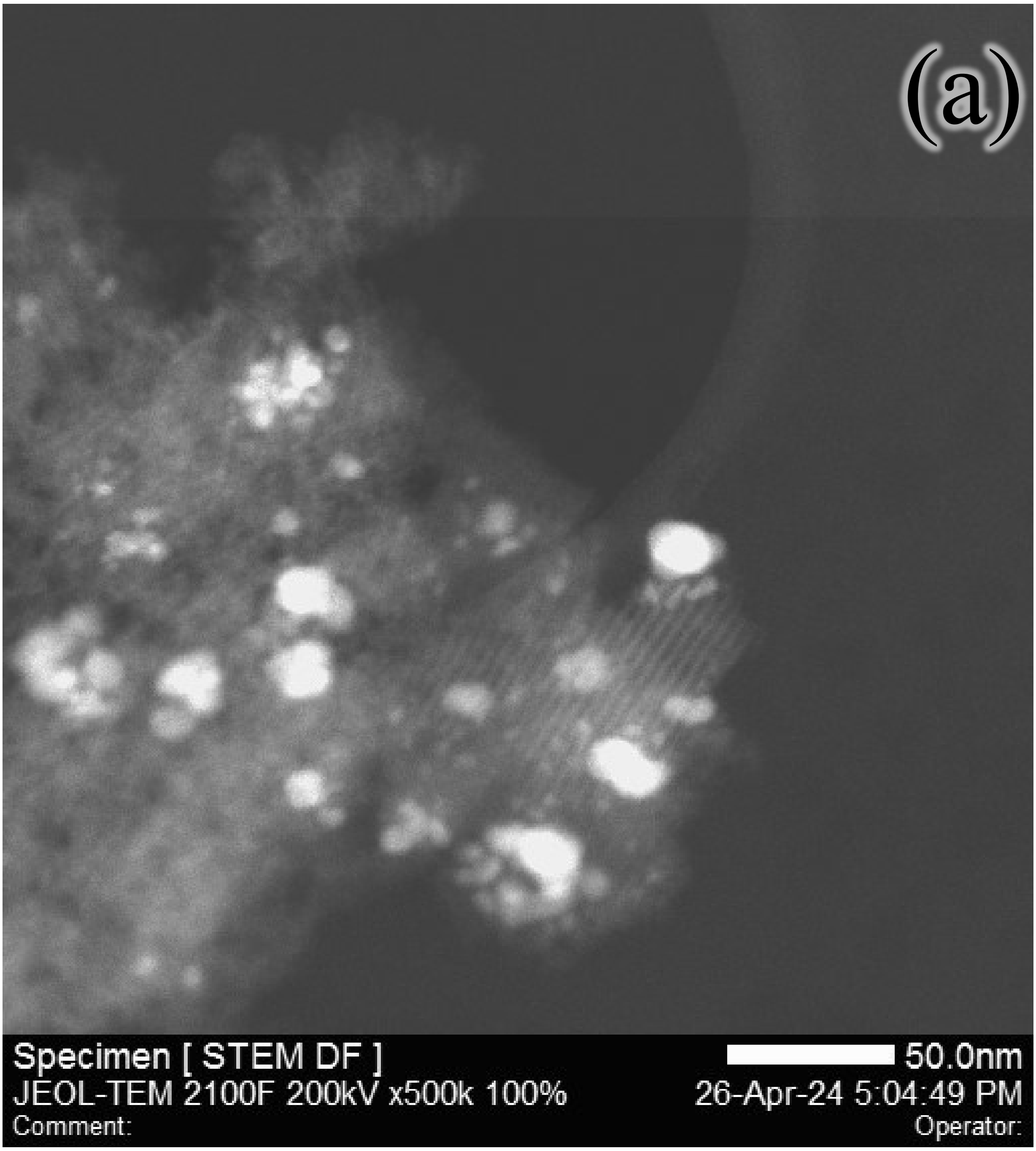
(a)
Specimen [STEM DF]
50.0nm
JEOL-TEM 2100F 200kV x500k 100%
26-Apr-24 5:04:49 PM
Comment:
Operator:

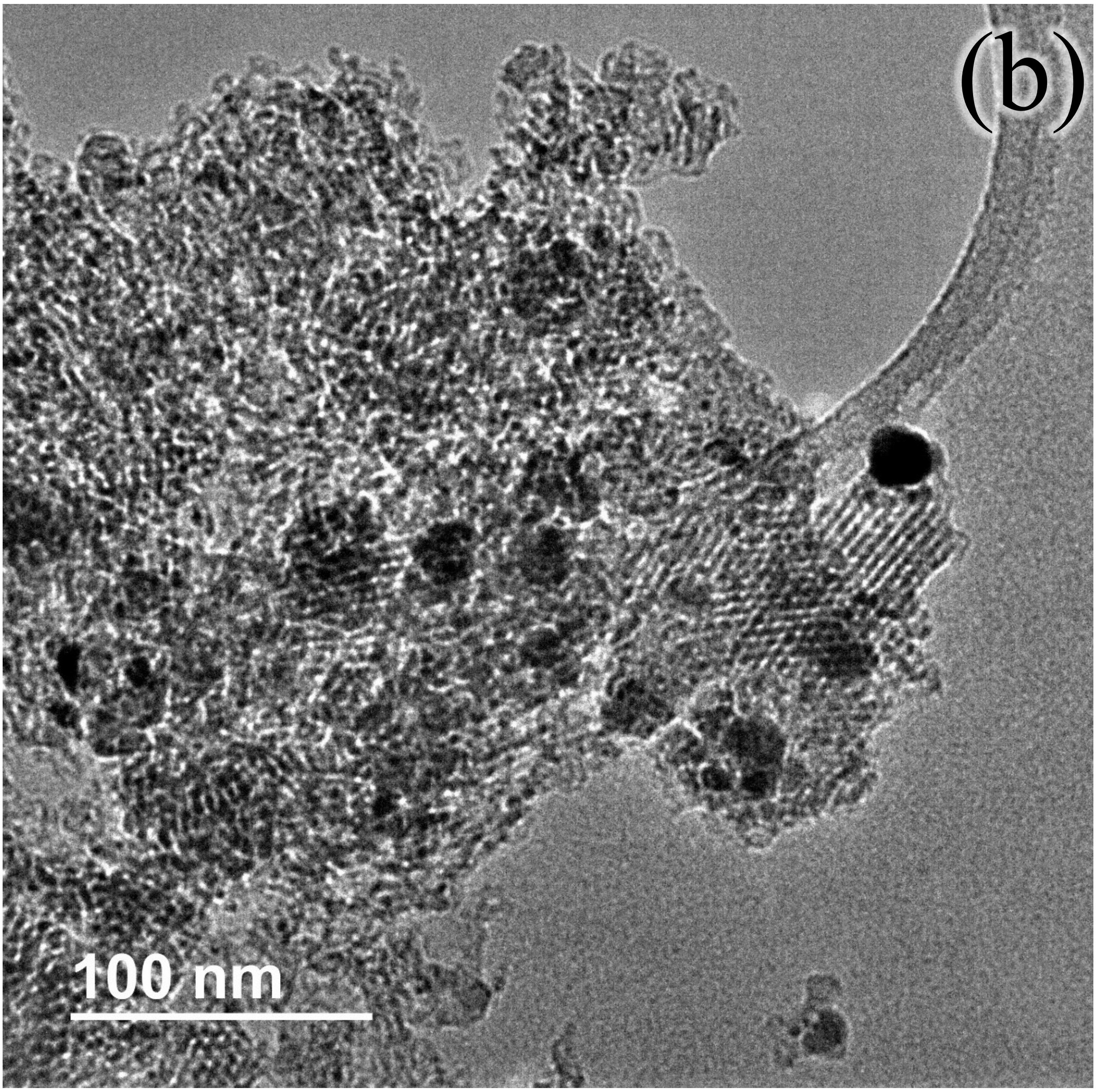
(b)
100 nm

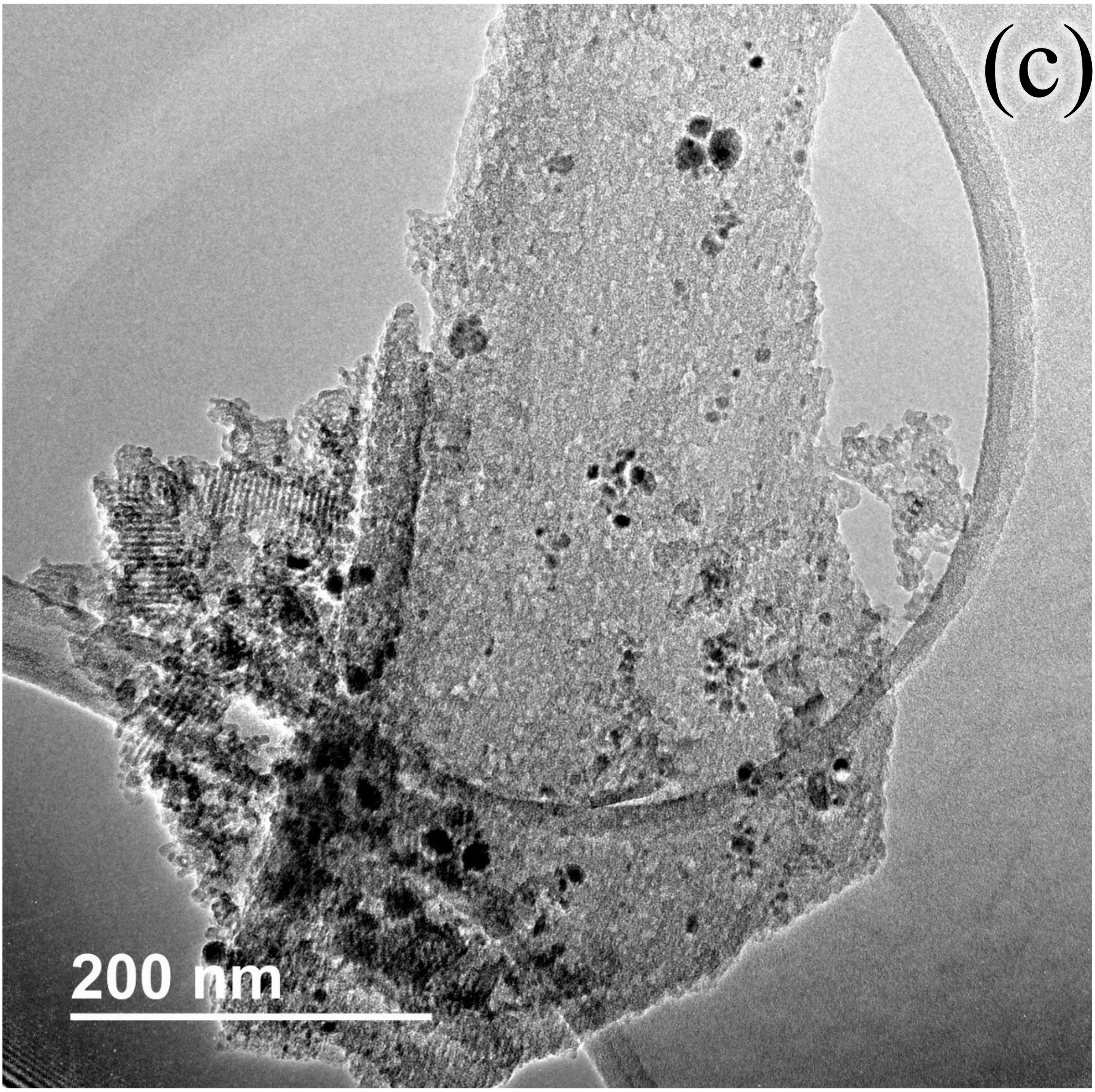

Figure 4.10. (a) HAADF-STEM dark field and (b), (c) TEM bright-field images for the 5Ni/ITQ-6 (∞).

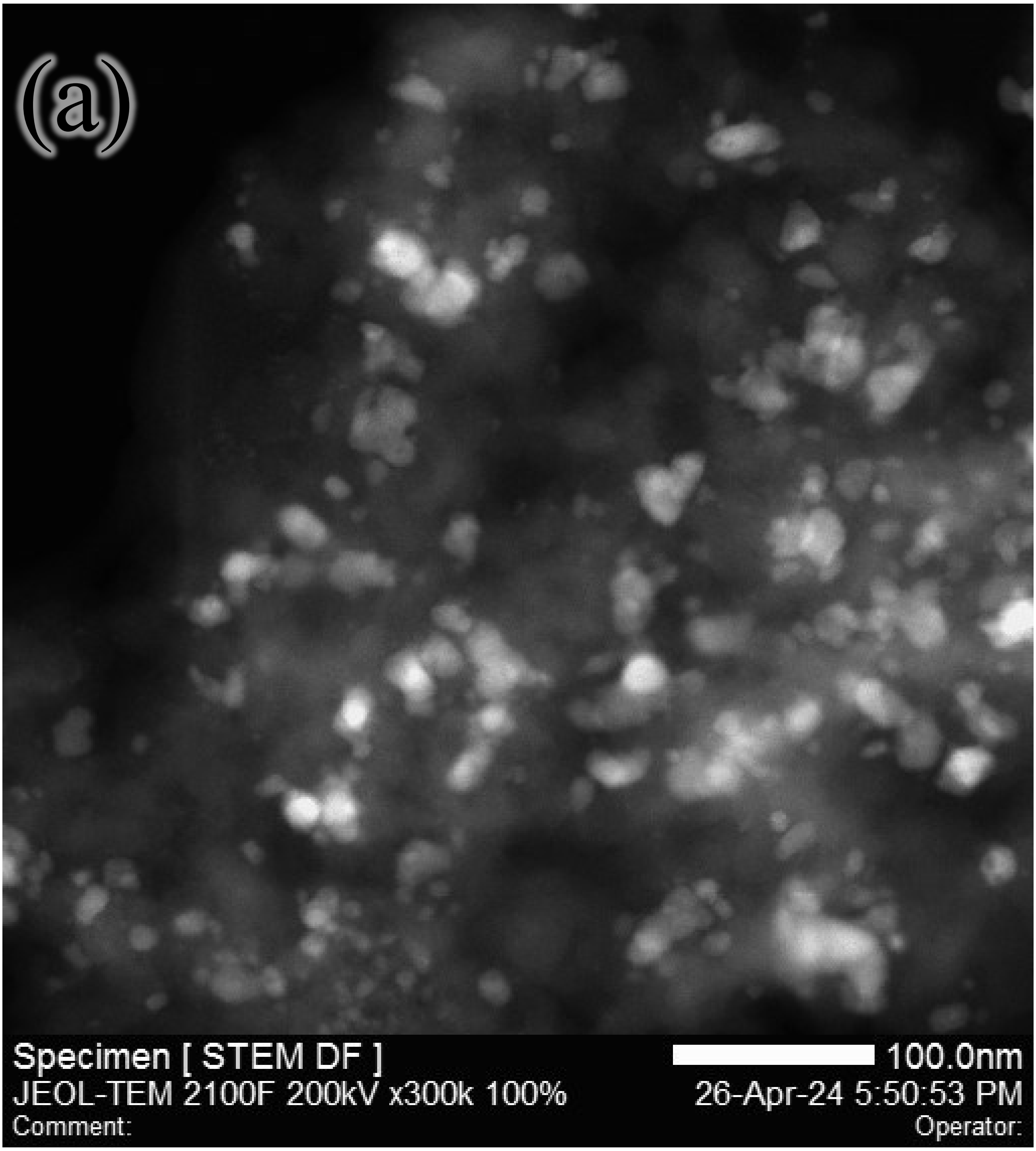
(a)
Specimen [STEM DF]
100.0nm
JEOL-TEM 2100F 200kV x300k 100%
26-Apr-24 5:50:53 PM
Comment:
Operator:

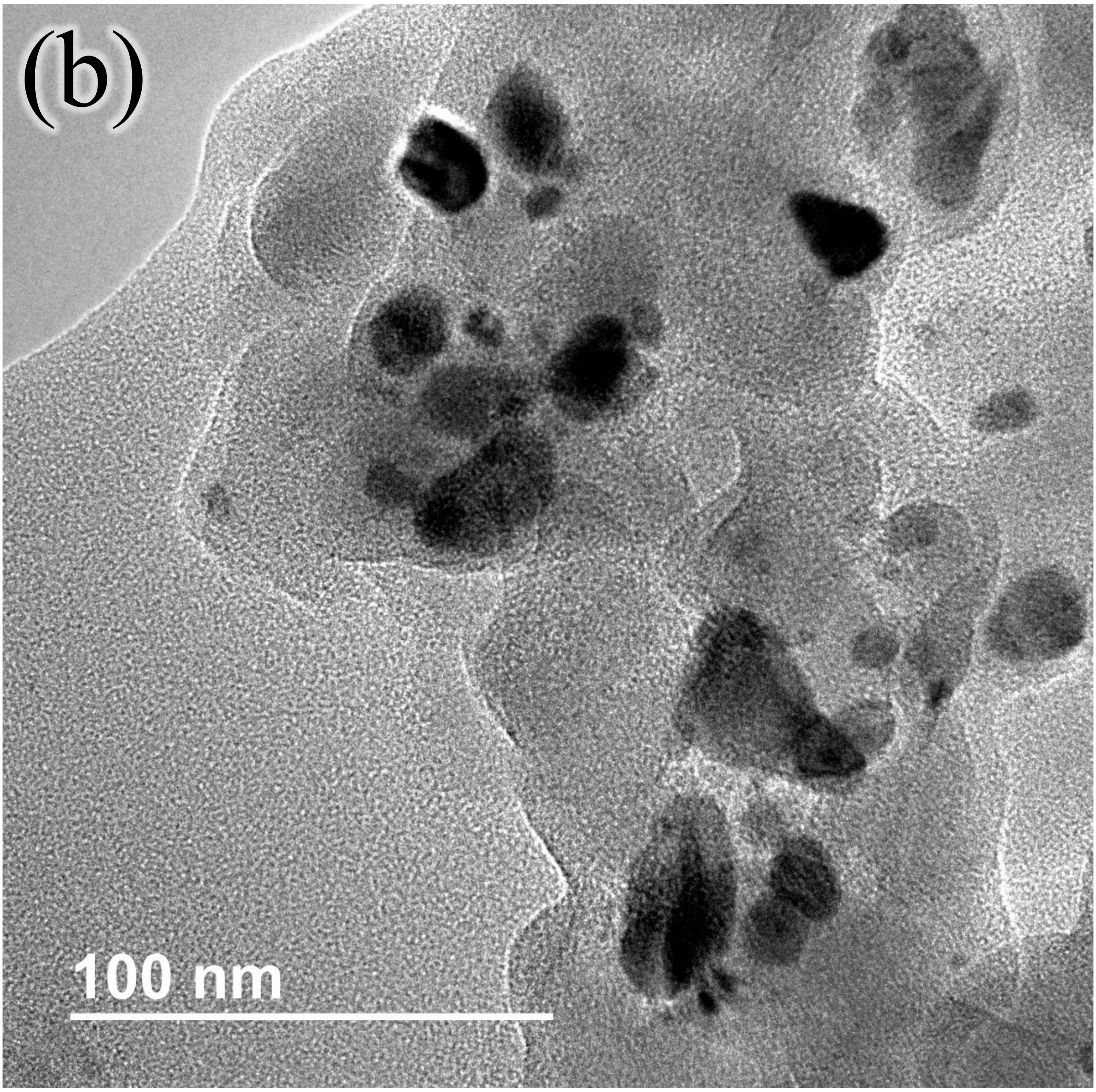

Figure 4.11. (a) HAADF-STEM dark field and (b)TEM bright-field images for the 5Ni/FER (30).

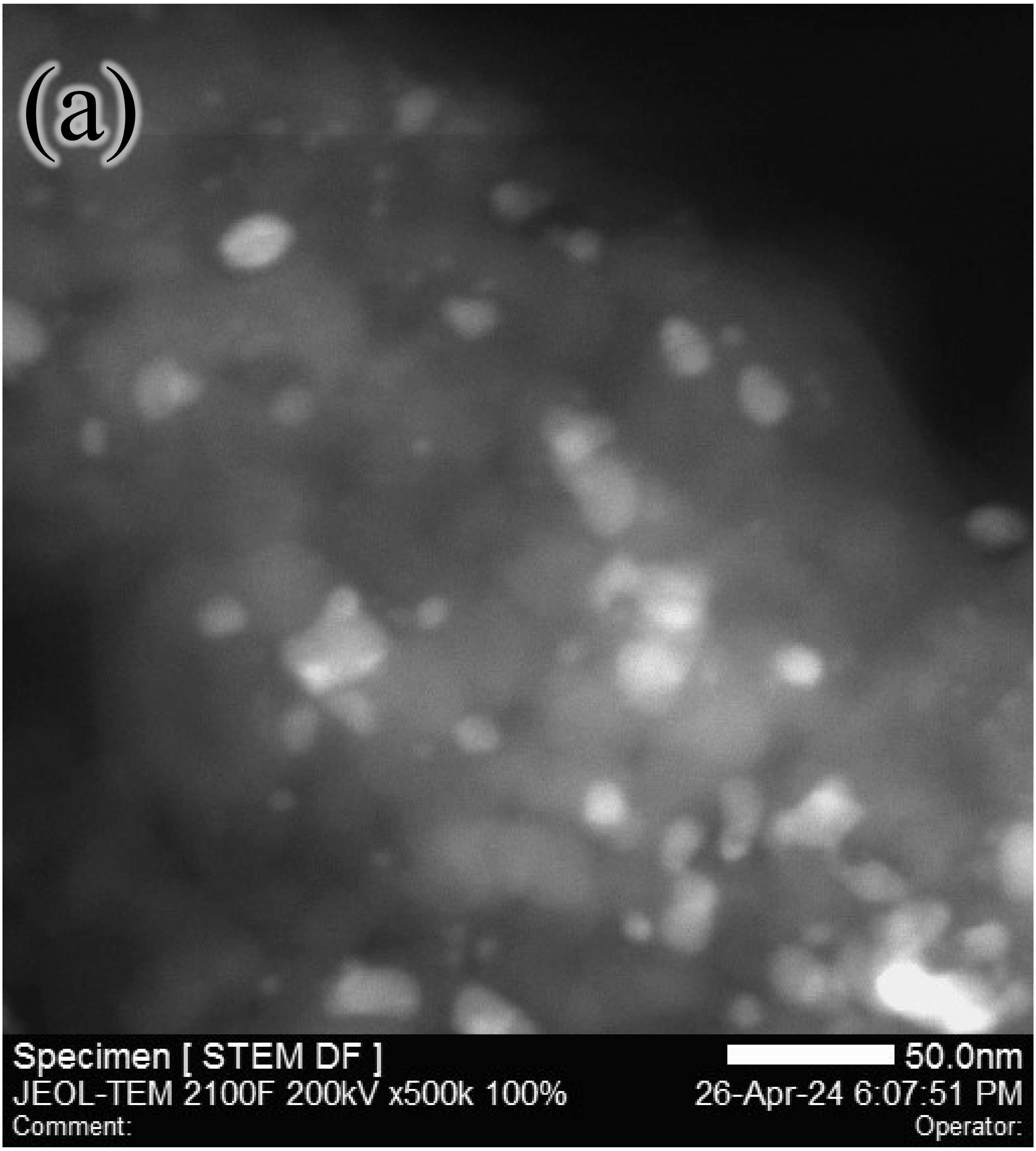
(a)
Specimen [STEM DF]
JEOL-TEM 2100F 200kV x500k 100%
Comment:
50.0nm
26-Apr-24 6:07:51 PM
Operator:

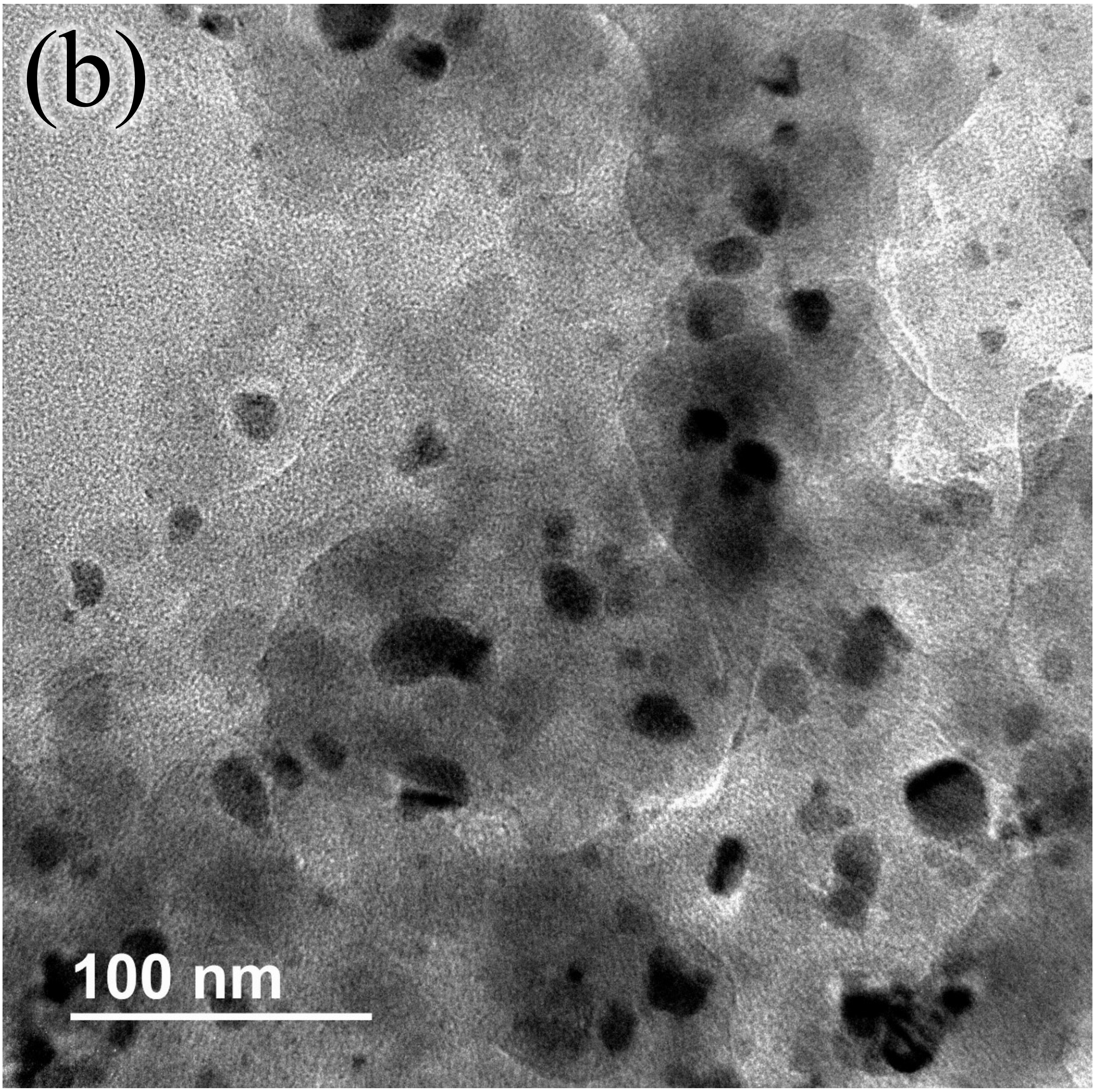

Figure 4.12. (a) HAADF-STEM dark field and (b) TEM bright-field images for the 5Ni/FER (∞).

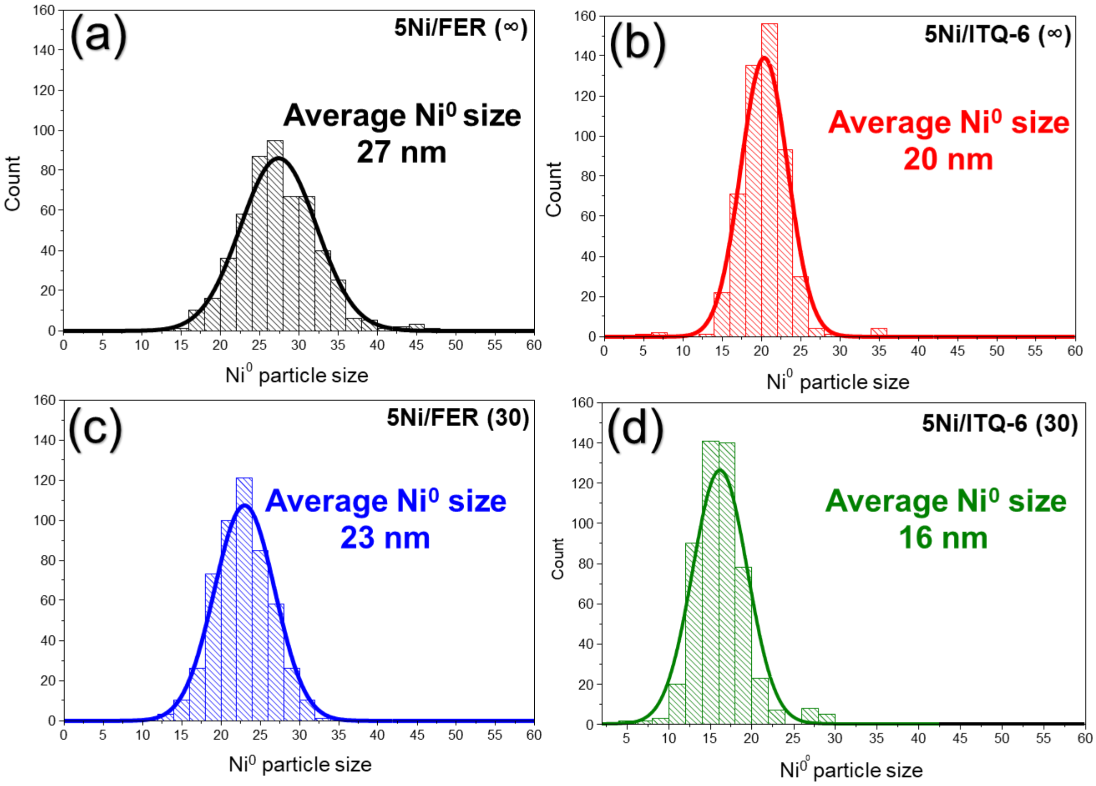

Figure 4.13. Ni^0 particle size distribution, normal fit, and average size for the 5 wt. % Ni-based catalysts: (a) 5Ni/FER (∞)_R, (b) 5Ni/ITQ-6 (∞)_R, (c) 5Ni/FER (30)_R and (d) 5Ni/ITQ-6 (30)_R. 500 particles were counted for each one of the catalysts using the TEM images and measured using the ImageJ software.

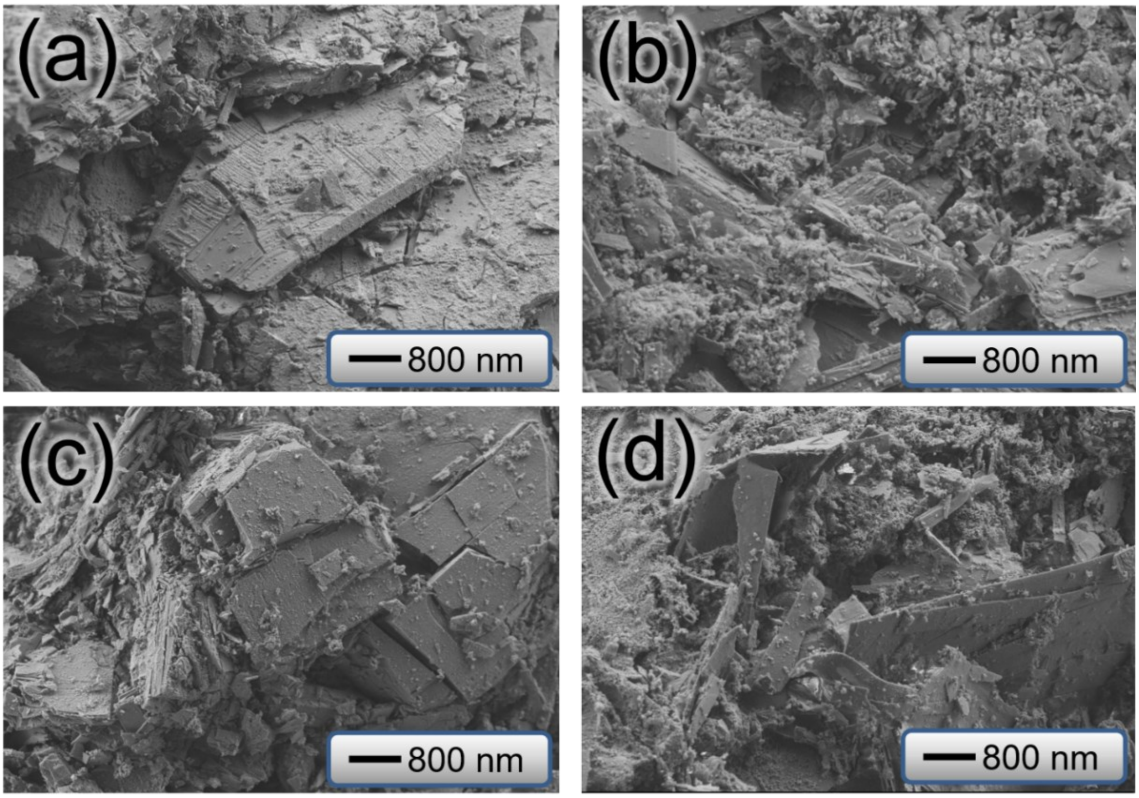

Figure 4.14. SEM images for the reduced version of (a) 5Ni/FER (∞), (b) 5Ni/ITQ-6 (∞), (c) 5Ni/FER (30), and (d) 5Ni/ITQ-6 (30).

The values observed by HAADF-STEM are higher than those observed by XRD because they pertain to the measurement of observable particles, while XRD measurements determine the average sizes of Ni^0 crystallites, which are crystalline domains contained within the actual Ni particles, seen in TEM. SEM images (**Figure 4.14**) reveal that for ITQ-6 catalysts, some of the delaminated layers are 50-100 nm thick, suggesting that these layers are composed of aluminosilicate multilayers not completely delaminated [29], which partly preserves the crystallographic order along the a-axis and accounts for the partial preservation of the (200) and (400) planes diffraction peaks (**Figure 4.3**).

The N_2 adsorption-desorption isotherms for the FER and ITQ-6-based catalysts (**Figure 4.15**) and their textural properties (**Table 4.3**) reveal that the isotherms of 5Ni/FER (∞) and 5Ni/FER (30) are type I, which is characteristic of microporous materials [44]. This profile is typical for materials whose pore sizes are not much larger than the kinetic molecular diameter of the adsorbate.

This is precisely the case for the FER zeolite, whose channels 10 MR (0.43 nm x 0.55 nm) and 8 MR (0.38 nm x 0.55 nm) are larger than the kinetic molecular diameter of N_2 (0.364 nm) [30]. Under these conditions, only one adsorbate layer is formed, reaching a plateau level of adsorbate for low P/Po values [45].

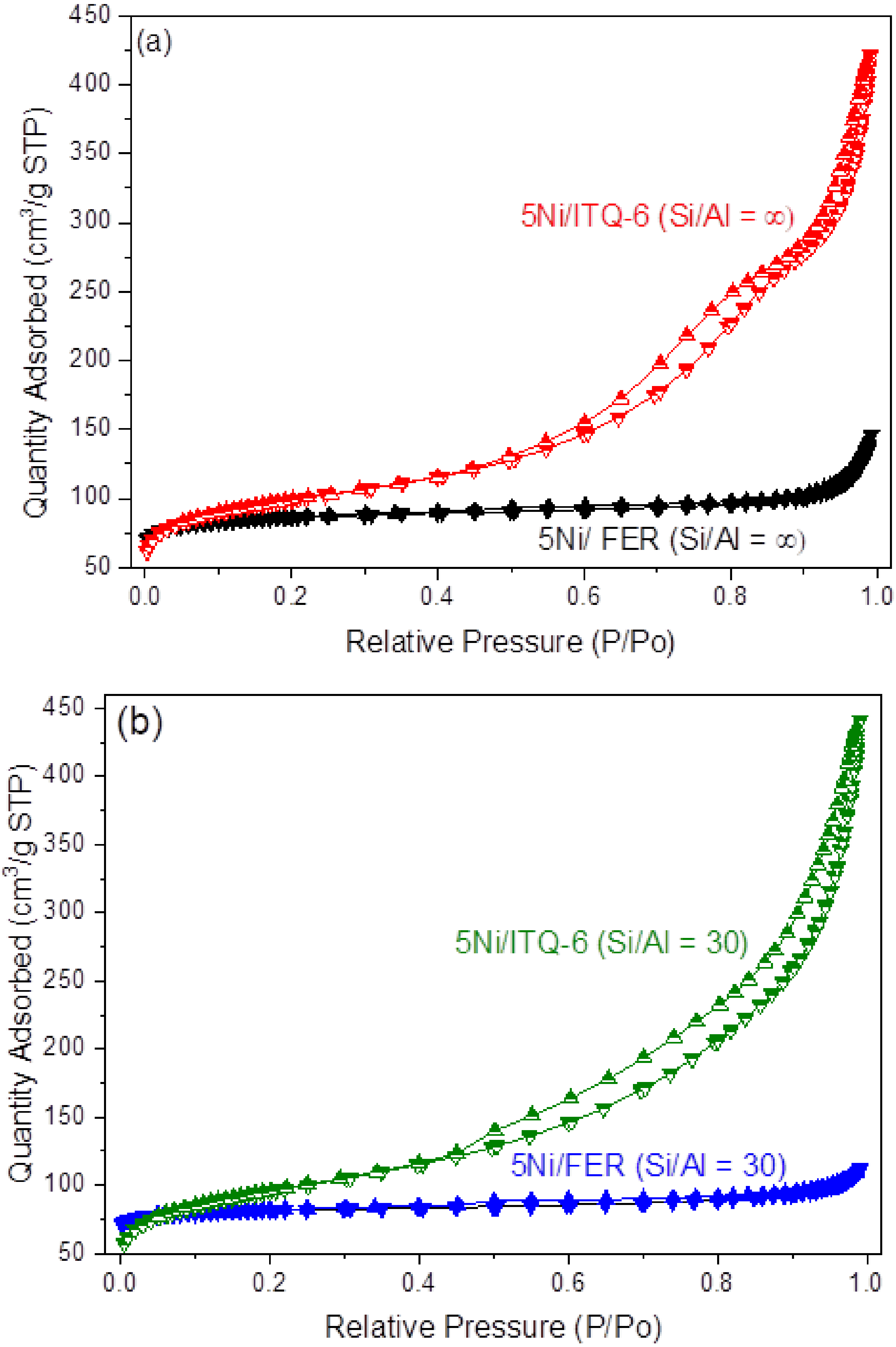

Figure 4.15. Nitrogen adsorption-desorption isotherms of the 5 wt. % Ni-based catalysts supported on the (a) Si/Al = ∞ zeolites and the (a) Si/Al = 30 zeolites.

Table 4.3. Textural properties for the zeolite samples: BET surface area (S_{BET}), t-plot micropore area (S_{MICRO}), t-plot external surface area ($S_{EXTERNAL}$), t-plot micropore volume (V_{MICRO}), and BJH mesopore volume, (V_{MESO}).

Sample	S_{BET} (m²/g)	S_{MICRO} (m²/g)	$S_{EXTERNAL}$ (m²/g)	V_{MICRO} (cm³/g)	V_{MESO} (cm³/g)
FER (∞)	315	292	23	0.142	0.081
5Ni/FER (∞)	278	255	23	0.125	0.035
ITQ-6 (∞)	605	71	534	0.018	0.381
5Ni/ITQ-6 (∞)	336	39	297	0.008	0.366
FER (30)	278	245	33	0.119	0.058
5Ni/FER (30)	250	222	28	0.113	0.027
ITQ-6 (30)	591	81	510	0.034	0.603
5Ni/ITQ-6 (30)	329	45	284	0.015	0.359

Adsorption isotherms for the 5Ni/ITQ-6 (∞) and 5Ni/ITQ-6 (30) catalysts, on the other hand, are type IV, characteristic of mesoporous materials, with an H3 hysteresis. This profile has been previously attributed to mesoporous materials with a wide distribution of mesopore sizes, as no plateau is reached up to higher P/Po values. This is the case for the ITQ-6 catalysts and their "house of cards" structure, which comprises mesopores formed by the random layer piling after the delamination process.

Micropore surface area of the FER-type zeolites significantly drops with reductions of over 60% when converted to ITQ-6-type zeolites, while the external surface increases due to the formation of a "house-of-cards"-type structure. The remaining micropore surface area in ITQ-6 is accounted for incomplete delamination [46], preserving aluminosilicate multilayers that maintain the 10MR channel structure, as seen in SEM images in **Figure 4.14**.

A higher delamination extension is observed for the Si/Al = 30 zeolites, for which the increase in the total BET surface area is higher than that observed for the Si/Al = ∞. This had already been suggested by the observation of the intensity of the remaining (200) plane peak in the XRD results when ITQ-6 (30) and ITQ-6 (∞) were compared with each other and was further confirmed by adsorption results.

Nickel-based catalysts present lower S_{BET} values than their corresponding bare supports, which is explained by two simultaneous phenomena: first, and on a smaller scale, due to a dilution effect, which has already been reported in previous results of our research group [47] and which takes place due to the deposition of a low surface area phase (NiO) over a higher surface area one (zeolite), decreasing the overall surface area per unit of mass. And secondly, on a more extended scale, the partial obstruction of the micro and mesopores by the NiO particles, leading to a decrease of the micro and mesopore volume (**Table 4.3).**

H_2-chemisorption results (**Table 4.4**) reveal that the trend is followed in the reduced version of these catalysts, in which the average Ni^0 particle size is smaller in the ITQ-6-based catalysts. However, the values are different than the ones measured by XRD or TEM, as they are measured in an indirect way. H_2-chemisorption employs H_2 molecules as a probe to analyze the Ni^0 particles surface area, as determined in the classic study conducted by Bartholomew et al. [48], and from this data, the Ni^0 particle size is determined considering the molecules with a hemispherical shape hypothesis.

Table 4.4. Textural and reducibility properties for reduced FER and ITQ-6 type catalysts: active metal surface area, S_{Ni}, Ni^0 average particle size, D_{Ni}, molar H_2 monolayer uptake, and percentual reducibility at 450 °C.

Catalyst	S_{Ni} (m²/g)[a]	D_{Ni} (nm)[a]	H_2 uptake (µmol/g)[a]	Reducibility (%)[b]
5Ni/FER (∞)_R	1.7	20	21	90
5Ni/ITQ-6 (∞)_R	2.1	16	27	86
5Ni/FER (30)_R	2.0	17	25	93
5Ni/ITQ-6 (30)_R	2.6	13	33	51
10Ni/ITQ-6 (30)_R	4.7	17	39	-
15Ni/ITQ-6 (30)_R	6.9	19	47	-
20Ni/ITQ-6 (30)_R	7.4	19	48	-

[a] Determined by H_2-chemisorption analyses

[b] Determined by TPR analyses

The nickel active metallic surface area is 25% higher for the 5Ni/ITQ-6 (∞) when compared to the 5Ni/FER (∞) and 31% higher for the 5Ni/ITQ-6 (30) when compared to the 5Ni/FER (30), which goes hand in hand with the observation of reduction of Ni crystallite size in the same sequence. HAADF-STEM images and the size distribution diagrams obtained from these images (**Figure 4.13**) reveal that, on the ITQ-6 supports, the average Ni^0 particle size is lower than in non-delaminated counterparts.

These measurements confirm the chemisorption results and reveal that in ITQ-6-based catalysts, the distribution of Ni^0 particle size is narrower, which is attributed to the higher support surface area, as seen in **Figure 4.13**. Regarding the Al addition, Al-containing catalysts also present, in general, a narrower distribution of the Ni^0 particles in comparison with the Al-free catalysts, which is accounted for the presence of zeolitic -OH groups, as detected by IR measurements, as it will still be discussed. These anchoring hydroxyl groups allow better dispersion of Ni precursors, as they interact with the nickel precursors during the preparation step and enhance their dispersion [49].

H_2-TPR results show peaks at different temperatures for all catalysts because the outcome profile is the overlap of three different profiles related to distinct reduction events for NiO particles (**Figure 4.16**). Peaks at lower temperatures regions (α region) refer to the reduction of bulk NiO, which presents weaker interaction with the support, while the ones at higher temperatures (β and γ regions) refer to the reduction of NiO that hold stronger interaction with the support [50, 51]. On the other hand, it is important to highlight that the reduction of Ni^{2+} as charge compensating cation would not take place since reduction peaks above 630 ºC are not detected [50].

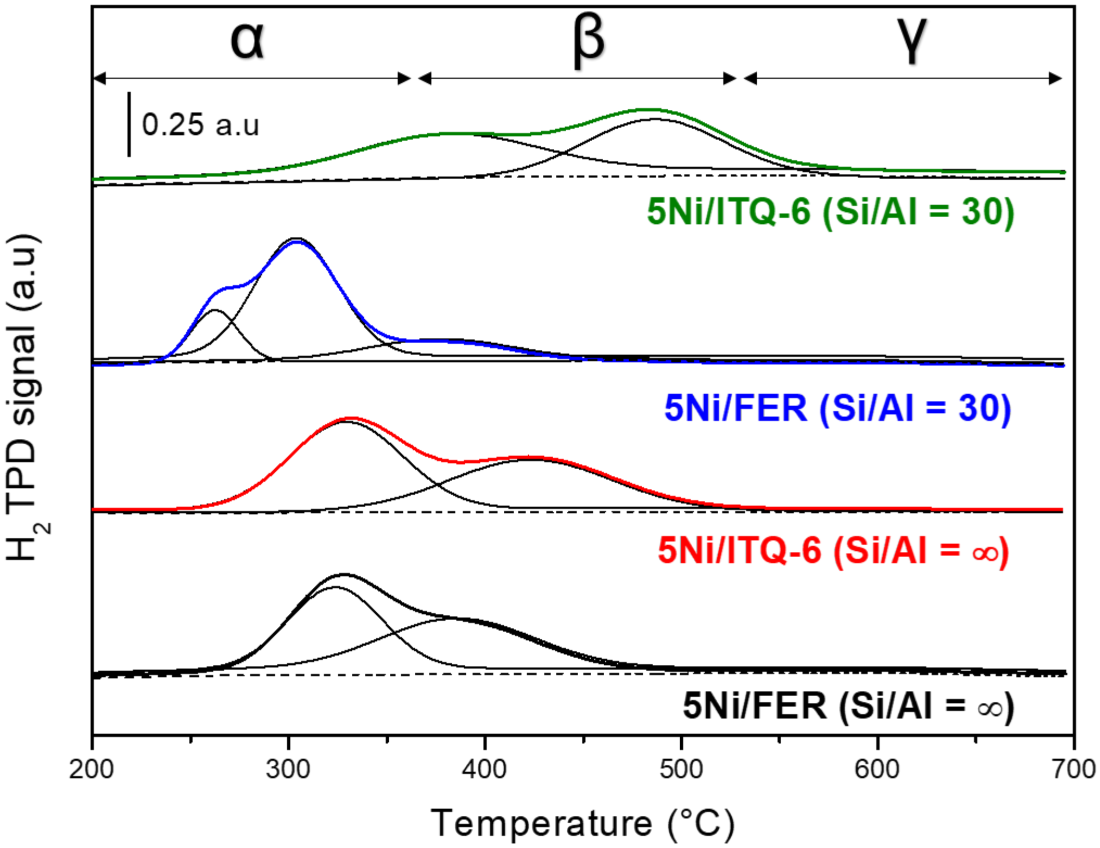

Figure 4.16. H_2-TPR profile of zeolite-based catalysts under H_2 flow over the range of temperatures between 200 °C and 700 °C.

For a given nickel loading for a series of catalysts and the same reduction conditions, the amount of available Ni^0 sites in the catalysts after reduction will rely on two factors, the reduction extension of the NiO phase and the resulting metallic dispersion, with these two factors being dependent of the strong metal-support interactions (SMSI) between the zeolite support and the nickel phase [52].

The results also reveal that the H_2-TPR profile is not strictly correlated with the Ni^0 particle size distribution, as it informs about the temperatures in which the NiO phase is reduced, depending on its interaction with the support. The Ni^0 particle size, on the other hand, is conditioned by other factors, such as the reduction temperature, time of reduction, and the sintering extension, as Ni^0 phase reduced below the activation temperature (450 °C) undergoes sintering, which leads to Ni^0 particles with different size.

By integrating the area below the curve in the H_2-TPR results up to the chosen temperature used for the activation by reduction of the catalysts (450 °C), the reduction extension degree is calculated for each catalyst. The higher reducibility at lower temperatures seen in FER-based catalysts is attributed to the bigger NiO crystallites, making most of the Ni species present in the bulk phase, with weaker interactions with the surface and most of the reduction events falling off in the α and β regions (**Figure 4.16**).

Meanwhile, in ITQ-6 catalysts, smaller NiO crystallites are formed, which exhibit stronger interactions with the Si and Al species on the zeolites' surface, making them harder to reduce and falling off on the β and γ regions of the H_2-TPR profiles. This is seen in **Figure 4.16** in the γ region peaks centered at **460 °C** for the **5Ni/ITQ-6 (**∞) and one centered at **490 °C** for the **5Ni/ITQ-6 (30)**.

Regarding the effect of Ni loading, as the nickel content increases, there is a clear shift of the main peak towards lower temperature values, as observed with the peak at 418 °C for 10Ni/ITQ-6 (30) and 398 °C for 15Ni/ITQ-6 (30) (**Figure 4.17**).

This is attributed to the fact that as the Ni content increases, the average size of NiO crystallites also increases, resulting in a higher proportion in the bulk phase, whose reduction is attributed to the aforementioned temperatures. The increase in Ni content also leads to the appearance of new peaks, which is consistent with previously reported results in the literature [53]. This is attributed to the fact that a higher amount of metal leads to greater heterogeneity in NiO particle sizes, which is reflected in the appearance of reduction events at different temperatures.

Costa-Serra had already previously described that higher surface area zeolites are supports that lead to better dispersion and smaller nickel oxide particles over the surface [47], and this is confirmed over the delaminated zeolites in this study.

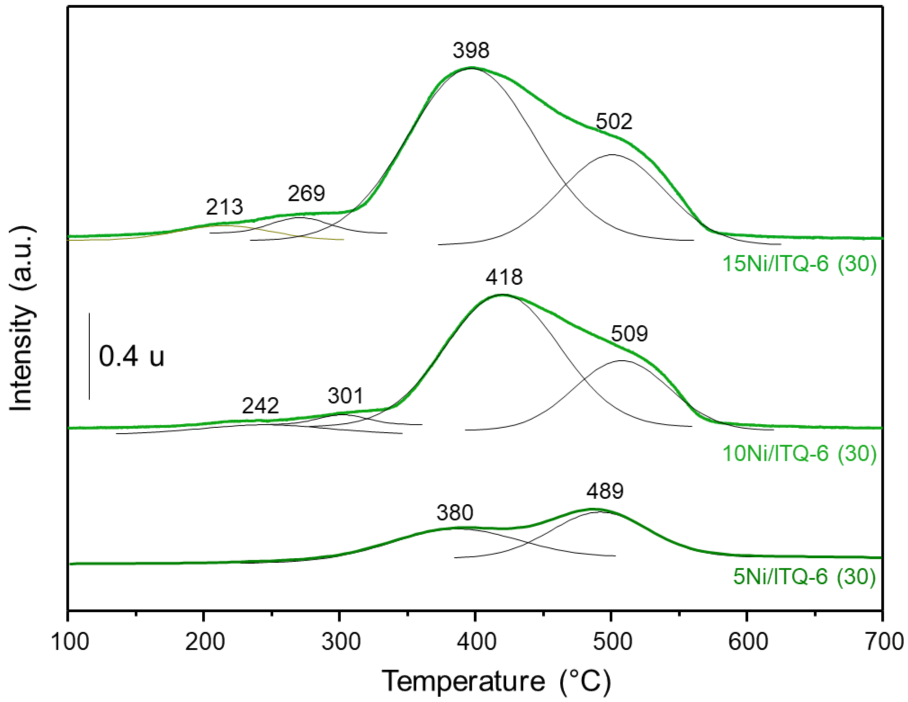

Figure 4.17. H_2-TPR profile of higher Ni loading catalyst supported on ITQ-6 (Si/Al = 30) over the range of temperatures between 200 °C and 700 °C.

Achieving higher dispersion of Ni particles over inorganic supports is related not only to the higher external surface area, but also to other properties, such as hydrophilicity, basicity, and concentration of surface hydroxyl groups, as previously described by other authors [54-56]

IR spectra from these catalysts exhibit three types of hydroxyl groups located in different zeolitic sites, depending on the presence or absence of Al ions inside the network (**Figure 4.18**).

IR spectra results reveal that the nickel impregnation did not significantly modify the profile of hydroxyl group vibrations, as support and catalyst spectra are practically the same, which is expected, as low nickel loading was employed for all catalysts (**Figure 4.19**).

Si/Al = ∞ catalysts only exhibit peaks associated with Si-OH hydroxyl groups, typical of Al-free zeolitic supports, found at 3741 cm^{-1} (**Figure 4.19**). On the other hand, Si/Al = 30 catalysts present a higher concentration of surface -OH groups due to the presence of not only Si-OH, but also Al-OH and Si-(OH)-Al groups. The vibration of these surface hydroxyl groups is located at lower wavenumbers, centered at 3640 and 3598 cm^{-1}, respectively, as previously described in the literature [57].

In FER zeolites, due to their microporous structure, most of their hydroxyl groups are located within them, while the FT-IR results reveal that the delaminated support, ITQ-6, exhibits a higher concentration of Si-OH groups. These groups are obtained by the cleavage of Si-O-Si dangling bonds during the delamination step treatment with NaOH, which, when split apart give rise to -terminal -OH groups as previously reported by Chica et al. [34].

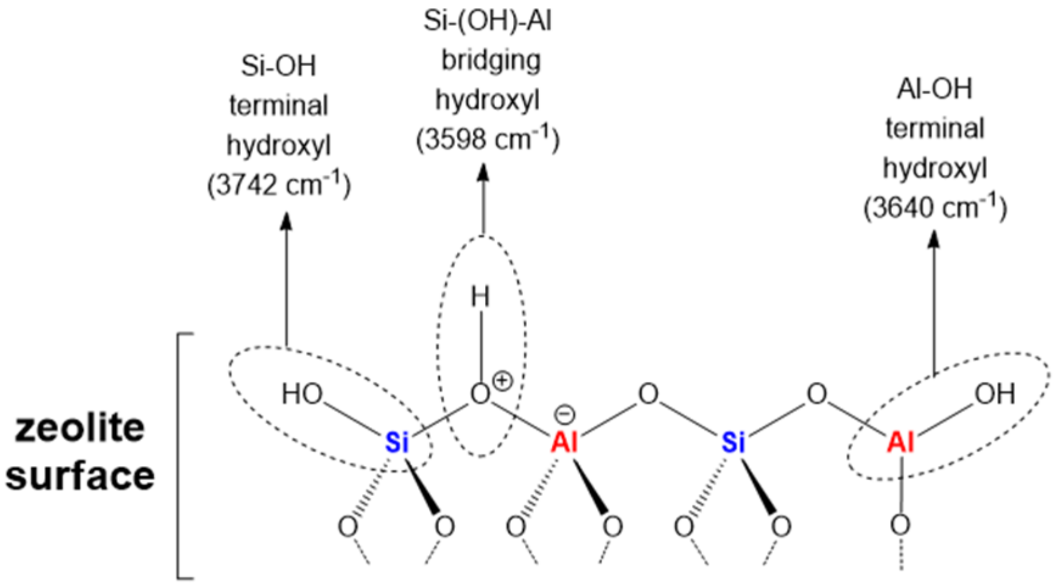

Figure 4.18. Schematic representation of the different types of surface hydroxyl groups found in an Al-containing zeolite. The presence of aluminum is associated with an increase of -OH groups on the zeolite surface due to the formation of bridging hydroxyls, Si-(OH)-Al, and terminal hydroxyls, Al-OH.

The higher concentration of -OH groups on the surface of delaminated and Al-containing zeolites favors the interaction between the support and nickel, which accounts for the higher Ni^0 dispersion in catalysts supported on Si/Al = 30 zeolites in comparison with the Si/Al =∞ ones (**Table 4.4**).

This is accounted for by the fact that by using the impregnation technique, the deposition of the metallic phase relies first on electrostatic interaction between the precursor and the support surface, followed by its subsequent calcination. This way, previous results from the literature reveal that an increase in the concentration of these surface -OH groups leads to catalysts with more dispersed metallic phase [58, 59], which is in consonance with the trend observed for the catalysts in this study.

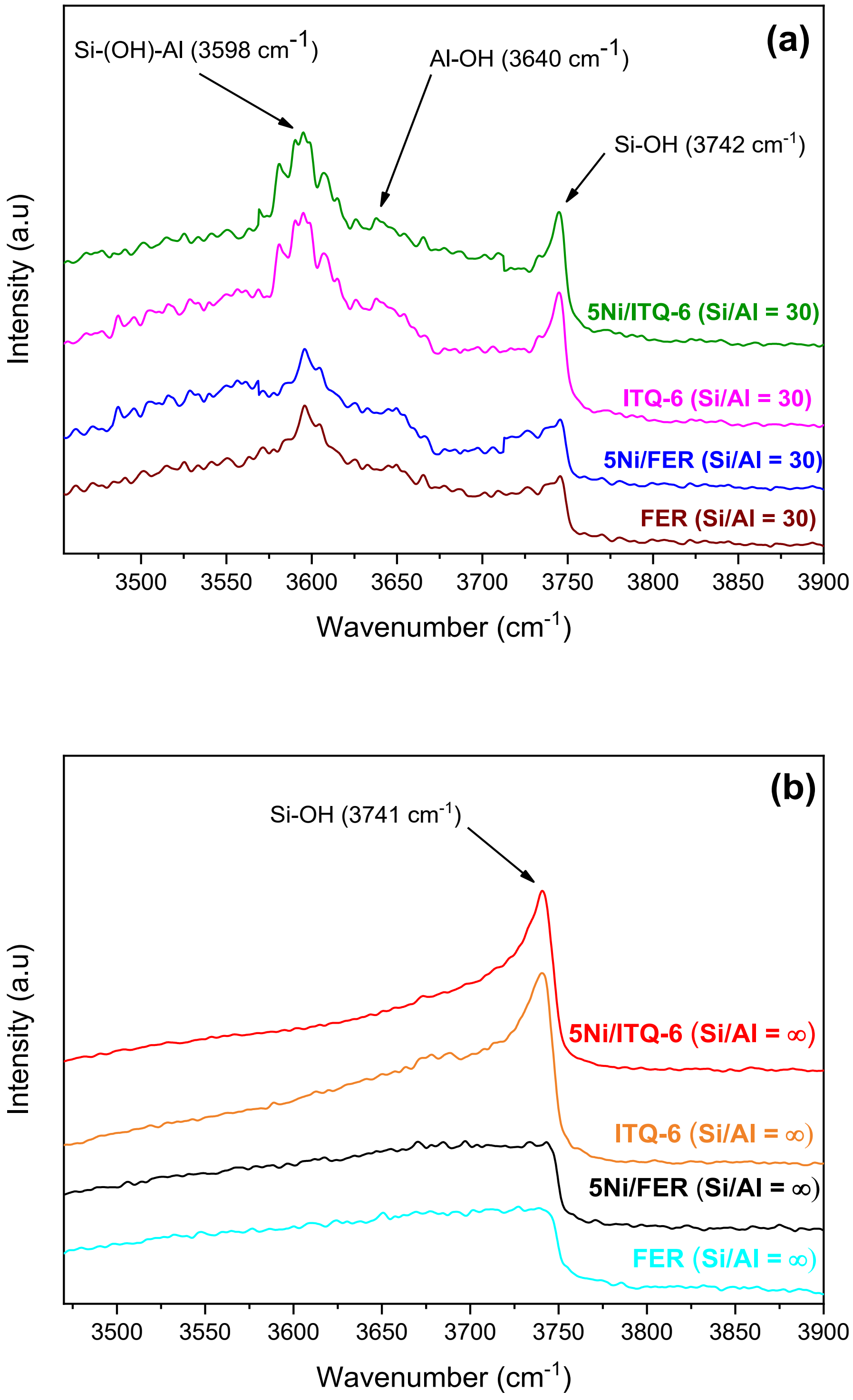

Figure 4.19. FTIR spectra for the Ni-based catalysts and respective supports for the **(a)** Si/Al = 30 and the **(b)** Si/Al = ∞ materials. The spectra exhibit hydroxyl vibrations at different zeolitic positions: terminal Si-OH and Al-OH, centered around 3742 cm^{-1} and 3640 cm^{-1}, respectively, and bridging Si-(OH)-Al, centered around 3598 cm^{-1}.

4.2.2 – Catalytic results and reaction mechanism

CO_2 conversion and CH_4 selectivity for all the 5% wt. Ni catalysts are presented in **Figure 4.20.** As it can be seen, the catalysts based on delaminated zeolite (ITQ-6) show higher CO_2 conversion and CH_4 selectivity values than their counterpart based on FER zeolite.

As previously discussed over the XRD and H_2-chemisorption results, the delaminated and Al-containing catalysts present smaller Ni crystallite sizes and, consequently, a larger metallic surface area (**Table 4.4**). This sequence aligns with the one observed for CO_2 conversion at 450 °C: 5Ni/ITQ-6 (30) > (5Ni/ITQ-6 (∞) > 5Ni/FER (30) > 5Ni/FER (∞) (**Figure 4.20**).

To provide insight into the mechanism taking place for these catalysts, kinetic studies were conducted to calculate the TOF values for the CO_2 methanation reaction (**Figure 4.20**). Furthermore, as CO might be an intermediate in the reaction mechanism, catalytic tests, and kinetic studies were also carried out for the CO methanation reaction, and the results are summarized in **Figure 4.21**.

Table 4.5. Turnover frequency values and apparent activation energy values (E^*_{a,CO_2}) towards CH_4 formation via CO_2 methanation (TOF_{CO_2} and E^*_{a,CO_2}) and CO methanation (TOF_{CO} and $E^*_{a,CO}$) for the 5% wt. Ni zeolite-based catalysts.

Catalyst	**TOF_{CO_2} (s^{-1})**				**E^*_{a,CO_2}(kJ mol^{-1})**
	250 °C	**300 °C**	**350 °C**	**400 °C**	
5Ni/FER (∞)	0.015	0.069	0.186	0.422	61
5Ni/ITQ-6 (∞)	0.104	0.226	0.466	0.731	40
5Ni/FER (30)	0.039	0.128	0.332	0.621	54
5Ni/ITQ-6 (30)	0.177	0.354	0.684	1.162	36
	TOF_{CO} (s^{-1})				**$E^*_{a,CO}$(kJ mol^{-1})**
5Ni/FER (∞)	0.009	0.022	0.070	0.149	54
5Ni/ITQ-6 (∞)	0.066	0.199	0.340	0.683	44
5Ni/FER (30)	0.026	0.065	0.153	0.271	49
5Ni/ITQ-6 (30)	0.168	0.415	0.812	1.395	41

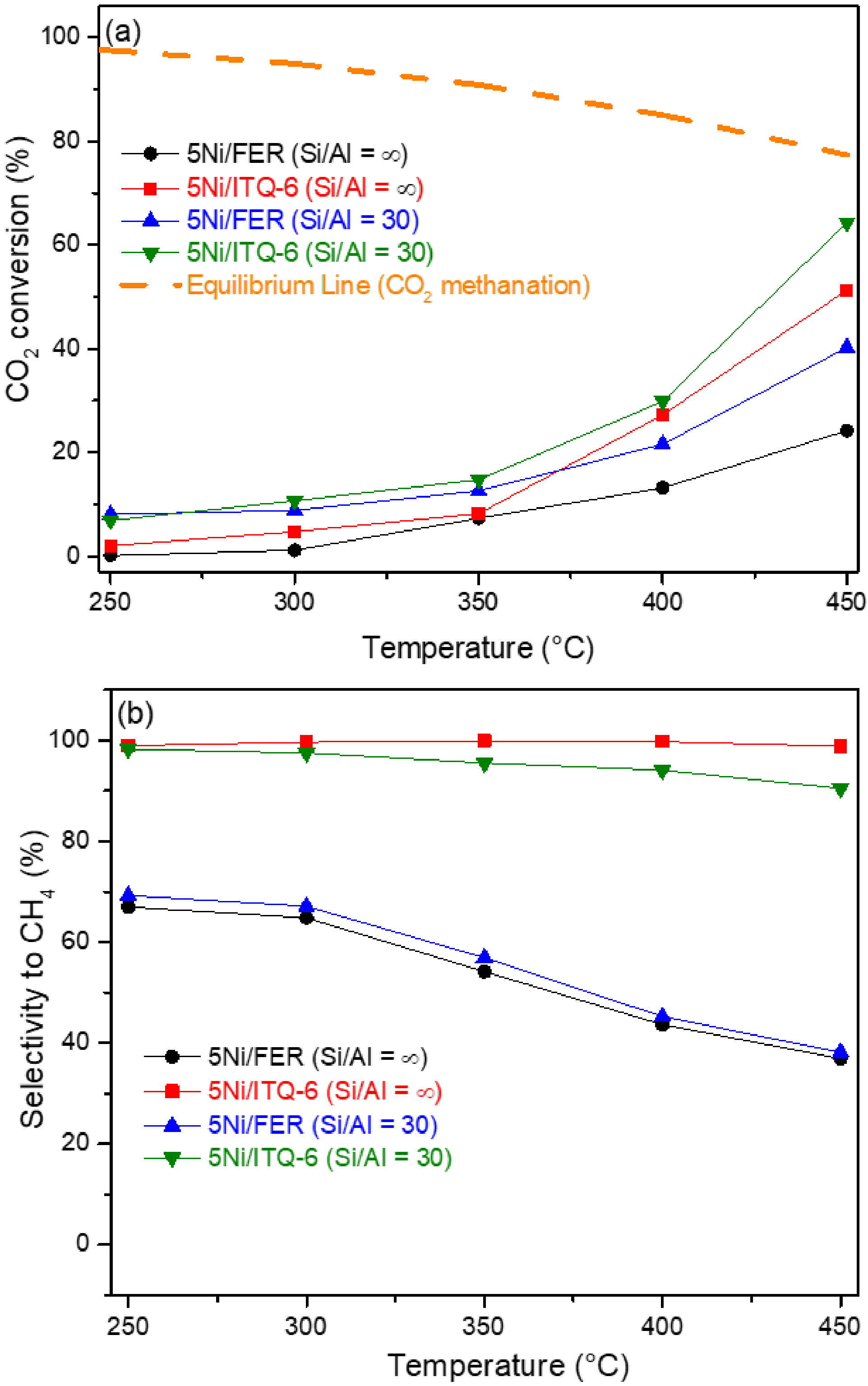

Figure 4.20. (a) CO_2 conversion and (b) selectivity towards CH_4 dependence on temperature for the catalysts based on FER and ITQ-6. Reaction conditions: 250 °C - 450 °C, Pressure: 1 atm, WHSV = 38,000 mL $(g_{cat}\ h)^{-1}$, $H_2/CO_2 = 4$. Equilibrium data were extracted from Gao [60].

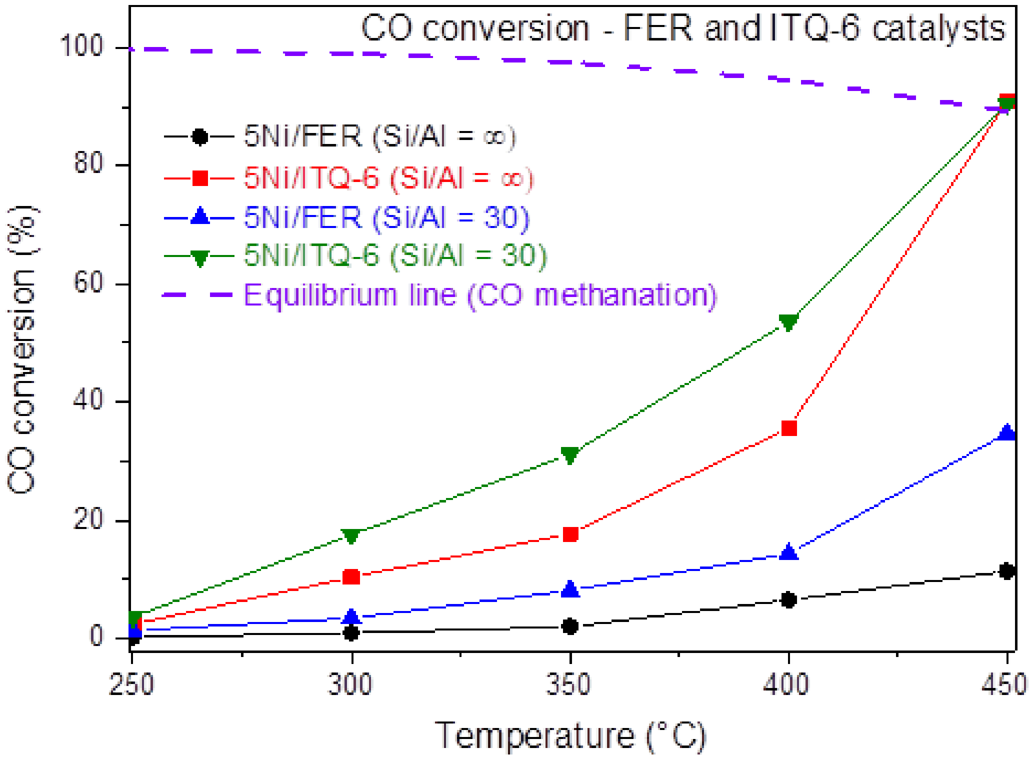

Figure 4.21. CO conversion dependence on temperature for the catalysts based on FER and ITQ-6. Reaction conditions: 250 °C - 450 °C, Pressure: 1 atm, WHSV = 38,000 mL $(g_{cat}\ h)^{-1}$, $H_2/CO = 3$. Equilibrium data were extracted from Gao et al. [60].

With these TOF values, the Arrhenius plots were performed to calculate the apparent activation energy for the CO_2 (E^*_{a,CO_2}) and CO methanation reactions ($E^*_{a,CO}$) (**Figure 4.22**). This will be further used in the mechanism discussion to account for the difference in CO_2 conversion and CH_4 selectivity found across the catalysts supported on different zeolitic supports.

Taking into account in-situ/operando results and DFT studies available in the literature [61-63], two main mechanistic pathways have been proposed for the CO_2 methanation reaction and presented in **Figure 4.23**:

(a) Associative pathway, by which CO_2 is first adsorbed, forming intermediate species, such as formates or bicarbonates that are, in the sequence, hydrogenated by adsorbed hydrogen atoms leading to CH_4 formation.

(b) Dissociative pathway, by which CO_2, after adsorption, undergoes dissociation to carbonyl (CO_{ads}), which is then hydrogenated.

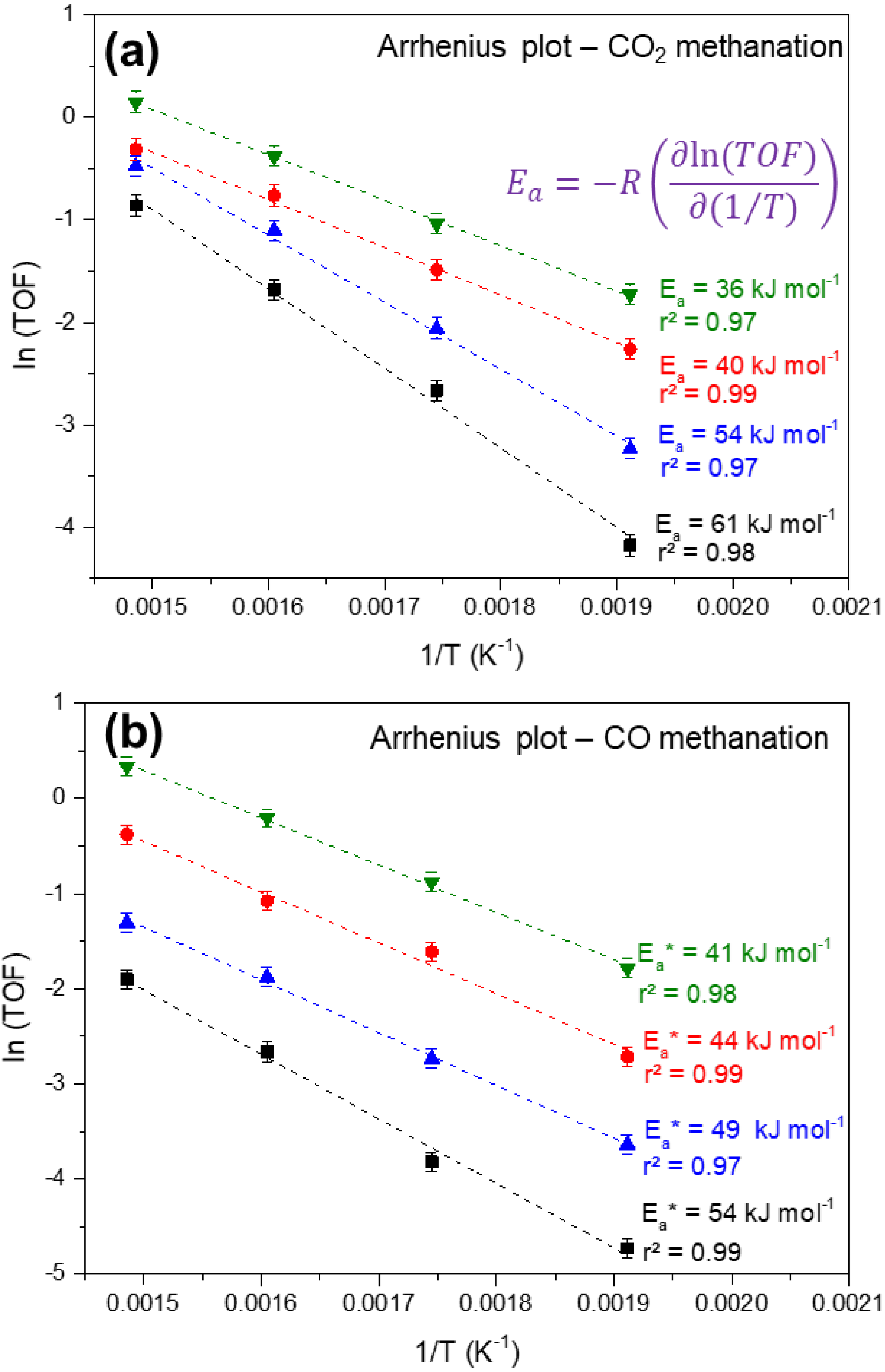

Figure 4.22. Arrhenius plot for (a) CO_2 methanation and (b) CO methanation. The apparent activation energy for the CO_2 methanation (E^*_{a,CO_2}) and CO methanation ($E^*_{a,CO}$) are obtained from the slope obtained from the data series.

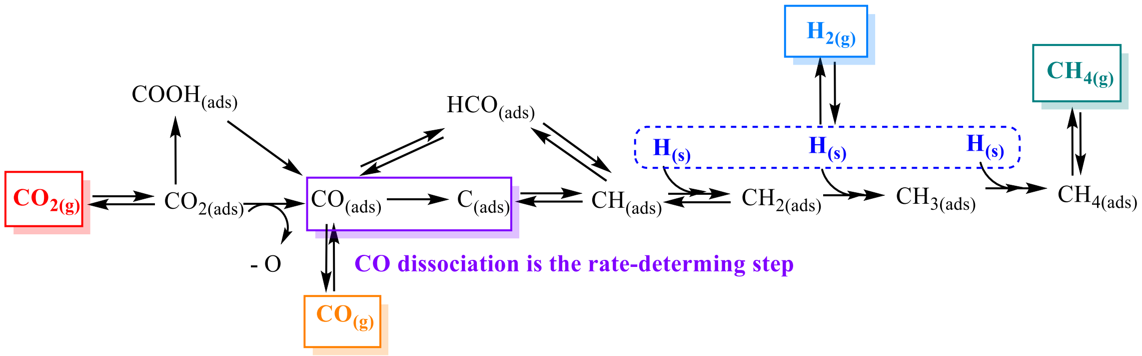

Figure 4.23. Schematic representation of the possible chemical reactions for the CO_2 methanation reaction, either by the associative or dissociative mechanistic pathways.

Despite the apparent stoichiometric simplicity of the reaction, there are still uncertainties regarding the nature and role of intermediate surface species in the formation of methane. Wu et al. determined from DRIFTS results that over siliceous supports, such as zeolites, the key intermediate to the formation of methane might either be HCOO species or CO, depending on the type of support, basicity, porous structure and experimental conditions, such as temperature and pressure [64].

As seen in **Table 4.5**, for ITQ-6-based catalysts, $E^*_{a,CO_2} < E^*_{a,CO}$, while for the FER-based catalysts, the opposite trend is observed, $E^*_{a,CO_2} > E^*_{a,CO}$ suggesting different mechanisms are taking place in both systems.

In the ITQ-6 catalysts, the fact that $\mathrm{E}^*_{\mathrm{a,CO_2}} < \mathrm{E}^*_{\mathrm{a,CO}}$ explains the low CO selectivity of these catalysts, as the formation of methane via the associative mechanism takes place without a relevant formation of $C_{(ads)}$ as an intermediate. Among all the possible reactions, Schmider et al reported that the disassociation steps, from $CO_{2(ads)}$ to $CO_{(ads)}$, and $CO_{(ads)}$ to $C_{(ads)}$, in the dissociative mechanism, are the ones with the highest activation energy, which makes this process a rate-determining step for the dissociative mechanism, favoring instead the associative mechanism [65], as seen in **Figure 4.23**.

The presence of surface -OH groups on ITQ-6 catalysts, as detected by IR spectroscopy, provides further evidence for the lower E^*_{a,CO_2} as these zeolitic surface hydroxyl groups take a role in the adsorption of CO_2 molecules on the ITQ-6 surface and the carbonated intermediates could be reduced by hydrogen species to CH_4, as previously reported for the CO_2 methanation reaction by Huang et al. [66].

Westermann et al., working on catalysts based on USY zeolite, reported that with the absence of the basic moieties to interact with the CO_2 molecules, no carbonate species are formed as intermediates, with most of the conversion taking place through formate dissociation to CO over Ni particles, significantly decreasing total CO_2 conversion and CH_4 selectivity [67], which corroborates the results found in this work.

While for the FER-based catalysts, $E^*_{a,CO_2} > E^*_{a,CO}$, which is accounted for the presence of larger metallic particles, which leads to a decrease in H_2 uptake, as confirmed by the chemisorption results, leading to a less efficient interaction of the H-derived species and the carbon intermediates formed from CO_2.

4.2.3 – Effect of the delamination of the support

In all the catalytic tests, elemental analysis of the spent catalysts revealed there was no significant carbon formation, and the mass balance between inlet and outlet flows was around 100%. For this reason, one can assume there is no significant occurrence of other undesired reactions, such as the Boudouard reaction ($2CO \rightarrow C + CO_2$), CH_4 cracking ($CH_4 \rightarrow 2H_2 + C$), and CO reduction ($CO + H_2 \rightarrow C + H_2O$), which would lead to coke formation.

For the CO_2 methanation reaction, ITQ-6-based catalysts exhibit higher CO_2 conversion values (**Figure 4.20a**), and higher TOF values than their FER-based counterparts (**Table 4.5**). The first apparent reason for this is that ITQ-6-based catalysts present higher H_2 uptake over the metallic surface than the FER-based catalysts, as shown by the H_2-chemisorption, which is a consequence of higher metallic dispersion and metallic surface area. H_2 uptake from the Ni particles is an important step in the mechanism of CO_2 hydrogenation in the associative mechanism, as higher availability of H_2 over the metallic particles allows a higher combination with CO_2 molecules.

The second reason is the higher peripheral zone between the metallic phase and the zeolite surface over the ITQ-6-based catalysts, as a consequence of smaller Ni^0 particles. As previously discussed in the last section, over ITQ-6-based catalysts, the reaction seems to proceed via the associative mechanism, and part of the CH_4 can be formed by the interaction of the carbonated species on the zeolite surface and hydrogen atoms carried out by spillover. This way, in ITQ-6 catalysts, a smaller distance between the hydrogen atoms over the Ni atoms and the CO_2 adsorbed on the zeolite surface enhances the interaction between both species.

Gao et al., in a study about CO methanation over Ni/α-Al_2O_3 catalysts, concluded there is an optimum range in size for the Ni nanoparticles to increase the hydrogenation of CO towards CH_4 [68]. Too small particles, smaller than 8 nm, presented lower H_2 coverage, which decreased CO_2 conversion and increased coke formation due to side reactions. At the other point of the size range, too large particles, larger than 20 nm, did not favor the interaction of carbon and hydrogen species, leading to a decrease in conversion. The catalysts with middle-sized particles were the ones that concerted both effects and presented higher conversions and selectivity toward CH_4.

In another study, Varvoutis et al. concluded that for a series of Ni-CeO_2 catalysts, the optimum Ni^0 size for CO_2 methanation was around 18-20 nm [69]. Smaller particles led to a decrease in the peripheral zone between the support and step/edge and kink/corner Ni^0 sites, which are known to be the active sites for the activation of CO_2 molecules in the reaction mechanism. Larger particles, on the other hand, decreased the step/edge and kink/corner and favored the formation of terrace sites, which are inactive for the activation of molecules.

The Ni^0 particle size distribution in the catalysts (**Figure 4.13**) reveals that most Ni^0 particles in the ITQ-6 catalysts are found between the 8-16 nm range, while in the FER-based ones, larger particles are found, mostly in the 17-30 nm. This confirms that most Ni^0 particles over the delaminated supports fall in the middle-size range, accounting for their higher CO_2 conversion and selectivity.

Regarding selectivity towards CH_4, it was found to be very dependent on the kind of support employed. First of all, for all supports, the selectivity towards CH_4 decreased when the temperature was increased. With the increase in temperature, the endothermic reverse water-gas shift reaction (RWGS) (Equation 7) is favored in relation to the exothermic CO_2 methanation (Equation 8), which accounts for the observed drop in CH_4 selectivity for all catalysts.

$$CO_2 + H_2 \rightleftharpoons CO + H_2O \quad \Delta H_{298\,K} = +41 kJ/mol \; (7)$$

$$CO_2 + 4H_2 \rightleftharpoons CH_4 + 2H_2O \quad \Delta H_{298\,K} = -165\, kJ/mol \; (8)$$

In the ITQ-6-based catalysts, where smaller Ni^0 crystallites were found, the main product of the reaction was CH_4, with selectivity towards CH_4 of over 90% over the whole range of studied temperatures, even for low CO_2 conversion values at lower temperatures (**Figure 4.20b**).

Meanwhile, for the FER-based catalysts, which present larger Ni^0 crystallites, the selectivity towards CH_4 did not surpass 70% at its highest value at 250 °C and significantly dropped to values as low as 40% at 450 °C.

The higher selectivity towards CH_4 on ITQ-6 catalysts is a consequence of the lower E^*_{a,CO_2} in these systems, as previously discussed in the last section, which is associated with the presence of smaller Ni^0 particles. **Figure 4.24** summarizes this discussion by showing that, over the range of average Ni crystallites analyzed, the higher the average Ni^0 crystallite size, the higher the E^*_{a,CO_2} value.

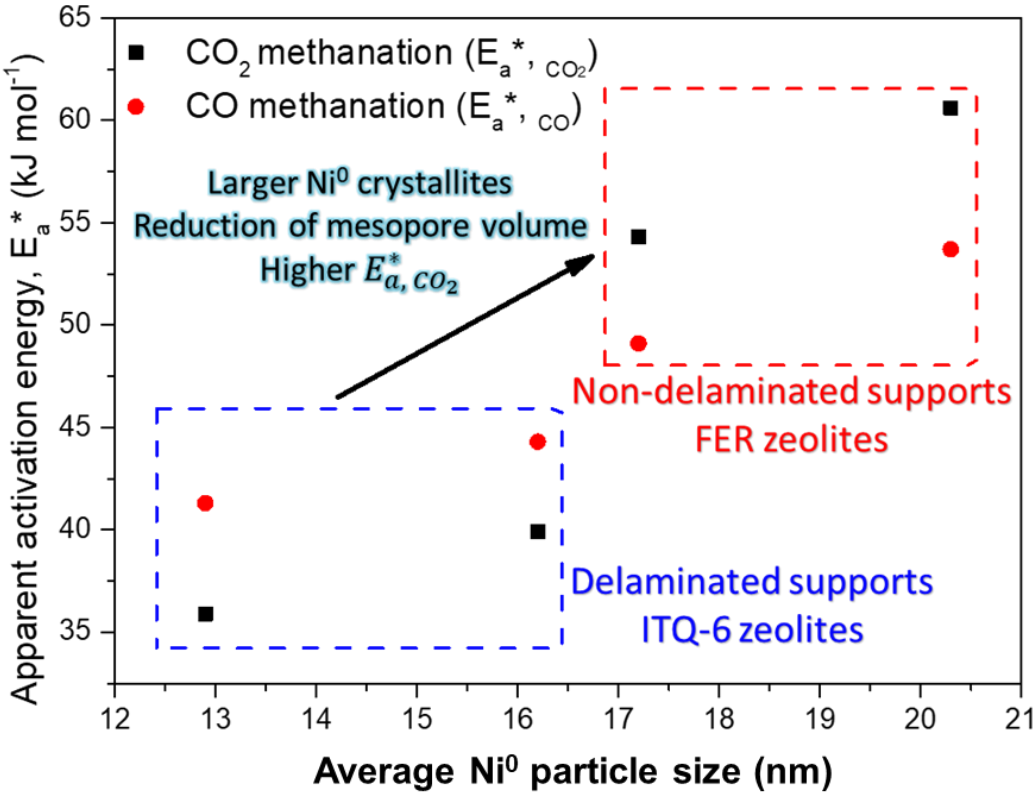

Figure 4.24. Apparent activation energy for the CO_2 methanation reaction, E^*_{a,CO_2} (■) and the CO methanation reaction, $E^*_{a,CO}$, (●) dependence of the average Ni^0 particle size.

4.2.4 – Effect of aluminum addition into the zeolite framework

Regarding the effect of aluminum addition on the catalytic performance, Bacariza et al. remark that higher Si/Al ratios lead to higher hydrophobicity, which favors the removal of the water molecules after their formation [24], which is a fundamental step so that the succession of hydrogenation steps might take place towards CH_4 formation. Contrastingly, a higher Si/Al ratio leads to lower interaction with the solvent during the catalyst preparation step by impregnation due to a lower concentration of surface hydroxyl groups, which leads to lower metallic dispersion catalysts [49].

At the same time, the lower concentration of -OH groups affects the material basicity, as these groups act as intermediate basicity sites, which might participate in the CO_2 sorption, as previously discussed.

Given these three opposite trends concerning the Si/Al ratio, Bacariza et al. report that a delicate balance of the best Si/Al ratio at intermediate values needs to be found for a compromise toward the best performance for the CO_2 methanation reaction [24]. In their study, Y zeolites were used as support for Ni-based catalysts, and they reported that the zeolites with Si/Al ratios as low as 3 performed worse than equivalent support with Si/Al = 38, which was attributed to the higher hydrophobicity of the latter, favoring the water removal from the reaction site and the formation of methane.

On the other extreme of high Si/Al ratios, Xu et al. employed Ni catalysts supported over low basicity MFI zeolite supports (Si/Al = ∞) and concluded that the absence of basic sites significantly increased the E^{*}_{a,CO_2} for the methanation reaction, due to the lack of interaction between basic sites and CO_2, as confirmed by TPD results [70]. When the system basicity was increased, conversion and CH_4 selectivity were significantly increased.

Outside of the zeolite field as supports, but still regarding the impact of the presence of basic sites at the support surface, Pan et al. evidenced the role of basicity by comparing the catalytic performance between $Ni/Ce_{0.5}Zr_{0.5}O_2$ and $Ni/\gamma\text{-}Al_2O_3$ and highlighting that the only difference between them is the strength of hydroxyl and CO_2 interactions [71]. While the adsorption of CO_2 over the medium basic sites of $Ni/Ce_{0.5}Zr_{0.5}O_2$ led to the formation of monodentate carbonates species and eventual CH_4 formation, the CO_2 molecules adsorbed on the stronger sites found in $Ni/\gamma\text{-}Al_2O_3$ did not take part in the reaction, even though they were detected by in-situ DRIFTS.

In the specific case of this work, the catalysts supported on Si-Al = 30 zeolites exhibited higher metallic dispersion, which was attributed to the higher hydrophilicity and consequent interaction between the support and the nickel precursors during the preparation step. This led to a higher proportion of nickel crystallites between 10-15 nm, known to be the most active for the methanation reaction. In addition to that, Si-Al = 30 zeolites exhibited higher TOF values over the whole range of analyzed temperatures, and lower E^{*}_{a,CO_2}.

Higher catalytic activity on the catalysts based on the Si-Al = 30 zeolites compared to their aluminum-free counterparts is rationalized by the favoring effect proportioned by the higher concentration of -OH groups, which is achieved by the inclusion of Al inside the zeolite framework and has a consequence on increasing the CO_2 uptake. The carbonated intermediates can take part and interact with adsorbed hydrogen atoms, eventually culminating in the formation of hydrogenated intermediates at a lower activation energy cost (**Table 4.5**).

The mechanism is even more favored when Si-(OH)-Al groups are present on the catalyst's surface, such as the ones found in ITQ-6 (30) support, which accounts for the fact that 5Ni/ITQ-6 (30) is the catalyst with higher CO_2 conversion and TOF values among the 5% wt. catalysts.

4.2.5 – Effect of nickel content on the catalytic performance

Once the ITQ-6 (30) zeolite was identified as the best support for the CO_2 methanation reaction, a series of tests was conducted with the 5Ni/ITQ-6 (30) at a lower space velocity [WHSV

= 10,000 mL (g_{cat} h)$^{-1}$] than in the first catalytic assessment tests. This was done to increase the contact time with the active phase and maximize CO_2 conversion [72].

Furthermore, a series of higher loading catalysts on ITQ-6 (30), 10Ni/ITQ-6 (30), 15Ni/ITQ-6 (30), and 20/ITQ-6 (30) were tested for the CO_2 methanation reaction by employing the 10,000 h^{-1} space velocity (**Figure 4.25**), and compared with other catalysts already published in the literature (**Table 4.6**).

Regarding the CH_4 selectivity, the higher the metallic content, the higher the selectivity, with the higher loading catalysts reaching > 99% selectivity values at temperatures as low as 350°C. (**Figure 4.25**). This is attributed to the fact that on higher-loading catalysts, the Ni particle sizes are larger, and, consequently, the available metallic surface area is also larger, as confirmed by XRD and chemisorption results.

This way, following the associative mechanism previously detected by the kinetic studies, more hydrogen is directly available to fully hydrogenate the carbonated intermediates to CH_4, increasing the selectivity values, which is in consonance with other studies published by our research group and other researchers [73-75].

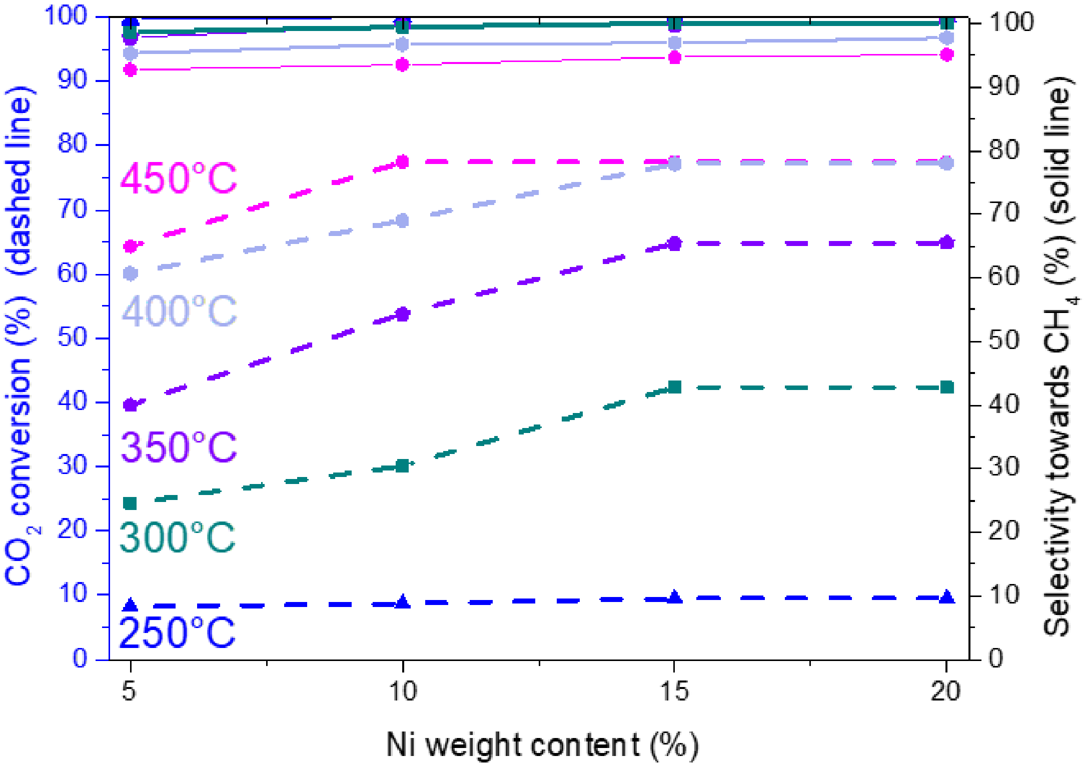

Figure 4.25. Effect of nickel loading on CO_2 conversion (dashed lines) and selectivity towards CH_4 (solid lines) on different temperatures for the catalysts based on ITQ-6 (30). Pressure: 1 atm, H_2/CO_2 = 4:1, WHSV = 10,000 mL (g_{cat} h)$^{-1}$

Table 4.6. Comparison of the best catalytic performance conditions achieved for a series of zeolite-based catalysts for the CO_2 methanation reaction, and the corresponding experimental conditions employed for the catalytic tests.

Catalyst	**Si/Al ratio**	**T_{red}(°C)**	**WHSV (h^{-1})**	**Best catalytic performance achieved**			**Reference**
				T (°C)	CO_2 conv. (%)	CH_4 select. (%)	
5Ni/ITQ-6	30	450	10,000	450	68	95	This work.
10Ni/ITQ-6	30	450	10,000	450	77	97	This work.
15Ni/ITQ-6	30	450	10,000	400	79	98	This work.
20Ni/ITQ-6	30	450	10,000	400	79	98	This work.
15Ni/USY	38	470	43,000	400	71	97	[24]
15Ni/BEA	38	470	43,000	400	70	96	[23]
15Ni/MOR	47	470	43,000	400	66	95	[23]
15Ni/ZSM-5	40	470	43,000	400	65	95	[23]
5Ni/S-1	∞	500	60,000	450	57	91	[76]
14Ni-7Ce/USY	3	700	43,000	400	68	95	[77]
10Ni-10La/BEA	12	500	10,000	350	65	99	[78]

The 15Ni/ITQ-6 (30) catalyst presented higher CO_2 conversion and CH_4 selectivity values than the ones reported by Bacariza et al. [23, 24], which carried out a work on Ni-based catalysts supported on 3D zeolites for CO_2 methanation.

The 15% wt. Ni catalyst in this work also exhibited higher CO_2 conversion and CH_4 selectivity than other types of zeolite-based catalysts, such as the one reported by Goodarzi et al., which consisted of cage-confined Ni particles inside the 1-silicalite structure [76]. It also displayed higher conversion and selectivity values than some zeolite-based catalysts, in which promoters had been added, such as a Ce-USY reported by Graça et al. [77] and a La-BEA one reported by Quindimil et al. [78]

Indubitably, as previously mentioned, it is necessary to critically consider the diversity of experimental aspects when this type of literature-oriented comparison is carried out, such as the metallic loading, reduction temperature, and duration, which affect metallic surface area availability, WHSV, contact time and other experimental factors. Nevertheless, the experimental results exhibited by the ITQ-6 (30) catalysts, particularly 15Ni/ITQ-6 (30), place them among the best zeolite-based catalysts reported for the moment, with much potential for an efficient CO_2 methanation implementation.

4.3 – Conclusions

Catalysts based on Ni supported on ITQ-6 and FER zeolites have been prepared and studied in the CO_2 and CO methanation reaction. N_2 adsorption results showed that the delamination process increased the zeolite total surface area while the microporous surface area drastically decreased, indicating a successful dissociation of the zeolitic aluminosilicate layers of the FER zeolite, which was confirmed by microscopy analyses. XRD results confirmed that a higher delamination extent was achieved for the Si/Al = 30 zeolite due to the presence of aluminum in the solid network and that the employed impregnation techniques deposited Ni^0 nanoparticles in the 8-20 nm crystallite size range.

Catalytic results for CO_2 methanation reaction showed that ITQ-6-based catalysts presented higher CO_2 conversion and TOF values, which has been attributed to the better dispersion of metallic Ni particles and confirmed by the particle size distribution determination with TEM images. As confirmed by chemisorption results, their smaller size led to higher H_2 uptake on the metallic phase, which, according to the associative mechanistic pathway taken by the reaction, favors the interaction between the reactants.

ITQ-6-based catalysts also exhibited higher selectivity values towards CH_4 (> 90%) than the ones shown by the FER-based catalysts, which did not surpass 70%. This has been rationalized by the experimentally determined apparent activation energies, which revealed that, in ITQ-6-based systems, the apparent activation energy for CH_4 methanation was lower than that observed for CO methanation. Based on a computational study already published in the literature [59], we then proposed a mechanistic pathway for these systems by which the associative mechanism is favored in the ITQ-6-based catalysts due to the higher Ni^0 available surface area, which leads to a higher H_2 uptake, favoring the complete reduction of carbon intermediates. Meanwhile, in the FER-based catalysts, lower metallic dispersions are found and, as a consequence, lower H_2 uptakes, which leads to partial reduction of CO_2 to CO and accounting for the lower selectivity to CH_4.

Regarding the impact of the addition of Al into the zeolitic network, the Si/Al = 30 catalysts exhibited higher CO_2 conversion and TOF values than the pure Si ones, which was attributed to their higher uptake of CO_2 on the metal-support interface, due to the presence of Si-(OH)-Al groups.

Finally, after ITQ-6 (30) was identified to be the best support for the CO_2 methanation reaction, higher metallic loading catalysts were also catalytically assessed. The 15% wt. one presented optimum results (high activity, selectivity, and stability after 24 hours of reaction time), comparable or even superior to some of the best zeolite-based catalysts reported in the literature.

In summary, the nature of support was confirmed to be paramount in developing promising catalysts for the CO_2 methanation reaction, and the effect of delamination was positive to improve the metallic dispersion of Ni^0 species and metal-support interaction in the reaction mechanism. This opens a wide window of prospects to explore the use of delaminated zeolites as support for developing new catalysts for CO_2 methanation reaction or, furthermore, for industrial-scale processes based on carbon capture and valorization.

4.4 – References

[1] Weckhuysen BM, Yu J. Recent advances in zeolite chemistry and catalysis. Chemical Society Reviews. 2015;44:7022-4.

[2] Król M. Natural vs. Synthetic Zeolites. Crystals. 2020;10:622.

[3] Li Y, Yu J. Emerging applications of zeolites in catalysis, separation and host–guest assembly. Nature Reviews Materials. 2021;6:1156-74.

[4] Boronat M, Corma A. Factors Controlling the Acidity of Zeolites. Catalysis Letters. 2015;145:162-72.

[5] Moliner M, Martínez C, Corma A. Multipore Zeolites: Synthesis and Catalytic Applications. Angewandte Chemie International Edition. 2015;54:3560-79.

[6] Shi W-y, Shao H-b, Li H, Shao M-a, Du S. Progress in the remediation of hazardous heavy metal-polluted soils by natural zeolite. Journal of Hazardous Materials. 2009;170:1-6.

[7] Yuna Z. Review of the Natural, Modified, and Synthetic Zeolites for Heavy Metals Removal from Wastewater. Environmental Engineering Science. 2016;33:443-54.

[8] Wang S, Peng Y. Natural zeolites as effective adsorbents in water and wastewater treatment. Chemical Engineering Journal. 2010;156:11-24.

[9] Tang R, Ullah N, Li Z. Unveiling the promotion effect of Zr species on SBA-15 supported nickel catalysts for CO2 methanation. International Journal of Hydrogen Energy. 2023;48:4694-707.

[10] Cataldo E, Salvi L, Paoli F, Fucile M, Masciandaro G, Manzi D, et al. Application of Zeolites in Agriculture and Other Potential Uses: A Review. Agronomy2021.

[11] Khaleque A, Alam MM, Hoque M, Mondal S, Haider JB, Xu B, et al. Zeolite synthesis from low-cost materials and environmental applications: A review. Environmental Advances. 2020;2.

[12] Martínez C, Corma A. Inorganic molecular sieves: Preparation, modification and industrial application in catalytic processes. Coordination Chemistry Reviews. 2011;255:1558-80.

[13] Weitkamp J. Zeolites and catalysis. Solid State Ionics. 2000;131:175-88.

[14] Degnan TF. Applications of zeolites in petroleum refining. Topics in Catalysis. 2000;13:349-56.

[15] Vermeiren W, Gilson JP. Impact of Zeolites on the Petroleum and Petrochemical Industry. Topics in Catalysis. 2009;52:1131-61.

[16] Ennaert T, Van Aelst J, Dijkmans J, De Clercq R, Schutyser W, Dusselier M, et al. Potential and challenges of zeolite chemistry in the catalytic conversion of biomass. Chemical Society Reviews. 2016;45:584-611.

[17] Andana T, Rappé KG, Nelson NC, Gao F, Wang Y. Selective catalytic reduction of NOx with NH3 over Ce-Mn oxide and Cu-SSZ-13 composite catalysts – Low temperature enhancement. Applied Catalysis B: Environmental. 2022;316.

[18] Wang S, Yin Q, Guo J, Ru B, Zhu L. Improved Fischer–Tropsch synthesis for gasoline over Ru, Ni promoted Co/HZSM-5 catalysts. Fuel. 2013;108:597-603.

[19] Bando KK, Soga K, Kunimori K, Ichikuni N, Okabe K, Kusama H, et al. CO2 hydrogenation activity and surface structure of zeolite-supported Rh catalysts. Applied Catalysis A: General. 1998;173:47-60.

[20] Aziz MAA, Jalil AA, Triwahyono S, Mukti RR, Taufiq-Yap YH, Sazegar MR. Highly active Ni-promoted mesostructured silica nanoparticles for CO2 methanation. Applied Catalysis B: Environmental. 2014;147:359-68.

[21] Scirè S, Crisafulli C, Maggiore R, Minicò S, Galvagno S. Influence of the support on CO2 methanation over Ru catalysts: an FT-IR study. Catalysis Letters. 1998;51:41-5.

[22] Guo X, Traitangwong A, Hu M, Zuo C, Meeyoo V, Peng Z, et al. Carbon Dioxide Methanation over Nickel-Based Catalysts Supported on Various Mesoporous Material. Energy and Fuels. 2018;32:3681-9.

[23] Bacariza MC, Maleval M, Graça I, Lopes JM, Henriques C. Power-to-methane over Ni/zeolites: Influence of the framework type. Microporous and Mesoporous Materials. 2019;274:102-12.

[24] Bacariza MC, Graça I, Lopes JM, Henriques C. Enhanced activity of CO2 hydrogenation to CH4 over Ni based zeolites through the optimization of the Si/Al ratio. Microporous and Mesoporous Materials. 2018;267:9-19.

[25] Bacariza MC, Bértolo R, Graça I, Lopes JM, Henriques C. The effect of the compensating cation on the catalytic performances of Ni/USY zeolites towards CO2 methanation. Journal of CO2 Utilization. 2017;21:280-91.

[26] Calleja G, Pau J, Calles JA. Pure and Multicomponent Adsorption Equilibrium of Carbon Dioxide, Ethylene, and Propane on ZSM-5 Zeolites with Different Si/Al Ratios. Journal of Chemical & Engineering Data. 1998;43:994-1003.

[27] Palomino M, Corma A, Rey F, Valencia S. New insights on CO2-methane separation using LTA zeolites with different Si/Al ratios and a first comparison with MOFs. Langmuir : the ACS journal of surfaces and colloids. 2010;26:1910-7.

[28] Zukal A, Pulido A, Gil B, Nachtigall P, Bludský O, Rubeš M, et al. Experimental and theoretical determination of adsorption heats of CO2 over alkali metal exchanged ferrierites with different Si/Al ratio. Physical Chemistry Chemical Physics. 2010;12:6413-22.

[29] Zukal A, Dominguez I, Mayerová J, Čejka J. Functionalization of delaminated zeolite ITQ-6 for the adsorption of carbon dioxide. Langmuir : the ACS journal of surfaces and colloids. 2009;25:10314-21.

[30] Van Daele S, Minoux D, Nesterenko N, Maury S, Coupard V, Valtchev V, et al. A highly selective FER-based catalyst to produce n-butenes from isobutanol. Applied Catalysis B: Environmental. 2021;284:119699-.

[31] Bonilla A, Baudouin D, Pérez-Ramírez J. Desilication of ferrierite zeolite for porosity generation and improved effectiveness in polyethylene pyrolysis. Journal of Catalysis. 2009;265:170-80.

[32] Corma A, Diaz U, Domine ME, Fornés V. New aluminosilicate and titanosilicate delaminated materials active for acid catalysis, and oxidation reactions using H2O2. Journal of the American Chemical Society. 2000;122:2804-9.

[33] Corma A, Diaz U, Domine ME, Fornés V. AlITQ-6 and TiITQ-6: Synthesis, Characterization, and Catalytic Activity. Angewandte Chemie International Edition. 2000;39:1499-501.

[34] Chica A, Diaz U, Fornés V, Corma A. Changing the hydroisomerization to hydrocracking ratio of long chain alkanes by varying the level of delamination in zeolitic (ITQ-6) materials. Catalysis Today. 2009;147:179-85.

[35] Radko M, Rutkowska M, Kowalczyk A, Mikrut P, Święs A, Díaz U, et al. Catalytic oxidation of organic sulfides by H2O2 in the presence of titanosilicate zeolites. Microporous and Mesoporous Materials. 2020;302.

[36] Concepción P, López C, Martínez A, Puntes VF. Characterization and catalytic properties of cobalt supported on delaminated ITQ-6 and ITQ-2 zeolites for the Fischer-Tropsch synthesis reaction. Journal of Catalysis. 2004;228:321-32.

[37] Solsona B, Lopez Nieto JM, Díaz U. Siliceous ITQ-6: A new support for vanadia in the oxidative dehydrogenation of propane. Microporous and Mesoporous Materials. 2006;94:339-47.

[38] Da Costa-Serra JF, Miralles-Martínez A, García-Muñoz B, Maestro-Cuadrado S, Chica A. Ni and Co-based catalysts supported on ITQ-6 zeolite for hydrogen production by steam reforming of ethanol. International Journal of Hydrogen Energy. 2023;48:26518-25.

[39] Machado-Silva RB, Da Costa-Serra JF, Chica A. Enhancement of catalytic activity in CO2 methanation in Ni-based catalysts supported on delaminated ITQ-6 zeolite. Journal of Catalysis. 2024;436:115609.

[40] Święs A, Kowalczyk A, Rutkowska M, Díaz U, Palomares AE, Chmielarz L. Ferrierite and its delaminated and silica-intercalated forms modified with copper as effective catalysts for NH3-SCR process. Catalysts. 2020;10:1-22.

[41] De Pietre MK, Bonk FA, Rettori C, Garcia FA, Pastore HO. [V,Al]-ITQ-6: Novel porous material and the effect of delamination conditions on v sites and their distribution. Microporous and Mesoporous Materials. 2011;145:108-17.

[42] Sun C, Wang H, Ren J, Wang X, Wang R. Inserting ultrafine NiO nanoparticles into amorphous NiP sheets by in situ phase reconstruction for high-stability of the HER catalysts. Nanoscale. 2021;13:13703-8.

[43] Nazemi MK, Sheibani S, Rashchi F, Gonzalez-DelaCruz VM, Caballero A. Preparation of nanostructured nickel aluminate spinel powder from spent NiO/Al2O3 catalyst by mechano-chemical synthesis. Advanced Powder Technology. 2012;23:833-8.

[44] Thommes M, Kaneko K, Neimark AV, Olivier JP, Rodriguez-Reinoso F, Rouquerol J, et al. Physisorption of gases, with special reference to the evaluation of surface area and pore size distribution (IUPAC Technical Report). 2015;87:1051-69.

[45] Ackley MW, Rege SU, Saxena H. Application of natural zeolites in the purification and separation of gases. Microporous and Mesoporous Materials. 2003;61:25-42.

[46] Marosz M, Samojeden B, Kowalczyk A, Rutkowska M, Motak M, Díaz U, et al. MCM-22, MCM-36, and ITQ-2 zeolites with different Si/Al molar ratios as effective catalysts of methanol and ethanol dehydration. Materials. 2020;13:2399-.

[47] da Costa-Serra JF, Cerdá-Moreno C, Chica A. Zeolite-Supported Ni Catalysts for CO2 Methanation: Effect of Zeolite Structure and Si/Al Ratio. Applied Sciences2020.

[48] Bartholomew CH, Farrauto RJ. Chemistry of nickel-alumina catalysts. Journal of Catalysis. 1976;45:41-53.

[49] Bacariza MC, Amjad S, Teixeira P, Lopes JM, Henriques C. Boosting Ni Dispersion on Zeolite-Supported Catalysts for CO2Methanation: The Influence of the Impregnation Solvent. Energy and Fuels. 2020;34:14656-66.

[50] Maia AJ, Louis B, Lam YL, Pereira MM. Ni-ZSM-5 catalysts: Detailed characterization of metal sites for proper catalyst design. Journal of Catalysis. 2010;269:103-9.

[51] Mohan V, Raghavendra C, Pramod CV, Raju BD, Rama Rao KS. Ni/H-ZSM-5 as a promising catalyst for vapour phase hydrogenation of levulinic acid at atmospheric pressure. RSC Advances. 2014;4:9660-8.

[52] Vitale G, Molero H, Hernandez E, Aquino S, Birss V, Pereira-Almao P. One-pot preparation and characterization of bifunctional Ni-containing ZSM-5 catalysts. Applied Catalysis A: General. 2013;452:75-87.

[53] Omoregbe O, Majewski AJ, Steinberger-Wilckens R, El-kharouf A. Investigating the Effect of Ni Loading on the Performance of Yttria-Stabilised Zirconia Supported Ni Catalyst during CO2 Methanation. 2023;2:86-102.
[54] Cho JM, Ahn CI, Pang C, Bae JW. Fischer–Tropsch synthesis on Co/AlSBA-15: effects of hydrophilicity of supports on cobalt dispersion and product distributions. Catalysis Science & Technology. 2015;5:3525-35.
[55] Sekkal KNEH, Ouargli-Saker R, Lachachi AK, Zekkari M, Beltrao-Nunes A-P, Michelin L, et al. Effect of copper dispersion on SBA-15 and SBA-16 affinity towards carbon dioxide—an approach through thermal programmed desorption. Journal of Nanoparticle Research. 2021;23:154.
[56] Das S, Sengupta M, Patel J, Bordoloi A. A study of the synergy between support surface properties and catalyst deactivation for CO2 reforming over supported Ni nanoparticles. Applied Catalysis A: General. 2017;545:113-26.
[57] Hadjiivanov K. Chapter Two - Identification and Characterization of Surface Hydroxyl Groups by Infrared Spectroscopy. In: Jentoft FC, editor. Advances in Catalysis: Academic Press; 2014. p. 99-318.
[58] Wang Y, Huang B, Xu J, Li N, Qu Z. Hydroxyl Groups Promoted Ag Dispersion and Excellent Performance of Ag/Al2O3 Catalyst for HCHO Oxidation. Catalysis Letters. 2021;151:2376-83.
[59] Fan Y, Wang F, Li R, Liu C, Fu Q. Surface Hydroxyl-Determined Migration and Anchoring of Silver on Alumina in Oxidative Redispersion. ACS Catalysis. 2023;13:2277-85.
[60] Gao J, Wang Y, Ping Y, Hu D, Xu G, Gu F, et al. A thermodynamic analysis of methanation reactions of carbon oxides for the production of synthetic natural gas. RSC Advances. 2012;2:2358-68.
[61] Lee SM, Lee YH, Moon DH, Ahn JY, Nguyen DD, Chang SW, et al. Reaction Mechanism and Catalytic Impact of Ni/CeO2–x Catalyst for Low-Temperature CO2 Methanation. Industrial & Engineering Chemistry Research. 2019;58:8656-62.
[62] Miao B, Ma SSK, Wang X, Su H, Chan SH. Catalysis mechanisms of CO2 and CO methanation. Catalysis Science and Technology. 2016;6:4048-58.
[63] Ren J, Guo H, Yang J, Qin Z, Lin J, Li Z. Insights into the mechanisms of CO 2 methanation on Ni(111) surfaces by density functional theory. Applied Surface Science. 2015;351:504-16.
[64] Wu HC, Chang YC, Wu JH, Lin JH, Lin IK, Chen CS. Methanation of CO2 and reverse water gas shift reactions on Ni/SiO2 catalysts: the influence of particle size on selectivity and reaction pathway. Catalysis Science and Technology. 2015;5:4154-63.
[65] Schmider D, Maier L, Deutschmann O. Reaction Kinetics of CO and CO2Methanation over Nickel. Industrial and Engineering Chemistry Research. 2021;60:5792-805.

[66] Huang J, Li X, Wang X, Fang X, Wang H, Xu X. New insights into CO2 methanation mechanisms on Ni/MgO catalysts by DFT calculations: Elucidating Ni and MgO roles and support effects. Journal of CO2 Utilization. 2019;33:55-63.

[67] Westermann A, Azambre B, Bacariza MC, Graça I, Ribeiro MF, Lopes JM, et al. Insight into CO2 methanation mechanism over NiUSY zeolites: An operando IR study. Applied Catalysis B: Environmental. 2015;174-175:120-5.

[68] Gao J, Jia C, Zhang M, Gu F, Xu G, Su F. Effect of nickel nanoparticle size in Ni/α-Al2O 3 on CO methanation reaction for the production of synthetic natural gas. Catalysis Science and Technology. 2013;3:2009-15.

[69] Varvoutis G, Lykaki M, Stefa S, Binas V, Marnellos GE, Konsolakis M. Deciphering the role of Ni particle size and nickel-ceria interfacial perimeter in the low-temperature CO2 methanation reaction over remarkably active Ni/CeO2 nanorods. Applied Catalysis B: Environmental. 2021;297:120401.

[70] Xu L, Wen X, Chen M, Lv C, Cui Y, Wu X, et al. Highly dispersed Ni-La catalysts over mesoporous nanosponge MFI zeolite for low-temperature CO2 methanation: Synergistic effect between mesoporous and microporous channels. Journal of Industrial and Engineering Chemistry. 2021;100:159-73.

[71] Pan Q, Peng J, Sun T, Wang S, Wang S. Insight into the reaction route of CO2 methanation: Promotion effect of medium basic sites. Catalysis Communications. 2014;45:74-8.

[72] Sachse A, Hulea V, Finiels A, Coq B, Fajula F, Galarneau A. Alumina-grafted macro-/mesoporous silica monoliths as continuous flow microreactors for the Diels–Alder reaction. Journal of Catalysis. 2012;287:62-7.

[73] Karelovic A, Ruiz P. Improving the hydrogenation function of Pd/γ-Al2O 3 catalyst by Rh/γ-Al2O3 Addition in CO2 methanation at low temperature. ACS Catalysis. 2013;3:2799-812.

[74] Kwak JH, Kovarik L, Szanyi J. Heterogeneous catalysis on atomically dispersed supported metals: CO 2 reduction on multifunctional Pd catalysts. ACS Catalysis. 2013;3:2094-100.

[75] Cerdá-Moreno C, Chica A, Keller S, Rautenberg C, Bentrup U. Ni-sepiolite and Ni-todorokite as efficient CO2 methanation catalysts: Mechanistic insight by operando DRIFTS. Applied Catalysis B: Environmental. 2020;264:118546-.

[76] Goodarzi F, Kang L, Wang FR, Joensen F, Kegnæs S, Mielby J. Methanation of Carbon Dioxide over Zeolite-Encapsulated Nickel Nanoparticles. ChemCatChem. 2018;10:1566-70.

[77] Graça I, González LV, Bacariza MC, Fernandes A, Henriques C, Lopes JM, et al. CO2 hydrogenation into CH4 on NiHNaUSY zeolites. Applied Catalysis B: Environmental. 2014;147:101-10.

[78] Quindimil A, De-La-Torre U, Pereda-Ayo B, González-Marcos JA, González-Velasco JR. Ni catalysts with La as promoter supported over Y- and BETA- zeolites for CO2 methanation. Applied Catalysis B: Environmental. 2018;238:393-403.

Chapter 5

Oxide-based catalysts

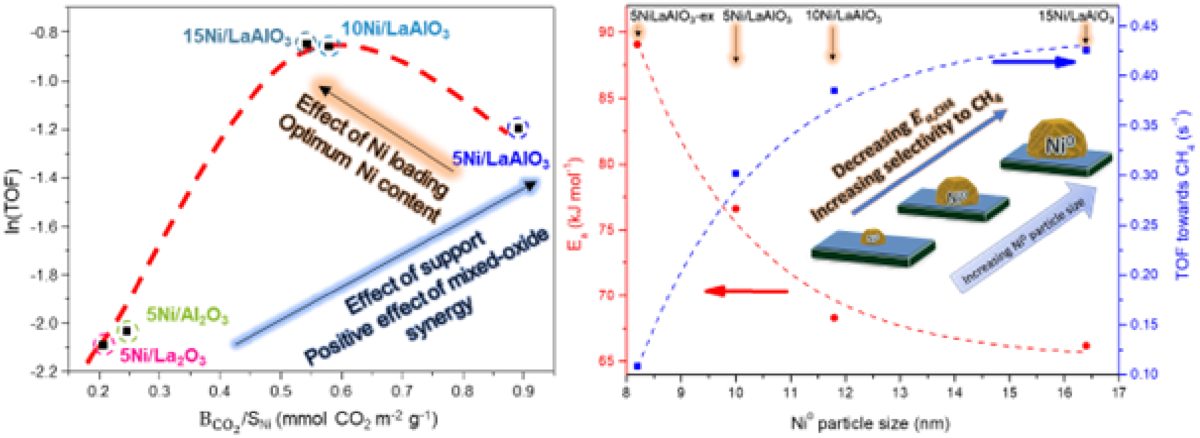

This chapter was adapted from the following manuscript:

Machado-Silva, R. B.; Andrés-Olmos, L.; Kosinov, N.; Hensen, E. J. M.; Chica, A.; Exploring mixed-oxide synergy in La and Al oxides as supports in Ni-catalysts for the CO$_2$ methanation reaction. (Under review).

5.1 – Introduction

Metal oxides are crystalline solids composed of oxide anions and one or more metallic cations. When a single metallic element is involved, the compound is termed a binary oxide; if multiple metallic elements are present, it is known as a mixed oxide [1, 2].

Most oxides are naturally occurring, where they are typically found as hydrated oxides, oxyhydroxides, hydroxides, or directly as oxides. [3]. Metal oxides (MO's) represent a compelling family of compounds with diverse properties, spanning various domains of materials science, engineering, chemistry and physics. Whether in bulk form, films, or as in different nanomorphologies, MO's exhibit a wide range of functional properties that make them ideal for numerous technological applications, including optoelectronic systems, passive-optical elements, catalytic processes, photovoltaic cells, environmental restoration, and gas monitoring [4-7].

Oxides are characterized by their surfaces terminating in lattice O^{2-} anions, which are frequently accompanied by various surface features and defects, including steps, terraces, and kinks. Since oxide-supported reactions are typically structure-sensitive, these structural irregularities are important for catalysis and contribute to metal oxides' sensitivity to some catalytic reactions [8, 9]. These structural imperfections affect the structure sensitivity of metal oxides in particular catalytic reactions, which has a substantial impact on catalysis. Unsaturation from surface flaws is often countered by the protonation of terminal oxide groups, which results in the formation of surface hydroxyls. For many catalytic processes involving oxide-based catalysts, these hydroxyl groups' dual functionality as proton donors and acceptors is essential.

Additionally, surface hydroxyls can influence the strength of adsorption, the rate of desorption, and the total catalytic activity by interacting with adsorbed reactants, intermediates, or products [8-10]. They can keep transition states stable during catalytic reactions. These groups can decrease the activation energy and speed up reaction rates by enhancing hydrogen bonding or proton transfer.

Metal oxide catalysts play a pivotal role in numerous catalytic processes, particularly in refining, petrochemical industries, and the synthesis of specialty chemicals. Recently, they have gained prominence in environmental applications, such as pollution control and achieving high selectivity in reactions to minimize unwanted by-products. The importance of metal oxide catalysts emerged significantly in the mid-1950s, when their effectiveness in catalyzing a broad spectrum of oxidation and acid-base reactions became widely recognized [11].

Metal oxides are primarily categorized into acidic, basic, and amphoteric oxides. Since the advent of solid oxide-based catalysts, each specific type of oxide has been employed according to the reaction mechanism of the chemical processes involved. Solid acid and base catalysts have seen significant development, particularly in the refining and petrochemical industries. These solid catalysts are increasingly replacing corrosive aqueous liquid catalysts, such as inorganic acids, as well as sodium and potassium hydroxides, which offers the advantage of reducing environmental impact.

Due to the mechanism of the CO_2 methanation reaction, it is widely recognized that the basic sites are important for the mechanism pathway, as they are involved in the capture and ulterior activation of the CO_2 molecules and their eventual hydrogenation [12].

As a result, when developing catalysts for this reaction, different basic oxides have been considered as both supports and promoters. The whole properties of the catalyst are influenced by the morphology, dispersion, and reducibility of the metal phase, all of which are influenced by the type of catalyst support. To improve the activity and long-term stability of Ni-based catalysts, various supports, such as Al_2O_3, SiO_2, TiO_2, ZrO_2, and CeO_2, have been studied [13]. Understanding the bonding and reactivity of chemisorbed species, as well as the interactions between nickel and the support, has also received a great deal of attention [14].

Since Al_2O_3-based supports have highly adjustable properties and advanced structural characteristics, they are commonly used in Ni-based methanation catalysts. Ni atom dispersion and anti-sintering stability can be improved by controlling the textural properties, porous structure, and surface basicity of Al_2O_3 supports by optimizing synthesis techniques [15]. For instance, γ-Al_2O_3 surfaces can anchor metallic atoms through strong interactions, ensuring that the metallic phase remains structurally stable and catalytically active during heterogeneous catalytic reactions [16].

In the literature, Al_2O_3-based catalysts commonly feature Ni as the primary metal [15-21], although other studies have explored the use of Ru [22-25], Rh [26, 27], and Pd [28].

The capacity of Al_2O_3 to adsorb CO_2 molecules on its surface, which can then interact with hydrogen species on the metallic phase, is primarily responsible for its efficacy as a support for this reaction. A study by Ewald et al. combined CO_2-TPD and DRIFTS techniques, concluding that carbonate species with varying degrees of coordination form on the surface of Al_2O_3 (**Figure 5.1**). Bicarbonate species are formed on sites with lower basicity, while monodentate and bidentate carbonates are formed on sites with intermediate basicity [29].

Another oxide considered for catalysts in the CO_2 methanation reaction is lanthanum (III) oxide (La_2O_3). This oxide is commonly used in Ni catalysts as an electronic modifier due to its capability to enhance the dispersion of the Ni phase and increase the system's basicity. However, it has also been explored as a support material in some studies [30].

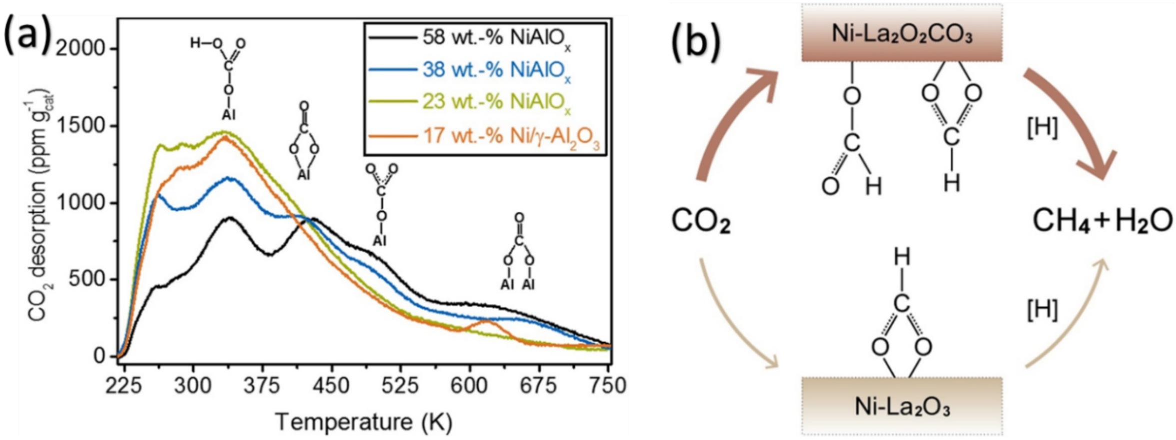

Figure 5.1. (a) CO_2-TPD diagram for a series of Ni-Al_2O_3 catalysts and corresponding coordination modes of surface carbonate species. Image adapted from Ewald [29]. (b) Intermediate formate species formed in the Ni-La_2O_3 and Ni-$La_2O_2CO_3$ catalysts during CO_2 hydrogenation. Image adapted from [31].

Dai et al., utilizing La_2O_3 and $La_2O_2CO_3$ as supports, compared Ni catalysts for the CO_2 methanation reaction [31]. Their thorough analysis validated the robustness of Ni-oxycarbonate catalysts for the CO_2 methanation reaction at high-temperature reductive conditions. It was discovered that a significant factor in the effective chemisorption and activation of CO_2 was the moderately basic sites on $La_2O_2CO_3$ surfaces.

Monodentate and bidentate formates were found to be the primary reaction intermediate species through analysis of DRIFT spectra. These species were further characterized as being highly active and resistant to CO poisoning during their conversion into CH_4.

This way, while Al_2O_3 and La_2O_3 have already been widely investigated as supports for CO_2 methanation catalysts, the mixed oxide $LaAlO_3$ has not yet been thoroughly investigated as a support for catalyst development in this reaction.

Lanthanum aluminate ($LaAlO_3$) is a mixed metal oxide ceramic compound that belongs to the perovskite-type oxide family with a unique combination of physical and chemical properties [32].

The perovskite-type structure is characteristic of many mixed oxides with the general chemical formula ABO_3, with 'A' and 'B' being two cations with distinct ionic radii. The 'A' cations are larger, typically ranging between 1.0 and 1.9 Å, while the 'B' cations are smaller, ranging between 0.5 and 1.2 Å. In the case of $LaAlO_3$, the ionic radii are r_A (La^{3+}) = 1.5 Å, r_B(Al^{3+}) = 0.675 Å, and r_O(O) = 1.26 Å [33].

With these cation sizes, the ideal structure with cubic symmetry has the La^{III} cation in a 12-fold cuboctahedral coordination and the Al^{III} cation in a 6-fold coordination (**Figure 5.2**).

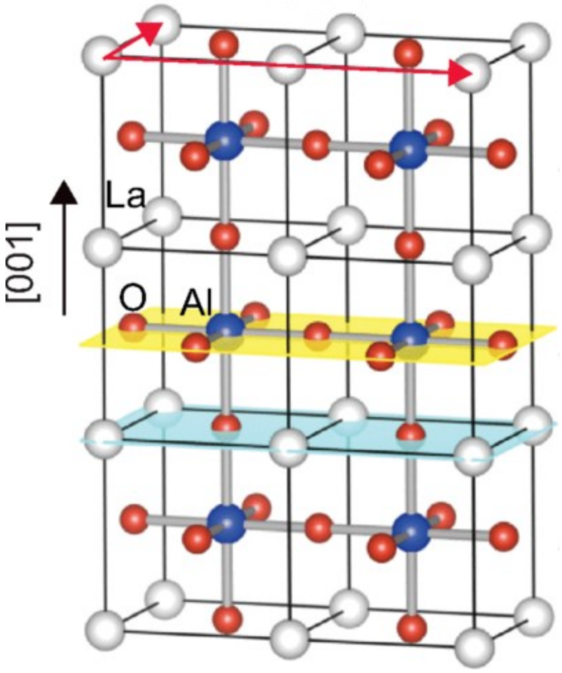

Figure 5.2. Structure of lanthanum aluminate, $LaAlO_3$, highlighting the 6-fold coordination around Al^{III} ions and 12-fold coordination around La^{III} ions. Image adapted from Krishnaswamy [34].

Strict requirements for relative ion size determine how stable this cubic structure is; even a small amount of buckling or distortion can result in lower-symmetry variants where the coordination numbers of the La^{III} or Al^{III} cations, or both, are lowered [34].

With these characteristics, the perovskite-type oxides, including $LaAlO_3$, have attracted significant interest due to their stable structure. The high lattice symmetry and short atomic distances confer unique physical properties, making them a subject of extensive research.

Among these properties, some of remarkable interest are high-temperature stability, robust mechanical properties, high ionic conductivity, and capability to stabilize metal nanoparticles. For this reason, $LaAlO_3$ has been widely investigated for applications in many fields, such as solid oxide fuel cells, catalysis, gas separation, and electronic devices [35-39]. Specifically in the catalysis field, it has found application for the development of catalysts for methane oxidative coupling [29], hydrocarbon steam reforming [40], NO reduction [41], CO-PROX [42], and soot oxidation [43].

As reported in previous results in the literature, mixed metal oxides can exhibit "*mixed-metal synergy*" due to the unique properties and interactions between the different metal oxides, resulting in a material that exhibits superior performance compared to its components.

Coleman et al., for example, studied catalysts for ethanol steam reforming and reported that a mixed metal oxide of Mg and Al exhibited superior catalytic activity compared to the individual oxides [44]. Liu et al. reported that a mixed oxide $La_{2-x}Sr_xCuO_{4\pm\lambda}$ also showed superior activity in comparison with the individual component oxides for phenol hydroxylation, with the catalytic performance dependent on the lanthanum content of the support [45].

There are also reports of the mixed-metal synergy and the use of mixed-metal oxide supports for different catalytic applications, such as N_2O decomposition [46], acetic acid steam reforming [47], and CH_4 dry reforming [48] reactions.

Therefore, taking into account this context and as no study has been published in the literature regarding the mixed-metal synergy effect of $LaAlO_3$ on the CO_2 methanation reaction and its use as support in Ni-based catalysts for biogas upgrade, this study was conceived. First, catalysts based on $LaAlO_3$ were compared to Al_2O_3 and La_2O_3 and exhibited a mixed-metal synergy effect, exhibiting higher X_{CO_2} and S_{CH_4}values, and, then, after the best support was identified, Ni loading was optimized. In the second phase, which will be described in Chapter 7, the catalyst with optimum Ni loading was tested for application for biogas upgrade.

These materials were assessed through a multi-technique analysis using XRD, N_2-adsorption, ICP, TEM, H_2-chemisorption, H_2-TPR, CO_2-TPD-MS, and operando FT-IR. This way, it was possible to provide a cross-sectional analysis of how available Ni^0 surface area, Ni^0 particle size, and concentration of moderate basic sites are mutually involved in the reaction mechanism.

The exact mechanism of this reaction remains a subject of debate, as the precise pathway is not universally accepted [49], and experimental studies have resulted in differing hypotheses regarding the specific pathway, including results from our research group [50-53]. Despite the uncertainty regarding the topic, it is suggested that intermediate strength basic sites engage in the CO_2 chemisorption step and eventual formation of intermediate species, even though more fundamental research is necessary to identify the role of these sites thoroughly [54].

To contribute to this ongoing discussion, novel time-resolved operando FT-IR analyses with a custom-made cell were carried out to identify participating intermediate species following the methodology followed in previous publications [55, 56], such as Ni^0-CO, bicarbonate, and carbonates. Coupled with the results obtained by kinetic studies and CO_2-TPD-MS, it was possible to formulate a series of hypotheses on how the basic sites participate in the mechanism for this class of catalysts.

More information was provided in Chapter 3 about the preparation of the catalysts used in this chapter, but their description is summarized in **Table 5.1**. The notation "_R" after the catalyst name indicates it was previously reduced, and the notation **"ex"** indicates that the active phase of the catalyst was prepared by ex-solution.

Table 5.1. Denomination employed in this chapter for the oxide-based catalysts. All Ni loading refers to nominal values established during their preparation.

5Ni/Al_2O_3	5% wt. Ni catalyst prepared commercial α-Al_2O_3
5Ni/La_2O_3	5% wt. Ni catalyst prepared commercial La_2O_3
5Ni/$LaAlO_3$	5% wt. Ni catalyst prepared over $LaAlO_3$
5Ni/$LaAlO_3$-ex	5% wt. Ni catalyst prepared by exsolution
10Ni/$LaAlO_3$	10% wt. Ni catalyst prepared over $LaAlO_3$
15Ni/$LaAlO_3$	15% wt. Ni catalyst prepared over $LaAlO_3$

5.2 – Characterization results

To evaluate the effect of the mixed oxide synergy, three different supports were initially assessed, La_2O_3, Al_2O_3, and $LaAlO_3$, and the corresponding 5 wt.% Ni catalysts prepared by IWI were analyzed by XRD (**Figure 5.3** and **Figure 5.4)** The La_2O_3 materials exhibit the typical diffraction peaks (JCPDS 05-0602), and also peaks associated with a $La(OH)_3$ phase (JCPDS 036-1481), which is typical for La_2O_3-based materials due to their hydrophilicity [57].

Regarding the Al_2O_3-based materials, the typical peaks for crystalline α-Al_2O_3 are identified (JCPDS 036-1481). For the $LaAlO_3$, which was synthesized by the Pechini method, it presented high crystallinity with the characteristic peaks at 2θ = 23.45° (012), 33.38° (110), 41.19° (202), 47.96° (024), 54.02° (116), 59.79° (018) and 70.23 (208). (JCPDS 31-0022). Furthermore, no peaks belonging to La_2O_3 or Al_2O_3 were identified, indicating that under the employed synthetic conditions, La^{III} and Al^{III} ions formed the perovskite structure, which was also confirmed by the ICP results (**Table 5.2**).

Concerning the synthesis of the Ni-based catalysts by impregnation, TG-DTA results (**see Chapter 9 - Supplementary Information**) confirmed that the decomposition of the Ni precursor, $Ni(NO_3)_2$, to nickel oxide, NiO, takes place below the calcination temperature (450 °C) [58].

ICP results (**Table 5.2**) revealed that the actual Ni weight content in the catalysts is close to the nominal content set during the synthesis, indicating that the metal incorporation was successful.

SEM-TEM images (**Figure 5.5**, **Figure 5.6**, and **Figure 5.7**) reveal that the $LaAlO_3$ nanoparticles exhibit a cylindrical rod-like morphology, with longitudinal length in the 100-500 nm range, as previously described in a work that employed the same synthetic conditions [59].

Table 5.2. Elemental weight percentage for lanthanum aluminate samples, as determined by ICP-OES, and La/Al molar ratio.

Sample	La(%)	Al (%)	Ni (%)	La/Al molar ratio
La_2O_3	84.0	-	-	-
5Ni/La_2O_3	78.5	-	5.4	-
Al_2O_3	-	50.8	-	-
5Ni/Al_2O_3	-	47.5	5.6	-
$LaAlO_3$	64.7	12.7	n/a	0.987
5Ni/$LaAlO_3$	59.4	11.7	5.4	0.983
10Ni/$LaAlO_3$	57.1	11.0	10.8	1.007
15Ni/$LaAlO_3$	53.5	10.5	15.5	0.988
5Ni$LaAlO_3$-ex	63.9	12.2	4.9	1.018

In the Ni-based supported on $LaAlO_3$, the DRX results (**Figure 5.8** and **Figure 5.9**) reveal that the NiO phase (2θ = 37.40° and 43.46°) (JCPDS:47-1049) is formed on the surface of the $LaAlO_3$ phase is corroborated by the TEM-EDS microscopy images (**Figure 5.7**). The higher the Ni loading in the impregnated samples, the higher the intensity of the peaks at 2θ = 37.40° and 43.46°.

After the reductive treatment under H_2, NiO phase peaks disappear, giving rise to metallic Ni^0 peaks (JCPDS: 01-045-1027) (**Figure 5.9** and **Figure 5.10**). The higher the Ni loading in the impregnated, the higher the Ni^0 average particle size, as seen by the distribution obtained from the TEM images, as expected (**Figure 5.11**).

For the sample where Ni was added into the aluminate phase by coprecipitation to prepare a Ni^0 active phase by ex-solution, **5Ni$LaAlO_3$-ex**, no NiO phase was detected (**Figure 5.8**). Instead, the typical peaks for the $LaAlO_3$ were slightly shifted to lower 2θ values. This is because, in this Ni-doped $LaAlO_3$ crystal, Ni is found with the oxidation state of 3+ and occupies the lattice position an Al^{III} ion would occupy, as previously described by Gibert [60]. As the Ni^{III} ion (60 pm) is faintly larger than the Al^{III} ion (50 pm), it leads to a crystal lattice expansion confirmed by the shift in the diffraction Bragg angle values.

As for 5Ni$LaAlO_3$-ex_R, smaller Ni^0 crystallite sizes are formed than in its counterpart prepared by impregnation, as confirmed by TEM images, which is attributed to the formation of the Ni^0 phase, coming out of the lattice very well dispersed, as previously discussed by Oliveira, and it will further be confirmed by the H_2-TPR results, which will be addressed in the sequence [61]. The formation of the Ni^0 phase after reduction is confirmed by TEM images when 5Ni$LaAlO_3$-ex is compared to 5Ni$LaAlO_3$ex_R (**Figure 5.5**).

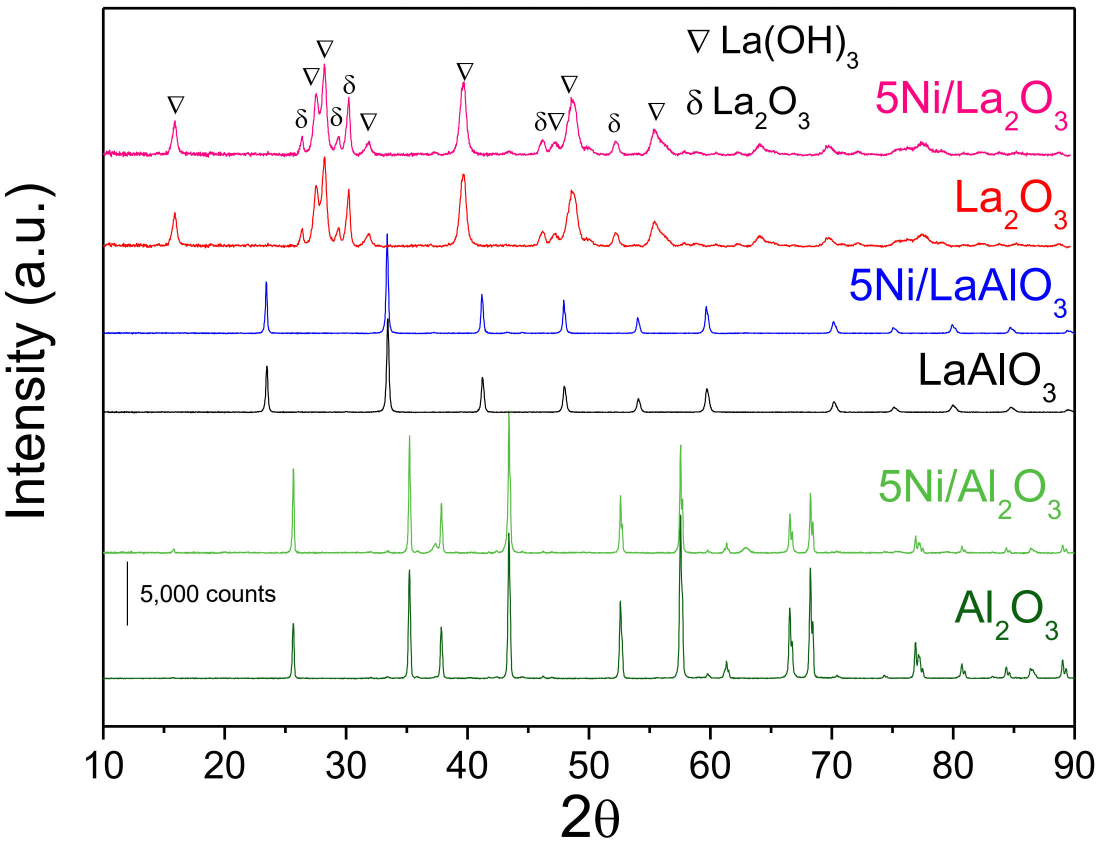

Figure 5.3. XRD diffractograms of the different supports and equivalent 5% wt. Ni-based catalysts.

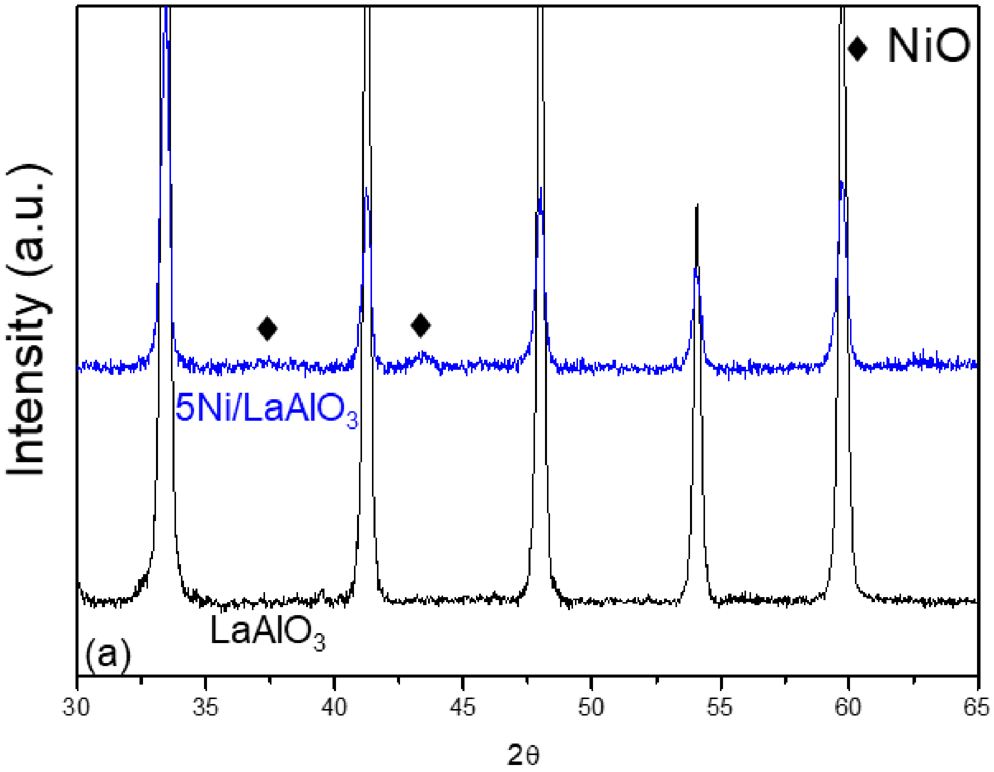
◆ NiO
5Ni/LaAlO3
LaAlO3
(a)
Intensity (a.u.)
30
35
40
45
50
55
60
65
2θ

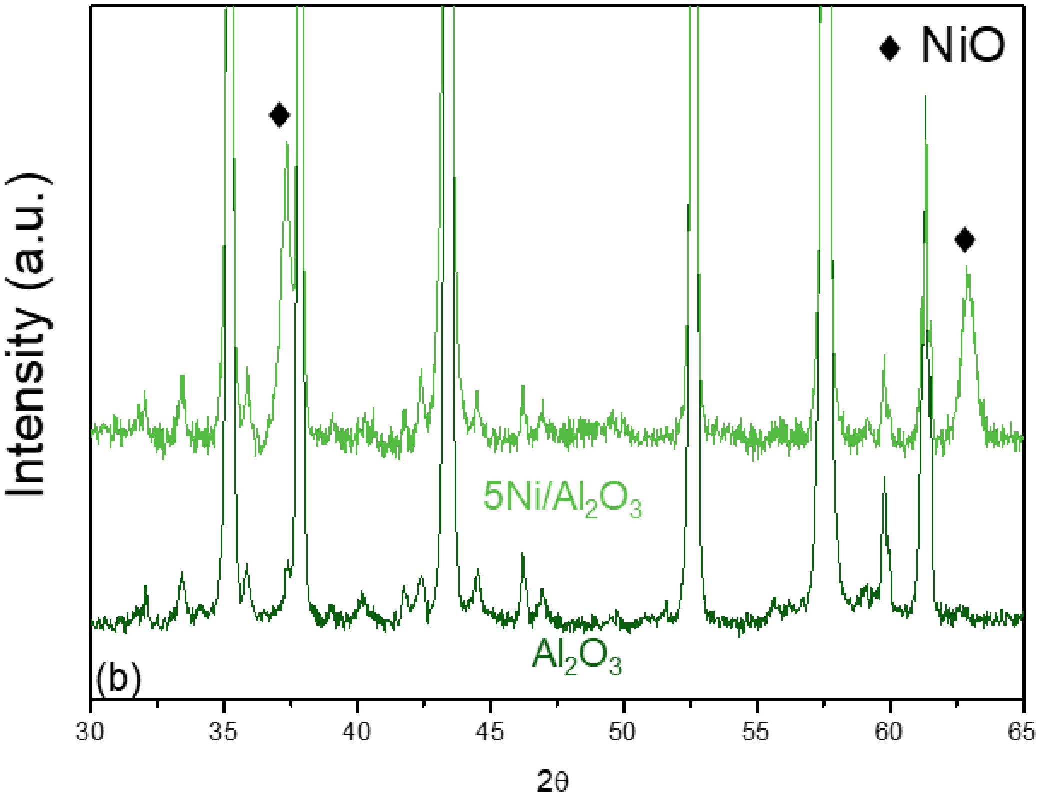
◆ NiO
5Ni/Al2O3
Al2O3
(b)
Intensity (a.u.)
30
35
40
45
50
55
60
65
2θ

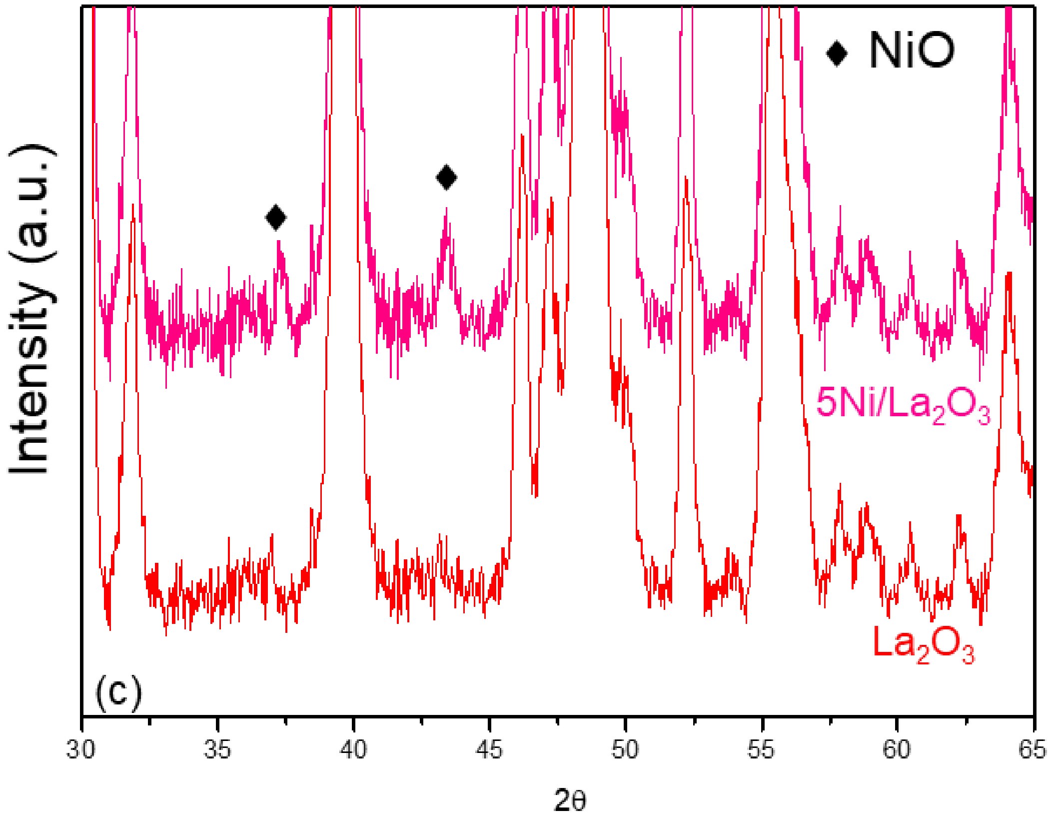

Figure 5.4. Magnification of specific ranges to highlight the presence of the peaks (♦) associated with the presence of NiO at 2θ = 37.40° and 43.46°.

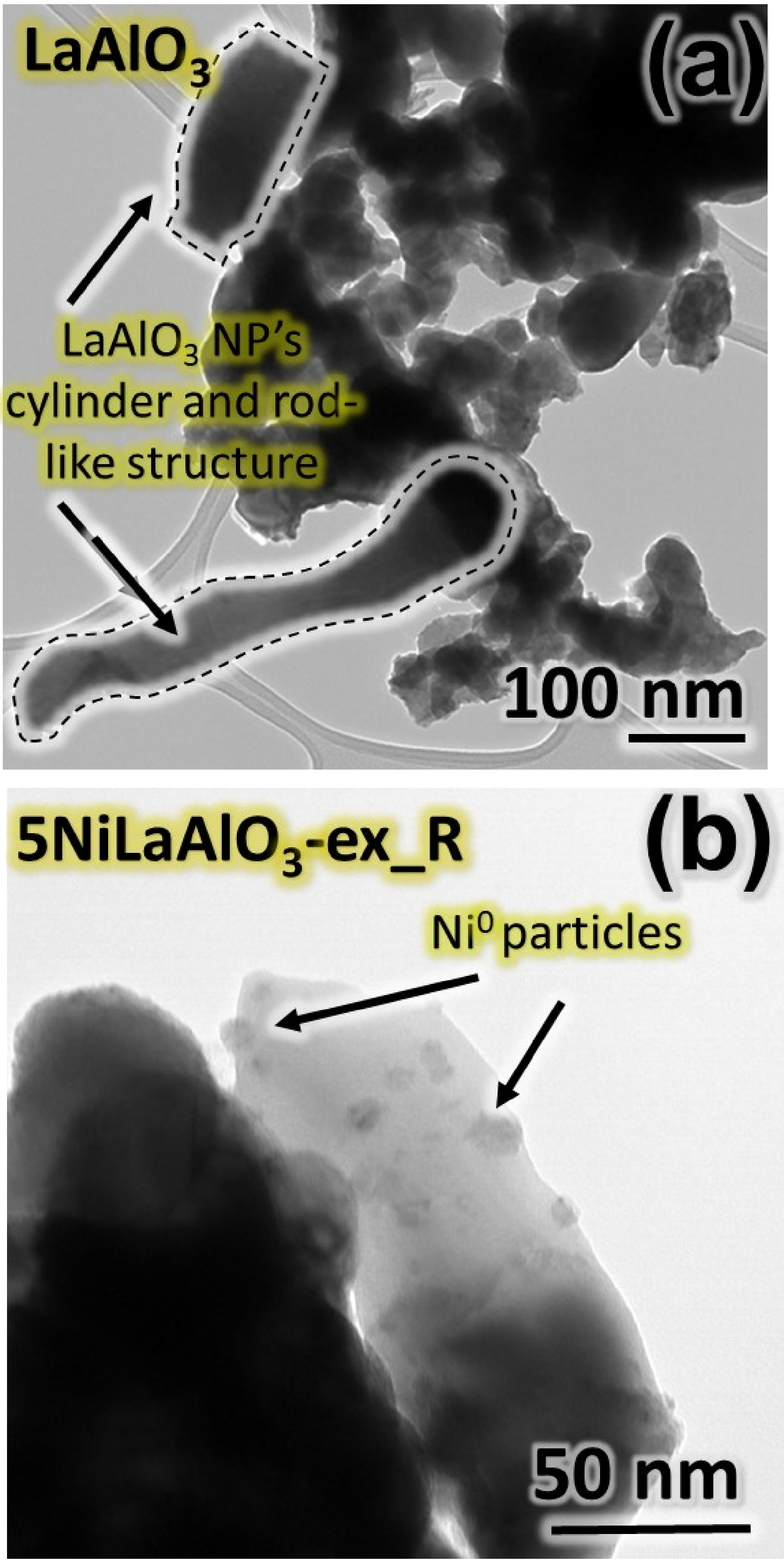
LaAlO3
(a)
LaAlO3 NP's cylinder and rod-like structure
100 nm
5NiLaAlO3-ex_R
(b)
Ni0 particles
50 nm

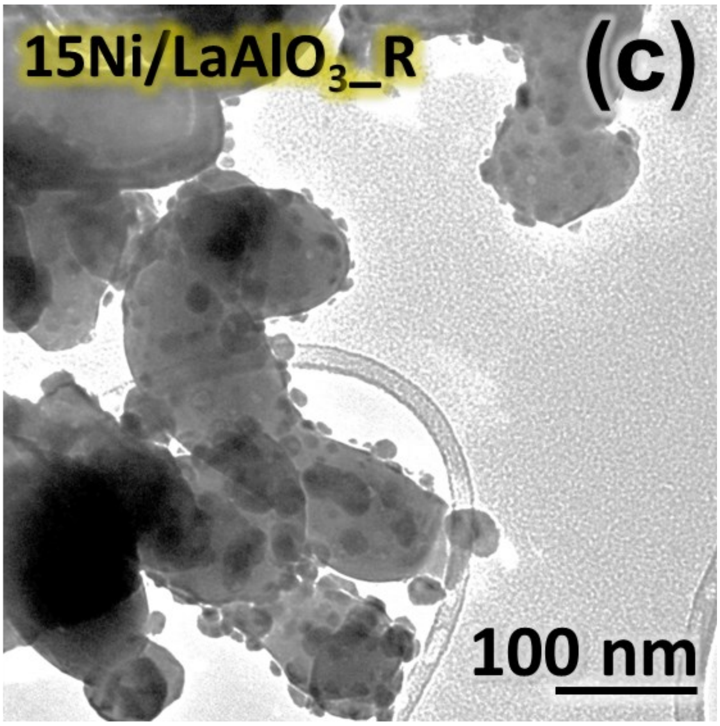

Figure 5.5. TEM images of: (a) $LaAlO_3$; (b) 5Ni/$LaAlO_3$_R; (c) 5Ni/$LaAlO_3$-ex_R; (d) 15Ni/$LaAlO_3$_R.

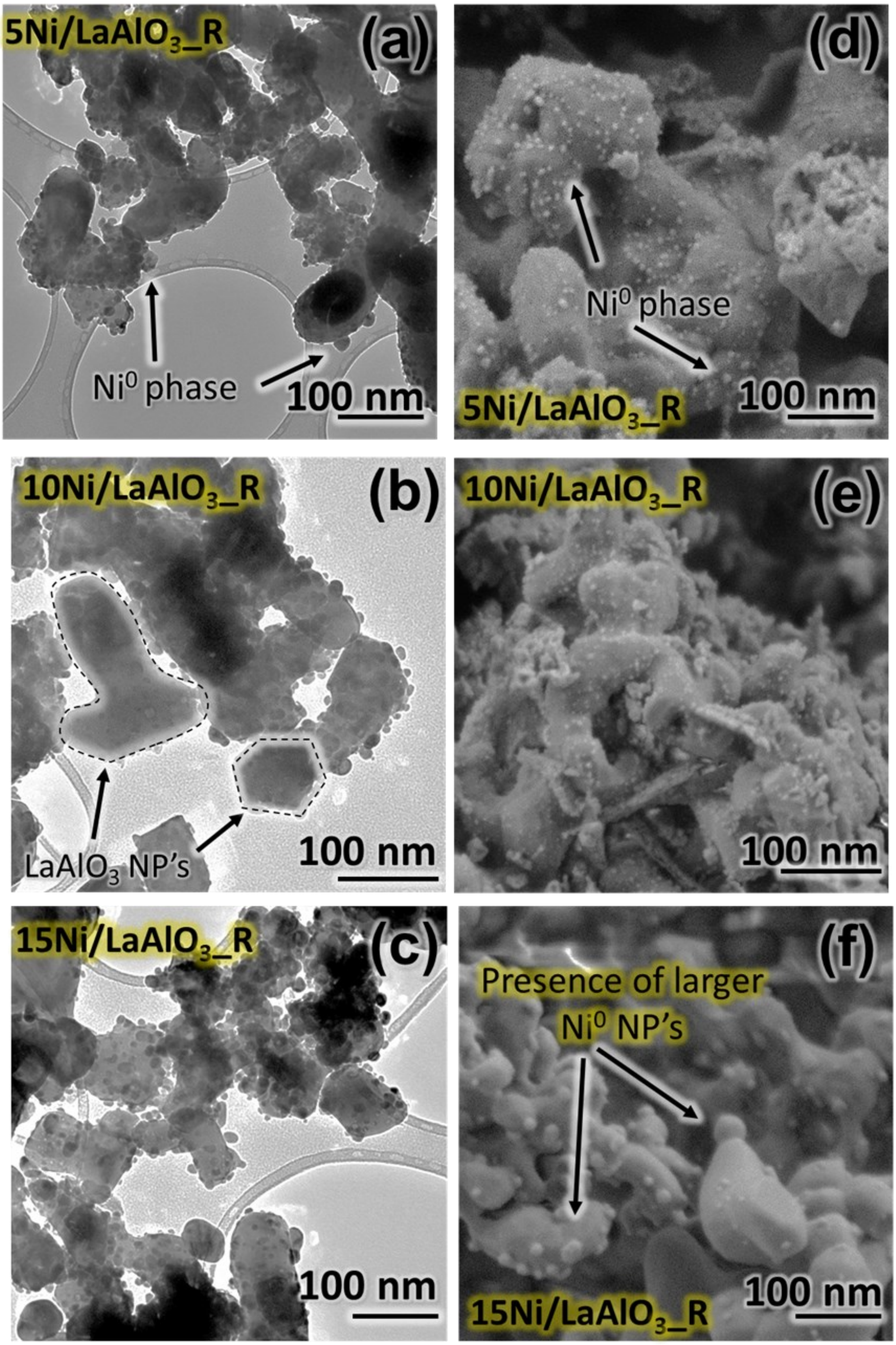

Figure 5.6. TEM/SEM images of the reduced catalysts with different Ni loading: 5Ni/$LaAlO_3$_R (a-TEM e-SEM), 10Ni/$LaAlO_3$_R (b-TEM e-SEM), and 15Ni/$LaAlO_3$_R (c-TEM f-SEM).

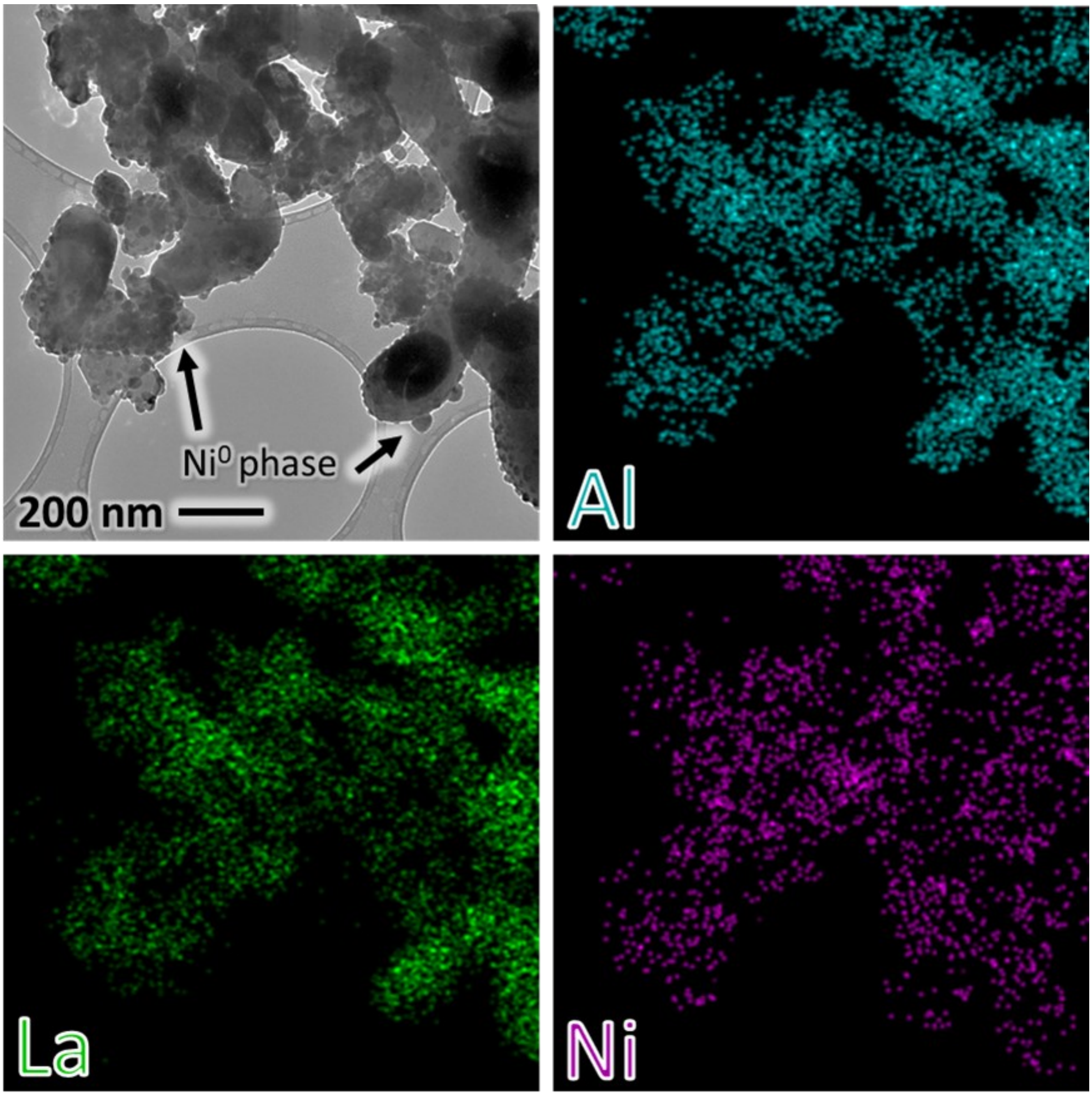

Figure 5.7. EDS-TEM results for the 15Ni/LaAlO$_3$_R and the response obtained for different elements: Al (cerulean); La (green), and Ni (purple).

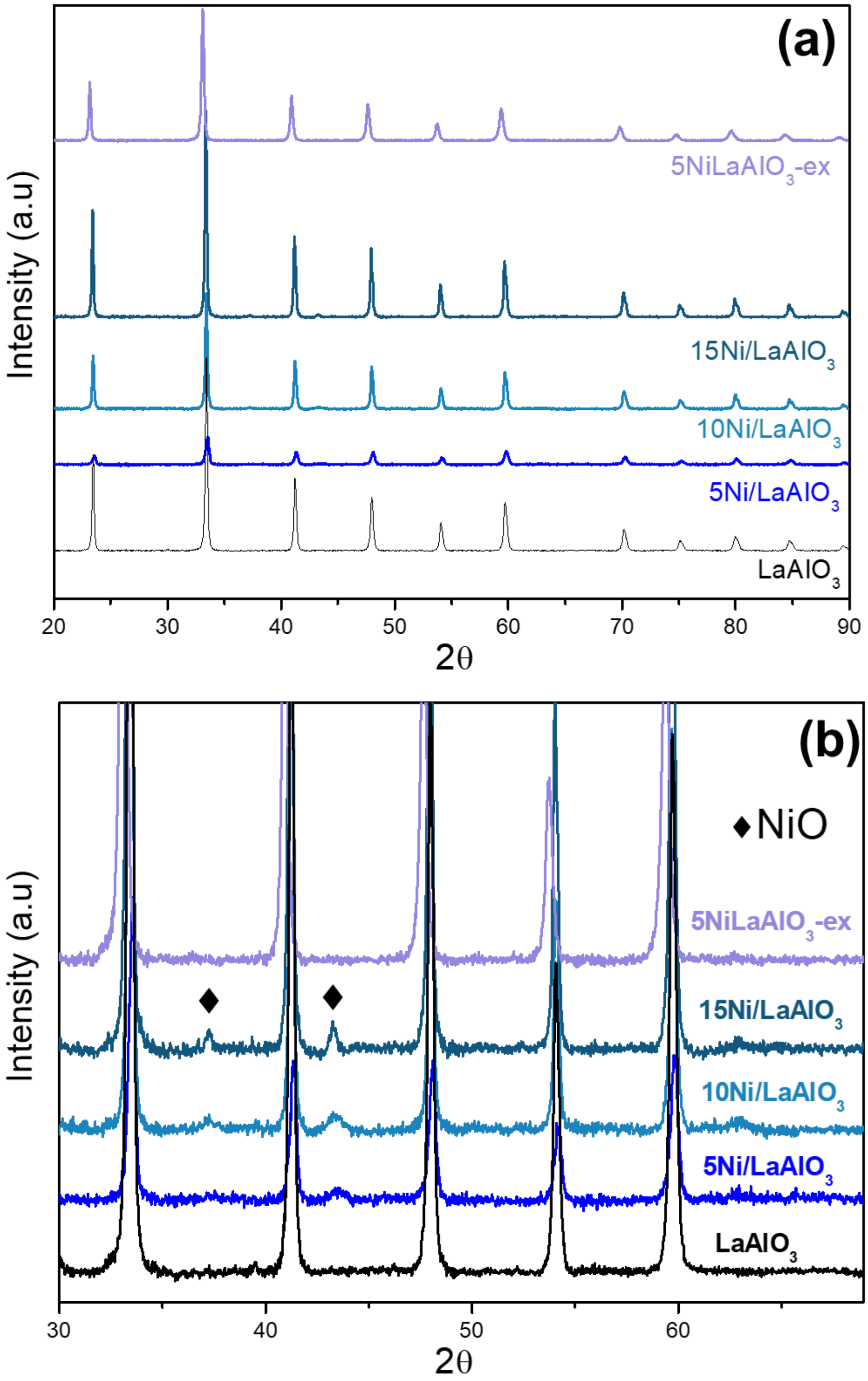

Figure 5.8. (a) XRD diffractograms of the calcined LaAlO$_3$-based catalysts prepared by different methods and metallic content. (b) Magnification of the region between 2θ = 30° and 70° to highlight diffraction peaks related to the presence of the NiO phase.

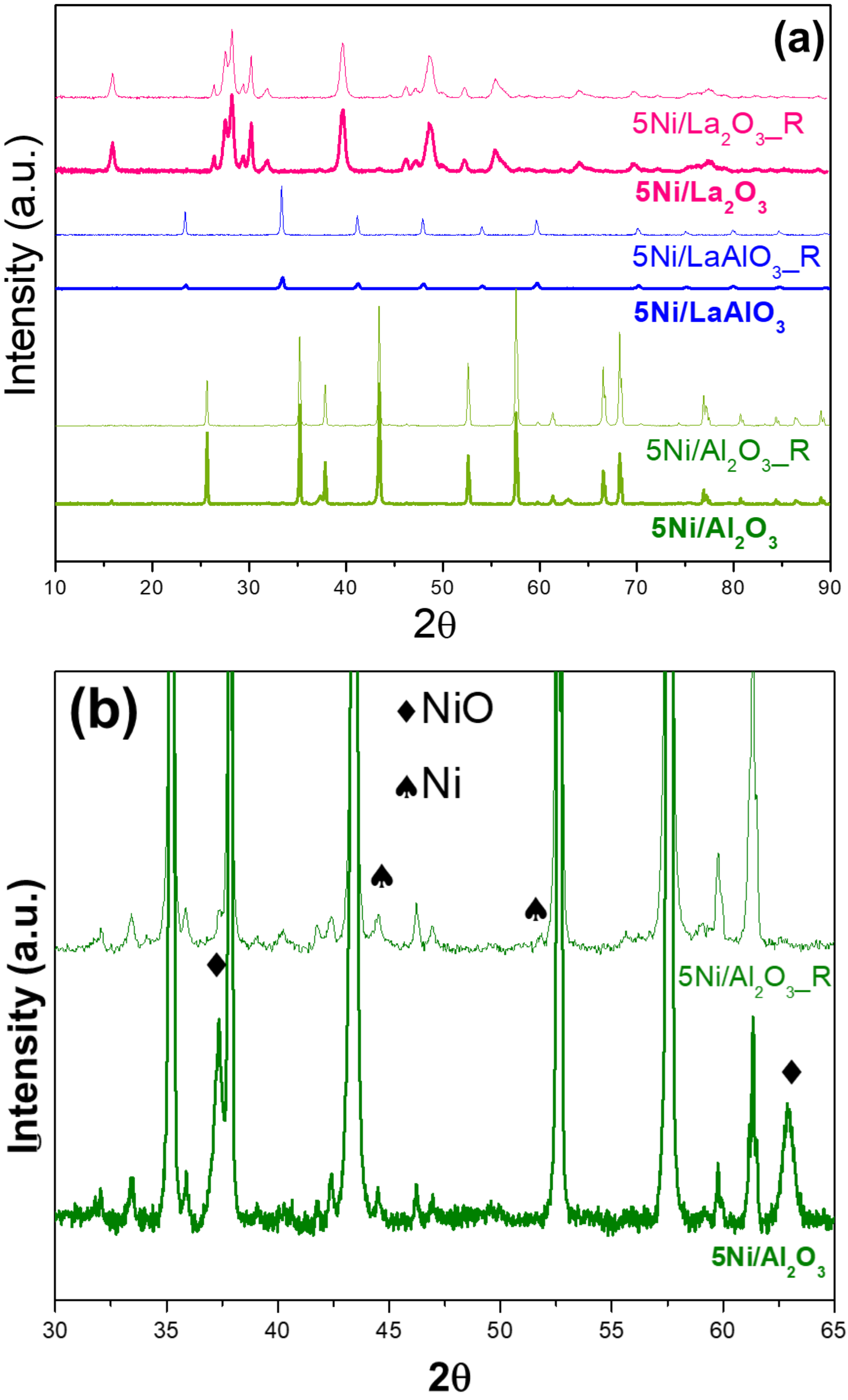
(a)
Intensity (a.u.)
5Ni/La$_2$O$_3$_R
5Ni/La$_2$O$_3$
5Ni/LaAlO$_3$_R
5Ni/LaAlO$_3$
5Ni/Al$_2$O$_3$_R
5Ni/Al$_2$O$_3$
10
20
30
40
50
60
70
80
90
2θ
(b)
◆NiO
♠Ni
Intensity (a.u.)
5Ni/Al$_2$O$_3$_R
5Ni/Al$_2$O$_3$
30
35
40
45
50
55
60
65
2θ

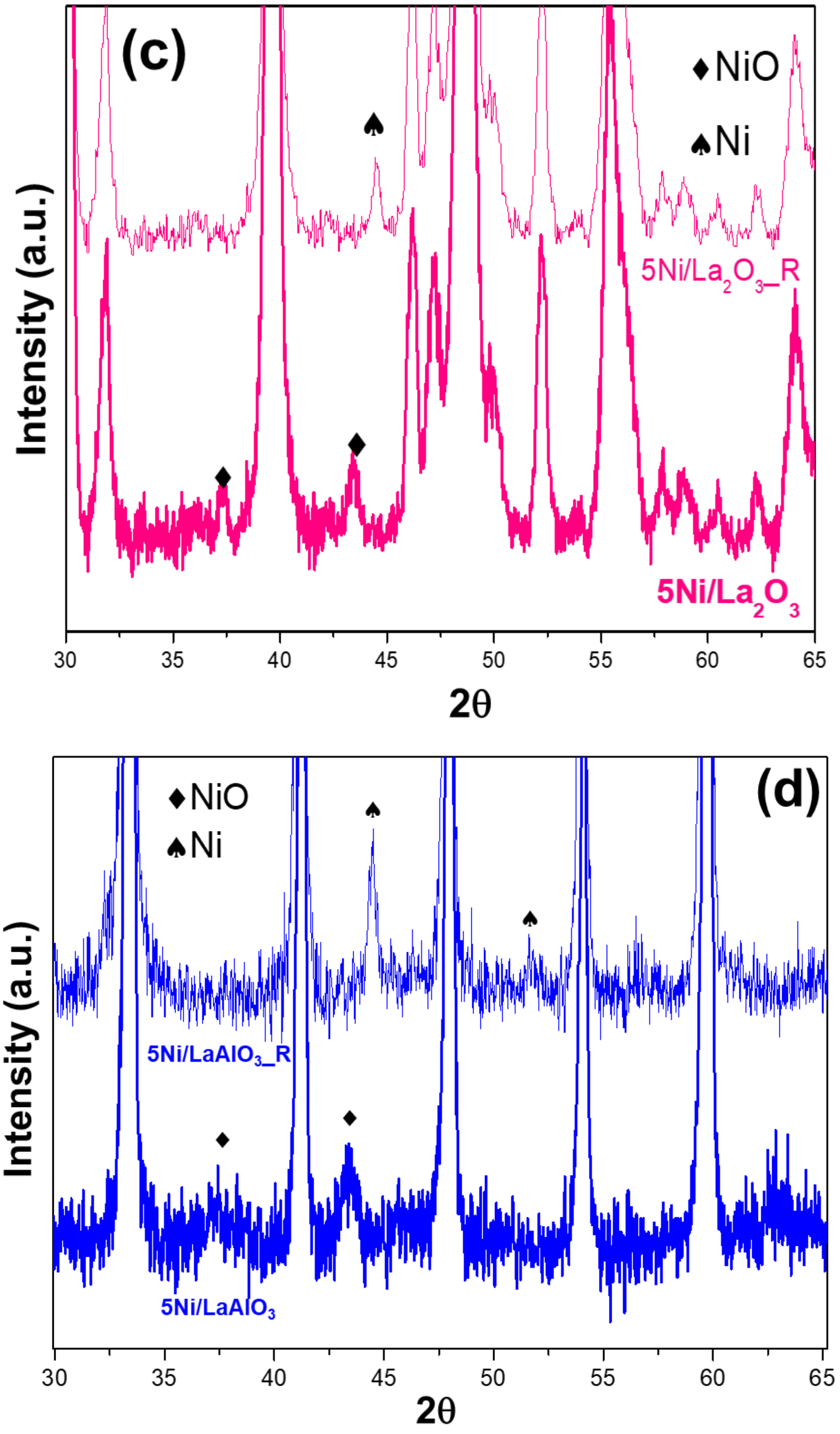

Figure 5.9. (a) Comparison of the XRD diffractograms of the reduced version of the 5% wt. catalysts with the calcined ones for the different supports and zoom-in of the region between 2θ = 30° and 65° for the (b) 5Ni/Al_2O_3_R and (c) 5Ni/La_2O_3_R catalysts.

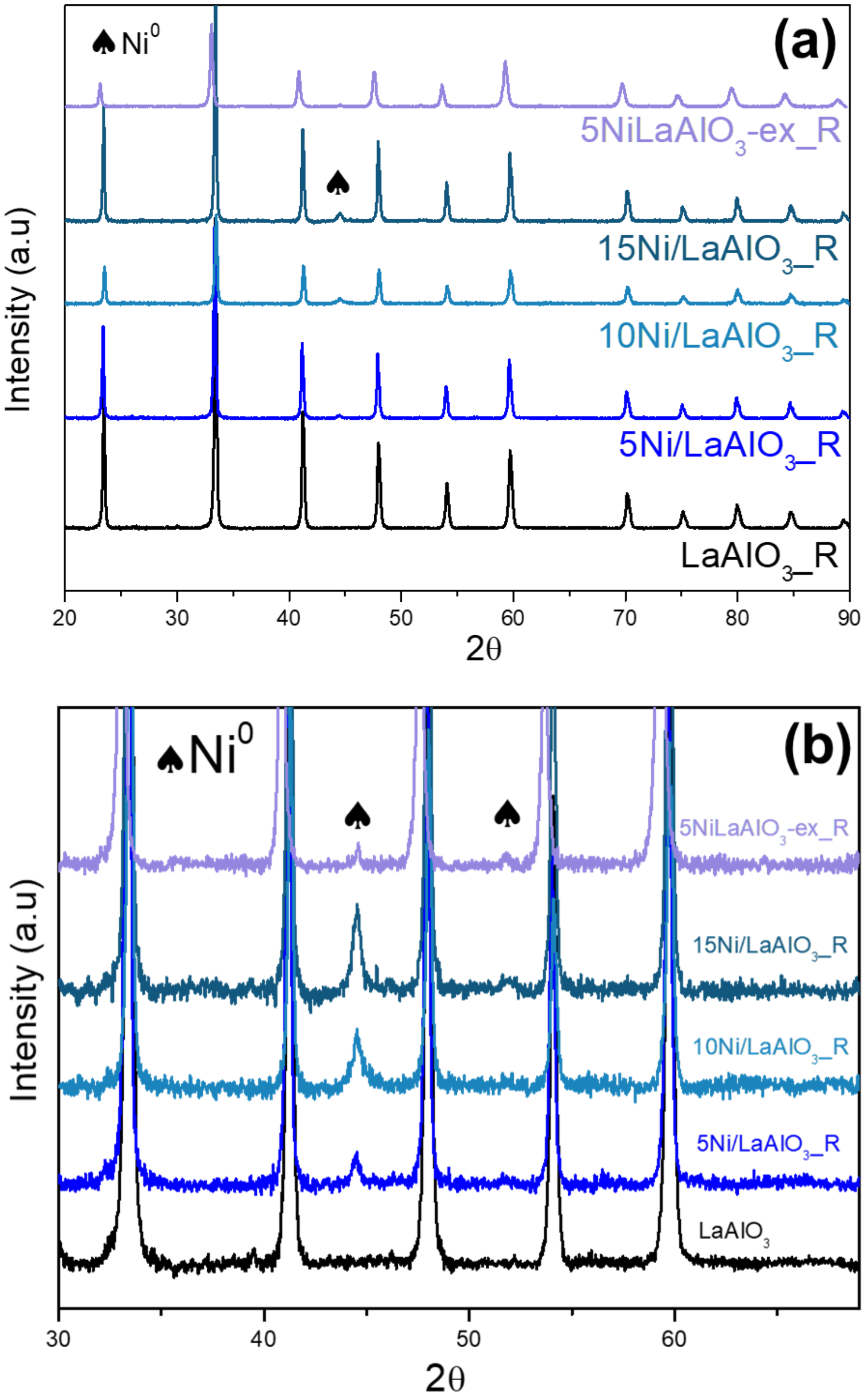

Figure 5.10. (a) XRD diffractograms of the reduced LaAlO$_3$-based catalysts. (b) Magnification of the region between 2θ = 30° and 70° to highlight the presence of diffraction peaks related to the presence of the Ni^0 phase.

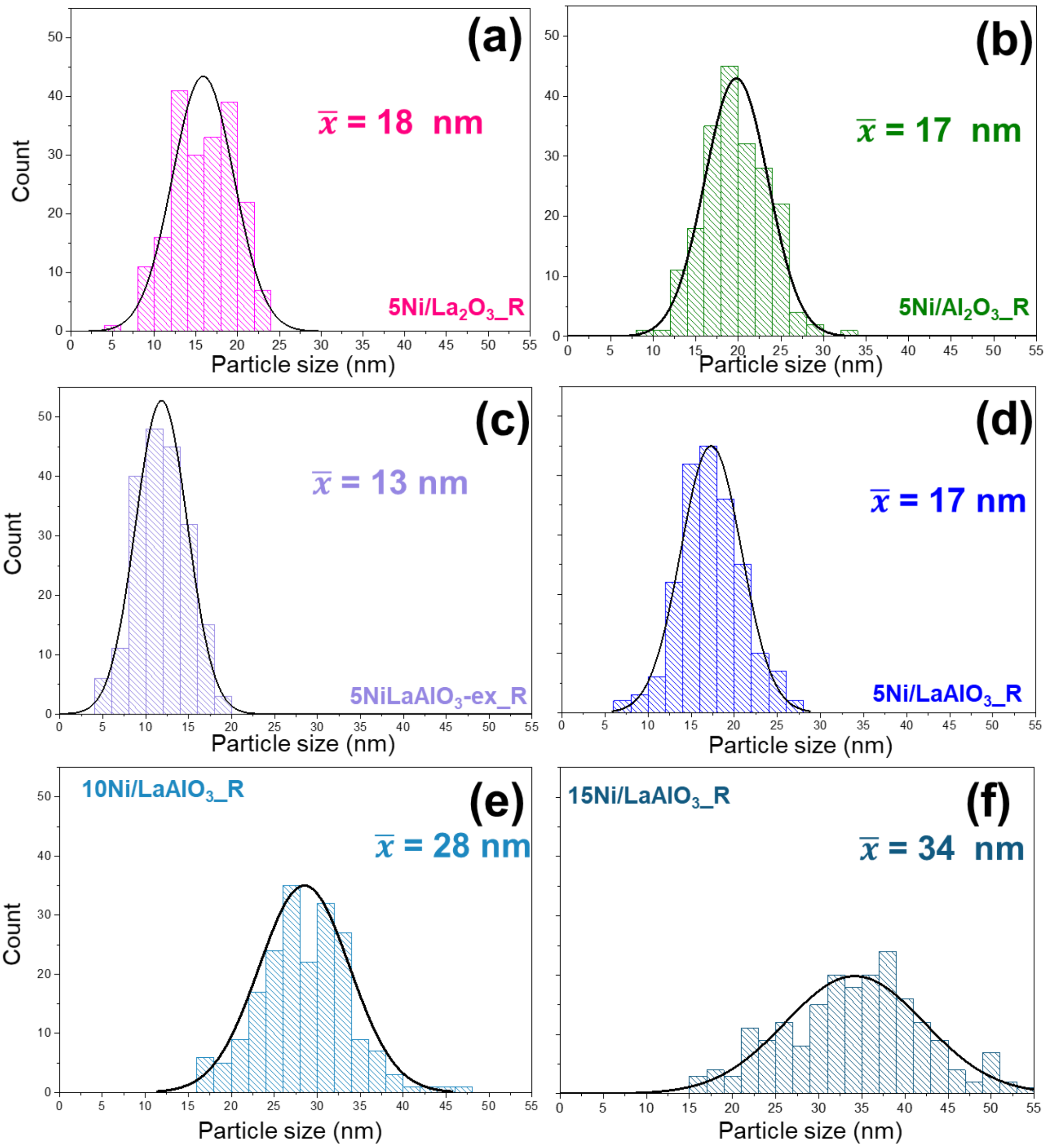

Figure 5.11. Size distribution for Ni^0 particles obtained, normal fit and average size for (a) 5Ni/La$_2$O$_3$_R; (b) 5Ni/Al$_2$O$_3$_R, (c) 5NiLaAlO$_3$-ex_R, (d) 5Ni/LaAlO$_3$_R; (e) 10Ni/LaAlO$_3$_R, and (f) 15Ni/LaAlO$_3$_R. 200 particles were measured for each one using the TEM images treated with the ImageJ software.

Textural properties (**Table 5.3**) reveal that the BET surface area, S_{BET}, of the synthesized $LaAlO_3$ is 15 m²/g, which aligns with previous results published in the literature [62]. The S_{BET} values determined for the commercial La_2O_3 and α-Al_2O_3 are also comparable to the ones previously described and in the same order of magnitude as the one determined for the $LaAlO_3$ [63, 64]. The objective in selecting α-Al_2O_3 was to use this material with low surface area and keep it comparable to the surface area values observed for La_2O_3 and $LaAlO_3$ to ensure that the sizes of impregnated Ni particles remain within the same order of magnitude. This allows for a focus on the study's main objective, which is the effect of the support on the catalytic performance.

Table 5.3. Textural properties: BET surface area (S_{BET}), t-plot mesopore area (S_{MESO}), t-plot mesopore volume (V_{MESO}), Ni^0 metallic surface area (S_{Ni}), Ni^0 average crystallite size, (D_{Ni}), and molar H_2 monolayer uptake.

Sample	S_{BET}[a]	S_{MESO}[a]	V_{MESO}[a]	S_{Ni}[b]	D_{Ni} (nm)[b]	H_2 uptake (µmol/g)[b]
La_2O_3	13	11.7	0.030	-	-	-
5Ni/La_2O_3	10	9.2	0.027	3.0	10	43.6
Al_2O_3	15	14.9	0.041	-	-	-
5Ni/Al_2O_3	11	9.6	0.035	3.7	11	54.3
$LaAlO_3$	15	11.6	0.032	-	-	-
5Ni$LaAlO_3$-ex	14	10.9	0.030	3.2	8	40.0
5Ni/$LaAlO_3$	15	11.3	0.026	3.4	10	48.3
10Ni/$LaAlO_3$	10	9.5	0.023	5.7	12	73.2
15Ni/$LaAlO_3$	7	8.0	0.021	6.2	16	78.8

[a] Estimated with BET surface area data obtained with N_2 adsorption-desorption isotherms. The surface data unit is m^2 g^{-1}, and the micropore volume is cm³ g^{-1}.

[b] Determined by H_2-chemisorption. The surface data unit is m^2 g^{-1}.

When Ni is deposited over these supports, there is a slight decrease in S_{BET}, which is attributed to two effects: on one side, the formation of the NiO crystallites seems to plug some of the mesopores of these materials, as seen by the reduction of the mesopore surface area. On the other, this can be attributed to a "dilution effect", which arises from the addition of a lower surface area phase (NiO) over another one with a higher area, leading to an overall effect of reducing the surface area per mass unit [65], and is more prominent in the higher-loading samples (**Table 5.3**).

H_2-TPR results (**Figure 5.12**) show that there are peaks between 200 and 500 °C. The lower temperature peaks correspond to the reduction of NiO to Ni^0, which exhibits a weaker interaction with the support. At higher temperatures, other peaks appear, which appear on this zone, due to their stronger interaction with the support [66].

At higher temperatures, small peaks are found, which are associated with the reduction of Ni^{II} species found in spinel phases, such as $NiAl_2O_4$ and $NiLa_2O_4$, which are formed at higher temperatures and are harder to reduce due to the stronger interaction of the Ni^{II} inside the lattice [67]. The temperature in which the high-temperature peak is centered follows the order: Al_2O_3 (663 °C) < $LaAlO_3$ (750 °C) < La_2O_3 (799 °C).

This order could be understood under the light that these materials present different oxophilicity, with Al being more oxophilic than La due to the higher polarizability effect, and $LaAlO_3$ presenting an intermediate behavior [68].

Regarding the samples supported on $LaAlO_3$ by impregnation, the higher the Ni loading, the higher the area under the curve, as there are more Ni^{II} species to be reduced. Higher metallic loadings also shift the peak towards lower temperatures: 5Ni/$LaAlO_3$ (380 °C) > 10Ni/$LaAlO_3$ (363 °C) > 15Ni/$LaAlO_3$ (347 °C), due to the larger size of crystallites and lower interaction with the support as described by Singha et al. [69]. The higher the metallic loading, the broader the peaks due to the wider range of particle size (**Figure 5.12**), and, consequentially, a broader range of strong metal support interactions (SMSI) strengths with the support.

As previously mentioned, 5Ni$LaAlO_3$-ex presents a different profile from the catalysts prepared by impregnation, as the first peak (311 °C) refers to the reduction of Ni^{III} to Ni^{II}, accompanied by the formation of La_2NiO_5 and La_2NiO_4 [61, 70]. The peaks at higher temperatures (441 and 467 °C) are associated with the reduction of surface Ni^{II} to Ni^0 which takes place in two phases due to different interactions of the Ni^{II} inside the lattice.

H_2-chemisorption results (**Table 5.3**) reveal that on the 5% wt. Ni catalysts prepared over different supports, their metallic surface, S_{Ni}, is around the same magnitude, with the Ni^0 dispersion and average crystallite size, D_{Ni}, following the trend. 5Ni/Al_2O_3 exhibits slightly larger H_2 uptake values, which might be attributed to the amphoteric nature of Al_2O_3 that presents a higher concentration of surface acid sites, which assist the stabilization of spilled-over atomic hydrogen [71]. 5Ni$LaAlO_3$-ex displays a slightly smaller S_{Ni} and H_2 uptake than 5Ni/$LaAlO_3$ because not all Ni inside the crystalline lattice is exsolved, which reduces the amount of available surface Ni^0 sites.

Regarding the CO_2-TPD analyses for the bare supports, the results were analyzed under the interpretation that CO_2 desorbs in three different temperature ranges, low (50 °C –200°C), intermediate (200°C – 400 °C) and high (400 °C – 900 °C), corresponding to weak, moderate and strong basicity sites, respectively (**Figure 5.13**), as described by Liu et al. [72]. The results (**Table 5.4**) reveal that among the three supports studied, $LaAlO_3$ has the highest values for total CO_2 uptake, followed by La_2O_3 and Al_2O_3.

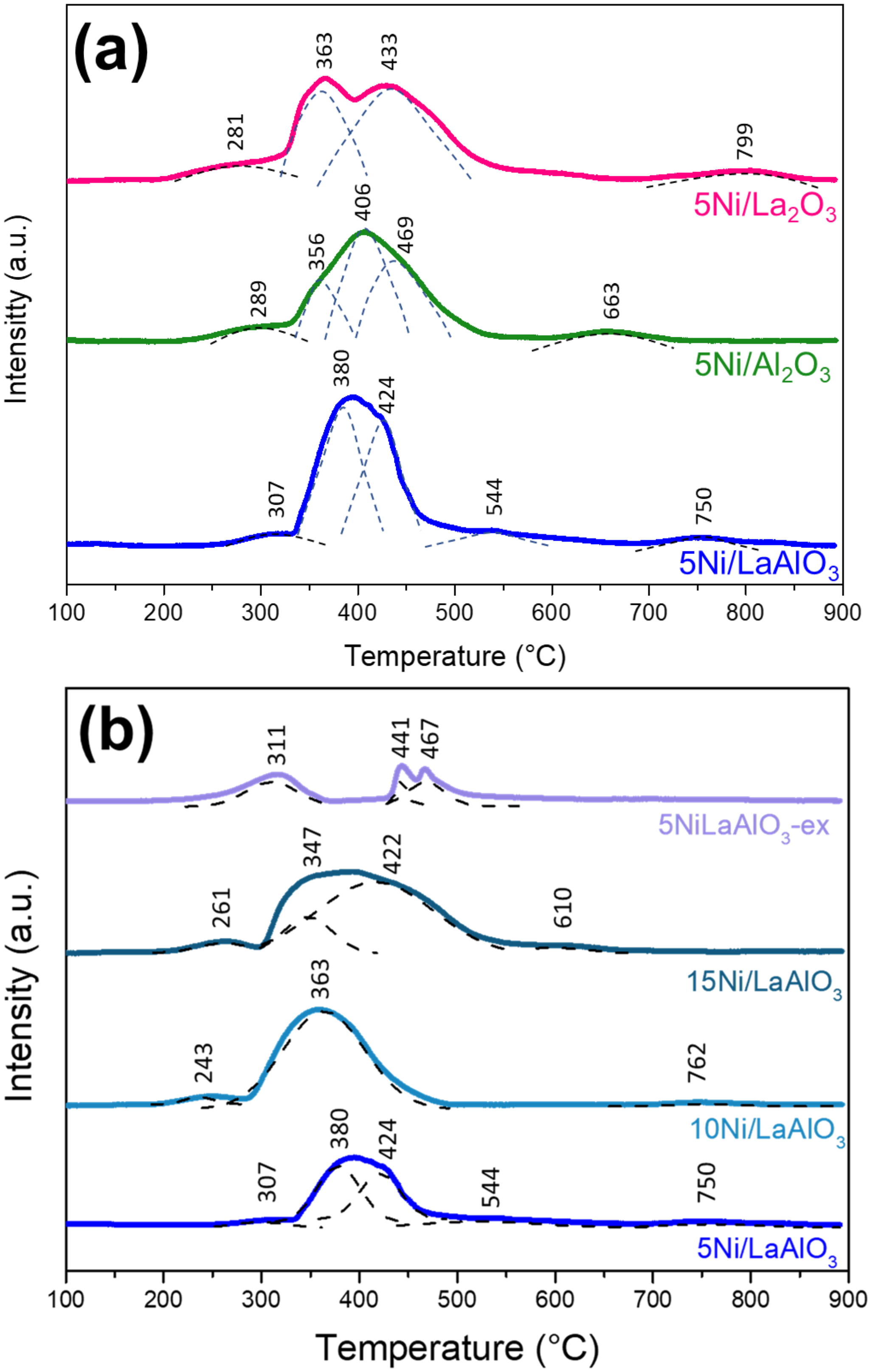

Figure 5.12. H_2-TPR profiles for the catalysts (a) on different supports and (b) with different Ni contents. The temperatures observed for the reduction events are shown next to the corresponding peaks.

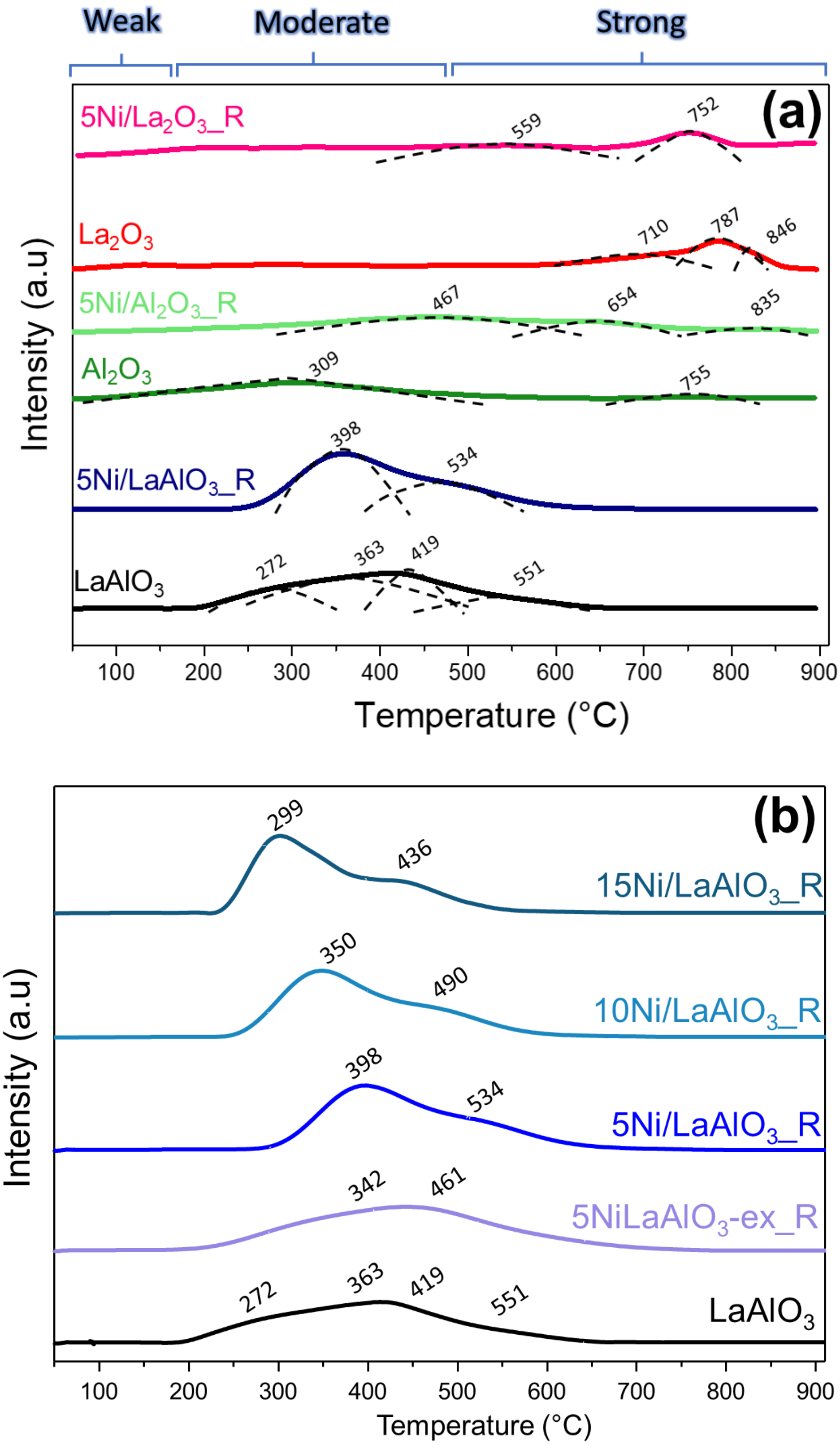

Figure 5.13. CO_2-TPD-MS profiles for the (a) different supports and (b) different Ni content used for the preparation of catalysts. The temperatures observed for the desorption events are shown next to the corresponding peaks.

Table 5.4. CO_2-TPD deconvolution for the concentration of weak (50-200 °C), moderate (200-400 °C), and strong (400-900 °C) basic sites and total basicity for the different supports and catalysts.

Sample	Deconvolution (mmol CO_2 g^{-1})			Total basicity
	Weak	Moderate (B_{CO2})	Strong	(mmol CO_2 g^{-1})
Al_2O_3	0.08	1.31	0.24	**1.63**
La_2O_3	0.11	0.45	1.69	**2.25**
$LaAlO_3$	0	2.32	0.95	**3.27**
5Ni/Al_2O_3_R	0.04	0.91	1.35	**2.30**
5Ni/La_2O_3_R	0.05	0.62	1.40	**2.07**
5Ni$LaAlO_3$-ex_R	0	2.64	1.12	**3.76**
5Ni/$LaAlO_3$_R	0	3.03	1.25	**4.28**
10Ni/$LaAlO_3$_R	0	3.30	1.29	**4.59**
15Ni/$LaAlO_3$_R	0	3.36	1.26	**4.62**

Concerning the distinct basicity strength in different ranges, $LaAlO_3$ is also the support with the highest concentration of moderate basicity sites (B_{CO2}), with desorption peaks centered at 363 °C and 419 °C. For the other two supports, the highest peak for La_2O_3 is shifted toward higher temperatures (787 °C), while the one in Al_2O_3, is towards lower temperatures (309 °C).

The formation of the thermally stable $La_2O_2CO_3$ phase has been linked to the strong sorption of CO_2 molecules, as evidenced by the peaks at high temperatures (710, 787, and 846 °C) in La_2O_3 [73]. This phase has been reported to provide resistance against coke formation in catalysts for methane dry reforming [74]. On the other hand, Al_2O_3 does not form oxocarbonates, and as evidenced by the peak centered at 309 °C, and CO_2 sorption primarily occurs on the surface oxide and hydroxide sites, which break down at lower temperatures [75].

For $LaAlO_3$, a middle-ground behavior seems to be taking place. As the surface is composed of Al^{III} and La^{III}, this leads to a high CO_2 uptake due to the formation of $La_2O_2CO_3$ and interaction with the oxide and hydroxide species on the surface. But, with the advantage of the presence of Al^{III} ions that facilitate the CO_2 desorption, lowering the temperature in which the highest peak is located in comparison with La_2O_3.

The peaks located for $LaAlO_3$ at different temperatures (272, 363, 419, 551 °C) refer to the desorption of carbonates with different coordination modes, which are known to desorb at different temperatures [29]. These different carbonate species formed over $LaAlO_3$ and their role in the CO_2 methanation reaction will be further corroborated by the operando FT-IR results, as discussed thereafter.

Recently studies were reported to provide more information on the effect of the moderate basic site concentration on the CO_2 methanation catalytic performance in different types of supports, such as phyllosilicates [76], SBA-16 [77], C_3N_4 [78], ZrO_2 [79], and Al_2O_3 [80].

Even though each one of these classes of materials presents its particularities regarding textural properties, type of active sites, reducibility, and metallic dispersion, the conclusions from the study seem to confirm that the concentration of moderate basic sites has an impact on the X_{CO_2} and S_{CH_4} values in all of them, as discussed over the next section.

5.3 – CO_2 methanation catalytic tests

5.3.1 – Support effect: La_2O_3, Al_2O_3 and $LaAlO_3$

The performance of all catalysts was evaluated for the CO_2 methanation reaction in terms of CO_2 conversion and selectivity towards CH_4 (**Figure 5.14**). The carbon balance between inlet and outlet composition closed up being kept within ±5%. For some of the most active catalysts, such as the ones with higher Ni loadings over $LaAlO_3$, X_{CO_2} values reach the equilibrium, following the profile of an exergonic reaction [81].

With respect to the support effect, at 350 °C, X_{CO_2} and $Y_{CH_4,}$ values follow the order: $5Ni/La_2O_3 < 5Ni/Al_2O_3 < 5Ni/LaAlO_3$ (**Figure 5.14**), and so do the TOF values at 250 °C, which is in consonance with the order observed for the activation energy toward CH_4 formation (E_{a,CH_4}) (**Figure 5.15** and **Table 5.5**).

Table 5.5. Catalytic data and selected properties: yield to CH_4 at 250 °C ($Y_{250\,°C}$), turnover frequency at 250 °C ($TOF_{250\,°C}$), activation energy towards CH_4, E_{a,CH_4}, intermediate basic sites concentration, B_{CO_2}, and average Ni^0 crystallite size, *D_{Ni}*.

Catalyst	$Y_{250\,°C}$ (%)	$TOF_{250\,°C}$ (s^{-1})	E_{a,CH_4} (kJ mol^{-1})[a]	B_{CO_2} (mmol CO_2 g^{-1})[b]	D_{Ni} (nm)[c]
$5Ni/La_2O_3$	4.7	0.124	89	0.62	11
$5Ni/Al_2O_3$	6.4	0.131	80	0.91	10
$5NiLaAlO_3$-ex	5.4	0.043	90	2.64	8
$5Ni/LaAlO_3$	8.5	0.302	75	3.03	11
$10Ni/LaAlO_3$	10.5	0.385	-	3.30	12
$15Ni/LaAlO_3$	17.3	0.429	-	3.36	16

[a] Determined with kinetic studies carried out between 250 °C-300 °C.

[b] Determined with CO_2-TPD-MS results.

[c] Determined with H_2-chemisorption results.

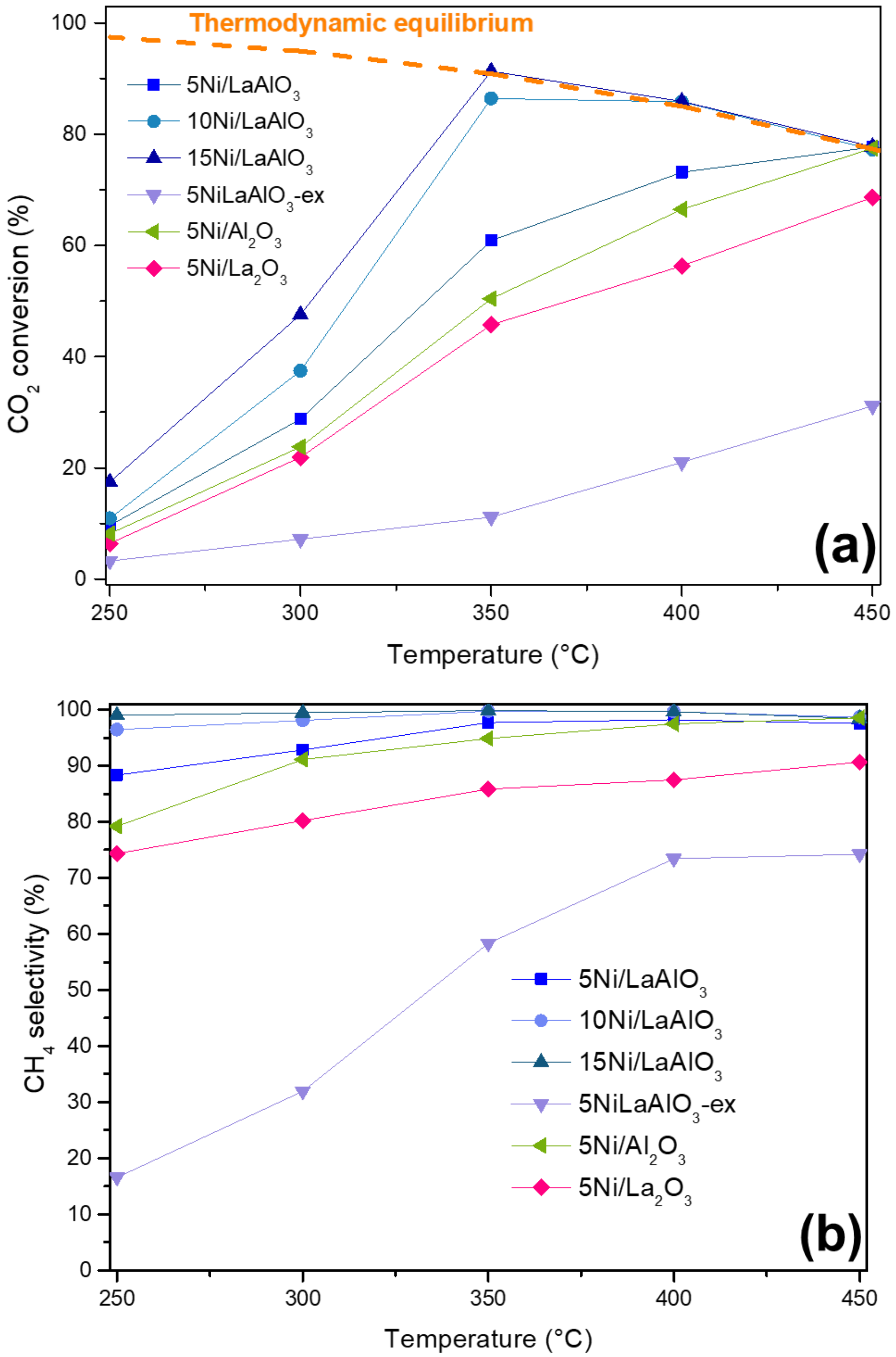

Figure 5.14. (a) CO_2 conversion and (b) CH_4 selectivity values. Conditions of experiment: 1 atm, 250 °C-450 °C, WHSV = 42,000 mL $(g_{cat}\ h)^{-1}$, H_2/CO_2 molar ratio = 4:1. Equilibrium data calculated on DWSIM software.

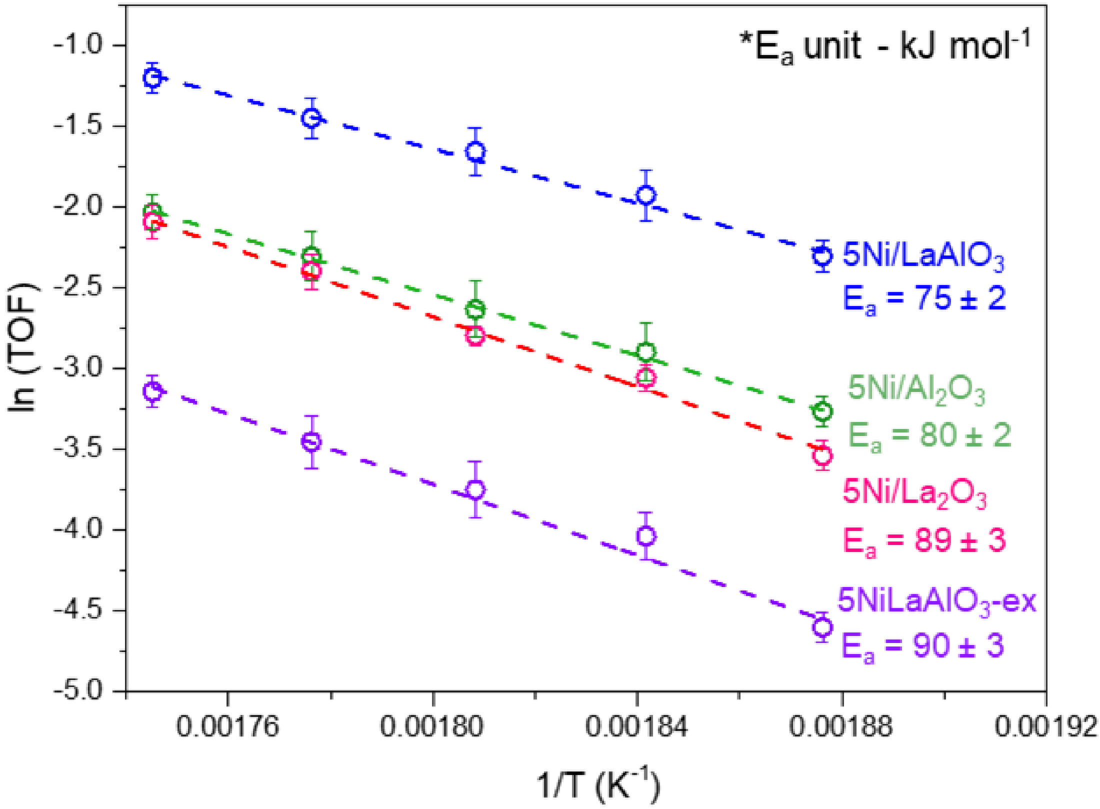

Figure 5.15. Arrhenius plot for the series of Ni-based catalysts prepared over different supports for the 260-300 °C. Linear regression on each set of data points was used to calculate the apparent activation energy, E_a.

Considering that the S_{Ni} and D_{Ni} values for these catalysts are around the same magnitude (**Table 5.3**), it seems that the metal oxide synergy in $LaAlO_3$, which increases the CO_2 uptake at moderate basicity strength sites, and, consequentially, the concentration of intermediate carbonated species. As confirmed by the mechanistic assessment with operando IR spectroscopy discussed in the following section, these carbonated species participate in the reaction mechanism so that a higher concentration of them increases the TOF values.

These results align with the ones observed by Italiano et al., whose work revealed that CO_2 methanation catalysts supported on Y_2O_3 displayed higher TOF values than ones supported on other metal oxides, due to Y_2O_3 higher intermediate basic site concentration [82]. Operando studies confirmed that on Y_2O_3, an associative mechanism was observed, and the intermediate basic sites were directly involved.

5.3.2 – Ni loading and method of incorporation effect

Once it was reported that $LaAlO_3$ was the most suitable support among the three, the effect of Ni content was assessed. As expected, higher Ni loading led to higher X_{CO_2} and S_{CH_4} values, which can be interpreted under the light of two trends: the Ni^0 particle size and the intermediate basic sites concentration.

To intertwine these catalytic results with the previous results, the catalyst with the optimum Ni loading, $15Ni/LaAlO_3$, was tested in operando FT-IR experiments to shed light on the formed intermediates (**Figure 5.16**). This is the first time in the literature that the $LaAlO_3$ support has been studied under operando conditions for the CO_2 methanation reaction, as far as we know.

First of all, upon introducing CO_2, carbonate species were formed, identified by the bands centered at 1378, 1495, 1603, and 1653 cm^{-1}, as summarized in **Table 5.6**. CO_2 introduction also led to the formation of metal-carbonyl groups with different degrees of coordination: linearly bonded μ_1- CO (2026 cm^{-1}), bridge bonded μ_2-CO (1918 cm^{-1}), and multi-bonded μ_3-CO (1859 cm^{-1}), located at different wavenumbers due to the difference in electronic density in the carbon-oxygen bond [83].

After the CO_2 flow is cut off, and a H_2 one is injected instead (**Figure 5.17**a), there is detection of $CH_{4(g)}$ with its typical rotovibrational profile and the peaks centered at 3016 cm^{-1} and 1302 cm^{-1}.

There is also modification of the monodentate carbonate bands at 1653 and 1609 cm^{-1}, which appear as shoulders to the more prominent bands that decrease in intensity after H_2 introduction, confirming their engagement in the reaction mechanism, as seen by the evolution of the normalized area of these peaks (**Figure 5.17**b)

Table 5.6. Vibration modes for different species in the $15Ni/LaAlO_3$ catalyst and corresponding wavenumber.

Vibration mode	Wavenumber (cm^{-1})	Reference
linear Ni^0-CO	2026	Cárdenas-Arenas et al.[83]
bridge Ni^0-CO	1918	Cárdenas-Arenas et al.[83]
Multi-bonded Ni^0-CO	1859	Cárdenas-Arenas et al.[83]
$CH_{4(g)}$	3016/1302	Cerdá Moreno et al.[53]
ν(C=O) monodentate carbonate	1653/1609	Cerdá Moreno et al.[53]
ν(C=O) bidentate carbonate	1495	Lorber et al. [84]
ν(C=O) formate	1378	Li et al.[85]

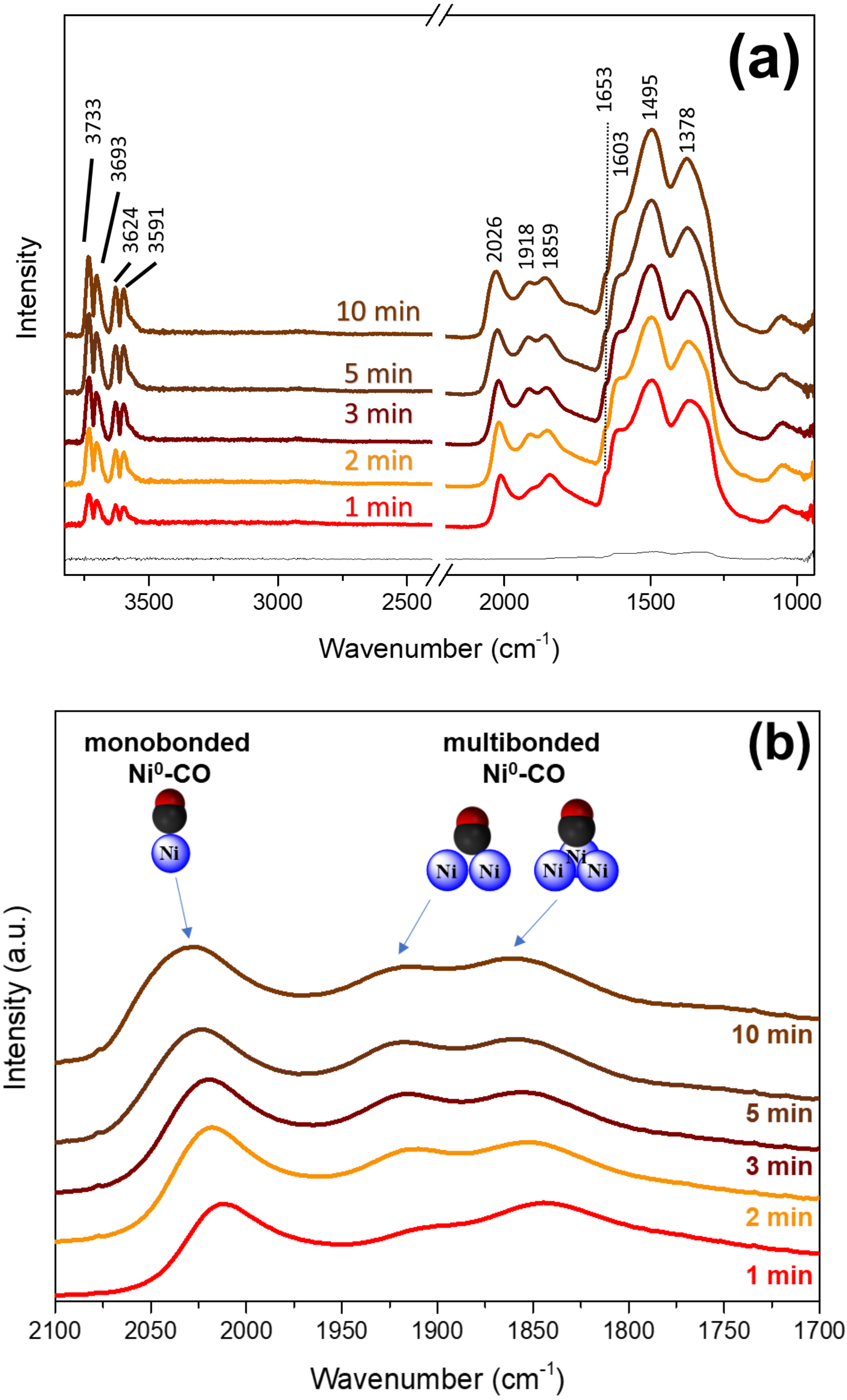
(a)
Intensity
3733
3693
3624
3591
2026
1918
1859
1653
1603
1495
1378
10 min
5 min
3 min
2 min
1 min
3500
3000
2500
2000
1500
1000
Wavenumber (cm^{-1})
(b)
monobonded
Ni^0-CO
multibonded
Ni^0-CO
Ni
Ni
Ni
Ni
Ni
Ni
Intensity (a.u.)
10 min
5 min
3 min
2 min
1 min
2100
2050
2000
1950
1900
1850
1800
1750
1700
Wavenumber (cm^{-1})

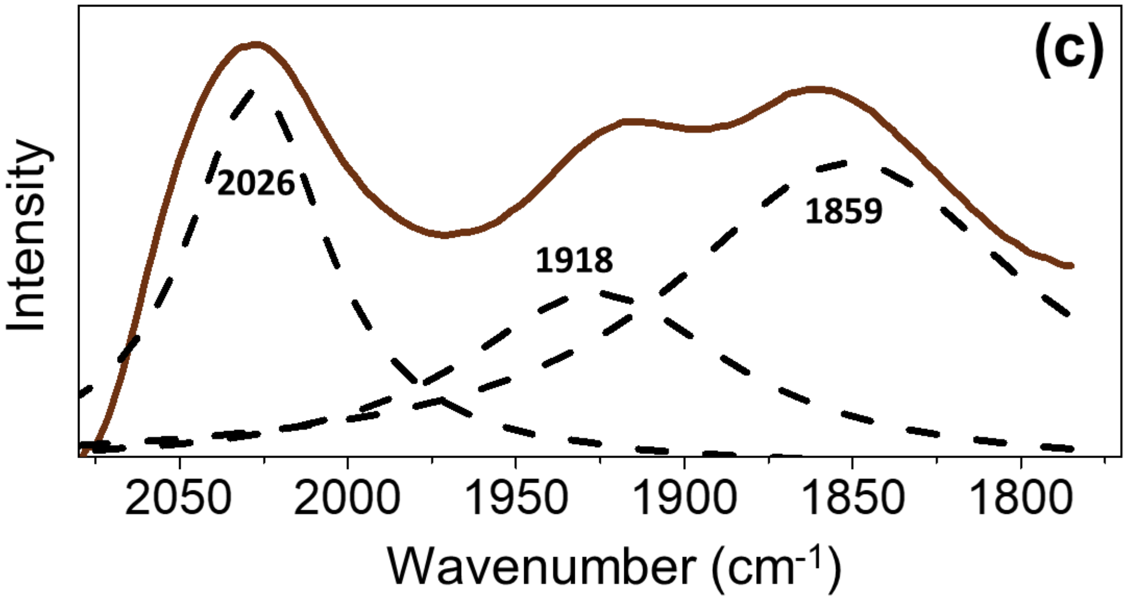

Figure 5.16. (a) Time-resolved transmission FT-IR measurements for the 15Ni/$LaAlO_3$ catalyst during CO_2 exposition. (b) Zoom-in of the region between 1750 and 2075 cm^{-1} showing the different Ni^0-CO bonding modes and (c) example of deconvolution profile for the 10 min sample for the different Ni^0-CO bonding modes.

The bidentate carbonate and formate intermediate (1495 and 1378 cm^{-1}, respectively) act as spectators, as their peaks do not change in intensity. The peaks of the aforementioned metal-carbonyl groups also decrease in intensity, suggesting their participation in the reaction mechanistic pathway.

Altogether, these results suggest that. in the 15Ni/$LaAlO_3$ catalyst, the reaction mechanism follows a H-assisted associative pathway, in which the bicarbonate species are being formed and hydrogenated to CH_4 via the associative mechanism. The intensity decrease of the metal-carbonyl peaks confirms that the dissociative mechanism takes place simultaneously.

Wrapping up the discussion and considering the current understanding of the reaction mechanism, these operando results reveal that the better performance over the higher loading samples can be attributed to two trends: the intermediate basicity site concentration, B_{CO_2}, and the available metallic surface area, S_{Ni}. For this reason, the ratio between these two parameters, B_{CO_2}/S_{Ni}, was calculated, and the dependence of the catalytic activity, expressed as ln (TOF) with B_{CO_2}/S_{Ni}, was studied (**Figure 5.18**).

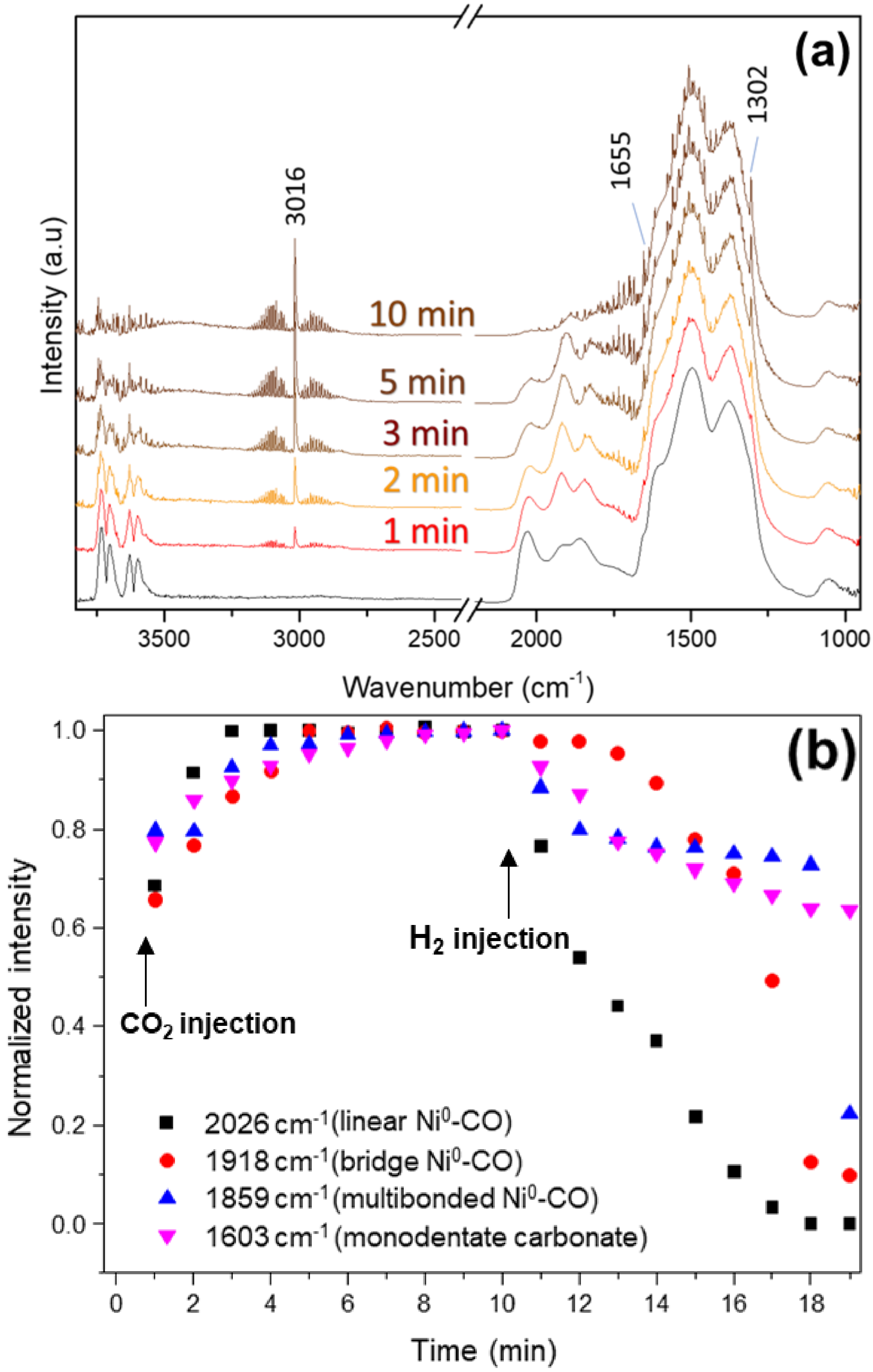

Figure 5.17. (a) Time-resolved in-situ FT-IR measurements for the 15Ni/$LaAlO_3$ catalyst during H_2 exposition after the CO_2 exposition step and (b) evolution of normalized intensity for selected peaks.

Regarding the effect of the support, as 5Ni/La_2O_3, 5Ni/Al_2O_3, and 5Ni/$LaAlO_3$ present similar metallic Ni^0 surface areas, the main difference resides in their basicity. As previously reported, Ni/Al_2O_3 and Ni/La_2O_3 also exhibit an associative mechanism towards CO_2 methanation, via a mechanism in which the moderate basicity sites are involved in forming participating monodentate carbonate intermediates [30, 86].

Therefore, the mixed oxide synergy in $LaAlO_3$ in increasing the moderate basicity sites has a positive effect on the reaction mechanism by increasing the monodentate carbonate intermediate formation and positively contributing to an increase in the catalytic activity, as confirmed by the operando FT-IR results.

The second factor to be considered is the S_{Ni}. As the $LaAlO_3$-based catalysts present similar B_{CO_2} values, the main difference resides in the properties regarding the Ni^0 phase (**Table 5.5**). Among the three, the higher the S_{Ni}, the higher the catalytic activity once a higher amount of Ni^0 sites at the support-Ni^0 interface positively impacts the amount of H_2 uptake (**Table 5.3**).

Another factor to consider about the effect of Ni loading beyond the available surface metallic surface is the structure-sensitiveness of the mechanism, directly linked to the Ni^0 particle sizes. In the 5NiLaAlO_3-ex catalyst, for example, the reduction conditions employed led to a catalyst with smaller Ni^0 particles (8 nm) than the others (**Figure 5.19**), which also affected E_{a,CH_4} and TOF values at 250 °C (**Table 5.5**).

The pattern reveals that for 5NiLaAlO_3-ex, the lower $Y_{250\,°C}$ values are due to the higher E_{a,CH_4} values accounted for the smaller Ni^0 particles. With an increase in the average Ni^0 particle size, the turnover frequency reveals a plateau-like behavior, confirming that the structure sensitiveness is more prominent for smaller particles (< 12 nm).

These findings are consistent with those of Varvoutis, who found that Ni^0 particles smaller than 10 nm reduced the interface region between the step and corner Ni^0 atoms, known to be the participating sites for the hydrogenation of CO_2 molecules [87]. On the other hand, larger particles of about 15-20 nm optimized the catalytic performance as they achieved a compromise by optimizing the interface region between the active sites of the Ni^0 particles and the support.

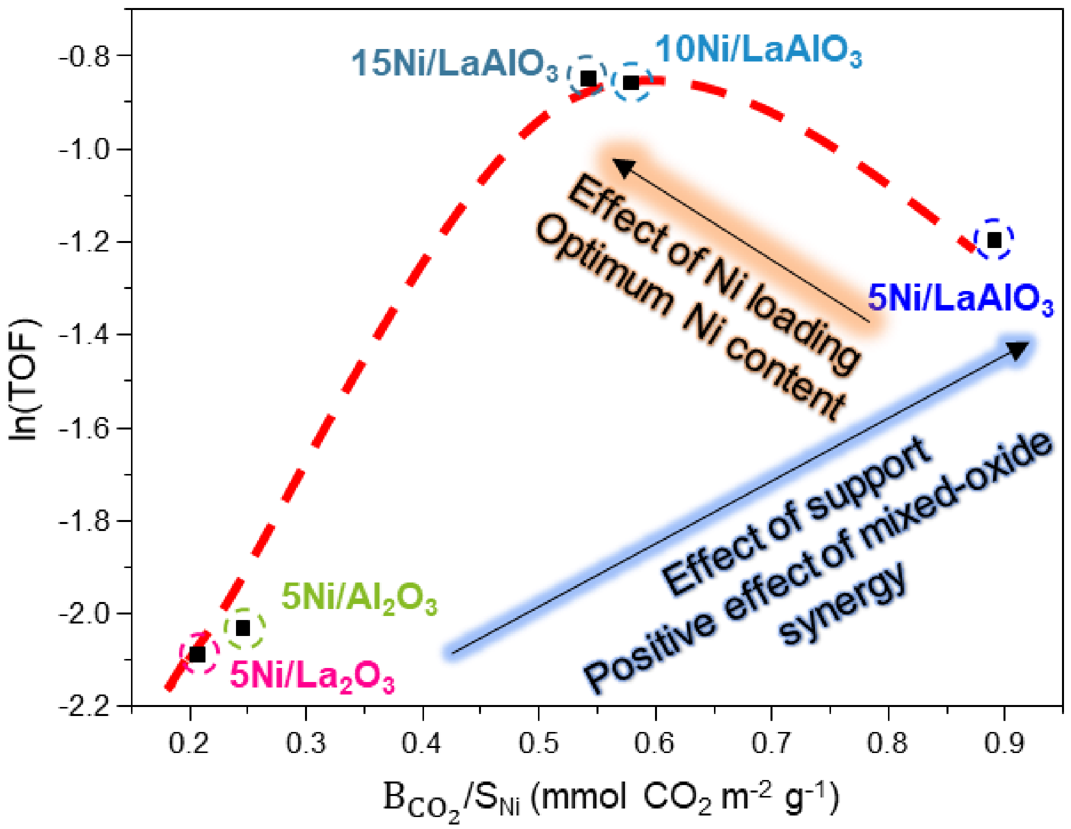

Figure 5.18. Dependence of catalytic activity on the ratio between moderate basic sites concentration, B_{CO_2}, and available metallic surface area, S_{Ni}. The red curve is added for better visualization of the data points.

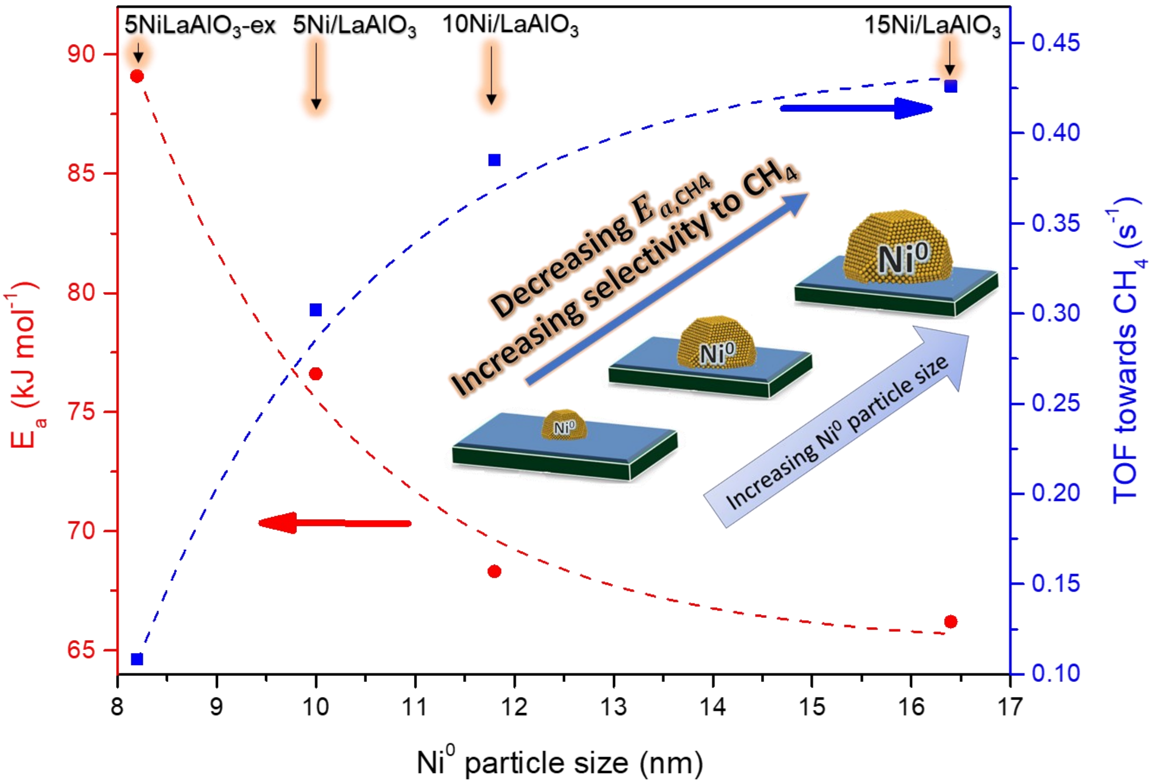

Figure 5.19. Correlation between Ni^0 particle size and CH_4 formation turnover frequency number (TOF) for the different catalysts supported on $LaAlO_3$.

5.4 – Conclusions

In this work, a comparison of Ni-based catalysts prepared over different lanthanum/aluminum oxides, La_2O_3, Al_2O_3, and $LaAlO_3$, was performed for the CO_2 methanation reaction. Initial catalytic tests proved that $LaAlO_3$-based catalysts exhibited metal oxide synergy, which was rationalized by a multi-technique approach based on different analyses (XRD, H_2-TPR, CO_2-TPD-MS, H_2-chemisorption, N_2 adsorption, and SEM-TEM).

The results revealed that, even though the Ni^0 crystallite size and metallic surface area are in the same order of magnitude, the catalyst supported on $LaAlO_3$ exhibited significantly higher catalytic activity than those supported on the individual oxides. This was attributed to a higher moderate basicity site concentration that led to the formation of carbonate species with different degrees of coordination.

Operando FT-IR revealed that, in this type of catalyst, the mechanism follows two pathways. The first is the dissociative one via the formation of Ni^0-CO intermediates. The second one is via the formation of monodentate carbonate species anchored in basic sites, which are of pivotal importance for the associative mechanism of the CO_2 methanation reaction. This led to the conclusion that positively tuning the moderate basicity site concentration has a positive impact on the catalytic performance.

After $LaAlO_3$ was identified as the most promising support, different methods of preparation and metallic loadings were tested for the CO_2 methanation reaction. The results revealed that the 15% wt. Ni one prepared by IWI (15Ni/$LaAlO_3$) presented the optimum catalytic results, which was due to a concerted effect of favorable reducibility of the Ni phase, higher available metallic phase, and formation of monodentate carbonate intermediates in the moderate basicity sites. The synergic interaction of the H-species and the carbonate ones contributed to CH_4 formation via the associative mechanism, which was confirmed by operando FT-IR results and corroborated by the kinetic studies.

Altogether, based on combined scrutiny with operando FT-IR results and CO_2-TPD-MS, the conclusions of this work contribute to the ongoing discussion about the effect of moderate basicity sites on the CO_2 methanation reaction and its mechanism, which is of underlying importance for the design of more efficient catalysts. Furthermore, it presents an innovative use of a catalyst based on $LaAlO_3$ for CO_2 methanation. It opens the perspective of future studies based on other mixed oxide materials with tuned surface basicity and different metallic compositions as catalysts for the CO_2 methanation reaction.

5.5 – References

[1] Gupta P, Maurya S, Pandey NK, Verma V. Metal-oxide based ammonia gas sensors: A review. Nanoscience and Nanotechnology - Asia. 2021;11:270-89.

[2] Mala NA, Dar MA, Sivakumar S, Dar TA, Manikandan E. Review article on the performance of electrochemical capacitors when altered metals doped with nickel oxide nanomaterials. Journal of Nanoparticle Research. 2022;24.

[3] Scheinost AC, Singh B. Metal oxides. In: Goss MJ, Oliver M, editors. Encyclopedia of Soils in the Environment (Second Edition). Oxford: Academic Press; 2023. p. 135-48.

[4] Laurent S, Boutry S, Muller RN. Chapter 1 - Metal Oxide Particles and Their Prospects for Applications. In: Mahmoudi M, Laurent S, editors. Iron Oxide Nanoparticles for Biomedical Applications: Elsevier; 2018. p. 3-42.

[5] Shen G, Chen PC, Ryu K, Zhou C. Devices and chemical sensing applications of metal oxide nanowires. Journal of Materials Chemistry. 2009;19:828-39.

[6] Visakh PM. Applications of Metal Oxide-Based Nanocomposites. Metal Oxide Nanocomposites: Synthesis and Applications2021. p. 303-26.

[7] Fiori G, Bonaccorso F, Iannaccone G, Palacios T, Neumaier D, Seabaugh A, et al. Electronics based on two-dimensional materials. Nature Nanotechnology. 2014;9:768-79.

[8] Yang D, Gates BC. Characterization, Structure, and Reactivity of Hydroxyl Groups on Metal-Oxide Cluster Nodes of Metal–Organic Frameworks: Structural Diversity and Keys to Reactivity and Catalysis. Advanced Materials. 2024;36:2305611.

[9] Tamura H, Tanaka A, Mita K, Furuichi R. Surface Hydroxyl Site Densities on Metal Oxides as a Measure for the Ion-Exchange Capacity. J Colloid Interface Sci. 1999;209:225-31.

[10] Tamura H, Mita K, Tanaka A, Ito M. Mechanism of Hydroxylation of Metal Oxide Surfaces. Journal of Colloid and Interface Science. 2001;243:202-7.

[11] Gawande MB, Pandey RK, Jayaram RV. Role of mixed metal oxides in catalysis science—versatile applications in organic synthesis. Catalysis Science & Technology. 2012;2:1113-25.

[12] Pan Q, Peng J, Sun T, Wang S, Wang S. Insight into the reaction route of CO2 methanation: Promotion effect of medium basic sites. Catalysis Communications. 2014;45:74-8.

[13] Muroyama H, Tsuda Y, Asakoshi T, Masitah H, Okanishi T, Matsui T, et al. Carbon dioxide methanation over Ni catalysts supported on various metal oxides. Journal of Catalysis. 2016;343:178-84.

[14] Siakavelas GI, Charisiou ND, AlKhoori S, AlKhoori AA, Sebastian V, Hinder SJ, et al. Highly selective and stable nickel catalysts supported on ceria promoted with Sm2O3, Pr2O3 and MgO for the CO2 methanation reaction. Applied Catalysis B: Environmental. 2021;282.

[15] Cai M, Wen J, Chu W, Cheng X, Li Z. Methanation of carbon dioxide on Ni/ZrO2-Al2O3 catalysts: Effects of ZrO2 promoter and preparation method of novel ZrO2-Al2O3 carrier. Journal of Natural Gas Chemistry. 2011;20:318-24.

[16] Erhan Aksoylu A, İlsenÖnsan Z. Hydrogenation of carbon oxides using coprecipitated and impregnated Ni/Al2O3 catalysts. Applied Catalysis A: General. 1997;164:1-11.

[17] Garbarino G, Bellotti D, Riani P, Magistri L, Busca G. Methanation of carbon dioxide on Ru/Al2O3 and Ni/Al2O3 catalysts at atmospheric pressure: Catalysts activation, behaviour and stability. International Journal of Hydrogen Energy. 2015;40.

[18] Garbarino G, Riani P, Magistri L, Busca G. A study of the methanation of carbon dioxide on Ni/Al2O3 catalysts at atmospheric pressure. International Journal of Hydrogen Energy. 2014;39:11557-65.

[19] Liu H, Zou X, Wang X, Lu X, Ding W. Effect of CeO2 addition on Ni/Al2O3 catalysts for methanation of carbon dioxide with hydrogen. Journal of Natural Gas Chemistry. 2012;21:703-7.

[20] Rahmani S, Rezaei M, Meshkani F. Preparation of highly active nickel catalysts supported on mesoporous nanocrystalline γ-Al2O3 for CO2 methanation. Journal of Industrial and Engineering Chemistry. 2014;20:1346-52.

[21] Song F, Zhong Q, Yu Y, Shi M, Wu Y, Hu J, et al. Obtaining well-dispersed Ni/Al2O3 catalyst for CO2 methanation with a microwave-assisted method. International Journal of Hydrogen Energy. 2017;42:4174-83.

[22] Garbarino G, Bellotti D, Finocchio E, Magistri L, Busca G. Methanation of carbon dioxide on Ru/Al2O3: Catalytic activity and infrared study. Catalysis Today. 2016;277:21-8.

[23] Kwak JH, Kovarik L, Szanyi J. CO2 Reduction on Supported Ru/Al2O3 Catalysts: Cluster Size Dependence of Product Selectivity. ACS Catalysis. 2013;3:2449-55.

[24] Wang X, Hong Y, Shi H, Szanyi J. Kinetic modeling and transient DRIFTS–MS studies of CO2 methanation over Ru/Al2O3 catalysts. Journal of Catalysis. 2016;343:185-95.

[25] Tada S, Ochieng OJ, Kikuchi R, Haneda T, Kameyama H. Promotion of CO2 methanation activity and CH4 selectivity at low temperatures over Ru/CeO2/Al2O3 catalysts. International Journal of Hydrogen Energy. 2014;39:10090-100.

[26] Beuls A, Swalus C, Jacquemin M, Heyen G, Karelovic A, Ruiz P. Methanation of CO2: Further insight into the mechanism over Rh/γ-Al2O3 catalyst. Applied Catalysis B: Environmental. 2012;113-114:2-10.

[27] Heyl D, Rodemerck U, Bentrup U. Mechanistic Study of Low-Temperature CO2 Hydrogenation over Modified Rh/Al2O3 Catalysts. ACS Catalysis. 2016;6:6275-84.

[28] Wang X, Shi H, Kwak J-H, Szanyi J. Mechanism of CO2 hydrogenation on Pd/Al2O3 catalysts: kinetics and transient DRIFTS-MS studies. ACS Catalysis. 2015;5:150917101014004.

[29] Ewald S, Hinrichsen O. On the interaction of CO2 with Ni-Al catalysts. Applied Catalysis A: General. 2019;580:71-80.

[30] Huang M-X, Liu F, He C-C, Yang S-Q, Chen W-Y, Ouyang L, et al. Interface promoted CO2 methanation: A theoretical study of Ni/La2O3. Chemical Physics Letters. 2021;768:138396.

[31] Dai Y, Xu M, Wang Q, Huang R, Jin Y, Bian B, et al. Enhanced activity and stability of Ni/La2O2CO3 catalyst for CO2 methanation by metal-carbonate interaction. Applied Catalysis B: Environmental. 2020;277.

[32] Rizwan M, Gul S, Iqbal T, Mushtaq U, Farooq M, Farman M, et al. A Review on Perovskite Lanthanum Aluminate (LaAlO3), Its Properties and Applications. Materials Research Express. 2019;6:2001.

[33] Lemański K, Sztolberg D, Brzostowski B, Drzewiecki A, Stefańska D, Dereń PJ. Spectroscopic and paramagnetic properties of LaAlO3 polycrystals doped with vanadium ions. Journal of Luminescence. 2020;221:117059.

[34] Krishnaswamy K, Dreyer CE, Janotti A, Van de Walle CG. Structure and energetics of LaAlO3 (001) surfaces. Physical Review B. 2014;90:235436.

[35] Alves N, Ferraz WB, Faria LO. Synthesis and investigation of the luminescent properties of carbon doped lanthanum aluminate (LaAlO3) for application in radiation dosimetry. Radiation Measurements. 2014;71:90-4.

[36] Filonova E, Medvedev D. Recent Progress in the Design, Characterisation and Application of LaAlO3-and LaGaO3-Based Solid Oxide Fuel Cell Electrolytes. Nanomaterials. 2022;12:1991.

[37] Figueredo GP, Medeiros RLBA, Macedo HP, de Oliveira ÂAS, Braga RM, Mercury JMR, et al. A comparative study of dry reforming of methane over nickel catalysts supported on perovskite-type LaAlO3 and commercial A-Al2O3. International Journal of Hydrogen Energy. 2018;43:11022-37.

[38] Kathiraser Y, Thitsartarn W, Sutthiumporn K, Kawi S. Inverse NiAl2O4 on LaAlO3-Al 2O3: Unique catalytic structure for stable CO2 reforming of methane. Journal of Physical Chemistry C. 2013;117:8120-30.

[39] Sekine Y, Mukai D, Murai Y, Tochiya S, Izutsu Y, Sekiguchi K, et al. Steam reforming of toluene over perovskite-supported Ni catalysts. Applied Catalysis A: General. 2013;451:160-7.

[40] Ma Y, Su P, Ge Y, Wang F, Xue R, Wang Z, et al. A Novel LaAlO3 Perovskite with Large Surface Area Supported Ni-Based Catalyst for Methane Dry Reforming. Catalysis Letters. 2022;152:2993-3003.

[41] Peter SD, Garbowski E, Perrichon V, Pommier B, Primet M. Activity enhancement of mixed lanthanum-copper-iron-perovskites in the CO+NO reaction. Applied Catalysis A: General. 2001;205:147-58.

[42] Lin Q, Qiao B, Huang Y, Li L, Lin J, Yan Liu X, et al. La-doped Al2O3 supported Au nanoparticles: highly active and selective catalysts for PROX under PEMFC operation conditions. Chemical Communications. 2014;50:2721-4.

[43] Tran QN, Martinovic F, Ceretti M, Esposito S, Bonelli B, Paulus W, et al. Co-doped LaAlO3 perovskite oxide for NOx-assisted soot oxidation. Applied Catalysis A: General. 2020;589:117304.

[44] Coleman LJI, Epling W, Hudgins RR, Croiset E. Ni/Mg–Al mixed oxide catalyst for the steam reforming of ethanol. Applied Catalysis A: General. 2009;363:52-63.

[45] Liu C, Zhao Z, Yang X, Ye X, Wu Y. Superconductor mixed oxides La2–SrCuO4 ±λ for catalytic hydroxylation of phenol in the liquid–solid phase. Chemical Communications. 1996:1019-20.

[46] Perez-Alonso FJ, Melián-Cabrera I, López Granados M, Kapteijn F, Fierro JLG. Synergy of FexCe1-xO2 mixed oxides for N2O decomposition. Journal of Catalysis. 2006;239:340-6.

[47] Vagia EC, Lemonidou AA. Investigations on the properties of ceria-zirconia-supported Ni and Rh catalysts and their performance in acetic acid steam reforming. Journal of Catalysis. 2010;269:388-96.

[48] García-García FR, Metcalfe IS. Chemical looping dry reforming of methane using mixed oxides of iron and cerium: Operation window. Catalysis Communications. 2021;160:106356.

[49] Schmider D, Maier L, Deutschmann O. Reaction Kinetics of CO and CO2Methanation over Nickel. Industrial and Engineering Chemistry Research. 2021;60:5792-805.

[50] Zhang T, Wang W, Gu F, Xu W, Zhang J, Li Z, et al. Enhancing the low-temperature CO2 methanation over Ni/La-CeO2 catalyst: The effects of surface oxygen vacancy and basic site on the catalytic performance. Applied Catalysis B: Environmental. 2022;312.

[51] Hongmanorom P, Ashok J, Chirawatkul P, Kawi S. Interfacial synergistic catalysis over Ni nanoparticles encapsulated in mesoporous ceria for CO2 methanation. Applied Catalysis B: Environmental. 2021;297.

[52] Hao Z, Shen J, Lin S, Han X, Chang X, Liu J, et al. Decoupling the effect of Ni particle size and surface oxygen deficiencies in CO2 methanation over ceria supported Ni. Applied Catalysis B: Environmental. 2021;286.

[53] Cerdá-Moreno C, Chica A, Keller S, Rautenberg C, Bentrup U. Ni-sepiolite and Ni-todorokite as efficient CO2 methanation catalysts: Mechanistic insight by operando DRIFTS. Applied Catalysis B: Environmental. 2020;264:118546-.

[54] Yang H, Wen X, Yin S, Zhang Y, Wu CE, Xu L, et al. The construction of the Ni/La2O2CO3 nanorods catalysts with enhanced low-temperature CO2 methanation activities. Journal of Industrial and Engineering Chemistry. 2023;128:167-83.

[55] Liu L, Mezari B, Kosinov N, Hensen EJM. Al Promotion of In2O3 for CO2 Hydrogenation to Methanol. ACS Catalysis. 2023;13:15730-45.

[56] Parastaev A, Muravev V, Osta EH, Kimpel TF, Simons JFM, van Hoof AJF, et al. Breaking structure sensitivity in CO2 hydrogenation by tuning metal–oxide interfaces in supported cobalt nanoparticles. Nature Catalysis. 2022;5:1051-60.

[57] Onrubia-Calvo JA, Bermejo-López A, Pérez-Vázquez S, Pereda-Ayo B, González-Marcos JA, González-Velasco JR. Applicability of LaNiO3-derived catalysts as dual function materials for CO2 capture and in-situ conversion to methane. Fuel. 2022;320:123842.

[58] Brockner W, Ehrhardt C, Gjikaj M. Thermal decomposition of nickel nitrate hexahydrate, Ni(NO3)2·6H2O, in comparison to Co(NO3)2·6H2O and Ca(NO3)2·4H2O. Thermochimica Acta. 2007;456:64-8.

[59] Zeng X, Zhang L, Zhao G, Xu J, Hang Y, Pang H, et al. Crystal growth and optical properties of LaAlO3 and Ce-doped LaAlO3 single crystals. Journal of Crystal Growth. 2004;271:319-24.

[60] Gibert M, Zubko P, Scherwitzl R, Íñiguez J, Triscone J-M. Exchange bias in LaNiO3–LaMnO3 superlattices. Nature Materials. 2012;11:195-8.

[61] Oliveira ÂAS, Medeiros RLBA, Figueredo GP, Macedo HP, Braga RM, Maziviero FV, et al. One-step synthesis of LaNiO3 with chitosan for dry reforming of methane. International Journal of Hydrogen Energy. 2018;43:9696-704.

[62] Torrez-Herrera JJ, Korili SA, Gil A. Effect of the synthesis method on the morphology, textural properties and catalytic performance of La-hexaaluminates in the dry reforming of methane. Journal of Environmental Chemical Engineering. 2021;9:105298-.

[63] Li K, Chang X, Pei C, Li X, Chen S, Zhang X, et al. Ordered mesoporous Ni/La2O3 catalysts with interfacial synergism towards CO2 activation in dry reforming of methane. Applied Catalysis B: Environmental. 2019;259:118092.

[64] Rytter E, Borg Ø, Enger BC, Holmen A. α-alumina as catalyst support in Co Fischer-Tropsch synthesis and the effect of added water; encompassing transient effects. Journal of Catalysis. 2019;373:13-24.

[65] da Costa-Serra JF, Cerdá-Moreno C, Chica A. Zeolite-Supported Ni Catalysts for CO2 Methanation: Effect of Zeolite Structure and Si/Al Ratio. Applied Sciences2020.

[66] Yuan X, Pu T, Gu M, Zhu M, Xu J. Strong Metal-Support Interactions between Nickel and Iron Oxide during CO2Hydrogenation. ACS Catalysis. 2021;11:11966-72.

[67] Mosinska M, Maniukiewicz W, Szynkowska-Jozwik MI, Mierczynski P. Influence of NiO/La2O3 Catalyst Preparation Method on Its Reactivity in the Oxy-Steam Reforming of LNG Process. Catalysts2021.

[68] Kalantar-zadeh K, Ou JZ, Daeneke T, Mitchell A, Sasaki T, Fuhrer MS. Two dimensional and layered transition metal oxides. Applied Materials Today. 2016;5:73-89.

[69] Singha RK, Shukla A, Yadav A, Sivakumar Konathala LN, Bal R. Effect of metal-support interaction on activity and stability of Ni-CeO2 catalyst for partial oxidation of methane. Applied Catalysis B: Environmental. 2017;202:473-88.

[70] Nair MM, Kaliaguine S, Kleitz F. Nanocast LaNiO3 Perovskites as Precursors for the Preparation of Coke-Resistant Dry Reforming Catalysts. ACS Catalysis. 2014;4:3837-46.

[71] Chen M, Wang C, Wang Y, Tang Z, Yang Z, Zhang H, et al. Hydrogen production from ethanol steam reforming: Effect of Ce content on catalytic performance of Co/Sepiolite catalyst. Fuel. 2019;247:344-55.

[72] Liu B, Li C, Zhang G, Yao X, Chuang SSC, Li Z. Oxygen Vacancy Promoting Dimethyl Carbonate Synthesis from CO2 and Methanol over Zr-Doped CeO2 Nanorods. ACS Catalysis. 2018;8:10446-56.

[73] Zhao H, Zhang W, Song H, Zhao J, Yang J, Yan L, et al. Highly coke-resistant Ni-La2O2CO3 catalyst with low Ni loading for dry reforming of methane with carbon dioxide. Catalysis Today. 2022;402:189-201.

[74] Li X, Li D, Tian H, Zeng L, Zhao Z-J, Gong J. Dry reforming of methane over Ni/La2O3 nanorod catalysts with stabilized Ni nanoparticles. Applied Catalysis B: Environmental. 2017;202:683-94.

[75] Montero C, Ochoa A, Castaño P, Bilbao J, Gayubo AG. Monitoring Ni0 and coke evolution during the deactivation of a Ni/La2O3–αAl2O3 catalyst in ethanol steam reforming in a fluidized bed. Journal of Catalysis. 2015;331:181-92.

[76] Han F, Liu Q, Li D, Ouyang J. An emerging and high-performance sepiolite-supported Ni catalyst for low-temperature CO2 methanation: The critical role of hydroxyl groups. Journal of Environmental Chemical Engineering. 2023;11:110331.

[77] Sun C, Świrk Da Costa K, Wang Y, Li L, Fabbiani M, Hulea V, et al. Unraveling catalytic properties by yttrium promotion on mesoporous SBA-16 supported nickel catalysts towards CO2 methanation. Fuel. 2022;317:122829.

[78] Ahmad KN, Samidin S, Rosli MI, Yusop MR, Kassim MB, Ayodele BV, et al. Alkaline earth metal modified nickel nanoparticles supported on exfoliated g-C3N4 for atmospheric CO2 methanation. Journal of Environmental Chemical Engineering. 2023;11:111109.

[79] Rabelo-Neto RC, Almeida MP, Silveira EB, Ayala M, Watson CD, Villarreal J, et al. CO2 hydrogenation: Selectivity control of CO versus CH4 achieved using Na doping over Ru/m-ZrO2 at low pressure. Applied Catalysis B: Environmental. 2022;315:121533.

[80] Bermejo-López A, Pereda-Ayo B, Onrubia-Calvo JA, González-Marcos JA, González-Velasco JR. Boosting dual function material Ni-Na/Al2O3 in the CO2 adsorption and hydrogenation to CH4: Joint presence of Na/Ca and Ru incorporation. Journal of Environmental Chemical Engineering. 2023;11:109401.

[81] Fan WK, Tahir M. Recent trends in developments of active metals and heterogenous materials for catalytic CO2hydrogenation to renewable methane: A review. Journal of Environmental Chemical Engineering. 2021;9.

[82] Italiano C, Llorca J, Pino L, Ferraro M, Antonucci V, Vita A. CO and CO2 methanation over Ni catalysts supported on CeO2, Al2O3 and Y2O3 oxides. Applied Catalysis B: Environmental. 2020;264:118494.

[83] Cárdenas-Arenas A, Quindimil A, Davó-Quiñonero A, Bailón-García E, Lozano-Castelló D, De-La-Torre U, et al. Isotopic and in situ DRIFTS study of the CO2 methanation mechanism using Ni/CeO2 and Ni/Al2O3 catalysts. Applied Catalysis B: Environmental. 2020;265:118538.

[84] Lorber K, Zavašnik J, Arčon I, Huš M, Teržan J, Likozar B, et al. CO2 Activation over Nanoshaped CeO2 Decorated with Nickel for Low-Temperature Methane Dry Reforming. ACS Applied Materials & Interfaces. 2022;14:31862-78.

[85] Li T, Dong M, Xu J, Zhang T, Sun Y, Li N, et al. Exploring the Promotion of γ-Al2O3 on Pd/CeO2-Catalyzed Low-Concentration Methane Oxidation Using Operando DRIFTS-MS. ChemCatChem. 2023;15:e202300194.

[86] Quindimil A, Onrubia-Calvo JA, Davó-Quiñonero A, Bermejo-López A, Bailón-García E, Pereda-Ayo B, et al. Intrinsic kinetics of CO2 methanation on low-loaded Ni/Al2O3 catalyst: Mechanism, model discrimination and parameter estimation. Journal of CO2 Utilization. 2022;57:101888.

[87] Varvoutis G, Lykaki M, Stefa S, Binas V, Marnellos GE, Konsolakis M. Deciphering the role of Ni particle size and nickel-ceria interfacial perimeter in the low-temperature CO2 methanation reaction over remarkably active Ni/CeO2 nanorods. Applied Catalysis B: Environmental. 2021;297:120401.

Chapter 6

Sepiolite-based catalysts

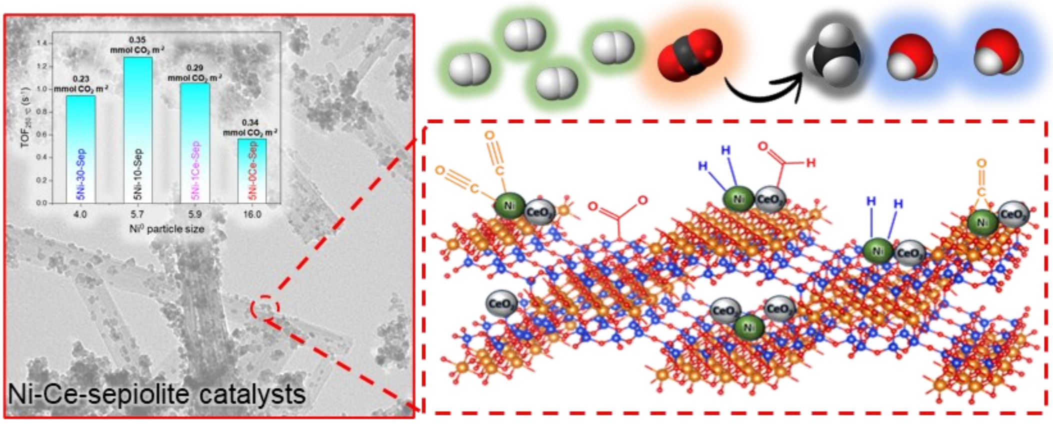

This chapter was adapted from the following manuscript:

Machado-Silva, R. B.; Kosinov, N.; Hensen, E. J. M.; Chica, A.; Operando IR spectroscopy and multi-technique characterization of ceria-nickel-based catalysts supported on sepiolite for the CO_2 methanation reaction. (Under review).

6.1 – Introduction

Clays are a group of naturally occurring materials that are abundantly found in the Earth's crust, with the most significant being kaolinite, illite, chlorite, smectite, vermiculite, palygorskite, and sepiolite [1]. Structurally, these materials are composed of layers of tetrahedral and octahedral sheets, and they can be classified as either 1:1 type, consisting of two layers, or 2:1 type, consisting of three layers [1]. Specifically, sepiolite contains tetrahedral sheets that contain Si and octahedral layers composed of Mg. These sheets are arranged to form the structural units of sepiolite, which comprise an octahedral layer between two tetrahedral layers. For this reason, sepiolite is typically categorized within the 2:1 phyllosilicate group [2-4].

However, this material exhibits the peculiarity that the octahedral layer is discontinuous, as once every six Si tetrahedra, an inversion of the tetrahedron takes place through Si-O-Si bonds (**Figure 6.1**). Consequently, at the junction of two structural units, the adjacent Si tetrahedra of both structural units are oriented in opposite directions [2-4]. This inversion of the Si tetrahedra also leads to the formation of channels or tunnels with dimensions of 10.6 x 3.7 Å along the longitudinal axis of the sepiolite fiber [5].

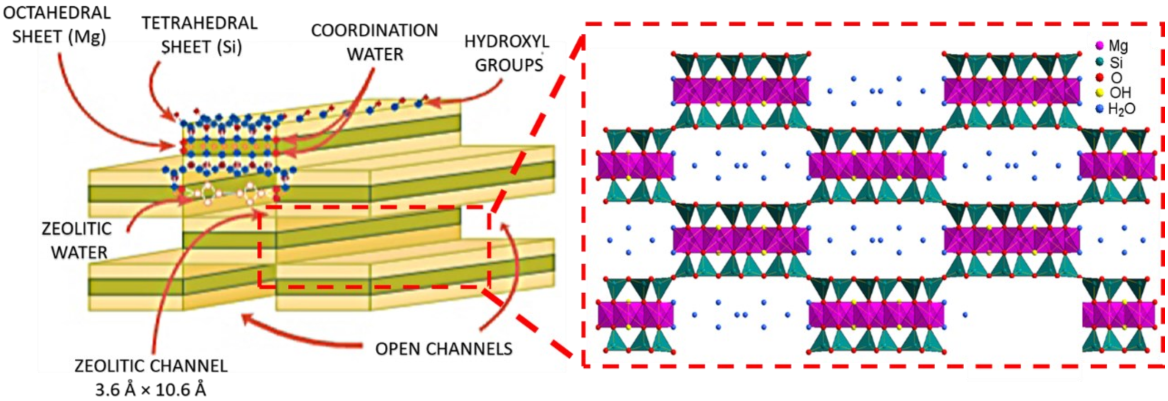

Figure 6.1. Schematic representation of the sepiolite structure, consisting of blocks formed by a Mg-containing octahedral layer, sandwiched between Si-containing tetrahedral layers. These blocks create channels or tunnels that are occupied by zeolitic water. Image adapted from Tadiello et al. [6].

Considering the structure of this material, three types of water can be distinguished based on their location: (i) zeolitic water contained within the channels, (ii) coordinated water bound to the terminal Mg atoms, and (iii) structural water associated with the OH- groups of the octahedral layers [4]. These three types of water are reflected in the theoretical formula of sepiolite, $Si_{12}O_{30}Mg_8(OH)_4(H_2O)_4\cdot nH_2O$, as reported by Bukas et al. [2]. Once this clay is naturally occurring, it may exhibit significant variations in chemical composition and properties depending on the conditions under which it was formed, such as the presence of dopant metals, such as iron and aluminum [3].

Sepiolite can also present high surface area values, which is a consequence of not only its channel structure but also due to its fibrous morphology and the reduced size of its particles. This aluminosilicate presents a hierarchical structure in which macropores, mesopores, and micropores can be found due to the hollow space between the fibers, as described in **Figure 6.2**. Due to this, sepiolites with surface area values as high as 500 $m^2 g^{-1}$ have been described, even though the specific area will depend on the material's origin [3].

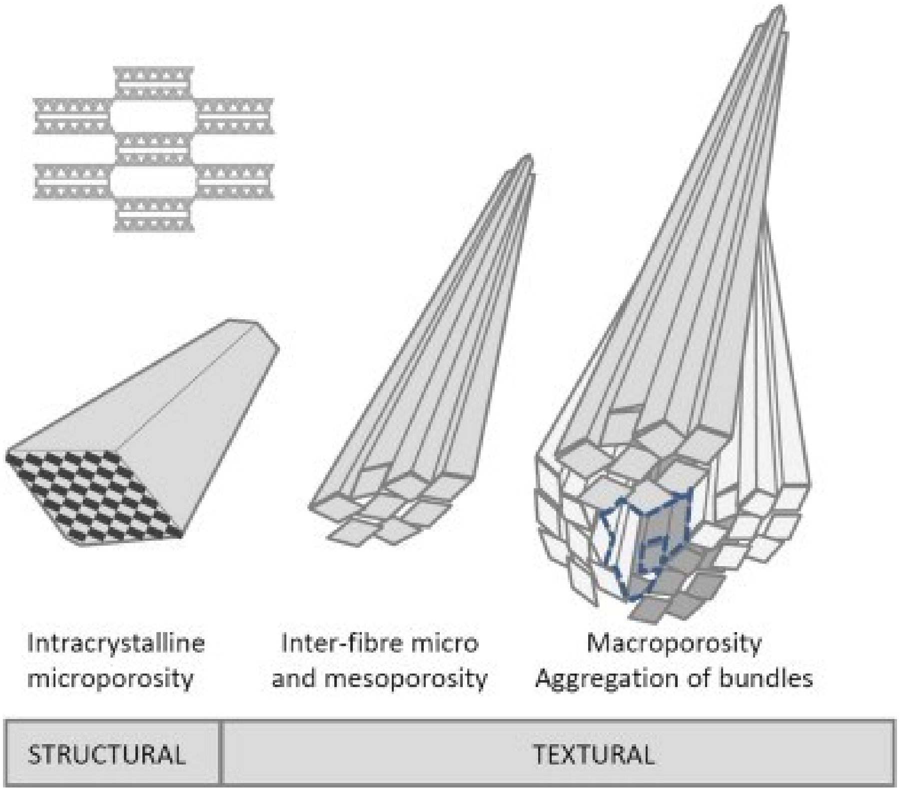

Figure 6.2. Hierarchical porous structure of sepiolite, in which macropores, mesopores and micropores can be detected. Image adapted from Suárez et al. [3].

Taken together, these structural, morphological, and textural characteristics make this material an attractive alternative for a wide range of applications that can be categorized into three groups: sorption, rheological, and catalytic [5, 7]. The primary characteristic of sepiolite is its high specific surface area, providing a significant adsorption capacity, either through direct application or after pretreatment. This material has been used for the removal of heavy metals such as Cd, Zn, and Pb from contaminated soils [8-10] and in the treatment of wastewater from various industries, including the wine and textile industries [11-13], as well as in water contaminated with herbicides, pesticides, or surfactants [14-17].

Apart from the ion sorption capability, sepiolite has already revealed that it presents high CO_2 sorption capability due to its basic properties, which makes it a potential material for the development of CO_2 methanation catalysts [18]. This material was employed for CO_2 capture, either directly or in combination with amines, such as DETA (diethylenetriamine), PEI (polyethyleneimine), or APTES (triethoxysilane) [19-21].

Cecilia et al. compared the CO_2 adsorption capacity of sepiolite with that of a similar clay, palygorskite, and reported that at 25 °C and 760 mm Hg, sepiolite exhibited a higher CO_2 adsorption capacity (1.48 mmol/g compared to 0.41 mmol/g), which was explained by the larger channels found in sepiolite [19]. The combined incorporation of APTES and PEI yielded the best results in this study, achieving an even higher CO_2 adsorption capacity (2.07 mmol/g, at 65 °C and 760 mm Hg).

Regarding its rheological applications, its ability to increase viscosity, stabilize suspensions, and form gels is utilized in applications such as oil drilling fluids, paints, cosmetics, sealants, and pharmaceuticals [22]. Sepiolite is especially effective in maintaining stability under extreme conditions, including high temperatures and salinity, opening the way for its use in environmental and agricultural sectors, such as wastewater treatment, soil stabilization, and pesticide suspension [23, 24]. Its versatility also extends to food products, ensuring consistent texture and preventing phase separation [25].

In addition to all the described applications, focusing on the applications regarding this work, sepiolite was also utilized as a catalyst or catalyst support in various chemical reactions. Its high specific surface area, channel system, and chemical composition make this material suitable as metal support.

Shimizu et al., for example, prepared Pd-based catalysts supported on sepiolite for the Suzuki reaction and compared its activity with other reference materials, such as SiO_2 and C [26]. Their results revealed that the sepiolite-based catalyst was the most stable, which was attributed to the strongest metal-support interaction between Pd^{II} species and the support and ensured catalyst reuse without leaching and loss of activity.

Additionally, Ma et al. studied Pt-based catalysts supported on sepiolite for formaldehyde oxidation and concluded that sepiolite allowed for good distribution of Pt nanoparticles, with sizes ranging between 2 and 4 nm [27]. Specifically, the catalyst with 1% wt. Pt yielded the best results and maintained good performance even after seven cycles of use. The favorable results for activity and stability were attributed to the synergistic effect between the OH groups of sepiolite and the high dispersion of Pt nanoparticles [28].

Moreover, this material has been employed in other reactions, such as the hydrogenation of organic molecules [28-32], the transesterification of glycerol and bio-oil [33, 34], pyrolysis of biomass [35, 36], NH_3-SCR [37], and Guerbet condensation [38].

Concerning the CO_2 methanation reaction, studies utilizing sepiolite are limited. In several works, Luo et al. investigated the effect of adding different metals to Ni or Ru catalysts, and the results led to improvement rates between 31.9% to 60.6% at 300 °C [39-41]. Laitao et al.

analyzed the addition of Sm as a promoter into Ni-based catalysts by XPS and concluded that Sm not only improved the dispersion of the Ni^0 phase but also increased the electronic density in the Ni phase [42]. Consequently, this strengthened the Ni-C bond and weakened the C-O, contributing to an increase in the CO_2 dissociation and increasing the yield to CH_4.

Liu et al. studied Ru-based catalysts on sepiolite and explored the effect of adding different promoters, such as Mn, Mo, Co, Cu, and Zr [39]. They note that some of them, such as Mo, shift the CO_2-TPD profiles to lower temperatures, while adding Cu causes the opposite effect, shifting the profiles to higher temperatures. Thus, they associate the improved activity observed with Mn, Mo, and Co with enhanced CO_2 mobility or desorption on the surface of the Ru catalyst supported on sepiolite [50].

In another study, Luo et al. [49], also using Ru-based catalysts, concluded that the best results are obtained by adding Mo, which led to an improvement of the dispersion and the number of active sites of the Ru^0 phase, and an improved resistance to poisoning by CS_2 [41]. Furthermore, in another study, the Y addition in a Ru-based catalyst on sepiolite resulted in increased activity and resistance to CS_2, as the yttria phase also improved the dispersion and reduction properties of the Ru^0 phase [40].

Furthermore, in a recent study published by our research group, Cerdá-Moreno et al. in an operando FT-IR spectroscopic study, reported that for a Ni-sepiolite catalyst, the reaction mechanism followed a dissociative mechanism, with Ni^0-CO species acting as the main reaction intermediates [43].

Due to the versatility offered by its unique structure, high specific surface area, natural origin, low cost, and high availability (with Spain being one of the world's leading producers of sepiolite), this material has been chosen for the present work as a support for the preparation of Ni-based catalysts for the CO_2 methanation reaction.

In summary, sepiolite has a wide range of applications, including its use in the synthesis of catalysts for CO_2 methanation. However, they do not conduct an in-depth analysis of the direct role of sepiolite as a support in the reaction mechanism. Additionally, there is a notable gap in the literature regarding studies that perform an operando spectroscopic analysis of the combined effect of the addition of a promoter to a Ni-sepiolite catalyst, which serves as a motivation for the study presented in this work.

In this work, delving deeper into the results published by our research group [43], Ce was added as a promoter to a Ni-sepiolite system. This was motivated by its capability to increase the reducibility and dispersion of the metallic phase and increase the system basicity, two critical properties involved in the mechanism of the CO_2 methanation reaction.

This way, catalysts with different Ni (ranging from 5% wt. to 20% wt.) and Ce loading (ranging from 0% wt. to 30% wt.) were tested to find the optimum composition to maximize CO_2

conversion and selectivity to CH_4. The catalysts were studied by different characterization techniques (H_2-chemisorption, TEM-SEM, CO_2-TPD-MS, XRD, N_2-adsorption) and a time-resolved operando FT-IR spectroscopy study.

This way, the objective of these crossed analyses was to observe the effect of Ce addition in the Ni^0 phase dispersion and intermediate basic sites concentration and the impact of the promoter's addition in forming reaction intermediates.

Finally, after identifying the optimum Ce loading, the Ni loading was also optimized to find the catalyst with optimum composition to maximize the yield to CH_4, and eventually also be tested for the biogas upgrade tests, as it will be discussed in Chapter 7.

More information was provided in Chapter 3 about preparing the catalysts used in this chapter, and their description is summarized in **Table 6.1**. The notation "_R" after the catalyst name indicates it was previously reduced.

Table 6.1. Denomination is employed in this chapter for the sepiolite-based catalysts. The number preceding the elements Ni and Ce refers to the nominal loading values established during their preparation.

5Ni-0Ce-Sep	5% wt. Ni and no Ce addition
5Ni-1Ce-Sep	5% wt. Ni and 1% wt. Ce
5Ni-10Ce-Sep	5% wt. Ni and 10% wt. Ce
5Ni-30Ce-Sep	5% wt. Ni and 30% wt. Ce
10Ni-10Ce-Sep	10% wt. Ni and 10% wt. Ce
15Ni-10Ce-Sep	15% wt. Ni and 10% wt. Ce
20Ni-10Ce-Sep	20% wt. Ni and 10% wt. Ce

6.2 – Characterization results

First of all, regarding the composition of the prepared catalysts, the ICP results of calcined catalysts (**Table 6.2**) reveal that Ni and Ce weight content values are close to the nominal one assumed during preparation, suggesting that all nickel and cerium were incorporated into the support.

The Si/Mg content ratio is kept upon the incorporation of Ni and Ce, which strongly suggests that these sepiolite-composing elements are not lost after incorporating Ni and Ce phases.

DRX results of the sepiolite support (JCPDS 00-013-0595) and the nickel-ceria calcined materials (**Figure 6.3** and **Figure 6.4**) reveal that the peak at $2\theta = 7.3°$, attributed to (110) crystalline plane, is maintained after Ni incorporation [44].

When Ni is not incorporated into the support and sepiolite is calcined, the peak at $2\theta = 7.3°$ significantly decreases in intensity, giving rise instead to peaks at $2\theta = 8.6°$ and $2\theta = 10.9°$.

This shift is attributed to a modification of the sepiolite crystalline structure to the sepiolite dihydrate phase due to the loss of water molecules from the channel framework during the calcination step [4, 45].

Table 6.2. Elemental weight percentage for nickel and cerium, and Mg/Si atomic ratio for nickel-ceria-sepiolite materials.

Sample	Ni load. (% wt.)[a]	Ce load. (% wt.)[a]	Mg/Si atomic ratio
Sep	-	-	1.3
5Ni-0Ce-Sep	5.5	-	1.4
5Ni-1Ce-Sep	5.6	1.3	1.4
5Ni-10Ce-Sep	5.0	9.8	1.4
5Ni-30Ce-Sep	5.2	29.4	1.4
10Ni-10Ce-Sep	10.6	9.6	1.4
15Ni-10Ce-Sep	15.6	9.4	1.4
20Ni-10Ce-Sep	20.9	9.8	1.4

Post et al., working with synchrotron powder X-ray diffraction with Rietveld treatment, confirmed this phenomenon and attributed this to a modification of the coordination sphere of the Mg ions due to the removal of water molecules [44], as seen in **Figure 6.5**.

The higher the cerium content in the samples, the more intense the peaks attributed to CeO_2 ($2\theta = 28.7°$, 33.3°, 47.8°, and 56.8°) (JCPDS 03-065-5923) [46]. In the samples where the Ce content is kept the same, the higher the Ni content, the more intense the NiO phase peaks ($2\theta = 37.40°$, 43.46°, and 63.24°) (JCPDS 00-022-1189), which is due to the presence of larger NiO crystallites. In the reduced catalyst, the same trend is observed for Ni^0 crystallite size, which is expected to follow the NiO crystallite trend, following previous results from Singhat et al. [47].

TEM images of the catalysts after the reduction step (**Figure 6.6** through **Figure 6.9**) confirm that the fiber-like structure of sepiolite is maintained after calcination and exposure to H_2, which is consonant with previous works reported by our group [43]. This confirms that even though the cross-sectional area microporous channels is structurally modified during the conversion of the sepiolite phase to sepiolite dihydrate, the structure running along the fibers is well maintained.

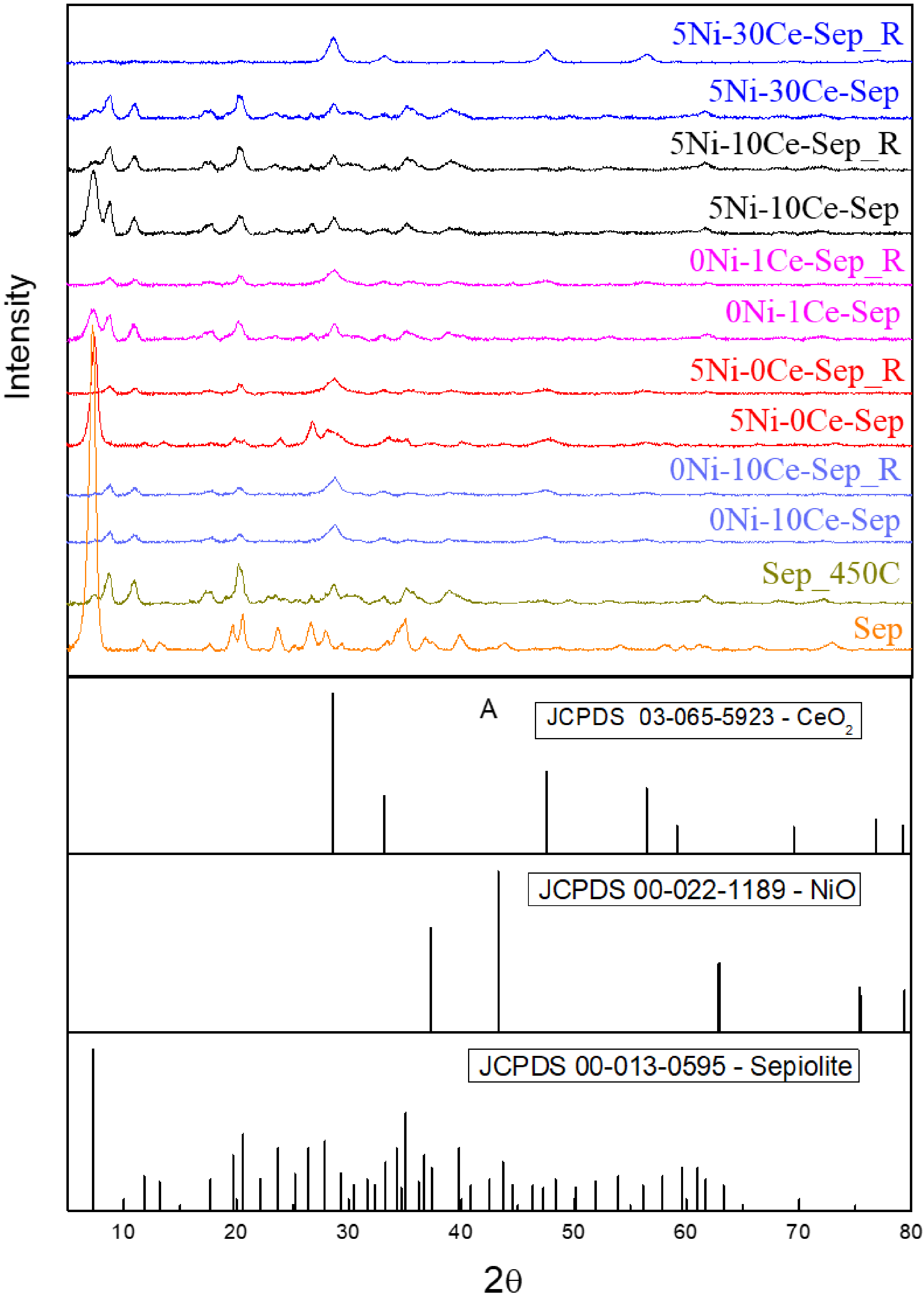

Figure 6.3. XRD patterns of cerium-nickel-sepiolite catalysts, the support and the reference patterns of different phases that make up the catalyst.

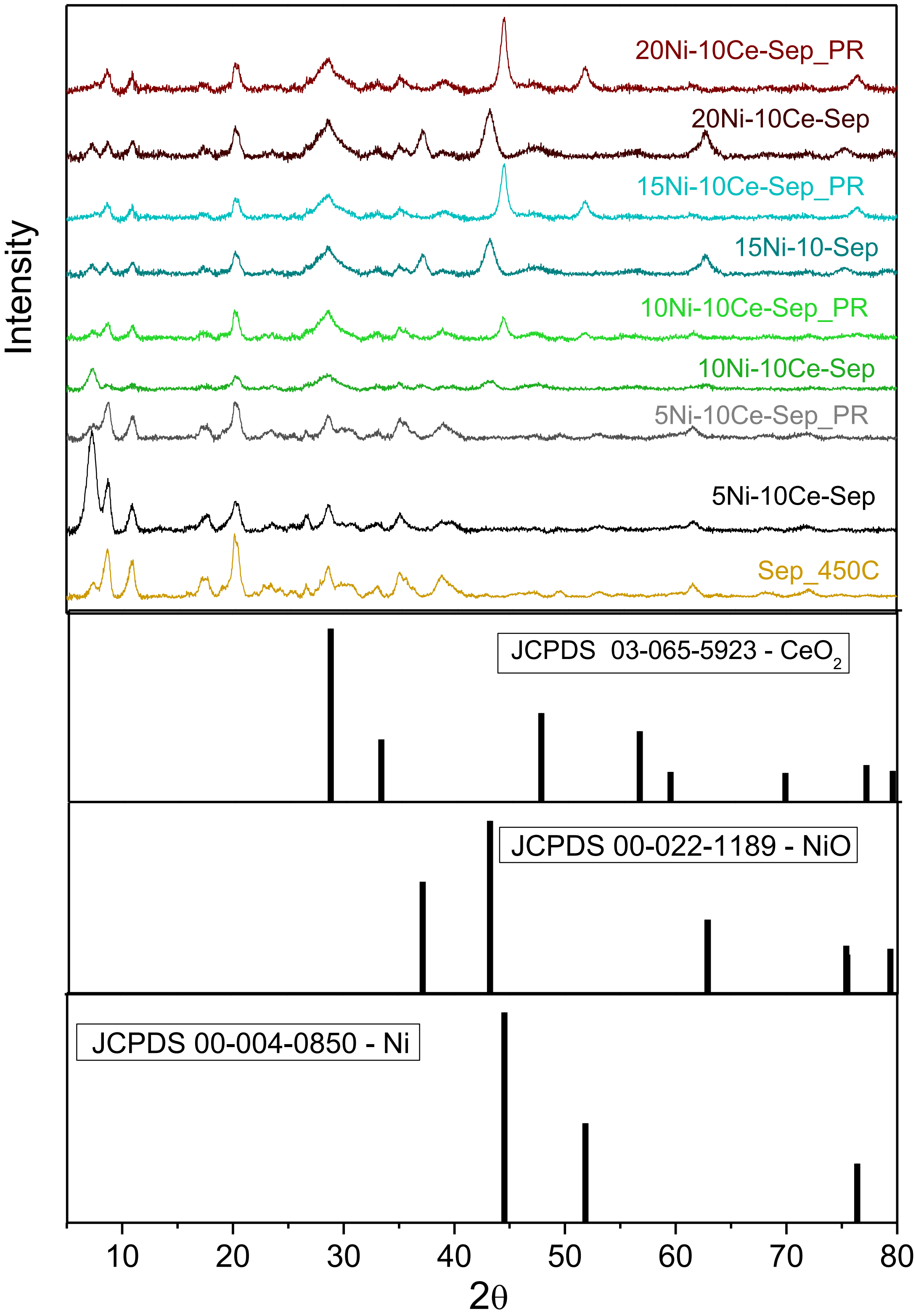

Figure 6.4. XRD patterns of the higher Ni loading cerium-nickel-sepiolite catalysts, the support, and the reference patterns of different phases that make up the catalyst.

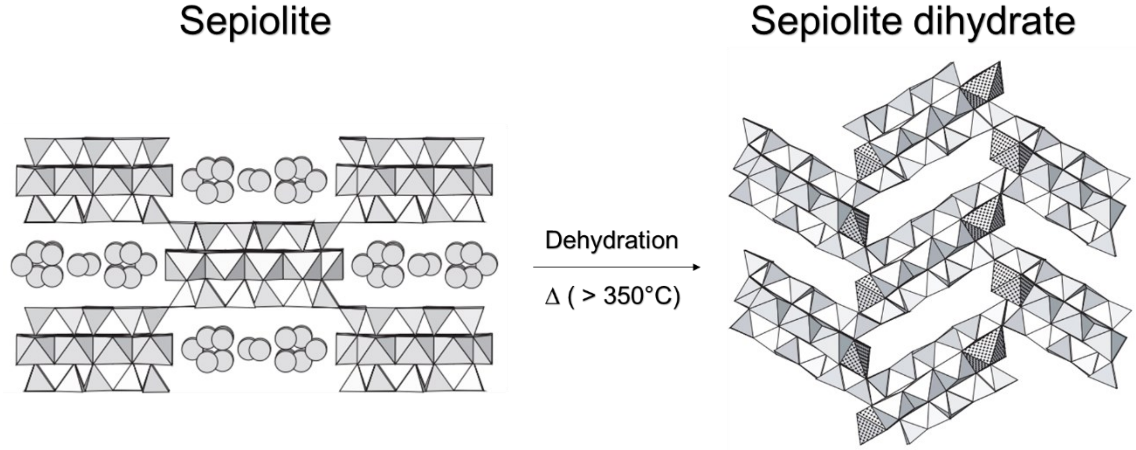

Figure 6.5. Structure of sepiolite and sepiolite dihydrate, the phase of the material that is stable at temperatures above 350 °C, due to the loss of the zeolitic H_2O molecules inside the channels. Gray molecules represent H_2O molecules. Image adapted from Post et al. [44].

Crystalline ceria is confirmed in the higher magnification TEM images, as confirmed the diffraction fringes of the (100) planes [48], confirming the XRD results. Crystalline Ni^0 nanoparticles are also detected, as seen by the fringes formed by diffraction of the (111) Ni^0 planes [49].

Ni^0 nanoparticles are observed with a truncated octahedron shape in which different crystalline facets, corners, and edges are formed (**Figure 6.10**) This is the most thermodynamically stable structure for aggregates of more than 200 atoms for elements with the face-centered cubic (fcc) structure, which is the case of elements like Ni, Cu, Pd, Ag, Pt, and Au [49].

These different spots on the surface of the Ni^0 particles are commonly regarded in the literature as the sites where H_2 disassociates to form Ni-H hydride species [50]. These are the participating species of the hydrogenation of CO_2 at the peripheral zone between the metallic phase and the support, as it will be covered in more depth in the mechanistic and catalytic results section.

Regarding the textural properties, all the samples exhibit type-IV adsorption-desorption isotherms with a type H3 hysteresis loop (**Figure 6.11**), which is typical of mesoporous materials, which are formed by the piling of the sepiolite fibers, as confirmed by the SEM-TEM images. The samples also show a significant microporous volume, which is due to the presence of fine microporous channels that run along sepiolite fibers, as previously reported by Suárez et al. [3].

The textural properties (**Table 6.3**) reveal that when the bare support sepiolite is calcined at 450 °C to form Sep_450C, a decrease in S_{BET} is observed. As previously mentioned, this is rationalized for the drastic decrease of micropore area due to the loss of water molecules and the consequent channel structure modification, as discussed based on the DRX results.

Regarding the effect of Ce addition, for a series of catalysts where the Ni loading is the same, the higher the Ce content, the lower the S_{BET} values. This is attributed to the obstruction of the support microporous framework, as confirmed by the more considerable decrease in the micropore volume, V_{micro}, with increasing cerium content.

For the same Ce content, the higher the Ni loading, the more significant the decrease in S_{BET}. This goes in consonance with previous results from our research group, and it is associated with a combined phenomenon of obstruction of the porous framework and a dilution effect that derives from the deposition of a lower surface area phase over another with a higher surface area [51].

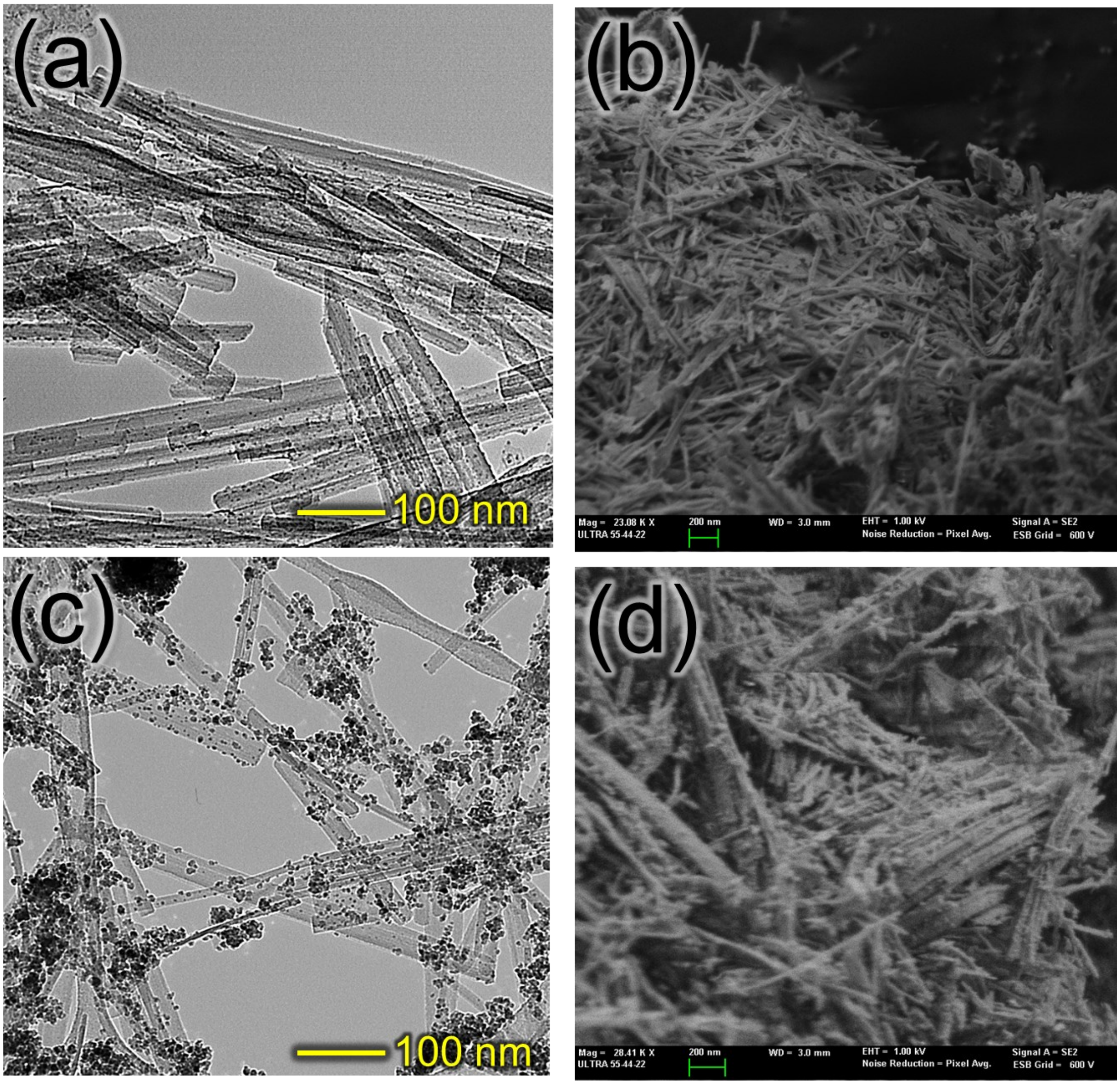

Figure 6.6. TEM-SEM images of the catalysts after the reduction step: 5Ni-0Ce-Sep_R (a-TEM, b-SEM) and 5Ni-1Ce-Sep (c-TEM, d-SEM).

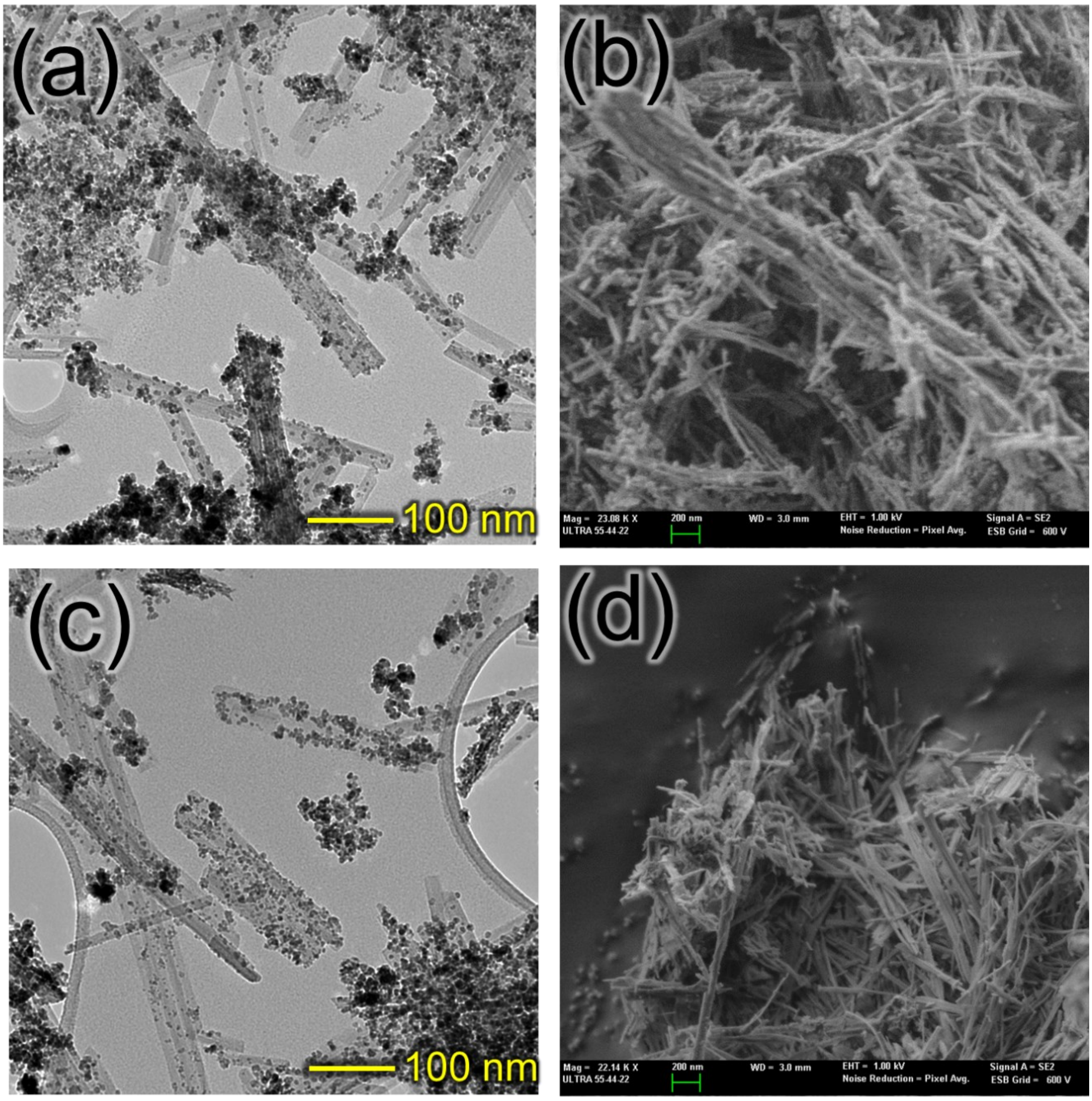

Figure 6.7. TEM-SEM images of the catalysts after the reduction step: 5Ni-10Ce-Sep_R (a-TEM, b-SEM) and 5Ni-30Ce-Sep (c-TEM, d-SEM).

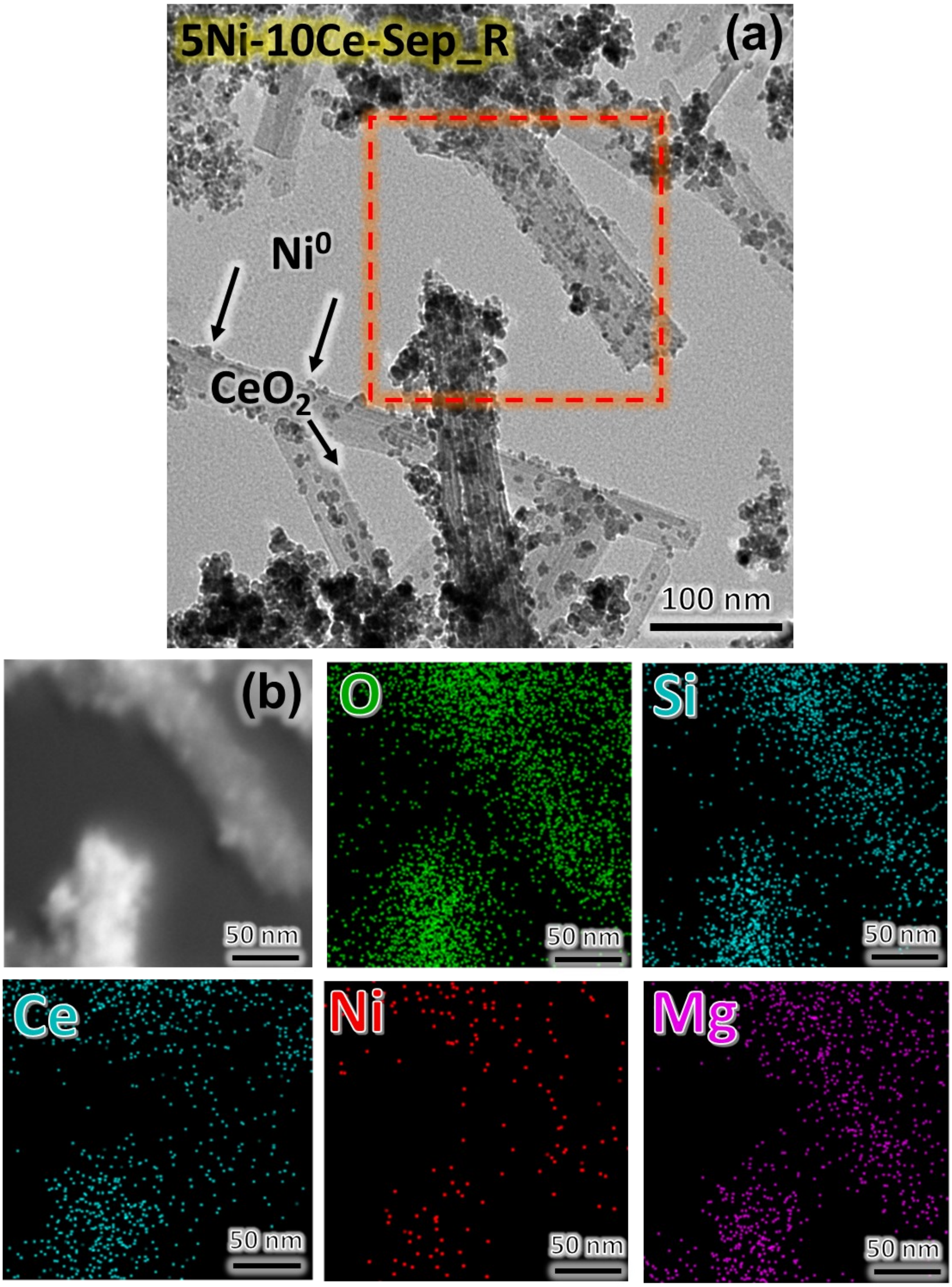

Figure 6.8. (a) bright-field TEM image of the 5Ni-10Ce-Sep_R catalyst after the reduction step and (b) dark field STEM of the highlighted area. EDS mapping of different composing elements was also obtained.

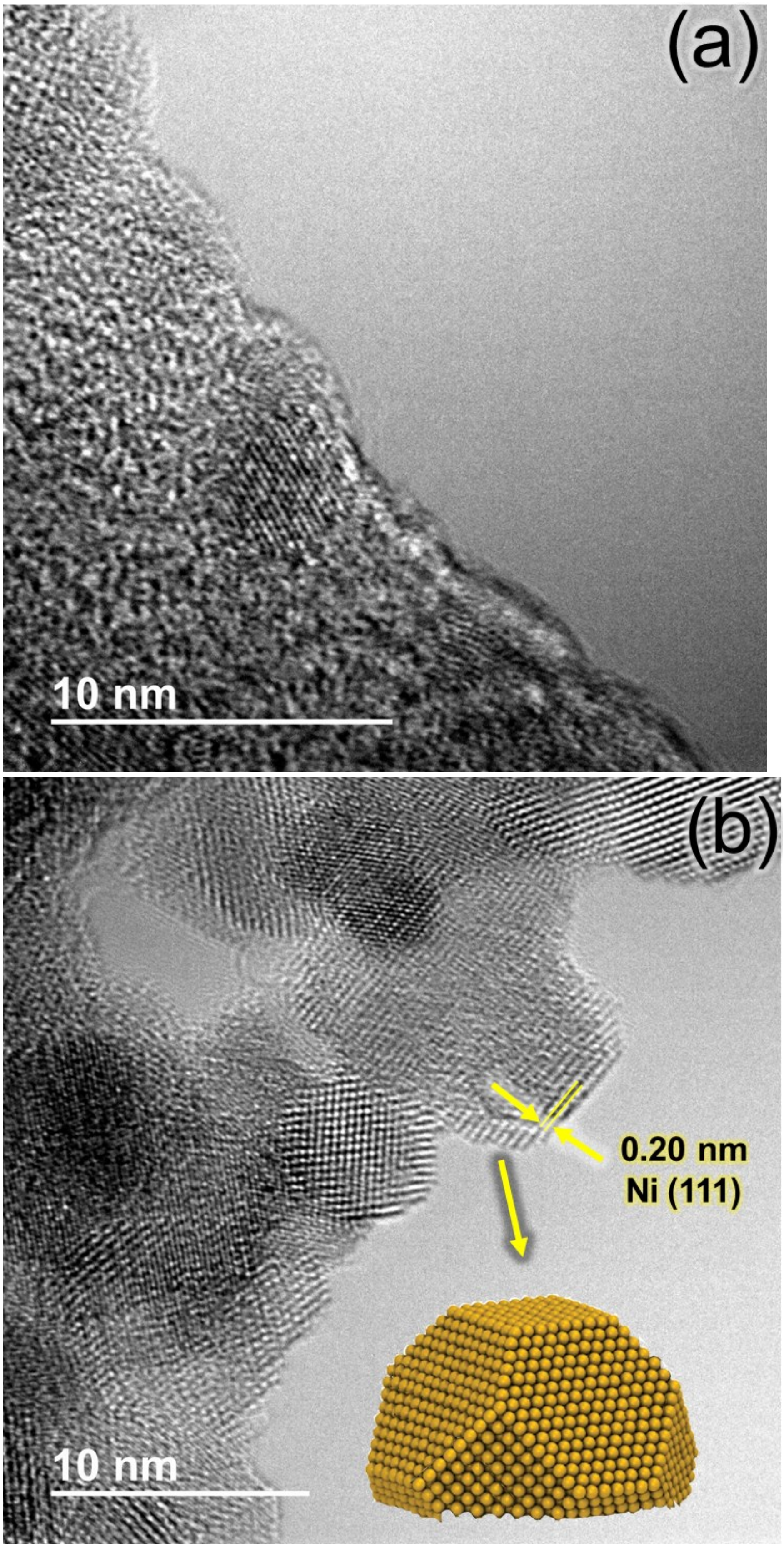
(a)
10 nm
(b)
0.20 nm
Ni (111)
10 nm

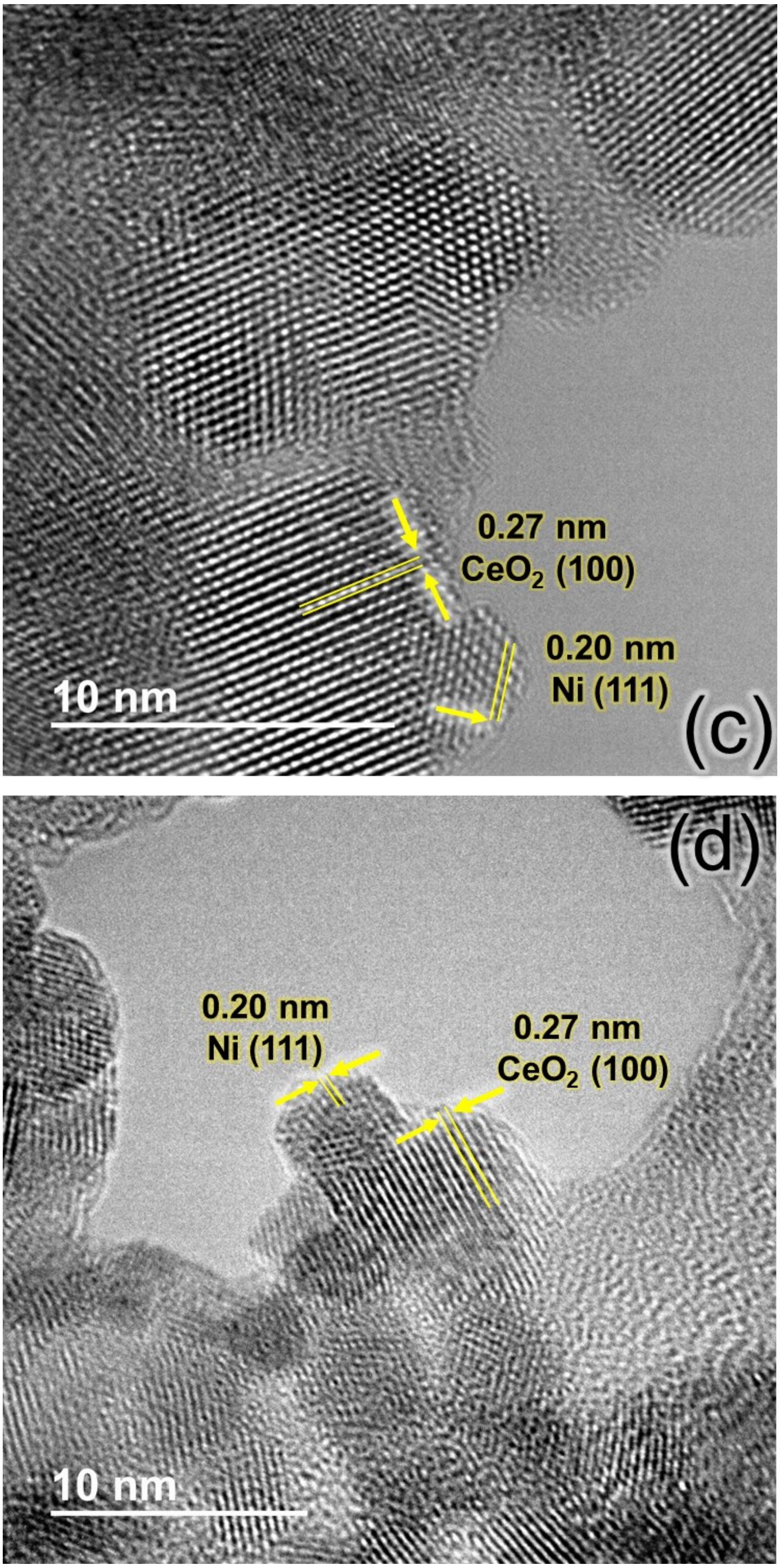

Figure 6.9. Higher magnification TEM image of the catalysts after the reduction step: (a) 5Ni-0Ce-Sep_R; (b) 5Ni-1Ce-Sep_R; (c) 5Ni-10Ce-Sep_R; 5Ni-30Ce-Sep_R.

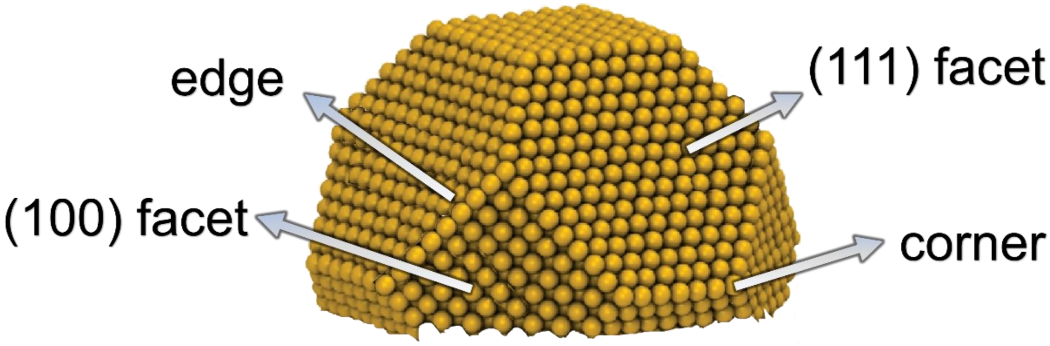

Figure 6.10. Structure of a partially truncated octahedron, observed for the Ni^0 nanoparticles, highlighting some geometrical elements of interest. Image adapted from Rana et al. [49].

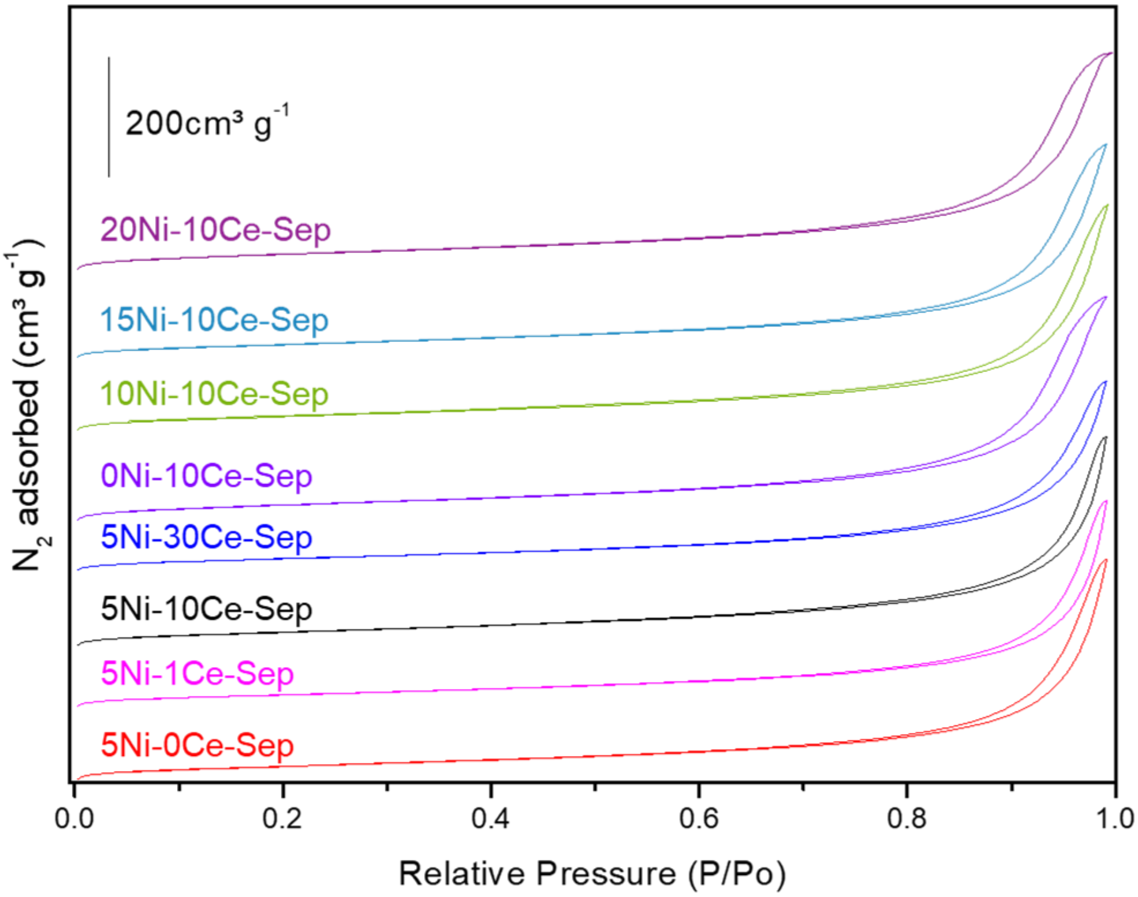

Figure 6.11. N_2 adsorption-desoprtion isotherms for the nickel-ceria-sepiolite calcined catalysts.

Table 6.3. Textural properties of ceria-nickel sepiolite catalysts: BET surface area, S_{BET}, t-plot micropore area, S_{micro}, t-plot external surface area, S_{ext}, and t-plot micropore volume, V_{micro}.

Sample	S_{BET} (m^2/g)	S_{ext} (m^2/g)	S_{micro} (m^2/g)	V_{micro} (cm^3/g)
Sep	471	210	261	0.127
Sep450C	151	124	27	0.012
0Ni-10CeO$_2$-Sep	158	136	22	0.009
5Ni-0CeO$_2$-Sep	148	123	25	0.012
5Ni-1CeO$_2$-Sep	147	127	20	0.009
5Ni-10CeO$_2$-Sep	129	116	13	0.005
5Ni-30CeO$_2$-Sep	121	112	9	0.004
10Ni-10CeO$_2$-Sep	125	113	12	0.004
15Ni-10CeO$_2$-Sep	120	108	12	0.004
20Ni-10CeO$_2$-Sep	118	107	11	0.004

H_2-TPR results reveal that Ce addition decreases the temperature in which the Ni reduction events take place (**Figure 6.12a**). First of all, in the Ni-free sample, two peaks, centered at 577 and 839 °C, are observed, which are associated with the formation of surface and bulk oxygen vacancies in the CeO_2 phase, respectively [52].

In the cerium-free sample, 5Ni-0Ce-Sep, a peak referring to the reduction of the NiO phase is observed centered at 493 °C, as previously reported in the works of our group [53].

This NiO reduction peak is shifted to lower temperatures in the cerium-containing samples. The higher the Ce loading, the more peaks are observed, which is attributed to the higher dispersion of the Ni phase, as it will be confirmed by the H_2-chemisorption results. The peaks are centered in different temperatures due to different SMSI strengths between NiO and the sepiolite and CeO_2 phases, which gives rise to different energy costs to reduce the NiO phase to Ni [54].

The decrease in temperature in which the reduction events occur is also attributed to the presence of oxygen vacancies present in the CeO_2 phase, which is in direct contact with the NiO one. As previously described by Puigdollers et al.[55], these vacancies on the NiO-CeO_2 boundary decrease the thermodynamical cost of removing an oxygen atom from the NiO phase due to the extra anionic mobility.

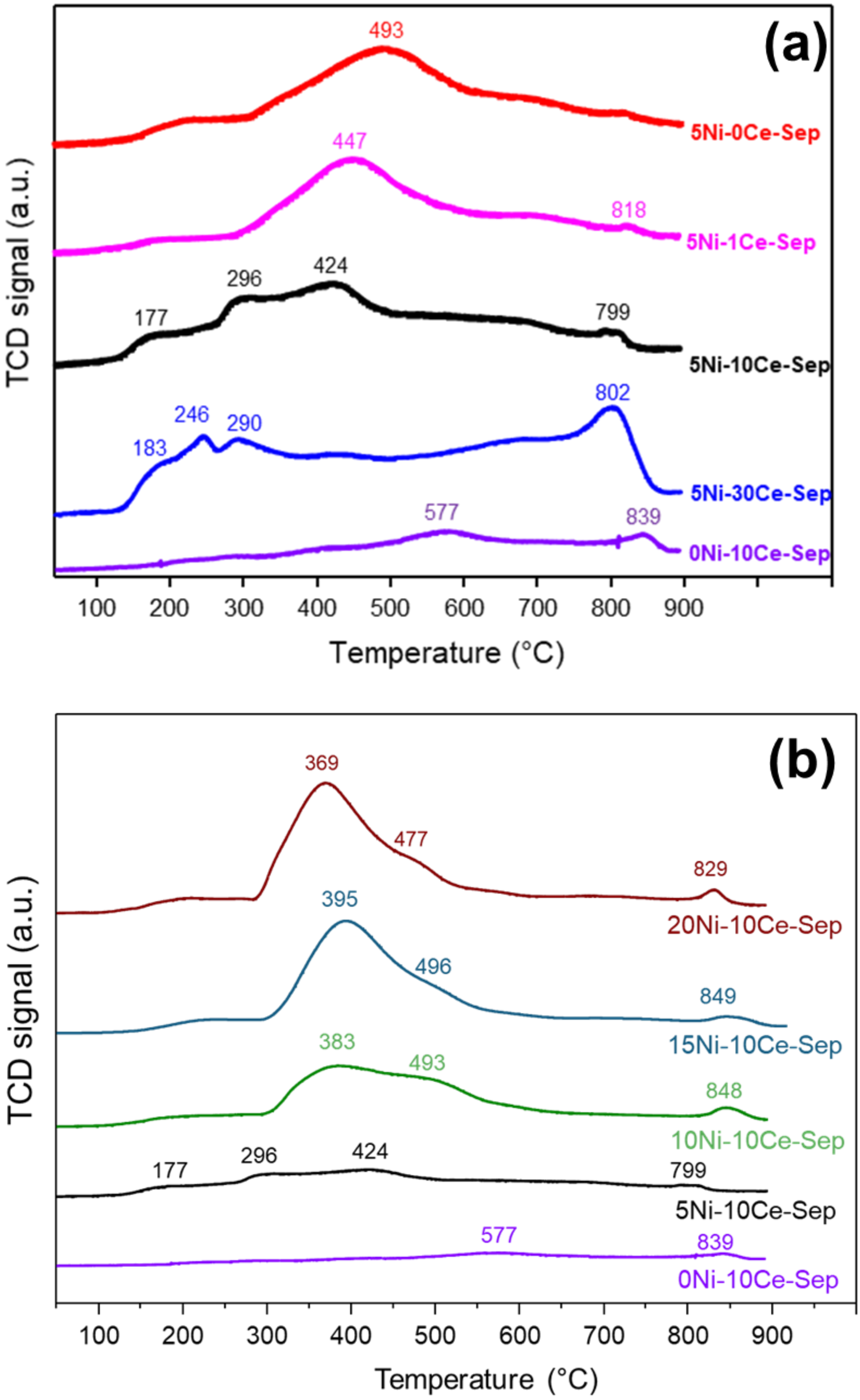

Figure 6.12. H_2-TPR profiles between 50 °C and 900 °C for the series of nickel-ceria catalysts supported over sepiolite.

Regarding the effect of Ni loading in the H_2-TPR profiles (**Figure 6.12**b), it is observed that the higher the Ni loading, the more prominent the peaks in the 350 – 500 °C range, with the observance of two overlapped peaks. This profile has been previously described in the works of our research group and refers to the reduction of surface and bulk NiO phase, with the surface NiO taking place at lower temperatures, as previously described by Machado-Silva [54].

H_2-chemisorption data (**Table 6.4**) provides information about the Ni^0 phase in the catalyst after the reduction step. First, for the 5% wt. Ni catalysts, the results reveal that the higher the Ce content, the higher the metallic dispersion of the Ni^0, which aligns with the H_2-TPR results previously mentioned.

Table 6.4. H_2-chemisorption data for nickel-ceria-based catalysts: metallic dispersion, active metal surface area, S_{Ni}, Ni^0 average particle size, D_{Ni}, and molar H_2 monolayer uptake.

Catalyst	Dispersion (%)	S_{Ni} (m²/g)	D_{Ni} (nm)	H_2 uptake (µmol g^{-1})
5Ni-0Ce-Sep	6.3	2.1	16.0	26.8
5Ni-1Ce-Sep	16.9	5.6	5.9	72.1
5Ni-10Ce-Sep	17.7	5.9	5.7	75.6
5Ni-30Ce-Sep	23.7	7.9	4.2	100.9
10Ni-10Ce-Sep	16.6	11.1	6.2	134.7
15Ni-10Ce-Sep	15.0	15.0	6.7	192.0
20Ni-10Ce-Sep	11.6	15.4	10.9	197.1

For the 10% wt. Ce catalysts with different Ni loadings, the higher the Ni loading, the lower the metallic dispersion, as larger Ni^0 crystallites are found on average, which is expected due to the higher metallic loading employed during the synthesis. Higher Ni loadings also lead to higher Ni^0 metallic surface area values, until reaching a plateau-like behavior for the samples with higher loadings, as seen by the values exhibited by the 15% wt. Ni and the 20% wt. Ni catalysts.

The CO_2-TPD profiles for the sepiolite-based catalysts (**Figure 6.13**) might be understood as a sequence of CO_2 desorption peaks that fall into three categories, as described by Liu et al. [56]: 1) low-temperature desorption (50-200 °C), associated with the presence of surface hydroxyl groups or loosely bound anions, 2) intermediate-temperature desorption (200-400 °C), associated with coordinatively unsaturated oxygen atoms or certain weakly bound anions and, 3) high-temperature desorption (400-900 °C), associated with the presence of strongly bound oxide anions, which can retain adsorbed molecules even at high temperatures. [57],[58].

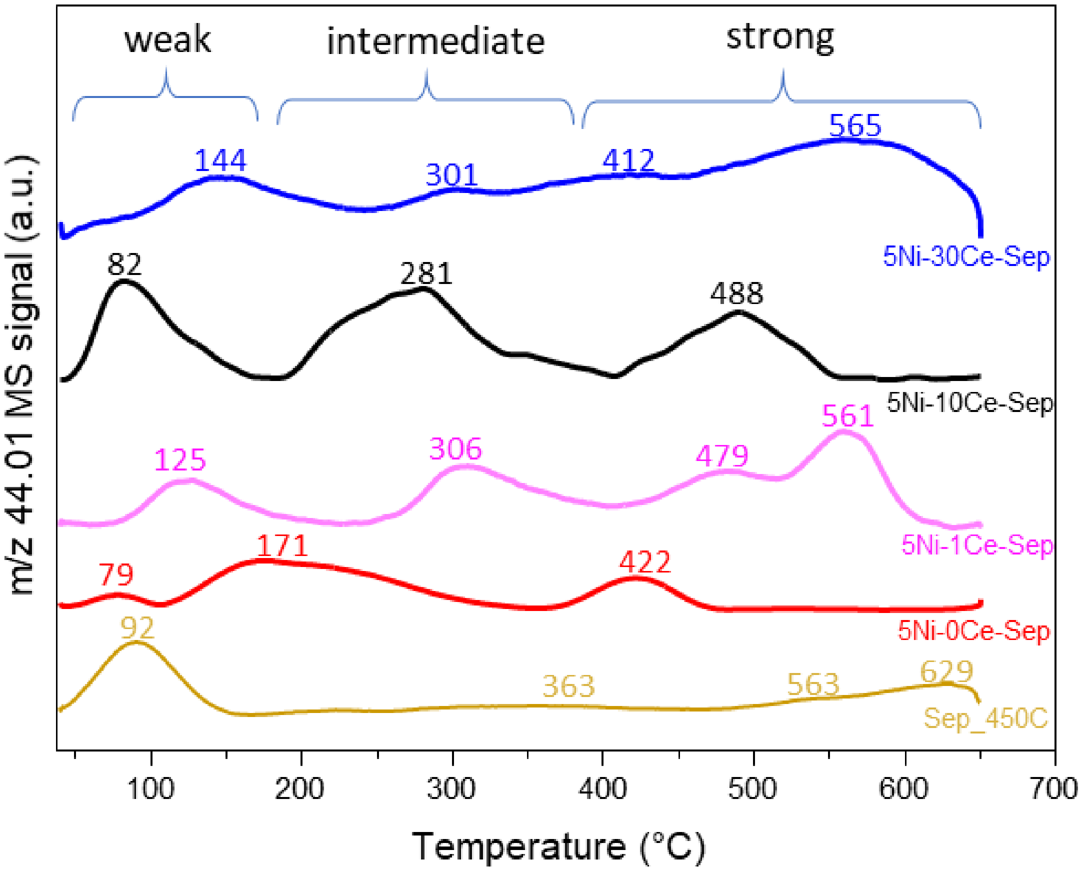

Figure 6.13. CO_2-TPD profiles for (a) calcined sepiolite, Sep_450C; (b) 5Ni-0Ce-Sep; (c) (b) 5Ni-1Ce-Sep; (d) 5Ni-10Ce-Sep; and (e) 5Ni-30Ce-Sep.

The deconvoluted results for each one of the regions and total basicity are shown in Chapter 9 – Supplementary Information and summarized in **Table 6.5**.

The sepiolite CO_2-TPD profile (**Figure 6.13a**) presents a profile similar to the one already described in the literature by Güngor et al. [59]. The peak centered at 92 °C is attributed to the weakly bonded CO_2 molecules on the sepiolite surface, while the small peaks in the intermediate zone (200 – 400 °C) are attributed to the desorption of CO_2 from the decomposition of carbonate species formed by the interaction with oxygen atoms on the support surface.

The peak at the higher temperature in this zone, centered at 363 °C, is attributed to the CO_2 molecules adsorbed on basic sites inside the sepiolite microporous channel structure, which require a higher temperature to be desorbed. Finally, the peaks at higher temperatures, 563 °C and 629 °C, are attributed to the decomposition of carbonate species formed by interaction with surface oxide anions from the magnesium silicate structure.

Table 6.5. CO_2-TPD deconvolution for the weak (50 – 200 °C), moderate (200 – 400 °C) and strong (400 – 600 °C) basic sites and total basicity for the sepiolite-based catalysts.

Sample	**Deconvolution (mmol CO_2 g^{-1})**			**Total basicity**
	Weak	**Medium**	**Strong**	**(mmol CO_2 g^{-1})**
Sep_450C	0.72	0.17	0.53	1.42
5Ni-0Ce-Sep	0.21	0.72	0.82	1.75
5Ni-1Ce-Sep	0.54	1.62	0.90	3.06
5Ni-10Ce-Sep	0.62	2.05	1.17	3.83
5Ni-30-Ce-Sep	0.83	1.85	2.65	5.33

Regarding the effect of Ni addition, 5Ni-0Ce-Sep presents higher CO_2 uptake than the Ni-free support, Sep_450C. This is attributed to the formation of carbonyl species on the Ni^0 phase, which had been previously described in the literature for the increase in CO_2 uptake when a Ni^0 phase is deposited over an inorganic support [60, 61]. Furthermore, these carbonyl species were detected in the operando spectroscopic studies that will be addressed in the sequence.

Ce addition also modulates the catalysts' basicity, as the higher the Ce content, the higher the total basicity (**Table 6.5**), in consonance with some works already published before [62, 63].

Regarding the weak basicity specifically, the higher the Ce content, the higher the weak basicity of the nickel-ceria catalysts. This goes in consonance with results reported by Daroughegi et al., which attributed that the increase of -OH groups concentration with higher loading of CeO_2 increases the interaction with CO_2 molecules and, consequently, leads to an increase in weak basicity [64].

Following this trend, the strong CO_2 basicity also increases with the increase in cerium content in the catalyst series. Yu et al. describe that for ceria-based catalysts, the high-temperature desorption peaks are associated with carbonated species formed by the interaction between CO_2 and oxygen vacancies [65]. Corroborating the CO_2-TPD results, these carbonated species were detected by the FT-IR transmission operando studies, as it will be discussed more thoroughly in the next section.

This trend is confirmed in the CO_2-TPD profile, in which it is seen that higher Ce concentration leads to more intense peaks at the high-temperature desorption zone. The higher the Ce concentration, the broader the peaks as well, which accounts for the wider distribution of oxygen vacancy types, as the concentration of oxygen vacancies is different on distinct CeO_2 crystalline facets [66]. This is clearly seen for the broad peaks centered at 490 °C and 563 °C for the 5Ni-10Ce-Sep and 5Ni-30Ce-Sep, respectively.

The medium basicity, on the other hand, presents a volcano-like behavior, with the maximum value being reached in the 5Ni-10Ce-Sep catalyst. The medium basicity is associated with the decomposition of HCO_3^- or HCO_2^- species, which are formed by the interaction between CO_2 surface -OH groups, and this volcano-like behavior takes place due to the observance of two opposite trends [67].

Even though the increase in the Ce content also increases the surface -OH groups concentration on the ceria surface, it also decreases the sepiolite surface -OH groups. This takes place because these latter OH groups serve as anchors for the CeO_2 phase deposition and also because CeO_2 deposition partially clogs the support microporous channel structure, as previously confirmed by the textural properties and TEM images.

This is further confirmed by the trend observed in **Figure 6.13**, in which the intermediate temperature desorption peak temperatures are shifted towards higher values for higher Ce contents. This confirms the diffusional hindrance that this phase imposes on CO_2 mass transfers inside the micropores, making it necessary higher temperatures to desorb these molecules.

6.3 – Catalytic and operando FT-IR characterization

6.3.1 – Operando FT-IR characterization

The catalytic results in the reactor (**Figure 6.14**) reveal that the nickel-free catalyst, 0Ni-10Ce-Sep, presents very low CO_2 conversion, below 3% for the whole range of temperatures, confirming that the nickel phase is crucial for the CO_2 methanation reaction catalysis. For all the 5 wt. % catalysts, X_{CO_2}values are relatively low at temperatures below 300 °C. At higher temperatures, however, the curves reach higher values in temperatures over 350 °C, reaching the equilibrium limit.

Ce addition has a positive effect on the CO_2 methanation reaction, as all cerium-containing samples exhibit higher X_{CO_2}values than the 5Ni-0Ce-Sep. Of all the Ce-containing samples, the 5Ni-10Ce-Sep is the one that shows the best results, which is quite clear at 350°C, confirming a volcano-like dependence of the CO_2 conversion on the cerium content.

Therefore, based on these catalytic results and previous results from our research group and from the literature regarding the mechanism of the CO_2 methanation, the effect of Ce loading was assessed with more in-depth operando studies of the intermediates species.

For the 5Ni-0Ce-Sep catalyst, by analyzing the ν(OH) region before the introduction of any reactant flow, the typical peaks for sepiolite are found (**Figure 6.15**). The peak at 3721 cm^{-1} is assigned to ν(Si-OH) groups, while the one at 3671 cm^{-1} is assigned to ν(Mg-OH). The bands at 3599/3533 cm^{-1} are assigned to ν(OH) of H_2O molecules coordinated to Mg sites, as previously described by Cerdá-Moreno et al. [43].

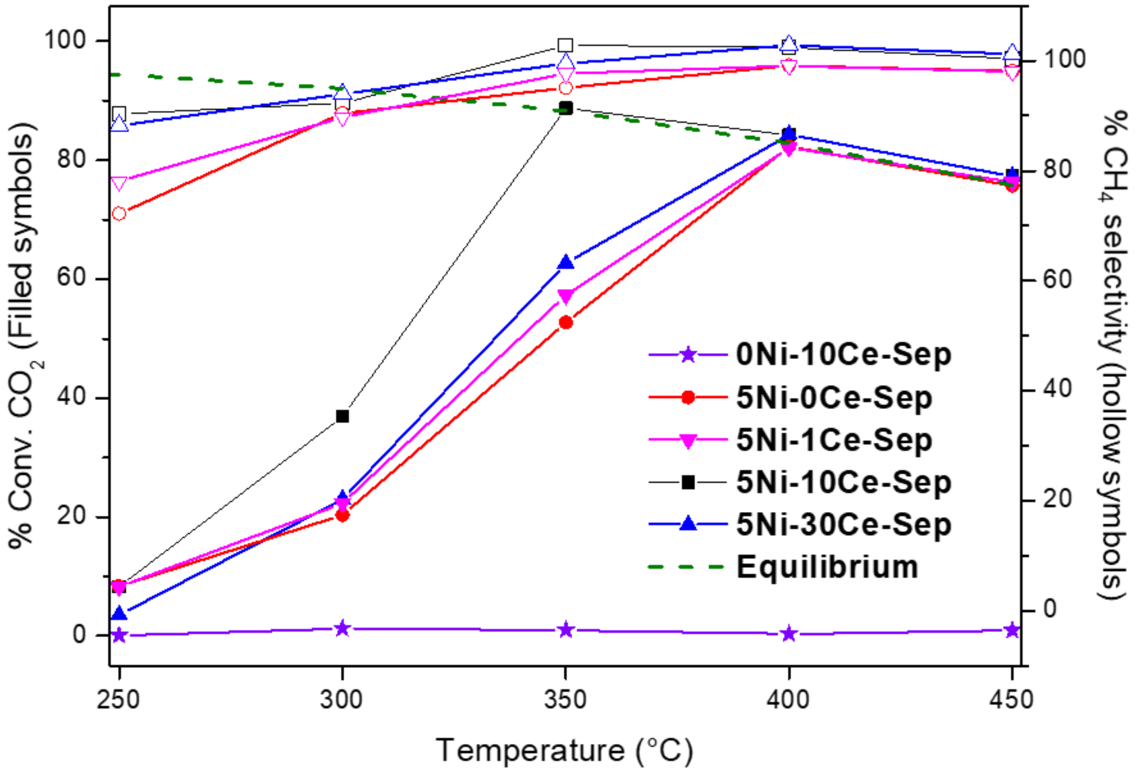

Figure 6.14. CO_2 conversion (filled symbols) and CH_4 selectivity (hollow symbols) for the nickel-cerium-sepiolite catalysts. Equilibrium data was calculated using the DWSIM simulator. Reaction conditions: 250 °C - 450 °C, 1 atm, WHSV = 38,000 mL $(g_{CAT}\cdot h)^{-1}$. $H_2/CO_2 = 4$.

The peak centered at 1630 cm^{-1} is attributed to the bending vibration of adsorbed H_2O molecules, $\delta(H_2O)$, indicating that they remain even after the thermal treatment, confirming the hydrophilic nature of the clay support. To simplify, the peak attributions are all summarized in **Table 6.6**.

In order to assess the reaction mechanism, a series of transient experiments were conducted at 250 °C. This temperature was chosen because the catalytic tests had proven that there is CO_2 conversion to a quantifiable extent (**Figure 6.14**). Other studies in the literature were also conducted at low temperatures for a series of factors, such as lower X_{CO_2} values, higher sensitivity to the formation of intermediate species and less observance of side reactions, which could lead to more complex interpretations [68].

First of all, the evolution of the IR bands over 5Ni-0Ce-Sep was assessed in two phases (**Figure 6.16**a). The lower part of the graph exhibits the evolution under CO_2 exposition over 20 minutes, while the upper one shows the subsequent phase when the CO_2 flow was cut off and H_2 flow was injected instead.

During the CO_2 injection, there is the formation of a series of peaks in the linear (2031 cm^{-1}), bridge (1909 cm^{-1}), and multibonded (1855 cm^{-1}) CO groups, respectively, on the Ni^0 phase surface (**Table 6.6**), as previously reported by Yan et al. [69].

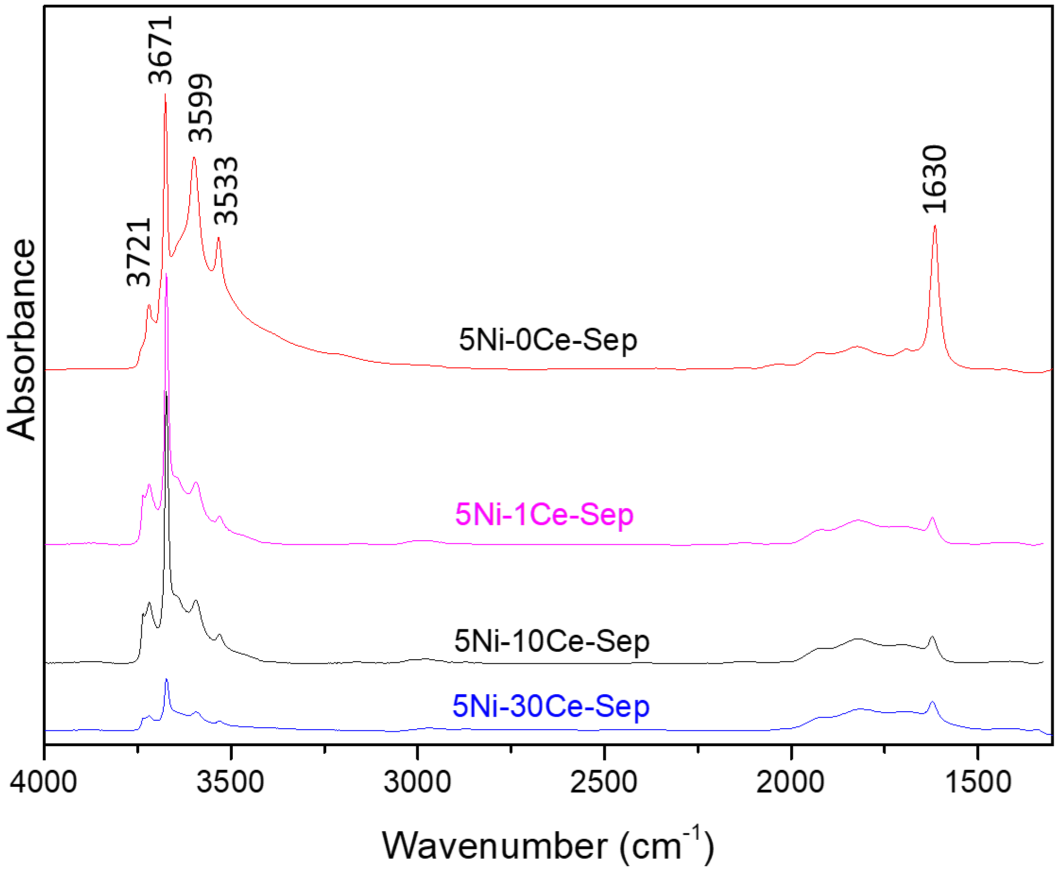

Figure 6.15. Transmission infrared results over the different calcined catalysts before introducing any reactants into the transmission IR analysis chamber.

Table 6.6. Assignation of the corresponding wavenumber to the vibration modes observed in the nickel-sepiolite-ceria catalysts.

Vibration mode	Wavenumber (cm^{-1})	Reference
ν(OH) – Si-OH	3721	Cerdá Moreno et al. [43]
ν(OH) – Mg-OH	3671	Cerdá Moreno et al. [43]
ν(OH) – adsorbed water	3599/3533	Cerdá Moreno et al. [43]
$CH_{4(g)}$	3016/1305	Cerdá Moreno et al. [43]
linear Ni^0-CO	2031	Yan et al. [69]
bridge Ni^0-CO	1909	Yan et al. [69]
multibonded Ni^0-CO	1855	Yan et al. [69]
-OCH_3	1733	Yan et al. [70]
Adsorbed H_2O	1630	Cerdá Moreno et al. [43]
Monodentate carbonate	1466/1391	Lorber et al.[71]
Bidentate carbonate	1458	Li et al. [72]
HCOO- formiate group	2848/1570/1710	Pozdnyakova et al. [73]

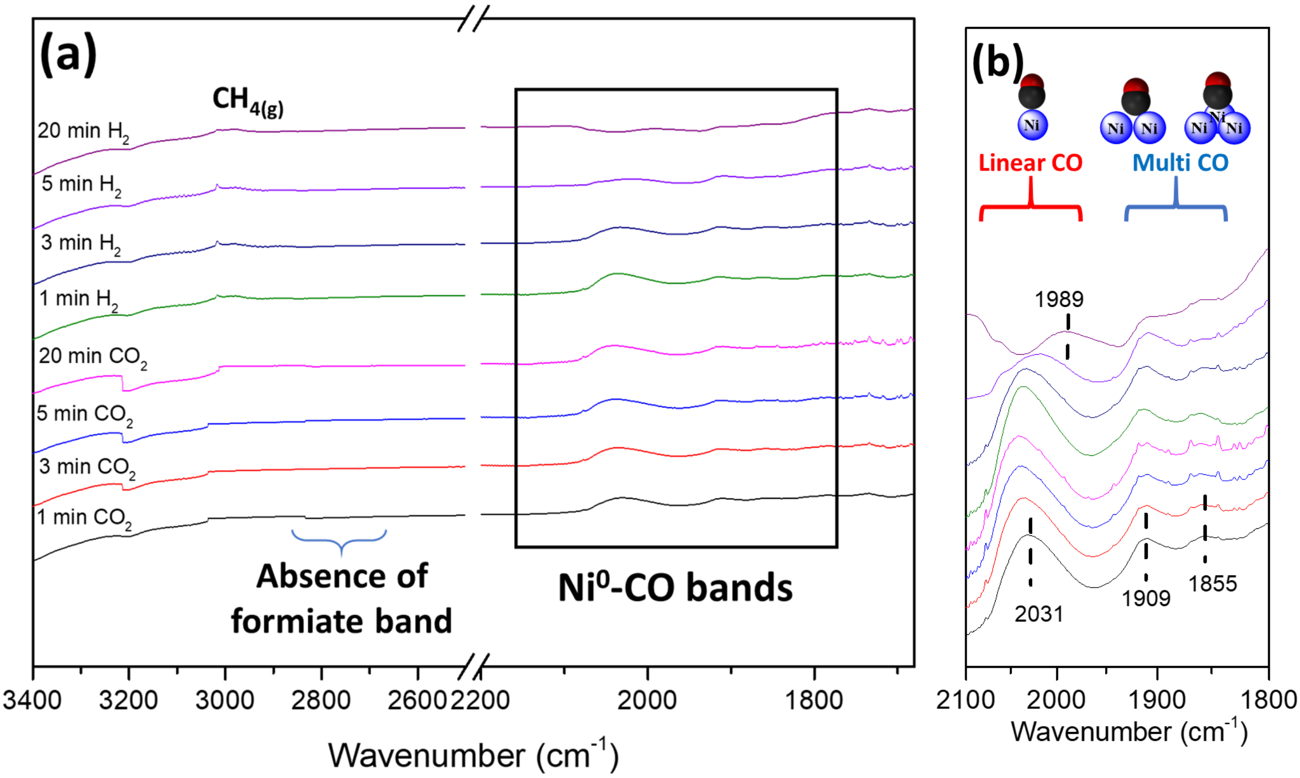

Figure 6.16. (a) Transmission FT-IR results for the transient experiments after alternate expositions to CO_2 and H_2 at 250 °C for 5Ni-0Ce-Sep. (b) Magnification of the carbonyl region between 2100 and 1800 cm^{-1}, showing the evolution of the Ni^0-CO bands during the transient experiments.

Previous results from our research group published by Cerdá-Moreno et al. had already discussed and proved that the CO_2 activation goes via the dissociative mechanism in the 5Ni-0Ce-Sep over the Ni^0 phase without the necessity of having H_2 in the reactant flow [43].

When H_2 is injected, the carbonyl peaks rapidly decrease in intensity, while there is an appearance of the CH_4 peak centered at 3013 cm^{-1}, accompanied by its typical rotovibrational profile. This strongly suggests that after dissociation over the Ni^0 phase, H_2 interacts with the Ni^0-CO species, which eventually leads to CH_4 formation.

Regarding the Ce-containing catalysts, as they presented higher X_{CO_2} and S_{CH_4} values than the cerium-free catalyst, 5Ni-0Ce-Sep, the operando IR studies were conducted in order to shed light on the mechanism taking place introduced by Ce addition (**Figure 6.17**).

The first difference in comparison with 5Ni-0Ce-Sep is the diversity and intensity of peaks in the fingerprint region, which is attributed to the formation of carbonated species, as it will be further discussed. Due to the complex nature of the support and the huge diversity of available surface hydroxyl in this system, as previously confirmed by CO_2-TPD results (**Figure 6.13**), this gives rise to a vast array of possible carbonated species vibration [74-76].

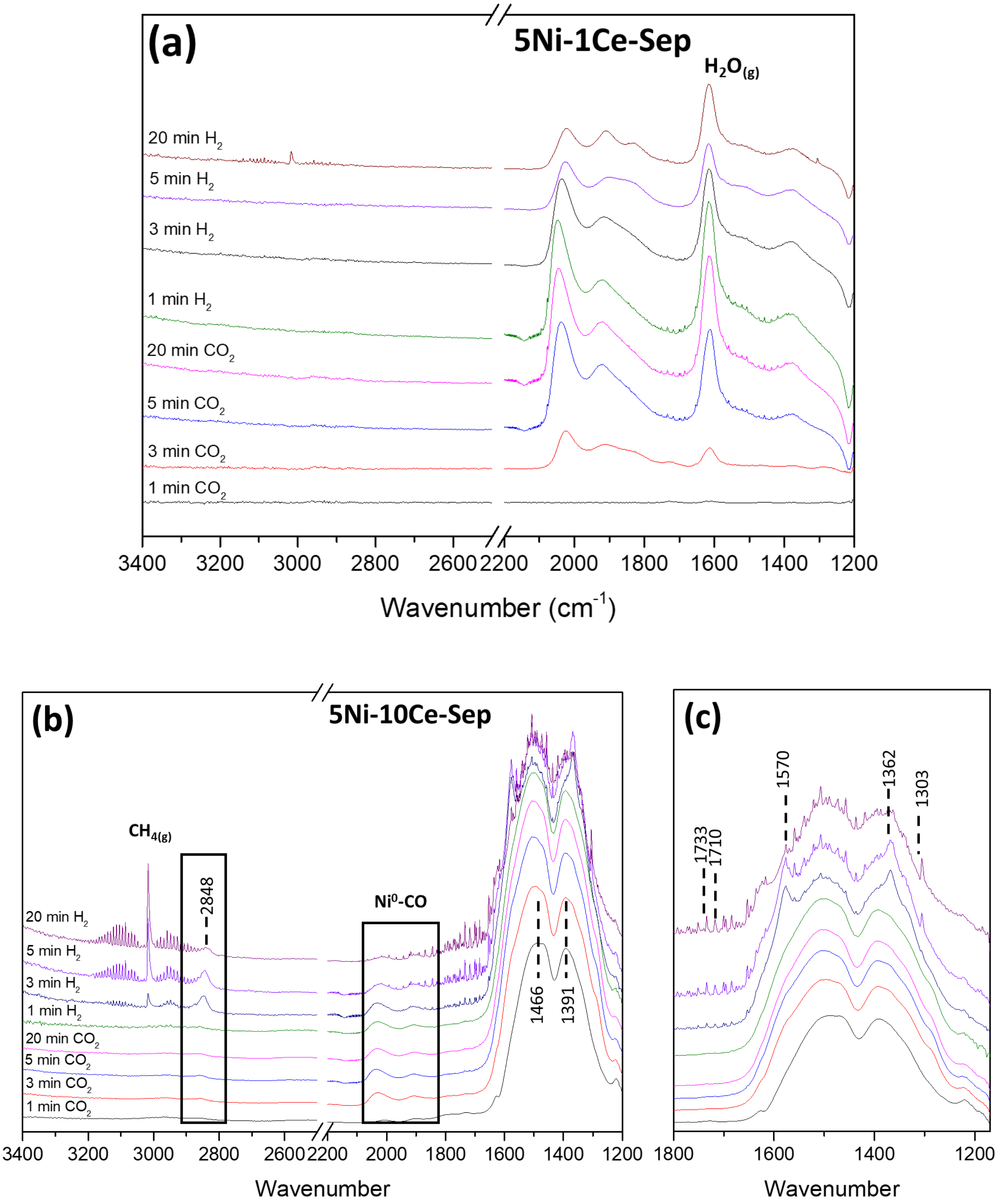
(a)
5Ni-1Ce-Sep
$H_2O_{(g)}$
20 min H_2
5 min H_2
3 min H_2
1 min H_2
20 min CO_2
5 min CO_2
3 min CO_2
1 min CO_2
3400
3200
3000
2800
2600
2200
2000
1800
1600
1400
1200
Wavenumber (cm^{-1})
(b)
5Ni-10Ce-Sep
$CH_{4(g)}$
2848
Ni^0-CO
1466
1391
20 min H_2
5 min H_2
3 min H_2
1 min H_2
20 min CO_2
5 min CO_2
3 min CO_2
1 min CO_2
3400
3200
3000
2800
2600
2200
2000
1800
1600
1400
1200
Wavenumber
(c)
1733
1710
1570
1362
1303
1800
1600
1400
1200
Wavenumber

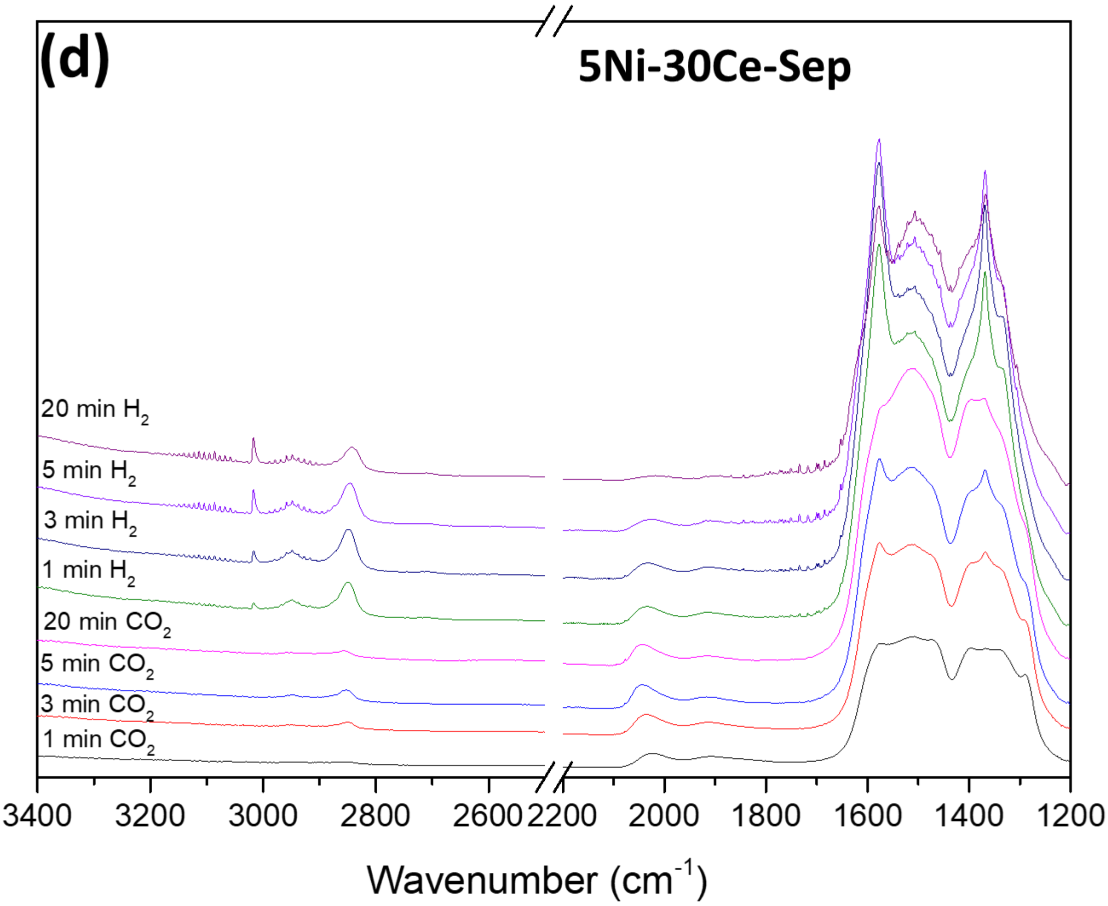

Figure 6.17. Transmission FT-IR results for the transient experiments after **alternate expositions** to CO_2 and H_2 at 250 °C at different times for: (a) 5Ni-1Ce-Sep, (b) 5Ni-10Ce-Sep and (d) 5Ni-30Ce-Sep. (c) Zoom-in of the 1200-1600 cm^{-1} region for the 5Ni-10Ce-Sep catalyst. Test conditions: T = 250 °C, 1 atm.

Another difference is that for the Ce-containing samples, particularly the higher loading ones, one can also observe a peak centered at 2848 cm^{-1}, characteristic of the ν(C-H) of formate groups, HCOO-.

When the transient experiments for the 5Ni-10Ce-Sep were conducted, upon CO_2 injection into the system, it interacted with surface hydroxyl groups, leading to the formation of carbonate species, as previously suggested by the CO_2-TPD results. These groups are detected by the peaks centered at 1466 and 1391 cm^{-1} and are attributed to monodentate carbonates [71] (**Figure 6.17b**).

In the next step of the transient experiment, when H_2 is injected, formate is formed (2848 cm^{-1} peak) but rapidly consumed, as more clearly seen in the time-resolved assessment of peak intensity time (**Figure 6.18**). The linear Ni^0-CO intermediate species are also consumed, as the decrease at the 2031 cm^{-1} band suggests that the associative and the dissociative mechanisms are taking place simultaneously.

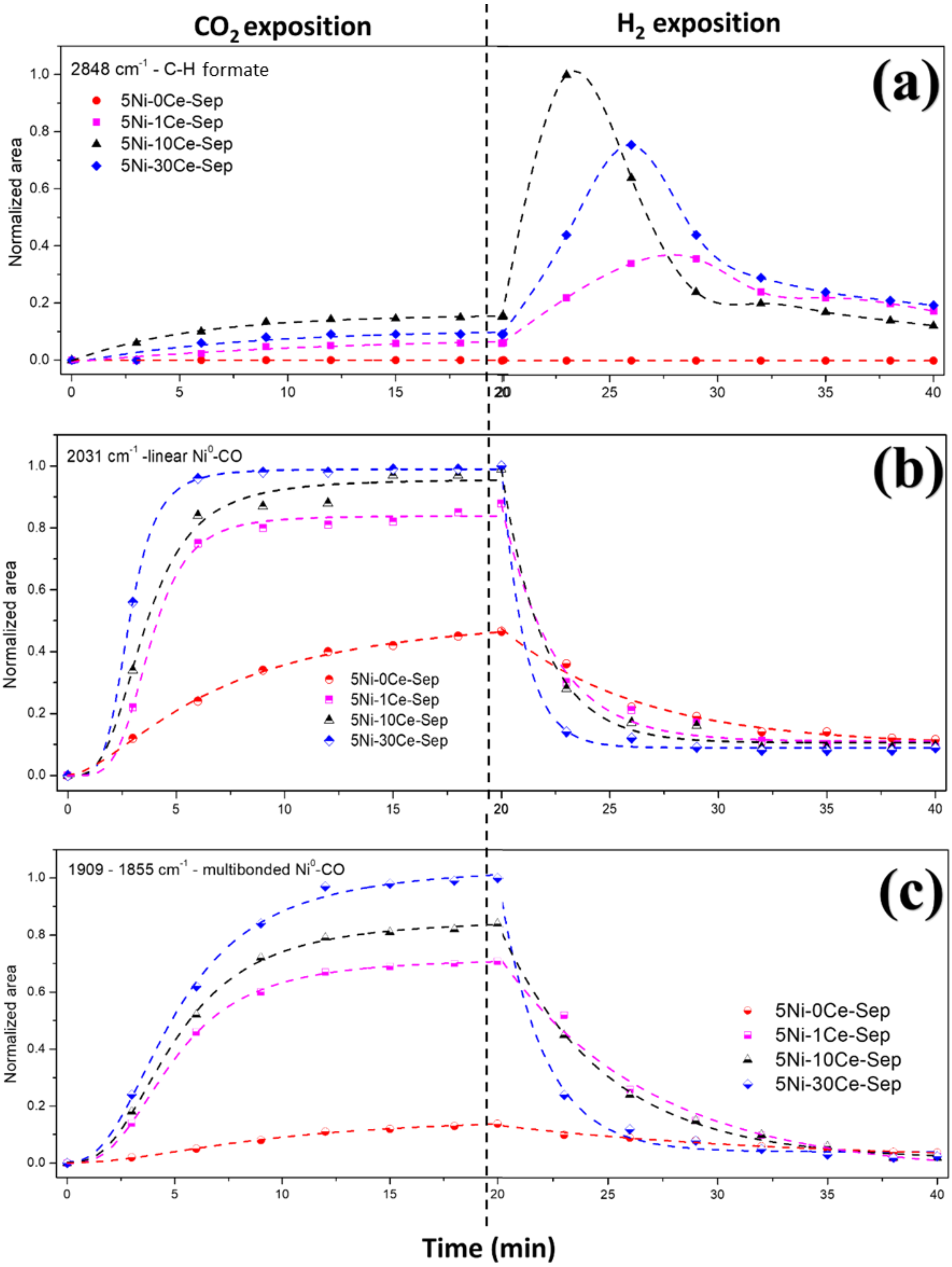

Figure 6.18. Time-resolved normalized intensity of infrared bands centered at: (a) 2848 cm^{-1}, formate, (b) 2031cm^{-1}, linear Ni^0-CO; (c) 1909-1855 cm^{-1}, multibonded Ni^0-CO, for t5Ni-10Ce-sep catalyst. Conditions: 250 °C, 1 atm, alternate expositions to CO_2 followed by H_2.

Also, with the H_2 introduction into the system, the broad peaks associated with strong monodentate carbonate peaks (1466 and 1391 cm^{-1}) reduce in intensity. This suggests that H_2 interacts with the monodentate carbonate species on ceria and leads to the formation of a complex mixture of bicarbonate, formate, and formyl groups, as seen by the formation of new peaks (1570 and 1362 cm^{-1}) (**Figure 6.17c**).

Previous reports in the literature show that the ceria phase contributes to forming these intermediates due to the thermodynamical stabilization of the oxygen vacancies. Some of these intermediates are monodentate bicarbonate (1421, 1405 cm^{-1}) [71], formate species (1570 and 1362 cm^{-1}) [77], and formyl species [73].

The formation of extra carbonated species due to the interaction of CO_2 and CeO_2 oxygen vacancies was also confirmed by the operando studies, as the CO_2-TPD results had previously suggested it.

Ebrahimi et al. also report that surface Ce^{III}/Ce^{IV} ions on the CeO_2 can also act as Lewis acid sites and behave as coordinating sites for the formation of bidentate carbonate and formates species due to their d orbital availability [78], which might also account for some of the carbonated species formed in the Ce-based catalysts.

Therefore, these spectroscopic findings suggest that the CeO_2 phase acts as a promoter by serving as an anchoring spot for carbonated species interacting with hydrogen, leading to the formation of intermediates detected by IR measurements. A proposed mechanism wrapping up these results combined is depicted in **Figure 6.19**.

Altogether, the presence of these intermediates detected by the transmission IR experiments strongly suggests that there are differences between the ceria-free catalyst and the cerium-containing ones. For the first one, the dissociative mechanistic pathway seemed to be the main one, while for the second, the associative mechanism seems to take place to a significant extent simultaneously with the dissociative mechanism, accounting for the higher X_{CO_2} and S_{CH_4} values.

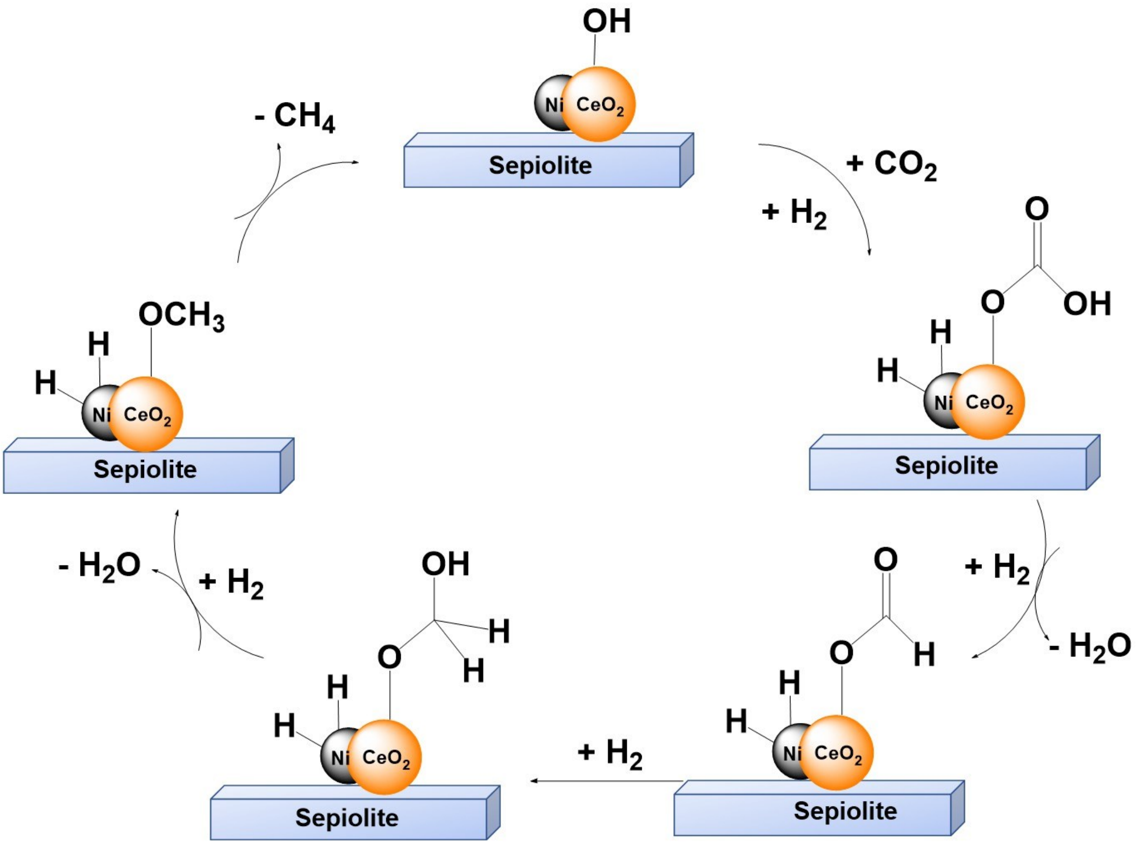

Figure 6.19. Depiction of the proposed catalytic cycle taking place in the 5Ni-10Ce-Sep catalyst for the H-assisted associative mechanism for the CO_2 methanation reaction via formate formation.

6.3.2 – Effect of cerium content

To assess the effect of the cerium content on the catalytic performance, the normalized area of some of the most remarkable peaks, such as the Ni^{0-}CO and the ν(C-H) of the -HCOO group, were analyzed in time-resolved experiments.

For the linear and the multibonded Ni^0-CO bands, the peak intensity follows the increase of Ce content. This can be interpreted by the fact that, as previously discussed, the higher the Ce content, the higher the Ni^0 dispersion in the catalysts after activation, and, as a consequence, the higher the Ni^0 metallic surface area.

Particularly for the linear Ni^0-CO band, there is a drastic increase between the 5Ni-0Ce-Sep and 5Ni-1Ce-Sep catalysts, even though between 5Ni-10Ce-Sep and 5Ni-30Ce-Sep, the difference is no longer that remarkable.

Concerning the ν(C-H) peak from the formate group (**Figure 6.18b**), one can see that its formation starts slowly and reaches a steady state for all cerium-containing catalysts after 20 minutes of CO_2 exposition, with a drastic increase takes place after the introduction of H_2 into the system. In the 5Ni -10Ce-Sep, it reaches the highest intensity and is the fastest one, followed by the 5Ni-30Ce-Sep and the 5Ni-1Ce-Sep.

This profile seems to confirm the mechanism discussed in the last section. Ce addition increases the formation of participating carbonated intermediate via the associative mechanism in which these species are transformed into formate groups. The trend goes hand in hand with the CO_2-TPD results, by which we observe that the medium basicity also follows the order 5Ni-10Ce-Sep > 5Ni-30Ce-Sep > 5Ni-1Ce-Sep.

Therefore, wrapping up this discussion and the current understanding of the reaction mechanism, it seems that intermediate basicity active sites and Ni^0 metallic sites are involved in the mechanistic pathway. Therefore, a delicate balance between intermediate strength sites and metallic sites available is necessary, and for this reason, the ratio between these two parameters, B_{CO_2}/S_{Ni}, was calculated (**Table 6.7**), and this data was correlated with the TOF values and the Ni^0 average particle size.

Table 6.7. Catalytic data regarding 5% wt. Ni catalysts and selected properties: TOF at 250 °C, $TOF_{CH_4, 250\,°C}$, moderate basicity concentration, B_{CO_2}, average Ni^0 crystallite size, D_{Ni}, and moderate basicity per unit of active metallic surface area, B_{CO_2}/S_{Ni}.

Catalyst	$TOF_{250\,°C}$ (s^{-1})	D_{Ni} (nm)^a	B_{CO_2} (mmol CO_2 g^{-1})	B_{CO_2}/S_{Ni} (mmol CO_2 m^{-2})
5Ni-0Ce-Sep	0.564	16.0	0.72	0.34
5Ni-1Ce-Sep	1.051	5.9	1.62	0.29
5Ni-10CeO$_2$-Sep	1.281	5.7	2.05	0.35
5Ni-30CeO$_2$-Sep	0.944	4.2	1.85	0.23

The results reveal that for the two samples with the same B_{CO_2}/S_{Ni} ratio, 5Ni-0Ce-Sep, and 5Ni-10Ce-Sep, the average Ni^0 crystallite size has an influence on the catalytic performance. This is confirmed as the catalyst with Ni^0 particles around 6 nm presented higher TOF values than the one with particles around 16 nm (**Figure 6.20**). This volcano-like behavior seems to be involved in optimizing the interfacial metal-support perimeter, which favors the interaction of reaction intermediates but also ensures enough metallic surface area to activate H_2.

On the other hand, the samples with almost the same Ni^0 average crystallite size, 5Ni-1Ce-Sep, and 5Ni-10Ce-Sep, the higher concentration of moderate basic sites in the second one accounted for the higher TOF value.

This novel approaches regarding the analysis of the B_{CO_2}/S_{Ni} ratio reinforces the importance of modulating the textural properties regarding basicity and metallic dispersion to obtain the best catalytic result. These results are in consonance with recent results published in the literature and shed more light on the ongoing discussion about the nature of the intricate CO_2 methanation reaction mechanism [79-81].

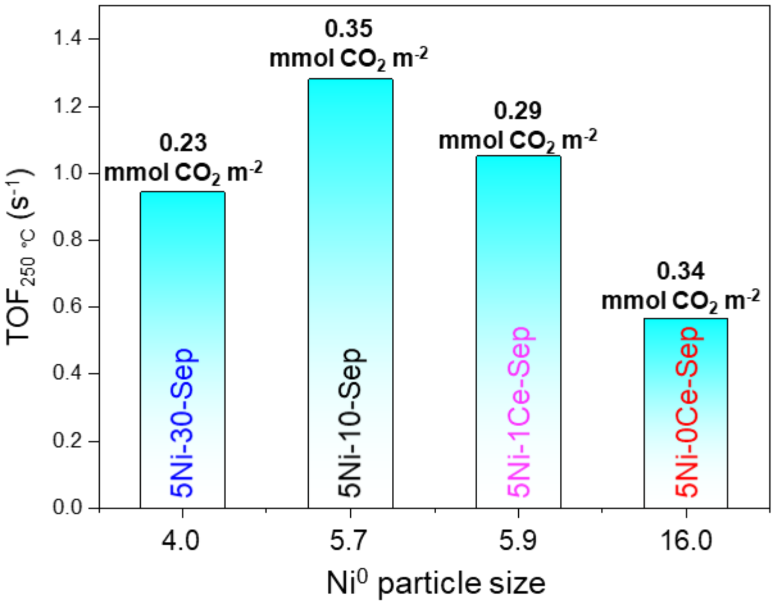

Figure 6.20. Dependence of TOF on Ni^0 particle size for 5% wt. Ni catalysts with different Ce loadings. The respective values of concentration of moderate basic site per unit of active metallic surface area, B_{CO_2}/ S_{Ni} are also indicated.

6.3.3 – Effect of nickel content

After thorough characterization of the 5% wt. Ni catalysts and determination of the optimum Ce amount as a promoter in 10% wt. Ce, the effect of Ni loading was also assessed to obtain catalysts with higher yield to CH_4 aiming to the application of biogas upgrade, as it will be discussed in Chapter 7 of the thesis.

Catalytic results for higher-loading catalysts reveal that the optimum X_{CO_2} and S_{CH_4} values are achieved at around 350 °C (**Figure 6.21**), decreasing at higher temperatures, which is expected due to the endothermic nature of the reaction, which limits the conversion at higher temperatures [82]. The only other hydrogenation product observed for all these tests was CO, and the higher S_{CH_4} values were achieved at around 350 °C, as higher temperature favored the RWGS reaction, which increases the selectivity to CO [83].

Regarding the Ni loading, the 15% wt. Ni catalyst, 15Ni-10Ce-Sep, optimized yield to CH_4, presenting similar results to the ones shown by the 20% wt. Ni one. As strongly suggested by the FT-IR data, the reaction mechanism takes place at the peripheral zone between Ni^0 and the support phase, and for this, there is a maximum level at which the Ni^0 active sites can actually take place in the formation of intermediates, as previously discussed by Quindimil et al. [84].

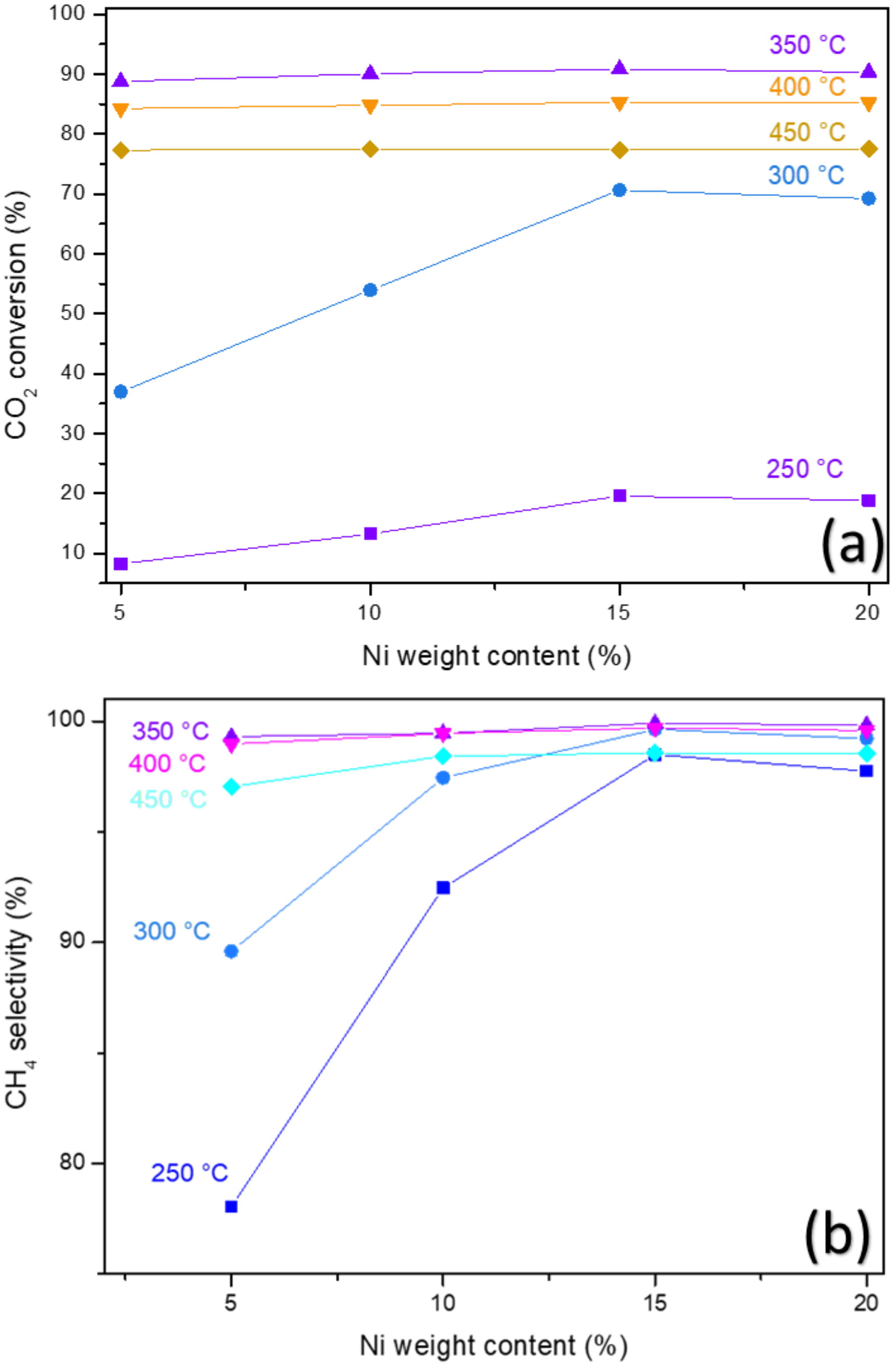

Figure 6.21. Effect of Ni loading on (a) CO_2 conversion and (b) CH_4 selectivity on different temperatures for the 10% Ce sepiolite catalysts. Pressure: 1 atm, $H_2/CO_2 = 4:1$, WHSV = 38,000 mL $(g_{cat} \cdot h)^{-1}$.

For lower temperatures, such as 250 °C and lower Ni loadings (5 and 10% wt.), lower values of S_{CH_4} are observed, since in the smaller Ni^0 particles, there are not enough step/edge and kink/corner Ni^0 sites, which are known to be the active sites for the activation of CO_2. For this reason, CO_2 is partially hydrogenated to CO, as discussed in one of our recent publications [54].

For higher loadings, on the other hand, such as the 15 and 20% wt. Ni ones, they present higher S_{CH_4} values with no difference. This is due to optimizing the number of active sites at the perimeter between the metallic and the support phase, attaining the saturation threshold, which optimized the complete reduction of CO_2 to CH_4.

6.4 – Conclusions

A series of nickel-cerium-based catalysts supported on the sepiolite clay as support with different Ce loadings (0, 1, 10, and 30%) and Ni loadings (0, 5, 10, 15. 20%) were synthesized by the coprecipitation procedure. ICP-OES results confirmed that the synthesis conditions were correct for depositing the metals close to the nominal content.

TPR and TEM-EDS results showed that Ni and Ce phases are deposited together and higher Ce contents decrease the temperature at which the NiO phase reduction event occurs. Ce addition also decreases the average Ni^0 particle size in the catalysts after the reduction step.

Operando transient transmission IR measurements confirmed that over the Ce-free catalyst, the mechanism for the CO_2 methanation reaction follows the dissociative pathway, with the CO_2 molecule dissociating into Ni^0-CO species (peaks in the 1800-2100 cm^{-1} region). These peaks rapidly decrease in intensity after H_2 introduction into the system, while a peak centered at 3013 cm^{-1} (CH_4) is formed, suggesting these Ni^0-CO species are directly hydrogenated to CH_4.

In the cerium-containing catalysts, the dissociative mechanism described for the aforementioned catalyst is also observed. However, besides that one, a H-assisted associative mechanism is also discerned by the decrease in intensity of the carbonate and bicarbonate bands (1300-1500 cm^{-1} region) after introducing H_2. Their decrease leads to an increase of a formate band (~ 2800 cm^{-1}), which subsequently decreases, leading to CH_4 formation.

Among the cerium-containing catalysts, the 5Ni-10Ce-Sep was the one that exhibited higher CO_2 conversion values at lower temperatures, reaching the equilibrium limit at 350 °C, a temperature in which it exhibited the highest CH_4 selectivity. This was rationalized by CO_2-TPD results, which pointed out that the 10Ce sample maximized the moderate basicity due to the CO_2 interaction with ceria, a step involved in the CO_2 methanation reaction. For this reason, it exhibited superior catalytic performance, and with all this seen, a mechanistic pathway was proposed to account for this catalytic and spectroscopic behavior.

Regarding the higher Ni loading samples, the 15% wt. Ni presented the optimum yield to CH_4, by maximizing the CO_2 conversion and selectivity to CH_4. This was attributed to the fact that this sample increased the surface Ni^0 metallic area, as demonstrated by the H_2-chemisorption results, favoring the hydrogenation of the intermediates species at the peripheral zone.

Therefore, this study demonstrates that moderate strength basicity sites are involved in the CO_2 methanation reaction mechanism and that the deposition of a dispersed phase of a basic promoter increases the concentration of moderate basic sites and leads to catalysts with higher yield values to CH_4.

6.5 – References

[1] Ewis D, Ba-Abbad MM, Benamor A, El-Naas MH. Adsorption of organic water pollutants by clays and clay minerals composites: A comprehensive review. Applied Clay Science. 2022;229.

[2] Bukas VJ, Tsampodimou M, Gionis V, Chryssikos GD. Synchronous ATR infrared and NIR-spectroscopy investigation of sepiolite upon drying. Vibrational Spectroscopy. 2013;68:51-60.

[3] Suárez M, García-Romero E. Variability of the surface properties of sepiolite. Applied Clay Science. 2012;67-68:72-82.

[4] Zhang Y, Wang L, Wang F, Liang J, Ran S, Sun J. Phase transformation and morphology evolution of sepiolite fibers during thermal treatment. Applied Clay Science. 2017;143:205-11.

[5] Álvarez A, Santarén J, Esteban-Cubillo A, Aparicio P. Chapter 12 - Current Industrial Applications of Palygorskite and Sepiolite. In: Galàn E, Singer A, editors. Developments in Clay Science: Elsevier; 2011. p. 281-98.

[6] Tadiello L, Guerra S, Giannini L. Sepiolite-Based Anisotropic Nanoparticles: A New Player in the Rubber Reinforcement Technology for Tire Application. Applied Sciences. 2022;12:2714.

[7] Galan E. Properties and applications of palygorskite-sepiolite clays. Clay Minerals. 1996;31:443-53.

[8] Abad-Valle P, Álvarez-Ayuso E, Murciego A, Pellitero E. Assessment of the use of sepiolite amendment to restore heavy metal polluted mine soil. Geoderma. 2016;280:57-66.

[9] Álvarez-Ayuso E, Garcı, x, a-Sánchez A. Sepiolite as a feasible soil additive for the immobilization of cadmium and zinc. Science of The Total Environment. 2003;305:1-12.

[10] Sun Y, Sun G, Xu Y, Wang L, Liang X, Lin D. Assessment of sepiolite for immobilization of cadmium-contaminated soils. Geoderma. 2013;193-194:149-55.

[11] Alkan M, Demirbaş Ö, Çelikçapa S, Doğan M. Sorption of acid red 57 from aqueous solution onto sepiolite. Journal of Hazardous Materials. 2004;116:135-45.

[12] Özcan AS, Tetik Ş, Özcan A. Adsorption of Acid Dyes from Aqueous Solutions onto Sepiolite. Separation Science and Technology. 2005;39:301-20.

[13] Rytwo G, Rettig A, Gonen Y. Organo-sepiolite particles for efficient pretreatment of organic wastewater: Application to winery effluents. Applied Clay Science. 2011;51:390-4.

[14] González-Pradas E, Socías-Viciana M, Ureña-Amate MD, Cantos-Molina A, Villafranca-Sánchez M. Adsorption of chloridazon from aqueous solution on heat and acid treated sepiolites. Water research. 2005;39:1849-57.

[15] Lemić J, Tomašević-Čanović M, Djuričić M, Stanić T. Surface modification of sepiolite with quaternary amines. Journal of Colloid and Interface Science. 2005;292:11-9.

[16] Sabah E, Çelik MS. Adsorption mechanism of quaternary amines by sepiolite. Separation Science and Technology. 2002;37:3081-97.

[17] Sanchez-Martin MJ, Rodriguez-Cruz MS, Andrades MS, Sanchez-Camazano M. Efficiency of different clay minerals modified with a cationic surfactant in the adsorption of pesticides: Influence of clay type and pesticide hydrophobicity. Applied Clay Science. 2006;31:216-28.

[18] Wang C, Wang Y, Chen M, Liang D, Cheng W, Li C, et al. Understanding relationship of sepiolite structure tailoring and the catalytic behaviors in glycerol steam reforming over Co/sepiolite derived Co-phyllosilicate catalyst. Renewable Energy. 2022;183:304-20.

[19] Cecilia JA, Vilarrasa-García E, Cavalcante CL, Azevedo DCS, Franco F, Rodríguez-Castellón E. Evaluation of two fibrous clay minerals (sepiolite and palygorskite) for CO2 Capture. Journal of Environmental Chemical Engineering. 2018;6:4573-87.

[20] Liu L, Chen H, Shiko E, Fan X, Zhou Y, Zhang G, et al. Low-cost DETA impregnation of acid-activated sepiolite for CO2 capture. Chemical Engineering Journal. 2018;353:940-8.

[21] Ouyang J, Gu W, Zheng C, Yang H, Zhang X, Jin Y, et al. Polyethyleneimine (PEI) loaded MgO-SiO2 nanofibers from sepiolite minerals for reusable CO2 capture/release applications. Applied Clay Science. 2018;152:267-75.

[22] López-Galindo A, Viseras C, Cerezo P. Compositional, technical and safety specifications of clays to be used as pharmaceutical and cosmetic products. Applied Clay Science. 2007;36:51-63.

[23] Zhuang G, Zhang Z, Jaber M. Organoclays used as colloidal and rheological additives in oil-based drilling fluids: An overview. Applied Clay Science. 2019;177:63-81.

[24] Zhuang G, Zhang Z, Peng S, Gao J, Jaber M. Enhancing the rheological properties and thermal stability of oil-based drilling fluids by synergetic use of organo-montmorillonite and organo-sepiolite. Applied Clay Science. 2018;161:505-12.

[25] Christidis GE. Industrial clays. European Mineralogical Union Notes in Mineralogy. 2011;9:341-414.

[26] Shimizu K-i, Maruyama R, Komai S-i, Kodama T, Kitayama Y. Pd–sepiolite catalyst for Suzuki coupling reaction in water: Structural and catalytic investigations. Journal of Catalysis. 2004;227:202-9.

[27] Ma Y, Zhang G. Sepiolite nanofiber-supported platinum nanoparticle catalysts toward the catalytic oxidation of formaldehyde at ambient temperature: Efficient and stable performance and mechanism. Chemical Engineering Journal. 2016;288:70-8.

[28] Anderson JA, Daza L, Damyanova S, Fierro JLG, Rodrigo MT. Hydrogenation of styrene over nickel/sepiolite catalysts. Applied Catalysis A: General. 1994;113:75-88.

[29] Meric P, Yu KMK, Tsang SC. Micelle-Hosted Palladium Nanoparticles Catalyze Citral Molecule Hydrogenation in Supercritical Carbon Dioxide. Langmuir : the ACS journal of surfaces and colloids. 2004;20:8537-45.

[30] Ravasio N, Zaccheria F, Gargano M, Recchia S, Fusi A, Poli N, et al. Environmental friendly lubricants through selective hydrogenation of rapeseed oil over supported copper catalysts. Applied Catalysis A: General. 2002;233:1-6.

[31] Shimizu K-i, Miyamoto Y, Satsuma A. Size- and support-dependent silver cluster catalysis for chemoselective hydrogenation of nitroaromatics. Journal of Catalysis. 2010;270:86-94.

[32] Tao R, Miao S, Liu Z, Xie Y, Han B, An G, et al. Pd nanoparticles immobilized on sepiolite by ionic liquids: efficient catalysts for hydrogenation of alkenes and Heck reactions. Green Chemistry. 2009;11:96-101.

[33] Algoufi YT, Akpan UG, Asif M, Hameed BH. One-pot synthesis of glycidol from glycerol and dimethyl carbonate over KF/sepiolite catalyst. Applied Catalysis A: General. 2014;487:181-8.

[34] Degirmenbasi N, Boz N, Kalyon DM. Biofuel production via transesterification using sepiolite-supported alkaline catalysts. Applied Catalysis B: Environmental. 2014;150-151:147-56.

[35] Liu S, Zhu J, Chen M, Xin W, Yang Z, Kong L. Hydrogen production via catalytic pyrolysis of biomass in a two-stage fixed bed reactor system. International Journal of Hydrogen Energy. 2014;39:13128-35.

[36] Veses A, Aznar M, López JM, Callén MS, Murillo R, García T. Production of upgraded bio-oils by biomass catalytic pyrolysis in an auger reactor using low cost materials. Fuel. 2015;141:17-22.

[37] Xie A, Tang Y, Huang X, Jin X, Gu P, Luo S, et al. Three-dimensional nanoflower MnCrOx/Sepiolite catalyst with increased SO2 resistance for NH3-SCR at low temperature. Chemical Engineering Journal. 2019;370:897-905.

[38] Balestra G, de Maron J, Tabanelli T, Cavani F, Nieto JML. The selective ethanol Guerbet condensation over alkali metal-doped sepiolite. Catalysis Today. 2023;423:114013.

[39] Luo L, Li S. Effect of Transition Metals on Catalytic Performance of Ru/Sepiolite Catalyst for Methanation of Carbon Dioxide. Journal of Natural Gas Chemistry. 2004;13:45-8.

[40] Luo L, Li S, Zhu Y. The effects of yttrium on the hydrogenation performance and surface properties of a ruthenium-supported catalyst. Journal of the Serbian Chemical Society. 2005;70:1419-25.

[41] Luo L, Li S, Ouyang Y. Effects of Promoters on a Ru/Sepiolite Catalyst for Carbon Dioxide Methanation. Journal of Natural Gas Chemistry. 2003;12:254-8.

[42] Laitao L, Songjun L, Gengfeng D, Fengyi L. Influence of samarium on the hydrogenation properties of supported nickel catalyst. Reaction Kinetics and Catalysis Letters. 2002;75:289-96.

[43] Cerdá-Moreno C, Chica A, Keller S, Rautenberg C, Bentrup U. Ni-sepiolite and Ni-todorokite as efficient CO2 methanation catalysts: Mechanistic insight by operando DRIFTS. Applied Catalysis B: Environmental. 2020;264:118546-.

[44] Post JE, Bish DL, Heaney PJ. Synchrotron powder X-ray diffraction study of the structure and dehydration behavior of sepiolite. American Mineralogist. 2007;92:91-7.

[45] Perraki T, Orfanoudaki A. Study of raw and thermally treated sepiolite from the Mantoudi area, Euboea, Greece. Journal of Thermal Analysis and Calorimetry. 2008;91:589-93.

[46] Osawa T, Nakai Y, Mouri A, Lee IYS. Studies of the preparation method of ceria-promoted nickel catalyst for carbon dioxide reforming of methane. Applied Catalysis A: General. 2014;474:100-6.

[47] Singha RK, Shukla A, Yadav A, Sivakumar Konathala LN, Bal R. Effect of metal-support interaction on activity and stability of Ni-CeO2 catalyst for partial oxidation of methane. Applied Catalysis B: Environmental. 2017;202:473-88.

[48] Xu B, Jia L, Yang H, Wang Y, Fan S-Y, Yuan S-S, et al. Improved photocatalytic performance of acetaldehyde degradation via crystal plane regulation on truncated octahedral CeO2. Rare Metals. 2024;43:2026-38.

[49] Rana S, Masli N, Monder DS, Chatterjee A. Hydriding pathway for Ni nanoparticles: Computational characterization provides insights into the nanoparticle size and facet effect on layer-by-layer subsurface hydride formation. Computational Materials Science. 2022;210:111482.

[50] Jia X, Zhang X, Rui N, Hu X, Liu CJ. Structural effect of Ni/ZrO2 catalyst on CO2 methanation with enhanced activity. Applied Catalysis B: Environmental. 2019;244:159-69.

[51] da Costa-Serra JF, Cerdá-Moreno C, Chica A. Zeolite-supported Ni catalysts for CO2 methanation: Effect of zeolite structure and Si/Al ratio. Applied Sciences (Switzerland). 2020;10.

[52] Elizalde-Martínez I, Ramírez-López R, Mederos F, Monterrubio C, Vazquez-Medina R, Manríquez ME. Optimization of O2/CH4 to oxide methane at 823 K by alumina-ceria supported Pt catalysts. Reaction Kinetics, Mechanisms and Catalysis. 2019;128.

[53] da Costa-Serra JF, Cerdá-Moreno C, Chica A. Zeolite-Supported Ni Catalysts for CO2 Methanation: Effect of Zeolite Structure and Si/Al Ratio. Applied Sciences2020.

[54] Machado-Silva RB, Da Costa-Serra JF, Chica A. Enhancement of catalytic activity in CO2 methanation in Ni-based catalysts supported on delaminated ITQ-6 zeolite. Journal of Catalysis. 2024:115609.

[55] Ruiz Puigdollers A, Schlexer P, Tosoni S, Pacchioni G. Increasing Oxide Reducibility: The Role of Metal/Oxide Interfaces in the Formation of Oxygen Vacancies. ACS Catalysis. 2017;7:6493-513.

[56] Liu B, Li C, Zhang G, Yao X, Chuang SSC, Li Z. Oxygen Vacancy Promoting Dimethyl Carbonate Synthesis from CO2 and Methanol over Zr-Doped CeO2 Nanorods. ACS Catalysis. 2018;8:10446-56.

[57] Reljic S, Martinez-Escandell M, Silvestre-Albero J. Effect of Porosity and Surface Chemistry on CO2 and CH4 Adsorption in S-Doped and S-/O-co-Doped Porous Carbons. Journal of Carbon Research2022.

[58] Liu H, Da Costa P, Hadj Taief HB, Benzina M, Gálvez ME. Mg-promotion of Ni natural clay-supported catalysts for dry reforming of methane. RSC Advances. 2018;8:19627-34.

[59] Güngör N, Işçi S, Günister E, Miśta W, Teterycz H, Klimkiewicz R. Characterization of sepiolite as a support of silver catalyst in soot combustion. Applied Clay Science. 2006;32:291-6.

[60] Cañón-Alvarado M, Blanco C, Daza C. Exploring dolomite as a promising support for Ni catalysts in CO2 methanation. Journal of Environmental Chemical Engineering. 2024;12:112224.

[61] Schreiter N, Kirchner J, Kureti S. A DRIFTS and TPD study on the methanation of CO2 on Ni/Al2O3 catalyst. Catalysis Communications. 2020;140:105988.

[62] Bonura G, Arena F, Mezzatesta G, Cannilla C, Spadaro L, Frusteri F. Role of the ceria promoter and carrier on the functionality of Cu-based catalysts in the CO2-to-methanol hydrogenation reaction. Catalysis Today. 2011;171:251-6.

[63] Bai J, Song Z, Liu L, Zhu X, Gao F, Chaudhari RV. Enhanced transformation of CO2 over microporous Ce-doped Zr metal-organic frameworks. RSC Advances. 2022;12:26307-18.

[64] Daroughegi R, Meshkani F, Rezaei M. Enhanced low-temperature activity of CO2 methanation over ceria-promoted Ni-Al2O3 nanocatalyst. Chemical Engineering Science. 2021;230:116194-.

[65] Yu Y, Bian Z, Wang J, Wang Z, Tan W, Zhong Q, et al. CO2 hydrogenation to CH4 over hydrothermal prepared ceria-nickel catalysts: Performance and mechanism study. Catalysis Today. 2021.

[66] Silva RBM, de Oliveira CS, Teixeira-Neto É, Sigoli FA, Mazali IO. Improvement of PROX-CO catalytical performance by modulation of the pore structure of CeO2 nanorods decorated with Au nanoparticles. Microporous and Mesoporous Materials. 2022;330:111574.

[67] Hu F, Tong S, Lu K, Chen C-M, Su F-Y, Zhou J, et al. Reduced graphene oxide supported Ni-Ce catalysts for CO2 methanation: The support and ceria promotion effects. Journal of CO2 Utilization. 2019;34:676-87.

[68] Cárdenas-Arenas A, Quindimil A, Davó-Quiñonero A, Bailón-García E, Lozano-Castelló D, De-La-Torre U, et al. Isotopic and in situ DRIFTS study of the CO2 methanation mechanism using Ni/CeO2 and Ni/Al2O3 catalysts. 2019.

[69] Yan B, Zhao B, Kattel S, Wu Q, Yao S, Su D, et al. Tuning CO2 hydrogenation selectivity via metal-oxide interfacial sites. Journal of Catalysis. 2019;374:60-71.

[70] Yan Z, Liu Q, Liang L, Ouyang J. Surface hydroxyls mediated CO2 methanation at ambient pressure over attapulgite-loaded Ni-TiO2 composite catalysts with high activity and reuse ability. Journal of CO2 Utilization. 2021;47:101489.

[71] Lorber K, Zavašnik J, Arčon I, Huš M, Teržan J, Likozar B, et al. CO2 Activation over Nanoshaped CeO2 Decorated with Nickel for Low-Temperature Methane Dry Reforming. ACS Applied Materials & Interfaces. 2022;14:31862-78.

[72] Li T, Dong M, Xu J, Zhang T, Sun Y, Li N, et al. Exploring the Promotion of γ-Al2O3 on Pd/CeO2-Catalyzed Low-Concentration Methane Oxidation Using Operando DRIFTS-MS. ChemCatChem. 2023;15:e202300194.

[73] Pozdnyakova O, Teschner D, Wootsch A, Kröhnert J, Steinhauer B, Sauer H, et al. Preferential CO oxidation in hydrogen (PROX) on ceria-supported catalysts, part II: Oxidation states and surface species on Pd/CeO2 under reaction conditions, suggested reaction mechanism. Journal of Catalysis. 2006;237:17-28.

[74] Tada S, Ochieng OJ, Kikuchi R, Haneda T, Kameyama H. Promotion of CO2 methanation activity and CH4 selectivity at low temperatures over Ru/CeO2/Al2O 3 catalysts. International Journal of Hydrogen Energy. 2014;39:10090-100.

[75] Panagiotopoulou P, Kondarides DI, Verykios XE. Mechanistic study of the selective methanation of CO over Ru/TiO 2 catalyst: Identification of active surface species and reaction pathways. Journal of Physical Chemistry C. 2011;115:1220-30.

[76] Wang S, Pan Q, Peng J, Wang S. In situ FTIR spectroscopic study of the CO2 methanation mechanism on Ni/Ce0.5Zr0.5O2. Catalysis Science and Technology. 2014;4:502-9.

[77] Saw ET, Oemar U, Tan XR, Du Y, Borgna A, Hidajat K, et al. Bimetallic Ni–Cu catalyst supported on CeO2 for high-temperature water–gas shift reaction: Methane suppression via enhanced CO adsorption. Journal of Catalysis. 2014;314:32-46.

[78] Ebrahimi P, Kumar A, Khraisheh M. A Review of CeO2 Supported Catalysts for CO2 Reduction to CO through the Reverse Water Gas Shift Reaction. Catalysts 2022, Vol 12, Page 1101. 2022;12:1101-.

[79] Hao Z, Shen J, Lin S, Han X, Chang X, Liu J, et al. Decoupling the effect of Ni particle size and surface oxygen deficiencies in CO2 methanation over ceria supported Ni. Applied Catalysis B: Environmental. 2021;286.

[80] Zhu M, Tian P, Cao X, Chen J, Pu T, Shi B, et al. Vacancy engineering of the nickel-based catalysts for enhanced CO2 methanation. Applied Catalysis B: Environmental. 2021;282.

[81] Yu Y, Bian Z, Wang J, Wang Z, Tan W, Zhong Q, et al. CO2 hydrogenation to CH4 over hydrothermal prepared ceria-nickel catalysts: Performance and mechanism study. Catalysis Today. 2023;424:113345.

[82] Sun C, Da Costa P. Transition metal-based catalysts for CO2 methanation and hydrogenation. Heterogeneous Catalysis: Materials and Applications2022. p. 59-93.

[83] Ridzuan NDM, Shaharun MS, Anawar MA, Ud-Din I. Ni-Based Catalyst for Carbon Dioxide Methanation: A Review on Performance and Progress. Catalysts. 2022;12.

[84] Quindimil A, De-La-Torre U, Pereda-Ayo B, Davó-Quiñonero A, Bailón-García E, Lozano-Castelló D, et al. Effect of metal loading on the CO2 methanation: A comparison between alumina supported Ni and Ru catalysts. Catalysis Today. 2020;356:419-32.

Chapter 7

Application for catalytic technologies

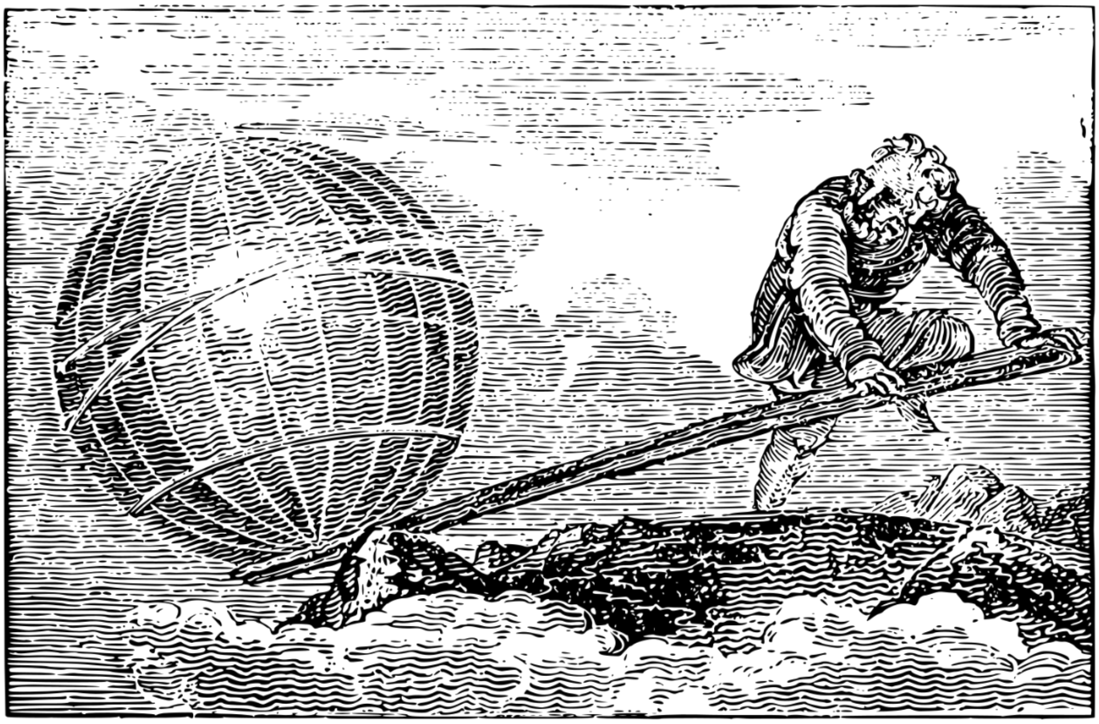

“Give me a place to stand, and I will move the world.”
Archimedes of Syracuse

Figure: Engraving from Mechanic’s Magazine, Volume II, Knight & Lacey, 1824.
Public Domain Image

7.1 - Introduction

One of the most promising applications of CO_2 methanation is in producing biomethane or synthetic natural gas (SNG). By integrating the CO_2 methanation reaction processes, which is exothermic, with water electrolysis, an endothermic process, it would be possible to integrate the use of green hydrogen to directly reduce CO_2 to CH_4 [1].

This application provides a means of storing renewable energy as CH_4 and leverages the existing natural gas infrastructure, facilitating a gradual transition to a more sustainable energy system.

Catalytic technologies based on the reaction could play a key role in the decarbonization of “hard-to-abate sectors”, such as cement and steel production, that could implement the process to reduce CO_2 emissions and generate fuel for sustaining the energy-consuming processes [2]. Besides this one, another catalytic technology that emerges as one of the most promising ones is using the CO_2 methanation reaction to upgrade biogas to biomethane or SNG, by converting the naturally existing CO_2 found in biogas to CH_4, enriching its energetic content.

Due to the relevance that the biogas market is projected to have over the following years, this chapter will include a study of implementing the catalysts developed over the last chapters for catalytic technologies for biogas upgrade via selective hydrogenation of CO_2 to CH_4.

To apply a material for catalytic technology, besides the factors previously explored in the earlier chapters, such as CO_2 conversion and CH_4 selectivity, other factors like space velocity and stability must also be analyzed.

Thus, the catalysts that showed optimal yield values for methane were selected for additional tests. These tests include analyses with different space velocity values and stability tests with simulated sweetened biogas mixtures.

Therefore, the three catalysts chosen for the additional tests in this chapter are summarized in the table below. As part of the notation that refers to these materials, “_R” after the catalyst name indicates that it was previously reduced under standard reduction conditions, and “_ST” indicates that the material was subjected to a stability test.

Table 7.1. Selected catalysts with optimum results from previous results used for the WHSV and stability tests with synthetic sweetened biogas.

15Ni/ITQ-6 (30)	15% wt. Ni catalyst prepared by IWI over the ITQ-6 (30) zeolite support
15Ni/$LaAlO_3$	15% wt. Ni catalyst prepared by IWI over the $LaAlO_3$ support
15Ni-10Ce-Sep	15% wt. Ni doped with 10% wt. Ce prepared over the sepiolite support

7.2 – Influence of the Weight Speed Space Velocity (WHSV)

Space velocity is a critical parameter in catalytic processes that significantly influences the catalytic performance of a reactor. In this work, the weight hourly space velocity (WHSV) was used, which is the volumetric flow rate of feed of the **reactant gases** per unit mass of catalyst, even though other definitions of space velocity are also available.

The catalytic performance is highly sensitive to space velocity because it determines the contact time (τ) between the reactants and the catalyst. In heterogeneous catalysis, where reactions occur on the surface of solid catalysts, the diffusion of not only reactants to the active sites but also of products away from them is critical to the reaction rate. At low WHSV, there is typically enough time for reactants to diffuse thoroughly into the catalyst's porous structure, allowing for higher yields of the desired product. However, this may also increase the likelihood of side reactions, potentially producing unwanted by-products.

Space velocity also has an effect on the deactivation behavior of catalysts. Over time, catalysts can lose their activity due to phenomena such as coking, fouling, or sintering. At lower space velocities, the prolonged contact between the catalyst and reactants can accelerate these deactivation processes, especially in reactions prone to carbon deposition or where contaminants in the feed can poison the catalyst.

Higher space velocities can reduce the extent of these deactivation processes by decreasing the residence time of potentially harmful species on the catalyst surface. However, if the space velocity is too high, it may lead to incomplete reactions and reduced catalyst efficiency, requiring more frequent regeneration or replacement cycles, which requires a fine tuning of the space velocity.

Another aspect influenced by space velocity is the pressure drop across the catalyst bed. Lower space velocities usually result in lower pressure drops, which can be beneficial for energy efficiency and reducing operational costs. However, excessively low space velocities may lead to non-uniform flow distribution and channeling within the reactor, where some regions of the catalyst bed are underutilized while others are overloaded.

In practice, the choice of WHSV is often a compromise between maximizing conversion, selectivity, and catalyst lifespan while minimizing pressure drop and operational costs. One must consider the specific reaction kinetics, the nature of the feedstock, and the desired product distribution when determining the optimal space velocity.

In the last three chapters, the typical WHSV employed was 38,000 mL $(g_{CAT}\ h)^{-1}$, as the focus was not maximizing the CO_2 conversion and CH_4 yield, but instead exploring the physical-chemical characteristics of the catalysts. In this phase of the study, however, as the objective is maximizing the yield to CH_4, lower WHSV values were tested, such as 20,000; 10,000 and 6,000 mL $(g_{CAT}\ h)^{-1}$.

Regarding the temperature used for these tests and the stability ones with synthetic sweetened biogas samples, the temperature of 320 °C was chosen. At this temperature, as it will be seen in the next section, reaction equilibrium conversion was not attained (93.5%), so any deactivation effect would be noticed.

7.2.1 – 15Ni/ITQ-6 (30)

The results (**Figure 7.1**a) reveal that upon using WHSV = 6,000 mL (g_{CAT} h)$^{-1}$, the maximum CO_2 conversion is achieved. The lower the WHSV, the higher the CO_2 conversion for the range of studied temperatures, indicating that the increase in contact time has a positive effect on the catalytic performance.

For a porous material, such as the 15/ITQ-6, which presents part of the Ni^0 phase inside mesopores, an increased contact time favors the interaction of the molecules with the active phase, in consonance with similar materials previously published in the literature.

7.2.2 – 15Ni-LaAlO$_3$

The results (**Figure 7.1**b) reveal that upon using WHSV = 10,000 mL (g_{CAT} h)$^{-1}$ WHSV, the maximum CO_2 conversion is achieved. This aligns with others previously published results, as a plateau behavior is expected when the time of contact of the reactants with the active phase is increased.

This seems to take place in this case since the reaction rate seems mass-transfer controlled. With these conditions, extending the contact time does not increase the reaction rate after a certain point because there is no further modification on the rate at which reactants reach the active sites or products are removed from these sites.

7.2.3 – 15Ni-10Ce-Sep

The findings (**Figure 7.1**c) demonstrate that employing WHSV = 20,000 mL (g_{CAT} h)$^{-1}$ leads to higher CO_2 conversion values, with lower WHSV values leading to similar values. This behavior is similar to the one observed for the 15Ni/LaAlO$_3$ catalyst and seems to indicate that, under these conditions, the reaction is mass-transfer controlled.

Further increases in the time of contact do not lead to an increase in the catalytic performance because there is no change in either the rate at which reactant molecules reach the active site or the rate at which the product molecules leave the active site.

This way, with these tests, the optimum WHSV values were determined for each one of the catalysts, and these were the ones used for the biogas upgrade tests, as discussed in the following section.

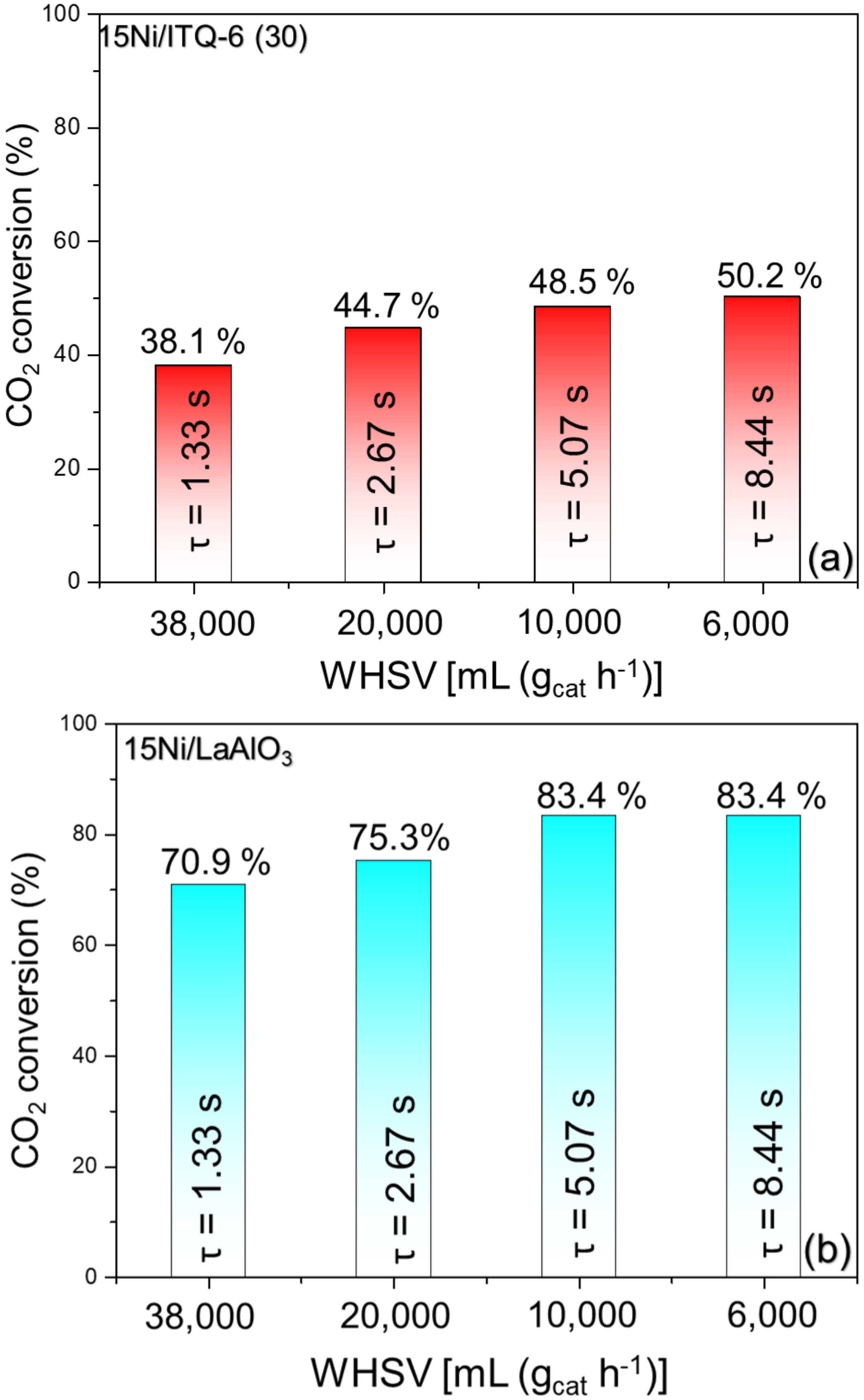
15Ni/ITQ-6 (30)
CO2 conversion (%)
0
20
40
60
80
100
38.1 %
44.7 %
48.5 %
50.2 %
τ = 1.33 s
τ = 2.67 s
τ = 5.07 s
τ = 8.44 s
(a)
38,000
20,000
10,000
6,000
WHSV [mL (gcat h-1)]
15Ni/LaAlO3
CO2 conversion (%)
0
20
40
60
80
100
70.9 %
75.3%
83.4 %
83.4 %
τ = 1.33 s
τ = 2.67 s
τ = 5.07 s
τ = 8.44 s
(b)
38,000
20,000
10,000
6,000
WHSV [mL (gcat h-1)]

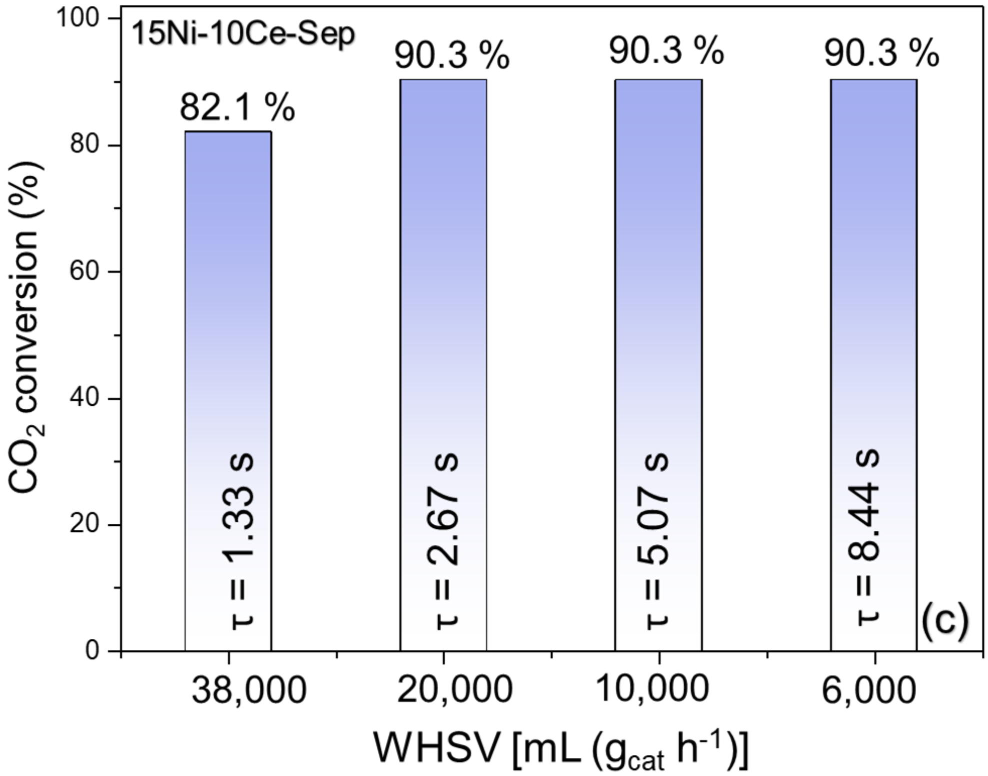

Figure 7.1. CO_2 conversion values dependence on the WHSV and correspondent time of contact (τ) between the reactants and the active phase is specified for (a) 15Ni/ITQ-6 (30), (b) 15Ni/$LaAlO_3$ and (c) 15Ni-10Ce-Sep. Reaction conditions: 320 °C, 1 atm, H_2:CO_2 = 4.

7.3 – Stability tests with synthetic sweetened biogas feed

As previously mentioned in Chapter 1, one of the most promising applications for the CO_2 methanation reaction is using it to develop catalytic technologies to upgrade the energetic content of biogas.

Biogas is obtained by anaerobic decomposition of organic waste materials and typically contains CH_4 and CO_2, along with contaminants, such as H_2S and NH_3, and others [3], which can be removed by sweetening. Technologies for the removal of the primary biogas contaminants are in a mature stage of development, as H_2S can be eliminated upon exposition to a catalytic bed containing iron oxides and salts and NH_3 by exposure to solutions containing inorganic acids or nitrogen-fixing microorganisms [4].

After the purification step, a mixture that is typically made up of CH_4 (50-75%) and CO_2 (25-50%) is obtained, with the exact composition depending on the organic source and conditions of the anaerobic digestion process [5, 6]. This biogas mixture can be upgraded by converting CO_2 into CH_4 [7].

In this way, sweetened biogas samples are converted into upgraded ones, such as biomethane (above 90% CH_4 [8]) or synthetic natural gas (SNG) (above 95% CH_4 [9]). Increasing the energy density of biogas this way represents a promising technological advance aimed at increasing its attractiveness in the renewable energy sector, as these upgraded samples could be transported by existing infrastructure [10, 11].

Considering the biogas characteristics, in the tests carried out in this study, a synthetic sweetened biogas sample with a composition of 60% CH_4 and 40 % CO_2 was employed. The stability tests consisted of a 24-hour long analysis with data collection every 24.7 min using the respective optimum WHSV identified in the 7.2 section.

7.3.1 – 15Ni//ITQ-6 (30)

The first data point exhibits X_{CO_2} = 45.7%, slightly lower than the one observed when CH_4 was absent (50.2%), which is attributed to a partial pressure reduction due to CH_4 addition (**Figure 7.2**). This impacts the reaction kinetics, as seen by the mathematical relation between the reaction rate and partial pressures of H_2 and CO_2, as described by Burger et al. [12].

According to the equation that governs the reaction kinetics, the introduction of CH_4 into the system, in comparison with the previous experiments, not only decreases the partial pressure of the reactants (H_2 and CH_4), but also increases the partial pressure of one of the products, which has the overall effect of decreasing the reaction rate, which leads to a decrease in CO_2 conversion.

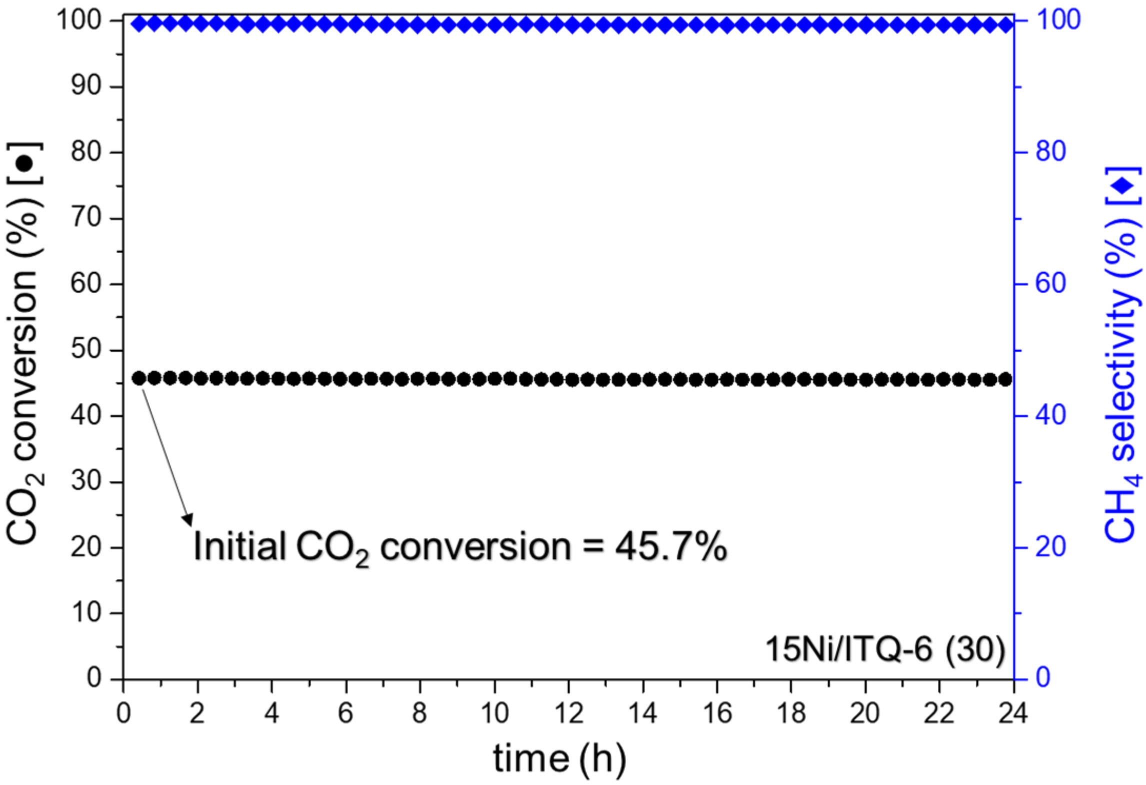

Figure 7.2. Stability test results regarding CO_2 conversion (●) and CH_4 selectivity (♦) values for the 15Ni/ITQ-6 (30) catalyst with emulated sweetened synthetic biogas sample. Reaction conditions: 1 atm, 320 °C, WHSV = 6,000 $(g_{cat}\,h)^{-1}$, CH_4: CO_2: H_2 = 3:2:8.

Throughout the extension of the experiment, the CO_2 conversions and CH_4 selectivity values are kept relatively the same throughout the extension of the stability. The results indicate that CH_4 remained unreactive throughout the experiment, as evidenced by its consistent inlet flow matching the outlet one, confirming the absence of any secondary reactions.

The catalyst after the stability test was assessed by XRD, elemental analysis, N_2 adsorption-desorption, and microscopy. XRD results (**Figure 7.3**) reveal no significant changes in the catalyst after the stability test. Furthermore, it is noteworthy that no peaks associated with $NiAl_2O_4$ phase are found, indicating that it was not formed under the conditions employed for the test.

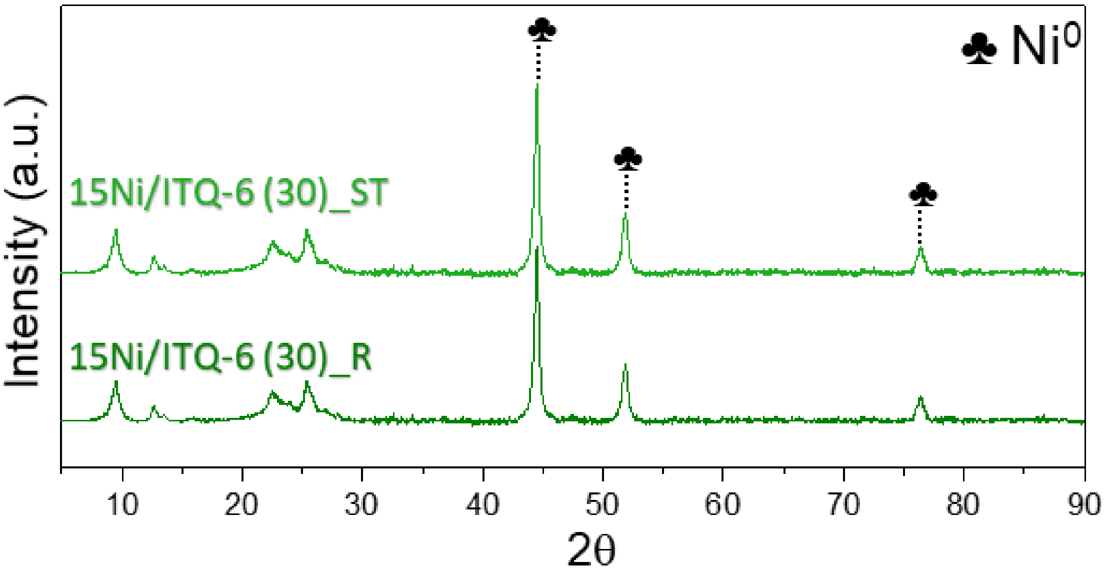

Figure 7.3. Comparison of the X-ray diffractograms of the 15Ni/ITQ-6 (30) catalyst after the reduction step and the stability test with a synthetic biogas sample.

H_2-chemisorption results (

Table 7.2) revealed that the Ni^0 average crystallite size changed from 19 to 21 nm (sintering extent = 10.7%).

Elemental analysis of the sample after the catalytic test detected the presence of carbon with 0.442% content, even though it was not possible to detect with the TEM images the formation of a specific carbon phase, such as carbon nanorods (**Figure 7.4**). The presence of carbon did not pose a problem for the catalytic stability, as revealed by the catalytic results, which did not change throughout the extension of the experiment.

TEM images further revealed that the delaminated structure of the ITQ-6 support was kept after the stability tests.

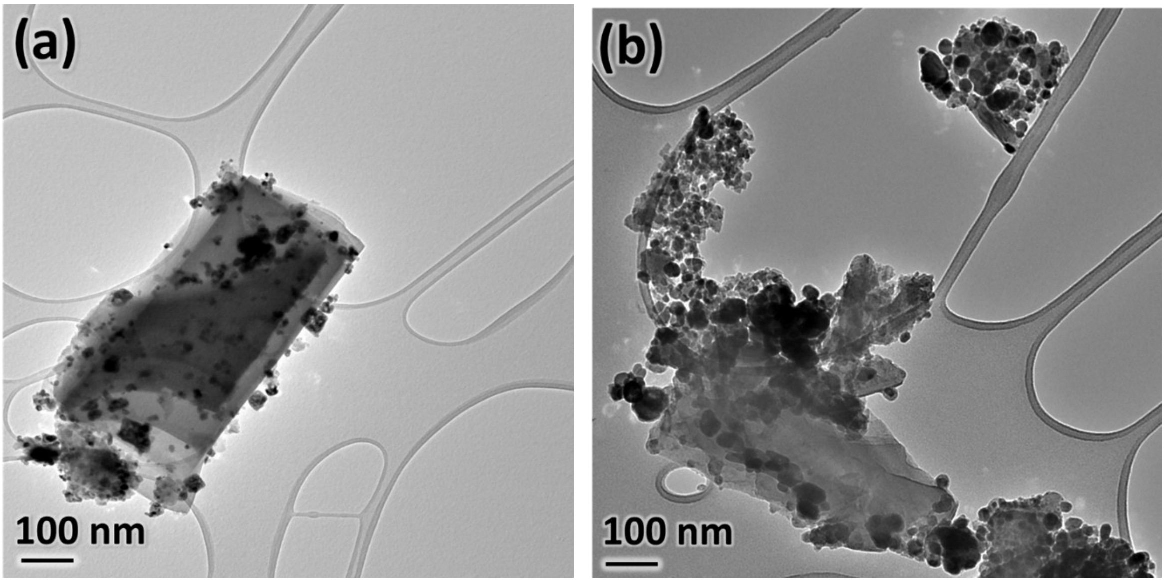

Figure 7.4. Comparison of the TEM of the 15Ni/ITQ-6 (30) catalyst (a) after the reduction step and (b) after the stability test with a synthetic biogas sample.

Table 7.2. Textural properties of selected catalysts used for the stability tests with synthetic sweetened biogas samples: Ni^0 crystallite size, D_{Ni}, sintering extent, carbon elemental content, C (wt. %), and BET surface area, S_{BET}.

Sample	D_{Ni} (nm) [a]	Sintering extent (%)	C (wt. %) [b]	S_{BET} (m^2 g^{-1}) [c]
15Ni/ITQ-6 (30)_R	19.6		-	287
15Ni/ITQ-6 (30)_ST	21.7	10.7	0.442	280
15Ni/$LaAlO_3$_R	16.0		-	7
15Ni/$LaAlO_3$_ST	22.6	41.3	0.248	7
15Ni-10Ce-Sep_R	7.6		-	120
15Ni-10Ce-Sep_ST	8.2	7.8	0.159	115

[a] Determined with H_2-chemisorption.

[b] Determined with elemental analysis.

[c] Determined with N_2 adsorption-desorption isotherms.

7.3.2 – 15Ni/LaAlO$_3$

The main difference from the previous one is that this catalyst exhibits an initial X_{CO_2}= 80.0 %, but then shows a significant decrease of the X_{CO_2}during the first six hours of the experiment (**Figure 7.5**). Despite encountering this decrease initially, the long-term results throughout the 24-hour test revealed that the X_{CO_2}values consistently hovered around 75.4%, while S_{CH_4} remained steadfast at 99.6%.

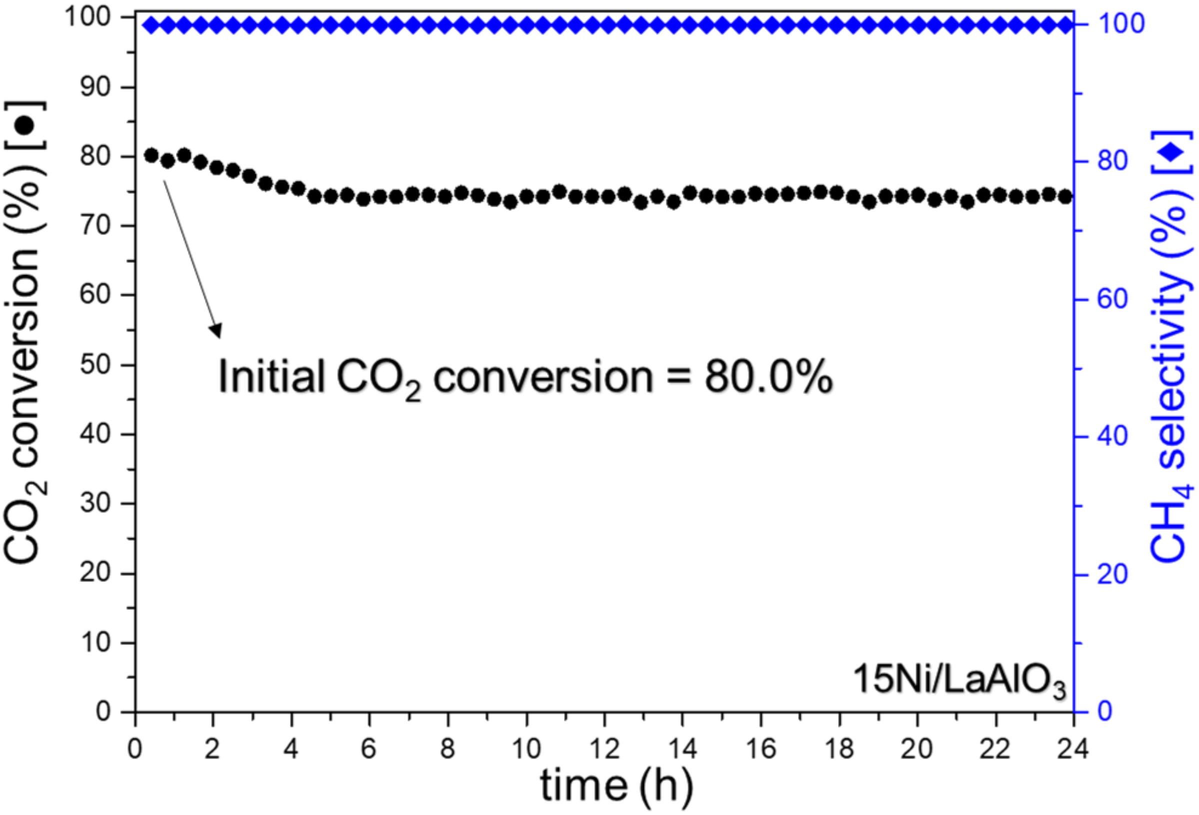

Figure 7.5. Stability test results regarding CO$_2$ conversion (●) and CH$_4$ selectivity (♦) for the 15Ni/LaAlO$_3$ catalyst with a sweetened synthetic biogas sample. Reaction conditions: 320 °C, 1 atm, WHSV = 10,000 mL (g$_{cat}$·h)$^{-1}$. Reaction conditions: 1 atm, 320 °C, WHSV = 10,000 mL (g$_{cat}$ h)$^{-1}$, CH$_4$: CO$_2$: H$_2$ = 3:2:8.

The results also reveal that the initial X_{CO_2} conversion value is lower than the one observed in the WHSV tests due to the introduction of CH$_4$ into the inlet flow, which has an impact on the partial pressure of the reactants, as previously discussed. In this experiment, CH$_4$ also remained unreactive, with the inlet and outlet flow for this gas remaining unchanged, indicating that it did not participate in side reactions.

H$_2$-chemisorption results reveal that the initial deactivation effect might be attributed to metallic sintering, as it is observed that the average Ni^0 crystallite size (

Table 7.2) increases from 16.0 nm (15Ni/LaAlO$_3$_R) to 24.1 nm (15Ni/LaAlO$_3$_ST) with a significant sintering extension. This sintering seems to take place due to the low surface area of the support, which is significantly lower than the other two catalysts, which contribute to an interaction in a higher extension between the Ni^0 particles.

XRD results also reveal that no $NiAl_2O_4$ phase was formed, and the phase composition after the 24-hour-long test was kept similar to the one found in the catalyst after reduction.

Elemental analysis of $15Ni/LaAlO_3$_ST reveals that carbon is formed to some extent, even though the TEM images taken from the catalyst after the stability test do not show explicitly the formation of a carbon phase (**Figure 7.7**). The formation of coke might also be attributed as one of the reasons for the initial deactivation observed for the catalyst, even though this does not prevent the catalysts from obtaining steadfast values for X_{CO_2} and S_{CH_4} towards the end of the experiment.

The TEM images also reveal that the rod-like structure of the support is maintained with no significant alterations.

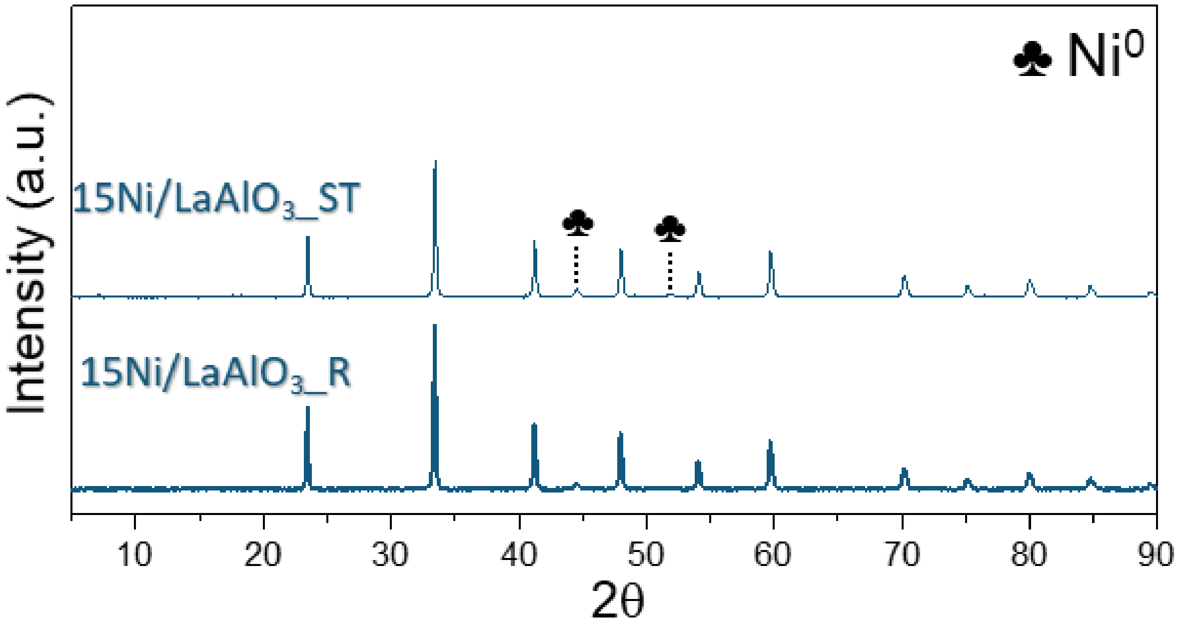

Figure 7.6. Comparison of the X-ray diffractograms of the $15Ni/LaAlO_3$ catalyst after the reduction step and the stability test with a synthetic biogas sample.

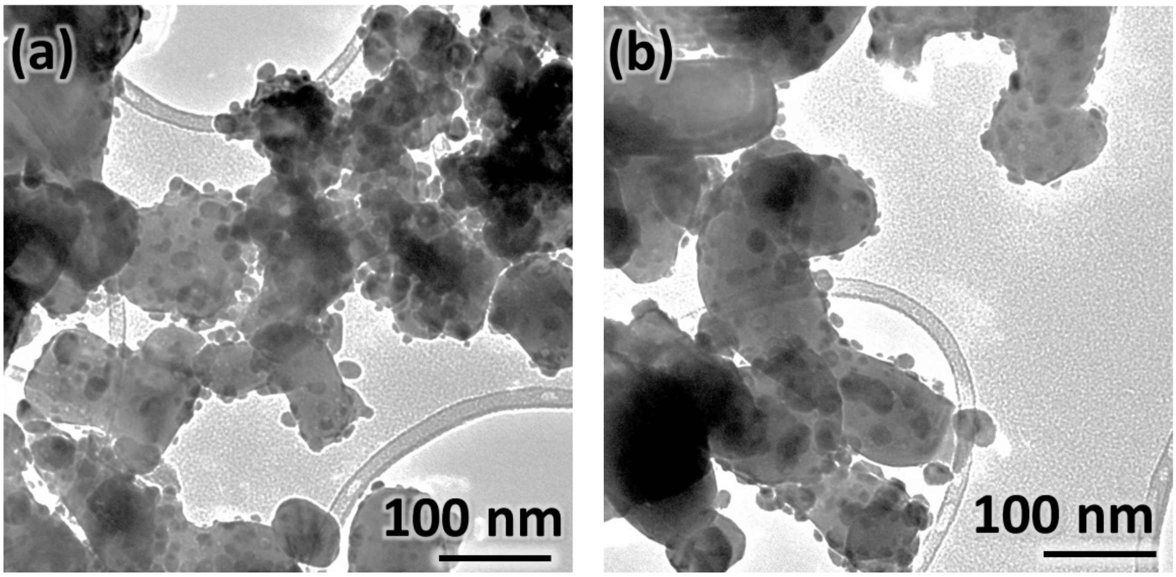

Figure 7.7. Comparison of the TEM of the 15Ni/LaAlO$_3$ catalyst (a) after the reduction step and (b) after the stability test with a synthetic biogas sample.

7.3.3 – 15Ni-10Ce-Sep

The results reveal that X_{CO_2} and S_{CH_4} values are kept relatively constant throughout the analysis with observance of X_{CO_2}= 87.5% and S_{CH_4}= 99.9% throughout the whole extension of the experiment (**Figure 7.8**).

Once again, in consonance with the results obtained for the other two catalysts, the initial observed X_{CO_2} value is lower than the one observed when CH_4 was not present in the inlet flow. This further confirms that introducing CH_4 into the system and the consequent drop in the partial pressure of the reactant gases lead to a reduction in CO_2 conversion. The injected CH_4 once again remained unreactive, as its inlet and outlet flows did not present modifications.

H_2-chemisorption results of the sample after the stability test reveal that there is a minor increase in the average Ni^0 particle size (D_{Ni} = **7.6 nm** in 15Ni-10Ce-Sep_R and **8.2 nm** in 15Ni-10Ce-Sep_ST) (

Table 7.2). This can be attributed to some sintering of the Ni^0 phase taking place to a limited extension, which is rationalized not only by the high surface area of the sepiolite support but overall, for the effect of CeO_2, which has been previously reported to prevent the sintering of the metallic phase in catalysts.

As previously discussed by Nagai et al., the Ni^0 phase can interact with the oxygen vacancies of the CeO_2 phase, creating Ni-O-Ce bonds, which prevents the interaction between Ni^0, hindering the sintering effect [13].

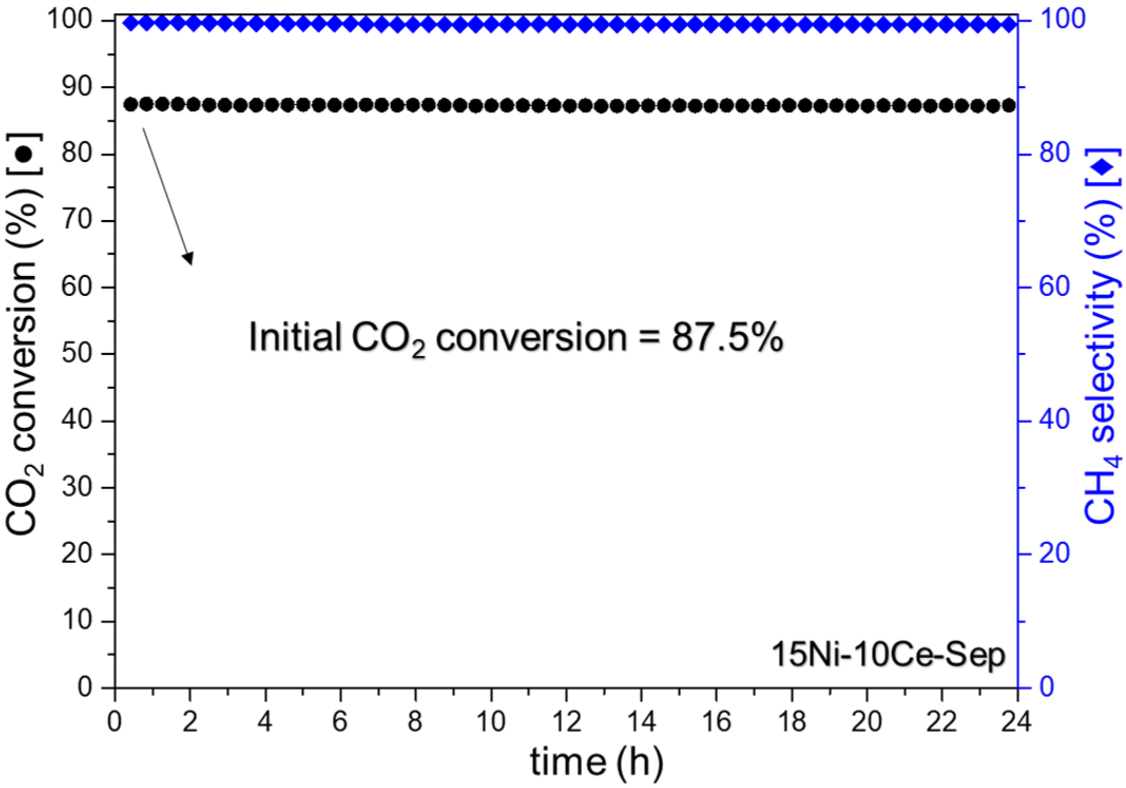

Figure 7.8. Stability test results regarding CO_2 conversion (●) and CH_4 selectivity (♦) for the 15Ni-10Ce-Sep catalyst with a sweetened synthetic biogas sample. Reaction conditions: 1 atm, 320 °C, WHSV = 20,000 mL $(g_{cat}\,h)^{-1}$, CH_4: CO_2: H_2 = 3:2:8.

XRD results (**Figure 7.9**) also reveal that no extra phases are formed between the interaction of the Ni^0 phase, neither with Si or Mg from sepiolite nor with cerium from the promoter phase.

Elemental analysis of 15Ni/$LaAlO_3$_ST reveals that it presents the lowest coke percentage (0.159 %) among the three tested catalysts. Previous results from the literature reveal that the extra anionic mobility provided by the CeO_2 oxygen vacancies decreases the activation energy for oxidation of the coke phase [14], which favors its elimination and seems to explain the lowest carbon content for this catalyst.

TEM images of the catalysts after the stability test (**Figure 7.10**) do not clearly show the formation of a carbon phase, with no observance of the typical structures, such as carbon nanotubes or nanorods. These images also reveal that the fibrous structure of the sepiolite support is kept after the stability tests.

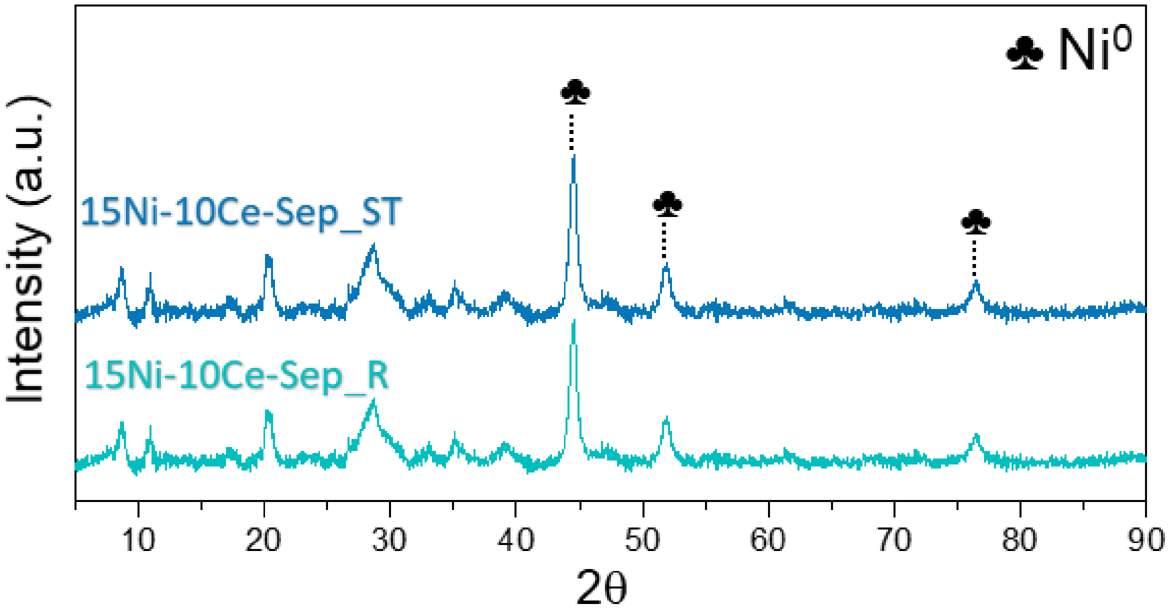

Figure 7.9. Comparison of the X-ray diffractograms of the 15Ni-10Ce-Sep catalyst after the reduction step and the stability test with a synthetic biogas sample.

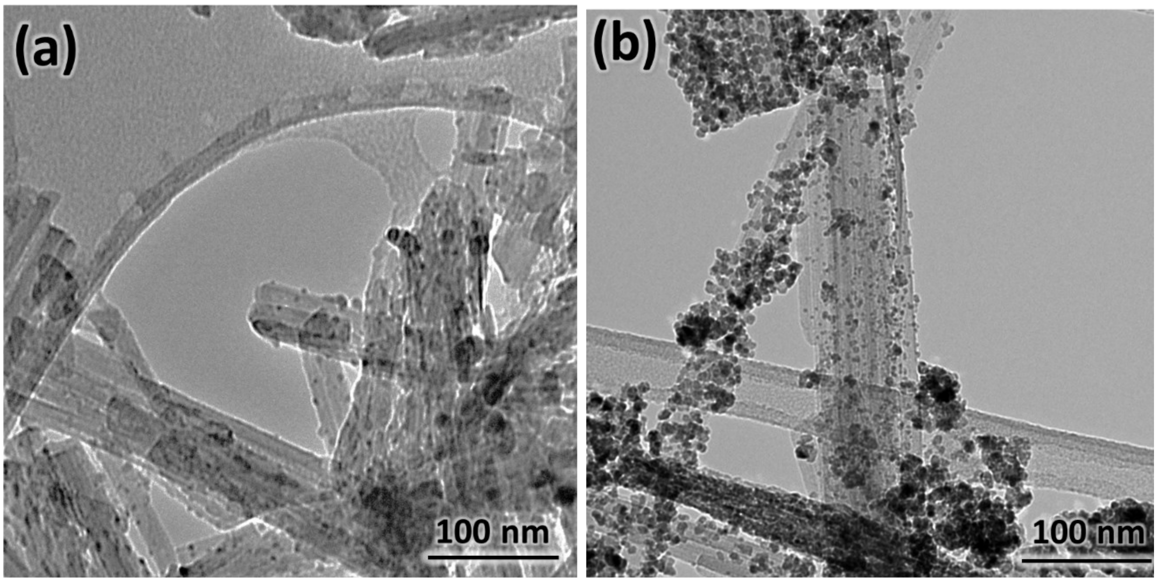

Figure 7.10. Comparison of the TEM of the 15Ni-10Ce-Sep catalyst (a) after the reduction step and (b) after the stability test with a synthetic biogas sample.

7.4 – Final considerations

Thus, as observed in the previous section, all three tested catalysts demonstrated stable CH_4 yield results after the 24-hour stability tests. The results of these experiments are summarized in **Table 7.3**, which calculates the CH_4 production rate for the catalysts after the stability tests.

Table 7.3. Results for selected catalysts at the end of the stability tests: used weight hourly speed velocity (WHSV), yield to CH_4 at the end of the test, Y_{CH_4}, and CH_4 production rate, F_{CH_4}.

Catalyst	WHSV used (mL $(g_{cat}\,h)^{-1}$)	Y_{CH_4}(%)	F_{CH_4} (mL $\cdot CH_4\,h^{-1}$)
15Ni/ITQ-6 (30)	6,000	44.4	186.8
15Ni/LaAlO$_3$	10,000	74.7	523.0
15Ni-10Ce-Sep	20,000	86.5	1211.0

These results show that the 15Ni-10Ce-Sep catalyst exhibits the highest production rate among the three catalysts studied (1211.0 mL CH_4 h^{-1}). The explanation for this observation has been addressed throughout this thesis but can be summarized as follows.

Given that all three catalysts contain the same metallic content, the 15Ni-10Ce-Sep catalyst was identified as having Ni^0 particles with an average crystallite size of 8.2 nm. As discussed in Chapter 6, Ni^0 particles around this size are the most efficient for maximizing TOF values by optimizing the interaction between the active metallic sites and the support.

Additionally, as discussed in Chapter 6, this catalyst retains the intrinsically basic characteristics of the sepiolite support due to Si and Mg ions in its structure. As explored in this thesis, basic sites are fundamentally important for the CO_2 reaction mechanism, as they participate in the activation process of this molecule, leading to its eventual reduction. Therefore, adding Ce as a promoter in this catalyst optimizes the Ni^0 particle size and increases the system's basicity, resulting in superior catalytic performance.

Finally, this catalyst is characterized by a fibrous structure and a significant surface area, with the active phase for the reaction located within mesopores. As previously discussed, this structure contributes to the interaction of reaction intermediates, promoting the observed high catalytic activity.

Therefore, for the stability test results observed for the catalyst with the best performance, 15Ni-10Ce-Sep, not considering the other component gas, the initial biogas mixture (60% CH_4/40% CO_2) was upgraded to a CH_4-enriched outlet flow (94.1% CH_4/5.9% CO_2). This composition represents a CH_4 content approximately 56.9% higher than the original biogas composition utilized prior to catalytic testing.

Given that this refined biogas sample exhibits a CH_4 content exceeding 90%, and considering the thresholds delineated by Kapoor et al. [8], it can be designated as biomethane.

Consequently, it can be seamlessly integrated into pre-existing pipeline infrastructures without technological upgrades [15].

Furthermore, another possibility is leaving part of the unreacted H_2 in the resulting flow, which would allow direct hydrogen blending in the biomethane flow obtained to some extent.

At this stage of technology development, blending H_2 in natural gas pipelines has been proposed as a promising procedure to attain near-term CO_2 emissions reductions and distribution of H_2 obtained by low carbon footprint processes, such as electrolysis [16].

These preliminary results reveal that the 15Ni-10Ce-Sep catalyst demonstrates significant potential for technological applications, particularly in developing biogas upgrading technologies through CO_2 methanation. Considering this promising outlook, further studies will be conducted as part of a recently approved research funding project. An example is the recently approved funding line for the CSIC COCREA project (Project number 2024/COCRE2310), aimed at developing novel catalysts for the CO_2 methanation reaction, which is being conducted in partnership with the Spanish company Tolsa.

7.5 – Conclusions

This chapter discusses the potential applications of the catalysts studied throughout this thesis for their use in biogas upgrading technologies through the selective hydrogenation of CO_2 to CH_4. The catalysts used for these tests were 15Ni/ITQ-6 (30), 15Ni/$LaAlO_3$, and 15Ni-10Ce-Sep.

Initially, screening tests with different WHSV values were conducted, revealing that a reduction in WHSV led to increased CO_2 conversion rates for all catalysts. This effect was attributed to the longer contact time between the reactants and the active phase, which favored the complete reduction of CO_2 to CH_4.

Subsequently, after determining the optimal space velocities for the catalysts, 24-hour stability tests were conducted using synthetic sweetened biogas samples (60% CH_4, 40% CO_2).

Among the three catalysts, 15Ni-10Ce-Sep exhibited the best performance, demonstrating good stability in conversion values throughout the experiment while minimizing coke formation. These results were attributed not only to the characteristics of the support but also to the addition of Ce as a promoter, which allowed the catalyst to present Ni^0 particles with an average size of around 8 nm. This particle size was identified in this study as the most efficient for CO_2 methanation. Furthermore, adding Ce optimized the concentration of moderate basic sites, another critical feature for the reaction mechanism, while also limiting coke formation compared to the other catalysts studied.

Finally, the 15Ni-10Ce-Sep catalyst exhibited a methane production rate of 1211.0 mL CH_4 h^{-1}, the highest among the three tested catalysts. The results demonstrated that considering the CH_4-CO_2 mixture used as synthetic biogas, it was possible to upgrade the mixture from an initial composition of 60% CH_4:40% CO_2 to a final composition of biomethane (94.1% CH_4/5.9% CO_2).

7.6 – References

[1] Held M, Schollenberger D, Sauerschell S, Bajohr S, Kolb T. Power-to-Gas: CO2 Methanation Concepts for SNG Production at the Engler-Bunte-Institut. Chemie-Ingenieur-Technik. 2020;92:595-602.

[2] Mertens J, Breyer C, Arning K, Bardow A, Belmans R, Dibenedetto A, et al. Carbon capture and utilization: More than hiding CO2 for some time. Joule. 2023;7:442-9.

[3] Wang D, Xin Y, Shi H, Ai P, Yu L, Li X, et al. Closing ammonia loop in efficient biogas production: Recycling ammonia pretreatment of wheat straw. Biosystems Engineering. 2019;180:182-90.

[4] Das J, Ravishankar H, Lens PNL. Biological biogas purification: Recent developments, challenges and future prospects. Journal of Environmental Management. 2022;304.

[5] Li Y, Alaimo CP, Kim M, Kado NY, Peppers J, Xue J, et al. Composition and Toxicity of Biogas Produced from Different Feedstocks in California. Environmental science & technology. 2019;53:11569-79.

[6] Kapoor R, Ghosh P, Kumar M, Vijay VK. Evaluation of biogas upgrading technologies and future perspectives: a review. Environmental Science and Pollution Research. 2019.

[7] Bauer F, Persson T, Hulteberg C, Tamm D. Biogas upgrading – technology overview, comparison and perspectives for the future. Biofuels, Bioproducts and Biorefining. 2013;7:499-511.

[8] Kapoor R, Subbarao PMV, Vijay VK, Shah G, Sahota S, Singh D, et al. Factors affecting methane loss from a water scrubbing based biogas upgrading system. Applied Energy. 2017;208:1379-88.

[9] Szima S, Cormos C-C. CO2 Utilization Technologies: A Techno-Economic Analysis for Synthetic Natural Gas Production. Energies2021.

[10] Aziz MAA, Jalil AA, Triwahyono S, Ahmad A. CO2 methanation over heterogeneous catalysts: Recent progress and future prospects. Green Chemistry. 2015;17:2647-63.

[11] Vogt C, Monai M, Kramer GJ, Weckhuysen BM. The renaissance of the Sabatier reaction and its applications on Earth and in space. Nature Catalysis. 2019;2:188-97.

[12] Burger T, Donaubauer P, Hinrichsen O. On the kinetics of the co-methanation of CO and CO2 on a co-precipitated Ni-Al catalyst. Applied Catalysis B: Environmental. 2021;282.

[13] Nagai Y, Hirabayashi T, Dohmae K, Takagi N, Minami T, Shinjoh H, et al. Sintering inhibition mechanism of platinum supported on ceria-based oxide and Pt-oxide–support interaction. Journal of Catalysis. 2006;242:103-9.

[14] Gurram VRB, Enumula SS, Mutyala S, Pochamoni R, Prasad PSS, Burri DR, et al. The advantage of ceria loading over V2O5/Al2O3 catalyst for vapor phase oxidative dehydrogenation of ethylbenzene to styrene using CO2 as a soft oxidant. Applied Petrochemical Research. 2016;6:427-37.

[15] Calero M, Godoy V, Heras CG, Lozano E, Arjandas S, Martín-Lara MA. Current state of biogas and biomethane production and its implications for Spain. Sustainable Energy & Fuels. 2023;7:3584-602.

[16] Pellegrino S, Lanzini A, Leone P. Greening the gas network – The need for modelling the distributed injection of alternative fuels. Renewable and Sustainable Energy Reviews. 2017;70:266-86.

Chapter 8

General conclusions

Thus, with the primary objective of developing catalysts for the selective hydrogenation of CO_2 to CH_4, Ni-based catalysts for this reaction supported on different supports were tested for the first time in the literature. These materials were characterized using various ex-situ and in-situ techniques to understand their physicochemical properties and were tested under different conditions to assess their catalytic activity. Finally, the most effective catalysts were tested to evaluate their applicability in catalytic technologies based on upgrading biogas through the selective hydrogenation of CO_2 to CH_4.

Each of the previous chapters includes a section dedicated to more thorough conclusions; however, this chapter resourcefully summarizes the main results obtained in each one of the chapters.

Chapter 4 – Zeolite based-catalysts

- Two types of zeolites, FER, and its delaminated counterpart, ITQ-6, with distinct Si/Al molar ratios, were compared as catalyst supports to assess zeolitic delamination's effect on the CO_2 methanation reaction.
- ITQ-6-based catalysts exhibited a more dispersed Ni^0 phase in comparison with the FER-supported ones due to the higher surface area values.
- ITQ-6-based catalysts presented higher CO_2 conversion and TOF values than the FER-based ones, attributed to the better dispersion of Ni^0 particles, which presented the optimum size (6-20 nm) for the catalytic performance, and also to a higher concentration of surface -OH groups.
- Regarding the effect of the Si/Al ratio, Si/Al = 30 catalysts exhibited higher CO_2 conversion and TOF values than the pure Si/Al = ∞, which was attributed to the presence of Si-(OH)-Al groups, which increased their CO_2 uptake.

Chapter 5 – Oxide-based catalysts

- The effect of mixed metal oxide synergy was evaluated for $LaAlO_3$ as catalytic support by comparing it with catalysts prepared for the individual oxides, Al_2O_3 and La_2O_3. The effect of Ni loading was also assessed.
- The $LaAlO_3$-based catalysts exhibited superior metal oxide synergy for the catalytic performance, attributed to a higher concentration of moderate basic sites.
- Time-resolved operando IR results revealed that these moderate basic sites are involved in the formation of monodentate carbonates, which are participating intermediates in the mechanism of reduction of CO_2 to CH_4.
- Regarding the Ni loading, 15% wt. Ni catalyst over $LaAlO_3$ presented the optimum results, attributed to a concerted effect of increased reducibility of the Ni phase and optimum

available Ni^0 metallic area. This favoured the formation of Ni^0-CO and monodentate carbonate participating intermediates in a mixed associative-dissociative mechanistic pathway.

Chapter 6 – Sepiolite-based catalysts

- Ce was evaluated as a promoter for a series of Ni-based catalysts supported over sepiolite. The effect of Ce loading (0, 1, 10, 30%) in a series of 5% wt. Ni catalysts was assessed. After its optimization, the effect of Ni loading (0, 5, 10, 15, 20) was also evaluated.
- The material in which 10% wt. Ce was added to a 5% wt. Ni catalyst exhibited the optimum CH_4 yield values at lower temperatures. Cerium increased the dispersion of the Ni^0 phase, leading to the obtention of Ni^0 particles with a size around 6 nm, which proved to be the most active for the CO_2 methanation reaction.
- Time-resolved operando IR measurements revealed that Ce-containing catalysts exhibited the dissociative-associative mechanism differently from the Ce-free one, which only exhibited the dissociative one. The Ce addition led to the formation of monodentate and formate, which were identified as participating intermediate species.
- Regarding the Ni loading, 15% wt. Ni catalyst with 10% wt. Ce presented the best results, attributed to an optimization of the Ni^0 particle size (around 7 nm) and the H_2 uptake, which reached a maximum at around 200 μmol H_2 g_{CAT}^{-1}.

Chapter 7 – Applications for catalytic technologies

- The best catalysts from each one of the previous were submitted to tests for the application of upgrading a synthetic biogas sample via the selective hydrogenation of CH_4: 15Ni/ITQ-6 (Si/Al = 30), 15Ni/$LaAlO_3$, and 15Ni-10Ce-Sep.
- Screening tests with different WHSV values revealed that, for all three catalysts, a reduction in WHSV led to increased CO_2 conversion rates.
- 15Ni-10Ce-Sep exhibited the best performance, demonstrating good stability in conversion values throughout the experiment while minimizing coke formation. This was attributed to the effect of Ce to optimize the Ni^0 dispersion and increase the concentration of moderate basic sites.
- Considering the CH_4 and CO_2 mixture, tests with 15Ni-10Ce-Sep catalysts upgraded a biogas mixture (60% CH_4:40% CO_2) to biomethane (94.1% CH_4/5.9% CO_2) with a CH_4 rate formation of 1211.0 mL CH_4 h^{-1}.

Chapter 9

Supplementary information

This chapter is dedicated to providing additional information necessary to understand this doctoral thesis, which was not included in the other chapters to maintain the text's fluidity and clarity.

9.1 – Example of calculation of a TOF value

To provide an example of how the Turnover Frequency values were calculated in this Thesis, here we provide examples of the calculations employed for the 5Ni/FER (Si//Al = ∞) catalyst, reported in Chapter 4.

TOF was calculated following the mathematical description already reported in the literature using the following equation:

$$TOF = \frac{number\ of\ reactions\ per\ second}{number\ of available\ active\ centers}$$

As the TOF regarding formation of CH_4 was studied, this expression can be remodeled to be:

$$TOF = \frac{\dot{n}_{CH_4,out}}{0.350\ \mathrm{g} \times \overline{N}_{available,\ Ni}}$$

Where $\dot{n}_{CH_4,out}$, is the CH_4 outlet molar flow, in mol s^{-1}, and $\overline{N}_{available,\ Ni}$ is the molar amount of Ni sites per catalyst gram calculated with the chemisorption technique and the in and out notations refer either to the inlet or outlet reactor flow, respectively.

Considering the stoichiometry of the reaction, this expression can be reformulated like:

$$TOF = \frac{\left(\dot{n}_{CO2,out} - \dot{n}_{CO2,in}\right) \cdot S_{CH_4}}{0.350\ \mathrm{g} \times \overline{N}_{available,\ Ni}}$$

As described in Chapter 3, the determination of $\overline{N}_{available,\ Ni}$, was carried out with H_2-chemisorption, where the approximations of a H_2 monolayer formation are considered. This way, the amount of chemisorbed H_2 per unit of mass of catalyst, N_m, is calculated with the following expression:

$$N_m = \frac{P \cdot V_{mono}}{m\ \cdot R \cdot T}$$

For example, for the 5Ni/FER (Si//Al = ∞) catalyst, the $V_{mono} = 8.044 \cdot 10^{-5}$ L H_2

Therefore, as the chemisorption temperature was 303 K:

$$N_m = \frac{(1\ atm) \cdot 8.044 \cdot 10^{-5}\ \mathrm{L}}{0.350\ g\ \cdot (0.082\ atm\ L\ mol^{-1}\ K^{-1}) \cdot (303\ K)}$$

$$N_m = 9.25 \cdot 10^{-6}\ mol\ g^{-1}$$

This way, the molar amount of available Ni sites to H_2 per catalyst gram is calculated by considering the stoichiometric factor (2 for Ni in these conditions).

$$\bar{N}_{available,\ Ni} = N_m \cdot 2$$

$$\bar{N}_{available,\ Ni} = 1.85 \cdot 10^{-5}\ mol\ g^{-1}$$

This way, at the temperature of 250 °C for the 5Ni/FER (Si//Al = ∞) catalyst, as described in Chapter 4, we have the following catalytic data:

$$TOF = \frac{(45\ ml\ min^{-1} - 44.784\ ml\ min^{-1}) \cdot 0.6696}{0.350\ \mathrm{g} \times 1.85 \cdot 10^{-5}\ mol\ g^{-1}}$$

As we want the TOF unit in inverse seconds, as typically reported in the literature for comparison purposes, a correction factor for time units can be added. The volume of gas can be converted into a molar amount by using the ideal gas equation:

$$TOF = \frac{(0.144\ ml\ min^{-1}) \cdot (10^{-3}\ L/1\ mL\,) \cdot (1\ min/60\ s)}{6.48\ \cdot 10^{-6}\ mol}$$

$$\cdot \frac{1\ atm}{(0.082\ atm\ L\ mol^{-1}\ K^{-1}) \cdot 298\ K}$$

$$TOF = \frac{9.82 \cdot 10^{-8}\ mol\ s^{-1}}{6.48\ \cdot 10^{-6}\ mol}$$

$$\boldsymbol{TOF = 0.0152\ s^{-1}}$$

Which is the value reported in Chapter 4 as the TOF value for the 5Ni/FER (Si/Al = ∞) referring to the temperature of 250 °C.

This method was employed to calculate TOF for all catalysts and at different temperatures for kinetic studies.

9.2 – Supplementary Figures

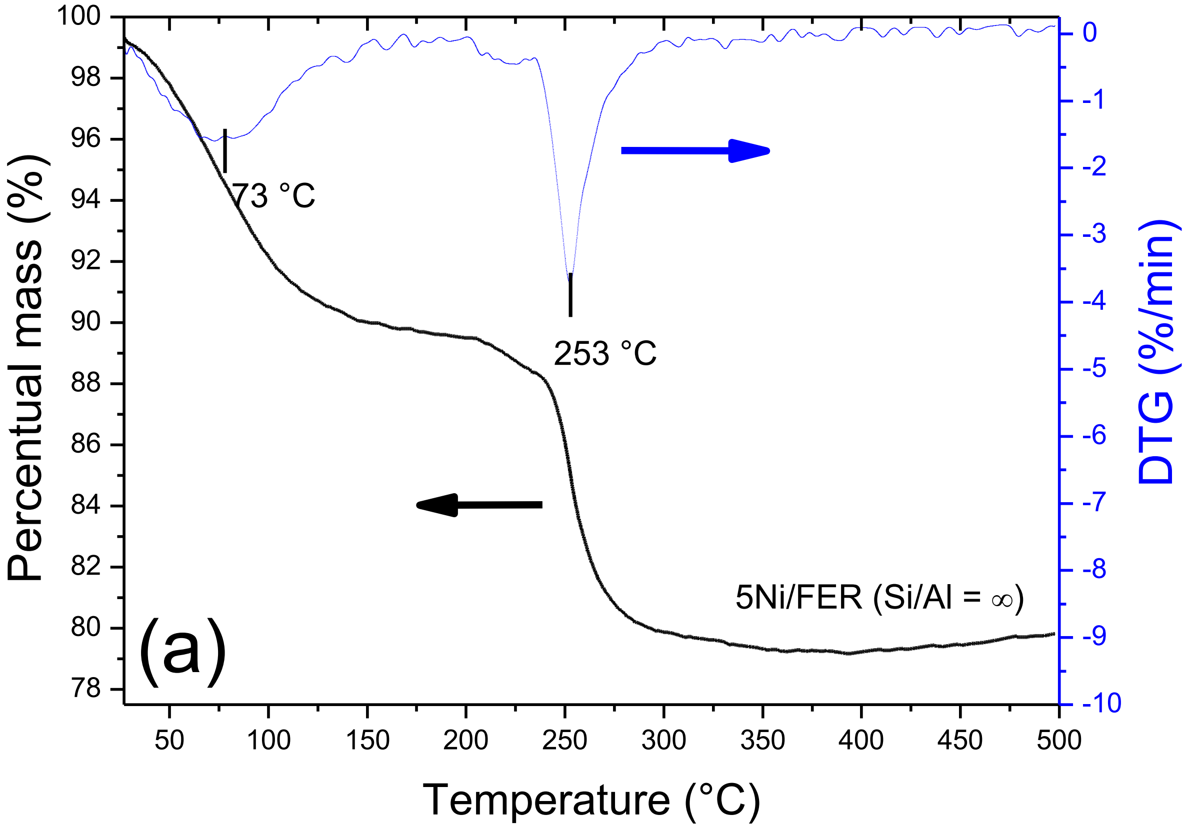

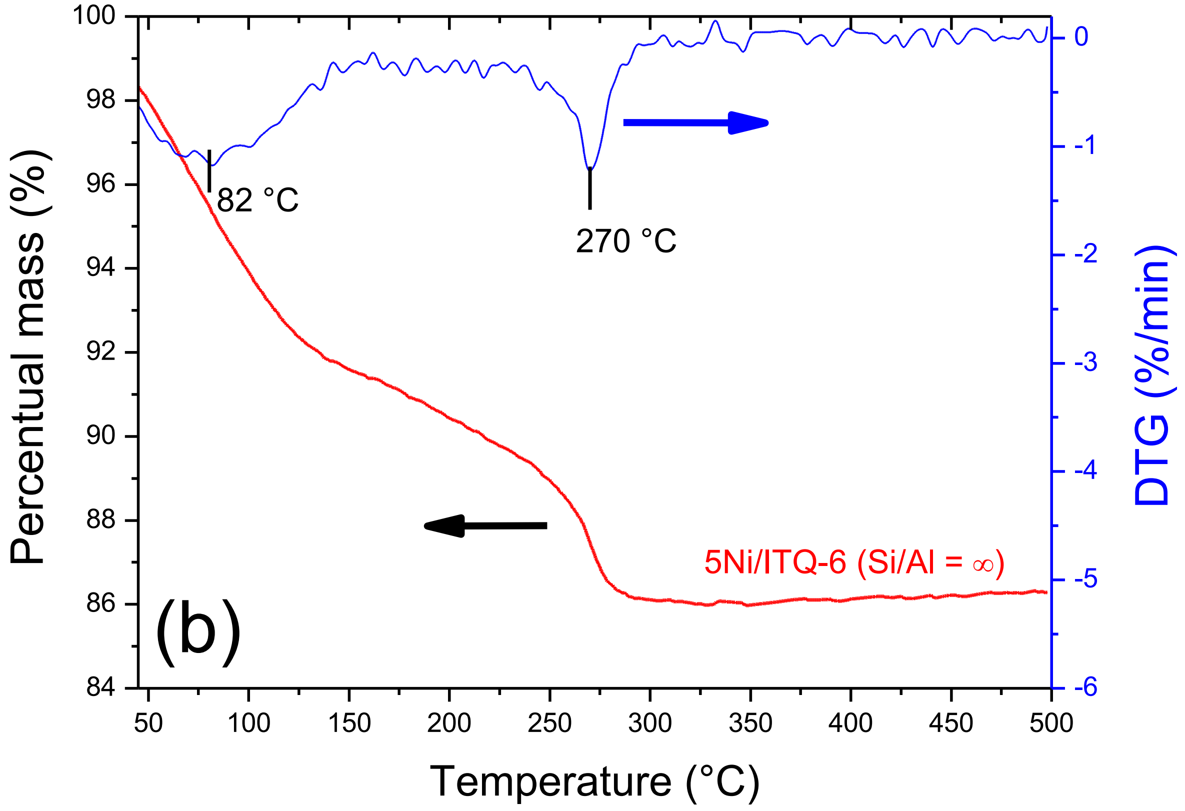

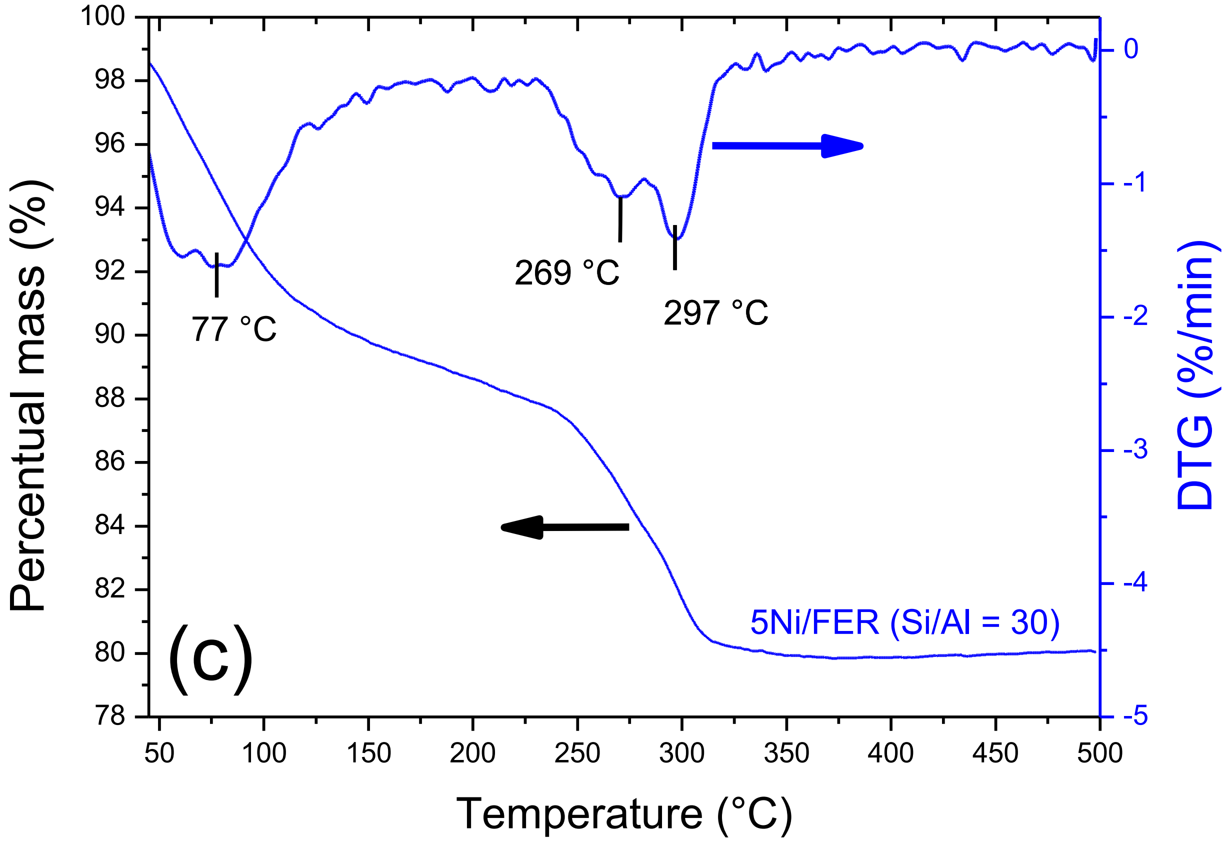
Percentual mass (%)
100
98
96
94
92
90
88
86
84
82
80
78
DTG (%/min)
0
-1
-2
-3
-4
-5
50
100
150
200
250
300
350
400
450
500
Temperature (°C)
77 °C
269 °C
297 °C
(c)
5Ni/FER (Si/Al = 30)

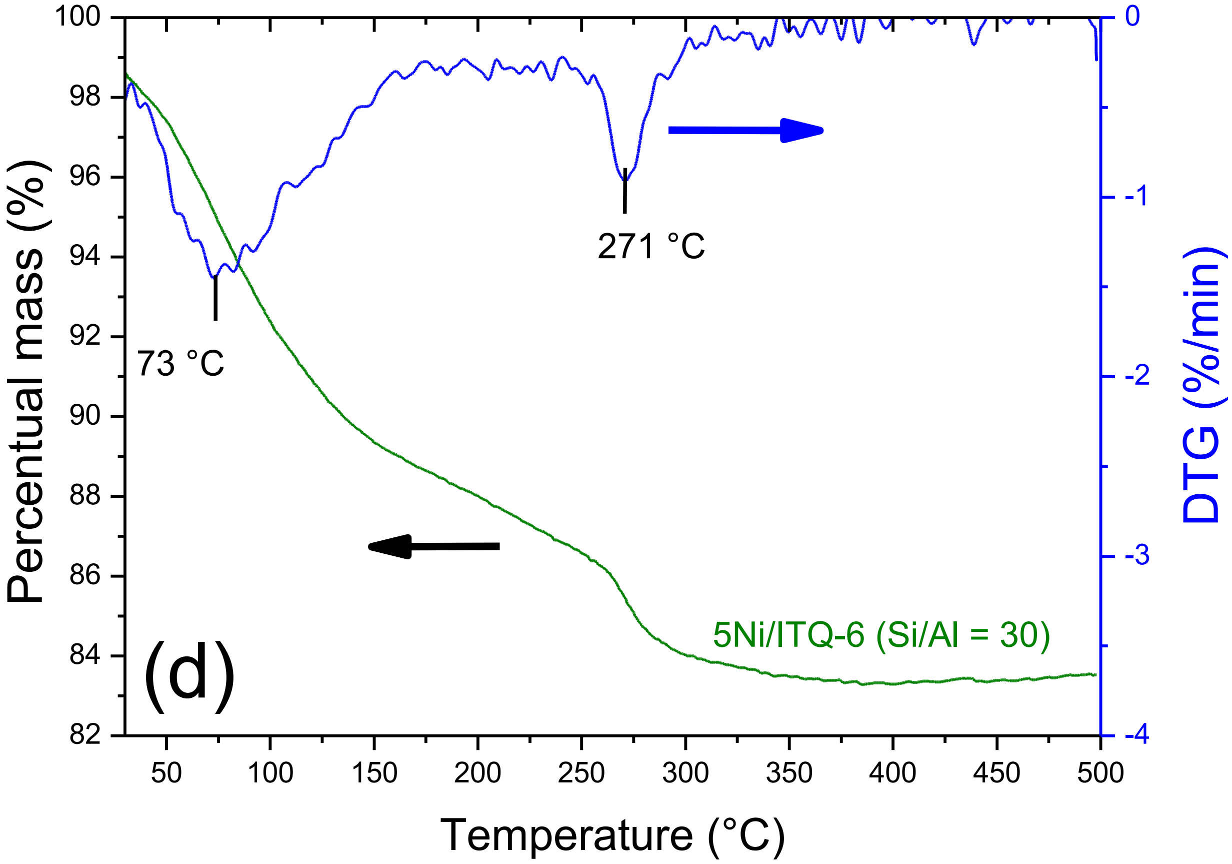
Percentual mass (%)
100
98
96
94
92
90
88
86
84
82
DTG (%/min)
0
-1
-2
-3
-4
50
100
150
200
250
300
350
400
450
500
Temperature (°C)
73 °C
271 °C
(d)
5Ni/ITQ-6 (Si/Al = 30)

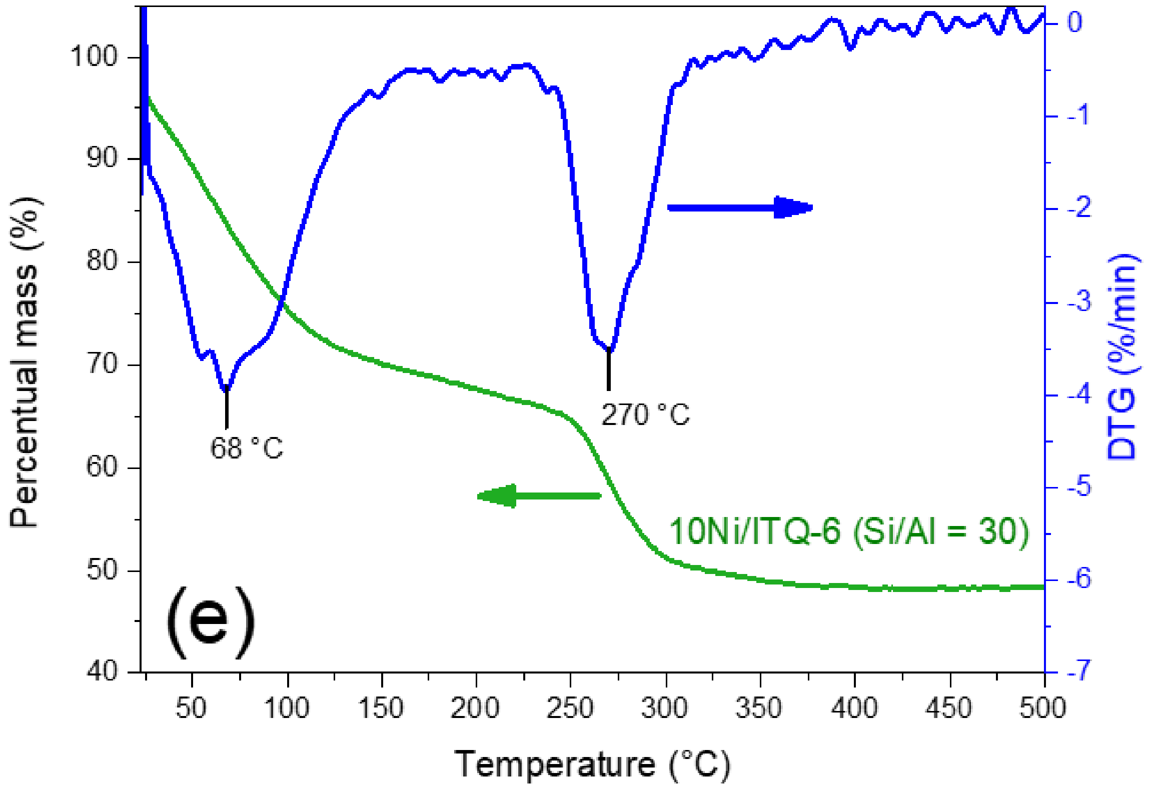
(e)
10Ni/ITQ-6 (Si/Al = 30)
68 °C
270 °C
Percentual mass (%)
DTG (%/min)
Temperature (°C)
100
90
80
70
60
50
40
0
-1
-2
-3
-4
-5
-6
-7
50
100
150
200
250
300
350
400
450
500

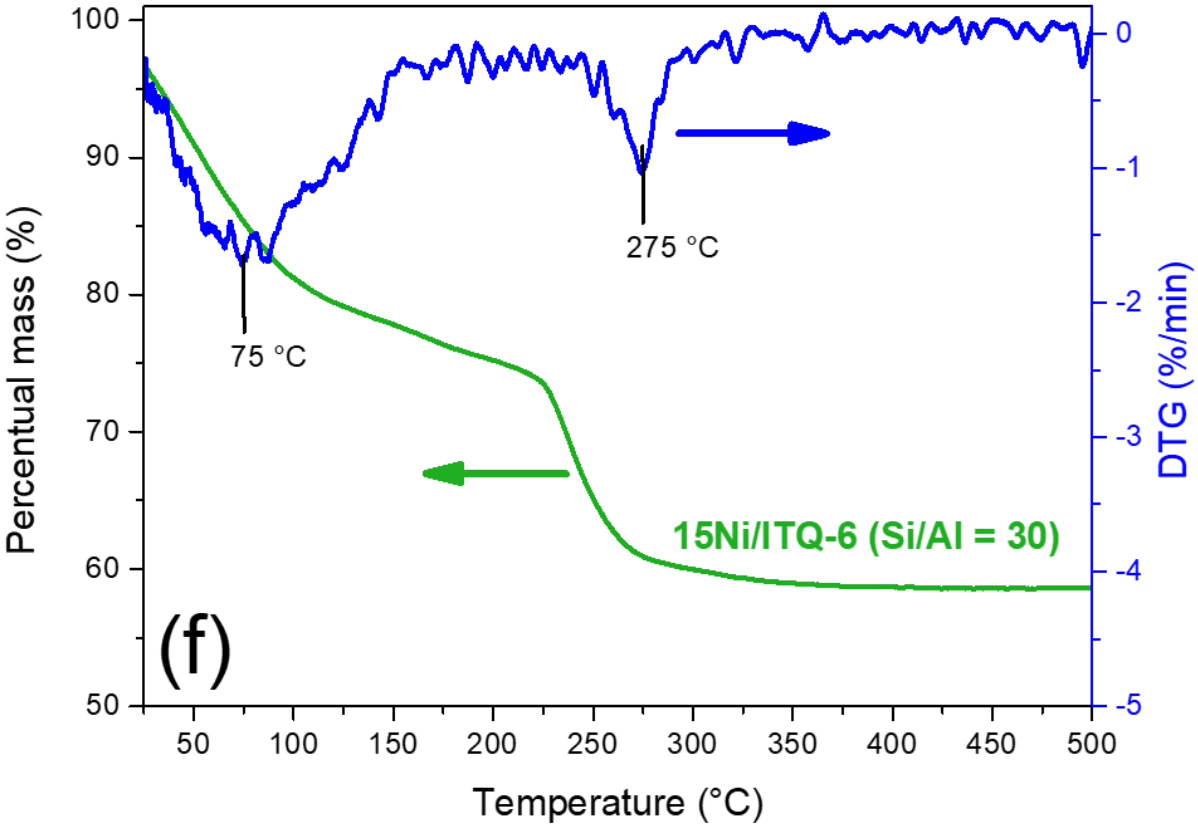
(f)
15Ni/ITQ-6 (Si/Al = 30)
75 °C
275 °C
Percentual mass (%)
DTG (%/min)
Temperature (°C)
100
90
80
70
60
50
0
-1
-2
-3
-4
-5
50
100
150
200
250
300
350
400
450
500

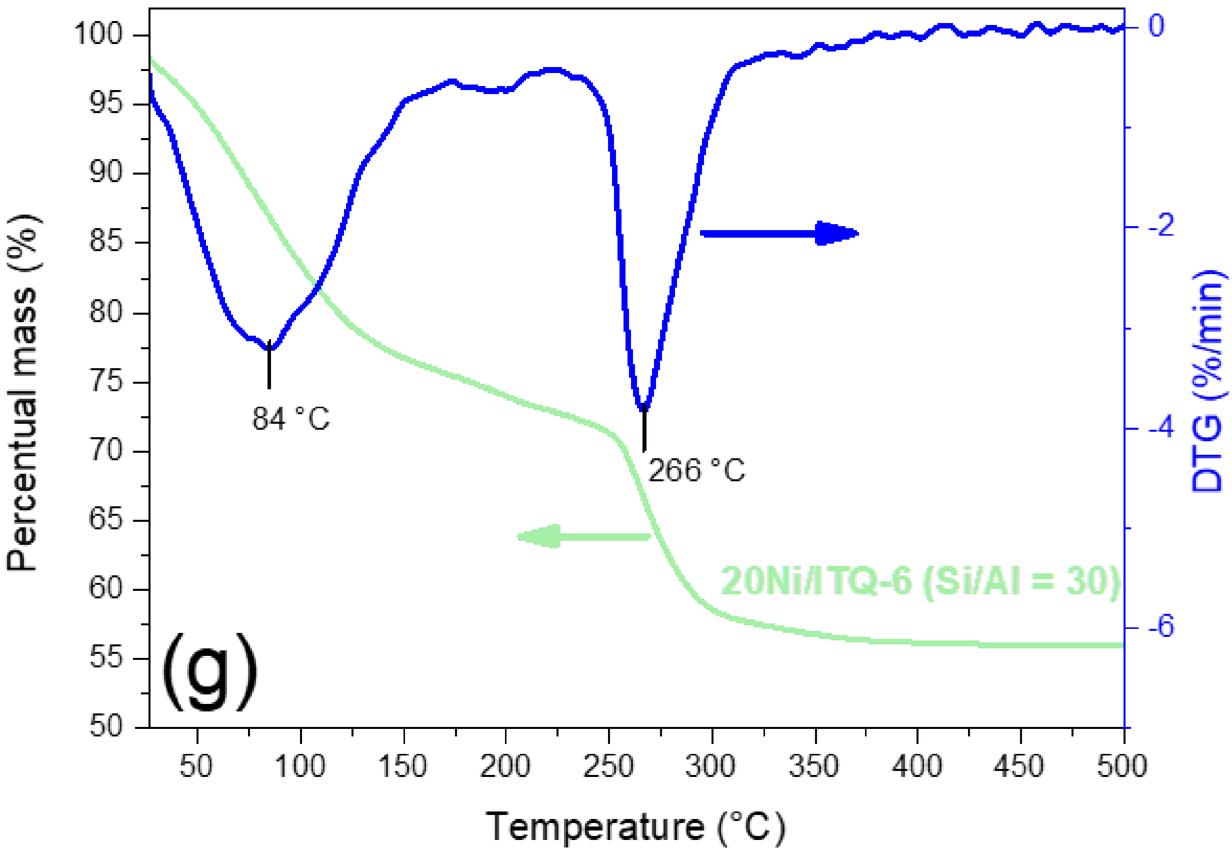

Figure 9.1. Thermogravimetric differential analysis (TG/DTA) of the zeolite-based catalysts after the impregnation step for the (a) 5Ni/FER (∞), (b) 5Ni/ITQ-6 (∞), (c) 5Ni/FER (30), (d) 5Ni/ITQ-6 (30), (e) 10Ni/ ITQ-6 (30), (f) 15Ni/ ITQ-6 (30), and (g) 20Ni/ ITQ-6 (30). The arrows next to the data point to the corresponding vertical axis.

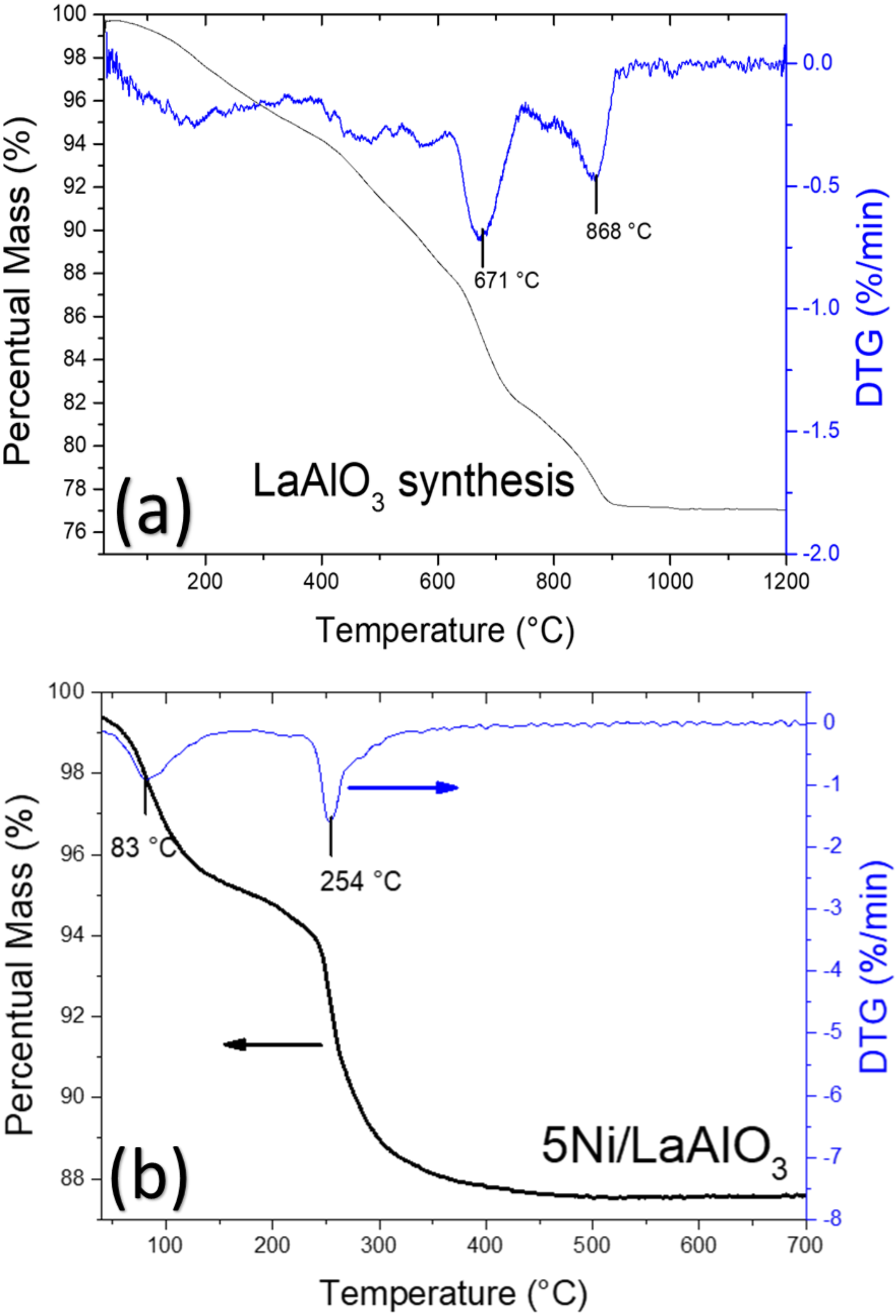
(a)
LaAlO3 synthesis
Percentual Mass (%)
100
98
96
94
92
90
88
86
84
82
80
78
76
DTG (%/min)
0.0
-0.5
-1.0
-1.5
-2.0
200
400
600
800
1000
1200
Temperature (°C)
671 °C
868 °C
(b)
5Ni/LaAlO3
Percentual Mass (%)
100
98
96
94
92
90
88
DTG (%/min)
0
-1
-2
-3
-4
-5
-6
-7
-8
100
200
300
400
500
600
700
Temperature (°C)
83 °C
254 °C

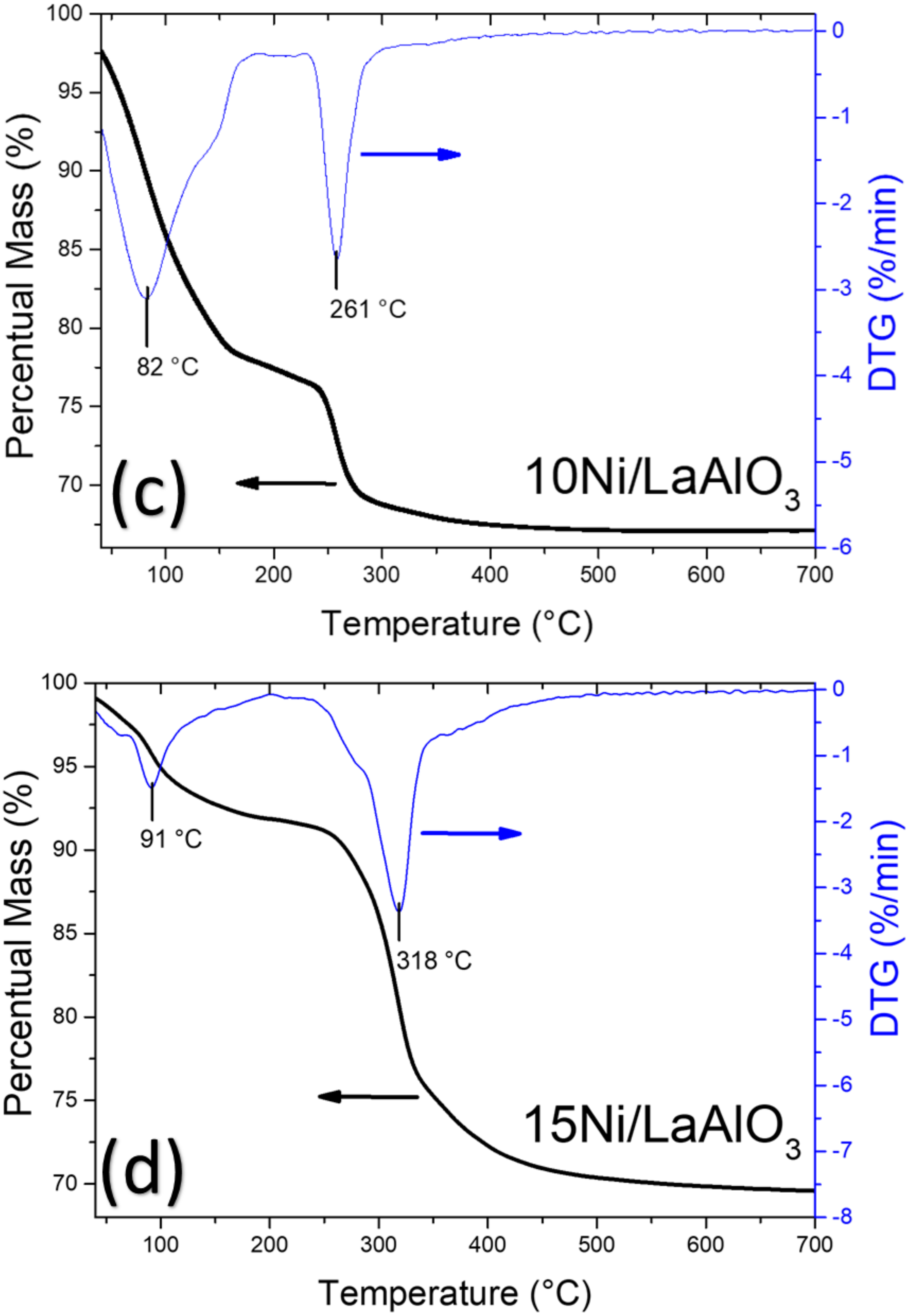

Figure 9.2. Thermogravimetric differential analysis (TG/DTA) for: (a) the support precursors for $LaAlO_3$ before the calcination, and the Ni-impregnated $LaAlO_3$ supports with different metallic loadings: (b) 5% wt.; (c) 10% wt.; (b) 15% wt. The arrows next to the data point to the corresponding vertical axis.

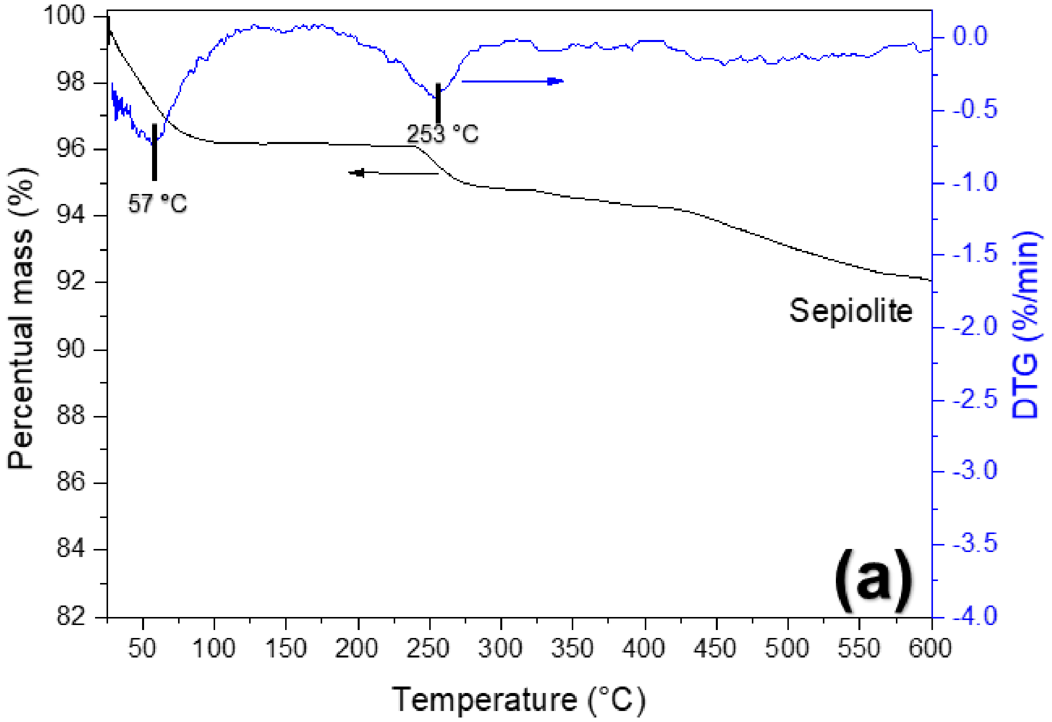
Percentual mass (%)
100
98
96
94
92
90
88
86
84
82
DTG (%/min)
0.0
-0.5
-1.0
-1.5
-2.0
-2.5
-3.0
-3.5
-4.0
57 °C
253 °C
Sepiolite
(a)
50
100
150
200
250
300
350
400
450
500
550
600
Temperature (°C)

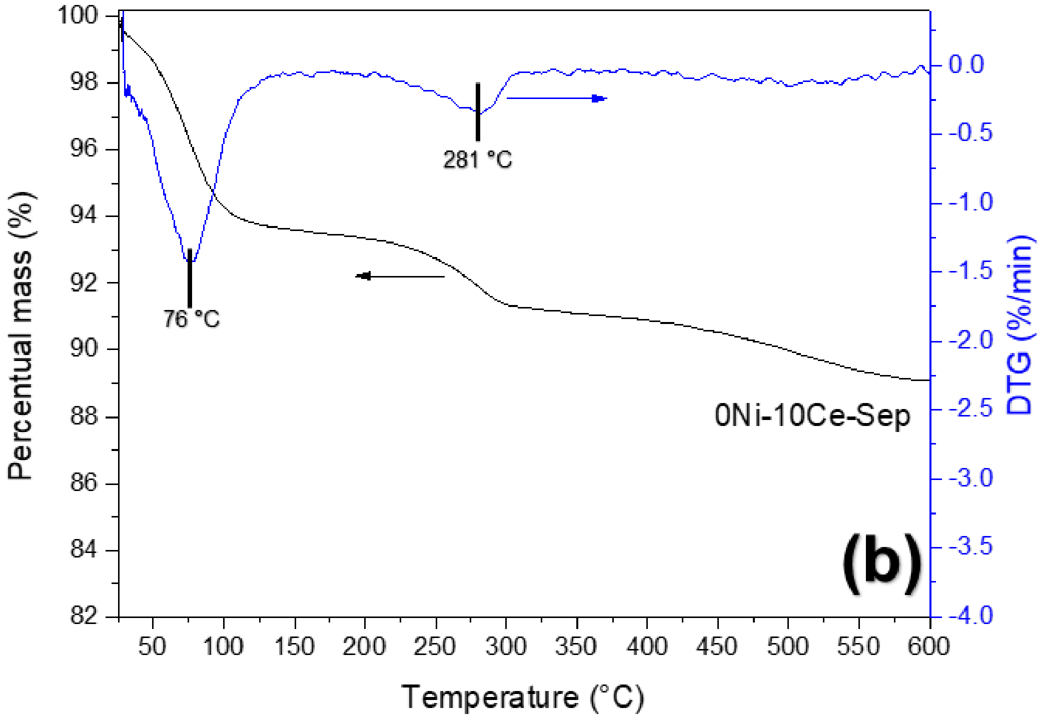
Percentual mass (%)
100
98
96
94
92
90
88
86
84
82
DTG (%/min)
0.0
-0.5
-1.0
-1.5
-2.0
-2.5
-3.0
-3.5
-4.0
76 °C
281 °C
0Ni-10Ce-Sep
(b)
50
100
150
200
250
300
350
400
450
500
550
600
Temperature (°C)

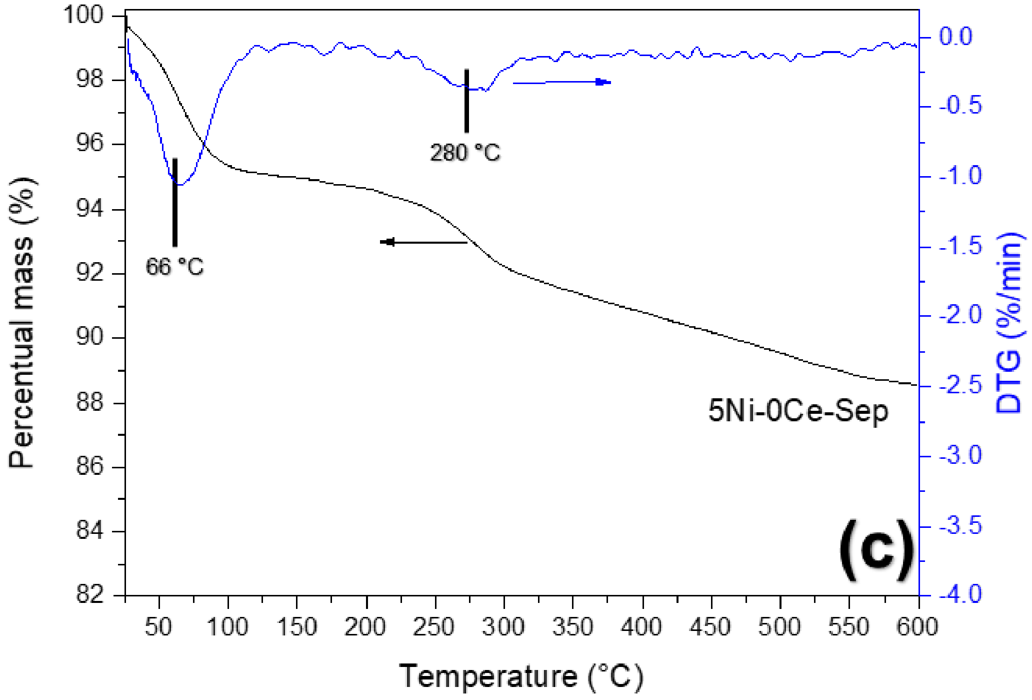
Percentual mass (%)
100
98
96
94
92
90
88
86
84
82
DTG (%/min)
0.0
-0.5
-1.0
-1.5
-2.0
-2.5
-3.0
-3.5
-4.0
Temperature (°C)
50
100
150
200
250
300
350
400
450
500
550
600
66 °C
280 °C
5Ni-0Ce-Sep
(c)

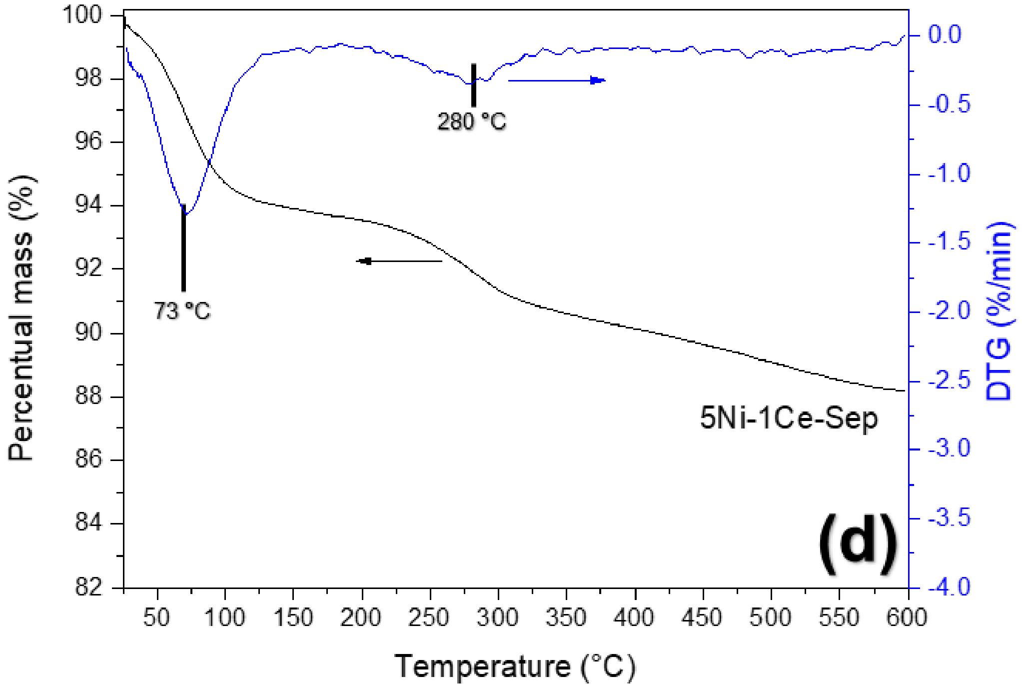
Percentual mass (%)
100
98
96
94
92
90
88
86
84
82
DTG (%/min)
0.0
-0.5
-1.0
-1.5
-2.0
-2.5
-3.0
-3.5
-4.0
Temperature (°C)
50
100
150
200
250
300
350
400
450
500
550
600
73 °C
280 °C
5Ni-1Ce-Sep
(d)

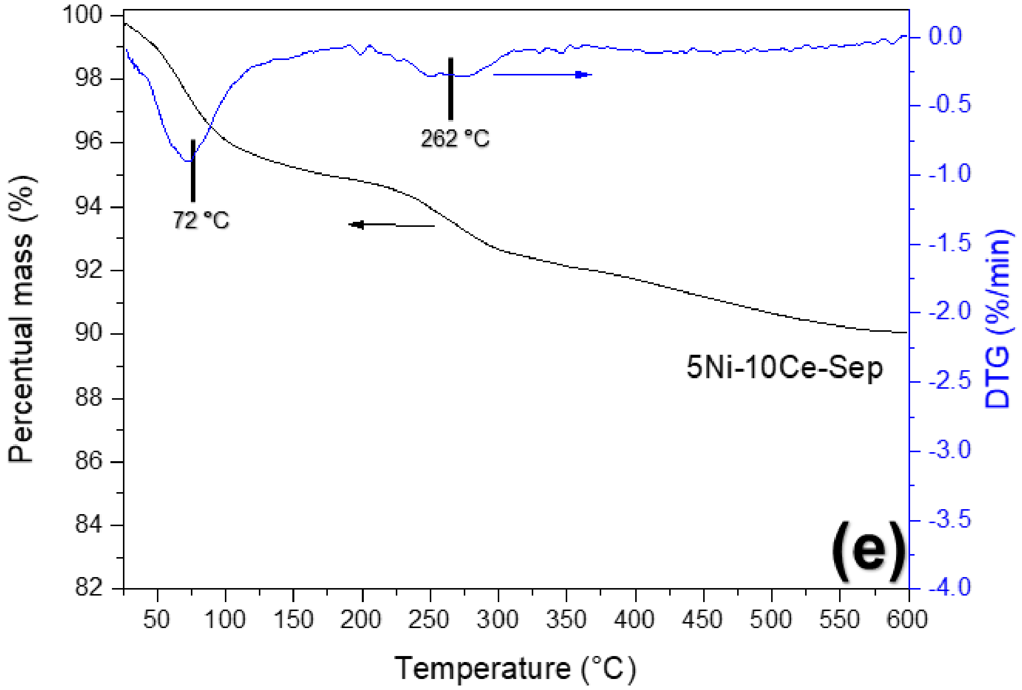
Percentual mass (%)
100
98
96
94
92
90
88
86
84
82
DTG (%/min)
0.0
-0.5
-1.0
-1.5
-2.0
-2.5
-3.0
-3.5
-4.0
50
100
150
200
250
300
350
400
450
500
550
600
Temperature (°C)
72 °C
262 °C
5Ni-10Ce-Sep
(e)

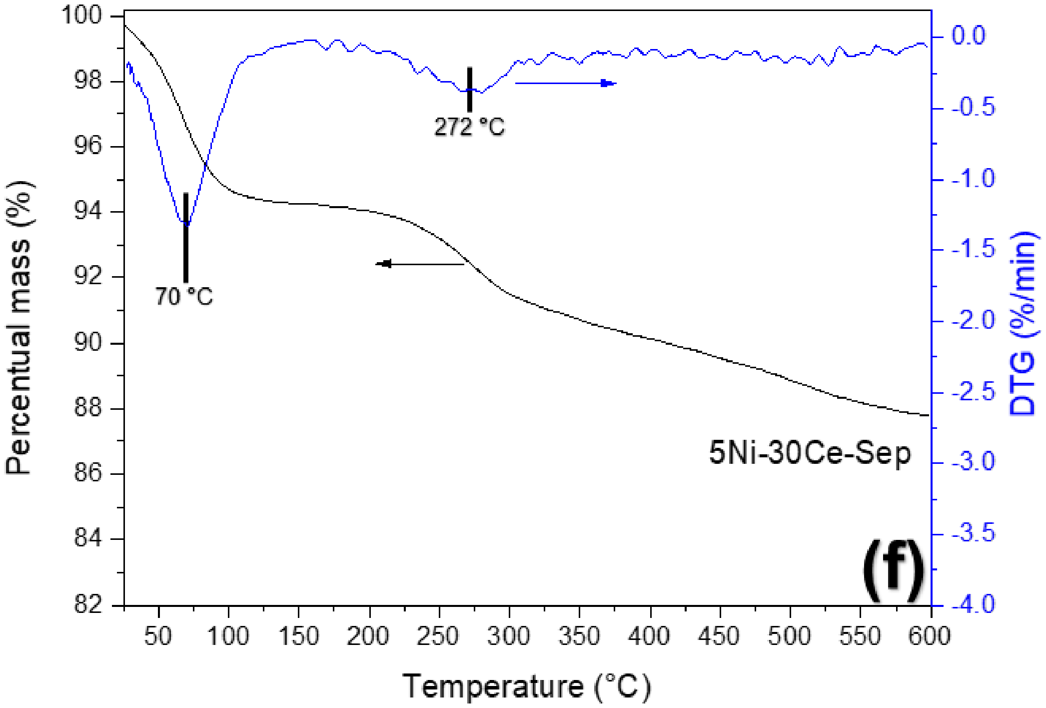
Percentual mass (%)
100
98
96
94
92
90
88
86
84
82
DTG (%/min)
0.0
-0.5
-1.0
-1.5
-2.0
-2.5
-3.0
-3.5
-4.0
50
100
150
200
250
300
350
400
450
500
550
600
Temperature (°C)
70 °C
272 °C
5Ni-30Ce-Sep
(f)

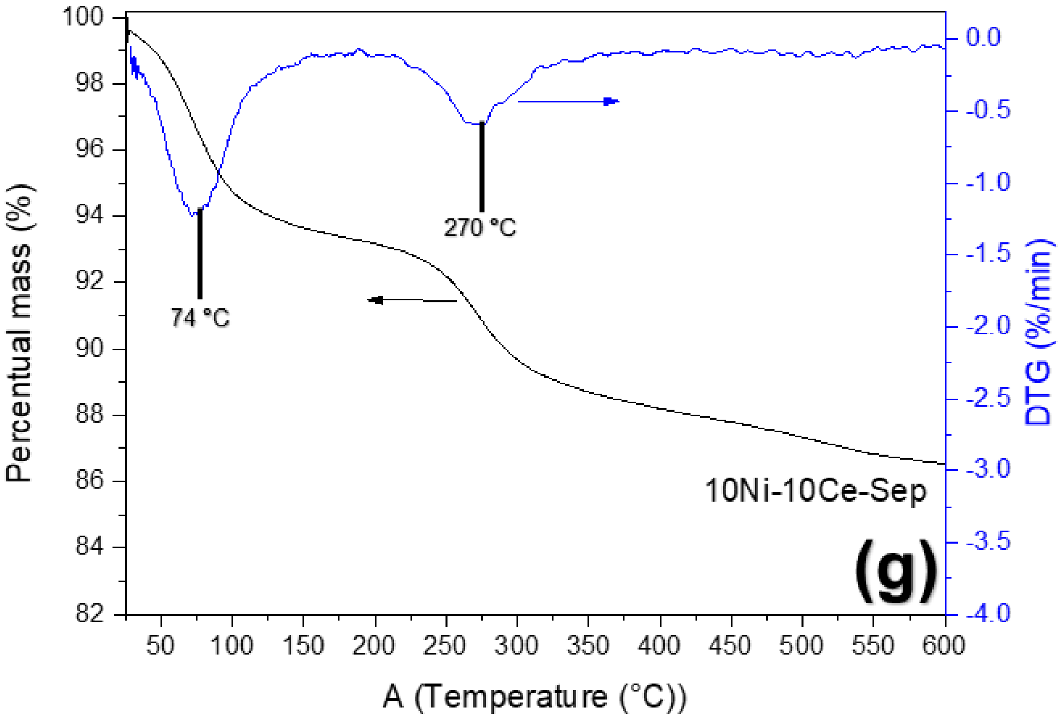

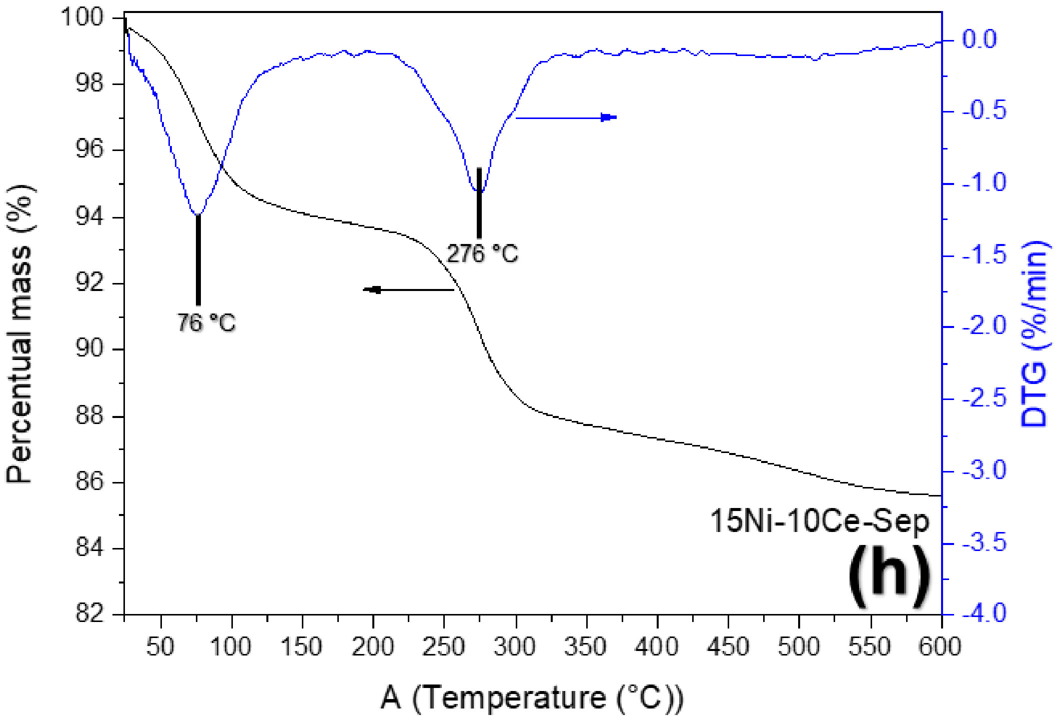

Figure 9.3. Thermogravimetric differential analysis (TG/DTA) for: (a) sepiolite, (b) 0Ni-10Ce-Sep, (c) 5Ni-0Ce-Sep, (d) 5Ni-1Ce-Sep, (e) 5Ni-10Ce-Sep, (f) 5Ni-30Ce-Sep, (g) 10Ni-10Ce-Sep, and (h) 15Ni-10Ce-Sep. The arrows next to the data point to the corresponding vertical axis.

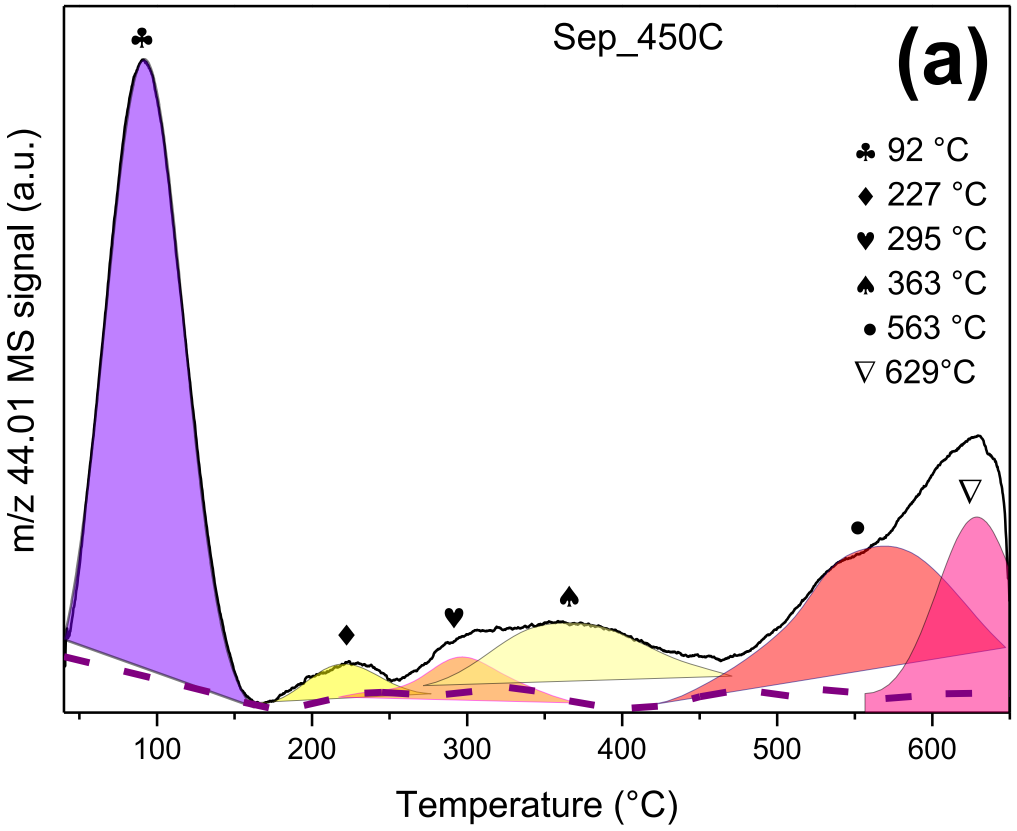
Sep_450C
(a)
♣ 92 °C
♦ 227 °C
♥ 295 °C
♠ 363 °C
● 563 °C
∇ 629°C
♣
♦
♥
♠
●
∇
m/z 44.01 MS signal (a.u.)
100
200
300
400
500
600
Temperature (°C)

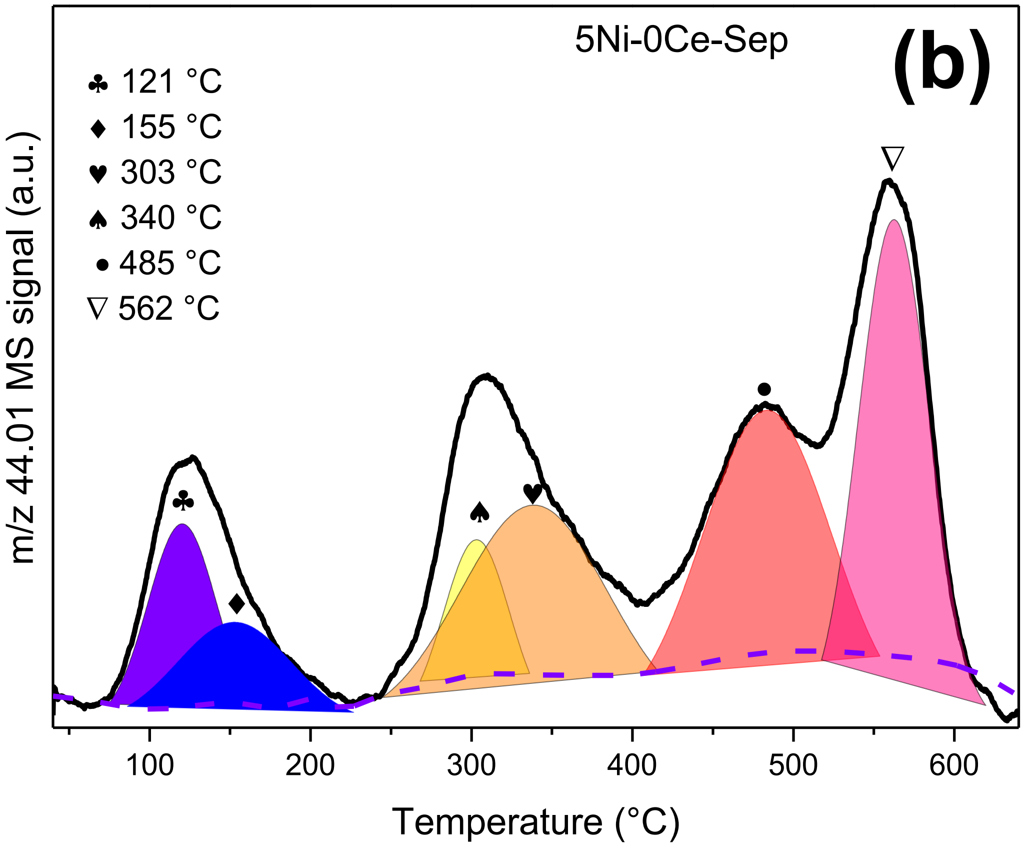
5Ni-0Ce-Sep
(b)
♣ 121 °C
♦ 155 °C
♥ 303 °C
♠ 340 °C
● 485 °C
∇ 562 °C
∇
●
♣
♦
♠
♥
m/z 44.01 MS signal (a.u.)
100
200
300
400
500
600
Temperature (°C)

]

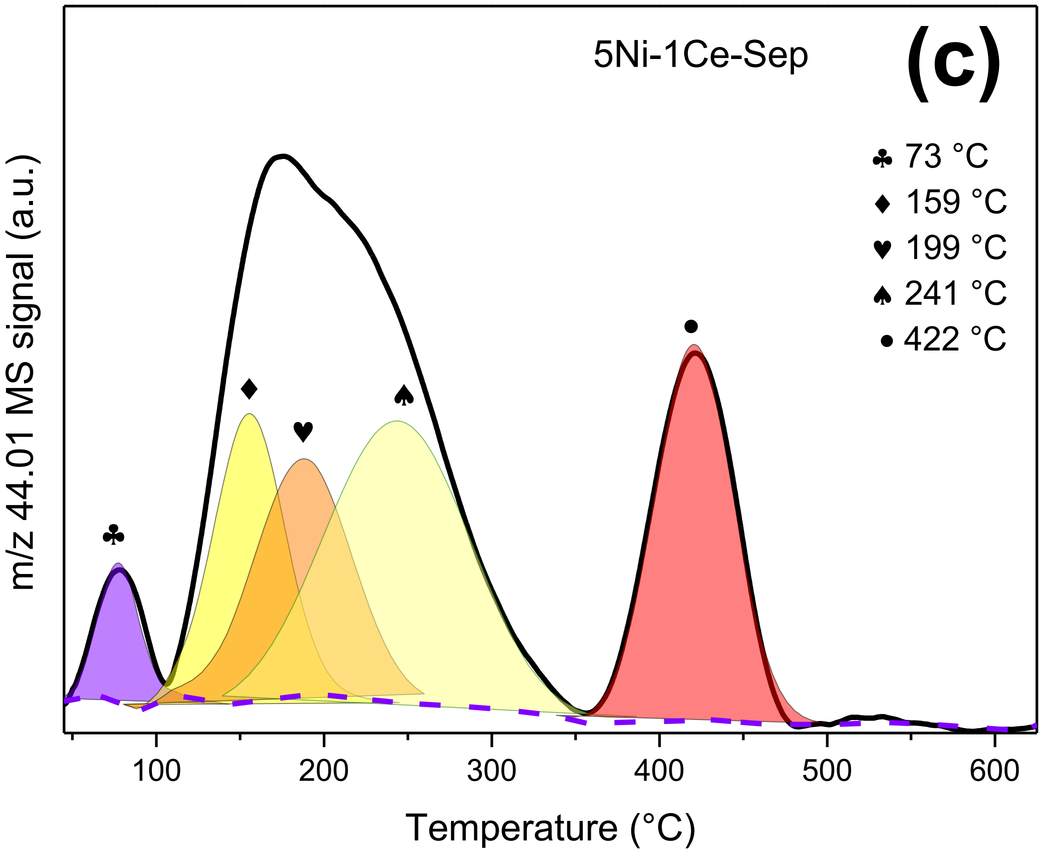
5Ni-1Ce-Sep
(c)
♣ 73 °C
♦ 159 °C
♥ 199 °C
♠ 241 °C
● 422 °C
♣
♦
♥
♠
●
m/z 44.01 MS signal (a.u.)
100
200
300
400
500
600
Temperature (°C)

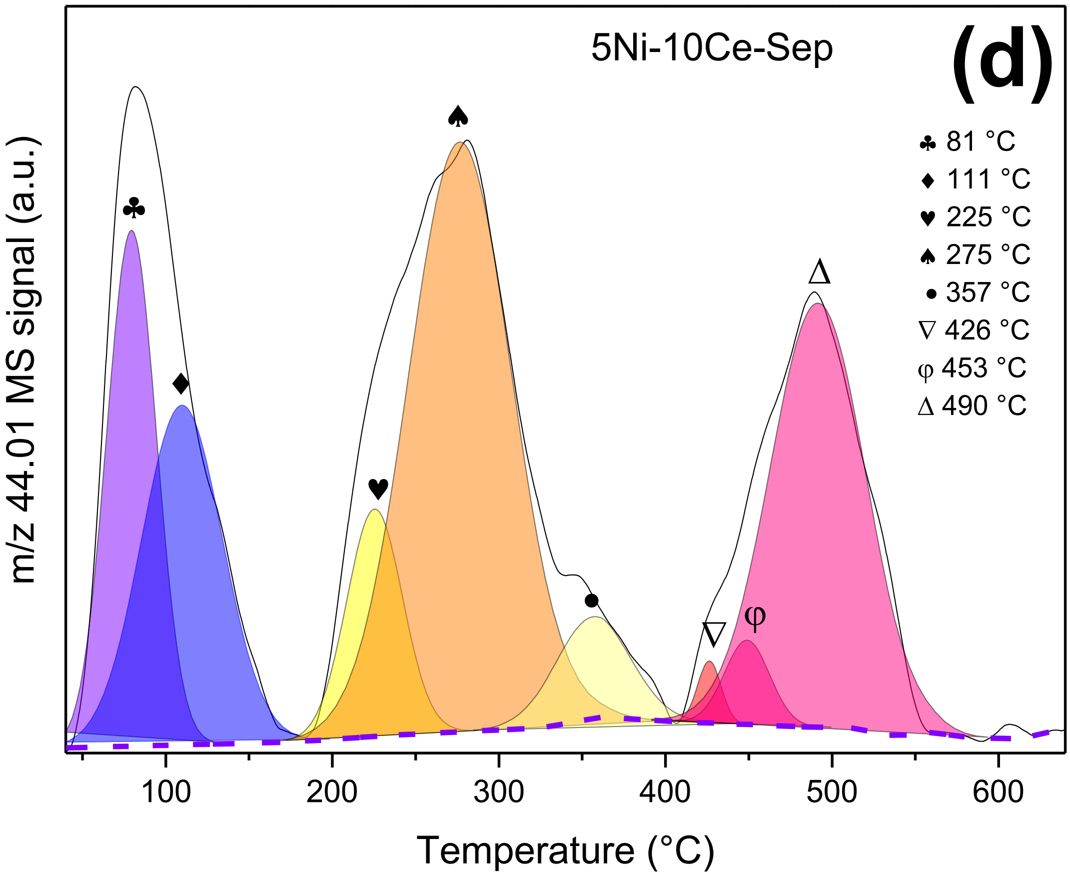
5Ni-10Ce-Sep
(d)
♣ 81 °C
♦ 111 °C
♥ 225 °C
♠ 275 °C
● 357 °C
∇ 426 °C
φ 453 °C
Δ 490 °C
♣
♦
♥
♠
●
∇
φ
Δ
m/z 44.01 MS signal (a.u.)
100
200
300
400
500
600
Temperature (°C)

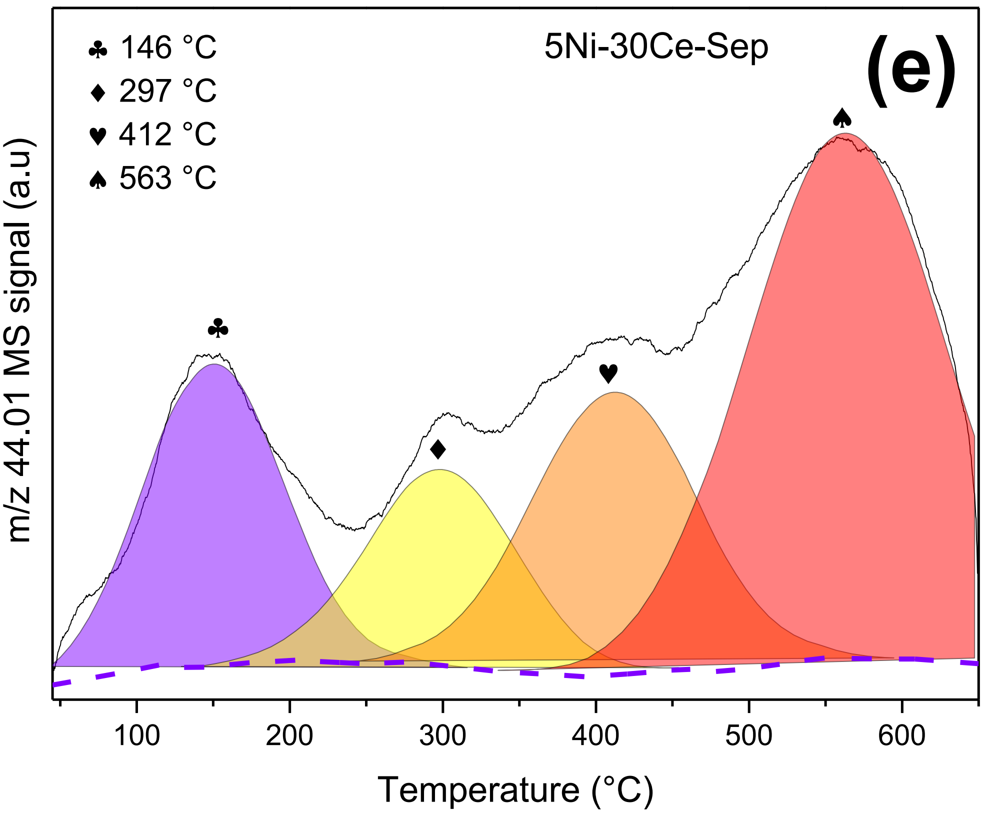

Figure 9.4. Individual deconvolution of CO_2-TPD profiles for (a) calcined sepiolite, Sep_450C; (b) 5Ni-0Ce-Sep; (c) (b) 5Ni-1Ce-Sep; (d) 5Ni-10Ce-Sep; and (e) 5Ni-30Ce-Sep.

Curriculum Vitae

The author

Raul B. Machado da Silva was born in Fortaleza, Brazil. During high school, he represented the Olympic Delegation in the International Chemistry Olympiads in 2010 and 2011, earning two Gold and two Bronze medals. In 2012, he was admitted to the Chemistry undergraduate program at the State University of Campinas (UNICAMP).

In 2015, he was also accepted into the engineering program at the *Grand École Chimie ParisTech* through a binational agreement with the French Eiffel Scholarship. While in Paris, he gained experience as a Research Assistant at *Saint Gobain Recherche*, working on the spectroscopic characterization of vitreous surfaces.

In 2017, he graduated from both courses, obtaining the titles of *Diplôme d'Ingénieur* and Bachelor in Industrial Chemistry, with the highest honors, receiving the Lavoisier Medal, awarded to the class valedictorian.

In 2019, he completed his Master's degree under the supervision of Dr. Italo Mazali at UNICAMP, focusing on novel methods to tune the microporous structure of CeO_2-based catalysts and the potential application of these materials for the PROX-CO reaction.

In 2020, he began his PhD studies in Valencia, Spain, under the supervision of Dr. Antonio Chica Lara at the Instituto de Tecnología Química, with an INPhINIT fellowship from LaCaixa Foundation. His project regarded the development of efficient catalytic technologies for the selective hydrogenation of CO_2 to CH_4. During his doctoral degree, he also obtained the dual Brazilian-Spanish double nationality after fulfilling all the requirements to be a citizen of both countries.

In 2023, he completed a research internship under the supervision of Dr. Emiel Hensen at the Eindhoven University of Technology in the Netherlands, where he gained experience with state-of-the-art *operando* IR spectroscopy analyses for characterizing intermediate species and proposing reaction mechanisms.

The results of his PhD project have been presented at several national and international congresses and published in scientific journals. This thesis summarizes the most relevant results obtained from this PhD project.

1. Education and Academic Formation

Year of title obtention	Title	Institution
2020	MSc Degree in Inorganic Chemistry	State University of Campinas (UNICAMP)
2018	Diplôme d'Ingénieur	Chimie ParisTech – Université Paris Science et Lettres (PSL)
2018	BSc in Industrial Chemistry	State University of Campinas (UNICAMP)
2012	High School Degree	Farias Brito High School

2. Scientific Prizes and Awards

[1] Young Scientist Prize in Catalysis, **2024**, International Association of Catalysis Communities (IACS).

[2] Doctoral INPhINIT Fellowship, **2020**, "la Caixa" Foundation.

[3] Lavoisier Prize for promotion's valedictorian student, **2018**, Regional Council of Chemistry, Brazil (Conselho Regional de Química).

[4] France Eiffel Excellence Scholarship, **2015**, French Ministry for Europe and Foreign Affairs.

[5] Cambridge Chemistry Challenge Award, **2014**, University of Cambridge.

[6] Gold Medal Winner and Top Scorer in 17th Ibero-american Chemistry Olympiad, **2011**, Federal University of Piauí, Brazil (UFPI).

[7] Bronze Medal Winner in 43rd International Chemistry Olympiad, **2011**, Middle East Technical University, Turkey (Orta Doğu Teknik Üniversites).

[8] Gold Medal Winner and Top Scorer in 16th Ibero-american Chemistry Olympiad, **2010**, National Autonomous University of Mexico (UNAM).

[9] Bronze Medal Winner in 42nd International Chemistry Olympiad, **2010**, University of Tokyo, Japan. (東京大学).

3. Scientific Production

3.1 Scientific Journal Publications

1. Machado-Silva, R. B.; Costa-Serra, J. F.; Chica, A.; Enhancement of catalytic activity in CO2 methanation in Ni-based catalysts supported on delaminated ITQ-6 zeolite. *Journal of Catalysis*, **2024**, 436, 115609.
   DOI: **10.1016/j.jcat.2024.115609**

2. Silva, R. B. M.; de Oliveira, C. S.; Teixeira-Neto, É.; Sigoli, F. A.; Mazali, I. O., Improvement of PROX-CO catalytical performance by modulation of the pore structure of CeO2 nanorods decorated with Au nanoparticles. *Microporous and Mesoporous Materials*, **2022**, 330, 111574. *

   DOI: **10.1016/j.micromeso.2021.111574**
3. Machado-Silva, R. B.; Andrés-Olmos, L.; Kosinov, N.; Hensen, E. J. M.; Chica, A.; Exploring mixed-oxide synergy in La and Al oxides as supports in Ni-catalysts for the CO2 methanation reaction. (Under review).
4. Machado-Silva, R. B.; Kosinov, N.; Hensen, E. J. M.; Chica, A.; Operando IR spectroscopy and multi-technique characterization of ceria-nickel-based catalysts supported on sepiolite for the CO2 methanation reaction. (Under review).
5. Machado-Silva, R. B.; Cerdá-Moreno, C.; Chica, A.; Development and multi-technique characterization of sepiolite-nickel-based catalysts for the CO2 methanation reaction (Under review).

*Not related to this doctorate thesis.

3.2 Congress Publications

1. Machado-Silva, R. B; Kosinov, N.; Hensen, E.; Chica, A.; Novel application for sepiolite-based catalysts for biogas upgrade to biomethane via CO2 methanation reaction, 5th Iberoamerican congress on Biorefineries, **October 2024**, Jaén, Spain, Poster Presentation.
2. Machado-Silva, R. B; Kosinov, N.; Hensen, E.; Chica, A.; Time-resolved operando mechanistic studies on nickel-ceria sepiolite-based catalysts for the CO_2 methanation reaction, 29th Ibero-American Catalysis Congress, **September 2024**, Bilbao, Spain, Oral Presentation.
3. Machado-Silva, R. B; Chica, A.; Kosinov, N.; Hensen, E.; Time-resolved operando IR studies on nickel-ceria-sepiolite catalysts for the exploration of the CO_2 methanation reaction mechanism, International Symposium Spectrocat, **July 2024**, Caen, France, Oral Presentation.
4. Machado-Silva, R. B; Chica, A.; Kosinov, N.; Hensen, E.; Operando IR studies on nickel-sepiolite-based catalysts for the CO_2 methanation reaction, 18th International Congress on Catalysis, **July 2024**, Lyon, France, Poster Presentation.
5. Machado-Silva, R. B; Chica, A.; Kosinov, N.; Hensen, E.; Multi-technique and operando studies for sepiolite-based catalysts for the CO_2 methanation reaction, 10th ENMIX Young Scientist Meeting, **March 2024**, online, Oral presentation.
6. Machado-Silva, R. B; Chica, A.; Development and multi-technique characterization of sepiolite-nickel-ceria-based catalysts for the CO_2 methanation reaction aimed at the storage

of green hydrogen, European Hydrogen Energy Conference 2024, **March 2024**, Bilbao, Spain, Oral Presentation.

7. Machado-Silva, R. B; Chica, A.; Kosinov, N.; Hensen, E.; Unravelling the mechanism of CO_2 methanation over ceria-nickel-based catalysts supported on sepiolite using operando IR spectroscopy and multi-technique characterization, Catalysis Hub Meeting, **September 2023**, Oxfordshire, United Kingdom, Poster Presentation.
8. Machado-Silva, R. B; Chica, A.; Effect of Ce content on the catalytic performance of Ni-sepiolite-based catalysts for the methanation of CO_2, Reunión Bienal de la Sociedad Española de Catálisis 2023, **June 2023**, Valencia, Spain, Oral Presentation.
9. Machado-Silva, R. B; Chica, A.; Catalysts supported on ITQ-6 and FER for CO_2 methanation and biogas upgrade, Encuentro de la Red de Biorrefinerías Sostenibles, **November 2022**, Donostia, Spain, Oral Presentation.
10. Machado-Silva, R. B; Chica, A.; Effect of delamination and Al addition on Ferrierite and ITQ-6 zeolites as supports in Ni-based catalysts for catalytic CO_2 methanation, 20th International Zeolite Conference, **July 2022**, Valencia, Spain, Poster Presentation.
11. Machado-Silva, R. B; Chica, A.; Ni supported on Ferrierite and ITQ-6 zeolites for catalytic methanation of CO_2 - Effect of delamination on the catalytic performance, European Hydrogen Energy Conference, **May 2022**, Madrid, Spain, Oral Presentation.
12. Machado-Silva, R. B; Chica, A.; Novel Ni-based catalysts supported on delaminated zeolites to convert green H_2 and CO_2 into synthetic methane, Reunión Bienal de la Sociedad Española de Catálisis 2021, **October 2021**, Valencia, Spain, Poster Presentation.
13. Machado-Silva, R. B; Chica, A.; Ni supported on Ferrierite and ITQ-6 zeolites for catalytic methanation of CO_2. Effect of delamination on the catalytic performance, 12th International Conference on Hydrogen Production, **September 2021**, online, Oral Presentation.
14. Machado-Silva, R. B; Chica, A.; Ni-based catalysts supported on Ferrierite and ITQ-6 zeolites for CO_2 methanation reaction: Effect of delamination on the performance of the reaction, 21º Congresso Brasileiro de Catálise, **July 2021**, online, Oral Presentation.
15. Machado-Silva, R. B; Cerdá-Moreno, C.; Chica, A.; Novel Ni-Based Catalysts on Sepiolite and Todorokite for the Selective Methanation of CO2, 3rd Winter Meeting, **December 2020**, Valencia, Spain, Oral presentation.
16. Machado-Silva, R. B; Cerdá-Moreno, C.; Chica, A.; Novel Ni-Based Catalysts on Sepiolite and Todorokite for the Selective Methanation of CO2, 7th ENMIX Young Researchers Meeting, **October 2020**, online, Oral Presentation.
17. Cerdá-Moreno, C.; Machado-Silva, R. B; Chica, A.; Novel Ni-Based Catalysts Supported on Sepiolite and Todorokite for the Selective Methanation of CO2, IV Encuentro de Jóvenes Investigadores de la SECAT, **September 2020**, Bilbao, Spain, Poster Presentation.

18. Silva, R. B. M.; de Oliveira, C. S.; Neto, E. T.; Sigoli, F. A.; Mazali, I. O.; Influence of the structural design of CeO2 porous nanorods decorated with gold nanoparticles upon the optimization of water gas shift reaction (WGSR), 42ª Reunião Anual da Sociedade Brasileira de Química, **May 2019**, Joinville, Brazil, Poster presentation. *
19. Silva, R. B. M.; de Oliveira, C. S.; Neto, E. T.; Rangel, M. C. Sigoli, F. A.; Mazali, I. O.; Novel nanostructured systems composed of ceria porous nanorods decorated with metallic nanoparticles with application on the catalytic optimization of the water-gas shift reaction (WGSR), 47th IUPAC World Chemistry Congress, **July 2019**, Paris, France, Oral presentation.*

*Not related to this doctorate thesis.

Appendix

List of Figures

Figure 3.2. Simplified representation on the synthetical route to obtain the FER or the ITQ-6, depending on whether the swelling step with cetyltrimethylammonium bromide (CTAB) is followed before the calcination step.

Figure 3.3. Representation of the different interference patterns that take place in X-ray diffraction: (a) destructive interference, when the leaving photons are out of phase, or (b) constructive interference when the leaving photons are in phase.

Figure 3.4. Classification of the six types of adsorption that might take place over a material according to the IUPAC guidelines.

Figure 3.5. Simplified scheme depicting the experimental setup for the analysis with the ICP-OES technique.

Figure 3.6. Schematic diagram of the experimental setup used for the CO_2-TPD-MS analyses carried out in this study.

Figure 3.7. Schematic representation of a generic mid-IR transmission spectrum showing typical absorption lines associated with vibrational modes of different chemical bonds.

Figure 3.8. Simplified depiction of the effects that take place by the interaction of an electron beam with matter.

Figure 3.9. Scheme of the catalytical unit used to perform the tests.

Figure 3.10. Schematic representation of the fixed-bed tubular reactor dimensions used for the catalytic tests.

Figure 3.11. Chromatograms obtained for the bypass analyses as detected by the (a) TCD and (b) FID. In the upper figure, a zoom-in of the highlighted region is depicted to show with more clarity the peak separation.

Figure 3.12. Chromatograms obtained for a typical analysis when a CO_2 hydrogenation catalytic test is carried out as detected by the (a) TCD and (b) FID. In the upper figure, a zoom-in of the highlighted region is depicted to show with more clarity the peak separation.

Figure 3.13. Nicolet 6700 FT-IR spectrometer used for the operando FT-IR measurements carried out in this work. The custom-made cell is located inside the spectrometer where the IR beam could orthogonally hit the catalyst's surface.

Figure 3.14. Photograph of the custom-made IR cell used in this study and schematic representation of the process used to obtain the operando FT-IR spectra. 15- µm-thick wafers were prepared from the solid samples and positioned orthogonally to the beam pathway.

Figure 4.1. Representation of the structure of the ferrierite zeolite along the [001] and [010] directions. The opening of the 8-MR and the 10-MR channels are highlighted.

Figure 4.2. Artistic representation of delaminated ITQ-6, revealing the “molecular cups” formed after delamination of the ferrierite structure.

Figure 4.3. X-ray diffraction patterns for FER, ITQ-6, PREFER, and swollen PREFER with Si/Al molar ratios of (a) ∞ and (b) 30.

Figure 4.4. X-ray diffractograms of 5 wt. % Ni-based catalysts supported on FER and ITQ-6 zeolites between the range 2θ =5°-70° with Si/Al ratios of (a) infinite and (b) 30. The diffractograms of the bare supports are also depicted for comparison.

Figure 4.5. X-ray diffractograms of (a) reduced 5% wt. Ni-based catalysts supported on FER and ITQ-6 zeolites, and (b) higher Ni loading catalysts supported on ITQ-6 (30).

Figure 4.6. HAADF-STEM dark field images of the reduced catalysts: (a) 5Ni/FER (∞), (b) 5Ni/ITQ-6 (∞), (c) 5Ni/FER (30), and (d) 5Ni/ITQ-6 (30).

Figure 4.7. TEM images of the reduced 5% wt. Ni-based catalysts supported on aluminum-free supports: (a) 5Ni/FER (Si/Al = ∞) and (b) 5Ni/ITQ-6 (Si/Al = ∞).

Figure 4.8. TEM images of the reduced 5% wt. Ni-based catalysts supported of the aluminum-containing catalysts: (a) 5Ni/FER (Si/Al = 30), and (b) 5Ni/ITQ-6 (Si/Al = 30).

Figure 4.9. (a), (b) HAADF-STEM dark field and (c) TEM bright-field images for the 5Ni/ITQ-6 (30).

Figure 4.10. (a) HAADF-STEM dark field and (b), (c) TEM bright-field images for the 5Ni/ITQ-6 (∞).

Figure 4.11. (a) HAADF-STEM dark field and (b)TEM bright-field images for the 5Ni/FER (30).

Figure 4.12. (a) HAADF-STEM dark field and (b) TEM bright-field images for the 5Ni/FER (∞).

Figure 4.13. Ni^0 particle size distribution, normal fit, and average size for the 5 wt. % Ni-based catalysts: (a) 5Ni/FER (∞)_R, (b) 5Ni/ITQ-6 (∞)_R, (c) 5Ni/FER (30)_R and (d) 5Ni/ITQ-6 (30)_R.

Figure 4.14. SEM images for the reduced version of (a) 5Ni/FER (∞), (b) 5Ni/ITQ-6 (∞), (c) 5Ni/FER (30), and (d) 5Ni/ITQ-6 (30).

Figure 4.15. Nitrogen adsorption-desorption isotherms of the 5 wt. % Ni-based catalysts supported on the (a) Si/Al = ∞ zeolites and the (a) Si/Al = 30 zeolites.

Figure 4.16. H_2-TPR profile of zeolite-based catalysts under H_2 flow over the range of temperatures between 200 °C and 700 °C.

Figure 4.17. H_2-TPR profile of higher Ni loading catalyst supported on ITQ-6 (Si/Al = 30) over the range of temperatures between 200 °C and 700 °C.).

Figure 4.18. Schematic representation of the different types of surface hydroxyl groups found in an Al-containing zeolite. The presence of aluminum is associated with an increase of -OH groups on the zeolite surface due to the formation of bridging hydroxyls, Si-(OH)-Al, and terminal hydroxyls, Al-OH.

Figure 4.19. FTIR spectra for the Ni-based catalysts and respective supports for the **(a)** Si/Al = 30 and the **(b)** Si/Al = ∞ materials. The spectra exhibit hydroxyl vibrations at different zeolitic positions: terminal Si-OH and Al-OH, centered around 3742 cm^{-1} and 3640 cm^{-1}, respectively, and bridging Si-(OH)-Al, centered around 3598 cm^{-1}.

Figure 4.20. (a) CO_2 conversion and (b) selectivity towards CH_4 dependence on temperature for the catalysts based on FER and ITQ-6. Reaction conditions: 250 °C - 450 °C, Pressure: 1 atm, WHSV = 38,000 mL $(g_{cat}\ h)^{-1}$, $H_2/CO_2 = 4$.

Figure 4.21. CO conversion dependence on temperature for the catalysts based on FER and ITQ-6. Reaction conditions: 250 °C - 450 °C, Pressure: 1 atm, WHSV = 38,000 mL $(g_{cat}\ h)^{-1}$, $H_2/CO = 3$.

Figure 4.22. Arrhenius plot for (a) CO_2 methanation and (b) CO methanation. The apparent activation energy for the CO_2 methanation (E^*_{a,CO_2}) and CO methanation ($E^*_{a,CO}$) are obtained from the slope obtained from the data series.

Figure 4.23. Schematic representation of the possible chemical reactions for the CO_2 methanation reaction, either by the associative or dissociative mechanistic pathways.

Figure 4.24. Apparent activation energy for the CO_2 methanation reaction, E^*_{a,CO_2} (■) and the CO methanation reaction, $E^*_{a,CO}$, (●) dependence of the average Ni^0 particle size.

Figure 4.25. Effect of nickel loading on CO_2 conversion (dashed lines) and selectivity towards CH_4 (solid lines) on different temperatures for the catalysts based on ITQ-6 (30). Pressure: 1 atm, $H_2/CO_2 = 4:1$, WHSV = 6,000 mL $(g_{cat}\ h)^{-1}$

Figure 5.1. (a) CO_2-TPD diagram for a series of Ni-Al_2O_3 catalysts and corresponding coordination modes of surface carbonate species. Image adapted from Ewald [29]. (b) Intermediate formate species formed in the Ni-La_2O_3 and Ni-$La_2O_2CO_3$ catalysts during CO_2 hydrogenation.

Figure 5.2. Structure of lanthanum aluminate, $LaAlO_3$, highlighting the 6-fold coordination around Al^{III} ions and 12-fold coordination around La^{III} ions.

Figure 5.3. XRD diffractograms of the different supports and equivalent 5% wt. Ni-based catalysts.

Figure 5.4. Magnification of specific ranges to highlight the presence of the peaks (♦) associated with the presence of NiO at 2θ = 37.40° and 43.46°.

Figure 5.5. TEM images of: (a) $LaAlO_3$; (b) 5Ni/$LaAlO_3$_R; (c) 5Ni/$LaAlO_3$-ex_R; (d) 15Ni/$LaAlO_3$_R.

Figure 5.6.TEM/SEM images of the reduced catalysts with different Ni loading: 5Ni/$LaAlO_3$_R (a-TEM e-SEM), 10Ni/$LaAlO_3$_R (b-TEM e-SEM), and 15Ni/$LaAlO_3$_R (c-TEM f-SEM).

Figure 5.7. EDS-TEM results for the 15Ni/$LaAlO_3$_R and the response obtained for different elements: Al (cerulean); La (green), and Ni (purple).

Figure 5.8. (a) XRD diffractograms of the calcined $LaAlO_3$-based catalysts prepared by different methods and metallic content. (b) Magnification of the region between 2θ = 30° and 70° to highlight diffraction peaks related to the presence of the NiO phase.

Figure 5.9. (a) Comparison of the XRD diffractograms of the reduced version of the 5% wt. catalysts with the calcined ones for the different supports and zoom-in of the region between 2θ = 30° and 65° for the (b) $5Ni/Al_2O_3$_R and (c) $5Ni/La_2O_3$_R catalysts.

Figure 5.10. (a) XRD diffractograms of the reduced $LaAlO_3$-based catalysts. (b) Magnification of the region between 2θ = 30° and 70° to highlight the presence of diffraction peaks related to the presence of the Ni^0 phase.

Figure 5.11. Size distribution for Ni^0 particles obtained, normal fit and average size for (a) $5Ni/La_2O_3$_R; (b) $5Ni/Al_2O_3$_R, (c) $5NiLaAlO_3$-ex_R, (d) $5Ni/LaAlO_3$_R; (e) $10Ni/LaAlO_3$_R, and (f) $15Ni/LaAlO_3$_R.

Figure 5.12. H_2-TPR profiles for the catalysts (a) on different supports and (b) with different Ni contents.

Figure 5.13. CO_2-TPD-MS profiles for the (a) different supports and (b) different Ni content used for the preparation of catalysts.

Figure 5.14. (a) CO_2 conversion and (b) CH_4 selectivity values. Conditions of experiment: 1 atm, 250 °C-450 °C, WHSV = 42,000 mL $(g_{cat}\ h)^{-1}$, H_2/CO_2 molar ratio = 4:1.

Figure 5.15. Arrhenius plot for the series of Ni-based catalysts prepared over different supports for the 260-300 °C. Linear regression on each set of data points was used to calculate the apparent activation energy, E_a.

Figure 5.16. (a) Time-resolved transmission FT-IR measurements for the $15Ni/LaAlO_3$ catalyst during CO_2 exposition. (b) Zoom-in of the region between 1750 and 2075 cm^{-1} showing the different Ni^0-CO bonding modes and (c) example of deconvolution profile for the 10 min sample for the different Ni^0-CO bonding modes.

Figure 5.17. (a) Time-resolved in-situ FT-IR measurements for the $15Ni/LaAlO_3$ catalyst during H_2 exposition after the CO_2 exposition step and (b) evolution of normalized intensity for selected peaks.

Figure 5.18. Dependence of catalytic activity on the ratio between moderate basic sites concentration, B_{CO_2}, and available metallic surface area, S_{Ni}. The red curve is added for better visualization of the data points.

Figure 5.19. Correlation between Ni^0 particle size and CH_4 formation turnover frequency number (TOF) for the different catalysts supported on $LaAlO_3$.

Figure 6.1. Schematic representation of the sepiolite structure, consisting of blocks formed by a Mg-containing octahedral layer, sandwiched between Si-containing tetrahedral layers. These blocks create channels or tunnels that are occupied by zeolitic water.

Figure 6.2. Hierarchical porous structure of sepiolite, in which macropores, mesopores and micropores can be detected.

Figure 6.3. XRD patterns of cerium-nickel-sepiolite catalysts, the support and the reference patterns of different phases that make up the catalyst.

Figure 6.4. XRD patterns of the higher Ni loading cerium-nickel-sepiolite catalysts, the support and the reference patters of different phases that make up the catalyst.

Figure 6.5. Structure of sepiolite and sepiolite dihydrate, the phase of the material that is stable at temperatures above 350 °C, due to the loss of the zeolitic H_2O molecules inside the channels. Gray molecules represent H_2O molecules.

Figure 6.6. TEM-SEM images of the catalysts after the reduction step: 5Ni-0Ce-Sep_R (a-TEM, b-SEM) and 5Ni-1Ce-Sep (c-TEM, d-SEM).

Figure 6.7. TEM-SEM images of the catalysts after the reduction step: 5Ni-10Ce-Sep_R (a-TEM, b-SEM) and 5Ni-30Ce-Sep (c-TEM, d-SEM).

Figure 6.8. (a) bright-field TEM image of the 5Ni-10Ce-Sep_R catalyst after the reduction step and (b) dark field STEM of the highlighted area. EDS mapping of different composing elements was also obtained.

Figure 6.9. Higher magnification TEM image of the catalysts after the reduction step: (a) 5Ni-0Ce-Sep_R; (b) 5Ni-1Ce-Sep_R; (c) 5Ni-10Ce-Sep_R; 5Ni-30Ce-Sep_R.

Figure 6.10. Structure of a partially truncated octahedron, observed for the Ni^0 nanoparticles, highlighting some geometrical elements of interest. Image adapted from Rana et al. [49].

Figure 6.11. N_2 adsorption-desoprtion isotherms for the nickel-ceria-sepiolite calcined catalysts.

Figure 6.12. H_2-TPR profiles between 50 °C and 900 °C for the series of nickel-ceria catalysts supported over sepiolite.

Figure 6.13. CO_2-TPD profiles for (a) calcined sepiolite, Sep_450C; (b) 5Ni-0Ce-Sep; (c) (b) 5Ni-1Ce-Sep; (d) 5Ni-10Ce-Sep; and (e) 5Ni-30Ce-Sep.

Figure 6.14. CO_2 conversion (filled symbols) and CH_4 selectivity (hollow symbols) for the nickel-cerium-sepiolite catalysts. Equilibrium data was calculated using the DWSIM simulator. Reaction conditions: 250 °C - 450 °C, 1 atm, WHSV = 38,000 mL $(g_{CAT} \cdot h)^{-1}$. $H_2/CO_2 = 4$.

Figure 6.15. Transmission infrared results over the different calcined catalysts before introducing any reactants into the transmission IR analysis chamber.

Figure 6.16. (a) Transmission FT-IR results for the transient experiments after alternate expositions to CO_2 and H_2 at 250 °C for 5Ni-0Ce-Sep. (b) Magnification of the carbonyl region between 2100 and 1800 cm^{-1}, showing the evolution of the Ni^0-CO bands during the transient experiments.

Figure 6.17. Transmission FT-IR results for the transient experiments after alternate expositions to CO_2 and H_2 at 250 °C at different times for: (a) 5Ni-1Ce-Sep, (b) 5Ni-10Ce-Sep and (d) 5Ni-30Ce-Sep. (c) Zoom-in of the 1200-1600 cm^{-1} region for the 5Ni-10Ce-Sep catalyst. Test conditions: T = 250 °C, 1 atm.

Figure 6.18. Time-resolved normalized intensity of infrared bands centered at: (a) 2848 cm^{-1}, formate, (b) 2031cm^{-1}, linear Ni^0-CO; (c) 1909-1855 cm^{-1}, multibonded Ni^0-CO, for t5Ni-10Ce-sep catalyst. Conditions: 250 °C, 1 atm, alternate expositions to CO_2 followed by H_2.

Figure 6.19. Depiction of the proposed catalytic cycle taking place in the 5Ni-10Ce-Sep catalyst for the H-assisted associative mechanism for the CO_2 methanation reaction via formate formation.

Figure 6.20. Dependence of TOF on Ni^0 particle size for 5% wt. Ni catalysts with different Ce loadings. The respective values of concentration of moderate basic site per unit of active metallic surface area, B_{CO_2}/ S_{Ni} are also indicated.

Figure 6.21. Effect of Ni loading on (a) CO_2 conversion and (b) CH_4 selectivity on different temperatures for the 10% Ce sepiolite catalysts. Pressure: 1 atm, $H_2/CO_2 = 4:1$, WHSV = 38,000 mL $(g_{cat}\cdot h)^{-1}$.

Figure 7.1. CO_2 conversion values dependence on the WHSV and correspondent time of contact (τ) between the reactants and the active phase is specified for (a) 15Ni/ITQ-6 (30), (b) 15Ni/$LaAlO_3$ and (c) 15Ni-10Ce-Sep. Reaction conditions: 320 °C, 1 atm, $H_2:CO_2 = 4$.

Figure 7.2. Stability test results regarding CO_2 conversion (●) and CH_4 selectivity (♦) values for the 15Ni/ITQ-6 (30) catalyst with emulated sweetened synthetic biogas sample. Reaction conditions: 1 atm, 320 °C, WHSV = 6,000 $(g_{cat} h)^{-1}$, CH_4: CO_2: H_2 = 3:2:8.

Figure 7.3. Comparison of the X-ray diffractograms of the 15Ni/ITQ-6 (30) catalyst after the reduction step and the stability test with a synthetic biogas sample.

Figure 7.4. Comparison of the TEM of the 15Ni/ITQ-6 (30) catalyst (a) after the reduction step and (b) after the stability test with a synthetic biogas sample.

Figure 7.5. Stability test results regarding CO_2 conversion (●) and CH_4 selectivity (♦) for the 15Ni/$LaAlO_3$ catalyst with a sweetened synthetic biogas sample. Reaction conditions: 320 °C, 1 atm, WHSV = 10,000 mL $(g_{cat}\cdot h)^{-1}$. Reaction conditions: 1 atm, 320 °C, WHSV = 10,000 mL $(g_{cat} h)^{-1}$, CH_4: CO_2: H_2 = 3:2:8.

Figure 7.6. Comparison of the X-ray diffractograms of the 15Ni/$LaAlO_3$ catalyst after the reduction step and the stability test with a synthetic biogas sample.

Figure 7.7. Comparison of the TEM of the 15Ni/$LaAlO_3$ catalyst (a) after the reduction step and (b) after the stability test with a synthetic biogas sample.

Figure 7.8. Stability test results regarding CO_2 conversion (●) and CH_4 selectivity (♦) for the 15Ni-10Ce-Sep catalyst with a sweetened synthetic biogas sample. Reaction conditions: 1 atm, 320 °C, WHSV = 20,000 mL $(g_{cat} h)^{-1}$, CH_4: CO_2: H_2 = 3:2:8

List of Tables

Table 5.5. Catalytic data and selected properties: yield to CH_4 at 250 °C ($Y_{250\,°C}$), turnover frequency at 250 °C ($TOF_{250\,°C}$), activation energy towards CH_4, E_{a,CH_4}, intermediate basic sites concentration, B_{CO_2}, and average Ni^0 crystallite size, D_{Ni}.

Table 5.6. Vibration modes for different species in the $15Ni/LaAlO_3$ catalyst and corresponding wavenumber.

Table 6.1. Denomination is employed in this chapter for the sepiolite-based catalysts. The number preceding the elements Ni and Ce refers to the nominal loading values established during their preparation.

Table 6.2. Elemental weight percentage for nickel and cerium, and Mg/Si atomic ratio for nickel-ceria-sepiolite materials.

Table 6.3. Textural properties of ceria-nickel sepiolite catalysts: BET surface area, S_{BET}, t-plot micropore area, S_{micro}, t-plot external surface area, S_{ext}, and t-plot micropore volume, V_{micro}.

Table 6.4. H_2-chemisorption data for nickel-ceria-based catalysts: metallic dispersion, active metal surface area, S_{Ni}, Ni^0 average particle size, D_{Ni}, and molar H_2 monolayer uptake.

Table 6.5. CO_2-TPD deconvolution for the weak (50 – 200 °C), moderate (200 – 400 °C) and strong (400 – 600 °C) basic sites and total basicity for the sepiolite-based catalysts.

Table 6.6. Assignation of the corresponding wavenumber to the vibration modes observed in the nickel-sepiolite-ceria catalysts.

Table 6.7. Catalytic data regarding 5% wt. Ni catalysts and selected properties: TOF at 250 °C, $TOF_{CH_4,250\,°C}$, moderate basicity concentration, B_{CO_2}, average Ni^0 crystallite size, D_{Ni}, and moderate basicity per unit of active metallic surface area, $B_{CO_2}/\mathbf{S_{Ni}}$.

Table 7.1. Selected catalysts with optimum results from previous results used for the WHSV and stability tests with synthetic sweetened biogas.

Table 7.2. Textural properties of selected catalysts used for the stability tests with synthetic sweetened biogas samples: Ni^0 crystallite size, D_{Ni}, sintering extent, carbon elemental content, C (wt. %), and BET surface area, S_{BET}.

Table 7.3. Results for selected catalysts at the end of the stability tests: used weight hourly speed velocity (WHSV), yield to CH_4 at the end of the test, Y_{CH_4}, and CH_4 production rate, F_{CH_4}.